Africa's last hunter-gatherers are under siege *p. 709*

The basics of turning CO_2 into ethylene *pp. 709 & 783*

A discredited biotech startup's fraud, revealed *p. 720*

Science

$15
18 MAY 2018
sciencemag.org

AAAS

SPECIAL ISSUE

THE RISE OF RESISTANCE

CONTENTS

709 & 758
A cellular view of kidney function

18 MAY 2018 • VOLUME 360 • ISSUE 6390

SPECIAL SECTION
Rise of resistance

ON THE COVER

Herbicides (dots) are designed to kill weeds, but some plants (such as the one shown at center) have become resistant to these substances. Whereas public awareness of antibiotic resistance is increasing, the alarming spread of resistance to chemicals used to protect crops against pests, weeds, and pathogens is less well appreciated. For more on the proliferation of biocide resistance, see page 726. *Illustration: Álvaro Valiño*

NEWS

INSIGHTS

CREDITS: (TOP TO BOTTOM) A. KITTERMAN/*SCIENCE*; ISTOCK.COM/FOTOKOSTIC; MATTHIEU PALEY

Published by AAAS

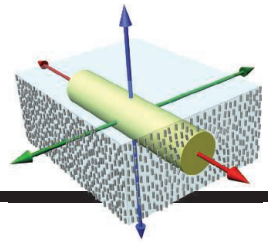

712 & 768
Biaxial phases

722
Einstein's travel diaries

RESEARCH

SCIENCE (ISSN 0036-8075) is published weekly on Friday, except last week in December, by the American Association for the Advancement of Science, 1200 New York Avenue, NW, Washington, DC 20005. Periodicals mail postage (publication No. 484460) paid at Washington, DC, and additional mailing offices. The title SCIENCE is a registered trademark of the AAAS. Domestic individual membership, including subscription (12 months): $165 ($74 allocated to subscription). Domestic institutional subscription (51 issues): $1808; Foreign postage extra: Mexico, Caribbean (surface mail) $55; other countries (air assist delivery): $89. First class, airmail, student, and emeritus rates on request. Canadian rates with GST available upon request, GST #125488122. Publications Mail Agreement Number 1069624. **Printed in the U.S.A.**
Change of address: Allow 4 weeks, giving old and new addresses and 8-digit account number. **Postmaster:** Send change of address to AAAS, P.O. Box 96178, Washington, DC 20090–6178. **Single-copy sales:** $15 each plus shipping and handling; bulk rate on request. *Science* is indexed in the *Reader's Guide to Periodical Literature* and in several specialized indexes.

Science
AAAS
1200 New York Avenue, NW, Washington, DC 20005
Clarendon House, Clarendon Road, Cambridge, UK CB2 8FH

SUBSCRIPTION SERVICES For change of address, missing issues, new orders and renewals, and payment questions: 866-434-AAAS (2227) or 202-326-6417, FAX 202-842-1065. Mailing addresses: AAAS, P.O. Box 96178, Washington, DC 20090-6178 or AAAS Member Services, 1200 New York Avenue, NW, Washington, DC 20005

INSTITUTIONAL SITE LICENSES 202-326-6730 **REPRINTS:** Author Inquiries 800-635-7181 **COMMERCIAL INQUIRIES** 803-359-4578 **PERMISSIONS** 202-326-6765, permissions@aaas.org **AAAS Member Central Support** 866-434-2227 www.aaas.org/membercentral.

INFORMATION FOR AUTHORS See www.sciencemag.org/authors/science-information-authors

Published by AAAS

EDITORIAL

NextGen postdocs

Postdoctoral scholars have been in the public eye of late. Less than a week after the National Postdoctoral Association (NPA) annual meeting last month, the U.S. National Academies of Sciences, Engineering, and Medicine (NASEM) released its report, "The Next Generation of Biomedical and Behavioral Sciences Researchers: Breaking Through." The NPA's meeting agenda covered major challenges for improving the postdoc experience. The NASEM report introduced bold recommendations that address challenges inherent in the postdoc experience. There is obviously more to be done to ensure the transition of postdocs to successful careers.

The NASEM report examines U.S. programs and policies that could support the next generation of researchers in the biomedical and behavioral sciences. It accurately identifies the nexus of career development, effective mentoring, and adequate funding as key components to improving postdoctoral training. Notably, several NASEM recommendations discuss career development training, emphasizing how essential it is to ensure that postdocs receive training beyond technical skills—what the NPA calls "core competencies." The good news is that over 200 U.S. academic institutions have dedicated staff for this purpose. And like the NASEM report, the NPA supports increased collection of outcomes data to determine the impact of career exploration, coaching, and professional development programs.

To support the NASEM recommendation for a mechanism to facilitate career counseling, the NPA encourages partnerships among federal funding agencies, private foundations, institutions, and professional societies. Successful examples include diverse experiential learning opportunities offered though the U.S. National Institutes of Health (NIH) BEST Award pilot programs and postdoctoral scholarships funded by professional societies. However, the 2017 NPA Institutional Policy Report showed wide variances in personnel, programmatic funding, and training offered across 102 institutions, which correlate with NIH funding and the number of postdocs at a given institution. Thus, the NPA continues to advocate for funding to provide career exploration services, in addition to professional development training, to ensure that postdocs are prepared for their chosen career track.

What about funding? The NASEM report and the NPA support more fellowships for early career researchers. This potentially requires an additional $1.1 billion dollars in NIH funding for these awards. Albeit at a lower capacity, a phased shift of funding toward early career researchers, who will sustain the research enterprise as senior researchers retire, could help in the meantime.

The NASEM report's recommendation that the NIH phase in a cap (3 years) on salary support for postdocs funded by NIH research project grants (RPGs) is controversial. Two major assumptions regarding that time frame are made: All postdocs have access to sufficient resources to facilitate career exploration and professional development, and all postdocs have access to sufficient fellowship funding to support an academic career track. This recommendation poses a major challenge because pursuing a tenure track faculty appointment often requires high-impact publications, early career funding, and sufficient preliminary data for immediate RPG applications, which are historically difficult to achieve within 3 years. The NPA advocates adopting a 5-year term limit for an individual's postdoctoral training support; currently, 54% of NPA member institutions adhere to this policy.

Recommendations from the NIH's Advisory Committee to the Director Working Group are imminent, providing another chance to contemplate the future of postdocs in science. Let's maximize these opportunities for progress.

–Tracy J. Costello

"There is obviously more to be done to ensure the transition of postdocs to successful careers."

Tracy J. Costello is chair of the Board of Directors of the National Postdoctoral Association and director of Postdoctoral Affairs at the H. Lee Moffitt Cancer Center & Research Institute in Tampa, FL, USA. tracy.costello@moffitt.org

PHOTOS: (INSET) IKON IMAGES/ALAMY STOCK PHOTO; (TOP RIGHT) NICHOLAS J. GOULD

10.1126/science.aau1303

> “We can regrow your Neanderthal brain.”
>
> **Gray Camp**, a cell biologist at the Max Planck Institute for Evolutionary Anthropology in Leipzig, Germany, in *The Guardian*. Camp is studying how Neandertal genes that persist in modern humans might affect brain development.

IN BRIEF

Edited by **Jeffrey Brainard**

PUBLIC HEALTH

Disputed HPV vaccine paper retracted

These women and others in Japan called a vaccine dangerous, although evidence is lacking.

Scientific Reports last week retracted a controversial paper that claimed to link a human papillomavirus (HPV) vaccine to neurological damage in mice. Critics had assailed the paper as “pseudoscience” that could have “devastating” health consequences in Japan by undermining public confidence in a childhood vaccine that can prevent cervical cancer. Public health officials in Japan and other countries worried the study seemed to provide scientific support for anecdotal reports of alleged HPV vaccine side effects, including headaches and fatigue. Japan’s national government distributed the vaccine for free starting in April 2013 but then stopped recommending it in June of that year, in reaction to reports of purported side effects and criticism from antivaccine campaigners. Although the vaccine is still provided for free, inoculations among girls plunged to near zero and have remained there. The retraction notice says that the paper, published online on 11 November 2016, “is not an appropriate approach to determine neurological damage from HPV vaccine alone.” In the study, mice were given a large dose of the HPV vaccine along with a pertussis toxin that makes the blood-brain barrier leaky. The retraction notice notes that the paper’s authors, led by Toshihiro Nakajima of Tokyo Medical University, “do not agree with the retraction.”

Europa’s plumes gain support

PLANETARY SCIENCE | NASA’s Galileo spacecraft may be dead, but it still has stories to tell. Fifteen years after the probe burned up in Jupiter’s atmosphere, a new analysis of magnetic and plasma data from the mission has bolstered evidence that Europa, the planet’s ice-bound moon, is venting water into space, according to a study published this week in *Nature Astronomy*. This phenomenon could help researchers hoping to discover whether Europa supports life or once did. Scientists believe Europa is home to a vast saltwater ocean trapped beneath a thick crust of ice, but sending a robot to land and drill through the ice for sampling is impractical. However, sensors aboard a robot probe named Europa Clipper, which NASA is planning to send to the moon within the next decade, could analyze the water plumes for clues to life. The new finding is based on data Galileo collected in 1997 during its closest pass of Europa. It adds to evidence collected in the past decade by the Hubble Space Telescope, which recorded faint clues that Europa ejects water in a region close to the one observed by Galileo.

FDA targets stem cell treatments

BIOTECHNOLOGY | Intensifying a crackdown on unapproved stem cell treatments, the U.S. Food and Drug Administration (FDA) last week asked a federal court to issue injunctions preventing two clinics from marketing their cellular products. The first, U.S. Stem Cell Clinic LLC, was previously warned by the agency that its therapy—cells obtained from a patient’s own fat intended to treat conditions including Parkinson’s disease, heart disease, and lupus—was a drug that required FDA review. Three patients went blind after getting eye injections at the company’s Sunrise, Florida, facility to treat macular degeneration. The second complaint targets the California Stem Cell Treatment Center, which has locations in Rancho Mirage and Beverly Hills, and the Cell Surgical Network, of which the treatment center is a member, for unauthorized treatments for conditions including cancer, arthritis, diabetes, and

PHOTO: THE YOMIURI SHIMBUN/AP IMAGES

The Hawaiian volcano's lava lake could trigger an explosion hurling large boulders.

VOLCANOLOGY

Kilauea runs risk of a steam-driven explosion

The steam watch is on at Hawaii's Kilauea volcano, which has spewed lava almost continuously since 1983. But this month, more than a dozen new fissures opened, causing a lava lake at its summit to plummet and raising the risk of a rare large explosion, scientists at the U.S. Geological Survey's Hawaiian Volcano Observatory on Uwekahuna Bluff warned last week. Kilauea's thin, runny lava tends not to trap the gases that lead to explosions. But as the lava lake drops, rocks falling from the sides of the volcano's throat can block the hole like a cork. When the lava drops below the groundwater line, steam, rather than dissolving into the lava, can build up under the rock plug like a pressure cooker until an explosion is triggered. Such an eruption, which last occurred in 1924, could hurl refrigerator-size boulders into the air.

stroke. In public responses to the suits, both the U.S. Stem Cell Clinic and the Cell Surgical Network argued that a person's own cells should not be regulated as a drug.

DNA banks reveal many cousins

POPULATION GENETICS | The arrest of the alleged Golden State Killer last month dramatically illustrated how the rapid expansion of DNA ancestry databases has potentially provided police with clues to investigate crimes. Police submitted a crime-scene DNA sample to a relatively small commercial database, GEDmatch, and identified about two dozen of the alleged killer's relatives, which allowed them to construct family trees and home in on the suspect. A larger ancestry database, one containing DNA data from 10 million people, could yield more than 350 fourth cousins and nearly 200 third cousins, population geneticists Doc Edge and Graham Coop at the University of California, Davis, estimate in a post on their lab blog. Searching databases for more distant relatives might produce diminishing returns for police because they would have to build and investigate even larger family trees, Coop and Edge write. The two largest existing DNA registries, AncestryDNA and 23andMe, are private, which means police cannot use them to match a suspect's DNA without a court order.

Number of people in DNA registries

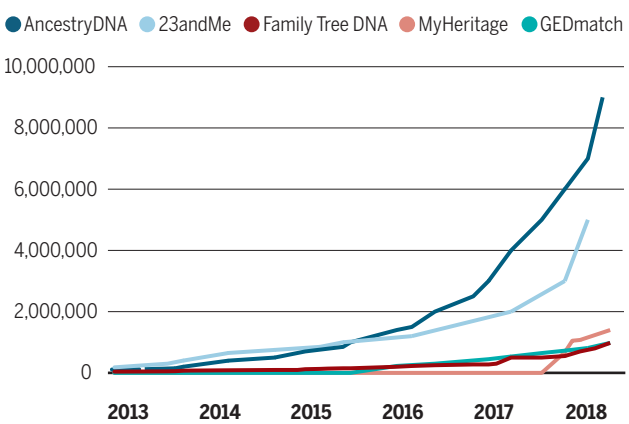

Note: Values for months with missing data are extrapolated.

From fuel plant to bombmaker

NUCLEAR WEAPONS | After years of cost overruns, last week the U.S. Department of Energy (DOE) formally abandoned a project at DOE's Savannah River Site in South Carolina to reprocess plutonium from dismantled nuclear weapons into fuel for nuclear power plants. Under a pact reached with Russia in 2000, the United States pledged to build the Mixed Oxide (MOX) Fuel Fabrication Facility to reprocess 34 metric tons of plutonium. Construction began in 2007, but DOE and Congress reconsidered when cost estimates grew to at least $17 billion. On 10 May, DOE announced plans to kill the MOX facility and convert it into a plant that could, by 2030, annually produce 50 plutonium pits, the grapefruit-size triggers at the heart of nuclear weapons. The Savannah site would become the second U.S. location making the bomb cores, along with Los Alamos National Laboratory in New Mexico. The plan will require approval from Congress.

Statistician faces Greek retrial

LAW | The former head of Greece's statistics agency, twice acquitted of

charges that he inflated the country's budget deficits in a case that critics call politically motivated, faces a third trial because of a legal ruling this week. After the European Union bailed Greece out of a debt crisis in 2010, EU officials praised the defendant, Andreas Georgiou, for ending the Greek government's past practices of underestimating budget deficits and for reporting higher ones that complied with international standards. Those moves angered Greek politicians, who accused him of inflating the estimates to justify the European Union's calls for Greece to take fiscal austerity measures. Greek authorities charged Georgiou with making a false statement. On 14 May, the country's Supreme Court overturned his latest acquittal and directed a lower court to decide whether he must undergo a third trial, according to *The Wall Street Journal*. The American Statistical Association in Washington, D.C., and other groups issued a statement this year asking Greek authorities to halt Georgiou's prosecution.

Detainees' release raises hopes

INTERNATIONAL RELATIONS | North Korea's release of three Americans last week was good news for the country's Pyongyang University of Science and Technology (PUST), where two of the prisoners had served on the faculty. Agricultural expert Hak-song Kim managed an experimental farm for PUST and Sang-duk "Tony" Kim taught accounting. Both were arrested in spring 2017 for alleged "hostile acts" against North Korea. PUST opened in 2010 as North Korea's first privately funded university with a goal of contributing to its economic development. Another 40 or so Americans on the PUST faculty had to leave the country after U.S. President Donald Trump's administration banned travel to North Korea by all U.S. citizens in September 2017. "We have very high hopes that because these three U.S. citizens have been released, the U.S. government will remove that travel ban," says Chan-Mo Park, a computer scientist and PUST's chancellor.

PLANETARY SCIENCE

Next Mars rover to launch eyes in the sky

NASA's next large rover on Mars, set for launch in July 2020, will bring along a little buddy for the ride: a softball-size helicopter. The 1.8-kilogram autonomous drone will be the first to hover over another planet, giving scientists views over rusty hills near the rover's landing site, NASA announced last week. The helicopter will be deployed from the belly of the SUV-size, $2.4 billion Mars 2020 rover before it rolls on to drill samples of the Red Planet's surface for eventual return to Earth. The chopper will achieve lift in the thin martian atmosphere by spinning its twin, counter-rotating blades 3000 times a minute, some 10 times faster than what's needed in Earth's thicker air. NASA plans five flights of increasing duration over a month to test the helicopter's ability to fly without active guidance from Earth. After the trials end, the rover will leave the helicopter behind.

THREE QS

Imagining how androids think

How realistic are the androids on HBO's *Westworld*? The show's scientific adviser, David Eagleman, a neuroscientist at Stanford University in Palo Alto, California, spoke with *Science* about whether we should fear the robot uprising. Read a longer version of this interview at https://scim.ag/QAWestworld.

Q: How did you get involved in the show?
A: I asked who their scientific adviser was. Turns out, they didn't have one. ... Then I went to [Los Angeles, California,] and had a long session with the producers and writers, for about 6 hours, maybe 8, about free will and the possibility of robot consciousness. I also showed them some tech that I'd invented ... this vest with vibratory motors on it. That's now part of the season two plot. ... The real vest vibrates in response to sound, for deaf people, but in *Westworld* it serves a different purpose, giving the wearers an important data stream.

Q: Can we make androids behave like humans, but without our selfishness and violence?
A: I certainly think so. I would hate to be wrong about this, but so much of human behavior has to do with evolutionary constraints. Things like competition for survival and for mating and for eating. Androids would certainly show up with a very different psychology. It would be more of an acting job—they wouldn't necessarily have the same kind of emotions as us, if they had them period. And this is tied into the question of whether they would even have any consciousness—any internal experience—at all.

Q: Are there any moments of especially humanlike behavior in the show?
A: I describe the brain as a team of rivals. If I offer you strawberry ice cream, part of your brain wants to eat it, part of your brain says, "Don't eat it, you'll get fat," and so on. One of the *Westworld* androids, Maeve, finally gets on a train to escape Westworld, and she decides she's going back in to find her daughter. She's torn. If the androids had a single internal voice, they'd be missing much of the emotional coloration that humans have, such as regret and uncertainty. Also, it just wouldn't be very interesting to watch.

SCIENCEMAG.ORG/NEWS
Read more news from *Science* online.

IMAGE: NASA/JPL-CALTECH

IN DEPTH

An aerial photo shows ancient linear roads that led to Pueblo Alto in Chaco Culture National Historical Park.

ARCHAEOLOGY

Drilling threatens ancient Chaco landscape

Lidar technology reveals ceremonial roads on land up for oil and gas development

By **April Reese**

About 1000 years ago, indigenous people built an elaborate network of great houses, kivas, and grand roads centered on Chaco Canyon, in the middle of the San Juan Basin of present-day New Mexico. Today, the region is one of the nation's most productive oil and gas basins. It is also the setting of a collision between burgeoning energy development and archaeology, as new discoveries reveal the importance of the larger landscape in understanding Chacoan society.

Taking advantage of advances in drilling technology, more than 4000 new wells will be developed in the area in the coming years, predicts the Bureau of Land Management (BLM), which manages development of federal mineral resources. Late last month, a federal judge issued a decision that may encourage the sale of oil and gas leases and eventual drilling near the Chaco Culture National Historical Park and known ancient roads. As a coalition of environmental and tribal groups mulls an appeal, they also await a new management plan from BLM, due as early as next month. With President Donald Trump's administration pushing for more oil and gas development on public lands, they worry the new plan may favor development at the expense of cultural and environmental protection.

Meanwhile, advances in remote sensing are revealing hundreds of previously unknown roads between Puebloan sites. As companies scrape well pads and access roads from the high desert scrub, archaeologists fear they will erase ancient roads before they have been fully studied—or even detected. "This real intense development that they're talking about essentially transforms the landscape into an industrial park," said John Roney, an independent cultural consultant based in Albuquerque, New Mexico, who formerly worked for BLM and conducted the first aerial survey of Chaco roads.

Although the park encompasses the largest pueblo, hundreds of smaller sites dot a 100,000-square-kilometer area surrounding the point where Arizona, Colorado, New Mexico, and Utah meet. Old aerial photos had traced roads extending from some sites (see map, left). But a 2017 paper in *Advances in Archaeological Practice* revealed previously unknown roads.

For this project, Anna Sofaer, an archaeo-astronomer who heads the nonprofit Solstice Project in Santa Fe, collaborated with Richard Friedman and Robert Weiner, who specialize in lidar, a technology that uses laser pulses from an airplane to reveal fine features on the landscape. Their analysis of three small areas near the park detected previously undocumented road segments and suggested that hundreds, perhaps thousands, of

Filling in a road map

Aerial and historic photos have revealed some ancient roads in the Chacoan region, especially near the national park (mapped below), but lidar analysis uncovered at least 5 kilometers of previously unknown thoroughfares, implying a far more extensive network.

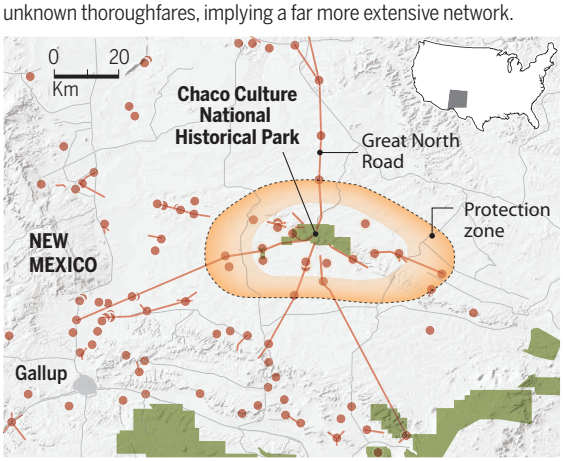

CREDITS: (PHOTO) ADRIEL HEISEY; (MAP) A. CUADRA/*SCIENCE*; (DATA) BUREAU OF LAND MANAGEMENT

ancient roadways traverse the San Juan Basin. The pilot study "told us what the potential would be for the whole Chaco region," Sofaer says. "Now we know that each of these great houses has spokes of roads [around it]."

The lidar work also "helps us understand just how much effort went into creating what we think of as this greater Chacoan world," adds Friedman, a Chaco expert and geographic information systems instructor at San Juan College in Farmington, New Mexico. "A 30-foot [9-meter] road … took a lot of labor just to create."

Many of the roads are more than twice as wide as modern two-lane thoroughfares, even though Ancient Puebloans had no wheeled transportation or beasts of burden. Some roads lead to Chaco Canyon, the epicenter of Ancient Puebloan society and now the heart of the national park. Others seem to lead nowhere. When Sofaer and colleagues explored one newly identified road from the ground, they found a mix of sherds from different pots strewn along the roadbed, lending credence to the theory that this road, at least, was for ceremonial use.

Few roads outside the park are protected. "Historically what was protected was the large building sites and the boundary around them" in the national park, Sofaer explains. "The question is how we protect the areas between the sites."

Although companies have pumped oil and gas from the basin for a century, development only recently spread into the Chaco area, after advances in directional drilling and hydraulic fracturing allowed companies to coax oil and gas from the previously impenetrable Mancos shale formation underneath the region. In March, BLM planned to offer 26 parcels for lease to oil and gas companies. One grazes the periphery of a 16-kilometer-wide temporary buffer that former President Barack Obama's administration imposed around the park; another parcel lies near a site along the Great North Road, a 9-meter-wide thoroughfare that leads 50 kilometers straight north from Chaco Canyon. After a Navajo group and environmental groups protested the leases, Secretary of the Interior Ryan Zinke suspended the sale.

On 23 April, however, Judge James Browning of the U.S. District Court for the District of New Mexico issued a ruling that may have implications for those shelved parcels. In 2015, environmental groups had sued BLM, arguing that it failed to protect cultural sites when approving drilling permits in the Chaco area. In the new ruling, Browning disagreed. He wrote that BLM only needed to survey the immediate area where the well would be drilled and that it had demonstrated that "Chaco Park and its satellites are outside of the wells' APEs [areas of potential effect]."

That decision could bring the 26 suspended parcels back into play, says Kyle Tisdel, an attorney with the Taos, New Mexico, office of the Western Environmental Law Center, which brought the suit on behalf of the groups. "I can imagine the judge's ruling emboldening the [BLM] field office to further prioritize oil and gas," he says. Meanwhile, New Mexico senators and indigenous groups are pressing BLM to place a moratorium on energy development in the area until the agency updates its 2003 resource management plan, which was crafted before heightened industry interest in the Mancos shale.

Zach Stone, a spokesperson for BLM's Farmington field office, says energy development has actually contributed to the archaeological record. He notes that BLM must conduct cultural surveys before drilling on a leased parcel can begin. "A lot of these sites would never have been found without oil and gas development, because we have to go out and look for them" before drilling starts, he said. BLM recently commissioned lidar surveys for the area around the park but has analyzed little of the data so far, and it's unclear whether the data will inform the new management plan.

> ***"This [development] is happening just as we're discovering the larger landscape."***
> **Anna Sofaer**, The Solstice Project

Friedman says BLM's ground surveys may miss the subtle signs of ancient roads. Sofaer estimates that as many as 80% of roads are still undocumented, and she fears that without costly lidar analysis, they never will be. Her team's $600,000 project to conduct a lidar survey of Chacoan lands in southeastern Utah failed to find funding. In March, BLM leased several parcels there, at least one of which abuts a Chacoan great house and, perhaps, roads that have yet to be found. "This [development] is happening just as we're discovering the larger landscape," she says.

Friedman is taking matters into his own hands: He recently acquired BLM's full lidar data set and will begin combing it for more roads in the area around the park. "That's in my spare time," he says. ■

April Reese is a journalist in Santa Fe.

INFECTIOUS DISEASES

Vaccine trial launched to stop Ebola

Fast response greets new Congo outbreak

By **Jon Cohen**

The first ever effort to use a vaccine to stop an Ebola outbreak in its initial stages is taking shape in the Democratic Republic of the Congo (DRC). The international response to health emergencies in sub-Saharan Africa is often maddeningly slow. But this time around, international agencies and the DRC government sprang into action, hoping to quickly extinguish the outbreak.

"Everything is organized," says virologist Yap Boum, who works with Doctors Without Borders (MSF) and is helping launch the vaccine effort. Boum, who lives in Yaoundé, Cameroon, began planning his trip to the DRC as soon as it confirmed on 8 May that two Ebola cases had occurred in the remote Bikoro health district in the Équateur province.

By tracing contacts between the infected people and others who had Ebola symptoms, such as high fevers and diarrhea, the DRC's Ministry of Public Health (MOPH) determined that the virus has likely been spreading since early April. As *Science* went to press, a total of 25 other probable cases and 14 suspected ones had been identified in Bikoro and two adjacent health districts. Nineteen of these people have died.

Boum says the most alarming news from the DRC so far is that two of the probable cases are in Mbandaka, a port city of 1.2 million people. "The possibility of the virus spreading is huge," adds Boum, noting that while Ebola is incubating undetected—which can take several weeks—the victim is already infectious. DRC President Joseph Kabila has authorized MOPH to use every tool at its disposal, including the experimental vaccine against Ebola, which worked spectacularly well in a clinical trial that Boum helped run in Guinea in 2015 at the tail end of the recent West African epidemic.

The World Health Organization (WHO) also acted quickly, immediately sending a team to the DRC to coordinate the response, which includes improved surveillance, introduction of safe medical and burial techniques, and the establishment of quar-

antine units operated by MSF and others. WHO Director-General Tedros Adhanom Ghebreyesus even visited Bikoro last week. WHO has been heavily criticized for its slow response to the West African epidemic, the worst Ebola outbreak on record, which sickened more than 28,000 people and killed an estimated 11,310 before traditional containment efforts ended it.

The DRC considered using the vaccine for an Ebola outbreak last year, but it met with hurdles including importing the vaccine and uncertainty about whether the virus had moved beyond remote villages. "This time they're much better prepared," says Seth Berkley, who heads Gavi, the Vaccine Alliance, a nonprofit based in Geneva, Switzerland, that purchased a stockpile of the experimental vaccine and is providing financial assistance to the DRC.

The vaccine consists of a harmless livestock virus genetically engineered to display Ebola surface proteins. It is made by Merck and not yet licensed for use by any country, but can be given as part of a trial under what are known as compassionate use regulations. The trial protocol, approved by the DRC last year, relies on a "ring" strategy in which only people who have come in contact with cases, their contacts, health care workers, and other front-line responders are vaccinated. At press time, surveillance teams had identified

> ***"The possibility of the virus spreading is huge."***
> **Yap Boum**, Doctors Without Borders

393 contacts. Some 8000 doses are being shipped to the DRC from WHO's Geneva headquarters and Merck's U.S. storage site. Special Arktek containers have arrived that can maintain the vaccine at below freezing temperatures for travel to remote locations.

MSF will sponsor the trial in collaboration with investigators from the DRC's health ministry. The team will follow vaccinated people for 84 days to assess whether any develop Ebola and to evaluate side effects.

The vaccine is but one of many tools being wielded to stop the outbreak as quickly as possible. All told, Gavi, WHO, the United Nations, and the Wellcome Trust have committed about $8 million to the DRC response, which includes sending mobile laboratories and equipment to the affected region, parts of which cannot be reached by car. "It's absolutely a dire scene in terms of infrastructure," said Peter Salama, who heads WHO's Health Emergencies Programme. "This is going to be tough and it's going to be costly to stamp out this outbreak." ■

The chicken in this nugget never clucked; it was cultured from cells.

PHOTO: MEMPHIS MEATS

BIOTECHNOLOGY REGULATION

U.S. lawmakers float plan to regulate cultured meat

Should agency that regulates meat from farms also oversee tissue grown from cells in bioreactors?

By **Kelly Servick**

A new wave of burgers and nuggets made of meat grown from cultured animal cells is heading to grocery shelves and restaurant menus in coming years. But these products of so-called cellular agriculture present a regulatory conundrum: Who should monitor the safety of food that comes from a culture medium, not a field?

Last week, lawmakers in the U.S. House of Representatives offered one answer, adding language to a draft spending bill that would put the Department of Agriculture (USDA) in charge of overseeing the manufacturing and labeling of cultured meat. But some lawmakers and industry groups argue the move could result in unnecessary new rules, and say the language was drafted with little input from food specialists or affected companies. "We should allow experts to weigh in before taking on this major policy" step, said Representative Rosa DeLauro (D–CT) during a 9 May hearing on the bill, which would set USDA's 2019 spending levels.

Unlike plant-based meat imitations that are already on the market, cultured meat starts with cells taken from livestock or poultry, which are then coaxed to grow into strands of muscle. Since the theatrical unveiling of the first lab-grown beef patty 5 years ago (*Science*, 9 August 2013, p. 602), several companies have crafted prototypes and announced plans to market products within 5 years.

Cultured meat proponents say the technology would spare animals from slaughter, require less energy and land, and emit fewer greenhouse gases than conventional meat production does. But its impending arrival has sparked disputes over what actually counts as meat. In February, the U.S. Cattlemen's Association in Washington, D.C., asked USDA to prevent cultured meat companies from labeling their products as "beef" or "meat," and to restrict those terms to products taken from animals "born, raised, and harvested in the traditional manner."

USDA is responsible for ensuring the quality of meat, poultry, and egg products, but some experts question whether it has the expertise to oversee cultured meat manufacturing—a process very different from the feedlots and slaughterhouses familiar to USDA inspectors. The manufacture of new meat products could more closely resemble that of therapies made from human cells and tissues, which the Food and Drug Administration (FDA) oversees. FDA is also responsible for the safety of processed foods, seafood, and genetically engineered animals. It's not yet clear what process either agency might use to assess the safety of cultured meat.

Opponents of the House provision will have several opportunities in coming weeks to remove it from the bill. And even if it survives, the Senate and the White House will have to agree to any new policy.

In the meantime, other countries are also contemplating cultured meat regulations. In the European Union, rules that went into effect in January declared cultured meat to be a category of "novel food" that can be marketed there if regulators decide it is safe, nutritionally equivalent to a food it is intended to replace, and labeled "so as not to mislead consumers." ■

Peruvians are among the world's shortest people, and one gene variant may explain why.

GENETICS

High altitude may have driven short stature in Peruvians

Study reveals new gene with a major impact on height

By **Elizabeth Pennisi**, *in Cold Spring Harbor, New York*

Hundreds of genes influence how tall a person is, but most make an imperceptible difference—perhaps a millimeter, for example. Now, a group studying the genetics of Peruvians, one of the world's shortest populations, has turned up a gene variant that cuts a person's height by more than 2 centimeters, on average. "It's amazing that they saw such a change," says Emma Farley, a genomicist at the University of California, San Diego. "It's quite a large effect."

Geneticists have diligently pursued genes for height; a 2014 analysis called GIANT examined 250,000 people. "That you can still pull out new players is very exciting," says Elaine Ostrander, a geneticist at the National Human Genome Research Institute in Bethesda, Maryland. "It speaks to the value of looking at isolated populations." So far, the gene variant is not known outside Peru, where the demands of living at high altitude may have driven its evolution, but it could offer clues about how other mutations influence height.

Postdoc Samira Asgari and Soumya Raychaudhuri's team, all at Harvard Medical School in Boston, originally wanted to know how a person's DNA influences the severity of tuberculosis. Together with epidemiologist Megan Murray's team at Partners in Health in Lima, they collected genetic information from 4002 residents there, along with other data including height. Peruvians are among the shortest people in the world, with men averaging 165 centimeters and women reaching about 153 centimeters—in both cases about 10 centimeters shorter than average people in the United States and 15 centimeters shorter than the Dutch, generally regarded as among the world's tallest people. So the team decided to search the DNA data for genetic factors underlying this short stature.

First, Asgari assessed the ancestry of their subjects by comparing their DNA to genomes of Africans, Europeans, and Native Americans. Peruvians are about 80% Native American, 16% European, and 3% African, she reported last week at the Biology of Genomes meeting here. "The more Native American ancestry, the shorter they were," she said. By correlating variation in the Native American portion of each person's genome with their height, Asgari found a specific gene variant that seems to influence the trait.

Short Peruvians have a version, or allele, of a gene called *FBN1* that differs by one base from the gene's usual DNA sequence. That subtle shift alters an amino acid in a carbohydrate-coated protein called fibrillin-1, which provides structural support in connective tissue. Other *FBN1* mutations are known to affect height in rare disorders: Marfan syndrome, which affects the skeleton, heart, and eyes and generally produces tall, thin people; and "stiff skin" syndrome, marked by shortness and a very thick, hard skin. This gene's new link to overall height "logically connects to [its] biology," Farley says.

Most of the 700 or so other genes tied to height can, with their individually small effects, together explain only about 7% of a Peruvian's height. The new allele accounts for another 1% all by itself, the researchers estimate. A person carrying just one copy of this *FBN1* variant is about 2.2 centimeters shorter than people with different versions of the gene and those with two copies can be more than 4 centimeters shorter, Asgari reported.

Her group estimates that 5% of Peruvians carry the newly identified *FBN1* allele, suggesting that evolution has favored short stature and perhaps thick skin among Peruvians. Many live at high altitudes, and animal studies show that species living at such elevations tend to be smaller, an apparent evolutionary adaptation to the scarcity of food in those places. Thick skin might also protect the body from the strong ultraviolet light at high altitudes.

Kousik Kundu, a genomicist at the Wellcome Sanger Institute in Hinxton, U.K., remains cautious about the role of this gene variant, calling for Asgari to get more detailed sequence data from her Peruvian subjects and to study larger populations there. Asgari also wants to study other short people, such as some groups in the Middle East, to see whether the same allele is at work elsewhere. With further genetic analysis, says geneticist Sarah Tishkoff at the University of Pennsylvania, Asgari might be able to say when the shortness variant arose. "It's a really cool story in the making." ■

PHOTO: HADYNYAH/GETTY IMAGES

NUCLEAR PHYSICS

Neutron stars' quark matter not so strange

Calculation also casts doubt on existence of Earth-gobbling strangelets

By **Adrian Cho**

Within a neutron star—the remains of an exploded, middle-weight star—pressures climb a billion billion times higher than in the sun's core. For decades, some theoretical physicists have speculated that under those conditions, a bizarre type of matter might emerge: a soup of the subatomic particles called quarks. Now, a new analysis indicates the recipe for that soup, called cold quark matter, needs revision. If correct, it suggests that particle accelerators on Earth might be able to produce stable bits of the quark matter. It also would put the kibosh on hypothetical particles called strangelets, which fearmongers once claimed could destroy the world.

"It's a speculative argument, but there is nothing obviously wrong with it," says Robert Pisarski, a nuclear theorist at Brookhaven National Laboratory in Upton, New York, who was not involved in the work.

Atomic nuclei consist of protons and neutrons, which themselves consist of trios of up and down quarks—two of the particles' six "flavors"—bound tightly by the strong nuclear force. Since the 1970s, some theorists have predicted that under extreme pressures like those in the hearts of neutron stars, quarks might break free of their strong-force chains to create a soup of cold quark matter. They also predicted that the soup's ingredients would differ from those of protons and neutrons. Their calculations suggested that to minimize its energy, quark matter should include a third flavor of quarks known as strange quarks.

Even though strange quarks emerge only fleetingly in collisions at particle accelerators, calculations suggested that such strange quark matter might have a lower energy than ordinary nuclear matter has. That means that specks of strange quark matter, or strangelets, could be stable and that, in principle, ordinary nuclei could change into them. That transformation would require simultaneous conversions of up and down quarks to strange quarks—something unlikely to happen spontaneously in the age of the universe. But strangelets generated in cosmic rays or lingering from violent astrophysical events might survive indefinitely. Scientists have searched for them in many ways, so far unsuccessfully.

Now, Bob Holdom, a nuclear theorist at the University of Toronto in Canada, and his colleagues say they have banished strange quark matter with better estimates of how, through quantum effects, quarks change the energy of the vacuum of space itself, a key component of quark matter's total energy. "Our model allows us to see how the vacuum energy depends on the flavor of the quark," Holdom says. Mixing in strange quarks incurs a bigger energy penalty than previously thought, so high that cold quark matter should consist of just up and down quarks, the researchers report in a paper in press at *Physical Review Letters*.

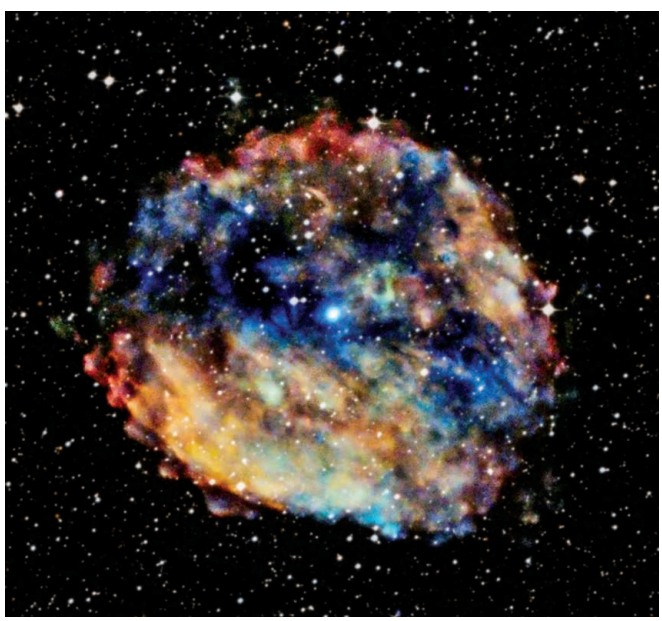

At its center, a supernova remnant harbors a neutron star, thought to contain a soup of quark matter. A new study suggests the soup may lack strange quarks.

IMAGE: (X-RAY) NASA/CXC/UNIVERSITY OF AMSTERDAM/N. REA *ET AL.*; (OPTICAL) DSS

Atomic nuclei clearly don't readily convert into up-down quark matter either. The team calculates that for masses below about 300 times that of the proton, ordinary nuclei are stable because effects akin to surface tension increase quark matter's energy. However, if experimenters striving to make new superheavy elements could push up in mass just a bit beyond the heaviest nucleus spotted yet—oganesson, with an atomic mass of 294—then they might make stable nuggets of up-down quark matter, the theorists predict.

Is this the end for strange quark matter? Probably not, Pisarski says. The theory of quarks is so mathematically intractable that, like everybody else, Holdom had to resort to approximate models, he says. Laura Paulucci, an astrophysicist at the Federal University of ABC in São Paulo, Brazil, adds that the analysis also doesn't quite rule out strange quark matter in neutron stars, where the density should be significantly higher than the theorists assume. "I'm not sure the theory they're using is adequate" for the conditions in neutron stars, she says.

Still, the study may be good news for scientists hunting stable quark matter, says Evan Finch, an experimenter at Southern Connecticut State University in New Haven who has searched for strangelets by running moon dust through a mass spectrometer and looking for particles with odd charge-to-mass ratios. "There's a suggestion that maybe we've been looking in the wrong place" for quark matter, he says. "I'm a bit skeptical, but it's fun."

The new picture of cold quark matter could also dispel a far-fetched threat to the world. Opponents of the Large Hadron Collider in Switzerland had argued that the atom smasher might produce negatively charged strangelets that would gobble up positively charged atomic nuclei in a runaway process. Physicists had countered that if such a catastrophe were possible, strangelets from space would have long since consumed the planet. Up-down quark matter would definitively rule out the doomsday scenario: It should be positively charged and repel atomic nuclei.

Still, a nugget of the stuff could be useful, Holdom says. Bombard it with neutrons and it would convert them to quark matter while generating energy, he predicts. ■

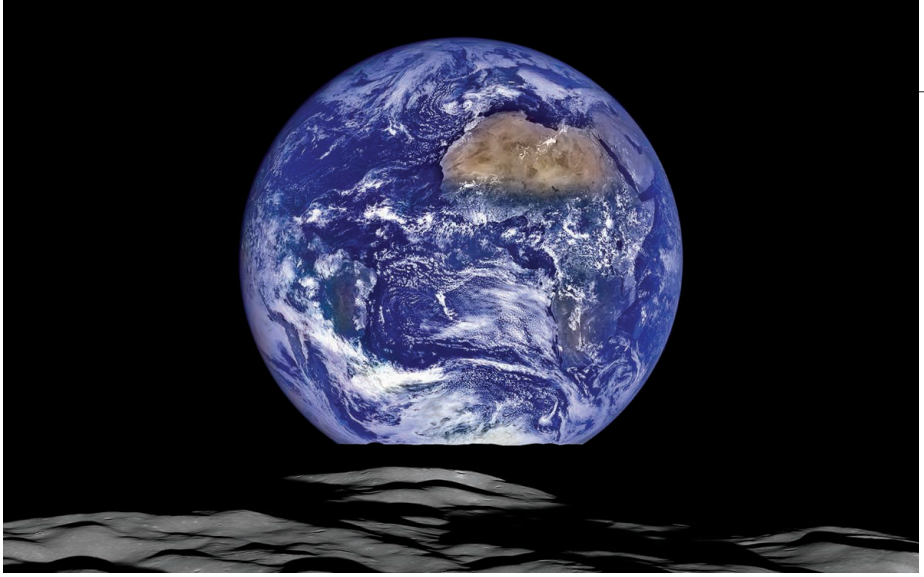

The lunar far side, always in shadow from Earth, can protect radio astronomy instruments from noise.

PHOTO: NASA/GODDARD/ARIZONA STATE UNIVERSITY

ASTRONOMY

China's moon mission is set to probe cosmic dark ages

Radio quiet environment near the moon will help Dutch-Chinese experiment explore time before the first stars

By **Daniel Clery**

On 21 May, China plans to launch a satellite with a vital but unglamorous mission. From a vantage point beyond the moon, Queqiao, as the satellite is called, will relay data from Chang'e 4, a lander and rover that is supposed to touch down on the lunar far side before the end of the year. But a Dutch-made radio receiver aboard Queqiao will attempt something more visionary. In the quiet lunar environment, it will listen to the cosmos at low frequencies that carry clues to the time a few hundred million years after the big bang, when clouds of hydrogen gas were spawning the universe's first stars.

The mission is a proof of principle for other efforts to take radio astronomy above the atmosphere, which blocks key radio frequencies, and far from earthly interference. "Putting the whole show into space is extremely appealing," says Michael Hecht of the Massachusetts Institute of Technology's Haystack Observatory in Westford, whose team is also developing small radio satellites that could be used to probe the cosmos. For Europe's astronomers, it is also a test of cooperation with China, something their U.S. counterparts at NASA are barred from doing.

The Netherlands-China Low-Frequency Explorer (NCLE) project stems from a 2015 Dutch trade mission to China, during which the two countries agreed to collaborate on space missions. The Netherlands is strong in radio astronomy: Its Low-Frequency Array (LOFAR) stretches across much of northern Europe (*Science*, 7 November 2014, p. 688). NCLE Principal Investigator Heino Falcke, of Radboud University in the Netherlands, has long advocated a "LOFAR on the moon." China has an ambitious program of moon missions, so he jumped at the chance to take a first step. "We put together a proposal in 2 weeks," he says. Once funded, the team had just 1.5 years to build the instrument. "Half of the experiment is how you work together" Falcke says. Jinsong Ping of the National Astronomical Observatories of China in Beijing, who leads the Chinese team working on the NCLE, agrees: "It is really challenging both sides. … Different culture, habit, language, working manner."

To see back into the dark age before the first stars, astronomers look for a signal emitted when electrons in the primordial neutral hydrogen gas spontaneously flipped their orientation. These photons started out with short radio wavelengths, but over their more than 13-billion-year journey to Earth, the universe's expansion stretched them out to long wavelengths, or low megahertz frequencies. After the gas clumped together to form the first stars, their radiation ionized the neutral gas and eventually snuffed out the faint signal.

Telescopes such as the LOFAR aim to detect the ancient signal and use it to map the distribution of primordial matter. But the signal is hard to discern in the maelstrom of radio noise from terrestrial sources and other objects across the universe. Only one detector, the Experiment to Detect the Global Epoch of Reionization Signature, a set of ground-based antennas in Australia, has so far claimed a detection (*Science*, 2 March, p. 969).

Queqiao, orbiting a gravitational balance point beyond the moon called L2, will offer a quieter vantage. In order to relay signals from the moon to Earth, the satellite can't be completely in the moon's shadow, which means that Earth noise could still be a problem, says Jack Burns, an astronomer at the University of Colorado in Boulder who has long campaigned for a lunar radio observatory. Burns adds that the spacecraft itself will also be a source of interference. But by testing hardware in space, the NCLE "will set the stage for other missions."

Once Queqiao arrives at L2, the NCLE will wait its turn until after the Chang'e 4 lander has achieved its main mission: exploring the South Pole-Aitken Basin, a huge far side depression. Then, around March 2019, the instrument will unspool three 5-meter-long carbon-fiber antennas, each at right angles to the others.

Because Earth's atmosphere blocks all radio signals below 30 megahertz, the data will delight a range of astronomers. Falcke says the team will study solar flares, the aurora of Jupiter, and the galaxy's radio emissions. "There's nothing as good as having real data," he says. The dark age signal is a long shot, he admits. Realistically, the mission is about "gaining expertise to build a follow-up."

The Chinese NCLE team has its own plans. It has placed basic receivers on the Chang'e 4 lander and two microsatellites that Queqiao will release into lunar orbit to study solar radio bursts. Ping says his team will also try to combine signals received by the NCLE with those taken by earth-bound detectors—a technique known as interferometry, which can improve resolution. "It is a demonstration," he says. It could show that, once detectors are sensitive enough, interferometry could help them map the newborn universe.

Burns and his colleagues are working on a proposal for a small satellite called the Dark Ages Polarimetry Pathfinder, which he says will be more sensitive to the dark age signal. But eventually, he wants to see an observatory on the lunar far side, deep with the moon's radio quiet shadow. He predicts a NASA-funded low-frequency telescope in the next 5 years. "There's great interest in the far side." ■

Corrected 18 May 2018. See full text.

Published by AAAS

ARTIFICIAL INTELLIGENCE

Boycott highlights AI's publishing rebellion

Researchers shun traditional journals for conference papers and open-review websites

By **Matthew Hutson**

Computer science was born of a rebellious, hacker culture, a spirit that lives on in the publishing culture of artificial intelligence (AI). The burgeoning field is increasingly turning to conference publications and free, open-review websites while shunning traditional outlets—sentiments dramatically expressed in a growing boycott of a high-profile AI journal. As of 15 May, about 3000 people, mostly academic computer scientists, had signed a petition promising not to submit, review, or edit articles for *Nature Machine Intelligence* (*NMI*), a new journal from the publisher Springer Nature set to begin publication in January 2019.

The petition, signed by many prominent researchers in AI, is more than just a call for open access. It decries not only closed-access, subscription-based journals such as *NMI*, but also author-fee publications: open-access journals that are free to read but require researchers to pay to publish. Instead the signatories call for more "zero-cost" open-access journals.

The purpose of the boycott is "to lower the barriers to research progress" for resource-strapped scientists, says Thomas Dietterich, a computer scientist at Oregon State University in Corvallis, who began the boycott last month. The field is moving too fast for traditional publishing, and AI's potential for both great benefit and great harm requires openness, he says. "Locking up our research papers behind a paywall would make public scrutiny more difficult."

Paul Ginsparg, a physicist at Cornell University and founder of the preprint repository arXiv, where computer scientists often publish, applauds what he calls "a principled stand." But, he adds, "I personally have no animus towards the subscription model." And he thinks the petition signers may have unrealistic hopes for zero-cost journals. Servers are cheap, but "systematic quality control is labor-intensive, and that costs real money."

Springer Nature is not backing away from its plans for the journal, Susie Winter, a Springer Nature spokesperson in London, said in a statement. "At present, we believe that the fairest way of producing highly selective journals like this one and ensuring their long-term sustainability as a resource for the widest possible community is to spread the associated costs among many readers." Dietterich says he did not include Springer Nature's flagship journal, *Nature*, in the boycott because computer scientists tend not to publish in general-interest journals anyway. (Google DeepMind, which published prominent papers on its AlphaGo AI in *Nature*, is an exception, although multiple DeepMind employees have signed the boycott.)

Journals from nonprofit societies such as AAAS (which publishes *Science* and *Science Robotics*), the Institute of Electrical and Electronics Engineers, and the Association for Computing Machinery also got a pass, Dietterich says, because of their missions and low fees.

In computer science, most of the action does not take place in journals, anyway. Often, papers are posted to arXiv and then submitted, generally for free, to conferences, where they get a limited form of peer review: comments, and acceptance or rejection. Computer scientists have gravitated to arXiv because of the slow reviewing process at journals, says Yann LeCun, Facebook's chief AI scientist in New York City. Moreover, for academic advancement in computer science, conference papers and not journal papers have become the coin of the realm, says Leslie Kaelbling, a computer scientist at the Massachusetts Institute of Technology in Cambridge. "We are all very practiced, everywhere, at arguing to our deans and provosts and so on at tenure time that, 'Yes, this person has almost no journal articles but it's OK.'"

AI is now moving toward not just open access, but open review. In 2013, Andrew McCallum, a computer scientist at the University of Massachusetts in Amherst, launched OpenReview, a site that allows authors to submit conference papers and invites reviewers to post their comments and decisions openly. Anyone else can add a review, too. Major AI conferences have begun using the site, and McCallum says fears of flame wars or soft reviews were unrealized. "Furthermore, some magical things happened." For example, for a 2013 AI paper on data analysis, a mathematician from outside computer science noted errors in a proof, and shared an idea to fix them. "This is the way science should be working, right?" McCallum says. He adds that he and Ginsparg have discussed using OpenReview to provide an independent overlay on arXiv articles, which don't currently allow comments.

Kaelbling says the explosion of AI research is stressing existing publications, and that sites such as OpenReview can help by spreading out the reviewing effort and curbing low-quality submissions. One upcoming conference, the Conference on Neural Information Processing Systems (NIPS), asked Kaelbling for help finding 2750 reviewers for submitted papers. "But I feel reasonably sure that it will be very hard to find 2750 qualified NIPS reviewers," she says. "It's crazy."

The torrent of AI publications may be unsustainable, but it is exhilarating, McCallum says. He tells a story about a colleague who posted a paper on computer vision to arXiv. Within months, other papers had built on it, been posted to arXiv, and been built on themselves. When one of those papers was presented at a conference, the authors didn't just discuss their own paper. They discussed a year of progress. "It was more like, 'Here, let me tell you a retrospective of seven generations of scientific research,'" McCallum says. "This never would have happened in a closed publishing world." ■

Matthew Hutson is a journalist in New York City.

Artificial intelligence explosion

In spite of a journal boycott, publication of artificial intelligence (AI) papers is nearly 10 times higher than it was in 1996, according to a study using the SCOPUS database.

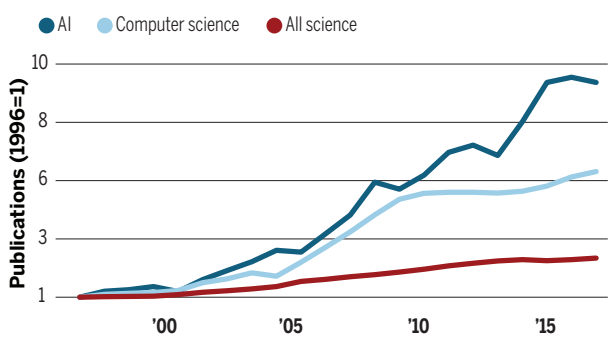

CREDITS: (GRAPH) E. HAND/*SCIENCE*; (DATA) YOAV SHOHAM *ET AL*., *THE AI INDEX 2017 ANNUAL REPORT* (2017)

HADZA ON THE BRINK

Farmers, tourists, and cattle threaten some of the world's last hunter-gatherers, long a magnet for researchers

By **Ann Gibbons**, *in the Yaeda Valley in Tanzania*

As we hike down a rocky slope, through thorny acacias that snag our clothes and past the emaciated carcass of a cow, we hear people singing. We are approaching a small camp of Hadza hunter-gatherers, and our Tanzanian guide thinks they must be celebrating something.

But as we near a few huts made of branches and draped with mosquito netting, a slender woman in a worn T-shirt and sari totters toward us. "She is drunk," says Killerai Munka, our guide.

The woman calls her children, and as she puts their small hands inside ours we get a sour whiff of diarrhea. That's when she tells Munka that her youngest child—a baby boy—died the night before. "He wanted to sleep some more and didn't wake up," Munka translates from Swahili.

A couple of pastoralist men, probably members of the local Datoga tribe, are also visiting. They carry wooden staffs, wear brass hoop earrings, and have brought a bottle of homemade alcohol. They have traded that bottle, and likely others, for honey gathered by the Hadza, who by now have had too much to drink.

Times are hard for the Hadza, who include some of the last people on the planet to live as nomadic hunter-gatherers.

Their way of life has been a magnet for researchers for 60 years, and the subject of hundreds of scholarly papers, because it may offer the closest analog to the way our African ancestors lived. The iconic lifestyle persists: Just that morning in another Hadza camp called Sengele, an hour's walk away, women and children were digging tuberous roots for food. Men were gathering honey by smoking out bees from baobab trees. But that lifestyle is quickly disappearing.

Today, of roughly 1000 Hadza living in the dry hills here between salty Lake Eyasi and the Rift Valley highlands, only about 100 to 300 still hunt and gather most of their food. Most of the others do forage—but they also buy, trade, or are given food, and sometimes alcohol and marijuana. Many live part of the year in larger semipermanent camps in the sprawling settlement of Mangola, where they depend on income from tourism and occasional jobs on farms or as guards.

PHOTO: MATTHIEU PALEY

Hadza men hunt on a ridge above the Yaeda Valley in Tanzania (left). The Hadza's hunting and gathering lifestyle fosters a diverse microbiome that researchers study with oral swabs (right) and by sampling fecal matter.

PHOTO: HUMAN FOOD PROJECT

Most Hadza now go to school for a few years, speak Swahili in addition to their own click language, and wear donated Western clothes. Some carry cellphones. But, "They are not integrating into a normal rural Tanzanian life," says evolutionary anthropologist Colette Berbesque of the University of Roehampton in London, who has studied the Hadza since 2007. Instead, she says, they are "transitioning to a life where they're at the absolute bottom of the barrel."

It is a tragic story that has played out many times before as hunter-gatherers around the world have been displaced by more politically powerful settlers. Although the Hadza have proved resilient in the past, researchers warn that they now face a daunting convergence of threats.

Their Brooklyn-size territory is being encroached on by pastoralists whose cattle drink their water and graze on their grasslands, farmers clearing woodlands to grow crops, and climate change that dries up rivers and stunts grass. All those pressures drive away the antelope, buffalo, and other wildlife the Hadza hunt. "If there are no animals, how are we going to feed our people?" asks Shani Msafir Sigwazi, a Hadza who is a law student at Tumaini University Makumira in Arusha, Tanzania. "How are we going to protect our life in the bush?"

"The last 5 years have drastically altered the landscape politically, socially, and ecologically," says human behavioral ecologist Alyssa Crittenden of the University of Nevada in Las Vegas, who has studied the Hadza since 2004. "It's clear to anyone who goes out to see the Hadza that we're dealing with small populations being pinched on all sides."

Worried about the Hadza's plight, researchers wonder about their responsibilities to the people they have studied intensively for decades. Many researchers are seeking ways to help, even as they vie to study the few Hadza who still hunt and gather full time. But some researchers have stopped fieldwork altogether, saying the Hadza lifestyle has changed too much. "The narrative that they are perfect hunter-gatherers has been eroding since the first researchers have worked with them," says paleobiologist Amanda Henry of Leiden University in the Netherlands, who has studied Hadza gut bacteria and diet; her team is not returning.

FROM THE VERY FIRST, researchers who studied the Hadza realized they were walking a tightrope—studying a traditional way of life that their very presence risked altering. James Woodburn was a 23-year-old graduate student in 1957, when he became the first anthropologist to study the Hadza. He quickly realized that the tire tracks of his Land Rover created new paths for the Hadza, so he sold it and walked everywhere with them instead. "I was most anxious not to affect their nomadic movements," says Woodburn, now retired from the London School of Economics.

All the Hadza he saw then were nomadic hunter-gatherers who ranged across 1000 square kilometers of bush, an area 20% larger than New York City. Yet even then, they were losing their traditional lands at a great rate, Woodburn says, and had less than half the 2500 square kilometers they inhabited when German geographer Erich Obst met them in 1911 (see map, p. 702).

Still, Woodburn recalls an "exceptional abundance of game" in the 1960s, including "a herd of 400 elephants, also lots of rhino, hyenas, lions, and many, many other animals." At the time, he found, the Hadza were healthier than farmers and herders, as he reported at the famous "Man the Hunter" symposium in Chicago, Illinois, in 1966. And although the Hadza traded with their agricultural neighbors, exchanging meat and skins for beads, pots, and iron knives, few people from other tribes had settled on their land. They did not intermarry much and kept to themselves.

The Hadza also resisted many attempts by governments and missionaries to move them into settlements to become farmers. So many Hadza died of infectious diseases in camps in the 1960s that Woodburn worried they would be wiped out. But survivors

always left the camps to return to the bush.

Woodburn realized that farming was antithetical to the Hadza's egalitarian values, as he described in a landmark paper in 1982 in the journal *Man*. He noted that they were vigilant in preventing any single person from acquiring assets or wealth, or asserting power or status over others. They shared the food they hunted and gathered the same day or soon after in an "immediate return" system. Woodburn contrasted that approach with "delayed return" societies, in which individuals invest in building personal assets that pay off later—for example, spending perhaps weeks crafting a boat and then storing caught fish for many months. Such societies, he argued, more readily adopt farming or herding, which allow individuals to acquire power, rank, and wealth.

bear more children; that men prefer to hunt large game because having reputations as good meat providers makes them desirable mates and allies; and that hunter-gatherer children forage for enough food that they are "cheap" to raise, boosting fertility and population. "The Hadza are just a touchstone for so much," says anthropologist Kristen Hawkes of The University of Utah in Salt Lake City, who did fieldwork with the Hadza from 1984 to the early 1990s.

Today, at least a dozen research groups from around the world have permits to study the Hadza. One is led by Jeff Leach, a visiting research fellow at King's College London, who helped show that the Hadza have more diverse gut bacteria than people on a Western diet do. "East Africa is ground zero for the human microbiome," he says.

A shrinking homeland

The Hadza hold deeds to a Brooklyn-size territory where they can hunt and gather, but this is only a fraction of their historic homeland. Today, farmers and pastoralists seeking grazing rights press in on all sides.

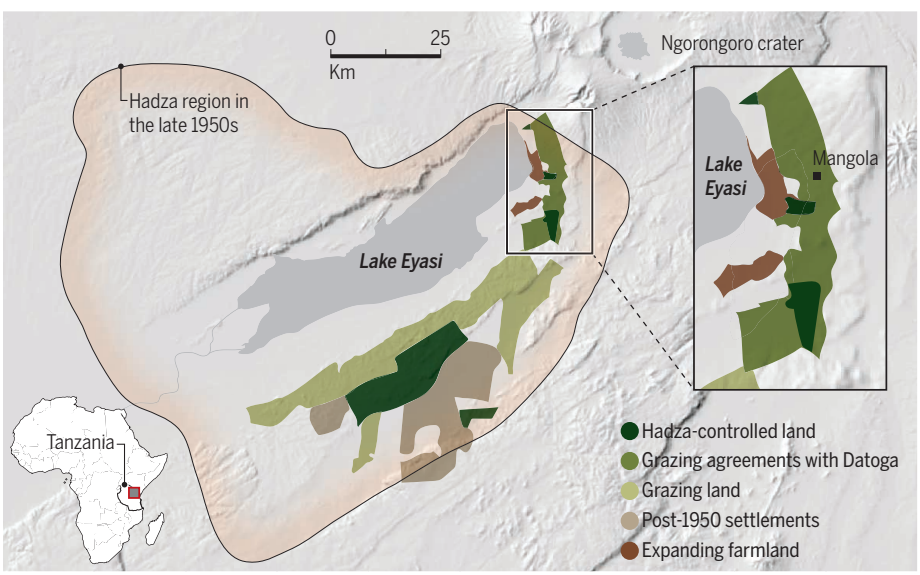

The Hadza are not living fossils "lost at the bottom of the Rift Valley for thousands of years," says Nicholas Blurton-Jones, professor emeritus at the University of California, Los Angeles (UCLA), who did fieldwork with the Hadza from 1982 to 2000. They also have evolved over the millennia and long ago adopted new tools, such as metal arrowheads and cooking pots. But in their rich and relatively undisturbed savanna home, the Hadza have offered a steady stream of researchers a unique view of the way of life and selection pressures that "many have suggested brought our species into being," he says.

Over the years, studies of the Hadza have revealed that grandmothers' food production boosts child survival so mothers can

"With the Hadza, who are exposed to the urine, blood, and feces of every animal they hunt, you can get a picture of all the microbes on that landscape."

Other studies focus on their lifestyle. Crittenden recently found that Hadza men who switched to an agricultural diet suffered less dental decay (probably because they ate less honey), but that women and children ended up with more cavities (*Science*, 28 April 2017, p. 362). A team led by UCLA biological anthropologist Brian Wood, who has studied the Hadza since 2004, learned that they use only as much energy every day as sedentary Westerners, suggesting that hunting and gathering can be remarkably efficient; and that the Hadza sleep less than recommended in Western guidelines.

EVEN AS STUDIES PROCEED, the Hadza's future is darkening. The biggest threat comes from farmers and pastoralists and their cattle encroaching on Hadza land. In 2011, after years of negotiation between a local nongovernmental organization (NGO) and government officials, the Tanzanian commissioner for lands gave the Hadza rights to a 230-square-kilometer area. That was a major victory, but the egalitarian Hadza have lacked the leadership or organization to protect their land.

"When you look at the Hadza, we have no leaders to represent us in government," Sigwazi says. Local governments enforce land and grazing rights, and the Hadza have far fewer representatives on village councils than the Datoga or Iraqw farmers who live nearby. As a result, the Hadza have had to agree to give away grazing rights on their land in the dry season. The laws do prevent the free-for-all hunting on Hadza land that happened in the mid-1980s when many elephants were poached, says Daudi Peterson, co-founder of Dorobo Safaris and the Dorobo Fund, which uses fees from research and sustainable tourism to protect wildlife and fund health care and education for the Hadza and other groups. (*Science* paid fees to the fund to visit Hadza land.) However, he adds, "Flagrant abuse of the laws" by herders has taken place.

The Hadza are particularly concerned about Datoga pastoralists who let their cattle graze on grass and drink from water holes on Hadza land year-round. In one Hadza camp, a woman named Tutu pointed to her people's huts. Their tree-branch frames were draped with clothes and bark instead of the traditional grass thatch. "The cows eat all the grass," she explained.

The Datoga are also moving in, building *bomas*—mud-walled huts encircled by acacia-thorn fences that contain livestock at night—near water sources. The settlements keep the nonconfrontational Hadza and their prey away from the water. "You can see from Google Earth where Datoga *bomas* are and how the Hadza—especially the women—adjust their spatial behavior to avoid them," Wood says.

"The Datoga come here and take over the area—they put in their permanent houses," said a Hadza man named Shakwa. "Our land is getting smaller and smaller. It is not like a human being that gets pregnant and can give us more and more land."

The incursions, with cattle grazing deep in the bush, have worsened in the past 3 years because of climate change, which has displaced the Datoga and other herders from lands outside the district, says Partala Dismas Meitaya, who works for the Ujamaa Community Resource Team in Arusha, the

CREDITS: (GRAPHIC) N. DESAI/*SCIENCE*; (DATA) DAUDI PETERSON/DOROBO FUND; CARBON TANZANIA

The outside world encroaches on Hadza land in many ways: A Hadza scout records cattle intruding on their lands using a GPS camera (top); Hadza put on baboon skins to impress a Lithuanian tourist in a camp in Mangola (bottom right); and a Hadza atop a truck watches a Maasai herder on a track through Hadza country (bottom left).

PHOTOS: (TOP TO BOTTOM) CARBON TANZANIA; MATTHIEU PALEY (2)

local NGO that negotiated the land rights. Half the Datoga's cattle died on their own grazing lands during the last rainy season from November 2017 to mid-January, which was unseasonably hot and dry. Their hardship makes them resent the rights deeded to the Hadza. "People ask, 'Why are the Hadza—a small number of people—taking a big part of the land?'" Meitaya says. "'Why don't they share the land?'"

A few signs of cooperation have emerged. Three Datoga are working with seven Hadza youth to patrol grazing on Hadza land. "They are cooperating in a peaceful way to make sure there isn't another fight between the Hadza and Datoga," Meitaya says.

But the threat from cattle is not the only force driving the Hadza from their ancestral land. Marina Butovskaya, a physical anthropologist from the Russian Academy of Sciences in Moscow, is stunned at how quickly woodland is being cleared for farming at the edges of Hadza land. "When we arrived there, in 2003, there was only bush, and there were plenty of wild animals," she recalls. "Now, along the road to Mangola, it's fields, fields, fields."

In her 5 months in the Mangola area, between September 2017 and February 2018, new power lines (which allow irrigation equipment) attracted an influx of farmers. They used tractors to clear a swath of land 10 kilometers closer to Hadza land. "You cannot imagine how fast it's going," Butovskaya says.

When the land is cleared, wild animals lose habitat, leaving fewer to hunt. The farmers also cut down wild fruit trees on which the Hadza depend, they told Wood recently. To survive, some Hadza take handouts of maize flour from missionaries or trade meat and honey for flour to make porridge. Or they head to one of a dozen "tourist camps" in the Mangola region, where they earn money by re-enacting their traditional ways. Thanks to a newly improved road, tourists from Ngorongoro Conservation Area, which draws 400,000 people a year, can "bomb down" to see the Hadza in Mangola in 1.5 hours, Peterson says.

RESEARCHERS ARE WELL AWARE of the irony that their research, which made the Hadza famous, also draws tourists, which in turn en-

courages the Tanzanian government to build roads. "If we never studied the Hadza, would they have been better off?" Hawkes wonders.

The tourism has a toxic impact. In the roughly 3 weeks that ecological anthropologist Haruna Yatsuka of Nihon University in Mishima, Japan, was in a tourist camp in Mangola in 2013, 40 tourist parties came from 19 nations. The tourists began arriving at 6 a.m. and watched the Hadza hunt (for show—they seldom got meat when with tourists), dig up tubers, or perform dances. In one camp, Hadza wore baboon skins, which is not their traditional dress but fits tourist expectations, Leach says. The Hadza also got money by selling souvenirs such as bead bracelets, or from tips. "Tourism now brings income to the Hadza and has had a tremendous effect on their livelihood, diet, residence, and nomadic patterns," Yatsuka says.

Nick Blurton-Jones (right) learns about the extensive support Hadza grandmothers give grandchildren as he interviews a great-grandmother (second from left) and her younger kinswoman (second from right) in 1999.

She observed the most destructive impact as soon as the tourists left in midafternoon, when the Hadza used their earnings to buy alcohol. "Everybody drinks: pregnant women, breastfeeding women, the men," says Monika Abels, a developmental psychologist at Tilburg University in the Netherlands, who compared child development between a tourist camp and Hadza bush camps. Sometimes the drinking starts early in the day, the children don't get fed, and drunk men beat women, Abels says.

Blurton-Jones has noted higher rates of alcoholism, disease, and early death for Hadza living in Mangola than in the bush. The Hadza themselves recognize that trend, and complain about being "tired" in camp, Yatsuka says. Turnover is high, as Hadza go into the bush to recover. Yatsuka is now studying how competition to sell souvenirs affects the Hadza's egalitarian culture. What happens when one Hadza woman makes money but another doesn't?

All those changes also affect research. Leach and others must stop data collection when missionaries give Hadza grain or antibiotics. "I think the way some of the recent papers report the situation they're studying is bordering on not very honest," Blurton-Jones says. "They need to tell us how much maize they get, how often do they get alcohol, how often do tourists come."

Others agree: "In my tenure, I've seen dramatic, dramatic change," Berbesque says. "There are Hadza keeping chickens; they have cellphones. It's not necessarily bad … but they are not pristine hunter-gatherers anymore." She has cut back her study of dietary preferences and will not take new students to study the Hadza until more protections are in place. Abels, too, probably will not return.

SOME RESEARCHERS THINK scientists have asked too much of the Hadza. "A woman said to me, 'My body is tired,'" Crittenden says. "'I'm tired giving my hair, my poop, my spit, my urine.'" Crittenden believes researchers now have a duty to their longtime subjects. "The Hadza have been desperately asking researchers to help them," she says, noting that Hadza have approached her at least a dozen times in the past few years for help with political advocacy, land rights, health care, and education.

Most researchers do step up. "You end up doing humanitarian work," Leach says. "I'm buying school clothes for 100 kids."

The top priority is to stop incursions on Hadza land so people who want to hunt and gather can continue to do so. One approach is to engage with local government and others on the Hadza's behalf. For example, Wood spoke with missionaries in 2014 who wanted to drill a well in an area that was "basically the last stand for the Hadza" who live in the bush. He told them a well would draw Datoga to water their cattle and thus harm the Hadza. But intervening carries risks, Wood warns: Evicting the Datoga and others from Hadza land could trigger a backlash.

Wood and other researchers are taking steps to respond to Hadza who increasingly want more say in who studies them and what kinds of studies are done. "What advantage do we get from your study?" Sigwazi asks. "I want to know the results of my poo. Tell us your important results."

Crittenden and Berbesque hope to help the Hadza develop a code of ethics like one unveiled last year by the San people of southern Africa, another intensively studied group. That code requires that the San Council approve and manage research protocols, says Bob Hitchcock, an anthropologist at The University of New Mexico in Albuquerque, who helped the San draft it. But Hitchcock foresees a challenge with the Hadza, who "don't have the same level of representation, the coordinated body" to do this, he says.

Researchers are sharply divided over a code, in part because many think scientists do more good than harm. They note that in 2007, scientists helped organize protests when the Tanzanian government evicted the Hadza from some of their land, proposing to turn it into a private hunting park for the United Arab Emirates's royal family. They also disagree that the Hadza are overstudied, arguing that many teams are there only for a month or so and don't overlap much. "I'm the only researcher in the field right now," Wood says.

As researchers, Hadza, and others consider how best to move forward, they agree on one thing: "It is important that every Hadza individual has the opportunity to choose a lifestyle for themselves," says Woodburn, who at age 84 still returns to camp with Hadza friends every few years. Sigwazi says: "I want to protect the culture of my people so the Hadza can enjoy their life—so they can wake up in the morning and hunt in the bush. It's a simple life, but a kind of wonderful life." ■

PHOTO: ANNETTE WAGNER FROM FILMING OF *TINDIGA—THOSE WHO ARE RUNNING* AND *HADZABE MEANS: US PEOPLE*

INSIGHTS

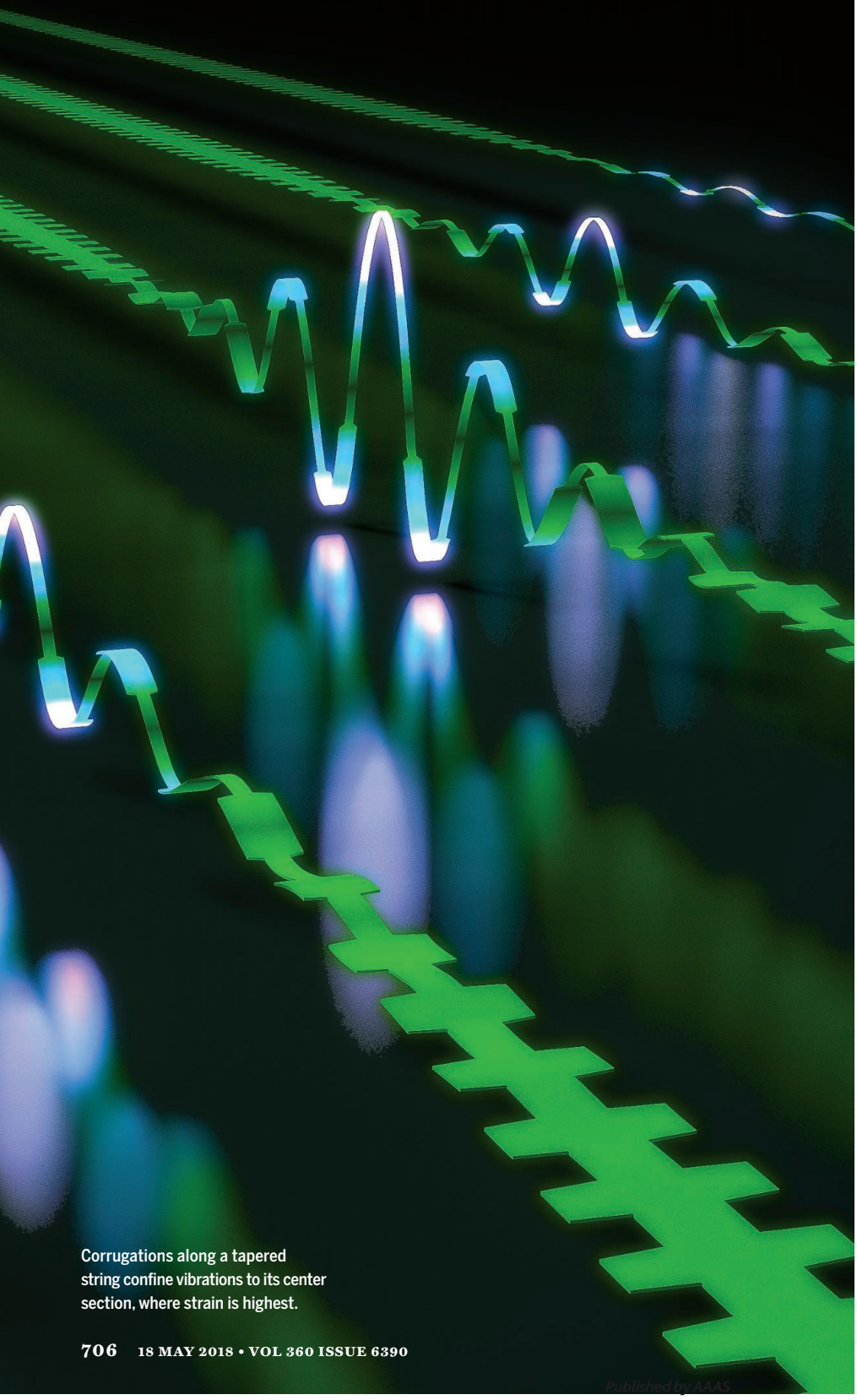

Corrugations along a tapered string confine vibrations to its center section, where strain is highest.

PERSPECTIVES

QUANTUM MATERIALS

Little is lost

Nanostrings can exploit strain engineering for unprecedented mechanical performance

By **Alexander Eichler**

Mechanical engineering is an ancient human craft, yet one that keeps emerging in ever-changing forms. Take the development of musical instruments as an example. Over the course of centuries, instrument makers mastered the selection of materials, geometrical design, and mechanical forces to generate new sounds and enable new musical styles. In recent years, physicists learned to apply similar engineering techniques to nanoscale mechanical resonators. Their efforts yielded immensely useful sensing tools, such as the atomic force microscope (*1*) and resonator devices that could play a decisive role in quantum information technology. On page 764 of this issue, Ghadimi *et al.* (*2*) demonstrate an important step in engineering the performance of such devices to an unprecedented level.

For many applications, the most important characteristic of a resonator is its quality factor Q. Roughly speaking, Q corresponds to the number of oscillations the resonator undergoes before its mechanical energy dampens out. To increase this number, one may either remove processes that cause damping or change the ratio between the energy stored in the resonator and the energy lost per oscillation cycle. Ghadimi *et al.* do both at the same time and achieve a record-high Q value of 400,000,000.

The authors build on previous work with membrane resonators by Tsaturyan *et al.* (*3*), in which a periodic pattern of holes was punched into a thin membrane, leaving only a small center island intact. The hole pattern acted as a shield that suppressed vibrations within a certain range of frequencies. Vibrations on the island interacted only very weakly with the rest of the experimental setup, almost as if they were surrounded completely by vacuum. This engineered isolation removed most of

Department of Physics, ETH Zürich, Otto-Stern-Weg 1, 8093 Zürich, Switzerland. Email: eichlera@phys.ethz.ch

the damping processes and thus increased the *Q* of the island vibrations tremendously. Ghadimi *et al.* implemented the same approach in a string resonator through a series of corrugations.

To push *Q* ever further, the authors used a technique called "damping dilution" (*4*–*6*). Through the application of strain, mechanical tension is generated within the material, and the energy stored in the resonator increases. Think of a skipping rope that you tauten by pulling on both ends—the elastic material stores energy, and the rope swings faster. Importantly, the energy lost per oscillation cycle does not increase by the same amount, so it takes more cycles for the energy to dampen out than it does without the tension. This dilution process effectively increases *Q*.

In contrast to previous work with membranes where strain was applied uniformly, Ghadimi *et al.* realized that the effect of damping dilution can be maximized through nonuniform elastic strain engineering (*7*). They applied the highest strain exactly where it matters, namely, in the central section of the string that hosts the shielded mechanical vibrations. The collocation of the shielded vibrations and the region of highest strain is the central element of the reported success, and it is realized with a surprisingly simple geometry (see the figure).

The result reported by Ghadimi *et al.* is the latest highlight in a tradition of impressive demonstrations with mechanical devices. Functionalized micro- and nanomechanical resonators can respond to almost any physical quantity, be it magnetic, electrical, or optical. In addition, mechanical devices act as bridges between the macroscopic world and microscopic objects. For example, an atomic force microscope cantilever may be visible to the naked eye, yet it scans surfaces with (near-)atomic resolution. Researchers have been fascinated by these attributes for decades. Aided by modern fabrication methods, they developed highly sophisticated mechanical sensors to probe the nanoworld. Today, it is possible to detect nanomechanical vibrations to a precision of a fraction of an atom's size (*8*), measure the magnetic moment of an individual electron (*9*), or discern the mass of a single molecule (*10*, *11*).

It has even become possible to control mechanical devices on the fundamental quantum level, and nanomechanical resonators are envisaged as components in future quantum sensing, communication, and computation architectures (*12*, *13*). In this context, a crucial figure of merit is the so-called "*Q*-times-*f* product," where *f* is the mechanical resonance frequency. This term determines over how many oscillations the resonator faithfully retains quantum information. The work of Ghadimi *et al.* establishes a new record for this number as well, approaching 10^{15} Hz at room temperature. This result means that millimeter-sized mechanical resonators (comprising trillions of atoms) can be used to process single quanta of energy, a truly staggering notion.

Finally, it is interesting to view the present work in the context of "bottom-up" versus "top-down" sensors. The two terms describe opposed approaches to device fabrication. Bottom-up devices are naturally small objects like carbon nanotubes, semiconducting nanowires, nanoparticles, or graphene sheets. Such devices are grown from basic materials and have exceptionally low masses, which makes them very sensitive but also hard to manipulate. Top-down devices are patterned out of bulk material and provide much more freedom for design. However, because materials cannot be carved or etched with atomic precision, top-down devices are larger than their grown counterparts and are inherently less sensitive. To some degree, this drawback can be compensated through high *Q* factors and extreme aspect ratios. Indeed, Ghadimi *et al.* find that their device, a string several millimeters long, offers a force sensitivity approaching that of single carbon nanotubes, which are about 100,000 times lighter (*14*).

We are now witnessing an era of unprecedented understanding and control of nanomechanics, with a view toward many new applications. Experimental prototypes have already demonstrated the potential for revolutionary new sensors. Future nanofabrication techniques and engineering feats will hopefully enable us to bring such applications into the realm of everyday life—with mechanical devices that even the master instrument builders of past centuries would have regarded with wonder. ■

REFERENCES

1. G. Binnig, C. F. Quate, C. Gerber, *Phys. Rev. Lett.* **56**, 930 (1986).
2. A. H. Ghadimi *et al.*, *Science* **360**, 764 (2018).
3. Y. Tsaturyan, A. Barg, E. S. Polzik, A. Schliesser, *Nat. Nanotechnol.* **12**, 776 (2017).
4. G. I. González, P. R. Saulson, *J. Acoust. Soc. Am.* **96**, 207 (1994).
5. Q. P. Unterreithmeier, T. Faust, J. P. Kotthaus, *Phys. Rev. Lett.* **105**, 027205 (2010).
6. S. Schmid, K. D. Jensen, K. H. Nielsen, A. Boisen, *Phys. Rev. B* **84**, 165307 (2011).
7. R. Zhang *et al.*, *App. Phys. Lett.* **107**, 131110 (2015).
8. J. D. Teufel, T. Donner, M. A. Castellanos-Beltran, J. W. Harlow, K. W. Lehnert, *Nat. Nanotechnol.* **4**, 820 (2009).
9. D. Rugar, R. Budakian, H. J. Mamin, B. W. Chui, *Nature* **430**, 329 (2004).
10. M. S. Hanay *et al.*, *Nat. Nanotechnol.* **7**, 602 (2012).
11. J. Chaste *et al.*, *Nat. Nanotechnol.* **7**, 301 (2012).
12. C. L. Degen, F. Reinhard, P. Cappellaro, *Rev. Mod. Phys.* **89**, 035002 (2017).
13. M. Aspelmeyer, T. J. Kippenberg, F. Marquardt, *Rev. Mod. Phys.* **86**, 1391 (2014).
14. J. Moser *et al.*, *Nat. Nanotechnol.* **8**, 493 (2013).

10.1126/science.aat1983

ENERGY STORAGE

Chemical storage of renewable energy

A stable electrochemical cell selectively produces ethylene from carbon dioxide

By **Joel W. Ager**[1] *and* **Alexei A. Lapkin**[2]

The conversion of carbon dioxide (CO_2) into fuels and chemicals using renewable energy is a potential pathway to mitigate increasing CO_2 concentration in the atmosphere and acidification of the oceans (*1*). In a process that is essentially the reverse of combustion and is analogous to photosynthesis, CO_2 can be electrochemically reduced to hydrocarbons by using renewable power sources such as wind and solar (*2*). This process would not compete with direct use of renewable energy as electricity, as the objective is to store excess energy for later use. On page 783 of this issue, Dinh *et al.* (*3*) show that ethylene can be generated selectively via electrochemical CO_2 reduction at rates that could yield a technologically feasible process.

The thermodynamics of reducing CO_2 are similar to those of splitting water into hydrogen and oxygen, which has been done commercially with an energetic efficiency as high as 80% (*4*). However, CO_2 reduction is considerably more challenging because of the unreactive nature of the CO_2 molecule and the demands of controlling multiple electron and proton transfer events (12, in the case of ethylene) on the surface of the electrocatalyst. Copper catalysts bind carbon monoxide (CO) and other reaction intermediates in such a way as to produce two-carbon products such as ethylene and ethanol (*5*). However, it has been difficult to steer the reaction toward any one product. Moreover, most experimental studies provide CO_2 to the electrode from aqueous solution, where its finite

[1]*Joint Center for Artificial Photosynthesis and Materials Sciences Division, Lawrence Berkeley National Laboratory and Department of Materials Science and Engineering, University of California, Berkeley, Berkeley, CA 94720, USA.* [2]*Department of Chemical Engineering and Biotechnology, University of Cambridge, Cambridge CB3 0AS, UK. Email: jwager@lbl.gov; aal35@cam.ac.uk*

Efficient conversion

Dinh *et al*. show that the use of very thin copper-catalyst layers in a gas diffusion electrode leads to efficient and selective electrochemical conversion of CO_2 to ethylene. Such a process could help to mitigate rising atmospheric CO_2 concentrations if the energy required for the conversion comes from renewable sources.

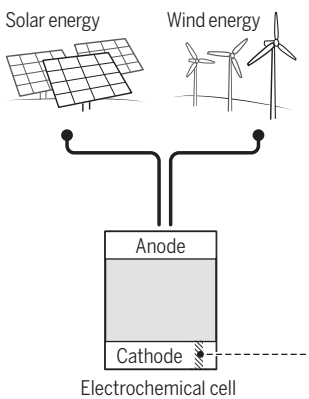

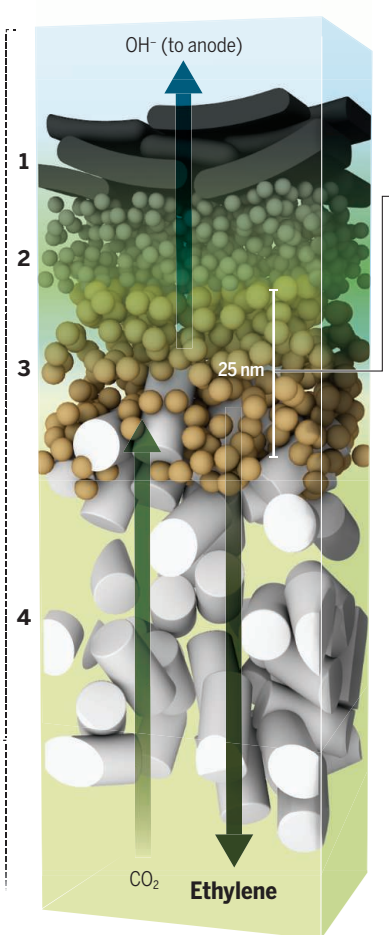

A stable and efficient system
Collocation of the catalyst layer and high concentrations of CO_2 and OH^- in a thin 25-nm layer lead to improvements in the conversion efficiency and selectivity for ethylene production. The use of base-stable PTFE for the porous gas transport layer enables continuous operation for 100 hours.

Gas diffusion electrode
1 Graphite
2 Carbon nanoparticles
3 Copper nanoparticles
4 Gas-porous PTFE

solubility leads to an upper, diffusion-limited current density of a few tens of milliamperes per square centimeter—far below what would be commercially relevant.

A breakthrough in efficiency can be achieved through intensification of mass transfer within the process. Process intensification is a chemical engineering approach that can achieve manyfold increases in product throughput by eliminating mass and energy transport limitations and exploiting potential synergies, such as combining multiple functions (for example, reaction and separation) (*6*). Use of a gas diffusion electrode similar to those in fuel cells can greatly reduce the mass-transfer constraint for CO_2 and has enabled current densities above 500 mA/cm² for formation of one-carbon products such as CO (*7*). However, careful management of the gas phase CO_2, liquid electrolyte, and solid electrocatalyst is required to maintain selectivity and minimize parasitic reactions such as water reduction.

Higher pH conditions can increase the yield of two-carbon products (*8*), but CO_2 itself is acidic, setting an upper limit to the pH attainable in a conventional experiment. Dinh *et al*. show that very high hydroxide (OH^-) concentrations can be maintained at the catalyst surface, provided that the electrochemical conversion is faster than the homogeneous reaction of CO_2 with OH^- to form bicarbonate. An optimal balance between these competing processes is attained through the use of very thin (~25 nm) Cu-catalyst layers deposited on the gas diffusion electrode (see the figure). The collocation of the electrocatalyst and high CO_2 and OH^- concentrations led to about 70% current efficiency to ethylene at current densities up to 750 mA/cm². When the authors used thicker catalyst layers (for example, 100 nm), a region of lower OH^- concentration formed, resulting in lower selectivity for ethylene.

To be economically viable, the process would need to operate continuously. Dinh *et al*. found that the highly basic conditions required to enhance ethylene yield led to deterioration of the carbon-based electrode material within an hour. As an alternative, they designed and implemented a gas diffusion electrode consisting of base-stable polytetrafluoroethylene (PTFE), with copper nanoparticles as the catalyst and carbon nanoparticles and graphite providing electrical contact. Use of this electrode led to a lower current density (~300 mA/cm²), but it was stable for 100 hours.

A full electrochemical CO_2-reduction system must also oxidize water to oxygen at the anode for sustained operation. Dinh *et al*. performed such a full-cell experiment, using a nickel iron oxide ($NiFeO_x$) to catalyze the oxygen-evolution reaction at the anode. They measured a full-cell energy conversion efficiency, which captures all losses (overpotentials at the cathode and anode and electrical resistance of the electrolyte), of 34%. This value is lower than the 60 to 80% achieved for water splitting but is comparable to CO_2-reduction cells, which make one-carbon products such as CO or formate and have lower cathode overpotentials (*9*).

Although the work of Dinh *et al*. is an important step toward chemical storage of renewable energy, challenges remain. Their reactor, and indeed nearly all CO_2-reduction reactors in the literature, makes products which are either entrained in the CO_2 stream or dissolved in the electrolyte, leaving product separation as an unsolved challenge (*10*).

There is a lively discussion in the literature regarding the prospective economics of electrochemical CO_2 reduction (*11*). Although there is consensus that a carbon tax would be required to provide an incentive for CO_2 conversion, opinions diverge on the economic viability of the conversion targets (such as CO and/or syngas, ethylene, and ethanol). Benchmark demonstrations such as that of Dinh *et al*. can be used to focus the discussion.

The products of electrochemical CO_2 reduction are simpler than those of natural photosynthesis, yet they are the most ambitious targets of preparative electrosynthetic chemistry; most work over the past 100 years or more has focused on simpler transformations involving far fewer electron transfers (*12*). Demonstrations such as that of Dinh *et al*., combined with increasing understanding of the mechanism, could lead to a commercially viable electrochemical CO_2-reduction process for mitigating rising atmospheric CO_2 concentrations and promoting the use of renewable energy. ■

REFERENCES

1. C. Graves, S. D. Ebbesen, M. Mogensen, K. S. Lackner, *Renew. Sustain. Energy Rev.* **15**, 1 (2011).
2. J. Qiao, Y. Liu, F. Hong, J. Zhang, *Chem. Soc. Rev.* **43**, 631 (2014).
3. C.-T. Dinh *et al*., *Science* **360**, 783 (2018).
4. A. Ursua, L. M. Gandia, P. Sanchis, *Proc. IEEE* **100**, 410 (2012).
5. X. Liu, J. Xiao, H. Peng, X. Hong, K. Chan, J. K. Nørskov, *Nat. Comm.* **8**, 15438 (2017).
6. A. I. Stankiewicz, J. A. Moulijn, *Chem. Eng. Prog.* **96**, 22 (2000).
7. S. Verma, X. Lu, S. Ma, R. I. Masel, P. J. A. Kenis, *Phys. Chem. Chem. Phys.* **18**, 7075 (2016).
8. K. J. P. Schouten, E. Pérez Gallent, M. T. M. Koper, *J. Electroanal. Chem.* **716**, 53 (2014).
9. D. T. Whipple, P. J. A. Kenis, *J. Phys. Chem. Lett.* **1**, 3451 (2010).
10. J. B. Greenblatt, D. J. Miller, J. W. Ager, F. A. Houle, I. D. Sharp, *Joule* **2**, 381 (2018).
11. J. M. Spurgeon, B. Kumar, *Energy Env. Sci.* 10.1039/C8EE00097B (2018).
12. H. Lund, *J. Electrochem. Soc.* **149**, S21 (2002).

10.1126/science.aat7918

GRAPHIC: V. ALTOUNIAN/*SCIENCE*

NEPHROLOGY

Mapping kidney cellular complexity

Simplifying complexity identifies cellular drivers of kidney disease

By **Benjamin D. Humphreys**

The prevalence of kidney disease in the United States is ~14%, with more than 600,000 patients with kidney failure. Despite the large and growing need for new therapies to treat kidney disease, few have been developed over the past two decades. The kidney's cellular complexity is partly to blame—its functional unit, the nephron, is composed of at least 13 different epithelial cell types, surrounded by an even larger array of supporting vascular, stromal, and immune cells. In disease states, various invading leukocytes and reactive parenchymal cell states further complicate the cellular landscape, making attempts to understand pathophysiology and identify therapeutic targets difficult. However, the advent of massively parallel single-cell RNA sequencing (scRNA-seq) is transforming our understanding of cellular diversity, offering an unbiased approach to profile not only complex tissues but entire organisms (*1, 2*). On page 758 of this issue, Park *et al.* (*3*) apply scRNA-seq to develop the first comprehensive gene expression atlas of the mouse kidney, use innovative analyses to transcriptionally characterize known cell types, and identify a new progenitor cell type. They also map the expression of monogenic and complex trait disease-associated genes to specific kidney cell types, providing new insight about cell types driving many kidney diseases.

Park *et al.* generated nearly 60,000 single-cell transcriptomes from adult mouse kidney and resolved them into 21 cell types based on unique transcriptional profiles. These include expected cell types—nine epithelial, three endothelial, one fibroblast, and five immune cell types—as well as three previously undescribed cell types. The authors mapped expression of human monogenic kidney disease genes onto cell types from their mouse data set. Proteinuria is a common manifestation of kidney disease, for example, and nearly all genes associated with inherited proteinuria were expressed only in podocytes. This is an epithelial cell type located in the glomerulus that helps to form the filtration barrier (*4*). Similarly, nearly all monogenic genes associated with blood pressure map to the distal parts of the nephron—segments that fine-tune sodium balance in the blood. These results validate scRNA-seq as a method to infer the cellular drivers of disease.

Diseases caused by alterations in single genes are relatively rare; most human genetic traits are complex, resulting from variation in multiple genes. Genome-wide association studies have identified thousands of disease-associated single-nucleotide polymorphisms (SNPs). Although most of these are noncoding and any individual SNP contributes only a small increased risk of disease, they often have large effects on gene expression (called expression quantitative trait loci, eQTL) that are usually cell-type specific (*5*). Understanding which cells express a particular gene with a disease-associated SNP can help to identify cellular drivers for complex traits. Using the same approach as with monogenic kidney disease genes, the authors mapped the expression of complex trait genes and found again that they were expressed in only single kidney cell types. The importance of this result is that the authors have illuminated potential cellular drivers of disease susceptibility—enabling hypothesis generation concerning the mechanism of action of genetic variants associated with disease and more accurate disease modeling.

By characterizing cell types in an unbiased fashion, scRNA-seq can identify new cell types. Park *et al.* characterized one of the new cell types identified in the collecting duct. This transitional cell type expressed markers for intercalated cells (which secrete acid and base) and principal cells (which regulate the sodium, potassium, and water content of urine) (see the figure). Because it was transcriptionally an intermediate cell type, the authors hypothesized that it may represent a cell transitioning from an intercalated to a principal cell, or vice versa. Although long-standing observations have suggested a lineage relationship between different intercalated cell subtypes (*6*), the idea that principal and intercalated cell types interconvert in adult kidney has less support (*7*).

Using a genetic lineage tracing strategy and immunostaining, Park *et al.* provide convincing evidence that the transitional population is present in adult mouse kidney. Prior results (*8*), coupled with an analysis of gene expression changes over the trajectory between intercalated to principal cell, implicated the Notch pathway in regulating this interconversion. By inducing expression of the Notch intracellular domain (which induces gene expression changes) in adult collecting ducts, the authors could shift the balance toward a principal cell fate and away from an

Interconversion of principal and intercalated cells

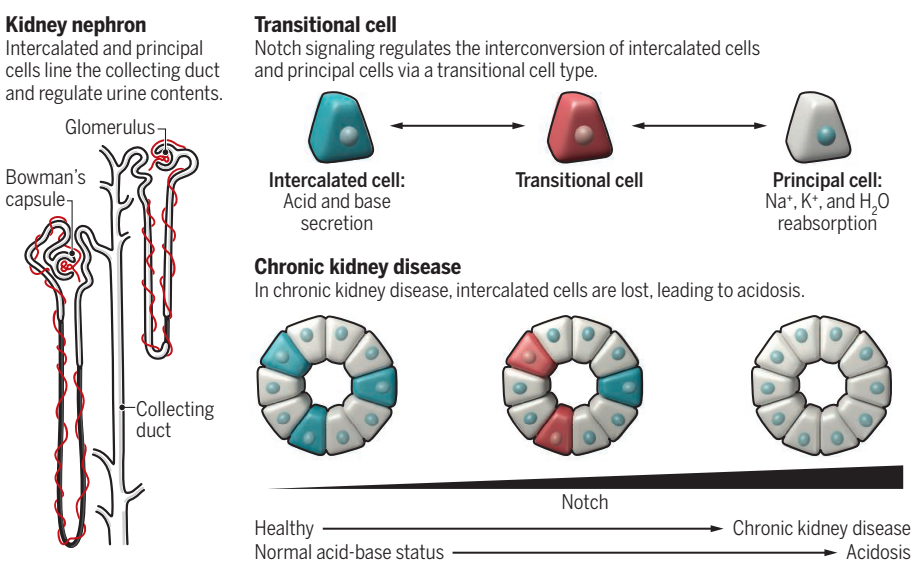

GRAPHIC: A. KITTERMAN/*SCIENCE*

Division of Nephrology, Washington University School of Medicine, St. Louis, MO 63110, USA. Email: humphreysbd@wustl.edu

intercalated cell fate. The transcription factor TFCP2L1 (transcription factor CP2-like 1) is a regulator of intercalated and principal cell specification via Notch signaling, further supporting the importance of this pathway in regulating collecting duct cell plasticity (*9*). A similar shift toward principal cells was observed in a mouse model of chronic kidney disease. By deconvoluting bulk transcriptional data from human kidneys with chronic kidney disease, they demonstrated increased principal and decreased intercalated cells, although they could not ascertain whether disrupted Notch signaling was involved. The authors propose that these results provide a molecular foundation for understanding the metabolic acidosis that accompanies chronic kidney disease, because loss of intercalated cells (through conversion to principal cells) impairs acid secretory capacity.

With reduced sequencing cost and commercialized workflows available, scRNA-seq will play an increasing role in understanding the cellular basis of kidney function as well as individual cell types driving disease that represent therapeutic targets. A future application of scRNA-seq is in defining the cellular complexity of kidney disease. In acute and chronic kidney diseases, the histologic appearance of tissue fibrosis can appear similar regardless of the root cause. For large diagnostic categories such as diabetic nephropathy or chronic kidney disease, it is almost certain that subphenotypes exist, but current diagnostic approaches lack the sensitivity to distinguish them (*10, 11*). A good example is the discovery that two variants in the gene encoding apolipoprotein L1 are responsible for the majority of end-stage renal disease in African Americans, and not simply hypertension, as was previously assumed (*12*).

Park *et al.* provide a powerful step toward a comprehensive understanding of the cellular basis for kidney homeostasis and disease, demonstrating the feasibility of scRNA-seq to unravel kidney complexity. ■

REFERENCES AND NOTES

1. C. Trapnell, *Genome Res.* **25**, 1491 (2015).
2. X. Han *et al.*, *Cell* **172**, 1091 (2018).
3. J. Park *et al.*, *Science* **360**, 758 (2018).
4. E. Machuca *et al.*, *Hum. Mol. Genet.* **18**, R185 (2009).
5. M. G. P. van der Wijst *et al.*, *Nat. Genet.* **50**, 493 (2018).
6. Q. Al-Awqati, *Am. J. Physiol.* **270**, C1571 (1996).
7. F. Trepiccione *et al.*, *Am. J. Physiol. Renal Physiol.* **305**, F919 (2013).
8. H.-W. Jeong *et al.*, *J. Clin. Invest.* **119**, 3290 (2009).
9. M. Werth *et al.*, *eLife* **6**, e24265 (2017).
10. A. F. Malone *et al.*, *Semin. Nephrol.* **38**, 31 (2018).
11. K. Ho, A. J. McKnight, *Adv. Chronic Kidney Dis.* **21**, 256 (2014).
12. D. J. Friedman, M. R. Pollak, *Trends Endocrinol. Metab.* **27**, 204 (2016).

ACKNOWLEDGMENTS

Work in the Humphreys lab is supported by grants from the U.S. National Institutes of Health and the Chan Zuckerberg Initiative.

10.1126/science.aat7271

METABOLISM

Ribosomes on the night shift

The universal protein-making machine becomes a nutrient source between meals

By **Michel Nofal** *and* **Joshua D. Rabinowitz**

From an evolutionary perspective, life involves two simple goals: survival and reproduction. But these goals are fundamentally at odds. Reproduction depends on growth, but attempts to grow when nutrients are scarce can jeopardize survival. In cells, growth is accomplished in large part by ribosomes, huge RNA-protein machines that translate nucleic acid messages into protein, the main biochemical constituent of cells. In nutrient-rich conditions, cells can be filled with ribosomes; they comprise more than a third of total biomass in rapidly growing *Escherichia coli* (*1*). But what happens to ribosomes when nutrient levels decline, as occurs sporadically in microbes and nightly in sleeping humans? Biosynthesis subsides, and ribosomes now serve as a reservoir of nutrients. Building on recent progress probing the regulation of protein synthesis and degradation from Gu *et al.* (*2*) and Abu-Remaileh *et al.* (*3*), on page 751 of this issue, Wyant *et al.* (*4*) elucidate a pathway in which ribosomes are selectively digested, promoting survival in starved cells.

Eukaryotic cells, from yeast to humans, can gobble up parts of their interior through a process called autophagy, encapsulating them in double membranes and forming an enclosed compartment known as an autophagosome. Autophagosomes then deliver their contents to the degradative compartment (lysosomes), where macromolecules are recycled into monomeric nutrients (*5*).

Autophagy was initially thought to be a nonspecific process, but it has become increasingly clear that cells can pick and choose what to digest in this manner. For example, defective mitochondria are detected and marked for autophagy through a system involving the proteins PINK1 (PTEN-induced putative kinase protein 1) and Parkin (*6*). In nutrient-poor conditions, however, mitochondria are valuable—they provide the most efficient way to generate energy from carbon—whereas ribosomes are no longer needed in large numbers to fuel biosynthesis. These dispensable ribosomes can be selectively degraded through ribophagy, autophagy of ribosomes.

How do cells balance growth and survival? The mammalian target of rapamycin complex 1 (mTORC1) kinase has emerged as an important regulator of this balance. When conditions are favorable for growth, mTORC1 stimulates the synthesis of all major biomaterials in cells, especially ribosomes, while suppressing autophagy. If growth conditions are poor—for example, during periods of starvation—mTORC1 is inactive, and autophagy proceeds.

To decide whether or not growth is appropriate, mTORC1 must sense and integrate a diverse set of environmental cues. One of these cues is amino acid availability. Cells must be well-stocked with amino acids, which are needed to make protein, in order to grow. Amino acids within the cytosol promote translocation of mTORC1 to the surface of the lysosome, where its activator, a small guanosine triphosphatase (GTPase) called RHEB (Ras homolog enriched in brain), resides (*7, 8*). Numerous specific amino acid–sensing proteins have been characterized. These include the Sestrin and CASTOR (cytosolic arginine sensor for mTORC1) families of proteins, which sense leucine and arginine, respectively (*9, 10*). Gu *et al.* added to this list when they identified SAMTOR [*S*-adenosylmethionine (SAM) sensor upstream of mTORC1], which indirectly senses the essential amino acid methionine by binding to SAM.

Why does the lysosome, which degrades macromolecules, play such a central role in the regulation of mTORC1, which promotes the construction of macromolecules? Accumulating evidence suggests that mTORC1 preferentially senses nutrients that are generated in the lysosome. Perhaps by sensing the products of degradation, mTORC1 can assess whether catabolic processes have generated enough nutrients.

This reasoning assumes that lysosomes differ from the rest of the cell not only in acidity and protein content but also in metabolite content. However, most methods for lysosomal purification involve ultracentrifugation in sucrose gradients for several hours, during which time metabolites have likely reacted or escaped and weakly associated lysosomal proteins have disassociated. Abu-Remaileh *et al.* reported a method for the rapid

Department of Chemistry and Lewis-Sigler Institute, Princeton University, Princeton, NJ, USA.
Email: joshr@genomics.princeton.edu

isolation of lysosomes, called LysoIP. Cells are genetically engineered to express a protein tag on lysosomal membranes. Magnetic beads linked to antibodies specific for the tag are added to lysed cells, and lysosomes are purified magnetically. This method has enabled systematic analysis of the metabolite content of lysosomes for the first time.

Using LysoIP, the authors compared the cytosolic and lysosomal concentrations of numerous metabolites. In cells grown in amino acid–rich conditions, metabolite levels were generally similar in both compartments, but upon impairment of the vacuolar adenosine triphosphatase (V-ATPase), which acidifies the lysosome, the lumenal concentrations of a large number of metabolites increased. These metabolites included most nonessential amino acids, which are apparently released from lysosomes in a proton-dependent manner. The lysosomal levels of most essential amino acids, however, did not change, suggesting their regulation by another factor.

A series of elegant experiments revealed that mTORC1 promotes the efflux from lysosomes of most essential amino acids, including leucine. Efflux is mediated by a lysosomal membrane protein called SLC38A9 (sodium-coupled neutral amino acid transporter 9). In amino acid–poor conditions, leucine transport out of lysosomes is required to activate mTORC1 (*11*). Taken together, these data suggest a paradox: mTORC1 activity induces SLC38A9-mediated efflux of leucine out of lysosomes, but mTORC1 remains inactive until leucine leaves the lysosome.

SLC38A9 has another important function, which may explain this paradox: Upon binding to the nonessential amino acid arginine in the lysosomal lumen, SLC38A9 helps to activate mTORC1. Thus, when amino acid levels accumulate in lysosomes, mTORC1 may initially become partially activated by SLC38A9. In this scenario, mTORC1 subsequently induces SLC38A9-mediated amino acid efflux from lysosomes. Last, effluxed leucine can augment mTORC1 activation. In other words, SLC38A9 may be at the center of a feed-forward loop in which nutrients derived from lysosomal catabolism activate mTORC1 only after accumulating above a threshold (see the figure).

Ribosomes as a source of nutrients

After meals, when nutrient amounts are high, ribosomes produce proteins. When nutrient intake stops—for example, during sleep—amino acid concentrations drop, which inactivates mTORC1. This triggers binding of NUFIP1 to ribosomes, leading to their recycling via ribophagy.

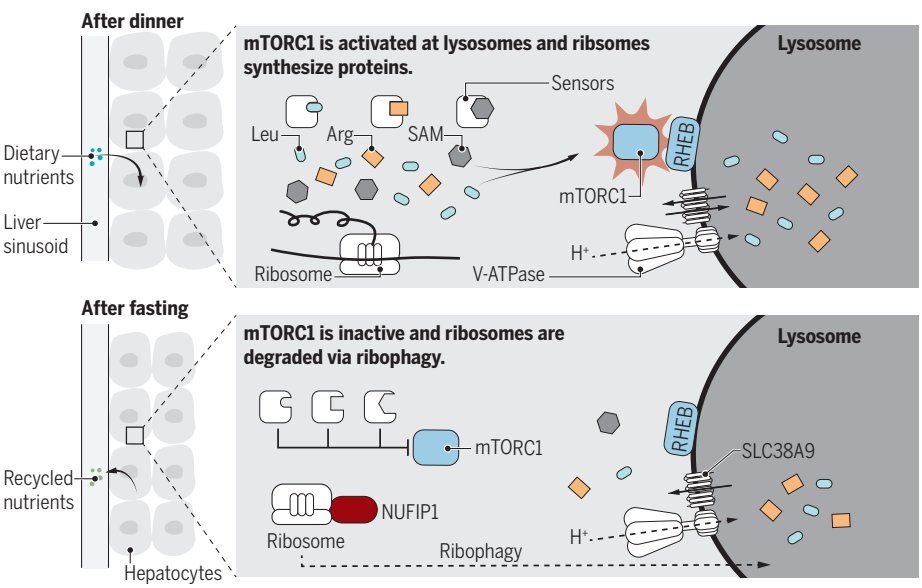

Why might SLC38A9 sense lysosomal arginine levels? Perhaps mTORC1 evolved to sense the degradation of proteins rich in arginine. One class of proteins stands out as arginine-rich: ribosomal proteins. These proteins contain high amounts of arginine and lysine, the positive charges of which help to bind the negatively charged phosphate backbone of ribosomal RNA.

How are ribosomes selectively delivered to lysosomes? Wyant *et al.* applied quantitative proteomics to identify proteins that increase their association with lysosomes in nutrient-starved cells. NUFIP1 (nuclear fragile X mental retardation–interacting protein 1), which has a previously annotated role in the nucleus, was found at higher concentrations in lysosomes of cells deprived of glucose and amino acids. The authors then showed that NUFIP1 binds to ribosomes when mTORC1 is inactive and delivers these ribosomes to autophagosomes for degradation.

Ribosomes are arguably the most important biochemical machine. But the importance of translation has overshadowed the role ribosomes can play as a nutrient source. By elucidating the function of NUFIP1, Wyant *et al.* provide a genetic handle with which to specifically probe the importance of ribosomes as nutrients. Indeed, genetic loss of NUFIP1 (that is, the inability to use ribosomes as nutrients) impairs survival of cells starved of glucose and amino acids.

Although it is easy to induce starvation of mammalian cells experimentally in a culture dish, cells in vivo are never exposed to glucose-free, amino acid–free environments. Rather, they are bathed in a steady stream of circulating nutrients. What prevents this stream from running dry? During extended periods between meals, macromolecules must be degraded. Proteins are depots of amino acids; glycogen is a depot of sugar. Ribosomes specifically are depots of amino acids, sugar, and nucleobases and as such can support diverse metabolic activity. A recent report showed that in mice, liver size and ribosome content oscillate with the diurnal cycle, increasing while the animals are awake (and eating at will) then gradually falling during sleep (*12*). Thus, after meals the liver fills with ribosomes. For a time, these ribosomes perform their canonical role: using ingested amino acids to make protein. But as nutrient levels drop, these ribosomes, via ribophagy, are recycled into nutrients for the rest of the body. These findings have not been validated in humans, but they raise intriguing possibilities. Whereas intact ribosomes are essential for diverse anabolic functions—protein synthesis is required for long-term memory formation (*13*)—degraded ribosomes may maintain nutrient levels as we sleep. Perhaps they quite literally fuel our dreams. Food for thought. ■

GRAPHIC: N. DESAI/*SCIENCE*

REFERENCES

1. M. Scott *et al.*, *Science* **330**, 1099 (2010).
2. X. Gu *et al. Science* **358**, 813 (2017).
3. M. Abu-Remaileh *et al., Science* **358**, 807 (2017).
4. G. A. Wyant *et al.*, *Science* **360**, 751 (2018).
5. M. Tsukada *et al.*, *FEBS Lett.* **333**, 169 (1993).
6. S. Geisler *et al.*, *Nat. Cell Biol.* **12**, 119 (2010).
7. Y. Sancak *et al.*, *Cell* **141**, 290 (2010).
8. C. Buerger *et al.*, *Biochem. Biophys. Res. Commun.* **344**, 869 (2006).
9. R. Wolfson *et al., Science* **351**, 43 (2015).
10. L. Chantranupong *et al., Cell* **165**, 153 (2016).
11. G. A. Wyant *et al.*, *Cell* **171**, 642 (2017).
12. F. Sinturel *et al.*, *Cell* **169**, 651 (2017).
13. H. P. Davis *et al.*, *Psychol. Bull.* **96**, 518 (1984).

10.1126/science.aat7121

MATERIALS SCIENCE

How to achieve a successful biaxial marriage

Coupling between organic and inorganic components results in a biaxial liquid crystal

By **Philippe Poulin**

Matter is generally divided into three states, namely solid, liquid, and gas. Liquid crystals form a fourth state of matter; they combine properties of liquids, such as fluidity and the ability to flow, with properties of crystalline solids, such as structural order and specific optical and electric properties. This unique combination makes liquid crystals valuable for numerous electro-optical applications, for example, in displays, cell phones, and televisions. They are also often found in living systems, for example in cell membranes made of phospholipids and in chromosomal DNA. On page 768 of this issue, Mundoor *et al.* (*1*) report a new class of liquid crystals made of long inorganic nanorods that are oriented in a perpendicular direction to the small organic molecules in which they are embedded.

Not all molecules or particles can reach the fourth state of matter. Liquid crystals are made of components—usually disks or rodlike molecules—that are anisotropic in shape. When the disks or rods are oriented along a single similar direction, but remain randomly positioned in space, they form a nematic phase. The nematic phase can have high fluidity and is often viewed as the simplest liquid crystalline phase. It is of great technological importance, because most electro-optical applications are based on nematic liquid crystals.

The ordering of a nematic phase made solely of disks or rods can be specified by a single direction and therefore forms a uniaxial system. A more complex situation would occur if the building blocks were in the shape of, for example, a parallelepiped (see the figure). In this case, the material should form a biaxial phase, because the orientation of the boardlike molecules themselves can be specified by two axes. A biaxial nematic phase can in principle also be obtained by mixing disks and rods (see the figure). Biaxial nematics are expected to have useful properties, including fast switching speeds in potential electro-optical applications and to serve as models for studying fundamental questions about defects and topology.

Because of their expected properties and potential technological interest, biaxial nematic phases have been the topic of extensive research—and controversy—for several decades (*2*). Yet, their experimental realization remains challenging. Disks and rods tend to phase separate, making it difficult or impossible to form biaxial phases by this approach. The use of boardlike molecules that adopt biaxial ordering has been the topic of controversies, with claims of biaxiality by some contradicted by others (*2*). The most encouraging results have been obtained with bent-core molecules and with some liquid-crystal polymers (*2*). The quest for biaxial nematics thus remains an open and exciting challenge.

Mundoor *et al.* report a strategy for making biaxial nematics that involves mixing inorganic nanorods and rodlike organic molecules. This approach differs from previous studies, which typically used mixtures of particles with different shapes or molecules with complex structures. In contrast, the particles in the authors' mixture have the same simple shape, but differ in size. The rodlike organic molecules are about 2 nm long, whereas the inorganic nanorods are about 1 μm (1000 nm) in length. On their own, the nanorods and the rodlike molecules can form uniaxial nematics. By controlling the chemistry of the nanorods, Mundoor *et al.* achieve their homogeneous dispersion and stabilization in the liquid crystal made of the rodlike organic molecules. In a well-defined concentration regime, the orientation of the nanorods is spontaneously orthogonal to that of the organic molecules (see the figure). This mixture thus forms a biaxial nematic liquid crystal.

The beauty of this achievement lies in the delicate control of the interactions between the nanorods and the organic molecules. If the interactions between them are too weak, the orientation of the nanorods and of the molecules would not be correlated. If the interactions are too strong, they would phase-separate and form other structures (*3*). By finely controlling the chemistry of the nanorods, Mundoor *et al.* have found the right balance to achieve a well-organized coupling of the inorganic and organic components. Because of this coupling, the nanorods disturb the ordering of the small molecules slightly, thereby making the liquid crystal state a bit less stable when heated. Thus, the small mol-

Centre de Recherche Paul Pascal – CNRS, University of Bordeaux, Avenue Schweitzer, 33600 Pessac, France. Email: poulin@crpp-bordeaux.cnrs.fr

How to make a biaxial nematic

Previous efforts to make biaxial nematics with either boardlike molecules or component mixtures have had limited success. Mundoor *et al.* used a different strategy to create a biaxial nematic by tuning the interactions between long inorganic nanorods and short organic molecules.

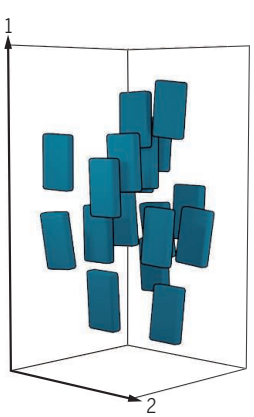

Boardlike molecules
Whether these molecules can adopt biaxial ordering remains controversial.

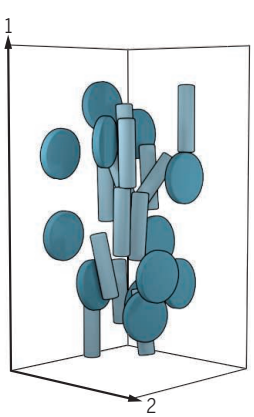

Disk- and rodlike components
Mixtures of similarly sized disk- and rod-shaped molecules tend to phase separate.

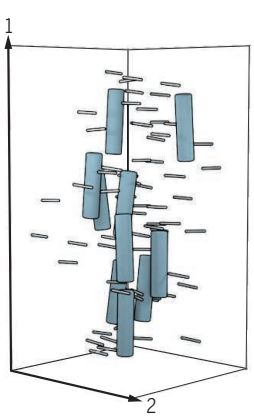

Hybrid mixture
Weak coupling between different components results in biaxial ordering.

GRAPHIC: V. ALTOUNIAN/*SCIENCE*

ecules must be cooled down a bit more to induce their transition from the isotropic to the nematic phase (*4*).

The authors convincingly characterize the materials with several optical methods. The results show that the biaxial nematic is not a simple superposition of two uniaxial nematics. Anisotropic interactions induce a biaxial orientation distribution of the nanorods, which in turn induce biaxility in the distribution of the organic molecules. Thus, the properties of the hybrid materials are even richer than would be expected from a simple superposition of uniaxial nematics. Furthermore, the present approach allows the use of organic liquid crystals with rather simple organic molecules, making it easier to control their stability and their temperature transitions and to make them suitable for applications. It would be more difficult to control and tune the thermodynamic properties of molecules and polymers with complex structures such as those that have been used in the past to make biaxial nematics.

"The beauty of this achievement lies in the delicate control of the interactions between the nanorods and the organic molecules [in the biaxial liquid crystal]."

Mundoor *et al.*'s study opens the door for a range of novel nematic liquid crystals. As demonstrated by the authors, the key is to achieve moderate coupling between the inorganic inclusions and the organic host. Tuning this coupling could lead to other states; following simple theoretical expectations (*4*), it may be possible to expect coexistence of nematic phases and even critical phase transitions. Use of other shapes, such as disks, boards, and chiral species, could further enrich this class of hybrid materials. The optical properties and response to external fields of these hybrid may form the basis for future applications in which the functionalities of organic and inorganic materials are combined. ■

REFERENCES

1. H. Mundoor *et al.*, *Science* **360**, 768 (2018).
2. C. Tschierske, D. J. Photinos, *J. Mater. Chem.* **20**, 4263 (2010).
3. I. Muševič, *Materials* **11**, 24 (2018).
4. P. Poulin, V. Raghunathan, P. Richetti, D. Roux, *J. Phys. II France* **4**, 1557 (1994).

10.1126/science.aat7399

TRANSCRIPTION

BRD4 and MYC—clarifying regulatory specificity

A study dissects the primary function of cancer-associated transcription factors

By **Arianna Sabò** *and* **Bruno Amati**

The transcriptional output of cells is governed by the interplay among sequence-specific transcription factors (TFs), epigenetic DNA and chromatin modifications, and their writers, readers, and erasers, along with the basal transcriptional machinery and RNA polymerase II (Pol2). Assessing the contribution of individual factors to specific transcriptional programs is an essential albeit elusive goal, as exemplified by studies of the chromatin-associated factor BRD4 (a BET family member) (*1*) or the oncogenic TF MYC (*2*). BET proteins interact with acetylated histones in active regulatory domains (promoters and enhancers) and promote Pol2 activity. Despite the general nature of this mechanism, BET inhibitors (BETis) have shown selective effects on gene expression—in particular, suppression of *MYC* and other oncogenes in tumor cells (*1*). MYC is a sequence-specific DNA-binding protein that has been proposed to function either as a selective regulator (*2*–*4*) or as a general activator ("amplifier") of transcriptional activity (*5*, *6*). Determining regulatory specificities is hampered by the need to identify productive DNA-binding events and to distinguish direct from indirect transcriptional responses. On page 800 of this issue, Muhar *et al.* (*7*) provide unprecedented resolution on the regulatory roles of MYC and BRD4, improving our understanding of these cancer-associated TFs.

The authors induced acute degradation of endogenous BRD4 or MYC in two cancer cell lines and profiled immediate transcriptional changes (see the figure). Inducing BRD4 degradation reduced the elongating form of Pol2 and globally down-regulated transcription, pointing to BRD4—rather than the whole BET family (*8*)—as a general coactivator of Pol2. Treatment of cells with the BETi JQ1 led to different outcomes, depending on the dosage: Whereas high doses suppressed all transcription, mimicking BRD4 degradation, lower doses—albeit still toxic to cancer cells—had more limited consequences, possibly because of a dose-dependent removal of BRD4 from chromatin (*9*). Such selective transcriptional responses to BETis have been the basis of their development as anticancer drugs because oncogenes—particularly *MYC*—were generally more sensitive than housekeeping genes to BET inhibition (*1*). Thus, understanding the molecular features that determine differential sensitivity to BETis is of crucial importance.

Neither the level of BRD4 binding to promoters (*7*, *10*, *11*) nor the presence of superenhancers (*7*, *11*, *12*) were sufficient to predict the sensitivity of a gene to JQ1. Although selectivity could also be due to the differential ability of promoters to undergo compensatory increases in Pol2 loading (*11*), data mining in genome binding profiles allowed Muhar *et al.* to identify other TFs and cofactors with predictive power, albeit not in a general manner; indeed, these factors were enriched on different subsets of JQ1-sensitive genes. Therefore, besides acetylated histones, other proteins may mediate BRD4 recruitment and/or activity on chromatin, contributing to the selective effects of BETis.

Of note, the global impairment of Pol2 elongation upon BRD4 degradation occurred without displacement of the elongation factor cyclin-dependent kinase 9 (CDK9), and BET and CDK9 inhibitors affected distinct groups of genes (*7*, *8*). Thus, besides recruiting CDK9, BRD4 may directly regulate Pol2 activity, possibly through intrinsic acetyltransferase and/or kinase activities (*1*).

The enhanced sensitivity of tumor cells to JQ1 is determined at least in part by its inhibitory action on MYC expression and/or activity. Thus, Muhar *et al.* addressed the consequences of acute MYC degradation in cancer cells, revealing a fundamentally different scenario from that observed with BRD4.

In recent years, the selectivity of MYC as a transcriptional regulator has been the subject of intense debate (*2*–*6*). In the work discussed here, only a few hundred genes showed decreased messenger RNA output upon loss of MYC, a large majority of the transcriptome remaining unaffected (*7*). Important insight was provided by the identity of MYC-dependent genes, which are involved in protein and nucleic acid biosynthetic pathways, among

Department of Experimental Oncology, European Institute of Oncology, Milan, Italy. Email: bruno.amati@ieo.it

others. This confirms that MYC contributes to the activation of select transcriptional programs, which in turn promote the wealth of secondary changes—including the general increase in RNA biosynthesis—associated with cell activation and transformation (*2*); most importantly, this accounts for all published data, without the need to invoke a direct amplifier function for MYC.

Muhar *et al.*, together with a series of recent reports, allow us to more precisely reformulate some of the key questions regarding MYC function. Although superactivating MYC above endogenous amounts in proliferating cells caused both up- and down-regulation of transcription (*3*, *4*, *13*, *14*), MYC degradation only led to down-regulation of select targets (*7*), which is at odds with the notion that MYC directly represses transcription. Thus, although overexpressed MYC can antagonize the activity of other TFs, such as MIZ1 (MYC-interacting zinc finger protein 1) (*2*, *4*), the extent of this phenomenon must be reevaluated; in particular, this may be relevant mainly in tumors with direct oncogenic activation of *MYC* (that is, genetic amplification or translocation, which is absent in the cells used by Muhar *et al.*). Moreover, repression by MYC may largely be a passive effect; in all data sets in which combined RNA expression and DNA-binding data are available, gene activation—as opposed to repression—correlates with the strongest gain in MYC binding to promoters (*4*, *7*, *13*, *14*); the contribution of enhancer binding (*3*–*6*, *15*) remains to be systematically addressed. A kinetic analysis in mouse fibroblasts (*14*) showed that activated genes not only gained the most MYC binding but also underwent rapid Pol2 loading. At the opposite end of the spectrum, repressed genes were less effectively bound by supernumerary MYC molecules, showed no increased loading, but instead lost Pol2 from their promoter; rather than being actively repressed by MYC, these genes may suffer from a competitive disadvantage in recruiting Pol2. Whether Pol2 levels are limiting and differentially affect promoter strength in vivo remains an open question. Notably, several genes encoding Pol2 subunits showed MYC-dependent expression (*7*), providing another indirect link between MYC and global transcriptional activity (*2*).

The data discussed here highlight the need to pursue kinetic, integrated analyses of DNA binding and RNA synthesis in cells. As exemplified by BRD4 and MYC, these approaches allow us to dissect the regulatory function of key cancer-associated transcription factors and, most importantly, to clearly distinguish primary from secondary events. ■

REFERENCES

1. Y. Xu, C. R. Vakoc, *Cold Spring Harb. Perspect. Med.* **7**, a026674 (2017).
2. T. R. Kress *et al.*, *Nat. Rev. Cancer* **15**, 593 (2015).
3. A. Sabò *et al.*, *Nature* **511**, 488 (2014).
4. S. Walz *et al.*, *Nature* **511**, 483 (2014).
5. C. Y. Lin *et al.*, *Cell* **151**, 56 (2012).
6. Z. Nie *et al.*, *Cell* **151**, 68 (2012).
7. M. Muhar *et al.*, *Science* **360**, 800 (2018).
8. G. E. Winter *et al.*, *Mol. Cell* **67**, 5 (2017).
9. J. Lovén *et al.*, *Cell* **153**, 320 (2013).
10. D. S. Tyler *et al.*, *Science* **356**, 1397 (2017).
11. E. Donato *et al.*, *Leukemia* **31**, 479 (2017).
12. S. Wang *et al.*, *Genome Res.* **26**, 1417 (2016).
13. F. Lorenzin *et al.*, *eLife* **5**, e15161 (2016).
14. S. de Pretis *et al.*, *Genome Res.* **27**, 1658 (2017).
15. R. Zeid *et al.*, *Nat. Genet.* **50**, 515 (2018).

10.1126/science.aat6664

Elimination of MYC and BRD4 differentially affects transcription

BRD4 and MYC (as a dimer with MAX; not shown here) are broadly bound to the regulatory regions of active genes. Whereas BRD4 degradation affects transcription of all genes, MYC is only required at select loci, enriched for genes involved in cell growth and proliferation. At later time points, indirect effects of MYC loss may lead to widespread gene repression. Although illustrated as stalled Pol2, the mechanism of shutdown upon MYC degradation remains to be addressed.

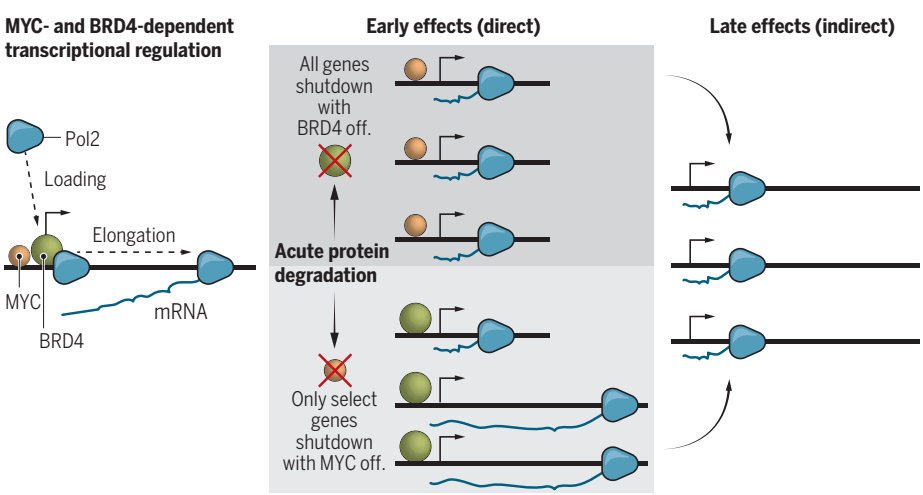

ECOLOGY

Narrowing pathways to a sustainable future

Limiting global warming to 1.5°C can protect species unless carbon sequestration threatens their habitats

By **Guy Midgley**

At the United Nations Framework Convention on Climate Change (UNFCCC) Conference of the Parties in Copenhagen in 2009, the Alliance of Small Island States, supported by African countries, called for a temperature target of 1.5°C above the preindustrial level, as opposed to the more broadly accepted 2°C limit, as the basis for a global multilateral climate agreement. A subsequent UNFCCC-established review concluded that 2°C of warming cannot be considered safe and that less warming would be preferable (*1*). The Paris Agreement, adopted in December 2015, formally recognized this notion in its stated aims to hold the increase to well below 2°C and to pursue efforts to limit it to 1.5°C above preindustrial levels (*2*). On page 791 of this issue, Warren *et al.* (*3*) provide a detailed analysis of the avoided risk to species' geographic ranges if a 1.5°C rather than a 2°C target is attained.

An IPCC review currently under way is assessing the broader impacts of global warming of 1.5°C above preindustrial levels and related global greenhouse gas emission pathways. This assessment, due for completion in September 2018, is critical especially given consistent confirmation of the long-term warming trend in global mean surface temperature (*4*) and of a reemerging rise in CO_2 emissions after 3 years of relative stabilization (*5*). Impact modeling in almost all sectors (such as agriculture, water, biodiversity, and human health) has tended to focus on higher levels of warming and more distant scenarios of climate change. Yet, observations of ongoing changes in climate-sensitive physical (*6*), biological (*7*), and

Department of Botany and Zoology, University of Stellenbosch, Stellenbosch, South Africa. Email: gfmidgley@sun.ac.za

GRAPHIC: N. DESAI/*SCIENCE*

Afforestation, as in this eucalyptus plantation in Argentina, can help to mitigate carbon dioxide emissions, but may reduce space for indigenous biodiversity.

PHOTO: AGE FOTOSTOCK/ALAMY STOCK PHOTO

human systems (*8*) are sounding an early warning of shorter-term impacts.

Model studies of the impacts of lower warming levels remain scarce, however, limiting quantitative assessment of the benefits of attaining a 1.5°C target. Nevertheless, a global synthetic analysis of modeling results identified an apparent accelerating trend in species extinction risk with increasing warming over the range of 1° to 5°C above preindustrial levels (*9*). Accelerating trends in impacts on biodiversity with greater warming might be expected, given that global average surface temperatures in the past 2 million years have rarely approached the levels projected (absent substantial mitigation) over the next few decades (*10*).

Warren *et al*. project accelerating increases in impacts on species' geographic ranges from 1.0°C to up to 4.5°C, thus indicating substantial avoided risk to biodiversity if global warming were to be held at lower levels. Their work builds on several earlier studies but is far more comprehensive, because the authors use a model with finer spatial scales and consider future climate uncertainty more accurately. They also use larger, more detailed data sets for model building and more reliable species distribution data. Avoided risks at 1.5°C versus 2°C include at least a halving in the number of species projected to lose more than 50% of their geographic range—range loss being the authors' main metric of impact. At higher levels of warming, substantial range loss spreads to greater numbers of species, indicating potential systemic ecological simplification. It remains to be seen whether rarer species are more sensitive than common species; this information would be particularly important for conservation planners in species-rich regions.

The authors further report that roughly one-tenth to a third of mobile organisms show positive and even large positive range responses. Might this imply the replacement of many "climate losers" with far fewer "climate winners" in a simplifying ecological landscape? What would the implications be for ecosystem resilience and functioning?

Policy-makers are increasingly focusing on solutions to climate change challenges. Much research is under way on the practicality of achieving the more stringent warming targets that would avoid the biodiversity risks highlighted by Warren *et al*. To do so, a transformative shift in energy production systems alone may not be enough, but negative emissions may be needed (*11*). However, integrated assessment modeling indicates that negative emissions technologies and in CO_2 removal approaches are likely to lead to increased land use (*12*), which itself may adversely affect biodiversity. Warren *et al*. suggest that implementation of "Article 2–compliant mitigation" may help to resolve this nexus between biodiversity, climate, and land-use priorities. This is a reference to the judiciously worded objective of the UNFCCC itself, crafted in the early 1990s, which calls for prevention of "dangerous anthropogenic interference with the climate system" but "within a time frame sufficient to allow ecosystems to adapt naturally to climate change, to ensure that food production is not threatened and to enable economic development to proceed in a sustainable manner" (*13*).

Warren *et al*. do not elaborate upon options under consideration that prioritize land-based carbon sequestration but that may themselves severely threaten biodiversity. This is particularly the case if ecosystems identified with high carbon sequestration potential are not considered valuable in biodiversity terms. For example, fire suppression to enhance carbon sequestration in the South American Cerrado has led to biodiversity losses (*14*), and ancient open tropical grasslands that are biodiversity-rich but shade-intolerant appear to be at risk of possible afforestation in pursuit of enhanced carbon sequestration (*15*).

Some integrated assessment modeling approaches that explore competing land-use objectives are being strengthened by incorporating explicit consideration of biodiversity concerns. Such analyses are vital for new assessments by the Intergovernmental Platform on Biodiversity and Ecosystem Services, which is well placed to integrate these diverse concerns. Nonetheless, as the nature of the trade-offs we face comes into sharper relief, it is clear that the pathways to a sustainable future have narrowed. ■

REFERENCES

1. Page 18, Message 5 in https://unfccc.int/sites/default/files/resource/docs/2015/sb/eng/inf01.pdf.
2. Article 2a of the Paris Agreement; https://unfccc.int/resource/docs/2015/cop21/eng/l09r01.pdf.
3. R. Warren *et al.*, *Science* **360**, 791 (2018).
4. S. Rahmstorf *et al.*, *Environ. Res. Lett.* **12**, 054001 (2017).
5. G. P. Peters *et al.*, *Nat. Clim. Chang.* **7**, 848 (2017).
6. L. Caesar, S. Rahmstorf, A. Robinson, G. Feulner, V. Saba, *Nature* **556**, 191 (2018).
7. T. P. Hughes *et al.*, *Science* **359**, 80 (2018).
8. C. Witt *et al.*, *Dtsch. Ärztebl. Int.* **112**, 878 (2015).
9. M. C. Urban, *Science* **348**, 571 (2015).
10. C. W. Snyder, *Nature* **538**, 226 (2016).
11. T. Gasser, C. Guivarch, K. Tachiiri, C. D. Jones, P. Ciais, *Nat. Commun.* **6**, 7958 (2015).
12. T. G. Benton *et al.*, *Curr. Opin. Environ. Sustain.* **31**, 88 (2018).
13. Article 2 of the United Nations Framework Convention on Climate Change; https://unfccc.int/resource/docs/convkp/conveng.pdf.
14. R. C. R. Abreu *et al.*, *Sci. Adv.* **3**, e1701284 (2017).
15. W. J. Bond, *Science* **351**, 120 (2016).

10.1126/science.aat6671

POLICY FORUM

RESEARCH CAREERS

Improving support for young biomedical scientists

Expand grant programs to encourage innovative research

By **Bruce Alberts,[1] Tony Hyman,[2] Christopher L. Pickett,[3,4] Shirley Tilghman,[4] Harold Varmus[5]**

Over the past several years, we and others in the biomedical research community have become increasingly concerned that younger scientists are not being adequately supported as independent academic investigators and that, of equal importance, these newly launched investigators are being strongly discouraged from tackling novel scientific problems (*1*–*6*). Both issues can prevent talented trainees from aspiring to careers in biomedical research, despite the extraordinary opportunities offered by new technologies and recent discoveries. We view this situation as an existential threat to our profession, demanding that we urgently confront the underlying problems.

It is widely recognized that career pathways for young scientists have changed dramatically and that over 80% of those who receive biomedical Ph.D.'s today will be employed in positions other than academic faculty (*1*, *5*). The U.S. National Academies of Sciences, Engineering, and Medicine recently released a report that addresses many important aspects of these cultural changes (*7*). Here we focus on the problems faced by those who will renew the ranks of academic research faculty, with proposals that complement the recommendations in that report. Drawing on lessons from Europe and the United States, we propose three steps that could be taken by funding agencies, specifically the U.S. National Institutes of Health (NIH) but also others across the world, to support young investigators in more constructive and effective ways.

THE NATURE OF THE DILEMMA

Major changes have occurred in the demographics of funded biomedical investigators in the United States, with a striking shift of awardees from younger to older scientists. This is evident from the number of those holding NIH R01 grants, the type most often awarded to independent investigators (see the figure, left). The factors responsible for this shift include the aging of the population, the elimination of a mandatory U.S. retirement age, the lengthening of graduate and postdoctoral training, and the often multiyear delay between assuming a faculty position and successfully competing for an NIH grant (*4*, *8*).

A cardinal feature of the shift is a dramatic reduction in NIH-funded investigators under the age of 37 (see the figure, right). Despite a large increase in the NIH budget and number of grants awarded since the early 1980s, there has been a greater than fivefold decrease in the number of investigators aged 36 or younger who hold R01-type grants: from more than 2500 grant holders to fewer than 500. Expressed in terms of NIH dollars, the proportion of all NIH funding awarded to scientists under the age of 36 has dropped from 5.6% in 1980 to 1.3% in 2012 (*1*). Although valuable support from philanthropic organizations is provided to a select set of young investigators, the scale of that support is much too small to compensate for the above changes. Thus, by these measures, the U.S. scientific community is doing a poor job of renewing itself.

> ***"...the U.S. scientific community is doing a poor job of renewing itself."***

The claim that investigators early in their careers are being discouraged from addressing the most challenging problems in biomedicine rests on less quantitative observations. But in our experience, the next generation of scientists report that the peer-review process for grant applications is perceived to be unduly conservative because of the hypercompetitive grant-funding environment, discouraging them from proposing to conduct highly original work (*7*, *9*). In conversations with trainees and young faculty, we have repeatedly heard that emerging scientists feel compelled to remain well within the bounds of the research that they and their mentors are already pursuing, because obtaining a research grant requires strong preliminary data and a high probability of success.

In addition, many junior and senior scientists operate with the conviction that essential components of the grant-making system, including peer reviewers and agency administrators, currently undervalue research that seeks to decipher the fundamental principles of living systems, in favor of projects with shorter-term objectives that focus directly on human diseases—so-called translational biomedical research. Yet the history of science has repeatedly shown that insightful studies of basic biological mechanisms in easily manipulated model organisms—such as bacteria, yeast, worms, and flies—provide revolutionary insights into life processes. Over the long term, these discoveries contribute to human health in profound ways (*10*).

ADDRESSING THE SITUATION IN THE EUROPEAN UNION AND THE UNITED STATES

Some ideas on how best to fund young scientists have recently come from Europe. In 2007, the European Research Council (ERC) launched its Starting Grants (StG) program, aimed at young scientists from all disciplines who received their Ph.D. within the previous 2 to 7 years. At the same time, the ERC initiated the parallel Advanced Grant program, open to applicants at any career stage, which likewise emphasizes innovative interdisciplinary research. Since then, the ERC has added a third category, the Consolidator Grant award, designed to support investigators who have previously received a single grant, such as a StG award, and are 7 to 12 years post-Ph.D. Importantly, the competitions for the three grant categories are conducted separately, and the awards are supported from three independent budgets (*2*).

This division of careers into three stages has a number of advantages. First and most crucially, investigators conducting their first independent projects and those stabilizing their laboratory programs are competing against scientists at the same career stage, not against senior scientists with longer careers and stronger reputations. Second, different criteria for review can be applied to applicants at different career stages. In this way, the StGs encourage applicants to pursue highly original projects when they start their own laboratories, without requiring extensive preliminary data.

[1]*University of California, San Francisco, San Francisco, CA, USA.* [2]*Max Planck Institute of Molecular Cell Biology and Genetics, Dresden, Germany.* [3]*American Association for the Advancement of Science, Washington, DC, USA.* [4]*Lewis-Sigler Institute, Princeton University, Princeton, NJ, USA.* [5]*Sandra and Edward Meyer Cancer Center, Weill Cornell Medicine, New York, NY, USA. Email: balberts@ucsf.edu*

Competition for these pan-European StGs is held annually, and each of the 100 to 200 successful applicants in the life sciences receives substantial funding, €1.5 million over 5 years. A critical feature of the process is the use of nine review panels, each composed of outstanding scientists coming from a broad range of disciplines and many European countries; this serves to minimize narrow specialization and to focus decisions on the broad implications of the proposals (*2*).

The ERC has recently completed a qualitative evaluation of the outcomes from the first several classes of investigators who completed the full course of funding from the ERC StGs. The results are very encouraging. Of the 199 individuals evaluated, 43 were judged to have produced a "scientific breakthrough," and 99 were thought to have generated a "major advance" (*11*). An ERC StG is now seen as a stamp of quality for a new investigator and his or her institution.

The NIH leadership has also been attentive to these problems. Over the past few decades, the agency has experimented with several programs designed to fund the next generation of biomedical scientists more effectively and at earlier ages (*2*). Some of these experiments, such as the R29 [First Independent Research Support and Transition (FIRST) Award] grant program, were discontinued after unfavorable evaluations that suggested the award stifled new investigators' careers. Other programs, such as the policy initiated in 2008 to raise the success rates of applications from Early Stage Investigators (ESIs; applicants within 10 years of receipt of their Ph.D. or completion of clinical training), have made a difference, and they continue. Additional experiments include the Early Independence (DP5) and the New Innovator (DP2) awards, popular programs that provide only a small number of research grants each year.

To be eligible for a DP2 grant, a scientist must be an ESI and cannot have received a major grant previously. The criteria for selection emphasize imaginative and original scientific goals without a requirement for preliminary results. These DP2 grants are generous with funds and time, providing $300,000 per year in direct research costs for 5 years. In addition, all of the money is provided at the start of the award period, so that expenditures can be tailored to the needs of each investigator (for example, to purchase major equipment). Although nearly 2200 DP2 applications were received in the initial year (2007), the fiscal allocation through the NIH Director's Common Fund allowed only 30 awards to be made. This presumably sent a discouraging signal, because only about 550 applications are now received each year, with 100 finalists selected by a single broad review group. After further evaluation, about 40 to 60 awards are made (*12*).

The NIH has just completed a careful external evaluation of the first three cohorts of DP2 recipients, compared to an equivalent control group, that deemed the program a success. This grant program is supporting "research that is more innovative, risky, and impactful than research that typically is reviewed and funded using the traditional R01 program." In addition, despite concerns that supporting ESIs to pursue highly original research topics might place their careers in jeopardy, the evaluation found that receiving a DP2 award did not hinder a young scientist's career (*13*).

Encouraged by directives in last year's 21st Century Cures Act enacted by Congress and responsive to concerns in the research community, the NIH has announced its intention to enlarge the cohort of young investigators who receive R01-type grants. NIH leadership has provided a list of mechanisms by which individual institutes and centers might increase the number of awards made to younger investigators and reaffirmed the NIH's commitment to improving prospects for ESIs (*3*). That announcement also defined a new category of applicant, the Early Established Investigator (EEI)—a scientist who has received only one R01-type grant and is thus formally analogous to a candidate for the ERC Consolidator Grant. This new NIH policy statement includes a pledge to increase the number of R01-type grants made each year to ESIs and EEIs by a few hundred in each category; however, the precise number of additional awards and the definitions of beneficiaries are still under review (*3*).

THREE SPECIFIC PROPOSALS

We are encouraged by the continued engagement of NIH leadership with the plight of young investigators. It is in that spirit that we propose three additional steps to enhance opportunities for early stage investigators.

Greatly expand use of the DP2 mechanism

The DP2 award has now been used for a decade and evaluated favorably. We believe it deserves expanded use and propose that the NIH move in a step-wise manner toward providing greater NIH resources to ESIs through this mechanism. In 2016, the NIH funded 908 of the 3937 applications from ESIs for R01-type grants, and the NIH now proposes to award grants to about 1100 ESIs annually (*3*, *14*). We suggest that the NIH move gradually toward making half of those awards (about 550) as DP2 grants. This number would greatly increase the probability that an ESI will explore new approaches to an important biological problem. The NIH

The increasing age of principal investigators funded by the NIH

(Left) The age distribution of NIH R01-type funded principal investigators (PIs) in 1980 and 2015. (Right) The percent of NIH PIs with R01-type funding plotted against year, selecting out older and younger age brackets. R01-type grants are defined as R01, R23, R29, and R37 awards. Data are from files posted for the NIH's Early Stage and Early Established Investigators at https://grants.nih.gov/policy/new_investigators/index.htm (file name "Age of RPG Awardees 1980 to 2015 from SARB File 191-16").

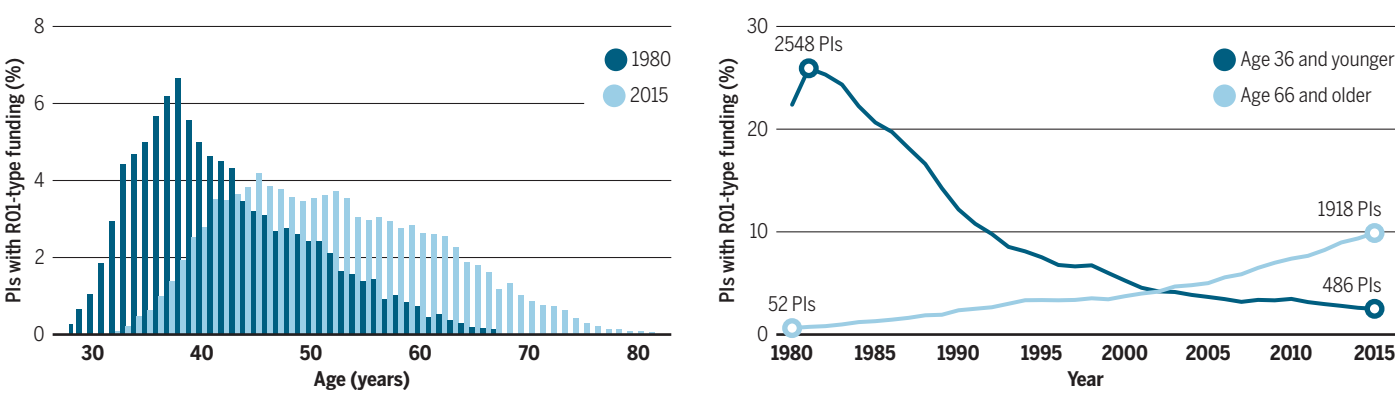

GRAPHIC: J. YOU/*SCIENCE*

should, of course, monitor expansion of the program to ensure that the quality of funded applications remains high and to identify any possible bias in making awards. The critical goal is to liberate new independent investigators, as well as the graduate students and postdoctoral fellows who will soon become independent, from the widely perceived tyranny of conventional thinking.

One can question whether a major expansion of the DP2 program would be able to reduce the average age at which new investigators in the United States are funded, given the large backlog of postdocs competing for a limited number of independent positions at U.S. research institutions. In the current funding environment, why would a university hire a scientist proposing to undertake an innovative research program after only a few years of postdoc training, when the institution could hire someone with several more years of training, many more publications, and a plan to continue an already productive research program? We propose that, by providing sufficient funds for new faculty without a preexisting publication record on a proposed research topic, the NIH would free university search committees to think more imaginatively about the type of science and scientists that they want for their institutions.

To encourage this type of hiring, we recommend that the NIH adopt two current practices of the ERC. The first is to allow postdocs to apply for a DP2 award, provided that he or she has secured a faculty position that is conditional on the award decision. This is the case for the ERC StGs, where, in addition, a successful applicant retains the option of shifting institutions after the grant has been awarded. The second is to restrict DP2 grants, over time, to applicants who completed their Ph.D. or clinical training between 2 and 7 years ago, with allowable exceptions, instead of the current 10-year limit. This recommendation recognizes that young investigators will often wait until the end of any eligibility period to apply, so as to expand their prior records. Reducing the number of years of eligibility for DP2 awards would thus encourage two healthy trends: less time in postdoctoral training and earlier research independence.

Much of the recommended expansion of the DP2 program could be accomplished within the NIH Director's Common Fund, which this year totals $588 million, perhaps by not replacing some of its special initiatives when they expire. In addition, the individual institutes should consider funding a greater number of DP2 grants, as an effective way to recruit a new generation of scientists to address institute missions.

Increase the funding of young investigators through requests for applications (RFAs)

It is often underappreciated that NIH institutes and centers issue substantial numbers of R01-type grants to applicants responding to RFAs—"top-down" initiatives, in which institutes identify priority topics to be funded, in contrast to the traditional "bottom-up" investigator-initiated awards. Ideally, RFAs can be used to attract more investigators into fields of research that warrant greater attention because the public health needs are great or because new findings or technologies offer unexpected opportunities for progress. In 2016, the total number of new NIH R01s was 4541; of these, 333 (7.3%) were awarded through an RFA.

We propose that the NIH mandate that a substantial percentage of grants be awarded to ESIs as part of both institute-sponsored RFAs and NIH-wide initiatives, such as the Cancer Moonshot and the Brain Research through Advancing Innovative Neurotechnologies (BRAIN) Initiative, and that the ESI competition be conducted using the selection criteria already used for DP2 awards. Reserving funds in each case for a separately reviewed, DP2-type competition that stresses experimental originality would both attract new scientists into the targeted field and encourage new approaches to an important problem.

> ***"...the NIH would free... search committees to think more imaginatively about the type of... scientists that they want for their institutions."***

Experiment with separate competitions for ESIs when awarding traditional investigator-initiated R01 grants

For several years, the NIH has encouraged its institutes to favor ESI applicants when selecting recipients of new grants. This has produced higher success rates for ESIs at some institutes, but it has not achieved a substantial change in workforce demographics (see the figure).

To reach a greater representation of young investigators among grant recipients, we suggest that the NIH experiment with the kind of strategy adopted by the ERC, in which ESIs compete separately for predesignated numbers of R01 awards, rather than against the entire pool of applicants.

An ideal funding program for young biomedical scientists would award enough independent grants to young investigators to inspire the most talented students to aim for scientific careers, while simultaneously encouraging them to attempt to solve important biological problems in new ways. We recognize, as does NIH leadership, that earmarking funds to support more young investigators will come at a cost to older investigators (*3*, *4*). Nevertheless, it is important to make this shift, which we consider essential for the future vitality of biomedical research. If properly implemented, our proposals could substantially increase the number of scientists under 40 years old who receive independent research support, while enhancing the originality of their research. These changes should also find support in Congress, which has repeatedly expressed concern about the status of young investigators. ■

REFERENCES AND NOTES

1. R. J. Daniels, *Proc. Natl. Acad. Sci. U.S.A.* **112**, 313 (2015).
2. T. Hyman, A. Desai, P. Walter, "On research funding and the power of youth," *ASCB Newsletter*, October 2016; www.ascb.org/newsletter/october-2016-newsletter/october-2016-newsletter-on-research-funding-and-the-power-of-youth/.
3. M. Lauer, L. Tabak, F. Collins, *Proc. Natl. Acad. Sci. U.S.A.* **114**, 11801 (2017).
4. M. Levitt, J. M. Levitt, *Proc. Natl. Acad. Sci. U.S.A.* **114**, 6498 (2017).
5. B. Alberts, M. Kirschner, S. Tilghman, H. Varmus, *Proc. Natl. Acad. Sci. U.S.A.* **111**, 5773 (2014).
6. A. Rzhetsky, J. G. Foster, I. T. Foster, J. A. Evans, *Proc. Natl. Acad. Sci. U.S.A.* **112**, 14569 (2015).
7. National Academies of Sciences, Engineering, and Medicine, *The Next Generation of Biomedical and Behavioral Sciences Researchers: Breaking Through* (The National Academies Press, Washington, DC, 2018).
8. D. M. Blau, B. A. Weinberg, *Proc. Natl. Acad. Sci. U.S.A.* **114**, 3879 (2017).
9. J. Mervis, *Science* **306**, 220 (2004).
10. J. Rine, *Mol. Biol. Cell.* **25**, 549 (2014).
11. European Research Council, "Qualitative evaluation of completed projects funded by the European Research Council," July 2016; https://erc.europa.eu/sites/default/files/qualitative_evaluation_of_completed_projects_funded_by_the_erc.pdf.
12. National Institutes of Health, NIH Research Portfolio Online Reporting Tools (RePORT), "Research project success rates by type and activity for 2016" (NIH, 2016); https://report.nih.gov/success_rates/Success_ByActivity.cfm.
13. S. S. Tinkle *et al.*, "An outcome evaluation of the National Institutes of Health Director's New Innovator Award program for fiscal years 2007–2009," (Institute for Defense Analyses Science and Technology Policy Institute, 2016); https://commonfund.nih.gov/sites/default/files/HRHR%20New%20Innovator%20Award%200utcomes%20Evaluation%202007-2009_508%20compliant.pdf.
14. National Institutes of Health, NIH Research Portfolio Online Reporting Tools (RePORT), "Special reports and current issues: Data on trends according to career stage" (NIH, 2017); https://report.nih.gov/special_reports_and_current_issues/index.aspx.

ACKNOWLEDGMENTS

The proposals in this piece reflect the views of the nonprofit organization Rescuing Biomedical Research, as approved by its Steering Committee (http://rescuingbiomedicalresearch.org/). We thank the Open Philanthropy Project for grant support, as well as numerous colleagues for their feedback on drafts of this manuscript.

10.1126/science.aar8405

BOOKS *et al.*

A driven entrepreneur, before the company's downfall Elizabeth Holmes was touted as "the next Steve Jobs."

DIAGNOSTIC MEDICINE

The rise and fall of Theranos

A biotech company's blood test proves too good to be true

By **Jennifer Couzin-Frankel**

In the opening pages of *Bad Blood,* the chief financial officer for the blood-testing company Theranos meets with his boss, Elizabeth Holmes, a charismatic 20-something Stanford University dropout, and warns her that the company must stop lying to its investors. Holmes's expression turns icy. She informs him that he's not a team player. Then she fires him on the spot.

Variations on this story recur throughout this engrossing new book by John Carreyrou, the *Wall Street Journal* reporter whose articles—guided by dozens of frightened but determined sources—brought down Theranos. The fraud that fooled everyone from Walgreens to U.S. statesmen is almost too fantastical to be believed. Holmes, vindictive and paranoid, and the company's number two, Ramesh "Sunny" Balwani, a bully almost 20 years her senior with whom she was in a romantic relationship, are pitted against employees frantic that patients will be harmed by a technology that doesn't work.

Holmes dreamed up Theranos in 2003, while at Stanford. She had recently completed an internship at the Genome Institute of Singapore, where she tested patient samples for the severe acute respiratory syndrome (SARS) virus that had devastated Asia. Determined to transform the clunky testing technology, Holmes imagined an arm patch that would diagnose and treat medical conditions. This morphed into Theranos testing devices, which she claimed could run hundreds of tests on a few drops of blood.

It was a remarkable idea. There was just one problem: Scientists and engineers at Theranos couldn't produce reliable results, at least not in the time frame demanded. That didn't stop Holmes and Balwani from raking in hundreds of millions of investor dollars or from deploying the error-prone machines for use on unsuspecting patients.

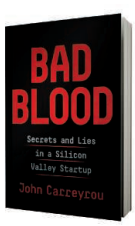

Bad Blood
Secrets and Lies in a Silicon Valley Startup
John Carreyrou
Knopf, 2018, 352 pp.

Venture capitalists—particularly ones less familiar with medical technologies—were riveted by Holmes's vision and her passionate pitches (no matter, Carreyrou writes, that she invented projected profits and falsely claimed that the U.S. military had stationed her devices on Humvees in Iraq). Companies such as Safeway and Walgreens feared missing out on a revolutionary technology that they imagined would vault them ahead of their competitors. And it's hard not to notice that many in thrall with Holmes were older men who often invested in the company or joined her board of directors: George Shultz, a secretary of state under President Ronald Reagan; Larry Ellison, the billionaire who cofounded the Oracle Corporation; and James Mattis, now U.S. secretary of defense, among others.

Theranos also benefited from uncertainty among regulators, who struggled to identify which agency should be charged with policing its services. Was the company offering simple blood tests, which fall under the Centers for Medicare and Medicaid Services? Did it have a diagnostic tool, governed by the U.S. Food and Drug Administration? Or was the Theranos product a "laboratory developed test," at the time a more unusual offering in a regulatory gray zone? Like many legitimate companies, Holmes pressed for whichever oversight would prove easier to navigate and managed to place her testing machines in drugstores without validation.

But if the scientific fraud is impressive, it's Holmes's reportedly ruthless treatment of anyone who challenged her that makes *Bad Blood* hard to put down. Theranos, Carreyrou writes, was a revolving door, as Holmes and Balwani fired anyone who voiced even tentative doubts. (He shares that Holmes stopped speaking to an employee whose sister turned down a Theranos job offer.) Company emails were strictly monitored; legal threats were frequent and aggressive. One former employee suspected being followed. The family of another shelled out hundreds of thousands of dollars in legal fees to protect themselves.

Bad Blood boasts movie-scene detail—indeed, a film based on the book is under way. In one passage, for example, Holmes's father flies a paper airplane toward her during Christmas dinner, with "P.H.D." written on the side. ("No, Dad, I'm not interested in getting a Ph.D., I want to make money," she tells him.) But the book's detail can be dizzying, making it hard to follow the various narrative threads and the dozens of named individuals.

Theranos employees are the story's heroes, with the force of journalism not far behind. In the last quarter of *Bad Blood*, Carreyrou describes the tip that ultimately led him to expose the company's misdeeds. Nailing the story required coaxing truth from physicians and former employees, many of them fearful of legal action, and, with his superiors, facing down Theranos's threats to the *Journal*.

What's frightening is how easy it is to imagine a different outcome, one in which the company's blood-testing devices continued to proliferate. That the story played out as it did is a testament to the many individuals who spoke up, at great personal risk. ■

10.1126/science.aat7771

The reviewer is on staff at Science *magazine.*
Email: jcouzin@aaas.org

PHOTO: JEFF CHIU/AP PHOTO

SCIENCE LIVES

Einstein goes east

Private travel diaries reveal the physicist's musings and moments of self-reflection

By **Andrew Robinson**

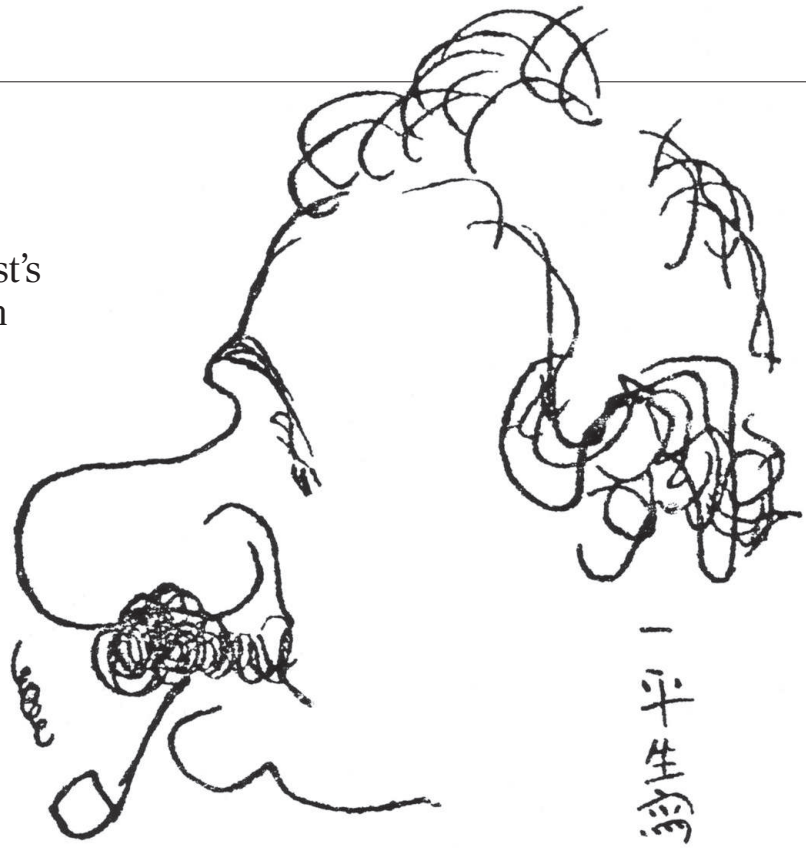

"Albert Einstein or The Nose as a Reservoir for Thoughts," by the Japanese cartoonist Ippei Okamoto, 1922.

From 1922 to 1923, Albert Einstein maintained a private travel diary, which is alive with his important and trivial adventures. Notably, however, he failed to record the news that he had been awarded the Nobel Prize.

This omission suggests both confidence in his scientific ideas and a lack of personal vanity but also suggests alienation from normal human emotion: that which he later deprecated as the "chains of the 'merely personal'" in his *Autobiographical Notes* (1949).

Having recently read the German psychiatrist Ernst Kretschmer's book *Physique and Character*, Einstein appears to recognize early in the diary, in a rare moment of self-analysis, that his own character might be defined by "Hypersensitivity transformed into indifference. During adolescence, inwardly inhibited and unworldly. Glass pane between subject and other people. Unmotivated mistrust. Substitute paper world. Ascetic impulses."

Einstein's travel diaries, kept under wraps during his lifetime, were posthumously quoted in biographies and studies, most extensively in Josef Eisinger's *Einstein on the Road* (2011). In 2012, the entire 1922–1923 diary appeared in translation in volume 13 of *The Collected Papers of Albert Einstein*. But until now it has not been published as its own, stand-alone book.

The Travel Diaries is a substantially revised version of the 2012 translation that comes with an illuminating introduction and astonishingly comprehensive endnotes by Ze'ev Rosenkranz, senior editor of the Einstein Papers Project and author of *Einstein Before Israel*, which includes his 1923 visit to Palestine.

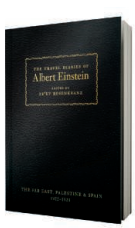

The Travel Diaries of Albert Einstein
The Far East, Palestine, and Spain, 1922–1923
Ze'ev Rosenkranz, Ed.
Princeton University Press, 2018. 377 pp.

Einstein's 1922–1923 travels were triggered by a request from a Japanese publisher to give lectures on relativity in Japan. The trip coincided with serious threats to Einstein's safety in Germany from anti-Semitic right-wing forces following the assassination in June 1922 of his friend and fellow Jew, Walther Rathenau, Germany's foreign minister. Accompanied by his second wife, Elsa, Einstein began his sea voyage in Marseilles in October 1922 and traveled to Japan via the Suez Canal, Ceylon, Singapore, Hong Kong, and Shanghai. The pair returned to Germany through Palestine and Spain in March 1923.

Rosenkranz enthuses in a preface, "Albert Einstein's travel diaries are, by far, my favorite documents penned by him. I have always enjoyed his quirky style, his acerbic quips about the individuals he met, and the colorful descriptions of the hustle and bustle in his ports of call." But then he confesses, "It was only later that I started to notice the more troublesome entries in his journal, in which he, at times, made what amounted to xenophobic comments about some of the peoples he encountered. I began to ask myself: how could this humanist icon be the author of such passages?"

Consider Einstein's entry written in Hong Kong on 10 November after observing the Chinese quarter on the mainland: "Industrious, filthy, lethargic people. Houses very formulaic, balconies like beehive-cells, everything built close together and monotonous. … Even the children are spiritless and look lethargic. It would be a pity if these Chinese supplant all other races." Comments Rosenkranz, "It seems clear that Einstein has bought—to some extent—into the perceived threat of 'the yellow peril.'"

Japan, by contrast, pushes Einstein to the opposite extreme. His diary reveals enchantment with the Japanese landscape, houses, temples, people, and painting (if not so much the music). In an article on his impressions written not long before departure, Einstein concludes, "The Japanese rightfully admires the intellectual achievements of the West and immerses himself successfully and with great idealism in the sciences. But let him not thereby forget to keep pure the great attributes in which he is superior to the West—the artful shaping of life, modesty and unpretentiousness in his personal needs, and the purity and calm of the Japanese soul." Nowhere in 6 weeks of Japanese travels does Einstein—despite his lifelong detestation of German militarism—anticipate Japan's forthcoming slide toward an authoritarian regime, as he did in Weimar Germany.

Only later, in Palestine, does Einstein regain a measure of balance. Although moved by his welcome from Jewish settlers, and by his key role in the opening ceremony of the fledgling Hebrew University, he tells his diary on 13 February, "I am wanted in Jerusalem at all costs. … My heart says yes but my mind says no." He never returned but worked assiduously for Jewish causes until the 1950s.

Anyone interested in Einstein's complex, sometimes self-contradictory, character will be enjoyably provoked by reading his piquant *Travel Diaries*. ■

The reviewer is the author of Einstein: A Hundred Years of Relativity *(Princeton University Press, Princeton, NJ, 2015). Email: andrew@andrew-robinson.org*

10.1126/science.aat4718

PHOTO: EMILIO SEGRE VISUAL ARCHIVES/AMERICAN INSTITUTE OF PHYSICS/SCIENCE PHOTO LIBRARY

Edited by **Jennifer Sills**

Beware silent waning of shark protection

On 2 October 2011, the Republic of the Marshall Islands (RMI) declared the world's largest shark sanctuary, adding 1,990,530 km^2 to the rapidly expanding shark sanctuary movement. News outlets praised the policy, citing its widespread local support and protection laws, the strongest to date (*1*, *2*). Moreover, it was hailed a substantial victory because the government chose to protect sharks despite pressures from politically influential fisheries and other interest groups (*3*). However, in 2016, mounting pressure from those same fishing interests convinced members of the government to weaken the sanctuary law (*4*), and the global conservation community has taken no action in response. Conservationists should determine at what point a weakened sanctuary—or any weakened protected area—should lose its title.

Expansion of shark sanctuaries has paralleled rapid designation of large-scale marine protected areas (LSMPAs) (*5*). Both have been criticized for being established in areas where political expediency outweighs ecological importance (*6*) and capacity for enforcement (*7*). However, unlike LSMPAs, shark sanctuaries have traditionally included two rigid regulations: They ban commercial retention of sharks and, in most cases, prohibit possession of shark parts on industrial fishing vessels (*8*). Yet, on 14 November 2017, the RMI Parliament amended regulations to allow vessels to possess shark parts obtained outside RMI (*4*), substantially weakening the potential for enforcement and the heralded benefits for sharks.

Advocates argue that governments protecting threatened species through either sanctuaries or LSMPAs should be publicly praised (*9*). They also argue for periodic, systematic evaluations of effectiveness after implementation (*10*–*12*). But if these evaluations, which are rare, reveal failures in real protection, we should publicly discuss these failures. Otherwise, we risk publicly accumulating square kilometers to meet conservation targets, while silently weakening progress and encouraging the belief that the work stops when the announcement is made.

Jessica E. Cramp,[1,2,3]* Colin A. Simpfendorfer,[2] Robert L. Pressey[1]
[1]Australian Research Council Centre of Excellence for Coral Reef Studies, James Cook University, Townsville, QLD 4811, Australia. [2]Centre for Sustainable Tropical Fisheries and Aquaculture & College of Science and Engineering, James Cook University, Townsville, QLD 4811, Australia. [3]Sharks Pacific, Rarotonga, Cook Islands.
*Corresponding author.
Email: jess.cramp@my.jcu.edu.au

REFERENCES

1. L. N. K. Davidson, *Science* **338**, 1538 (2012).
2. Pew Charitable Trusts, Press Release, "World's Largest Shark Sanctuary Declared In Central Pacific" (2011); www.pewenvironment.org/news-room/press-releases/worlds-largest-shark-sanctuary-declared-in-central-pacific-85899364555.
3. E. Tripp, "Marshall Islands Shark Sanctuary: A success story," Marine Science Today (2012); http://marinesciencetoday.com/2012/10/27/marshall-islands-shark-sanctuary-a-success-story/.
4. Republic of the Marshall Islands, Fisheries (Amendment) Act 2016, Bill Number 42, 1 P.L. 2017-49 (2017).
5. J. S. Jones, E. M. De Santo, *Mar. Pol.* **73**, 231 (2016).
6. R. Devillers *et al.*, *Aquat. Conserv. Mar. Freshw. Ecosyst.* **25**, 480 (2015).
7. E. M. De Santo, *J. Environ. Manage.* **124**, 137 (2013).
8. C. A. Ward-Paige, *Mar. Pol.* **82**, 87 (2017).
9. R. L. Singleton, C. M. Roberts, *Mar. Pollut. Bull.* **87**, 7 (2014).
10. R. L. Pressey, *Conserv. Biol.* **18**, 1677 (2004).
11. J. Day, M. Hockings, G. Jones, *Great Barrier Reef Mar. Park Auth.* January (2003).
12. M. Hockings *et al.*, *Evaluating Effectiveness: A Framework for Assessing Management Effectiveness of Protected Areas, 2nd Edition* (IUCN, 2006).

10.1126/science.aat3089

PHOTO: DESIGN PICS INC/ALAMY STOCK PHOTO

Gray reef sharks swim through the waters of the Marshall Islands, home to the largest shark sanctuary to date.

Marine protected areas: Just for show?

In March 2018, Brazil's government announced two sets of large marine protected areas (MPAs) in the open ocean (about 400,000 km^2 each). According to the government's ambitious plan (*1*), the total coverage of MPAs under Brazilian national jurisdiction will rise sharply from 1.5 to 25%, in line with an emerging global trend in designation of large MPAs (*2*). Although these new MPAs presented an opportunity to make progress toward biological priorities, the decision-making process instead reflected uninformed opportunism (*3*). Rather than meeting conservation goals, the proposed MPAs exemplify poor adherence to best practices in MPA planning in three ways.

First, large no-take MPAs—i.e., those that prohibit fishing and mining—were designated in areas where these activities are already unlikely or rare, rather than placed where they would be most useful to conservation (*4*). For example, Brazil will fully "protect" vast areas in depths below 5000 m, covering ecosystems that are already de facto protected by poor prospects for extractive activities, regardless of the level of management applied (*4*). Shallow seamounts with vulnerable habitats and high endemism (*5*, *6*) will remain unprotected or within multiple-use zones, with ongoing extraction and negative impacts on marine biodiversity.

Second, unlike well-designed MPA networks, Brazil's MPAs fail to account for spatial dependencies between areas to ensure that they achieve their core ecological objective: the maintenance of biodiversity over time (*7*). For example, population persistence on the protected deep seamounts will depend largely upon larvae transported from unprotected seamounts closer to the continental shelf (*6*), which are likely to be under high fishing pressure. If populations on protected seamounts are not self-recruiting, or fail to receive enough larvae from fished areas, they will also decline, and may fail to persist.

Third, designing large MPAs in the open ocean to regulate fishing of mobile pelagic

species (such as tuna and pelagic sharks) has long been considered a challenge for conservation planning (*8*). To be adequate, MPAs should encompass the home range and territory of adults of targeted species (*9*). The maximum horizontal dimension of the new Brazilian MPAs is 740 km; this range would not meet the requirements for species that display high mobility, which have home ranges wider than 1000 km (*9*). The success of remote MPAs in managing pelagic species also depends highly on compliance (*10*), which will require substantial resources devoted to enforcement. Brazil's government has committed such resources, but funding of management in already-established Brazilian MPAs is known to be inadequate (*11*).

Large MPAs can be flagships for meeting global conservation aspirations such as Aichi Target 11 (*12*) yet still fail to contribute to marine conservation, giving a false sense of conservation achievement. We encourage Brazilian authorities to embrace biodiversity values as they work to meet policy targets, rather than merely protecting a certain percentage of the ocean.

Rafael A. Magris[1]* and Robert L. Pressey[2]
[1]Chico Mendes Institute for Biodiversity Conservation, Brasilia-DF, 70.670-350, Brazil.
[2]Australian Research Council Centre of Excellence for Coral Reef Studies, James Cook University Townsville, QLD 4811, Australia.
*Corresponding author.
Email: rafael.jcu@gmail.com

REFERENCES

1. Ministry of the Environment. "UCs marinhas serão criadas ainda neste mês" (2018); www.mma.gov.br/index.php/comunicacao/agencia-informma?view=blog&id=2860 [in Portuguese].
2. L. Boonzaier, D. Pauly, *Oryx* **50**, 27 (2016).
3. R. L. Pressey, M. C. Bottrill, *Conserv. Biol.* **22**, 1340 (2008).
4. M. R. Clark, L. Watling, A. A. Rowden, J. M. Guinotte, C. R. Smith, *Ocean Coast. Manage.* **54**, 19 (2011).
5. M. R. Rosa *et al.*, *Coral Reefs* **35**, 113 (2016).
6. H. T. Pinheiro *et al.*, *PLOS One* **10**, e0118180 (2015).
7. R. A. Magris *et al.*, *Conserv. Lett.* **11**, e12439 (2018).
8. E. T. Game *et al.*, *Trends Ecol. Evol.* **24**, 360 (2009).
9. A. L. Green *et al.*, *Biol. Rev.* **90**, 1215 (2014).
10. A. Arias, R. L. Pressey, R. E. Jones, J. G. Álvarez-Romero, J. E. Cinner, *Oryx* **50**, 18 (2016).
11. L. C. Gerhardinger, E. A. Godoy, P. J. Jones, G. Sales, B. P. Ferreira, *Environ. Manage.* **47**, 630 (2011).
12. B. C. O'Leary *et al.*, *BioScience.* **68**, 5 (2018).

10.1126/science.aat6215


A marae (Māori meeting place) in New Zealand.

PHOTO: DAVE WARREN, UNIVERSITY OF OTAGO

OUTSIDE THE TOWER

Sharing chemistry with Māori students

I am bubbling dry ice in a beaker of sea water, showing how global warming is affecting our oceans, in front of Waikawa marae (a Māori meeting place) in Waikawa Bay, New Zealand. Fifty 14- to 16-year-old Māori students watch the demonstration intently. I have traveled for 6 hours to stay on this marae and show the students of the local iwi (tribe) that science isn't always carried out in a lab with a white coat on. Science, I tell them, is all around us in our everyday lives and works alongside Māori traditional knowledge. By linking traditions of caring for the environment with modern science, I hope to encourage Māori students to become the scientists our country needs.

After the last experiment in the chemistry show, I sit down with the students and share some chemistry YouTube videos on my laptop. One student, a young girl who spends any spare moment trying to start a game of rugby, marvels at how much the university is paying to fly me to the marae and provide materials for the program. She asks, "Why pay all that money just to come and do science with us?"

"Your teachers believe in you, and we think you're worth it."

Silence.

By the end of the visit, 50 students, local teachers, and I have slept in the same room for nearly a week, shared the cooking and cleaning, and worked together to test the water quality of the local river. To me, the essence of the Science Wānanga program (a Māori learning forum that involves rich and dynamic sharing of knowledge; www.otago.ac.nz/science-wananga) is to show Māori students that they are worth investing in.

Although the program aims to inspire Māori students to take an interest in science, scientists such as myself learn a great deal during our stay. Māori traditions of caring for the environment have been passed on for hundreds of years, and through Science Wānanga I gained a great deal of respect for New Zealand's indigenous people. The Māori people's relationship with their environment makes clear that these students already have the background they need to be fantastic scientists. We simply must invest in their education.

Marina Roxburgh
Department of Chemistry, University of Otago, Dunedin, 9010, New Zealand.
Email: mroxburgh@chemistry.otago.ac.nz

10.1126/science.aat6040

TECHNICAL COMMENT ABSTRACTS

Comment on "Maxima in the thermodynamic response and correlation functions of deeply supercooled water"

Frédéric Caupin, Vincent Holten, Chen Qiu, Emmanuel Guillerm, Max Wilke, Martin Frenz, José Teixeira, Alan K. Soper

Kim *et al*. recently measured the structure factor of deeply supercooled water droplets (Reports, 22 December 2017, p. 1589). We raise several concerns about their data analysis and interpretation. In our opinion, the reported data do not lead to clear conclusions about the origins of water's anomalies.
Full text: dx.doi.org/10.1126/science.aat1634

Response to Comment on "Maxima in the thermodynamic response and correlation functions of deeply supercooled water"

Kyung Hwan Kim, Alexander Späh, Harshad Pathak, Fivos Perakis, Daniel Mariedahl, Katrin Amann-Winkel, Jonas A. Sellberg, Jae Hyuk Lee, Sangsoo Kim, Jaehyun Park, Ki Hyun Nam, Tetsuo Katayama, Anders Nilsson

Caupin *et al.* have raised several issues regarding our recent paper on maxima in thermodynamic response and correlation functions in deeply supercooled water. We show that these issues can be addressed without affecting the conclusion of the paper.
Full text: dx.doi.org/10.1126/science.aat1729

TECHNICAL COMMENT

WATER THERMODYNAMICS

Comment on "Maxima in the thermodynamic response and correlation functions of deeply supercooled water"

Frédéric Caupin,[1]* Vincent Holten,[1] Chen Qiu,[2] Emmanuel Guillerm,[1] Max Wilke,[3] Martin Frenz,[2] José Teixeira,[4] Alan K. Soper[5]

Kim *et al*. recently measured the structure factor of deeply supercooled water droplets (Reports, 22 December 2017, p. 1589). We raise several concerns about their data analysis and interpretation. In our opinion, the reported data do not lead to clear conclusions about the origins of water's anomalies.

The structure factor of a fluid, $S(q)$, where q is the wave vector change, is related by Fourier transform to the pair correlation function of molecules in the fluid. In water, $S(q)$ exhibits a rise at low q, whose amplitude increases as temperature decreases and water becomes supercooled, as observed by Kim *et al.* (*1*). This anomalous behavior is related to κ_T (compressibility at constant temperature T) increasing upon cooling, because $S(0) = (\rho/m)\, k_B T \kappa_T$, where ρ is the liquid density, m is the molecular mass, and k_B is the Boltzmann constant. The analysis in (*1*) involves Ornstein-Zernike formalism, which is reliable near a critical point when $S(0)$ and κ_T diverge, density fluctuations are enhanced, and their correlation length ξ becomes much larger than the molecular spacing. However, in (*1*), $S(0)$ and ξ remain small [$S(0) <$ 0.1 and $\xi <$ 0.42 nm], making ξ very sensitive to the choice of splitting $S(q)$ between normal and anomalous components (*2*). Note also that ξ is not a cluster size, as figure 4B of (*1*) could suggest.

Kim *et al.* also deduced κ_T from $S(0)$. Knowledge of ρ is required but is only available above 239.74 K (*3*). To analyze data down to ~227.7 K, Kim *et al.* used an extrapolation intermediate between two formulas (*3*, *4*) [figure S8A of (*1*)]. Wölk and Strey (*4*) overestimated available ρ (*3*) by 2.6 kg m^{-3} at low temperature and their formula should not be used. The intermediate choice in (*1*) has a similar issue. The remaining formula (*3*) is a higher-quality, polynomial fit (maximum deviation 0.24 kg m^{-3}). We tried an empirical power law, $\rho_0 + \rho_1 T + \rho_\gamma (T/T_s - 1)^\gamma$, suggested by Speedy and Angell (*5*), where T_s and γ are adjustable parameters. The fit has the same quality as the polynomial, but it extrapolates to lower densities. For a given value of $S(0)$, changing the extrapolation from ρ to ρ' multiplies κ_T by ρ/ρ'. Using the power law with T_s between 225 and 227 K yields an extremely flat trend for κ_T at low temperature (Fig. 1), which, taking into account the error bars, casts doubt on the existence of a maximum.

Any choice of extrapolation for the density is arbitrary. Still, if a choice yields a maximum in κ_T at a temperature T_m, one can discuss its statistical significance. In their supplementary materials, Kim *et al.* tested the null hypothesis "Measured value at T_m is lower than the values at lower temperatures" with a p-value analysis: "Given the probability densities corresponding to the measured data points, [the authors] draw a set of values and evaluate whether it fulfills the null hypothesis or not." For the probability p to get no maximum in κ_T, the procedure gives $p = 11.8\%$ for H_2O. However, the premise of the test is questionable. It starts by assuming that the actual $\kappa_T(T)$ curve exhibits a maximum, and calculates the probability for an experiment to miss it. Here, instead, we first assume that the actual $\kappa_T(T)$ curve is monotonic, and we calculate the probability that an experiment gives an artificial maximum. We have tried two ansätze for the assumed monotonic curve, which both fit the data in (*1*) within their standard error: (i) a parabola; (ii) a flatter function, $a \tanh[b(x/c - 1)] + d$ (Fig. 1). For each temperature reported in the experiment, we drew synthetic data from a Gaussian distribution around the ansatz function, with a standard deviation equal to the experimental standard error. We repeated the procedure for 10^6 data sets and measured the probability p^* to find a maximum value at a temperature strictly above the lowest one. The result is $p^* = 35.3\%$ for the parabolic ansatz and 61.2% for the flatter ansatz. The maximum in κ_T reported in (*1*) is not statistically significant.

We have not considered other effects, such as a possible revision of the temperature estimate (*6*), nor have we considered how changing the extrapolation for ρ would change the normal component [calculated from hard spheres at density ρ (*1*)] used to decompose $S(q)$, which would in turn alter the results for ξ and κ_T. In our opinion, from the $S(q)$ data in (*1*), there is no definitive evidence for or against a maximum in ξ or in κ_T. No conclusion can be drawn about which scenario should be preferred to explain the strange behavior of water.

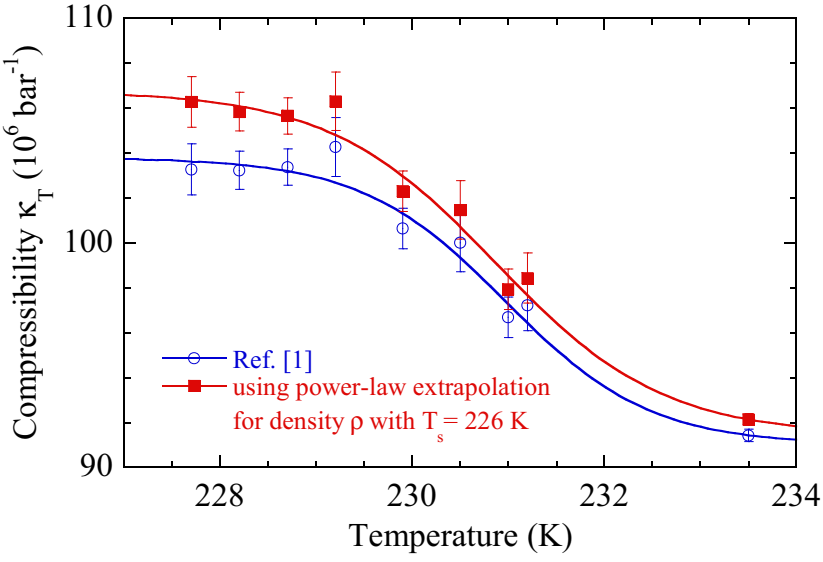

Fig. 1. A choice of extrapolation for the density ρ different from that in Kim *et al*. yields a very flat isothermal compressibility κ_T at low temperature. The solid lines show monotonic hyperbolic tangent functions that fit the data sets within their standard error (reduced $\chi^2 = 0.7$).

[1]Université de Lyon, Université Claude Bernard Lyon 1, CNRS, Institut Lumière Matière, F-69622 Villeurbanne, France. [2]Institute of Applied Physics, University of Bern, 3012 Bern, Switzerland. [3]Universität Potsdam, Erd- und Umweltwissenschaften, 14476 Potsdam, Germany. [4]Laboratoire Léon Brillouin (CEA/CNRS), CEA Saclay, F-91191 Gif-sur-Yvette, France. [5]ISIS Facility, STFC Rutherford Appleton Laboratory, Didcot, Oxon OX11 0QX, UK.
*Corresponding author. Email: frederic.caupin@univ-lyon1.fr

An argument is also put forward in (*1*) to rule out the critical point–free model (*7*): If the evaporating droplets cross a liquid-liquid transition at ambient pressure, the authors would "expect a discontinuous change with the coexistence of two peaks in the structure factor." We agree that a first-order phase change would be directly observable in $S(q)$ if a phase change occurred. However, we note that when the droplet temperature crosses 273.15 K, although $S(q)$ changes continuously, this is not sufficient to conclude that ice does not exist. What happens is that water remains liquid in a metastable state with respect to ice, beyond the line of liquid-ice equilibrium. Metastability is a characteristic feature of first-order transitions. Typical conditions to avoid nucleation of the more stable phase and promote metastability are cleanliness, small sample size, and short experimental time scales. These conditions are met by micrometer-sized droplets evaporating in vacuum. Even if they cross the location of a first-order equilibrium line (either the well-known ice-liquid line or the putative liquid-liquid line), they might therefore still remain metastable with respect to the other phase, without any abrupt change in $S(q)$.

We conclude by mentioning the first experimental report (*8*) of the long-sought line of maxima in κ_T along isobars, overlooked by Kim *et al.* It was proposed (*9*) that such a line, possibly hidden by the line of homogeneous ice nucleation at positive pressure, might emerge in the experimentally accessible region at negative pressure. Early experiments in this region (*9*) found a minimum in sound velocity along an isochore, and a first equation of state for stretched water was obtained from interpolation of sound velocity (*10*). However, because of the limited amount of data, different interpolations of similar quality yielded curves for κ_T at negative pressure either monotonic or with maxima (*10*). Recently, more sound velocity minima were measured in samples at other densities, which further constrained the possible interpolations: They all consistently lead to a line of maxima in κ_T along isobars around −100 MPa and 265 K (*8*). We emphasize that although a κ_T maximum is a necessary condition for the validity of both the second critical point scenario (*11*) and the singularity-free interpretation (*12*), it is not sufficient to allow a decision between them. The exciting possibility of observing more anomalies of water at positive pressure by reaching extreme supercooling, as in (*1*) and (*6*), calls for more experiments.

REFERENCES

1. K. H. Kim *et al.*, *Science* **358**, 1589–1593 (2017).
2. G. N. I. Clark, G. L. Hura, J. Teixeira, A. K. Soper, T. Head-Gordon, *Proc. Natl. Acad. Sci. U.S.A.* **107**, 14003–14007 (2010).
3. D. E. Hare, C. M. Sorensen, *J. Chem. Phys.* **87**, 4840–4845 (1987).
4. J. Wölk, R. Strey, *J. Phys. Chem. B* **105**, 11683–11701 (2001).
5. R. J. Speedy, C. A. Angell, *J. Chem. Phys.* **65**, 851–858 (1976).
6. C. Goy *et al.*, *Phys. Rev. Lett.* **120**, 015501 (2018).
7. C. A. Angell, *Science* **319**, 582–587 (2008).
8. V. Holten *et al.*, *J. Phys. Chem. Lett.* **8**, 5519–5522 (2017).
9. G. Pallares *et al.*, *Proc. Natl. Acad. Sci. U.S.A.* **111**, 7936–7941 (2014).
10. G. Pallares, M. A. González, J. L. F. Abascal, C. Valeriani, F. Caupin, *Phys. Chem. Chem. Phys.* **18**, 5896–5900 (2016).
11. P. H. Poole, F. Sciortino, U. Essmann, H. E. Stanley, *Nature* **360**, 324–328 (1992).
12. S. Sastry, P. G. Debenedetti, F. Sciortino, H. E. Stanley, *Phys. Rev. E* **53**, 6144–6154 (1996).

31 January 2018; accepted 13 April 2018
10.1126/science.aat1634

TECHNICAL RESPONSE

WATER THERMODYNAMICS

Response to Comment on "Maxima in the thermodynamic response and correlation functions of deeply supercooled water"

Kyung Hwan Kim,[1] Alexander Späh,[1] Harshad Pathak,[1] Fivos Perakis,[1] Daniel Mariedahl,[1] Katrin Amann-Winkel,[1] Jonas A. Sellberg,[2] Jae Hyuk Lee,[3] Sangsoo Kim,[3] Jaehyun Park,[3] Ki Hyun Nam,[3] Tetsuo Katayama,[4] Anders Nilsson[1]*

Caupin *et al*. have raised several issues regarding our recent paper on maxima in thermodynamic response and correlation functions in deeply supercooled water. We show that these issues can be addressed without affecting the conclusion of the paper.

Caupin *et al.* (*1*) question our application (*2*) of the Ornstein-Zernike (OZ) approach for noncritical divergence when the correlation length ξ becomes small, of similar magnitude as the intermolecular distance, such that the division of $S(q)$ into normal and anomalous components strongly affects the resulting value of ξ. First, ξ is not related to a specific distance in real space but is the damping factor in the asymptotic decay of the pair correlation (*3*). Second, we have followed exactly the same procedure in our determination of ξ as earlier outlined by one of the authors of (*1*) [in (*4*)] for noncritical divergence based on OZ theory of 253 K water, using a division of $S(q)$ into anomalous and normal components.

Third, the argument against that approach given in reference 2 of (*1*) is valid for 298 K where the low-q enhancement is extremely small, contrary to 280 K (see our determined structure factor variation in Fig. 1A where a detectable enhancement is clearly observed, which increases rapidly upon cooling). Figure 1B shows ξ as a function of temperature, and indeed the error bars are large in the estimation of ξ at high temperatures (~280 K). At the lower temperatures, the enhancement of $S(q)$ at $q = 0$ is approaching a factor of 2 in comparison to the minimum at $q = 0.5$ Å^{-1}, and the estimation of ξ becomes increasingly independent of the choice of the normal component and the density ρ used, resulting in small error bars as indicated in (*2*).

Figure 4B in (*2*) does not show clusters but is an illustration of fluctuating regions that vary in size as a function of temperature, as described in the caption. It is similar to the description from one of the authors of (*1*) [in (*5*)] as "transient hydrogen-bonded patches supported experimentally by the observation of small-angle x-ray scattering."

In (*2*), the compressibility κ_T values are reported by using the extrapolated density ρ below 239.74 K, and the exact shape of $\kappa_T(T)$ depends on the choice of extrapolation to lower temperatures. We already tested the effect from the various extrapolations and have shown that it does not change the overall shape of the curve [supplementary text and figure S8 of (*2*)]. Caupin *et al.* propose to use a power law with T_s between 225 and 227 K that would yield a flatter temperature dependence instead of a maximum. There is a clear reason why T_s between 225 and 227 K should not be used in a power-law fit: ρ would go significantly below the density of low-density amorphous ice at 228 and 229 K and would even become negative just above 225 and 227 K, respectively, which would be unphysical. We note that two authors of (*1*) [in reference 6 of (*1*)] did not use what they propose in (*1*), but instead applied extrapolations of ρ similar to those tested in (*2*).

The definition of the null hypothesis given in (*1*) [reproduced from (*2*)] is unusual. Although we did not assume any functional form for the test, specific functional forms were used in (*1*) (a parabola or a hyperbolic tangent function) even though the correct form is not known. In this case, the statistical hypothesis testing will relate to whether this specific functional form explains the experimental data well or not, and it is no longer related to the question regarding the presence or absence of a maximum; needless to say, there are an infinite number of other functional forms that do not exhibit a maximum. We also note that the appearance of a common maximum in all the eight plots, intensity of the small-angle x-ray scattering (SAXS), derivative of the first diffraction peak, ξ, and κ_T for H_2O and D_2O, shown in figures 2 and 3 of (*2*) adds further statistical significance to its existence.

The temperature has been estimated using the Knudsen evaporation model exactly in the same fashion as by two authors of (*1*) [in reference 6 of (*1*)]. The difference is that in reference 6 of (*1*), they determined the droplet diameter using Raman spectroscopy, but in (*2*) we could rely on the image from an optical microscope, as our droplet sizes are much larger.

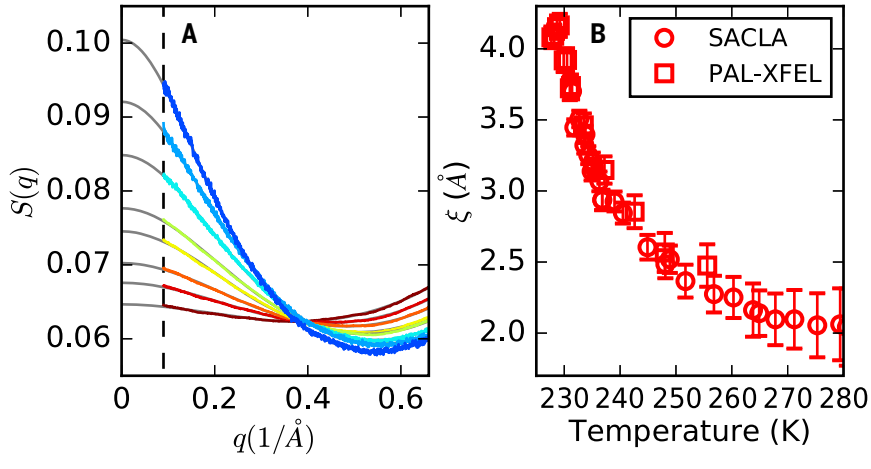

Fig. 1. OZ analysis of SAXS curves and correlation length. (**A**) Structure factor of H_2O measured at SACLA from (*2*) for temperatures between 280 K (dark red) and 231 K (dark blue). Gray lines show the OZ fit using the q range up to 0.65 Å^{-1}. (**B**) Correlation length obtained from the OZ fit for both the SACLA and PAL-XFEL data. The standard errors vary depending on the anomalous increase of the structure factor in (A) and are relatively large at high temperatures and small at low temperatures.

[1]Department of Physics, AlbaNova University Center, Stockholm University, SE-10691 Stockholm, Sweden. [2]Biomedical and X-Ray Physics, Department of Applied Physics, AlbaNova University Center, KTH Royal Institute of Technology, SE-10691 Stockholm, Sweden. [3]Pohang Accelerator Laboratory, Pohang, Gyeongbuk 37673, Republic of Korea. [4]Japan Synchrotron Radiation Research Institute, Kouto 1-1-1, Sayo, Hyogo 679-5198, Japan.
***Corresponding author. Email: andersn@fysik.su.se**

It is true that metastability can occur for a hypothetical liquid-liquid phase transition, but the singularity point–free model would imply that the diverging temperature for the response functions would correspond to the spinodal of the transition where the metastability would be lifted exactly as stated by one of the authors of (*1*) [in (*4*)]. Because no phase transition is observed at the maxima of the response and correlation functions, there is no indication of a spinodal and therefore the critical point–free model is inconsistent with our experimental data. Furthermore, the change in the structure factor with temperature goes through a maximum, followed by a slower change and finally reaching a value close to that of low-density amorphous ice, indicating that a sharp but continuous transition has occurred.

Caupin *et al*. claim that we have in (*2*) overlooked their study [reference 8 of (*1*)], which cannot be the case when considering the dates: The journal receipt date of (*2*) is almost 1 month earlier than that of reference 8 of (*1*). We also note that reference 8 of (*1*) suggests that there are maxima in κ_T at negative pressures, which is fully consistent with our findings—the existence of maxima of κ_T at positive pressures—given in (*2*).

REFERENCES AND NOTES

1. F. Caupin *et al*., *Science* **360**, eaat1634 (2018).
2. K. H. Kim *et al*., *Science* **358**, 1589–1593 (2017).
3. A. Nilsson, C. Huang, L. G. M. Pettersson, *J. Mol. Liq.* **176**, 2–16 (2012).
4. L. Bosio, J. Teixeira, H. E. Stanley, *Phys. Rev. Lett.* **46**, 597–600 (1981).
5. M. C. Bellissent-Funel, J. Teixeira, L. Bosio, J. Dore, P. Chieux, *Europhys. Lett.* **2**, 241–245 (1986).

ACKNOWLEDGMENTS

Supported by a European Research Council Advanced Grant under project no. 667205 and the Swedish National Research Council. The experiments were performed at beamline NCI of PAL-XFEL (proposal no. 2017-1st-CXI-006) funded by the Ministry of Science and ICT of Korea and at beamline BL3 of SACLA with the approval of the Japan Synchrotron Radiation Research Institute (proposal no. 2016A8015).

12 February 2018; accepted 13 April 2018
10.1126/science.aat1729

SPECIAL SECTION

REVIEWS

RELATED ITEM ► PODCAST

MEETING

RESISTANCE

By **Caroline Ash**

Almost as soon as antibiotics were discovered to be valuable in medicine, resistance emerged among bacteria. Whenever mutating or recombining organisms are faced with extirpation, those individuals with variations that avert death will survive and reproduce to take over the population. This can happen rapidly among organisms that reproduce fast and outpace our efforts to combat them. Thus, our use of chemical entities to rid ourselves of clinical, domestic, and agricultural pathogens and pests has selected for resistance.

Today, we find ourselves at the nexus of an alarming acceleration of resistance to antibiotics, insecticides, and herbicides. Through chemical misuse, resistance also brings widespread collateral damage to natural, social, and economic systems. Resistance to antifungal agents poses a particular challenge because a limited suite of chemicals is used in both agricultural and clinical settings.

Evolution will always circumvent head-on attack by new biocides, and we may not be able to invent all the new products that we need. We must therefore harness evolutionary approaches to find smarter ways to minimize the erosion of chemical susceptibility. We now have it in our means to integrate a variety of approaches to pest and pathogen management, including rigorous regulation of prescription behavior, consistent use of clinical hygiene measures, physical barriers to crop pests, and alternative cropping regimes. We urgently need to revisit our reliance on chemicals to ensure our future medical and food security.

A farmer sprays pesticides on crops. Our health and food security are threatened by escalating resistance to such biocides.

PHOTO: ISTOCK.COM/FOTOKOSTIC

REVIEW

Wicked evolution: Can we address the sociobiological dilemma of pesticide resistance?

Fred Gould,[1,2]* Zachary S. Brown,[1,3] Jennifer Kuzma[1,4]

Resistance to insecticides and herbicides has cost billions of U.S. dollars in the agricultural sector and could result in millions of lives lost to insect-vectored diseases. We mostly continue to use pesticides as if resistance is a temporary issue that will be addressed by commercialization of new pesticides with novel modes of action. However, current evidence suggests that insect and weed evolution may outstrip our ability to replace outmoded chemicals and other control mechanisms. To avoid this outcome, we must address the mix of ecological, genetic, economic, and sociopolitical factors that prevent implementation of sustainable pest management practices. We offer an ambitious proposition.

The first documentation of resistance evolving to an insecticide was published in 1914, and the researcher who discovered the problem emphasized that if we did not develop approaches for more judicious use of insecticides, the problem of resistant pests would continue (*1*). Although agriculturalists have developed the field of "resistance management," with more than 3000 publications since 1980 (*2*), we mostly continue to use insecticides and herbicides (hereafter collectively called pesticides) as if resistance is a temporary issue that will be solved by commercialization of new products with novel modes of action (*3*). Evolution of resistance by arthropods and weeds to control measures costs billions of U.S. dollars per year (*4*, *5*) and may lead to loss of millions of lives (*6*). Breakthroughs in chemistry and molecular biology may provide many new pesticides and novel methods for pest control, but there is also a considerable chance that the evolution of pest resistance will outpace human innovation.

Consider the case of malaria, where the use of insecticide-treated bednets (ITNs) and indoor residual sprays (IRS) is estimated to have averted more than 0.5 billion cases of malaria between 2000 and 2015 (*7*). Resistance is evolving to the insecticides used, and there is growing concern over resurgence of the malaria-vector mosquito populations (*6*). Although efforts are being made to develop new insecticides aimed at mosquitoes (*8*), it is not clear that the new compounds will become available soon enough and be as cost-effective as the current ones.

[1]Genetic Engineering and Society Center, North Carolina State University, Raleigh, NC 27695-7613, USA. [2]Department of Entomology and Plant Pathology, North Carolina State University, Raleigh, NC 27695-7613, USA. [3]Department of Agricultural and Resource Economics, North Carolina State University, Raleigh, NC 27695-7613, USA. [4]Department of Public Administration, North Carolina State University, Raleigh, NC 27695-7613, USA.
*Corresponding author. E-mail: fred_gould@ncsu.edu

In 1996, companies commercialized genetically engineered crops that were not harmed by glyphosate, an herbicide that has broad-spectrum toxicity to weed species. The flexibility and profits that these crops brought to farmers resulted in over 90% of U.S. maize (corn), soybean, and cotton hectares planted to herbicide-tolerant varieties by 2014 (*9*). The accompanying widespread use of glyphosate resulted in more than 40 weed species evolving resistance and consequently diminished the utility of the herbicide-tolerant crop varieties (*10*) (Fig. 1, left). To address this problem, companies have reengineered crops to be tolerant of the plant hormone (auxin)–mimicking herbicides 2,4-D and Dicamba. These herbicides were first commercialized in 1945 and 1967, respectively. This reaching back to the past has become necessary because no herbicides with new modes of action have been commercialized in more than 30 years (*11*). Weed species have evolved resistance to every herbicide class in use (Fig. 1, right), and more than 550 arthropod species have resistance to at least one insecticide (Fig. 2). Cases have emerged where no pesticide remains effective. In Australia, weeds in wheat became resistant to all herbicides available and resulted in farmers designing machines to harvest weed seeds for population suppression [e.g., *12*].

If we are to address this recalcitrant issue of pesticide resistance, we must treat it as a "wicked problem," in the sense that there are social, economic, and biological uncertainties and complexities interacting in ways that decrease incentives for actions aimed at mitigation. Here, we summarize the interacting factors and conclude with a call for government support of ambitious landscape-level experiments to assess which pesticide use strategies decrease resistance risks.

Ecology and genetics

Insecticides and herbicides are typically designed to disrupt or mimic a single biologically active protein that is critical to survival of a pest organism. Protein targets in insects are typically involved in function of the nervous system, but some more recently developed insecticides affect growth and development. Herbicides often target enzymes involved in photosynthesis or growth patterns.

Resistance can emerge from a single mutation making a protein less susceptible to action of the pesticide. Alternatively, a single mutation can increase the amount or efficiency of an enzyme that degrades the insecticide or herbicide. These two modes of resistance are common (*13*, *14*), but other forms of resistance have been found that involve gene duplication or multiple genes acting together, each with a small but additive impact on resistance (*15*).

One or two locus population genetic models permit a general understanding of pesticide resistance evolution. More realistic, predictive models require combining population genetics with empirical data on population biology (e.g., life history, mating behavior, and gene flow) of the pest species and the fitness of each genotype in environments with and without the pesticide (i.e., fitness cost). Accurate data on these parameters are difficult to collect and can vary among localities. Most insecticides are sprayed at a specific concentration on a given crop, but over time the insecticide decays, so insects contacting a sprayed plant 1 day versus 10 days after the spraying encounter different doses. The dose on day 1 might kill 90% of insects homozygous for the susceptible allele and only 10% of those homozygous for the resistant allele, while on day 10, only 20% of the susceptible homozygotes would die. If most of the insects were encountering the insecticide-treated plant on day 1, the rate of resistance evolution would be predicted to be faster than if most of the encounters were on day 10. To further complicate matters with insecticides and herbicides, not every sprayed plant or plant leaf receives the same amount of pesticide. In sexually reproducing weeds and insects, the rate of resistance evolution is strongly influenced by the relative fitness (dominant to recessive) of heterozygotes, and this sometimes depends on the dose of pesticide encountered in the field (Fig. 3). Thus, it is difficult (and controversial) to determine whether resistance is expected to evolve more rapidly to higher or lower application concentrations of a pesticide [e.g., *16, 17*].

Even more complexity arises in attempts to predict resistance evolution when combinations of pesticides are applied (*18*, *19*). Although the idea that such combinations will slow resistance evolution is theoretically controversial and lacks empirical support, mixtures are often recommended at the field level (*15*).

Although there is high uncertainty regarding many resistance management choices, under almost all circumstances entomologists agree that using an integrated pest management (IPM) approach that results in fewer insecticide applications

should decrease the rate of resistance evolution (*18*).

Toxins derived from the bacterium *Bacillus thuringiensis* (Bt) have been widely used in engineered insecticidal crops. Here, variation in the dose of toxin received by insects is less of a problem (*20*). Engineered plants can produce season-long Bt-toxin concentrations that, for some insect pests, kill all susceptible individuals and almost all heterozygotes (*21*). Season-long consistently high toxin doses, when coupled with a percentage of the crop planted to a nontoxic variety (i.e., that act as refuges for susceptibility) is predicted to slow resistance evolution by a factor of 10 to 100. This strategy is known as the high-dose/refuge approach (*17*) and has been used for more than 20 years with some target pests. Tabashnik and Carrière (*22*) have examined 30 cases of long-term planting of Bt-toxin–producing crops: In nine cases where a high dose of Bt was achieved, neither economically important target pest resistance nor early warnings of resistance were found, but in 17 of 21 cases in which high doses were not achieved, resistance had evolved or showed evidence of emergence. Some of the cases of resistance occurred in low- or middle-income nations where refuges were not planted or where the crop varieties were not engineered for the relative susceptibility of the local pests and therefore did not maintain a high enough toxin dose.

The focus in the resistance management literature is on resistance to chemical control, but widespread use of other control tactics—including biological control, crop rotation, and hand weeding—also faces the challenges of resistance evolution (*23*). For example, the northern and western corn rootworms, which are mostly restricted to feeding on maize (corn) roots as larvae, have evolved resistance to the rotation of maize and soybean. One species has evolved to mostly overwinter as an egg for 2 years instead of 1, so when there is a typical 2-year rotation of maize and soybean, the larvae emerge from the hatching eggs in time for the next maize planting. The other species evolved to lay some of its eggs in the soil beneath soybean plants, "anticipating" maize in the next season. Most amazingly, some weeds have evolved to look like rice plants and thus avoid hand hoeing, and others have evolved seeds that mimic those of the crop they infest and are replanted along with crop seeds (*23*).

"...we must treat it [resistance] as a 'wicked problem,' in the sense that there are social, economic, and biological uncertainties and complexities interacting in ways that decrease incentives for actions aimed at mitigation."

Whenever humans act in any way to decrease the fitness of an insect or weed, natural selection is likely to result in a response. Insect growth regulators that mimic hormones were at one time considered resistance-proof insecticides, but in the end this tactic did not deter evolution of resistance (*23*). Ultimately, even with all of the biological uncertainties involved in resistance management, it remains the only current option for limiting the economic and social impact of pest evolution.

Economic perspectives

Pesticide resistance has both economic causes and economic consequences. Agricultural benefits lost from resistance in the United States have been estimated at about US$10 billion per year (*5*). Globally, reliance on pesticides has been increasing (*24*), exacerbating the impact of resistance. Pesticides also bear costs for the environment and public health (*24*). Some pesticides, such as Bt toxins (used either in engineered crops or in organic agriculture), have replaced broader-spectrum pesticides that were more toxic to nontarget organisms (*24*). Hence, a loss in the effectiveness of Bt toxins owing to resistance has environmental consequences if we revert to a less target-specific replacement. This rationale has been used in the formulation of government regulations for managing resistance to Bt crops (*17*).

Insecticide resistance in public health is also imposing substantial damages, although fewer studies are available that quantify the economic costs. Model-based analysis has shown that if disease vector resistance to pyrethroids becomes widespread, cases of malaria averted with ITNs could decline by 40% (*25*). Coupled with the estimate that bednets averted more than 65 million clinical malaria cases in sub-Saharan Africa in 2015 (*7*), and assuming that this figure provides a lower bound for potential cases averted in subsequent years, this would imply around 26 million additional clinical cases of malaria per year as a result of widespread vector resistance. Assuming an approximate lower bound cost of illness of at least $10 per malaria episode (*26*), insecticide resistance could

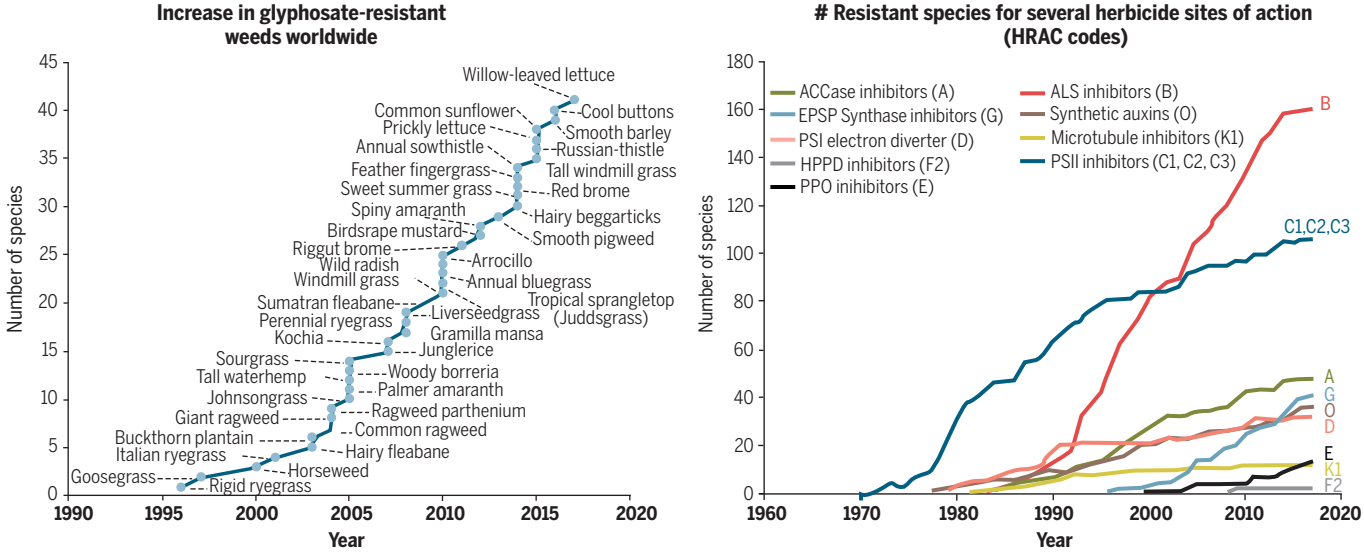

CREDIT: I. HEAP, WEEDSCIENCE.ORG 2018, ADAPTED BY H. BISHOP

Fig. 1. Weed species with resistance to herbicides. (**Left**) Cumulative number of weed species with resistance to glyphosate. (**Right**) Cumulative number of weed species with resistance to herbicides in the major mechanism of action groupings.

conservatively cost sub-Saharan Africa at least $260 million per year.

Although these numbers make clear that the potential costs are large enough to warrant stronger policies for managing pesticide resistance, they do not tell us exactly what return society might expect from different investments in resistance management. The most basic insight from economics is that efficient pesticide use should weigh current net benefits of use against the costs of lost future effectiveness (*27*). To assess these future costs, economic discounting and the uncertainty of developing replacement pest control technologies must be factored in. As yet, the user costs of resistance are not computed in any systematic way, although recent methods for computing prices for natural capital and ecosystem services could be applied (*28*).

Laxminarayan and Simpson (*29*) have analyzed the optimal refuge sizes for managing pest resistance to Bt crops. They found that fitness costs of resistance are critical for determining whether refuges are economically efficient in the long run. Fitness costs determine whether susceptibility can be renewed after accumulating high levels of resistance in the pest population. If this renewal rate is less than an expected rate of return on financial assets, then it is optimal in the long run to deplete pesticide susceptibility. Likewise, the importance of fitness costs has been shown for economic management of resistance to pyrethroid insecticides in malaria control (*30*) and agriculture (*31*).

Fitness costs, dominance, and initial frequencies of resistance genes remain highly uncertain in field settings for many pesticides. However, reducing uncertainty is costly, and better information may be more actionable for some of these factors than others, as has been shown for malaria vectors (*32*). For example, more certainty about the efficacy of noninsecticidal alternatives may be more valuable than better information about the fitness costs of resistance.

Ultimately, the costs of pesticide resistance to users depend on available control alternatives. However, no herbicides with new modes of action have been commercialized in more than 30 years, and the estimated cost of discovery of new insecticides has increased by a factor of eight in the past 50 years (*33*). Other tools with demonstrated effectiveness at managing resistance within an IPM framework range from biocontrol (*34*) to the sterile insect technique (*35*), but the implementation of these approaches is costly and complicated.

Pesticide susceptibility shares properties of a common pool resource (*36*). One party's use of a pesticide draws down the stock of susceptibility to that pesticide available not only to that party but also to other users. Furthermore, one user cannot limit use of the stock by others. The result is that users overexploit the resource relative to what would be economically efficient. One solution is to tax pesticide use to reflect the marginal user costs of resistance and the negative environmental impacts of pesticides. Four European countries have implemented pesticide taxes based on these motivations, although practical challenges impede their broader adoption (*37*).

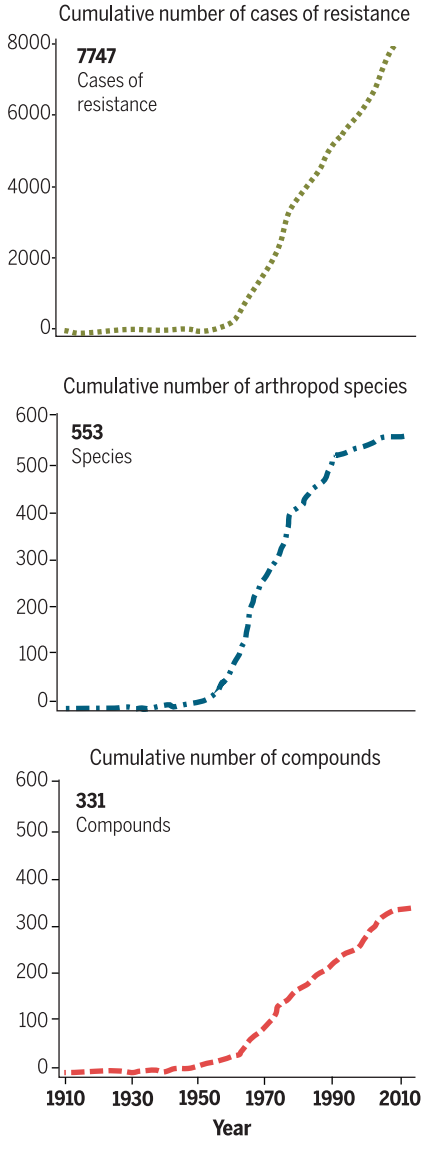

Fig. 2. Arthropods with resistance to insecticides. Data from 1910 to 2010 showing total number of species (dark blue dotted and dashed line), total number of cases of resistance to any insecticidal compound reported from a new location (green dashed line), and total number of compounds with resistance found in at least one arthropod species (light blue dashed line) (*56*).

One rationale supporting the laissez-faire management of weed resistance to glyphosate was the erroneous assumption that weeds were relatively immobile (*3*). This contrasts with extensive regulation of Bt crops to manage insect resistance, where the mobility of target pests of Bt crops was explicitly used as one rationale in refuge policies (*17*).

Because the use of Bt crops and other control tactics can result in suppression of the target pest over wide areas, incentives for overexploitation of susceptibility can be counterbalanced by the public good of areawide pest suppression. For example, areawide suppression of the European corn borer in the U.S. Midwest from use of Bt maize reduced pest damages by $2.4 billion among growers of non-Bt maize (*38*). Subsequent modeling shows that this areawide protection incentivizes planting of non-Bt varieties (*39*), which is predicted to slow resistance evolution further.

Sociopolitical perspectives

Efforts to decrease the uncertainties of pest resistance are critical to effective management, but an understanding of how these aspects intersect with social and political factors is also needed. Currently, the emphasis is on educational and incentive programs. However, these have not substantially improved resistance management and, as Ervin and Jussaume explain, "often fail to take into account the fact that farm-level decision-making takes place within complex social-cultural settings" (*40*). Sociopolitical research in this area applies at the level of the individual (micro level), the community (meso level), and the federal government or nation-state (macro level). Sociopolitical approaches have rarely been applied to resistance management, so concepts and examples must be drawn from other settings.

Individual level

The individual level of decision-making about pesticide use and resistance management mostly resides with farmers. In public health, households are often the key micro-level decision-makers, as in the case of whether or how to use a bednet. Most research on individuals' perceptions and decisions about pesticide use is framed around economic models of demand for pest control and risk reduction (*41*, *42*) and does not specifically address resistance. Resistance management could benefit from risk perception studies that have been used to analyze other technologies. Such studies would shed light on how factors associated with (i) technological options (e.g., controllability and familiarity), (ii) individuals themselves (e.g., culture, demographics, and worldviews), or (iii) risk managers and communicators (e.g., level of trust and perceived fairness) influence people's perception of risk and motivate them to take action for reducing resistance.

Community level

At the community level, social systems can support or interfere with resistance management programs and compliance. Social capital has been correlated with positive effects on IPM and sustainability, especially in developing nations (*43*). Research on network ties and social capital among U.S. farmers, and their relationship

to the successful implementation of resistance management programs, could shed light on how to enhance collective action.

Because pest susceptibility can often be considered a common pool resource, Ostrom's work on the governance of such resources suggests that resistance may sometimes be better managed by on-the-ground, networked communities generating their own rules and norms for pesticide use (*44*) than by more formal, top-down governance. Regional programs, such as weed management areas, in which local farmers vote to implement different resistance management strategies (*40*), fit this model. In another example, pink bollworm resistance to Bt cotton in the southwest United States has been effectively delayed through voluntary cooperative initiatives and cost-sharing between regional grower associations and the U.S. Department of Agriculture (*35*). In terms of management tools, policy process frameworks, such as institutional analysis and development, can inform the design, implementation, and evaluation of common pool resource governance systems (*44*, *45*). Behavioral tools, such as social marketing, to engender norms for resistance management have also shown recent promise (*46*), but further research is needed.

Macro level

Systems theory and thinking at the macro level can help to uncover the underlying factors contributing to policy problems, such as resistance management, by taking complexity and multiple types of competing and intersecting forces into account (*47*). In complex situations, quite often the most intuitive policies have immediate benefits but over time exhibit counterintuitive behavior (i.e., policy resistance) and fail owing to unanticipated feedback (*48*). For example, the price of maize rose in the first decade of the 21st century in large part due to ethanol mandates in midwestern states, as well as subsidies and higher oil prices. This led to a near-term economic advantage for farmers who stopped rotating maize with soybeans and instead planted maize continuously (*49*). The continuous planting of Bt maize could have led to higher pest resistance to Bt in those areas, an issue that requires further investigation.

Political economy studies at the macro level can also uncover underlying tensions and barriers to effective solutions. For example, chemical companies will desire to sell more pesticides and increase short-term company profits. Sales tactics will compete with government regulators' desires to contain pesticide use to mitigate health and environmental risk. However, recognizing the need to protect the efficacy of their products over the long term, some biotechnology companies selling Bt crop seed have partnered with federal agencies and farmers to implement resistance management programs. For instance, the selling of seed bags with a mixture of Bt and non-Bt seeds allows companies to maintain their level of product sales while complying with regulatory guidelines. It also improves compliance by farmers, although it decreases a farmer's ability to control the situation and might therefore increase their perception of risk and decrease trust at the micro level.

"Lacking data from bold experiments, we will likely just learn that heavy use of 2,4-D and Dicamba results in weed resistance and that we have an even more critical need for herbicides with new modes of action."

National research policy affects how much knowledge and data we have on all of the factors relating to pest resistance and management. Gaps in biological and economic research are affected by the national priorities of each political administration but have traditionally been underresourced, despite their importance to the growing challenge of resistance management (*50*).

A way forward?

We have seen how pesticide resistance is a "wicked problem" arising from interacting uncertainties and competing interests that decrease incentives for action. A pessimistic conclusion would be that the status quo of little action will hold until a major crisis arises. A more proactive stance is challenging but likely to be less costly in the long run, so we conclude by suggesting two optimistic ways forward.

First, in the case of engineered insecticidal crops, a natural experiment has already been performed, and we know with some certainty what action needs to be taken to develop high-dose/refuge approaches that when tailored to specific systems will slow resistance evolution. Still, we must overcome competing interests that hinder our ability to build the political will on the part of governments to work with companies and farmers to ensure appropriate development and use. As observed by Foley (*51*), "GMOs [genetically modified organisms] have

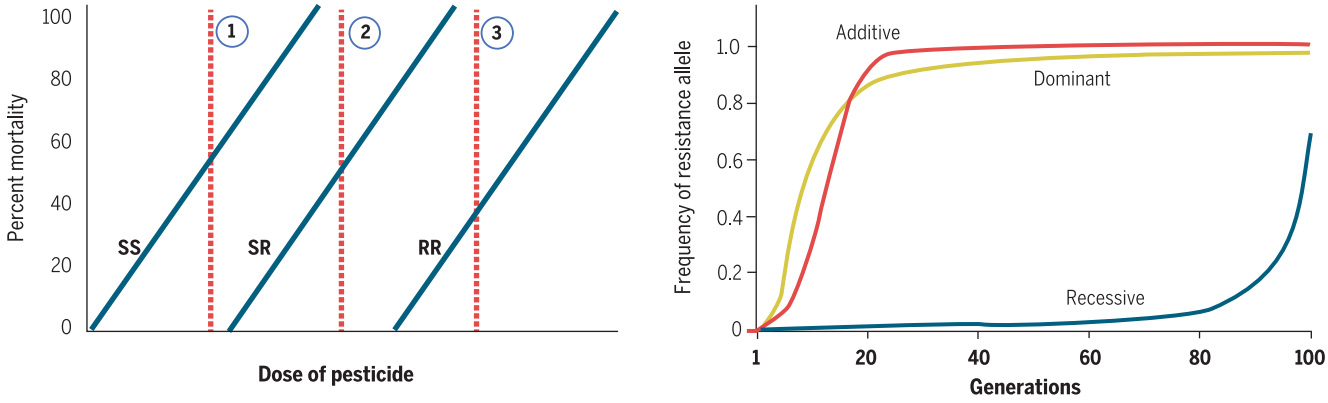

CREDIT: ADAPTED BY H. BISHOP

Fig. 3. Response to selection for resistance to toxins. (**Left**) The solid dark blue lines show the generally expected relationship between the dose of toxin and the mortality of pests that are homozygous for susceptibility alleles (SS), heterozygous (RS), and homozygous for resistance (RR). The vertical, dashed red lines (numbered 1, 2, and 3) show the expected mortality of the three genotypes at different toxin doses. At dose 1, the RS and RR individuals similarly have no mortality, whereas the SS individuals have 50% mortality, so the resistance trait is dominant. At dose 2, the RS mortality is intermediate between SS and RR, so resistance is additive. At dose 3, there is 100% mortality of SS and RS and only 30% mortality of RR, so resistance is recessive. (**Right**) Trajectories of increase over time in resistance allele frequency when resistance is dominant, additive, and recessive.

frequently failed to live up to their potential, not because they are inherently flawed, but because they have been deployed poorly into the complex social and environmental contexts of the real world." Governments should insist on feasible plans for strict enforcement of appropriate use as a condition for commercialization. Knowledge from the social and natural sciences will be needed to guide such governance.

The second and more complex challenge to tackle is for conventional pesticides where there is still a high degree of uncertainty about what the best approaches are to stymie resistance. Although we have data from small-scale experiments, these are not sufficient for understanding resistance dynamics at a landscape level. For crop insects and weeds, large-scale, experimental agriculture, coupled with technical innovation, must go hand in hand. New breakthroughs in genomics and bioinformatics are providing tools that enable detection of genomic responses of insects and weeds to selection with pesticides [e.g., (*52*)]. These tools will put us in a good position to conduct landscape-level experiments on the order of thousands of hectares to decrease uncertainty about the effectiveness of various resistance management practices. It should be possible to detect early genomic and biological signs of resistance and to change management practices before resistance becomes an economic problem. Although these measures will be expensive, complex experiments even with the most localized pests, similar, large-scale endeavors have been tried for eradication of specific insects and weeds, so some of the groundwork has been laid. In addition, such studies will require input from the social sciences to gain appropriate community involvement. Although large-scale experimentation is a substantial investment, in the United States the cost to the federal government (i.e., to taxpayers) for crop insurance to cover crop failures in 2011 was estimated at more than $11 billion, with 265 million acres enrolled (*53*). Policies are being pursued to encourage other agricultural practices, such as cover crops for soil conservation, by tying cover-crop planting to discounts on crop insurance premiums (*54*). Similar approaches could be used for pesticide resistance management. The United States is not the only country with crop subsidies. Certainly, there is a way to use these public investments for the public good of avoiding the long-term costs of resistance.

The United States is about to begin a huge experiment with the commercialization of engineered crops resistant to the action of 2,4-D and Dicamba. These two herbicides will likely be used alone and in combination with glyphosate, despite a lack of knowledge about what usage pattern would be best for decreasing the emergence of resistance in weed populations while maintaining economic viability. This ignorance is reflected in the literature from the EPA and companies that simply tells farmers that diversified approaches to weed management are best for delaying resistance, but with no supporting evidence or incentives (*55*).

Governments and universities could adopt incentive systems to create landscape-level experiments to test different spray combinations, rotations, or combined cultural and chemical controls on large acreages. Genomic responses of weeds would be monitored carefully enough to eliminate any failed strategy before troublesome resistance evolved. Setting up such experiments would require large investments and highly skilled management of people and technologies. This may seem radical, but governments do make similar investments to decrease erosion, maintain conservation reserve programs, and subsidize crop-loss insurance. Lacking data from bold experiments, we will likely just learn that heavy use of 2,4-D and Dicamba results in weed resistance and that we have an even more critical need for herbicides with new modes of action.

REFERENCES AND NOTES

1. A. L. Melander, *J. Econ. Entomol.* **15**, 400–404 (1914).
2. Web of Science, 25 February 2018; https://webofknowledge.com/).
3. A. S. Davis, G. B. Frisvold, *Pest Manag. Sci.* **73**, 2209–2220 (2017).
4. G. B. Frisvold, M. V. Bagavathiannan, J. K. Norsworthy, *Pest Manag. Sci.* **73**, 1110–1120 (2017).
5. S. R. Palumbi, *Science* **293**, 1786–1790 (2001).
6. H. Ranson, N. Lissenden, *Trends Parasitol.* **32**, 187–196 (2016).
7. S. Bhatt, D. J. Weiss, E. Cameron, D. Bisanzio, B. Mappin, U. Dalrymple, K. Battle, C. L. Moyes, A. Henry, P. A. Eckhoff, E. A. Wenger, O. Briët, M. A. Penny, T. A. Smith, A. Bennett, J. Yukich, T. P. Eisele, J. T. Griffin, C. A. Fergus, M. Lynch, F. Lindgren, J. M. Cohen, C. L. J. Murray, D. L. Smith, S. I. Hay, R. E. Cibulskis, P. W. Gething, *Nature* **526**, 207–211 (2015).
8. J. Hemingway, B. J. Beaty, M. Rowland, T. W. Scott, B. L. Sharp, The Innovative Vector Control Consortium, *Trends Parasitol.* **22**, 308–312 (2006).
9. United States Department of Agriculture (USDA), Recent trends in GE adoption in "Adoption of Genetically Engineered Crops in the U.S." (USDA, 2017; https://www.ers.usda.gov/data-products/adoption-of-genetically-engineered-crops-in-the-us/recent-trends-in-ge-adoption/).
10. I. Heap, "The International Survey of Herbicide Resistant Weeds" (Weed Science, 2017; www.weedscience.org).
11. S. O. Duke, *Pest Manag. Sci.* **68**, 505–512 (2012).
12. M. J. Walsh, S. B. Powles, *Pest Manag. Sci.* **70**, 1324–1328 (2014).
13. S. B. Powles, Q. Yu, *Annu. Rev. Plant Biol.* **61**, 317–347 (2010).
14. R. Feyereisen, W. Dermauw, T. Van Leeuwen, *Pestic. Biochem. Physiol.* **121**, 61–77 (2015).
15. C. Délye, M. Jasieniuk, V. Le Corre, *Trends Genet.* **29**, 649–658 (2013).
16. J. Gressel, *Pest Manag. Sci.* **67**, 253–257 (2011).
17. F. Gould, *Annu. Rev. Entomol.* **43**, 701–726 (1998).
18. R. T. Roush, *Parasitol. Today* **9**, 174–179 (1993).
19. R. Slater, P. Stratonovitch, J. Elias, M. A. Semenov, I. Denholm, *Pest Manag. Sci.* **73**, 1364–1372 (2017).
20. H. Z. Dong, W. J. Li, *J. Agron. Crop Sci.* **193**, 21–29 (2007).
21. B. E. Tabashnik, F. Gould, Y. Carrière, *J. Evol. Biol.* **17**, 904–912 (2004).
22. B. E. Tabashnik, Y. Carrière, *Nat. Biotechnol.* **35**, 926–935 (2017).
23. F. Gould, *Am. Sci.* **79**, 496–507 (1991).
24. L. Epstein, *Annu. Rev. Phytopathol.* **52**, 377–402 (2014).
25. O. J. T. Briët, M. A. Penny, D. Hardy, T. S. Awolola, W. Van Bortel, V. Corbel, R. K. Dabiré, J. Etang, B. G. Koudou, P. K. Tungu, N. Chitnis, *Malar. J.* **12**, 77 (2013).
26. M. Basili, F. Belloc, *J. Econ. Surv.* **29**, 896–916 (2015).
27. D. Hueth, D. U. Regev, *Am. J. Agric. Econ.* **56**, 543–552 (1974).
28. E. P. Fenichel, J. K. Abbott, *J. Assoc. Environ. Resour. Econ.* **1**, 1–27 (2014).
29. R. Laxminarayan, R. D. Simpson, *Environ. Resour. Econ.* **22**, 521–536 (2002).
30. Z. S. Brown, K. L. Dickinson, R. A. Kramer, *J. Econ. Entomol.* **106**, 366–374 (2013).
31. M. J. Livingston, G. A. Carlson, P. L. Fackler, *Am. J. Agric. Econ.* **86**, 1–13 (2004).
32. D. Kim, Z. Brown, R. Anderson, C. Mutero, M. L. Miranda, J. Wiener, R. Kramer, *Risk Anal.* **37**, 231–244 (2017).
33. T. C. Sparks, *Pestic. Biochem. Physiol.* **107**, 8–17 (2013).
34. S. E. Naranjo, P. C. Ellsworth, G. B. Frisvold, *Annu. Rev. Entomol.* **60**, 621–645 (2015).
35. B. E. Tabashnik, M. S. Sisterson, P. C. Ellsworth, T. J. Dennehy, L. Antilla, L. Liesner, M. Whitlow, R. T. Staten, J. A. Fabrick, G. C. Unnithan, A. J. Yelich, C. Ellers-Kirk, V. S. Harpold, X. Li, Y. Carrière, *Nat. Biotechnol.* **28**, 1304–1307 (2010).
36. J. A. Miranowski, G. A. Carlson, in *Pesticide Resistance: Strategies and Tactics for Management* (National Research Council, National Academy Press Washington, DC, 1986), pp. 436–448.
37. M. Lefebvre, S. R. H. Langrell, S. Gomez-y-Paloma, *Agron. Sustain. Dev.* **35**, 27–45 (2015).
38. W. D. Hutchison, E. C. Burkness, P. D. Mitchell, R. D. Moon, T. W. Leslie, S. J. Fleischer, M. Abrahamson, K. L. Hamilton, K. L. Steffey, M. E. Gray, R. L. Hellmich, L. V. Kaster, T. E. Hunt, R. J. Wright, K. Pecinovsky, T. L. Rabaey, B. R. Flood, E. S. Raun, *Science* **330**, 222–225 (2010).
39. A. E. Milne, J. R. Bell, W. D. Hutchison, F. van den Bosch, P. D. Mitchell, D. Crowder, S. Parnell, A. P. Whitmore, *PLOS Comput. Biol.* **11**, e1004483 (2015).
40. D. Ervin, R. Jussaume, *Weed Sci.* **62**, 403–414 (2014).
41. E. M. Liu, J. Huang, *J. Dev. Econ.* **103**, 202–215 (2013).
42. V. T. Covello, in *Risk Communication in Occupational Health Practice* (Oxford Univ. Press, New York, 2005), pp. 82–100.
43. J. Pretty, *Science* **302**, 1912–1914 (2003).
44. E. Ostrom, *Policy Stud. J.* **39**, 7–27 (2011).
45. J. Kuzma, F. Gould, Z. Brown, J. Collins, J. Delborne, E. Frow, K. Esvelt, D. Guston, C. Leitschuh, K. Oye, S. Stauffer, *J. Responsib. Innov.* **5** (suppl. 1), S13–S39 (2017).
46. Z. S. Brown, *Am. J. Agric. Econ.* **100**, 844–867 (2018).
47. K. Cockerill, L. Daniel, L. Malczynski, V. Tidwell, *Policy Sci.* **42**, 211–225 (2009).
48. N. Ghaffarzadegan, J. Lyneis, G. P. Richardson, *Syst. Dyn. Rev.* **27**, 22–24 (2011).
49. S. W. Fausti, *Environ. Sci. Policy* **52**, 41–50 (2015).
50. J. Kuzma, *J. Responsib. Innov.* **2**, 109–112 (2015).
51. J. Foley, GMOs, Silver Bullets and the Trap of Reductionist Thinking. Ensia. Retrieved from http://ensia.com/voices/gmos-silver-bullets-and-the-trap-of-reductionist-thinking/ (2014).
52. M. L. Fritz *et al.*, *Mol. Ecol.* **27**, 167–181 (2018).
53. J. W. Glauber, *Am. J. Agric. Econ.* **95**, 482–488 (2013).
54. C. O'Connor, "Soil Matters: How the Federal Crop Insurance Program should be reformed to encourage low-risk farming methods with high-reward environmental outcomes," 2013 AAEA: Crop Insurance and the Farm Bill Symposium, October 8-9, Louisville, KY, no. 156789, Agricultural and Applied Economics Association (2013).
55. https://monsanto.com/app/uploads/2017/05/2017_tug.010617final.pdf.
56. M. E. Whalon, D. Mota-Sanchez, R. M. Hollingworth, in M. E. Whalon, D. Mota-Sanchez, R. M. Hollingworth, Eds., *Global Pesticide Resistance in Arthropods* (CABI International, Wallingford, UK, 2008), pp. 5–31.

ACKNOWLEDGMENTS

We thank two anonymous reviewers and B. Tabashnik for helping us improve the manuscript. **Funding:** All authors acknowledge support from the North Carolina State University Genetic Engineering and Society Center. F.G. acknowledges support from USDA National Institute of Food and Agriculture grants 2012-33522-19793 and 2016-33522-25640. Z.S.B. acknowledges support from USDA National Institute of Food and Agriculture HATCH project NC02520. **Competing interests:** The authors declare no competing interests.

10.1126/science.aar3780

REVIEW

Genomic insights into the emergence and spread of antimicrobial-resistant bacterial pathogens

Stephen Baker,[1,2,3]* Nicholas Thomson,[4,5] François-Xavier Weill,[6] Kathryn E. Holt[5,7]

Whole-genome sequencing (WGS) has been vital for revealing the rapid temporal and spatial evolution of antimicrobial resistance (AMR) in bacterial pathogens. Some antimicrobial-resistant pathogens have outpaced us, with untreatable infections appearing in hospitals and the community. However, WGS has additionally provided us with enough knowledge to initiate countermeasures. Although we cannot stop bacterial adaptation, the predictability of many evolutionary processes in AMR bacteria offers us an opportunity to channel them using new control strategies. Furthermore, by using WGS for coordinating surveillance and to create a more fundamental understanding of the outcome of antimicrobial treatment and AMR mechanisms, we can use current and future antimicrobials more effectively and aim to extend their longevity.

When antimicrobial drugs were introduced into clinical usage in the mid-20th century, they had an astonishing impact on human health. Infectious bacteria that had threatened our survival were now at the mercy of a chemical arsenal. Previously fatal infections, from whooping cough and scarlet fever to tuberculosis and syphilis, were no longer considered a threat. Antimicrobials substantially reduced the risks associated with child birth, injuries, and invasive medical procedures. What has followed in the subsequent 70 years or so has been an uncontrolled microbiological experiment conducted on an unprecedented scale. Initially we identified a plethora of new antimicrobial classes targeting different essential bacterial functions, but we deployed them haphazardly in ever-increasing quantities. Now antimicrobial resistance (AMR) poses a genuine threat to human health, with the potential to return us to a situation where common infections are as untreatable as they were in the pre-antimicrobial era (*1*).

Humans did not create AMR; we simply promoted it by applying evolutionary pressure. Almost all antimicrobials have chemical similarities with compounds that can be found naturally; AMR genes have been found deep in the permafrost (*2*) and arose long before humankind's ability to synthesize antibacterial chemicals and use them en masse. Therefore, AMR in bacterial populations is a largely predictable phenomenon; the more commonly a specific antimicrobial compound is used, the more likely it is that resistance will emerge and be maintained in an exposed microbial population. The specific dynamics of the processes associated with AMR are, however, less predictable. The rapidity with which diverse AMR phenotypes have emerged and become established within human, animal, and wider environmental populations of microbes has been astonishing and most likely accelerated by concurrent advances in human development, mobilization, and population growth.

[1]Oxford University Clinical Research Unit, Ho Chi Minh City, Vietnam. [2]Centre for Tropical Medicine and Global Health, Oxford University, Oxford, UK. [3]The Department of Medicine, University of Cambridge, Cambridge, UK. [4]The Wellcome Trust Sanger Institute, Cambridge, UK. [5]The London School of Hygiene and Tropical Medicine, London, UK. [6]Institut Pasteur, Paris, France. [7]Department of Biochemistry and Molecular Biology, Bio21 Molecular Science and Biotechnology Institute, University of Melbourne, Parkville, Victoria, Australia.
*Corresponding author. Email: sbaker@oucru.org

"The first reports of penicillin-resistant infections occurred early in the 1940s, but a penicillinase was described even before the continued clinical usage of the prototype antibiotic."

The evolutionary dynamics of antimicrobial resistance

How resistance is maintained and distributed within bacterial populations is a function of the organism's lifestyle (i.e., transmission mode, colonization, and pathogenicity) and the genetic basis for resistance, which can be either intrinsic (i.e., the organism naturally lacks the specific pathway targeted by the drug), mutation associated (i.e., induced changes are passed vertically to descendants), or acquired via horizontal gene transfer (HGT) between organisms (with acquired genes then being passed vertically to progeny). The first reports of penicillin-resistant infections occurred early in the 1940s, but a penicillinase was described even before the continued clinical usage of the prototype antibiotic (*3*). Since then, there have been numerous examples of the rapid emergence of bacteria exhibiting resistance to a specific antimicrobial class soon after its introduction (*4*). However, in the past decade, through the advent of high-throughput whole-genome sequencing (WGS), we have been able to make substantive advances in understanding the dynamics of AMR evolution and spread in bacterial populations.

WGS has become the key technology for understanding pathogen evolution, population dynamics, and genomic epidemiology, as it provides a far greater degree of reproducibility, standardization, and resolution than previous genotyping methods (*5*). By capturing both the neutral evolution of the population—for tracking transmission and diversification of the organism—and the genetic determinants of AMR, WGS can reveal detailed temporal and spatial dynamics of AMR evolution and simultaneously infer the impact of AMR selection on pathogen populations. Much of the pioneering WGS-based AMR work was focused on the opportunistic Gram-positive human pathogen *Staphylococcus aureus*, particularly with respect to the emergence of methicillin resistance (MRSA) in health care facilities in Europe (*6*). MRSA is still among the best examples of how AMR variants can rapidly emerge, be efficiently maintained, and spread at different spatiotemporal scales, ranging from individual hospital wards to health care networks, and internationally within human populations (Fig. 1). MRSA was first observed in 1960, within a year of the introduction of second-generation β-lactams, such as methicillin, into clinical practice. However, phylogenetic reconstruction showed that MRSA actually emerged in the 1940s via HGT of the staphylococcal cassette chromosome *mec* (SCC*mec*) element, as a consequence of the initial mass usage of penicillin (*7*). WGS data shows that MRSA has arisen on numerous occasions independently in different subpopulations on different continents (e.g., USA300, ST22 in Europe, and ST93 in Australia) through parallel HGT events and spread throughout health care systems (*6*). The history of health care–associated MRSA in the later part of the 20th century was punctuated by frequent epidemics associated with highly successful clones, such as EMRSA-15 (ST22), which was first described in the United Kingdom in the 1990s and then spread throughout Europe, and then intercontinentally (Fig. 1) (*8*). Notably, a fluoroquinolone-resistant EMRSA-15 variant arose in the United Kingdom soon after clinical trials with ciprofloxacin in the 1980s, with point mutations in the DNA gyrase and topoisomerase IV genes. This critical event was the apparent trigger for the subsequent pandemic spread of a fluoroquinolone-resistant MRSA variant (Fig. 1) (*8*).

The global dissemination of antimicrobial-resistant clones

MRSA epitomizes a now all-too-familiar evolutionary route by which successful AMR clones

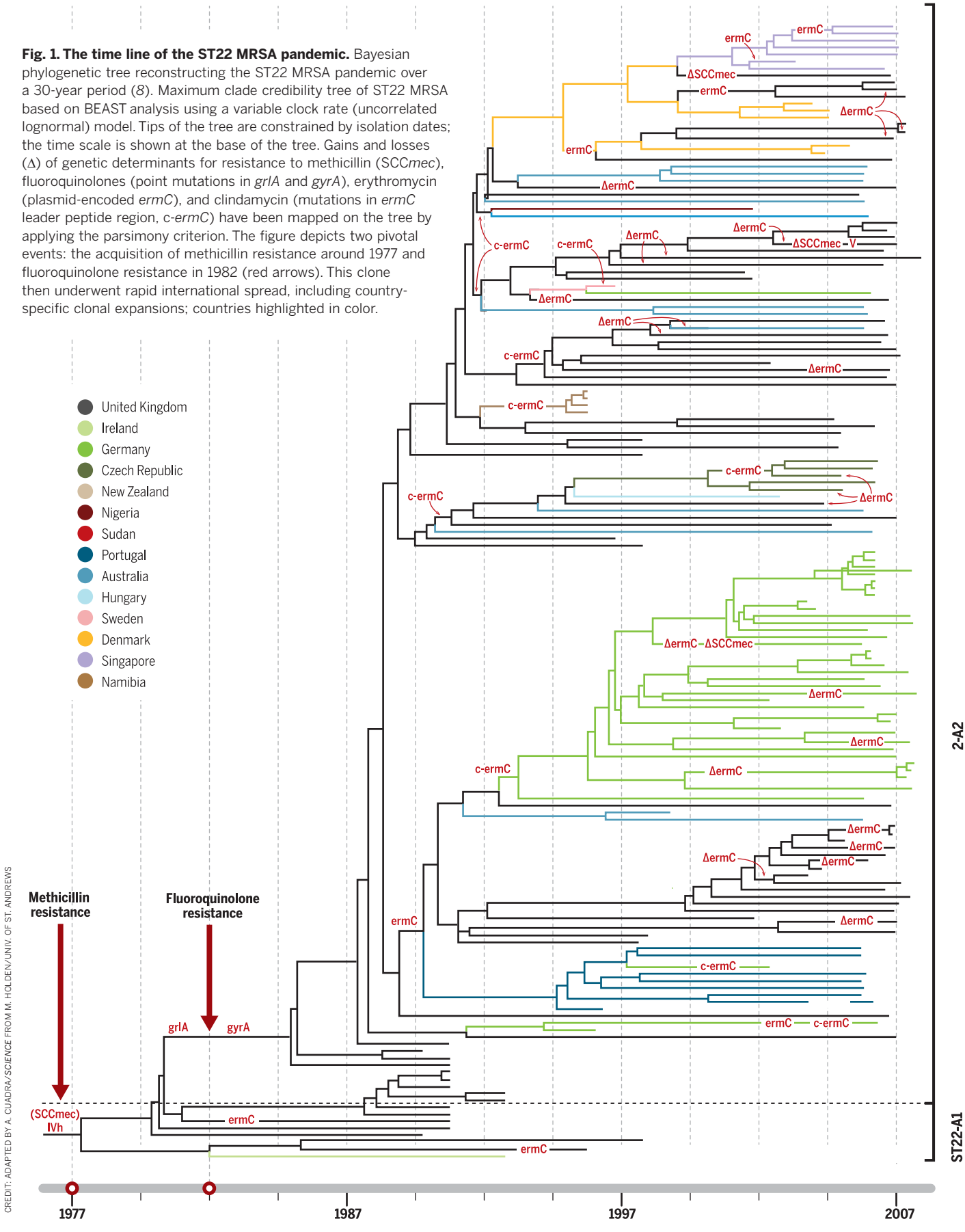

Fig. 1. The time line of the ST22 MRSA pandemic. Bayesian phylogenetic tree reconstructing the ST22 MRSA pandemic over a 30-year period (*8*). Maximum clade credibility tree of ST22 MRSA based on BEAST analysis using a variable clock rate (uncorrelated lognormal) model. Tips of the tree are constrained by isolation dates; the time scale is shown at the base of the tree. Gains and losses (Δ) of genetic determinants for resistance to methicillin (SCC*mec*), fluoroquinolones (point mutations in *grlA* and *gyrA*), erythromycin (plasmid-encoded *ermC*), and clindamycin (mutations in *ermC* leader peptide region, c-*ermC*) have been mapped on the tree by applying the parsimony criterion. The figure depicts two pivotal events: the acquisition of methicillin resistance around 1977 and fluoroquinolone resistance in 1982 (red arrows). This clone then underwent rapid international spread, including country-specific clonal expansions; countries highlighted in color.

CREDIT: ADAPTED BY A. CUADRA/*SCIENCE* FROM M. HOLDEN/UNIV. OF ST. ANDREWS

emerge in response to local antimicrobial usage, undergo population expansion under selection from sustained antimicrobial exposure, and then explode into pandemic spread. The finer details are organism specific and dependent on their particular evolutionary landscape (e.g., mechanisms of resistance, fitness costs, modes of transmission, and host range), but all follow a similar basic trajectory, mirroring that observed in the recent MEGA-plate experiment (*9*). Briefly, exposure of susceptible bacteria to antimicrobial drugs will result in the local emergence of resistant mutants. This happens continuously, as a genetically diverse pool of pathogens are exposed to a range of different compounds at different concentrations. Most resistant mutants will be purged quickly from the population, either through genetic drift or because they are less fit for onward transmission. For example, WGS data have shown that that a few common resistance mutations emerge repeatedly in *Mycobacterium tuberculosis* during the treatment of individuals but that these are rarely transmitted (*10*). However, occasionally a resistant mutant will have a sufficient fitness advantage to undergo local clonal expansion in a subset of infections. This occurs through a combination of ongoing antimicrobial exposures and/or a genetic background that moderates the fitness cost, e.g., the compensatory mutations in rifampicin-resistant *M. tuberculosis* (*11*); the increased replication rate of *Salmonella* Typhi with fluoroquinolone resistance–associated DNA gyrase mutations (*12*); or chromosomal variants that ameliorate the cost of AMR plasmid carriage (*13*). Once established, the locally successful AMR clone may face opportunities for further expansion, including potentially broader geographical dissemination and/or spillover into other host populations, depending on the mode of transmission and the extent of antimicrobial selection it encounters.

WGS investigations show that clonal expansion and ensuing geographical dissemination of pathogens can mostly be traced to the acquisition of a specific AMR determinant(s) like SCC*mec* in MRSA. This suggests the AMR element(s) function as the "king maker" within the various pathogen populations, determining which clones dominate locally, regionally, and globally. Some mobile AMR genes have played this role in multiple organisms and clones; e.g., CTX-M-15 has driven the success of *Escherichia coli* ST131 and several *Klebsiella pneumoniae* clones (CG14/15, ST101) (*14*, *15*). Equally, AMR genes also benefit by association with certain plasmid vectors or host bacterial clones, which act as vehicles for dissemination. *K. pneumoniae* is host to several key mobile AMR genes and has played a pivotal role in the global dissemination of various extended spectrum β-lactamases (ESBLs) and the carbapenemases KPC and NDM-1 (*15*). This association may be linked to *K. pneumoniae*'s broad ecological range and propensity for HGT, which provide a conduit for AMR gene trafficking from a very large gene pool into the smaller subpopulations of human-associated bacteria.

Another common reoccurring observation is the accumulation of additional resistance mechanisms in an already established AMR clone, such as fluoroquinolone resistance in EMRSA-15 (*8*). This phenomenon is likely driven by escalating antimicrobial use to tackle AMR infections, accompanied by a relaxation of selective constraints and an increased effective population size of the successful clone. It is particularly common in organisms that can accumulate multiple AMR genes through HGT, particularly within the Enterobacteriaceae (*14*, *15*), but is also evident in the highly clonal and evolutionarily constrained *M. tuberculosis*, in which resistance to isoniazid via a mutation in *katG* commonly precedes further AMR mutations (*10*).

Health care–associated "superbugs"

AMR organisms are highly destructive in hospitals. Modern medicine relies on antimicrobial therapy and prophylaxis to protect against opportunistic infections, which affect approximately 1 in 10 hospitalized patients globally. In industrialized countries, health care–associated infections account for the vast majority of the communicable disease burden (*16*), but hospitals on all continents are now plagued by AMR infections. The combination of intensive antimicrobial exposure in hosts whose immune systems are struggling to defend against infecting bacteria can rapidly select for resistance. Several WGS studies have documented local emergence of resistance in hospitalized patients in response to specific antimicrobial exposures, which have been studied in individual infections, treatment episodes (*17*), and at the ward level (*18*). These studies show that many of the same mutational events arise repeatedly in different patients and in different host backgrounds, demonstrating that the emergence of AMR in many organisms within health care facilities is often predictable. Examples include the repeated acquisition of SCC*mec* (methicillin resistance), *walKR* mutations (vancomycin resistance) in *S. aureus* (*18*), and *lpx* disruptions (colistin resistance) in *Acinetobacter baumannii* (*17*).

Although AMR organisms arise continuously, national- and international-level WGS snapshots show that most AMR infections are attributable to a few clones within the broad population of the specific pathogen. Thus, only a small fraction of emergent AMR variants is sufficiently fit for broader dissemination. WGS investigations of Gram-negative opportunistic pathogens mimic the pattern of MRSA, with clonal spread that begins as localized expansions, rapidly progressing to intercontinental spread (within years) and even global dissemination (within decades). Particularly concerning is *K. pneumoniae* clone ST258, which carries the plasmid-borne *K. pneumoniae* carbapenemase gene *KPC* that confers resistance to all β-lactams, including carbapenems and cephalosporins (*15*). KPC ST258 arose in the United States, where it began causing hospital outbreaks around 2005. After first spreading to Israel, by 2009, KPC ST258 was endemic in Greece and Italy and has since spread across Europe and South America and into Asia and Australia (Fig. 2). The arrival of the clone in new locations is linked to patients with a history of recent international travel to KPC ST258–endemic areas. Other carbapenemase-producing *K. pneumoniae* clones have also emerged (e.g., OXA-48 ST405 in Spain and KPC ST11 in China), but these have remained relatively localized. Why a combination of the *KPC* gene in the ST258 *K. pneumoniae* host background has been so successful remains an important unanswered question.

Other relevant Gram-negative health care–associated AMR clones include the ESBL-producing *E. coli* ST131, whose global dissemination has been so rapid that its initial geographical origins were obscured (*14*). *A. baumannii* Global Clone 1 (GC1) is probably the oldest multidrug-resistant (MDR) hospital clone of *A. baumannii* and emerged in the 1980s after acquisition of a genomic island conferring resistance to all first-line antimicrobials. GC1 latterly accumulated resistance against fluoroquinolones and carbapenems (*19*). The prevention and management of infections with these highly resistant clones is a major health care challenge, and alternative strategies, such as vaccines and targeted immunotherapies, are urgently needed. However, *K. pneumoniae* KPC ST258, *E. coli* ST131, and *A. baumannii* GC1 all display extensive surface antigen diversification, complicating such approaches (*15*, *19*).

Antimicrobial resistance in community-acquired infections

AMR is not only a substantial problem in health care systems but is also prevalent among a wide range of pathogens associated with community-acquired infections. WGS studies show that AMR in the community setting, as in hospitals, is similarly dominated by a small number of globally disseminated clones that have accumulated AMR determinants over time. The waterborne enteric diseases typhoid fever and dysentery provide two salient examples. The vast majority of MDR typhoid fever cases globally are caused by the *Salmonella* Typhi H58 clone, which emerged in South Asia in the early 1990s in association with an MDR plasmid and has since spread throughout Asia and into East Africa, accumulating fluoroquinolone resistance mutations in the genes encoding DNA gyrase and topoisomerase IV (Fig. 2) (*20*). Most pediatric cases of MDR shigellosis are caused by a *Shigella sonnei* clone that carries a mobile genetic element conferring resistance to almost all first-line drugs on its chromosome. The clone emerged in the 1970s and is now globally disseminated (Fig. 2) (*21*), with the same fluoroquinolone resistance mutations as in *S.* Typhi arising subsequently and spreading out from South Asia (*22*).

Sexually transmitted infections (STIs) present particular complications for understanding AMR in community-acquired disease, as their transmission is driven by complex human behavior. AMR in STIs share the same general evolutionary characteristics as AMR in health care–acquired infections, but have distinct transmission, diagnosis, and treatment parameters that result in distinct spatiotemporal dynamics. AMR in STIs are a major concern; data from locations with good STI surveillance systems suggest a general upward trend in bacterial STI incidence disproportionately associated with specific communities (*23*). In 2014, men-who-have-sex-with-men (MSM) represented <2% of the London adult population; however, 28% of all new STIs were diagnosed in this community. More specifically, 69% of all new cases of gonorrhea diagnosed in London were in MSM, and the emergence of some AMR variants of *Neisseria gonorrhoeae* have been specifically linked to MSM communities (*23*). AMR in *N. gonorrhoeae* is such a potential problem that it has been acknowledged by the World Health Organization (WHO) as being a major threat to human health (*24*). MDR variants leave increasingly limited treatment options, and there is a very real prospect of widespread resistance to ceftriaxone, the last remaining option for empirical monotherapy. Indeed, there have already been isolated reports of *N. gonorrhoeae* that exhibit resistance to all current treatments (*24*). One of the first epidemiological studies exploiting WGS for *N. gonorrhoeae* aimed to understand how particular AMR phenotypes had emerged. This study showed that reduced susceptibility against third-generation cephalosporins in the United States between 2000 and 2014 was the consequence of the expansion of two particular clones arising within the MSM community that possessed the mosaic *penA* resistance allele (*25*).

For other STIs, the situation is less clear. Despite reports of mutations in *Chlamydia trachomatis* conferring in vitro resistance against macrolides (the first-line treatment for chlamydia), there is no evidence for the stable maintenance of these mutations during human infection (*26*). Similarly, intramuscular injection with benzathine penicillin appears to remain generally effective for treating syphilis (*Treponema pallidum*). However, we are missing key epidemiological information on many STIs. In well-resourced clinical settings, there is a move away from microbiological culture as the "gold standard" for the diagnosis of bacterial STIs and increasing reliance on molecular testing (*24*). Although molecular tests have the advantage of being rapid and sensitive, they have the disadvantage of being destructive and do not screen for potential AMR phenotypes (*24*). This situation is exacerbated in resource-limited settings where any form of diagnostic testing is rare, which results in a substantial underreporting of STIs and almost no AMR or pathogen prevalence data (*24*).

"Sexually transmitted infections present particular complications for understanding AMR in community-acquired disease, as their transmission is driven by complex human behavior."

Another issue complicating AMR detection in STIs is the challenge of individual case management. A lack of diagnostic testing imposes a reliance on empirical syndromic therapy, which can have undesired consequences for driving the emergence of new AMR-STIs because of undirected antibiotic treatment. *Shigella* spp. are fecal-oral pathogens with a notoriously low infectious dose and are adept at acquiring new functions via HGT. *Shigella* has emerged as an enteric STI with a capacity for global dissemination of AMR genotypes. *Shigella* outbreaks in MSM communities have been sporadically observed since the 1970s (*27*). An increase in MSM-associated dysentery has been reported recently in the United Kingdom with a *Shigella flexneri* resistant to azithromycin in individuals with no history of travel to countries with highly endemic *Shigella* (*28*). Azithromycin is not routinely used to treat dysentery in the United Kingdom, but is the front-line treatment for gonococcal urethritis, syphilis, and chlamydia. The emergence of this *S. flexneri* variant was linked to the acquisition of a conjugative plasmid carrying various macrolide resistance genes, which was likely driven by azithromycin treatment for other STIs. Transmission of organisms via oro-anal sex, coupled with HIV-associated immunodeficiency, multiple sexual partners, and greater

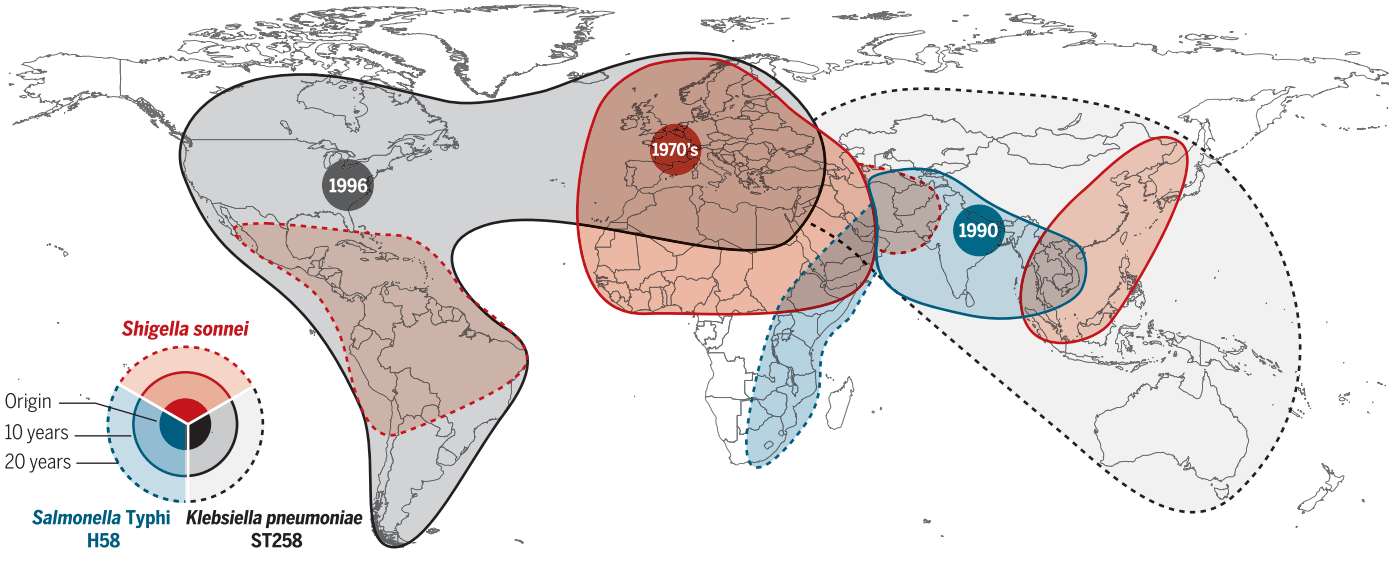

CREDIT: ADAPTED BY A. CUADRA/*SCIENCE* FROM S. BAKER *ET AL.*

Fig. 2. Origin and blast radius for the clonal expansion for three multidrug-resistant Gram-negative bacteria clones. The map summarizes data for the global dissemination of: dysentery causing *Shigella sonnei* clone lineage III-global, with a chromosomal insertion of a mobile genetic element encoding resistance to streptomycin, trimethoprim-sulfamethoxazole, and tetracycline (red); the typhoid fever pathogen *Salmonella* Typhi, clone H58, with a plasmid encoding resistance to chloramphenicol, ampicillin, trimethoprim-sulfamethoxazole, streptomycin, and tetracycline (blue); health care–associated *Klebsiella pneumoniae* clone ST258, carrying the KPC carbapenemase encoding resistance to all β-lactam antimicrobials, including carbapenems and third-generation cephalosporins (gray).

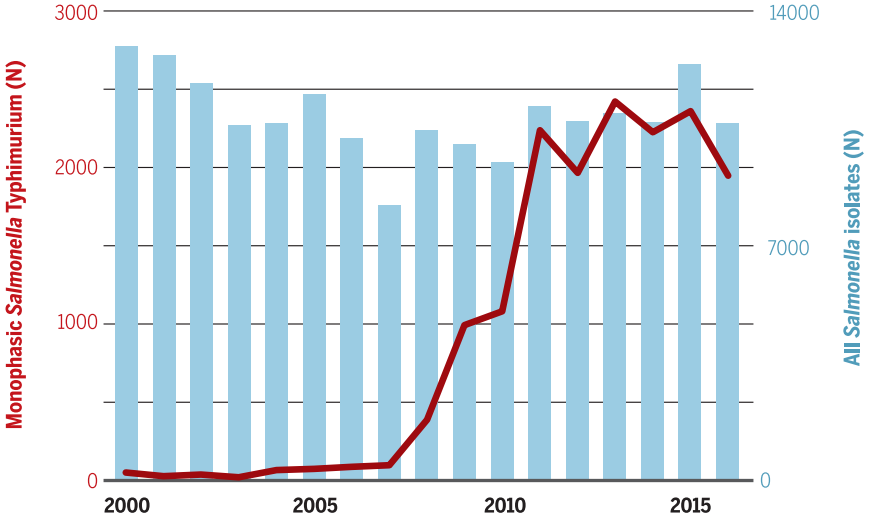

Fig. 3. The epidemic of monophasic *Salmonella* Typhimurium (1,4,[5],12:i:-). The graph shows the number of *Salmonella* isolates from human infections at the French National Reference Centre for *Salmonella* during 2000 to 2016. The blue bars depict the total number of *Salmonella* spp. isolated by year over the defined period; the red plot depicts the number of *Salmonella* Typhimurium (1,4,[5],12:i:-) isolated by year.

exposure to STIs alongside therapeutic antimicrobials, created the "perfect storm" for the emergence of this specific MSM-associated AMR lineage.

Foodborne dissemination of antimicrobial resistance

Humans are exposed to animal sources of AMR genes and bacteria through the food chain. The need for a "one-health" (i.e., considering the span of humans, animals, and their environment) strategy for AMR and infectious disease for surveillance and containment across the different sectors is well recognized. Nontyphoidal *Salmonella* (NTS), which is among the most common pathogens of humans and animals, are key for understanding AMR dynamics from a one-health perspective. In 2004, the Infectious Disease Society of America (IDSA) issued a report that presented a plausible catastrophic scenario of a highly fatal epidemic of MDR-NTS, illustrating how virulent AMR strains could rapidly escalate into major foodborne outbreaks threatening our food security. Indeed, large foodborne NTS outbreaks have been observed in recent decades, and NTS exhibiting resistance to last-line antimicrobials are beginning to be isolated.

The continued occurrence of MDR *Salmonella* Typhimurium (one of the most common types of NTS) as a cause of human infection personifies the one-health aspect of AMR and also highlights repeating patterns of AMR evolution. Antimicrobials have been used to treat and prevent infections in livestock since their discovery but were also used as growth promoters from the 1950s. In the early part of the 1960s, an increasing number of *S.* Typhimurium with transferable MDR phenotypes began to be isolated in the United Kingdom, with the first outbreak of MDR *S.* Typhimurium (phage type 27) in humans reported in 1959. This outbreak affected 102 patients; ~5% of isolates were resistant to streptomycin, sulfonamides, and tetracycline (*29*). In 1963, *S.* Typhimurium phage type DT29 emerged in the United Kingdom following the adoption of intensive farming methods using antibiotics for the rearing of calves (*30*). Subsequently, in 1965, >1200 and >500 MDR *S.* Typhimurium were isolated from cattle and humans, respectively. A recent WGS NTS investigation revealed that the AMR gene cassettes present in these early U.K. *Salmonella* outbreaks differed from those in historical *Salmonella* outbreaks in France, despite geographic proximity (*31*). This observation suggests that the emergence of MDR *S.* Typhimurium was caused by the independent acquisition of multiple AMR determinants followed by country-specific clonal expansions.

> ***"...globalization of the food industry means that inappropriate antimicrobial use in one part of the world has implications even for countries with strong controls on their own usage."***

Observations from the 1960s were repeated in the 1980s when *S.* Typhimurium phage type DT104 with a genomic island encoding resistance against ampicillin, chloramphenicol, streptomycin, sulfonamides, and tetracyclines emerged in U.K. cattle (*32*). This epidemic strain successively acquired resistance to quinolones and trimethoprim. Over the coming years, DT104 became widely distributed in cattle, poultry, pigs, and sheep and in 1996, >4000 human infections were associated with MDR DT104 in the United Kingdom. MDR DT104 spread internationally throughout the 1990s, particularly in continental Europe and North America, and became established in multiple domestic animal populations. By 2001, DT104 represented >50% of all *S.* Typhimurium isolates in Eastern Europe (*33*). Local and global transmission routes were reconstructed by WGS, and the role of this zoonotic pathogen in the spread of AMR through interspecies transmission was elucidated (*34*). These data may have cast doubt on the dominance of local animals in spreading MDR DT104 to humans, but importantly, they highlighted substantial gaps in our AMR surveillance. Notably, the general contribution of imported food in spreading AMR bacteria to humans remains poorly understood.

The latest foodborne *S.* Typhimurium epidemic was associated with swine and attributed to a monophasic variant (1,4,[5],12:i:-), which emerged in Europe in the mid-2000s, as highlighted by spread of the clone in France from 2008 (Fig. 3) (*35*). Sequence data identified these organisms as one clone, despite belonging to multiple phage types, that was distinct from monophasic *S.* Typhimurium previously described in Spain and North America. These were found to have become MDR through the acquisition of a composite transposon, which replaced the flagella operon. These isolates had also acquired a genomic island, which encoded resistance to several heavy metals in pig-feed supplements. This European monophasic variant has now been reported in swine in the Midwestern United States, where it has become resistant to quinolones and third-generation cephalosporins (*36*).

It was proposed relatively early on that use of penicillins and tetracyclines in livestock was responsible for the emergence of MDR *S.* Typhimurium. This hypothesis was controversial, owing to the complexities of NTS epidemiology and the lack of molecular tools allowing high-resolution tracking of the incriminated bacteria in the different ecosystems. In the 1980s, epidemiology, combined with early molecular typing techniques, concluded that most AMR variants of NTS in the United States could be traced to animals (*37*). Antimicrobial use for growth promotion was banned by the European Union in 2006 and heavily regulated in the United States in 2017. However, globalization of the food industry means that inappropriate antimicrobial use in one part of the world has implications even for countries with strong controls on their own usage. The recent example of the worldwide dissemination of MDR *Salmonella* Kentucky ST198 via African poultry further highlights the requirement for global one-health approaches to tackle AMR (*38*).

Staying one step ahead

It is indisputable that efforts to kill bacteria with chemicals will result in the selection, propagation, and dissemination of resistant variants. Data generated through WGS have revealed the rapid pace at which the bacteria can adapt to these chemicals. It is evident that some AMR pathogens have outpaced us, with untreatable infections appearing in hospitals and the community; but WGS studies have provided us with the tools and knowledge to initiate an intelligence-driven fightback. In particular, population genomics data at various spatiotemporal scales highlight many repeating patterns in the emergence and spread of AMR. The predictability of these evolutionary processes offers the opportunity to develop strategies to minimize the chance that new AMR clones are generated during individual treatment that will spread locally. For example, combination and sequential therapies may create conditions that constrain the fitness of emerging resistant mutants (*39*). These strategies are based broadly on the principle that adaptation to one class of antimicrobial drug may incur collateral sensitivity to another, such that their coordinated use imposes a roadblock to the emergence and spread of resistance. As diagnostics are generally lacking, the most practical option is likely to be empirical antimicrobial rotation as opposed to patient-tailored therapies. In theory, antimicrobial combinations or cycling can be employed at different levels (e.g., patients, wards, hospitals) and time scales (e.g., hours, days, months), depending on whether the goal is to limit the emergence of AMR within patients, or to confine the transmission of AMR variants. However, much work is required to determine the most effective way to restrict emergence and spread of differing resistance phenotypes in different settings (*40*). These approaches have the potential to lengthen the life of current antimicrobials and are vital for sustaining the efficacy of new antimicrobials as they are introduced.

A further important insight from WGS is that while resistance arises constantly during individual infections, most AMR variants represent a minimal risk with limited potential for transmission beyond the index patient. Hence, the major burden of AMR is associated with a few high-risk clones that spread easily and accumulate additional AMR phenotypes. It is these clones that represent the greatest risk beyond the individual patient and should be targeted more aggressively for containment. Work is still needed to understand the mechanisms underlying these apparently superfit AMR clones, and WGS studies will be vital for this process. Even in the absence of precise mechanisms, WGS can be deployed immediately for hospital infection control and public health surveillance to identify and target clones with epidemic potential as they arise.

The spatiotemporal dynamics of AMR evolution revealed by WGS studies clearly illustrate that microbial populations do not respect political boundaries; hence, it is imperative that AMR genomic surveillance data are combined internationally between different sectors in a one-health approach (i.e., across medical, veterinary, agricultural, and environmental settings). Such data sharing is essential to harness the power of genomic surveillance to identify and monitor evolutionary trends and population dynamics and to identify superfit AMR clones as they emerge and spread. The rapid pace of the global spread of AMR organisms, such as fluoroquinolone-resistant *Shigella* (*22*), indicates that these efforts have to be implemented in real time, as has been argued for the emergence of novel pathogens (*5*). This is the vision of the Global Microbial Identifier Project, the WHO, and other international bodies, but it has yet to gain international support from governments and industries.

AMR is a truly global health problem, one that we cannot ignore or attempt to counter with increasingly powerful antimicrobial agents. WGS has allowed us to understand the dynamics of AMR and the chaos we have created through haphazard antimicrobial usage. The data are stark. However, recognizing the complexity and assessing the magnitude of the task ahead is the first fundamental step in tackling the global AMR crisis. We are now at a pivotal point, and what happens next is likely to dictate the future of infectious disease control. Genomics has outlined several repeating patterns in the emergence and spread of AMR bacteria, and although we cannot stop bacterial evolution, we can try to channel it. Through coordinated efforts, intelligent surveillance, and a more fundamental understanding of AMR mechanisms, we can learn to use antimicrobials more effectively and extend their longevity.

REFERENCES AND NOTES

1. S. Baker, *Science* **347**, 1064–1066 (2015).
2. V. M. D'Costa, C. E. King, L. Kalan, M. Morar, W. W. L. Sung, C. Schwarz, D. Froese, G. Zazula, F. Calmels, R. Debruyne, G. B. Golding, H. N. Poinar, G. D. Wright, *Nature* **477**, 457–461 (2011).
3. E. P. Abraham, E. Chain, *Rev. Infect. Dis.* **10**, 677–678 (1988).
4. K. Lewis, *Nat. Rev. Drug Discov.* **12**, 371–387 (2013).
5. J. L. Gardy, N. J. Loman, *Nat. Rev. Genet.* **19**, 9–20 (2018).
6. J. R. Fitzgerald, M. T. G. Holden, *Annu. Rev. Microbiol.* **70**, 459–478 (2016).
7. C. P. Harkins *et al*., *Genome Biol.* **18**, 130 (2017).
8. M. T. G. Holden, L.-Y. Hsu, K. Kurt, L. A. Weinert, A. E. Mather, S. R. Harris, B. Strommenger, F. Layer, W. Witte, H. de Lencastre, R. Skov, H. Westh, H. Zemlicková, G. Coombs, A. M. Kearns, R. L. R. Hill, J. Edgeworth, I. Gould, V. Gant, J. Cooke, G. F. Edwards, P. R. McAdam, K. E. Templeton, A. McCann, Z. Zhou, S. Castillo-Ramírez, E. J. Feil, L. O. Hudson, M. C. Enright, F. Balloux, D. M. Aanensen, B. G. Spratt, J. R. Fitzgerald, J. Parkhill, M. Achtman, S. D. Bentley, U. Nübel, *Genome Res.* **23**, 653–664 (2013).
9. M. Baym, T. D. Lieberman, E. D. Kelsic, R. Chait, R. Gross, I. Yelin, R. Kishony, *Science* **353**, 1147–1151 (2016).
10. A. L. Manson *et al*., *Nat. Genet.* **49**, 395–402 (2017).
11. T. Song, Y. Park, I. C. Shamputa, S. Seo, S. Y. Lee, H.-S. Jeon, H. Choi, M. Lee, R. J. Glynne, S. W. Barnes, J. R. Walker, S. Batalov, K. Yusim, S. Feng, C.-S. Tung, J. Theiler, L. E. Via, H. I. M. Boshoff, K. S. Murakami, B. Korber, C. E. Barry 3rd, S.-N. Cho, *Mol. Microbiol.* **91**, 1106–1119 (2014).
12. S. Baker, P. T. Duy, T. V. T. Nga, T. T. N. Dung, V. V. Phat, T. T. Chau, A. K. Turner, J. Farrar, M. F. Boni, *eLife* **2**, e01229 (2013).
13. W. Loftie-Eaton, K. Bashford, H. Quinn, K. Dong, J. Millstein, S. Hunter, M. K. Thomason, H. Merrikh, J. M. Ponciano, E. M. Top, *Nat. Ecol. Evol.* **1**, 1354–1363 (2017).
14. A. J. Mathers, G. Peirano, J. D. D. Pitout, *Clin. Microbiol. Rev.* **28**, 565–591 (2015).
15. K. L. Wyres, K. E. Holt, *Trends Microbiol.* **24**, 944–956 (2016).
16. A. Cassini *et al*., *PLOS Med.* **13**, e1002150 (2016).
17. T. P. Lim, R. T.-H. Ong, P.-Y. Hon, J. Hawkey, K. E. Holt, T. H. Koh, M. L.-N. Leong, J. Q.-M. Teo, T. Y. Tan, M. M.-L. Ng, L. Y. Hsu, *Antimicrob. Agents Chemother.* **59**, 7899–7902 (2015).
18. B. P. Howden, A. Y. Peleg, T. P. Stinear, *Infect. Genet. Evol.* **21**, 575–582 (2014).
19. K. Holt *et al*., *Microb. Genom.* **2**, e000052 (2016).
20. V. K. Wong, S. Baker, D. J. Pickard, J. Parkhill, A. J. Page, N. A. Feasey, R. A. Kingsley, N. R. Thomson, J. A. Keane, F.-X. Weill, D. J. Edwards, J. Hawkey, S. R. Harris, A. E. Mather, A. K. Cain, J. Hadfield, P. J. Hart, N. T. V. Thieu, E. J. Klemm, D. A. Glinos, R. F. Breiman, C. H. Watson, S. Kariuki, M. A. Gordon, R. S. Heyderman, C. Okoro, J. Jacobs, O. Lunguya, W. J. Edmunds, C. Msefula, J. A. Chabalgoity, M. Kama, K. Jenkins, S. Dutta, F. Marks, J. Campos, C. Thompson, S. Obaro, C. A. MacLennan, C. Dolecek, K. H. Keddy, A. M. Smith, C. M. Parry, A. Karkey, E. K. Mulholland, J. I. Campbell, S. Dongol, B. Basnyat, M. Dufour, D. Bandaranayake, T. T. Naseri, S. P. Singh, M. Hatta, P. Newton, R. S. Onsare, L. Isaia, D. Dance, V. Davong, G. Thwaites, L. Wijedoru, J. A. Crump, E. De Pinna, S. Nair, E. J. Nilles, D. P. Thanh, P. Turner, S. Soeng, M. Valcanis, J. Powling, K. Dimovski, G. Hogg, J. Farrar, K. E. Holt, G. Dougan, *Nat. Genet.* **47**, 632–639 (2015).
21. K. E. Holt *et al*., *Nat. Genet.* **44**, 1056–1059 (2012).
22. H. Chung The *et al*., *PLOS Med.* **13**, e1002055 (2016).
23. D. A. Lewis, *Sex. Transm. Infect.* **89** (suppl. 4), iv47–iv51 (2013).
24. M. Unemo, W. M. Shafer, *Clin. Microbiol. Rev.* **27**, 587–613 (2014).
25. Y. H. Grad *et al*., *Lancet Infect. Dis.* **14**, 220–226 (2014).
26. J. Hadfield *et al*., *Genome Res.* **27**, 1220–1229 (2017).
27. S. K. Dritz, A. F. Back, *N. Engl. J. Med.* **291**, 1194 (1974).
28. K. S. Baker *et al*., *Lancet Infect. Dis.* **15**, 913–921 (2015).
29. N. Datta, *J. Hyg. (Lond.)* **60**, 301–310 (1962).
30. E. S. Anderson, *BMJ* **3**, 333–339 (1968).
31. A. Tran-Dien, S. Le Hello, C. Bouchier, F.-X. Weill, *Lancet Infect. Dis.* **18**, 207–214 (2018).
32. E. J. Threlfall, *J. Antimicrob. Chemother.* **46**, 7–10 (2000).
33. M. Helms, S. Ethelberg, K. Mølbak; DT104 Study Group, *Emerg. Infect. Dis.* **11**, 859–867 (2005).
34. A. E. Mather *et al*., *Science* **341**, 1514–1517 (2013).
35. K. L. Hopkins *et al*., *Euro Surveill.* **15**, 19580 (2010).
36. E. Elnekave *et al*., *Clin. Infect. Dis.* **5**, 877–885 (2017).
37. M. L. Cohen, R. V. Tauxe, *Science* **234**, 964–969 (1986).
38. S. Le Hello *et al*., *Lancet Infect. Dis.* **13**, 672–679 (2013).
39. M. Baym, L. K. Stone, R. Kishony, *Science* **351**, aad3292 (2016).
40. P. J. van Duijn *et al*., *Lancet Infect. Dis.* **18**, 401–409 (2018).

ACKNOWLEDGMENTS

We thank M. Holden at the University of St. Andrews for providing Fig. 1. **Funding:** S.B. is a Sir Henry Dale Fellow, jointly funded by the Wellcome Trust and the Royal Society (100087/Z/12/Z). K.E.H. is a Viertel Foundation of Australia Senior Medical Research Fellow and HHMI-Gates International Research Scholar. The funders had no role in study design, data collection and analysis, decision to publish, or preparation of the manuscript. **Competing interests:** S.B., N.R.T., and K.E.H. declare no competing interests; F.-X.V. wishes to declare he is a Member of the Scientific Council of the Pasteur Institutes of Guadeloupe and French Guiana.

10.1126/science.aar3777

REVIEW

Worldwide emergence of resistance to antifungal drugs challenges human health and food security

Matthew C. Fisher,[1]* Nichola J. Hawkins,[2] Dominique Sanglard,[3] Sarah J. Gurr[4,5]*

The recent rate of emergence of pathogenic fungi that are resistant to the limited number of commonly used antifungal agents is unprecedented. The azoles, for example, are used not only for human and animal health care and crop protection but also in antifouling coatings and timber preservation. The ubiquity and multiple uses of azoles have hastened the independent evolution of resistance in many environments. One consequence is an increasing risk in human health care from naturally occurring opportunistic fungal pathogens that have acquired resistance to this broad class of chemicals. To avoid a global collapse in our ability to control fungal infections and to avoid critical failures in medicine and food security, we must improve our stewardship of extant chemicals, promote new antifungal discovery, and leverage emerging technologies for alternative solutions.

The rapid emergence of multidrug-resistant pathogenic fungi and the better-publicized threat of antibiotic-resistant bacteria together pose a considerable threat to disease control across diverse anthropogenic systems. These microbes respond adroitly to human-induced natural selection through chemical treatments and nimbly hijack human globalization pathways (*1*), thus disseminating the problems worldwide. Today, crop-destroying fungi account for perennial yield losses of ~20% worldwide, with a further 10% loss postharvest. Fungal effects on human health are currently spiraling, and the global mortality rate for fungal diseases now exceeds that for malaria or breast cancer and is comparable to those for tuberculosis and HIV (*2*). Fungal infections have hitherto been greatly neglected relative to other classes of infectious disease, despite their ubiquity.

The first antifungal chemicals used in human health care, nystatin and the polyenes, were discovered in the 1950s, and copper and sulfur fungicides were first used to control crop disease more than 150 years ago. Today, systemic antifungals and fungicides are used as frontline treatments for fungal diseases in humans and plants. Fungal pathogen control can, however, be ephemeral because of the rapid development of resistance to the chemicals. Fungi have highly plastic genomes and reproduce rapidly. The combination of these properties quickly generates variants selected for resistance. For plant pathogens, the pace of breakdown of antifungal protection is enhanced by monoculture cropping practices, as large swathes of genetically uniform crops provide ideal breeding and feeding grounds for the rapid emergence of fungicide-resistant variants. In humans, long periods of prophylactic treatment in at-risk patients can similarly lead to the emergence of antifungal resistance (*3*). Resistance of clinical pathogens to all licensed systemic antifungals has been documented, although the rate of emergence varies among drug classes (Fig. 1) (*3*). Likewise, despite the wider range of fungicides licensed for use in agriculture, resistance to each main class of fungicides has emerged in some major pathogens (Fig. 1). This threat is exacerbated by the additional threat of withdrawal of some chemical classes because of regulatory changes in jurisdictions such as the European Union (EU).

Antifungals for the treatment of fungal diseases in the clinic and the field

The chemical control of fungal pathogens that cause diseases in animals and crops has progressed from the use of inorganic chemicals to the use of organic surface protectant chemicals and then to the use of systemically acting fungicides. Approximately nine times more antifungal compounds are available to control crop diseases than to treat systemic animal infections. Licensed treatments for humans are limited to four frontline classes of drugs (Fig. 1): The polyenes (such as amphotericin B) disrupt the structure of cell membranes by sequestering the fungal membrane sterol ergosterol. The pyrimidine analog 5-fluorocytosine (5-FC) blocks pyrimidine metabolism and DNA synthesis. The newest class of antifungals, the echinocandins, inhibits (1-3)-β-D-glucan synthase and disrupts cell wall biosynthesis. The fourth and most widely used class of fungicides, the azoles, blocks ergosterol biosynthesis through inhibition of lanosterol 14-α-demethylase. Most fungicides for crop disease target mitochondrial function, the cytoskeleton, or ergosterol biosynthesis (Fig. 1), although some specialized chemicals, such as the azanaphthalenes for powdery mildew control, target other pathways. However, the azoles remain the dominant chemicals in the treatment of fungal infections in crops, humans, and livestock, with five licensed clinical azole antifungals and 31 available for crop protection.

Parallel drivers of fungicide resistance in the clinic and the field

Human population growth, urbanization, and economic prosperity have fueled demands for increasing quantities and varieties of food. Intensive agriculture has too often responded to this demand with crops bred for maximum productivity under the protection of broad-scale pesticide applications, inadvertently breeding out the plants' own defenses. In parallel, the number of humans at risk from fungal infections is rising rapidly with increases in populations that are particularly susceptible because of age, medical interventions, or HIV infection. Medical advances resulting in greater initial survival rates for patients with cancer or organ transplantation can leave these patients susceptible to secondary attacks from opportunistic fungi, leading to increasing use of antifungal drugs in clinical practice (Fig. 2 and table S1).

The global movement of people and global trade in produce have hastened the free flow of fungal pathogens from country to country, bringing pathogens into contact with naïve hosts (*1*) (Fig. 3). In the clinical setting, new species of multidrug-resistant pathogenic fungi are emerging. *Candida auris,* first described in Japan in 2009 after isolation from a patient's ear, is responsible for rapidly increasing hospital-acquired invasive infections worldwide (*4*). This fungus is now resistant to all clinical antifungals (*5*) and presents a threat to intensive care units because it can survive normal decontamination protocols (*6*). The emergence of resistance in *Candida glabrata* has coincided with this species becoming the predominant bloodstream pathogen recovered from patients, largely because of the increasing prophylactic use of echinocandins and azoles (*7*). There is also a growing threat from filamentous pathogenic fungi that are intrinsically resistant to a broad range of antifungals, such as *Aspergillus terreus* (*8*), *Scedosporium* spp. (*9*), *Fusarium* spp. (*10*), and members of the Mucorales (*11*).

Simultaneously, we are witnessing the continual emergence of new races of plant-infecting fungi able to overcome both host defenses and chemical treatments (*12*), as well as the evolution of these traits in existing major pathogens (*13*, *14*). The first case of resistance against the benzimidazoles (MBCs) was reported in 1969 (*15*), and now MBC resistance is known to occur in more than 90 plant pathogens (*16*). Azole resistance in a plant pathogen was first reported in 1981 (*17*), but azole resistance is generally partial, in contrast to the complete control failures seen for MBCs (*18*). Resistance to strobilurins (QoIs) was reported in field trials even before commercial introduction and in wider field

[1]MRC Centre for Global Infectious Disease Analysis, School of Public Health, Imperial College London, London W2 1PG, UK. [2]Department of Biointeractions and Crop Protection, Rothamsted Research, Harpenden AL5 2JQ, UK. [3]Institute of Microbiology, University of Lausanne and University Hospital, Lausanne CH-1011, Switzerland. [4]Department of BioSciences, University of Exeter, Exeter EX4 4QD, UK. [5]Department of BioSciences, Utrecht University, Padualaan 8, Netherlands.
*Corresponding author. Email: matthew.fisher@imperial.ac.uk (M.C.F.); s.j.gurr@exeter.ac.uk (S.J.G.)

populations within 2 years of release (*19*). A new generation of succinate dehydrogenase inhibitors (SDHIs) was introduced in 2007, but by 2017 resistant field isolates were found in 17 pathogen species (*20*). Pathogens with resistance to MBCs, azoles, QoIs, and SDHIs include the major wheat pathogen *Zymoseptoria tritici*, banana black sigatoka pathogen *Mycosphaerella fijiensis*, cereal powdery mildew fungus *Blumeria graminis*, the emerging barley pathogen *Ramularia collo-cygni*, and the apple scab fungus *Venturia inaequalis*. For *Botrytis cinerea* (a generalist pathogen that causes gray mold, particularly on soft fruits), resistance against 15 different classes of systemic and protectant fungicides has been reported (*21*).

Parallel evolution of resistance mechanisms in the clinic and the field

The selective pressure exerted on fungi by single-site–inhibiting fungicides has resulted in similar adaptations arising over time in disparate fungal species. Parallel evolution of resistance extends across clinical and plant-pathogenic fungi, with the same key resistance mechanisms occurring independently in both.

Mutations resulting in conformational changes to the drug target site are the most common form of resistance in pathogenic fungi. Target-site mutations have been reported in candin-resistant clinical pathogens and MBC-, QoI-, and SDHI-resistant plant pathogens, as well as azole-resistant strains in agricultural and clinical settings. A single mutation, Gly^{143}→Ala in cytochrome *b*, has emerged in the field in more than 20 species under selection by QoIs (*14*). Moreover, the Tyr^{137}→Phe substitution in CYP51 (P450 cytochrome) has been found in multiple plant pathogens with partial azole resistance, and Tyr^{132}→Phe also occurs at the equivalent residue in *Candida albicans* (*18*). Promoter changes resulting in up-regulation of the fungicide target are also common across clinical and plant-pathogenic fungi (*22*). In *Aspergillus fumigatus*, tandem repeats in the CYP51A promoter region occur together with downstream single-nucleotide polymorphisms (SNPs) in the coding region, conferring a multi-azole resistance phenotype (*23*).

A third resistance mechanism involves reducing intracellular drug accumulation by up-regulation of efflux pumps, such as adenosine triphosphate–binding cassette transporters or major facilitators. Their up-regulation may result from promoter insertions or transcription factor gain-of-function mutations (*3*, *24*).

Further resistance mechanisms have been identified in clinical pathogens. Activation of stress response pathways by Hsp90 can unleash cryptic diversity, potentiating the evolution of resistance to azoles, echinocandins, and polyenes in *Candida* and *Aspergillus* species (*25*). Structural genomic plasticity can result in resistance, with chromosome arm duplications leading to efflux pump and target-site overexpression in *C. albicans* (*24*, *26*). Hypermutator strains of *C. glabrata* and *Cryptococcus neoformans*, with the potential to evolve rapidly in response to host and drug selection, were recently reported (*27*, *28*).

Dual use of azoles in the clinic and the field

The azoles are the most widely deployed class of fungicides in crop protection, totaling in excess of 26% of all fungicides across the EU (*29*). Azoles are also frontline drugs used in humans and animals; however, such multiple use seems to have promoted azole resistance in an opportunistic pathogen of humans (*29*, *30*), the saprotroph *A. fumigatus*. This species colonizes decaying vegetation in fields, forests, and compost heaps but is also capable of invading immunocompromised humans. Multi-azole–resistant *A. fumigatus* has been recovered from environmental and clinical samples globally. In the Netherlands, more than 25% of clinical *Aspergillus* strains carry azole resistance alleles (*31*). Azoles are increasingly failing as frontline therapies, with associated patient mortality approaching 100% (*31*). Population genomic analyses have shown that azole-resistant alleles in *A. fumigatus*

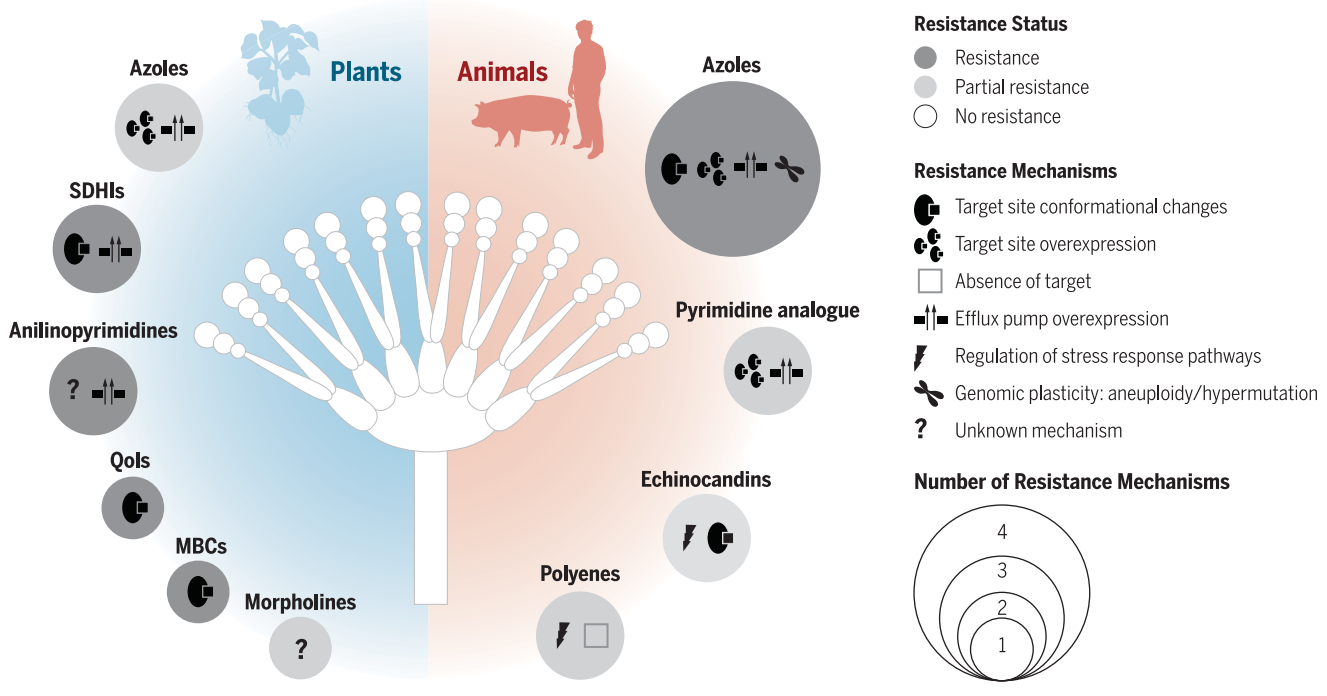

Fig. 1. Current classes of drugs used against plant and animal fungal infections and known mechanisms of resistance to them. The six main classes of fungicides are the morpholines, which inhibit two target sites within the ergosterol biosynthetic pathway, Δ14-reductase and Δ8-Δ7-isomerase (this reduces the risk of target-site resistance, but their intrinsic antifungal activity spectrum is narrower than those of other antifungals); the azoles (used also in animal infections), which target the ergosterol biosynthetic pathway; the benzimidazoles (MBCs), which interfere with the cytoskeleton by binding to β-tubulin, thus preventing the assembly of microtubules; the strobilurins (QoIs) and succinate dehydrogenase inhibitors (SDHIs), which both inhibit the electron transfer chain of mitochondrial respiration, with the SDHIs inhibiting complex II (succinate dehydrogenase) and the QoIs inhibiting complex III (the quinone outside binding pocket of cytochrome *b*); and the anilinopyrimidines, which may target mitochondrial signaling pathways. Three other antifungal classes are used for animal fungal infections: the echinocandins, which inhibit cell wall biosynthesis; the pyrimidine analogs, which interfere with nucleic acid biosynthesis; and the polyenes, which bind ergosterol.

ILLUSTRATION: CHARLOTTE GURR, ADAPTED BY K. KHOLOSKI

are associated with selective sweeps when azole use is high, as in India (*32*). Moreover, recombination in *A. fumigatus* generates new combinations of azole resistance alleles (*32*). Investigations are now under way to assess the relative contributions of clinical and environmental selection to azole resistance in *A. fumigatus* and to identify the most problematic environmental applications of azoles. The potential conflict between the level of agricultural use and the durability of clinical effectiveness of azoles highlights how limited the antifungal toolbox is, where neither "side" can afford to lose a mode of action (*33*).

Most cases of fungicide and antifungal resistance across field and clinic settings appear to have arisen by the repeated independent evolution of resistance to successive fungicides within numerous fungal species. This is where evolution of antifungal resistance differs fundamentally from that of antibacterial resistance, which is frequently transferred between pathogens of animals and humans via the "mobilome" of plasmids and phage (*34*). Some evidence indicates horizontal gene transfer among fungi (*35*), but this fungal gene transfer occurs over longer time scales than gene transfer among bacteria and the dynamics of resistance arising by this route is thus far negligible.

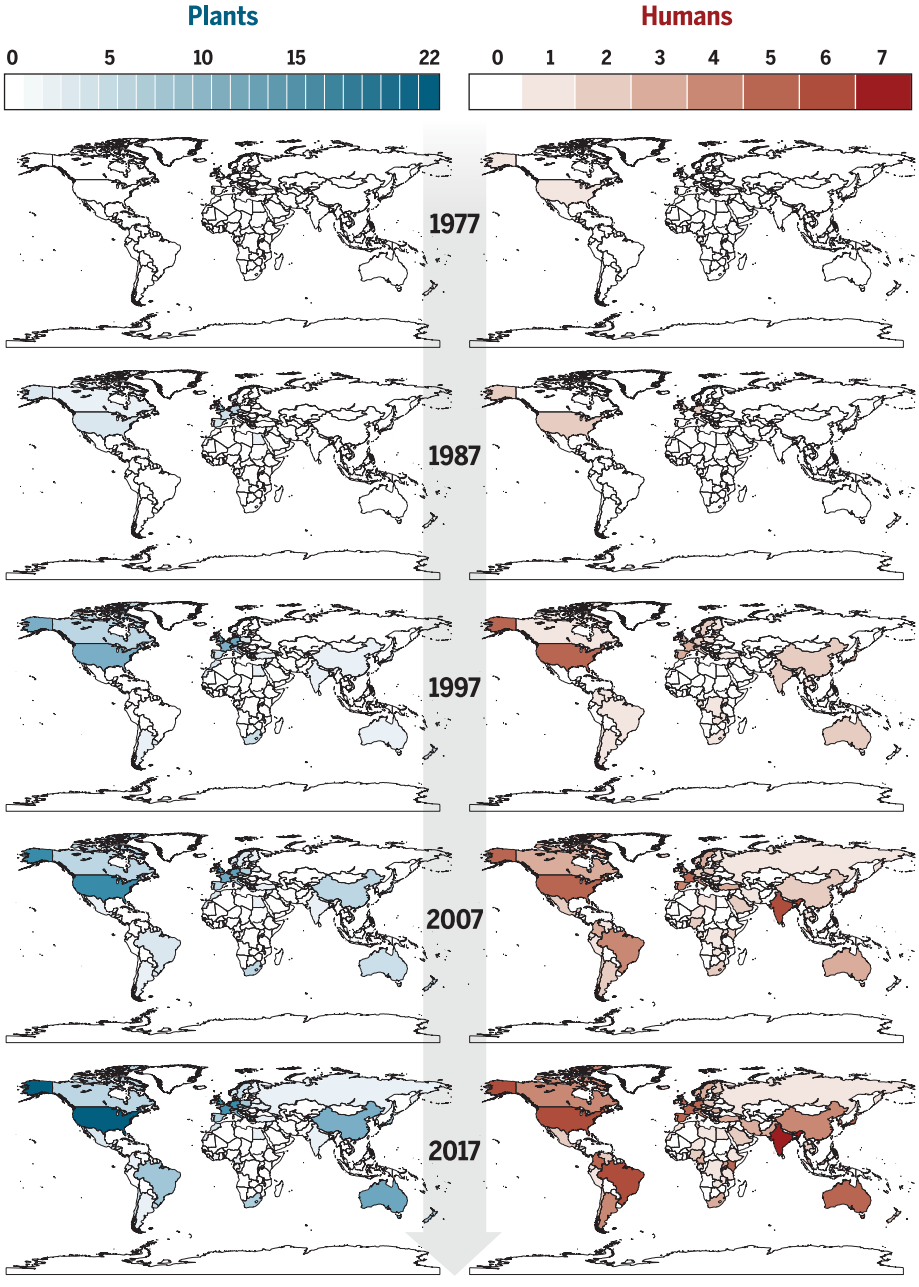

Fig. 2. Fungal species with reported antifungal resistance, by country. Increasing color intensity reflects a growing number of reports. The plant maps depict spatiotemporal records of resistance of crop pathogens to azoles (blue scale). The human maps depict spatiotemporal records of resistance of the pathogens *A. fumigatus*, *C. albicans*, *C. auris*, *C. glabrata*, *Cryptococcus gattii*, and *Cryptococcus neoformans* to azoles (red scale). The data are derived from peer-reviewed publications as of March 2018, reporting the occurrence of cases of resistance up to 2017 (the list of publications is available in table S1).

Prospects for diversifying the toolbox for fungal control

To counter the escalating risks of fungal disease, we need to discover antifungal chemicals with new modes of action, hinder the emergence of resistance in extant chemicals by better stewardship, and develop new disease control strategies to avoid overreliance on fungicides.

Development of new antifungals

The rate of emergence of fungicide resistance (Fig. 2) is greater than the pace of fungicide discovery, and the long registration process for new compounds adds further delays. This situation parallels the situation for antibiotics. Increased research activity is thus needed to develop new antifungal drugs (*36*). Recently, substantial progress has occurred in this field, with at least 11 antifungals in phase 1 and 2 clinical trials and at least two in the agricultural chemicals pipeline. Several of these are derivatives of commonly used antifungal chemicals, such as ergosterol biosynthesis and cell wall biosynthesis inhibitors, engineered for higher efficacy, and others have new modes of action. Combining molecular modeling, combinatorial chemistry, and high-throughput screening has the potential to develop chemicals with reduced resistance risk (*37*).

Stewardship of existing compounds

Robust global strategies are needed to slow the development of antifungal resistance. Combining different modes of action, either in mixtures or in alternating treatments, may slow the emergence of resistance. For example, combinations of fluconazole, flucytosine, and amphotericin B can effectively treat HIV-associated cryptococcal meningitis (*38*). In agriculture, mixtures of fungicides with different modes of action are already widely recommended (*39*), with some formulations available only as mixed products. Where target-site mutations confer high levels of resistance, lower doses of antifungals should be favored (*40*, *41*). However, this results in a trade-off between the immediate gain of treatment effectiveness and the longer benefit from slowing the selection of resistance. Improvements in molecular diagnostics are also needed, both for the identification of fungal pathogens so that antifungals can be used appropriately and for the detection of specific resistance alleles, as the monitoring of resistance is a vital part of stewardship (*42*).

Integrated disease management

To reduce our reliance on chemical control alone, we must develop more nonchemical control measures to use where effective fungicides are no longer available or to use in combination with fungicides to reduce the selective pressure

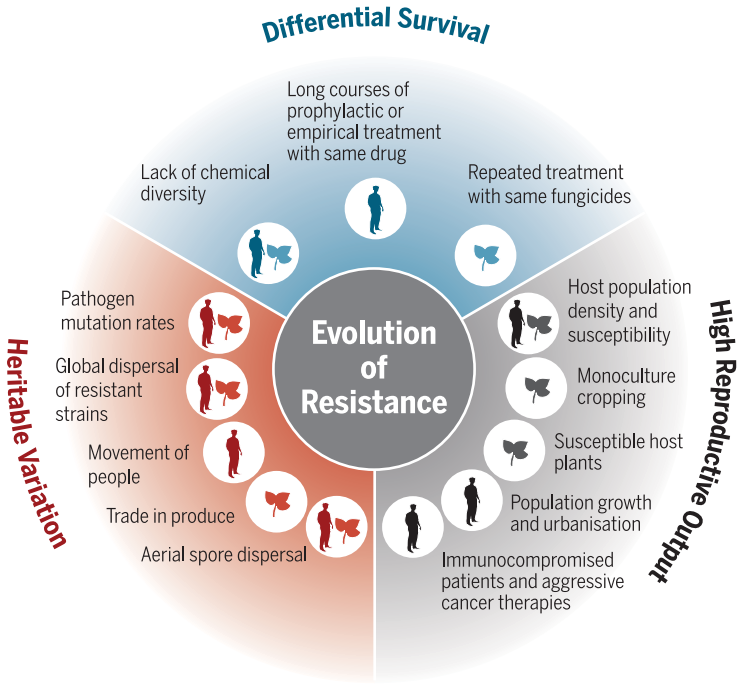

Fig. 3. Evolutionary drivers of antifungal resistance: heritable variation, high reproductive output, and differential survival.

on each component. In crops, the development of innate disease resistance through the selection of major pathogen-resistance alleles is widely used to breed disease-resistant cultivars. However, this approach is slow, with a 20-year lag from finding a suitable disease-resistance gene to releasing it in commercial lines. Marker-assisted breeding can speed up the recombination of multiple disease-resistance alleles, but it still takes approximately a decade (*43*). Transgene cloning, or gene editing, is faster still (requiring ~2 years), but no crops with transgenic antifungal disease resistance have yet been released commercially. The high degree of specificity between host and pathogen for major resistance genes (*44*) means that pathogens can also rapidly evolve to overcome this strategy. However, "evolution-smart" disease-resistant crops with pyramided pathogen-resistance genes or mosaic deployment of resistant varieties may provide greater durability of disease control. Minor resistance genes, such as those for the antifungal chitinases and glucanases, carry the advantage of broad-spectrum activity (*45*) but introduce the possible disadvantage of yield penalties, as well as providing incomplete protection. Further sources of genetic disease resistance can be found in the gene pools of crops' wild relatives, which may be introduced into modern crop varieties through introgression or transgenesis (*43*).

In humans, advances in combination antiretroviral therapy to halt HIV-AIDS progression, gene therapies under development for cystic fibrosis, and tissue engineering for rejection-free transplantation can reduce vulnerability to fungal infections in the corresponding patient cohorts. Also, the first antifungal vaccine against *C. albicans* is undergoing clinical trials (*46*), and the use of bioengineered T cells to augment host immunity is being explored (*47*). Lastly, the identification of human genetic biomarkers associated with susceptibility to fungal diseases, such as SNPs in the immune mediator *PTX3* (*48*), provides a new path to identify patient groups in which antifungal treatments could be reduced.

The rapidly growing fields of synthetic biology and epigenomics are now converging to develop antifungal treatments on the basis of RNA interference (RNAi). Bidirectional cross-kingdom microRNA (miRNA) trafficking between plants and fungi is being developed to fight pathogens (*49*) such as *B. cinerea*, which uses miRNA virulence effectors to silence host plant immune genes (*50*, *51*). Current research avenues include identifying new targets for RNAi and, crucially, developing systems for the stable and targeted delivery of RNA silencing through genetic engineering of the host plant or exogenous application of synthetic RNA (*50*–*52*). Although such approaches have not yet been used to treat fungal infections in the clinic, the discovery of RNAi as a promising clinical antifungal strategy is potentially transformational.

REFERENCES AND NOTES

1. M. C. Fisher *et al.*, *Nature* **484**, 186–194 (2012).
2. G. D. Brown *et al.*, *Sci. Transl. Med.* **4**, 165rv13 (2012).
3. N. Robbins, T. Caplan, L. E. Cowen, *Annu. Rev. Microbiol.* **71**, 753–775 (2017).
4. A. Chowdhary, C. Sharma, J. F. Meis, *PLOS Pathog.* **13**, e1006290 (2017).
5. S. R. Lockhart *et al.*, *Clin. Infect. Dis.* **64**, 134–140 (2017).
6. S. Schelenz *et al.*, *Antimicrob. Resist. Infect. Control* **5**, 35 (2016).
7. B. D. Alexander *et al.*, *Clin. Infect. Dis.* **56**, 1724–1732 (2013).
8. R. Hachem *et al.*, *J. Antimicrob. Chemother.* **69**, 3148–3155 (2014).
9. M. Lackner *et al.*, *Antimicrob. Agents Chemother.* **56**, 2635–2642 (2012).
10. A. M. Al-Hatmi, F. Hagen, S. B. Menken, J. F. Meis, G. S. de Hoog, *Emerg. Microbes Infect.* **5**, e124 (2016).
11. M. Slavin *et al.*, *Clin. Microbiol. Infect.* **21**, 490.e1–490.e10 (2015).
12. M. T. Islam *et al.*, *BMC Biol.* **14**, 84 (2016).
13. M. S. Hovmøller, S. *et al.*, *Plant Pathol.* **65**, 402–411 (2016).
14. J. A. Lucas, N. J. Hawkins, B. A. Fraaije, *Adv. Appl. Microbiol.* **90**, 29–92 (2015).
15. W. T. Schroeder, R. Provvidenti, *Plant Dis. Rep.* **53**, 271–275 (1969).
16. N. J. Hawkins, B. A. Fraaije, *Front. Microbiol.* **7**, 1814 (2016).
17. J. T. Fletcher, M. S. Wolfe, in *British Crop Protection Conference—Pests and Diseases*, Brighton, UK, 16 to 19 November 1981 (British Crop Protection Council, 1981), vol. 2, pp. 633–640.
18. H. J. Cools, B. A. Fraaije, *Pest Manag. Sci.* **64**, 681–684 (2008).
19. S. P. Heaney, A. Hall, S. A. Davies, G. Olaya, paper presented at the 2000 BCPC Conference—Pests and Diseases, Brighton, UK, 13 to 16 November 2000.
20. Fungicide Resistance Action Committee (FRAC), "FRAC list of plant pathogenic organisms resistant to disease control agents, revised December 2017" (FRAC, 2017).
21. M. Hahn, *J. Chem. Biol.* **7**, 133–141 (2014).
22. H. Hamamoto *et al.*, *Appl. Environ. Microbiol.* **66**, 3421–3426 (2000).
23. E. Snelders *et al.*, *Fungal Genet. Biol.* **48**, 1062–1070 (2011).
24. N. J. Hawkins *et al.*, *Mol. Biol. Evol.* **31**, 1793–1802 (2014).
25. L. E. Cowen, S. Lindquist, *Science* **309**, 2185–2189 (2005).
26. A. Selmecki, M. Gerami-Nejad, C. Paulson, A. Forche, J. Berman, *Mol. Microbiol.* **68**, 624–641 (2008).
27. J. Rhodes *et al.*, *G3* **7**, 1165–1176 (2017).
28. K. R. Healey *et al.*, *Nat. Commun.* **7**, 11128 (2016).
29. European Centers for Disease Control, "Risk assessment on the impact of environmental usage of triazoles on the development and spread of resistance to medical triazoles in *Aspergillus* species" (European Centers for Disease Control, 2013).
30. J. F. Meis, A. Chowdhary, J. L. Rhodes, M. C. Fisher, P. E. Verweij, *Philos. Trans. R. Soc. London Ser. B* **371**, 20150460 (2016).
31. J. van Paassen, A. Russcher, A. W. In 't Veld-van Wingerden, P. E. Verweij, E. J. Kuijper, *Euro Surveill.* **21**, 30300 (2016).
32. A. Abdolrasouli *et al.*, *mBio* **6**, e00536-15 (2015).
33. C. J. Swanton, H. R. Mashhadi, K. R. Solomon, M. M. Afifi, S. O. Duke, *Pest Manag. Sci.* **67**, 790–797 (2011).
34. J. A. Perry, G. D. Wright, *Front. Microbiol.* **4**, 138 (2013).
35. T. A. Richards *et al.*, *Proc. Natl. Acad. Sci. U.S.A.* **108**, 15258–15263 (2011).
36. D. W. Denning, M. J. Bromley, *Science* **347**, 1414–1416 (2015).
37. J. L. Nishikawa *et al.*, *Nature* **530**, 485–489 (2016).
38. M. Molefi *et al.*, *Trials* **16**, 276 (2015).
39. H. Dooley, M. W. Shaw, J. Spink, S. Kildea, *Plant Pathol.* **65**, 124–136 (2016).
40. F. van den Bosch, N. Paveley, M. Shaw, P. Hobbelen, R. Oliver, *Plant Pathol.* **60**, 597–606 (2011).
41. A. Mikaberidze, N. Paveley, S. Bonhoeffer, F. van den Bosch, *Phytopathology* **107**, 545–560 (2017).
42. R4P Network, *Trends Plant Sci.* **21**, 834–853 (2016).
43. S. Ashkani *et al.*, *Front. Plant Sci.* **6**, 886 (2015).
44. S. J. Gurr, P. J. Rushton, *Trends Biotechnol.* **23**, 275–282 (2005).
45. H. F. Eissa *et al.*, *Plant Methods* **13**, 41 (2017).
46. J. E. Edwards Jr., *J. Med. Microbiol.* **61**, 895–903 (2012).
47. P. R. Kumaresan *et al.*, *Proc. Natl. Acad. Sci. U.S.A.* **111**, 10660–10665 (2014).
48. C. Cunha *et al.*, *N. Engl. J. Med.* **370**, 421–432 (2014).
49. M. Z. Ratajczak, J. Ratajczak, *Clin. Transl. Med.* **5**, 7 (2016).
50. A. Weiberg *et al.*, *Science* **342**, 118–123 (2013).
51. M. Wang *et al.*, *Nat. Plants* **2**, 16151 (2016).
52. L. Kudsiova *et al.*, *Mol. Biosyst.* **12**, 934–951 (2016).

ACKNOWLEDGMENTS

We thank C. Thornton and G. Steinberg for their critical appraisal of the manuscript, C. Gurr for infographics based on ideas from N.J.H., and A. Abdolrasouli for assistance with literature searches. **Funding:** M.C.F. was supported by the Natural Environmental Research Council (NERC; NE/K014455/1) and the Medical Research Council (MRC; MR/K000373/1), N.J.H. was supported through the BBSRC's Industrial Strategy Challenge Fund (BBS/OS/CP/000001), D.S. was supported by the Swiss National Science Foundation (FN 301003A-172958), and S.J.G. was supported by BBSRC (BB/P018335, awarded to G. Steinberg and S.J.G.). **Competing interests:** None declared.

SUPPLEMENTARY MATERIALS

www.sciencemag.org/content/360/6390/739/suppl/DC1
Table S1
References (*53*–*323*)

10.1126/science.aap7999

ILLUSTRATION: CHARLOTTE GURR, ADAPTED BY K. KHOLOSKI

REVIEW

Prospects for harnessing biocide resistance for bioremediation and detoxification

Siavash Atashgahi,[1] Irene Sánchez-Andrea,[1] Hermann J. Heipieper,[2] Jan R. van der Meer,[3] Alfons J. M. Stams,[1,4] Hauke Smidt[1]*

Prokaryotes in natural environments respond rapidly to high concentrations of chemicals and physical stresses. Exposure to anthropogenic toxic substances—such as oil, chlorinated solvents, or antibiotics—favors the evolution of resistant phenotypes, some of which can use contaminants as an exclusive carbon source or as electron donors and acceptors. Microorganisms similarly adapt to extreme pH, metal, or osmotic stress. The metabolic plasticity of prokaryotes can thus be harnessed for bioremediation and can be exploited in a variety of ways, ranging from stimulated natural attenuation to bioaugmentation and from wastewater treatment to habitat restoration.

Microorganisms in pristine ecosystems as well as those in anthropogenically disturbed habitats are constantly challenged by combinations of chemicals and physical stresses. Natural habitats can experience combinations of conditions from high salinity and osmolarity, desiccation, ultraviolet radiation, high pressure, or extremes of pH or temperature (*1*). Industrial, agricultural, and domestic activities lead to the release of organic and inorganic compounds toxic to a wide range of organisms in the environment. Microbes exposed to such conditions can rapidly develop physiological and/or genetic adaptations to resist environmental constraints. Harnessing the metabolic capacities of prokaryotes and their adaptive potential is of interest for a broad range of applications for environmental clean-up as well as for treatment of domestic and industrial waste.

Microbial tolerance and resistance mechanisms

The mechanisms that enable bacteria to survive typical environmental stressors, such as toxic concentrations of organic pollutants and changes in temperature or osmolarity, are well understood (*2*–*4*). Preventing damage to the cell envelope and cellular membranes are pivotal for prokaryote survival (*5*). Hence, one of the first responses to toxic assault is membrane repair to reestablish membrane fluidity and rigidity. In Gram-negative bacteria, this occurs with the insertion of saturated and *trans*-configurated unsaturated fatty acids, whereas in Gram-positive bacteria, *iso*-branched fatty acids are inserted (*6*). Cell-surface properties can also be modified during exposure to stressors by the release of outer-membrane vesicles, which increase surface hydrophobicity. This phenomenon can stimulate biofilm formation, making bacteria yet more tolerant to environmental stressors (*7*). Bacteria can also change their morphology in the presence of toxic concentrations of organic pollutants, increasing their overall size and decreasing surface-to-volume ratio (*5*).

Many bacteria respond to stresses by inducing synthesis of specific membrane efflux pumps. This response is well understood in bacteria capable of withstanding high concentrations of organic solvents such as benzene, toluene, ethylbenzene, and xylene (BTEX). BTEX are excreted from membranes by energy-driven protein pumps belonging to the root nodulation (RND) family of membrane proteins. RND proteins are known in other bacteria to transport antibiotics and contribute to multidrug resistance (*3*). Cross-protection to different stresses is common. For example, bacterial cells that adapt to a given solvent also show increased tolerance to other solvents, heavy metals, antibiotics, and several forms of physical-chemical stress. Because bacterial adaptive physiological responses are inducible, it is therefore possible to pre-adapt the cells for potential applications at contaminated sites (*5*).

Role of environments in tolerance and resistance selection

Although any environment ultimately selects for the survival and proliferation of specific microbial genotypes, extreme and polluted environments showcase the power of such selective forces. Polluted environments are frequently characterized by high concentrations of toxic substances that can appear in sudden, infrequent, but ephemeral bursts such as oil spills (*8*), but equally, chronic pollution can arise from long-term input of pollutants (*9*). An influx of high concentrations of toxic compounds can lead to dramatic shifts in microbial community composition and diversity (Fig. 1, top) (*10*). Consequently, carbon and nutrients in the system that are no longer used by sensitive phenotypes can be used for growth by resistant phenotypes (Fig. 1, top) (*11*). Additionally, polluting compounds can become an exclusive source of assimilable nutrients or electron donors or acceptors for resistant microorganisms (Fig. 1, bottom) (*11*). For example, oil-degrading bacteria occur at typically low abundances in marine environments but respond with astonishingly rapid blooms during oil spills (*12*). Even for synthetic chemicals considered to be xenobiotic—such as chlorinated solvents, pesticides, and the plastic poly(ethylene terephthalate)—release into the environment, and long-term pollution selects for the appearance and proliferation of mutants with naturally recombined metabolic pathways, which profit from the exclusivity of the toxic compound for growth (*13*–*15*). Natural recombination is largely the result of abundant horizontal gene flow in prokaryote communities. Diverse mechanisms have been implicated in gene flow, such as plasmid conjugation, natural transformation, and integrative and conjugative or transposable elements (*11*). Extreme toxicity resistance as a result of RND-type efflux mechanisms may thus be a prerequisite for further adaptation by keeping the intracellular concentration of the toxicant low enough to permit its metabolism (*16*).

As worldwide environmental concerns shift from high contamination loads of legacy chemicals—such as oil, polycyclic aromatic hydrocarbons, and polychlorinated biphenyls—toward low concentrations of biologically very active molecules—including antibiotics, other pharmaceuticals, and ingredients of household and consumer care products—the question is what types of microbial resistance will be selected by low and chronic concentrations of these chemicals. Although low concentrations of chemicals can be toxic to some lineages and may result in selection of resistant phenotypes, as the widespread emergence of antibiotic resistances attests, the distinct proliferation of "compound-degrader" phenotypes may be more difficult to discern. Conceivably, micropollutant degraders might have more advantage in oligotrophic environments (*17*), where available nutrients are scarce and the ability to metabolize micropollutants may be particularly competitive.

Concepts for harnessing toxicant-tolerant or -resistant bacteria

An important outcome of adaptation and selection in contaminated environments is that sites chronically polluted with organic compounds naturally restore over time and diminish the pollution load (*18*). Such natural attenuation and restoration processes may, however, take decades (*19*). Nevertheless, they require little technical intervention or cost. The spontaneous adaptation and selection that has led to the appearance of (naturally recombinant) bacteria capable of resisting or degrading contaminants has since long attracted interest for potential applications

[1]Wageningen University & Research, Laboratory of Microbiology, Stippeneng 4, 6708 WE Wageningen, Netherlands. [2]Department of Environmental Biotechnology, Helmholtz Centre for Environmental Research–UFZ, Leipzig, Germany. [3]Department of Fundamental Microbiology, University of Lausanne, Lausanne, Switzerland. [4]Centre of Biological Engineering, University of Minho, Braga, Portugal.
*Corresponding author. Email: hauke.smidt@wur.nl

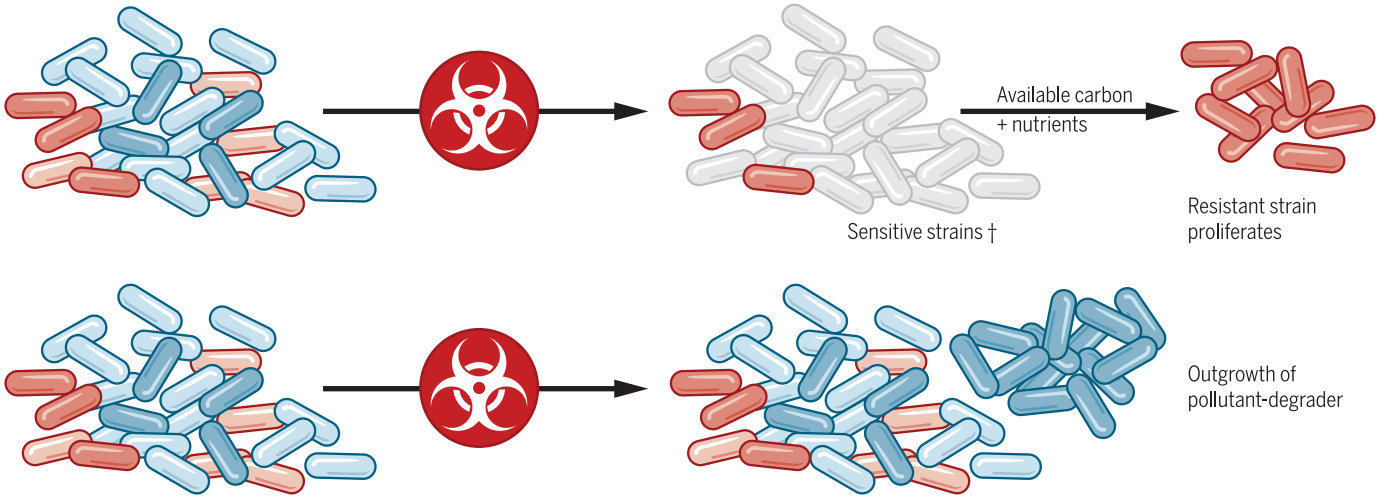

Fig. 1. Environmental selection of adaptive phenotypes to toxic compound stresses. (**Top**) Exposure of a diverse bacterial community to toxic concentrations of chemicals inhibits or kills sensitive individuals. Resistant organisms profit from the availability of unused carbon and nutrients in the system to proliferate. (**Bottom**) Toxic organic compounds themselves can be used as an exclusive growth substrate for low numbers of preexisting specialist bacteria in the community or for newly arising mutants. These lineages will proliferate by consuming the toxic compound, potentially leading to the spontaneous natural attenuation of a contaminated site. Specialist degrader bacteria may additionally profit from toxicity-resistance mechanisms.

elsewhere. The enrichment or isolation of promising pollutant-degrading bacteria, growth under laboratory conditions, and formulation for use in similar conditions and context—a process called bioaugmentation—could potentially shorten the long on-site adaptation process and accelerate remediation.

Bioaugmentation has been successfully applied at sites contaminated with organohalogen compounds. Organohalide-respiring bacteria (OHRB) such as *Dehalococcoides mccartyi*, *Dehalogenimonas* spp., and *Dehalobacter* spp. use chlorinated solvents and/or pesticides as their sole terminal electron acceptors for growth (*20*). Organohalide respiration is probably evolutionarily ancient (*21*), but traces of recent or even ongoing genetic adaptation are detectable in the genomes of these species. Precultured stocks of microbial consortia containing OHRB have been successfully applied so as to improve bioremediation of sites contaminated with chlorinated solvents such as tetrachloroethene (Fig. 2) (*20*, *22*). OHRB augmentation has been shown to be essential for on-site chlorinated solvent bioremediation because stimulation of the autochthonous OHRB frequently leads to accumulation of a more toxic transformation product, vinyl chloride (*23*).

Widespread pollution with hexachlorocyclohexanes (HCHs) arose around the world during production of the currently largely banned pesticide, the γ-HCH isomer lindane. Bacteria adapted to using HCHs as their sole carbon and energy sources have been discovered at HCH-contaminated sites (*24*) as a result of natural recruitment and recombination of existing genes and subsequent mutations. Such bacteria have been isolated, cultured in larger quantities, specifically formulated, and successfully used in the bioaugmentation of HCH-contaminated areas (*25*).

ADAPTED BY K. KHOLOSKI

Oil bioremediation

Crude oil is toxic to metazoan life yet is a supply of extremely energy-rich carbon sources for hydrocarbonoclastic bacteria. Hydrocarbonoclastic bacteria are ubiquitous and evolutionarily old lineages that have adapted to oil components released at natural oil seeps (*26*, *27*). Typically, their population size in the absence of oil spills is very small, but they bloom during oil contamination. For example, *Oceanospirillales* spp. can compose 90% of the local marine bacterial community after oil spillage (*27*). Two well-known species, *Alcanivorax borkumensis* and *Oleispira antarctica*, have evolved several adaptive strategies to optimize access to their poorly water-soluble aliphatic hydrocarbon substrates (*27*, *28*). These include an increase in cell surface hydrophobicity that is thought to favor partitioning of substrates into the cell envelope, as well as production of biosurfactants to increase the ambient solubility of the aliphatic hydrocarbons. Interestingly, *A. borkumensis* is also able to directly incorporate fatty acids, resulting from oxidation of aliphatic hydrocarbons, into its cell membrane (*28*).

"Although any environment ultimately selects for the survival and proliferation of specific microbial genotypes, extreme and polluted environments showcase the power of such selective forces."

Although bioaugmentation of oil spills is often revisited, the application of large quantities of precultured marine hydrocarbonoclastic bacteria has not been very successful. A more effective measure for major spills seems to be through stimulation of the growth and activity of indigenous hydrocarbonoclastic bacteria with the application of lipophilic nitrogen-phosphorous–rich fertilizers, both in the open sea as well as on rocks and beaches contaminated with crude oil (*29*).

Oil spills in arid terrestrial environments are accompanied by the simultaneous occurrence of high pH, high salinity, and high loads of toxic organic compounds. In general, adaptation to osmotic stress under high salinity and pH requires increased intracellular salt concentration or accumulation of organic osmotic solutes (*30*). At elevated salinity, the microbial cell surface tends to become more hydrophilic, which will further limit physiological activity on hydrophobic hydrocarbons. High salt concentrations are also characterized by reduced dissolved oxygen, but some organisms can metabolize oil under these conditions, although the mechanisms are not well understood. Successful large-scale bioaugmentation has been implemented in a water pit (3600 m^3) heavily polluted with crude oil in northern Oman, where the addition of halophilic cultures reduced hydrocarbon concentrations from 10 to 40% (w/w) to below 1% (w/w) within a year (Fig. 3) (*31*).

Resistance to low pH and high concentrations of heavy metals

Metal extraction and metal leachate decontamination offers contrasting examples of microbial resistance and its potential use for bioremediation.

Fig. 2. Bioaugmentation with OHRB. (**Left**) Injection of microbial cultures containing OHRB in an injection well or (**Right**) direct push injection without the use of wells in aquifers contaminated with chlorinated solvents. [Reprinted by permission from Springer Nature, (*22*).]

Bioextraction and recovery of valuable metals from sulfidic ores (biohydrometallurgy) depends on the activity of sulfur- and iron-oxidizing prokaryotes to solubilize the mineral pyrite (FeS_2) to H_2SO_4 and Fe^{3+}, during which protons and other metals trapped within the pyrite matrix are released. Biohydrometallurgic suspensions have extreme physicochemical characteristics, sometimes with negative pH values, and metal and sulfate concentrations between 10 and 100 g liter^{-1} (*32*).

Consortia of acidophilic prokaryotes used for biohydrometallurgy, mainly belonging to the genera *Acidithiobacillus* and *Leptospirillum*, are typically derived from natural acid rock drainage environments, such as the Tinto river in Spain, or from spontaneous enrichments derived from mine drainage. These acidophiles can grow at extremely low pH and high metal concentrations. Although growth at low pH has some advantages for cellular energy conservation because it builds a spontaneous pH gradient for the proton motive force across the cytoplasmic membrane, the protons still have to be neutralized within the cytoplasm. Some extreme acidophiles prevent ingress of protons by importing K^+ ions, which inverts the membrane potential (positive inside). They can also have highly impermeable membranes owing to the presence of tetraether lipids and specific membrane transporters, such as antiporters, symporters, H^+–adenosine triphosphatases (ATPases), or metal-transporting P-type ATPases, which remove excess protons and metal ions from the cytoplasm. Additionally, specific chaperones have been reported in acidophilic bacteria that stabilize DNA and proteins, which would otherwise be damaged by the low pH (*33*).

Metal leachates from mines are highly problematic because of their low pH, high sulfate, and high dissolved metal content. Sulfate-reducing bacteria (SRB) release sulfide, which will increase the pH and will react with the dissolved metal ions to precipitate in the form of poorly soluble metal sulfides. Stimulation of sulfidogenic activity has been tested in pilot-scale treatment of metal leachate from the zinc smelter Nyrstar in the Netherlands, and also for leachates from the gold mine Pueblo Viejo in the Dominican Republic. Both applications, however, required prior neutralization of the leachates before biological treatment. Nevertheless, acid- and metallotolerant SRB, such as *Desulfosporosinus acididurans* (*34*), have been isolated from low-pH environments and successfully deployed for initial biological leachate neutralization and subsequent metal detoxification in laboratory-scale reactors (*35*). The prior growth of acidophilic SRB in pH-controlled reactors may further improve the biological recovery of precipitated metallic sulphides and allow potential reuse in industrial processes (*36*).

Resistance to antibiotics and nonantibiotic biocides

Application of antibiotics and nonantibiotic biocides has increased dramatically in recent decades and has resulted in widespread selection of resistant or tolerant mutants. Resistance to antibiotics by the selection of RND efflux pump mechanisms can provide cross-resistance to a wide range of other adverse conditions and compounds. Hence, antibiotic resistance also frequently co-occurs with resistance to biocides and heavy metals. This results from the colocalization and/or comigration of genes conferring multiple resistance mechanisms (*37*, *38*). Antibiotic resistance genes occur in microbes in natural environments without obvious anthropogenic exposure to antibiotics. This indicates that they confer additional biological advantages (*39*), such as resistance to other environmental stressors or to interspecies competition strategies, and metabolism of toxic compounds structurally similar to antibiotics. Several previously unknown dioxygenases have been retrieved from soil metagenomic libraries screened for resistance against β-lactam antibiotics (*40*). These enzymes were also shown to transform other aromatic compounds (*40*). Some microbes can use these antibiotics as substrates for growth, although the mechanistic basis for this antibiotic subsistence has not been identified unequivocally (*41*).

Nonantibiotic biocides can also select for proliferation of resistant microorganisms capable of their biotransformation, as has been shown for a river sediment microbial community degrading benzalkonium chlorides (*42*). Strains of *Pseudomonas putida* and *Alcaligenes xylosoxidans*—which are capable of resisting high levels of the polychlorinated antimicrobial triclosan and using it as a sole carbon source—have been isolated from soil (*43*). Biocide resistance could potentially be put to good use—for instance, for biocides removal from the filters of drinking water treatment plants (DWTPs). However, success has been limited so far. Augmentation of *Aminobacter* sp. MSH1 to sand filters in recent pilot-scale studies of DWTPs only temporarily increased 2,6-dichlorobenzamide degradation. The loss of activity was attributed to starvation of the introduced bacteria because the micropollutant concentrations were low,

Fig. 3. Bioaugmentation with halophilic microorganisms. A bioaugmented open-air bioreactor in northern Oman (**Left**) just before and (**Right**) 1 year after seeding, as an example of hypersaline oil remediation technology. [Reprinted by permission from Springer Nature, (*31*).]

and metabolic competition occurred with more abundant assimilable organic carbon in the water (*44*, *45*).

Concluding remarks

The metabolic and stress-resistance traits that emerge in microorganisms in response to toxic compounds can be exploited for the bioremediation of spills of oil and chlorinated solvents, dissolution of valuable metals, and treating waste streams. However, designing sustainable bioremediation solutions, including those targeted at emerging micropollutants, is a major scientific challenge. The conceptual simplicity of bioaugmentation and attractiveness is deceptive, especially for single microbial strains (*44*–*46*). Microbiologists still have very little knowledge of the traits and conditions that need to be met to allow survival and population growth of nonnative microbes introduced into foreign ecosystems. The few studies that have measured the metabolic activities of inoculated bacterial strains in complex ecosystems have unveiled how divergent the biochemistry becomes in field conditions compared with the laboratory (*47*, *48*). Transposon library selection and sequencing have further shown just how many specific traits determine survival and proliferation in, for example, soil compared with the well-controlled conditions in the laboratory (*49*). Detailed experiments will be crucial for unraveling stress and resistance responses in inoculated strains and consortia and will be necessary to understand how productive metabolic traits can be deployed in order to functionally complement and restore contaminated ecosystems.

Genomic and allied technologies will permit better characterization of the prevailing resident microbial community in contaminated sites and inform community composition, xenometabolic potential, and adaptive capacity to adverse conditions. Meta-omic site diagnosis will provide inputs for advanced biogeochemical models (*50*, *51*). Such insights could be applied to diagnosing microbial communities for xenometabolic function at contaminated sites and for forecasting the success of specific measures, such as biostimulation or bioaugmentation, for accelerated bioremediation. Models could be expanded to address the potential roles of protozoan grazers and phage parasites that regulate microbial populations. For example, although phages can infect and eradicate populations of key detoxifier strains (*52*), they can also facilitate horizontal distribution of genes essential for bioremediation and as such promote degradation capacity.

REFERENCES AND NOTES

1. J. Seckbach, A. Oren, H. Stan-Lotter, Eds., *Polyextremophiles* (Springer, 2013), vol. 27.
2. H. J. Heipieper, F. J. Weber, J. Sikkema, H. Keweloh, J. A. de Bont, *Trends Biotechnol.* **12**, 409–415 (1994).
3. J. L. Ramos *et al*., *Annu. Rev. Microbiol.* **56**, 743–768 (2002).
4. J. Sikkema, J. A. de Bont, B. Poolman, *Microbiol. Rev.* **59**, 201–222 (1995).
5. H. J. Heipieper, G. Neumann, S. Cornelissen, F. Meinhardt, *Appl. Microbiol. Biotechnol.* **74**, 961–973 (2007).
6. Y.-M. Zhang, C. O. Rock, *Nat. Rev. Microbiol.* **6**, 222–233 (2008).
7. T. Baumgarten *et al*., *Appl. Environ. Microbiol.* **78**, 6217–6224 (2012).
8. J. Kemsley, *Chem. Eng. News* **93**, 8–12 (2015).
9. T. S. Galloway, *Mar. Pollut. Bull.* **53**, 606–613 (2006).
10. A. Herzyk *et al*., *J. Contam. Hydrol.* **207**, 17–30 (2017).
11. J. R. van der Meer, *Front. Ecol. Environ.* **4**, 35–42 (2006).
12. T. C. Hazen *et al*., *Science* **330**, 204–208 (2010).
13. T. A. Müller, C. Werlen, J. Spain, J. R. Van Der Meer, *Environ. Microbiol.* **5**, 163–173 (2003).
14. N. Sangwan *et al*., *ISME J.* **8**, 398–408 (2014).
15. S. Yoshida *et al*., *Science* **351**, 1196–1199 (2016).
16. K. Czechowska, C. Reimmann, J. R. van der Meer, *Front. Microbiol.* **4**, 203 (2013).
17. D. Li, M. Alidina, J. E. Drewes, *Appl. Microbiol. Biotechnol.* **98**, 5747–5756 (2014).
18. Z. Lu *et al*., *ISME J.* **6**, 451–460 (2012).
19. J. R. van der Meer Jr., C. Werlen, S. F. Nishino, J. C. Spain, *Appl. Environ. Microbiol.* **64**, 4185–4193 (1998).
20. L. Adrian, F. E. Löffler, Eds., *Organohalide-Respiring Bacteria* (Springer, 2016).
21. S. Atashgahi, M. M. Häggblom, H. Smidt, *Environ. Microbiol.* **20**, 934–948 (2018).
22. C. E. Aziz, R. A. Wymore, R. J. Steffan, in *Bioaugmentation for Groundwater Remediation*. Springer, pp. 141-169 (2013).
23. S. Atashgahi *et al*., *Environ. Microbiol.* **19**, 968–981 (2017).
24. R. Lal *et al*., *Microbiol. Mol. Biol. Rev.* **74**, 58–80 (2010).
25. N. Garg *et al*., *Biodegradation* **27**, 179–193 (2016).
26. M. Kube *et al*., *Nat. Commun.* **4**, 2156 (2013).
27. M. M. Yakimov, K. N. Timmis, P. N. Golyshin, *Curr. Opin. Biotechnol.* **18**, 257–266 (2007).
28. D. J. Naether *et al*., *Appl. Environ. Microbiol.* **79**, 4282–4293 (2013).
29. E. Z. Ron, E. Rosenberg, *Curr. Opin. Biotechnol.* **27**, 191–194 (2014).
30. A. Oren, *Environ. Microbiol.* **13**, 1908–1923 (2011).
31. H. Patzelt, in *Adaptation to Life at High Salt Concentrations in Archaea, Bacteria, and Eukarya* (Springer, 2005), pp. 105–122.
32. D. K. Nordstrom, C. N. Alpers, *Proc. Natl. Acad. Sci. U.S.A.* **96**, 3455–3462 (1999).
33. C. Baker-Austin, M. Dopson, *Trends Microbiol.* **15**, 165–171 (2007).
34. I. Sánchez-Andrea, A. J. Stams, S. Hedrich, I. Ňancucheo, D. B. Johnson, *Extremophiles* **19**, 39–47 (2015).
35. I. Sánchez-Andrea, J. L. Sanz, M. F. Bijmans, A. J. Stams, *J. Hazard. Mater.* **269**, 98–109 (2014).
36. I. Ňancucheo, D. B. Johnson, *Microb. Biotechnol.* **5**, 34–44 (2012).
37. R. Cantón, P. Ruiz-Garbajosa, *Curr. Opin. Pharmacol.* **11**, 477–485 (2011).
38. C. Pal, J. Bengtsson-Palme, E. Kristiansson, D. G. Larsson, *BMC Genomics* **16**, 964 (2015).
39. D. Versluis *et al*., *Sci. Rep.* **5**, 11981 (2015).
40. D. F. K. dos Santos, P. Istvan, E. F. Noronha, B. F. Quirino, R. H. Krüger, *Biotechnol. Lett.* **37**, 1809–1817 (2015).
41. Tde. J. Bello González, T. Zuidema, G. Bor, H. Smidt, M. W. van Passel, *Front. Microbiol.* **6**, 1550 (2016).
42. S. Oh, M. Tandukar, S. G. Pavlostathis, P. S. Chain, K. T. Konstantinidis, *Environ. Microbiol.* **15**, 2850–2864 (2013).
43. M. J. Meade, R. L. Waddell, T. M. Callahan, *FEMS Microbiol. Lett.* **204**, 45–48 (2001).
44. C. N. Albers, L. Feld, L. Ellegaard-Jensen, J. Aamand, *Water Res.* **83**, 61–70 (2015).
45. B. Horemans *et al*., *Environ. Sci. Technol.* **51**, 1616–1625 (2017).
46. A. Mrozik, Z. Piotrowska-Seget, *Microbiol. Res.* **165**, 363–375 (2010).
47. M. Morales *et al*., *PLOS ONE* **11**, e0165850 (2016).
48. S. K. Moreno-Forero, J. R. van der Meer, *ISME J.* **9**, 150–165 (2015).
49. C. Roggo *et al*., *Environ. Microbiol.* **15**, 2681–2695 (2013).
50. D. H. Parks *et al*., *Nat. Microbiol.* **2**, 1533–1542 (2017).
51. K. Anantharaman *et al*., *Nat. Commun.* **7**, 13219 (2016).
52. D. E. Holmes *et al*., *ISME J.* **9**, 333–346 (2015).

ACKNOWLEDGMENTS

We thank H. Stroo (Stroo Consulting) and C. Aziz (Ramboll) for providing photographs of bioaugmentation with OHRB, and H. Patzelt (Mazoon Environmental and Technological Services) for providing photographs of bioaugmentation with halophilic microorganisms. **Funding:** S.A., I.S.-A., and A.J.M.S. are supported by the Netherlands Ministry of Education, Culture and Science (project 024.002.002) and advanced ERC grant (project 323009). H.S. and S.A. were supported by a grant of BE-Basic-FES funds from the Dutch Ministry of Economic Affairs. H.S., J.R.v.d.M., and H.J.H. were supported by the European Commission (BACSIN, contract 211684; P4SB, contract 633962). **Competing interests:** The authors have no competing interests.

10.1126/science.aar3778

RESEARCH

Thermometry probe to measure hot electrons

Weng et al., *p. 775*

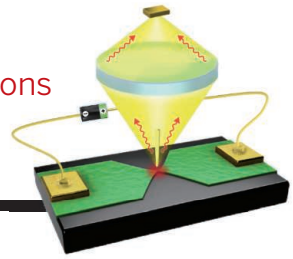

IN *SCIENCE* JOURNALS

Edited by **Caroline Ash**

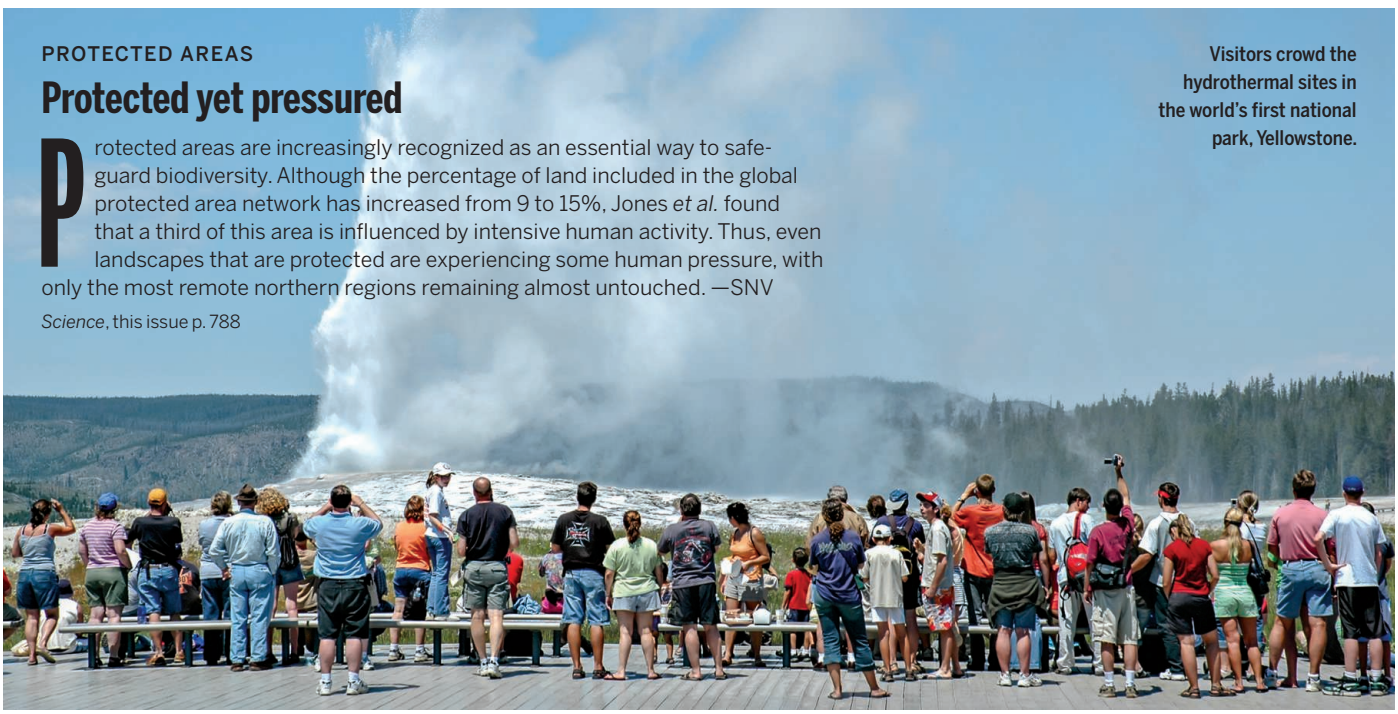

PROTECTED AREAS

Protected yet pressured

Protected areas are increasingly recognized as an essential way to safeguard biodiversity. Although the percentage of land included in the global protected area network has increased from 9 to 15%, Jones *et al.* found that a third of this area is influenced by intensive human activity. Thus, even landscapes that are protected are experiencing some human pressure, with only the most remote northern regions remaining almost untouched. —SNV

Science, this issue p. 788

Visitors crowd the hydrothermal sites in the world's first national park, Yellowstone.

INFECTIOUS DISEASES

Mycobacteria and metabolism

Since the discovery of *Mycobacterium tuberculosis* more than a century ago, great progress has been made in defining mechanisms of host resistance to tuberculosis (TB). In contrast, our understanding of how 90 to 95% of infected individuals live with chronic TB is extremely limited. Tzelepis *et al.* examined the role of mitochondrial matrix protein cyclophilin D (CypD) in T cells by using a mouse model of *M. tuberculosis* infection. CypD-deficient mice were more susceptible to infection, despite enhanced *M. tuberculosis*–specific T cell responses. Specific T cells apparently had no impact on curbing bacterial loads but did substantially increase lung immunopathology. —CNF

Sci. Immunol. **3**, eaar4135 (2018).

THERMOELECTRICS

SnSe doped a different way

Heat can be converted into electricity by thermoelectric materials. Such materials are promising for use in solid-state cooling devices. A challenge for developing efficient thermoelectric materials is to ensure high electrical but low thermal conductivity. Chang *et al.* found that bromine doping of tin selenide (SnSe) does just this by maintaining low thermal conductivity in the out-of-plane direction of this layered material. The result is a promising n-type thermoelectric material with electrons as the charge carriers—an important step for developing thermoelectric devices from SnSe. —BG

Science, this issue p. 778

ELECTROCHEMISTRY

A very basic pathway from CO_2 to ethylene

Ethylene is an important commodity chemical for plastics. It is considered a tractable target for synthesizing renewable resources from carbon dioxide (CO_2). The challenge is that the performance of the copper electrocatalysts used for this conversion under the required basic reaction conditions suffers from the competing reaction of CO_2 with the base to form bicarbonate. Dinh *et al.* designed an electrode that tolerates the base by optimizing CO_2 diffusion to the catalytic sites (see the Perspective by Ager and Lapkin). This catalyst design delivers 70% efficiency for 150 hours. —JSY

Science, this issue p. 783; see also p. 707

CLIMATE CHANGE

One and a half degrees on biodiversity

Insects are the most diverse group of animals on Earth and are ubiquitous in terrestrial food webs. We have little information about their fate in a changing climate; data are scant for insects compared with other groups of organisms. Warren *et al.* performed a global-scale

CREDITS: (FROM TOP) Q. WENG *ET AL.*; SHARON DAY/SHUTTERSTOCK.COM

Published by AAAS

analysis of the effects of climate change on insect distribution (see the Perspective by Midgley). For vertebrates and plants, the number of species losing more than half their geographic range by 2100 is halved when warming is limited to 1.5°C, compared with projected losses at 2°C. But for insects, the number is reduced by two-thirds. —AMS

Science, this issue p. 791; see also p. 714

MICROBIOTA

Benign colonization of the gut

Microbial communities in the gut can be highly individual. What engenders this specificity? The gut characteristically produces gram quantities of immunoglobulin A (IgA) antibody, which is presumed to protect the gut from pathogen attack. Donaldson *et al*. engineered strains of *Bacteroides fragilis*, a common human commensal, to modify its surface capsule, which affects its ability to colonize the germ-free mouse gut. Capsule changes altered the capacity of IgA to bind to the different mutants. It seems that this commensal species exploits IgA sticking power specifically to give it a competitive edge and to promote its establishment in the gut. —CA

Science, this issue p. 795

GENE REGULATION

Profiling transcription—a SLAM dunk

Identification of the direct target genes of transcription factors could shed light on how healthy cells become malignant. Muhar *et al*. applied a modified version of a transcript-mapping method called SLAM-seq to identify the target genes of two transcriptional regulators of major interest in cancer research (see the Perspective by Sabò and Amati). The MYC oncoprotein selectively activates transcription of just a few genes, primarily those involved in basic cell metabolism. In contrast, BRD4, a bromodomain-containing protein that is being targeted for cancer therapy, activates transcription of many genes. —PAK

Science, this issue p. 800; see also p. 713

SOCIAL SCIENCES

Incentives drive disclosure

Some scientists disclose their research results before publication, but many others do not. What factors explain such differences? Thursby *et al.* analyzed survey responses and publication data from 7103 active faculty researchers in the United States, Germany, and Switzerland across nine scientific fields. Perceived norms, competition, and commercial orientation explain 70% of disclosure variation across fields. Results were disclosed before publication by 67.2% of respondents, largely to solicit feedback, but sometimes to attract collaborators. Engineers and computer scientists, for whom commercial interests are important, were the least likely to disclose, whereas social scientists and mathematicians were the most likely. —PJB

Sci. Adv. 10.1126/sciadv.aar2133 (2018).

QUANTUM MATERIALS

Better performance under stress

Engineering stress or strain into materials can improve their performance. Adding mechanical stress to silicon chips, for instance, produces transistors with enhanced electron mobility. Ghadimi *et al*. explore the possibility of enhancing the vibrational properties of a micromechanical oscillator by engineering stress within the structure (see the Perspective by Eichler). By careful design of the micromechanical oscillator, and by building in associated stresses, exceptional vibrational properties can be produced. Such enhanced oscillators could be used as exquisite force sensors. —ISO

Science, this issue p. 764; see also p. 706

IN OTHER JOURNALS

Edited by **Caroline Ash** *and* **Jesse Smith**

Specialist plant cells contain gravity sensors to guide upright growth.

PLANT SCIENCE

Plants work out which way is up

Gravity-sensing cells in plants contain tiny grains of starch called statoliths. The orientation of the statoliths changes with the plant's orientation. The gravity-sensing cells respond to even the slightest tilt off of the established plane. Plant statoliths seem to evade the rules of physics that govern other granular materials. In live-cell imaging of young wheat shoots, Bérut *et al.* observed that statolith piles behave more like slowly creeping liquids than like granular accumulations. The reason is that the individual statoliths are always jiggling around, perhaps because of interactions with the plant cytoskeleton. —PJH

Proc. Natl. Acad. Sci. U.S.A. 10.1073/pnas.1801895115 (2018).

CIRCADIAN REGULATION

Timing metabolism in human muscle

Circadian rhythms are driven by intrinsic biological clocks that regulate and coordinate activity and metabolism. Skeletal muscle is fueled by glucose, but if glucose sensing by the skeletal muscle clock is disrupted, metabolic disease can result. Perrin *et al.* used genome-wide transcription analysis to

PHOTO: MARTIN SHIELDS/SCIENCE SOURCE

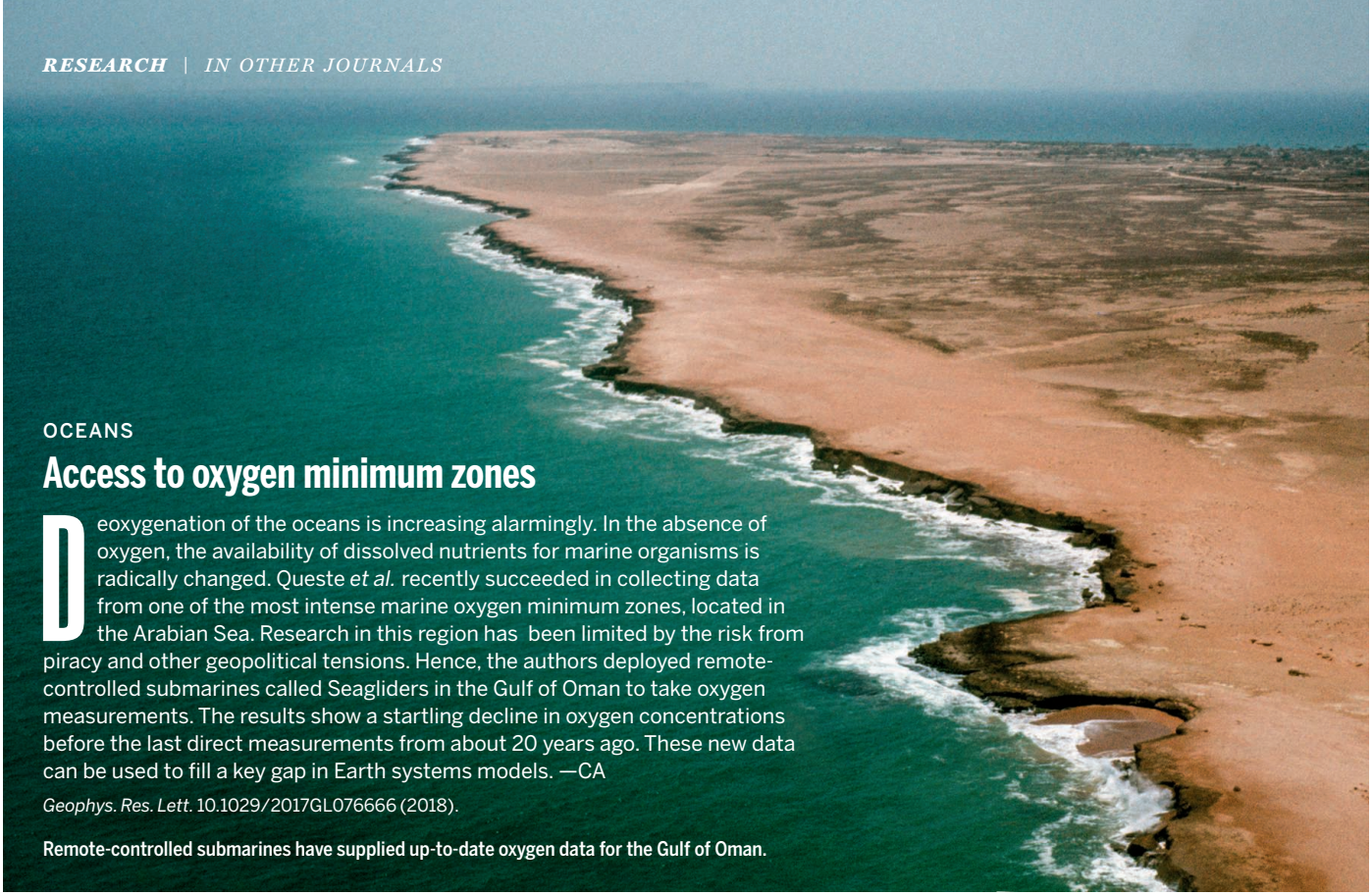

OCEANS

Access to oxygen minimum zones

Deoxygenation of the oceans is increasing alarmingly. In the absence of oxygen, the availability of dissolved nutrients for marine organisms is radically changed. Queste *et al.* recently succeeded in collecting data from one of the most intense marine oxygen minimum zones, located in the Arabian Sea. Research in this region has been limited by the risk from piracy and other geopolitical tensions. Hence, the authors deployed remote-controlled submarines called Seagliders in the Gulf of Oman to take oxygen measurements. The results show a startling decline in oxygen concentrations before the last direct measurements from about 20 years ago. These new data can be used to fill a key gap in Earth systems models. —CA

Geophys. Res. Lett. 10.1029/2017GL076666 (2018).

Remote-controlled submarines have supplied up-to-date oxygen data for the Gulf of Oman.

investigate clock-controlled circadian transcription in skeletal muscle and myotubes in vitro. Human biopsy samples exhibited rhythmic transcription, which occurred in two phases: Immune response genes were transcribed early in the day, whereas muscle contraction genes were expressed in the afternoon. In the absence of a fully functional clock, expression patterns of genes related to insulin response, myokine secretion, and lipid metabolism were strongly affected. —BAP

eLife 10.7554/eLife.34114 (2018).

OPTICAL DEVICES

Tunable on-chip optical beam splitter

Integrated optical approaches potentially offer a robust and compact platform to develop quantum-enhanced sensing and metrology technology. Bishop *et al.* describe an on-chip beam splitter in which the emission mode can be selected by electromechanically tuning the coupling of two suspended gallium arsenide waveguides. Using a quantum dot as a source of single photons pumped into the input arm of the waveguide, they show that the output port for the emitted photons can be selected by applying a small actuation voltage. Being compact, versatile, and scalable, the technique can be applied to tune other optical components, providing a powerful platform for the fabrication of on-chip quantum optical circuits. —ISO

Opt. Lett. **43**, 2142 (2018).

PHYSICS

Watching magnetic atoms thermalize

A multiparticle system displaced from its equilibrium state usually goes back to equilibrium in short order. Some systems, such as one-dimensional (1D) quantum gases, thermalize very slowly, first reaching an intermediate prethermalized state. To study how the prethermalized state evolves toward equilibrium, Tang *et al.* used ultracold dysprosium atoms arranged along hundreds of parallel 1D tubes. The atoms, which have high magnetic moments, interacted with other atoms in the same tube and with those in other tubes. The researchers found that both processes affected the dynamics of the system, which were nearly exponential after an initial prethermalization phase. —JS

Phys. Rev. X **8**, 021030 (2018).

AIR POLLUTION

A pause in progress on air pollution

Air pollution regulations in the United States have led to dramatic improvements in air quality over the past several decades. It therefore is discouraging to learn, as Jiang *et al.* report, that the reduction of nitrogen oxide and carbon monoxide emissions slowed sharply between 2011 and 2015. This is important because controlling these species is necessary for reducing tropospheric ozone pollution. A variety of factors likely caused this slowing of pollution reduction, including growing industrial contributions and a variety of vehicle-related trends. Improved satellite and model inversion technologies would help monitor changes in pollutant emissions and more precisely identify their sources. —HJS

Proc. Natl. Acad. Sci. U.S.A. 10.1073/pnas.1801191115 (2018).

APPETITE

Heating up suppresses appetite

Exercise can transiently suppress appetite, and it also makes you hot. Jeong *et al.* investigated whether loss of appetite is caused by increased body temperature. Hypothalamic neurons that express proopiomelanocortin control food intake. In mice, these neurons express a thermoreceptor called transient receptor potential vanilloid 1 (TRPV1). TRPV1s are activated when exercise increases physiological temperature, suppressing appetite. So, the heat of the moment directly mediates appetite, without invoking canonical nutrient-hormone pathways. —GKA

PLOS Biol. 10.1371/journal.pbio.2004399 (2018).

PHOTO: LLOYD CLUFF/GETTY IMAGES

ALSO IN *SCIENCE* JOURNALS

Edited by **Caroline Ash**

NEPHROLOGY

Touring the kidney, cell by cell

Our kidneys play a critical role in keeping us healthy, a fact of which we are reminded several times each day. This organ's cellular complexity has hindered progress in understanding the mechanisms underlying chronic kidney disease, which affects 10% of the world's population. Using single-cell transcriptional profiling, Park *et al*. produced a comprehensive cell atlas of the healthy mouse kidney (see the Perspective by Humphreys). An unexpected cell type in the collecting duct appears to be a transitional state between two known cell types. The transition from one cell type to the other is regulated by the Notch signaling pathway and is associated with metabolic acidosis. The authors also find that genetically distinct kidney diseases with common clinical features share common cellular origins. —PAK

Science, this issue p. 758; see also p. 709

BIOCHEMISTRY

A selective autophagy receptor identified

Autophagosomes engulf and degrade cellular components in lysosomes. Degradation of ribosomes is called ribophagy and is an important source of nutrients. Using a recently reported method to isolate lysosomes, Wyant *et al*. profiled the dynamics of the lysosomal proteome under different nutrient conditions (see the Perspective by Nofal and Rabinowitz). The protein NUFIP1 is an autophagy receptor for ribosomes during starvation-induced ribophagy. NUFIP1 shuttles out of the nucleus and targets its ribosome cargo directly by binding to an autophagosome protein. Loss of NUFIP1 means failure to provide sufficient nucleotides during starvation and, therefore, loss of cells under low nutrient conditions. —SYM

Science, this issue p. 751; see also p. 710

LIQUID CRYSTALS

Finding order in twos

In nematic liquid crystals, the local orientation of the molecules hovers around an average direction. The orientational control bestows unusual optical properties. In theory, with the right sort of two-dimensional shape, it should be possible to create nematics with biaxial ordering, but this has proven elusive. Mundoor *et al*. dispersed colloidal rods into a nematic solvent (see the Perspective by Poulin). Within a range of temperature and concentration, the rods ordered orthogonally to the solvent molecules, thus giving the mixture the type of properties that one would expect from a biaxial liquid crystal. —MSL

Science, this issue p. 768; see also p. 712

INORGANIC MATERIALS

Plastic in the dark

Inorganic semiconductors, such as silicon and gallium arsenide, are brittle materials. This property means that large single crystals are cleaved into thin sheets. Oshima *et al*. show that zinc sulfide is, in contrast, a plastic material if deformed in total darkness. Plastic deformation is likely inhibited when light is present because photoexcited charge carriers become trapped at these sites and pin them through electrostatic effects. —PDS

Science, this issue p. 772

FATTY LIVER DISEASE

Fat, microRNAs, and liver disease

Obesity and high-fat diets are linked to fatty liver disease. One hallmark of disease is repression of the cell-stress protein IRE1α. In livers from mice fed a high-fat diet and from patients with hepatic steatosis, Wang *et al*. found that IRE1α activity was repressed because of a post-translational modification called *S*-nitrosylation. The decrease in IRE1α activity enabled the biogenesis of microRNAs that decreased the levels of enzymes involved in lipid metabolism, leading to lipid accumulation in the liver. —LKF

Sci. Signal. **11**, eaao4617 (2018).

STROKE

Stroke therapy goes local

The complement system is activated by ischemic stroke to promote tissue repair. However, long-lasting systemic activation causes neurological impairments. Alawieh *et al*. show that specific local complement inhibition reduced cell death and inflammation and promoted functional recovery in a mouse model of stroke. Complement was targeted by linking a complement inhibitor to an antibody recognizing neoepitopes locally and transiently expressed in the ischemic area of the mouse brain. The targeted neoepitope was overexpressed in the ischemic region of brain tissue from stroke patients, indicating that the same approach might be effective in the clinic. —MM

Sci. Transl. Med. **10**, eaao6459 (2018).

NANOTHERMOMETRY

Taking the temperature of hot electrons

As electronic chips become smaller, efficient heat dissipation becomes a greater challenge. Electrons in such devices quickly accelerate over small distances, becoming "hot"—that is, out of equilibrium with the rest of the system. Weng *et al*. designed a thermometry probe that measures the effective temperature of hot electrons with a spatial resolution of about 50 nanometers. The method is based on the optical measurement of current noise and provides a glimpse into where heat is naturally dissipated in a working device. —JS

Science, this issue p. 775

RESEARCH ARTICLE

BIOCHEMISTRY

NUFIP1 is a ribosome receptor for starvation-induced ribophagy

Gregory A. Wyant,[1,2,3,4]* Monther Abu-Remaileh,[1,2,3,4]* Evgeni M. Frenkel,[1,2,3,4] Nouf N. Laqtom,[1,2,3,4] Vimisha Dharamdasani,[1,2,3,4] Caroline A. Lewis,[1] Sze Ham Chan,[1] Ivonne Heinze,[5] Alessandro Ori,[5]† David M. Sabatini[1,2,3,4]†

The lysosome degrades and recycles macromolecules, signals to the master growth regulator mTORC1 [mechanistic target of rapamycin (mTOR) complex 1], and is associated with human disease. We performed quantitative proteomic analyses of rapidly isolated lysosomes and found that nutrient levels and mTOR dynamically modulate the lysosomal proteome. Upon mTORC1 inhibition, NUFIP1 (nuclear fragile X mental retardation–interacting protein 1) redistributes from the nucleus to autophagosomes and lysosomes. Upon these conditions, NUFIP1 interacts with ribosomes and delivers them to autophagosomes by directly binding to microtubule-associated proteins 1A/1B light chain 3B (LC3B). The starvation-induced degradation of ribosomes via autophagy (ribophagy) depends on the capacity of NUFIP1 to bind LC3B and promotes cell survival. We propose that NUFIP1 is a receptor for the selective autophagy of ribosomes.

The capacity of lysosomes to degrade macromolecules is necessary for cells to clear damaged components and to recycle nutrients for maintaining homeostasis upon starvation. In the context of disease, lysosomes are best known for their dysfunction in the rare lysosomal storage diseases, but also play roles in neurodegeneration and cancer as well as the aging process [reviewed in (*1*–*3*)]. Over the past decade, it has become apparent that mTOR complex 1 (mTORC1), the major nutrient-sensitive regulator of growth (mass accumulation), has an intimate relationship with lysosomes [reviewed in (*4*)]. Most components of the nutrient-sensing machinery upstream of mTORC1 localize to the lysosomal surface, and nutrients generated by lysosomes regulate mTORC1 by promoting its translocation there—a key step in its activation. In turn, mTORC1 regulates the flux of macromolecules destined for lysosomal degradation by controlling autophagosome formation as well as lysosomal biogenesis through the TFEB transcription factor (*4*).

Using our recently developed LysoIP method to rapidly isolate highly pure lysosomes (*5*), we profiled the dynamics of the lysosomal proteome under conditions that inhibit mTORC1 signaling. We identify NUFIP1, a protein not previously associated with lysosomes, as necessary for the starvation-induced degradation of ribosomes and show that it fulfills multiple criteria for being an autophagy receptor for ribosomes.

[1]Whitehead Institute for Biomedical Research and Department of Biology, Massachusetts Institute of Technology, Cambridge, MA 02142, USA. [2]Howard Hughes Medical Institute, Department of Biology, Massachusetts Institute of Technology, Cambridge, MA 02139, USA. [3]Koch Institute for Integrative Cancer Research, Massachusetts Institute of Technology, Cambridge, MA 02142, USA. [4]Broad Institute of Harvard and MIT, Cambridge, MA 02142, USA. [5]Leibniz Institute on Aging–Fritz Lipmann Institute, 07745 Jena, Germany.
*These authors contributed equally to this work.
†Corresponding author. Email: sabatini@wi.mit.edu (D.M.S.); alessandro.ori@leibniz-fli.de (A.O.)

mTORC1 and nutrients regulate the lysosomal proteome

To define the mTORC1-regulated lysosomal proteome, we used high-resolution quantitative proteomics to analyze lysosomes isolated from human embryonic kidney (HEK) 293T cells cultured in nutrient-replete media (full media), starved of nutrients (amino acids and glucose), or treated with the mTOR inhibitor Torin1 for 1 hour (Fig. 1A and fig. S1A). Nutrient starvation and Torin1 both inhibited mTORC1 signaling (fig. S1A) but had distinct effects, because Torin1 inhibits mTORC1 more strongly than nutrient deprivation and because there are mTORC1-independent mechanisms for sensing nutrients. Nutrient starvation and Torin1 had no impact on the abundance of most proteins associated with the purified lysosomes, but even a cursory view of the data sets revealed many proteins affected by one or both treatments (Fig. 1B). Gratifyingly, these included proteins with established nutrient- and Torin1-sensitive associations with lysosomes (*6*–*11*), including components of mTORC1 (mTOR, Raptor, and mLST8) and the folliculin complex (FLCN, FNIP1, and FNIP2) (Fig. 1, B and C) as well as the TFEB, MITF, and TFE3 transcription factors (Fig. 1B). Proteins previously connected to lysosomes but not known to have regulated associations with them were also identified. For example, Torin1 decreased and amino acid starvation increased the lysosomal abundance of SPG11 and ZFYVE26 (Fig. 1, B and C, and table S1), which are associated with hereditary spastic paraplegia and interact with each other as well as the Adaptor-5 complex (*12*, *13*), whose components (AP5B1, AP5M1, AP5S1, and AP5Z1) behaved similarly in the data sets (table S1) (*13*).

Although these examples hinted at the utility of the proteomics data for discovery, we needed a way to a priori designate a protein as associated with lysosomes upon mTOR inhibition and/or nutrient deprivation; no set of such proteins had been previously defined. To do so, we generated a control data set of proteins that bind nonspecifically to magnetic beads coated with antibody to hemagglutinin (HA), used in the immune-isolation of the lysosomes. We defined as "lysosomal" any protein that was more abundant in purified lysosomes than on the control beads by a factor of at least 1.5 (at a significance value of $q < 0.1$; Fig. 1, A and D). We arrived at this value using a sliding-window method to identify a relative change that captured a protein set significantly enriched for those annotated as lysosomal in the UniProt database (fig. S1B). This approach yielded a total of 828 unique proteins that associated with lysosomes in any of the three experimental conditions (Fig. 1D), with 343 proteins designated as lysosomal under all conditions (Fig. 1D and table S2).

NUFIP1-ZNHIT3 accumulates on autophagosomes and lysosomes upon mTORC1 inhibition

Of the many proteins whose lysosomal abundance increased upon Torin1 treatment (table S1), nuclear fragile X mental retardation–interacting protein 1 (NUFIP1) piqued our interest because previous work indicated that although NUFIP1 is largely a nuclear protein, it has also been observed in the cytoplasm of some cell types (*14*). NUFIP1 forms a heterodimer with a smaller protein, zinc finger HIT domain–containing protein 3 (ZNHIT3) (*15*, *16*), whose lysosomal abundance also increased upon Torin1 treatment (table S1), albeit to a lesser extent. Similar to the behavior of many constitutively interacting proteins, CRISPR/Cas9-mediated loss of NUFIP1 caused the concomitant loss of ZNHIT3 (fig. S2A).

Previous work implicated NUFIP1-ZNHIT3 in the assembly of the box C/D small nucleolar ribonucleoprotein (snoRNP) (*17*–*19*). Consistent with such a role, NUFIP1 coimmunoprecipitated not only ZNHIT3 but also snoRNP core components such as fibrillarin (FBL), NOP58, SNU13/15.5K, and NOP17/PIH1D1 (fig. S2B). In addition, its loss caused modest reductions in the interaction of FBL with NOP58 and SNU13/15.5K as well as the expression of small nucleolar RNAs (snoRNAs) of the box C/D (U3 and U14), but not H/ACA (U19) or U4, class (fig. S2, C and D). Although these results confirm a role for NUFIP1 in the function of the box C/D snoRNP, none of its core components were in our proteomics data; this suggested that NUFIP1-ZNHIT3 might have a previously unappreciated role involving lysosomes.

Acute inhibition of mTORC1 in HEK-293T cells, by either Torin1 treatment or amino acid starvation, strongly increased the lysosomal abundance of NUFIP1 and ZNHIT3 (Fig. 2A). mTORC1

inhibition did not change the total cellular amount of NUFIP1 or ZNHIT3, so we reasoned that it must affect their subcellular localization. Indeed, upon Torin1 treatment and amino acid starvation, NUFIP1-ZNHIT3, but not SNU13/15.5K, redistributed from the nuclear fraction to the postnuclear supernatant, which contains lysosomes (Fig. 2B). Imaging studies using HEK-293T cells stably expressing FLAG-NUFIP1 confirmed that Torin1 caused NUFIP1 to translocate from the nucleus to LAMP2-positive lysosomes (Fig. 2C). Consistent with this shift in localization, Torin1 reduced the amount of NUFIP1-ZNHIT3 that coimmunoprecipitated with FBL, a C/D snoRNP component, without affecting the FBL-SNU13/15.5K interaction (fig. S2E). Thus, mTOR inhibition promotes the lysosomal accumulation of NUFIP1-ZNHIT3 at the expense of its interaction with the nuclear C/D snoRNP.

Because mTORC1 inhibition strongly induces autophagy, we hypothesized that NUFIP1-ZNHIT3 may travel to lysosomes through an association with incipient autophagosomes. Indeed, NUFIP1 and ZNHIT3 were absent from lysosomes isolated from cells lacking the ATG7 protein (Fig. 2D), which is necessary for the formation of autophagosomes (*20*), and in Torin1-treated cells FLAG-NUFIP1 colocalized with LC3B-positive autophagosomes (Fig. 2E).

NUFIP1-ZNHIT3 interacts with LC3B

Sequence analyses predicted that NUFIP1, but not ZNHIT3, has four potential LC3B-interacting regions (LIRs) (Fig. 2F). LIRs are found in autophagy receptors that physically link their cargo to the autophagosomal membrane through an LC3B/ATG8-binding domain that contains the Trp/Phe-X-X-Leu/Ile/Val sequence motif [reviewed in (*21*)]. Consistent with the presence of LIRs in NUFIP1, endogenous LC3B coimmunoprecipitated endogenous NUFIP1 and ZNHIT3 from detergent lysates of HEK-293T cells cultured in full media and, to a much greater extent, in cells treated with Torin1 or starved of amino acids (Fig. 2G). Even when overexpressed, ZNHIT3 did not coimmunoprecipitate with LC3B in cells lacking NUFIP1 (fig. S3A). In vitro, purified NUFIP1-ZNHIT3 bound to purified LC3B but not to GABARAP, another autophagosome-associated protein, or to the Rap2A control protein (Fig. 2H).

We sought a NUFIP1 mutant that dissociates its function in the nuclear C/D snoRNP from its capacity to bind LC3B. We generated NUFIP1 mutants with point mutations in each of the four potential LIRs and identified one, $Trp^{40} \rightarrow Ala$ (W40A) NUFIP1, that no longer interacted with LC3B (Fig. 2I). When expressed in NUFIP1-null cells, neither W40A NUFIP1 nor ZNHIT3 associated with lysosomes, whether or not mTORC1 was inhibited (fig. S3B). The W40A NUFIP1 mutant was indistinguishable from the wild-type protein in its capacity to coimmunoprecipitate FBL and reverse the modest reductions in U3 and U14 snoRNA expression caused by NUFIP1 loss (fig. S3, C and D). Thus, NUFIP1 interacts with LC3B, and the W40A mutant distinguishes between the role of NUFIP1 in C/D snoRNP function and its capacity to bind LC3B and localize to lysosomes.

NUFIP1-ZNHIT3 associates with ribosomes in a nutrient-dependent manner

Because NUFIP1 binds to LC3B, we hypothesized that it might serve as a selective autophagy

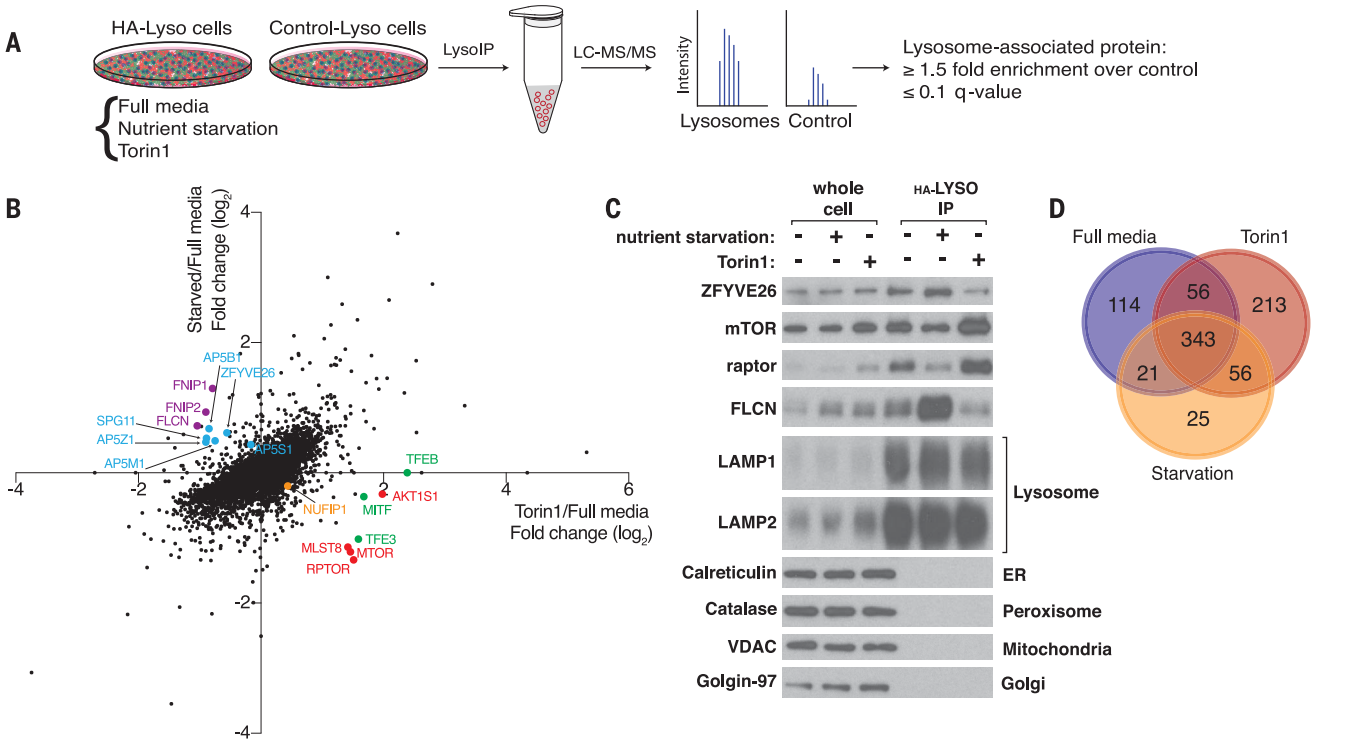

Fig. 1. Regulation of the lysosomal proteome in response to nutrient starvation and mTOR inhibition. (**A**) Schematic depicting the workflow for the LysoIP proteomics method. HA-Lyso and Control-Lyso cells refer to cells stably expressing 3×HA-tagged TMEM192 or 2×FLAG-tagged TMEM192, respectively. (**B**) Nutrient starvation and mTOR inhibition regulate the lysosomal proteome. The scatterplot shows relative (fold) changes in protein abundances in lysosomes captured from the HA-Lyso cells starved for 1 hour of nutrients (amino acids and glucose) or treated for 1 hour with 250 nM Torin1 versus lysosomes from cells cultured in nutrient-replete media (full media). For each condition, three independent isolations were compared. Colors indicate proteins mentioned in the text. The dots denote the 5339 unique proteins detected among all the prefiltered samples. The majority of these are in the immunoprecipitates from both the HA-Lyso and Control-Lyso cells. TFEB was detected only in the Torin1–full media comparison and was arbitrarily assigned a fold change value of 0 in the starved–full media comparison. (**C**) Validation of changes observed in the lysosomal abundances of some of the proteins highlighted in Fig. 1B. The immunoblot shows analyses for the indicated proteins in whole-cell lysates or lysosomes purified from HEK-293T cells subjected to the indicated treatments for 1 hour. ER, endoplasmic reticulum. (**D**) Venn diagram representation of the number of proteins defined as lysosomal in each of the three conditions. A protein was deemed lysosomal if it had a significant ($q \leq 0.1$) enrichment by a factor of at least 1.5 (>0.58, $\log_2$). Proteins not detected at all on the control beads were also classified as lysosomal.

receptor for an unknown cargo in the cytoplasm. Given its role in modifying ribosomal RNA and its reported colocalization with ribosomes in some cell types (*14*), we considered the possibility that NUFIP1-ZNHIT3 can associate with ribosomes. We began by fractionating cell lysates to determine the amount of NUFIP1-ZNHIT3 that comigrates with ribosomes pelleted through a 50% sucrose cushion. In lysates from control cells, NUFIP1-ZNHIT3 did not enter the sucrose cushion, whereas in lysates from cells treated with Torin1 or deprived of amino acids, both proteins shifted markedly to the ribosome-containing pellet (Fig. 3A and fig. S4A). Consistent with this finding, amino acid starvation increased the amount of ribosomes, as monitored via small (40*S*) and large (60*S*) ribosomal subunit proteins, that coimmunoprecipitated with NUFIP1 (Fig. 3B). To probe which ribosomal subunit NUFIP1-ZNHIT3 might associate with, we took advantage of the capacity of EDTA to dissociate ribosomes into their 40*S*

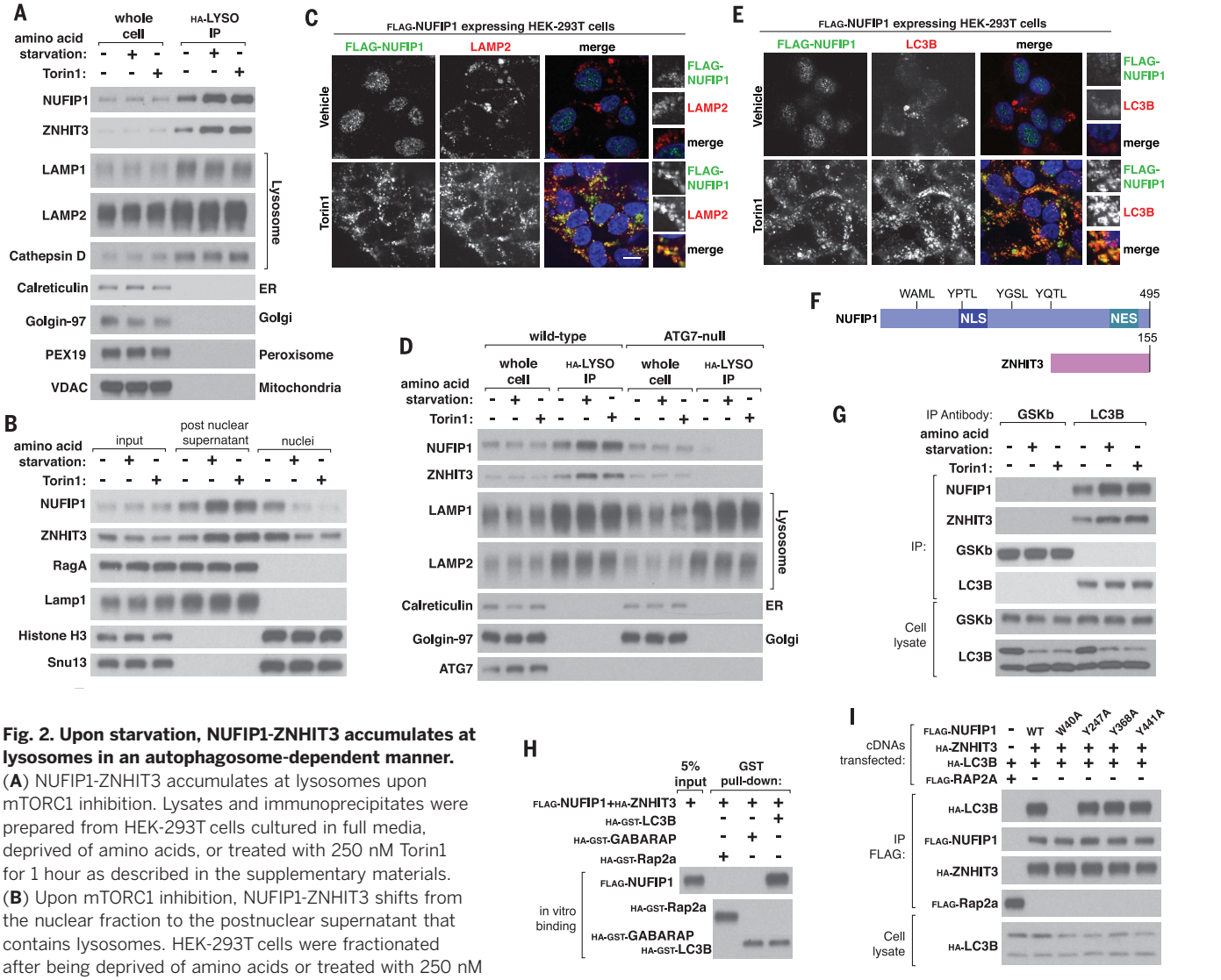

Fig. 2. Upon starvation, NUFIP1-ZNHIT3 accumulates at lysosomes in an autophagosome-dependent manner. (**A**) NUFIP1-ZNHIT3 accumulates at lysosomes upon mTORC1 inhibition. Lysates and immunoprecipitates were prepared from HEK-293T cells cultured in full media, deprived of amino acids, or treated with 250 nM Torin1 for 1 hour as described in the supplementary materials. (**B**) Upon mTORC1 inhibition, NUFIP1-ZNHIT3 shifts from the nuclear fraction to the postnuclear supernatant that contains lysosomes. HEK-293T cells were fractionated after being deprived of amino acids or treated with 250 nM Torin1 for 1 hour, and amounts of endogenous NUFIP1 and ZNHIT3 were analyzed by immunoblotting. RagA and LAMP1 are lysosome-associated proteins; histone H3 and SNU13 are nuclear. (**C**) mTOR inhibition shifts NUFIP1 from the nucleus to LAMP1-positive lysosomes. HEK-293T cells stably expressing FLAG-NUFIP1 were treated with 250 nM Torin1 for 1 hour and analyzed as described in the supplementary materials. Scale bar, 10 μm. (**D**) Loss of ATG7 greatly decreases the amount of NUFIP1-ZNHIT3 on lysosomes. Wild-type and ATG7-null HEK-293T cells stably expressing the HA-Lyso tag were deprived of amino acids or treated with 250 nM Torin1 for 1 hour, and the amounts of NUFIP1 and ZNHIT3 on lysosomes and in total cell lysates were analyzed as in (A). (**E**) mTOR inhibition shifts NUFIP1 from the nucleus to LC3B-positive puncta. HEK-293T cells stably expressing FLAG-NUFIP1 were treated with 250 nM Torin1 for 1 hour and processed as in (C). (**F**) Schematic depicting the localization of the four putative LC3B-binding regions (LIRs) in NUFIP1. (**G**) mTORC1 inhibition increases the interaction between endogenous LC3B and NUFIP1-ZNHIT3. Anti-LC3B immunoprecipitates were prepared from HEK-293T cells deprived of amino acids or treated with 250 nM Torin1 for 1 hour, and lysates and immunoprecipitates were analyzed for the indicated proteins. Immunoprecipitates prepared with an antibody to GSKb were used as negative controls. (**H**) NUFIP1-ZNHIT3 interacts with LC3B in vitro. Purified HA-GST-LC3B immobilized on a glutathione affinity resin was incubated with the purified FLAG-NUFIP1–HA-ZNHIT3 complex. HA-GST-Rap2a and HA-GST-GABARAP were used as negative controls. Proteins captured in the glutathione resin pull-down were analyzed by immunoblotting for the indicated proteins, using antibodies to epitope tags. GST, glutathione *S*-transferase. (**I**) Identification of a NUFIP1 mutant that does not bind LC3B. Wild-type (WT) FLAG-NUFIP1 or a series of point mutants in its putative LIR motifs were coexpressed with HA-ZNHIT3 and HA-LC3B. HA-Rap2A was used as a negative control. FLAG immunoprecipitates and lysates were prepared and analyzed by immunoblotting.

and 60*S* subunits. When lysates of amino acid–starved cells were fractionated through a 10 to 45% sucrose gradient, endogenous NUFIP1 and ZNHIT3 comigrated with monosomes (80*S*) and polysomes. The addition of EDTA to the same lysates increased the amount of NUFIP1-ZNHIT3 that migrated with the large ribosomal subunits (fig. S4B). Collectively, these results suggest that upon mTORC1 inhibition, NUFIP1 binds to LC3B and associates with the ribosome, likely through its large subunit.

Given that mTORC1 inhibition increases the interaction of NUFIP1-ZNHIT3 with ribosomes, we considered the possibility that an mTORC1-dependent modification of either NUFIP1-ZNHIT3 or ribosomes regulates the interaction. To test this idea, we purified ribosomes or NUFIP1-ZNHIT3 from cells cultured in full media or treated with Torin1 and examined their capacity to interact with each other in vitro. Interestingly, only ribosomes from Torin1-treated cells bound strongly to NUFIP1-ZNHIT3, whereas the source of NUFIP1-ZNHIT3 did not affect the strength of the interaction (Fig. 3, C and D). These results suggest that mTOR inhibition leads to a stable alteration of ribosomes that promotes their interaction with NUFIP1-ZNHIT3. In contrast, the in vitro interaction of NUFIP1-ZNHIT3 with LC3B was unaffected by the source of either (i.e., control or Torin1-treated cells) (fig. S4C). Taken together, these data suggest that the loss of nuclear NUFIP1 and the increase in the LC3B-NUFIP1 interaction caused by mTORC1 inhibition results from the binding and trapping of NUFIP1 by modified ribosomes in the cytoplasm. We cannot exclude the possibility that an mTORC1-dependent modification of NUFIP1 also regulates its nuclear entry or exit, but we have failed to identify mTORC1-regulated phosphorylation sites on NUFIP1.

NUFIP1 is required for ribosomal degradation induced by nutrient starvation

The proteasome is known to degrade ribosomal proteins that do not incorporate into ribosomal subunits, which we verified (fig. S5, A to C); however, the process by which intact ribosomes are degraded is less well understood, particularly in mammalian cells (*22*–*26*). Upon amino acid deprivation or Torin1 treatment, ribosomal proteins decreased in a time-dependent manner in a fashion that depended on ATG7 and a low lysosomal pH (Fig. 4A and fig. S6, A and B), in accord with previous work in yeast showing that intact ribosomes are degraded via autophagy (*27*). In GATOR1 mutant (DEPDC5 KO) cells that have

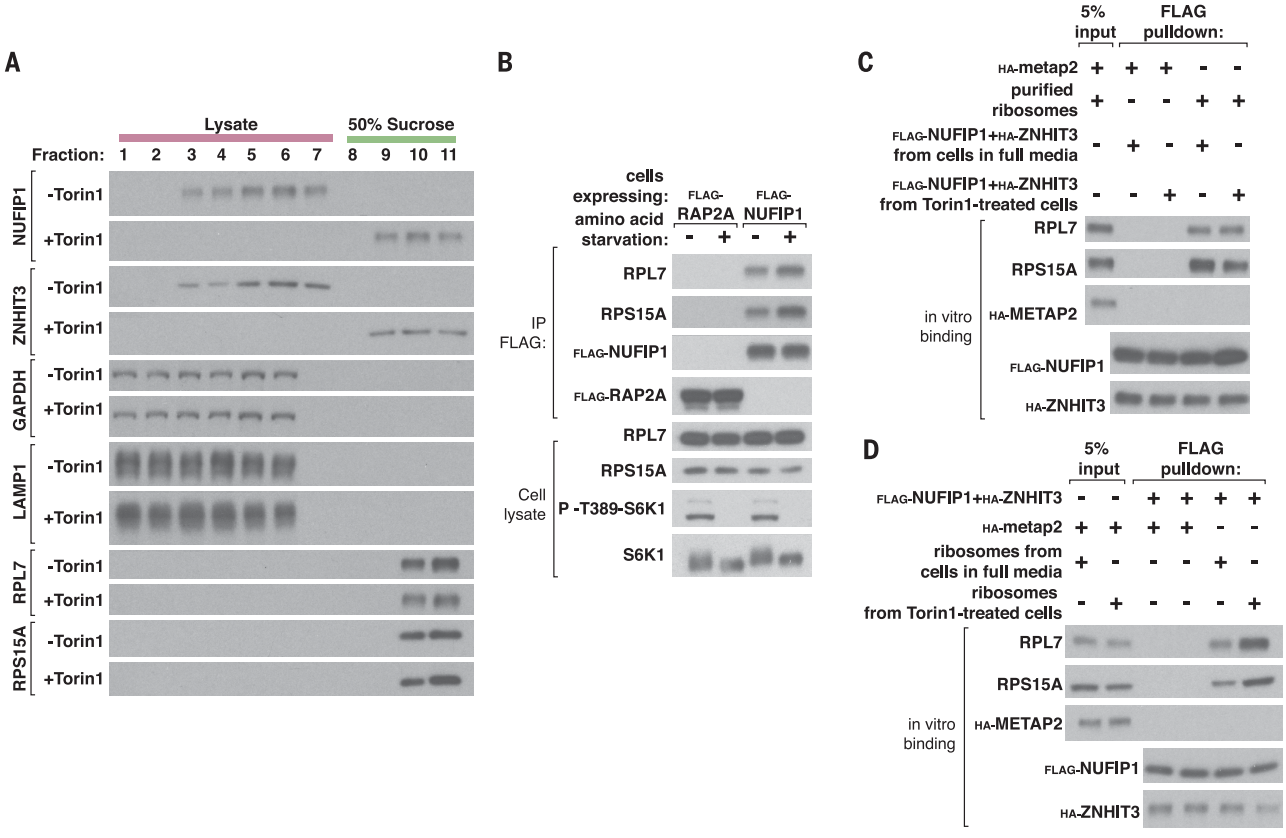

Fig. 3. NUFIP1-ZNHIT3 interacts with ribosomes in an mTORC1-dependent fashion. (**A**) mTOR inhibition increases the amount of NUFIP1-ZNHIT3 that comigrates with ribosomes. HEK-293T cell lysates prepared from cells in full media or treated with 250 nM Torin1 were fractionated over a 50% sucrose cushion. Fractions were collected and the indicated proteins were analyzed by immunoblotting. (**B**) Amino acid deprivation increases the amount of ribosomes that coimmunoprecipitate with NUFIP1. HEK-293T cells stably expressing FLAG-NUFIP1 were deprived of amino acid for 1 hour. Lysates and FLAG immunoprecipitates were prepared and analyzed for the indicated proteins by immunoblotting. FLAG-Rap2A was used as a negative control. (**C**) In vitro, purified NUFIP1-ZNHIT3 binds to ribosomes, and the interaction is not affected by whether NUFIP1-ZNHIT3 was obtained from cells with inhibited mTOR. The FLAG-NUFIP1–HA-ZNHIT3 complex was purified from HEK-293T cells in full media or treated with 250 nM Torin1 for 1 hour and immobilized on a FLAG affinity resin. Equal amounts of ribosomes obtained from cells in full media were added to the immobilized FLAG-NUFIP1–HA-ZNHIT3 complex, and the captured proteins were analyzed by immunoblotting. Ribosomes were purified as described in the supplementary materials. Purified HA-METAP was used as a negative control. (**D**) In vitro, ribosomes purified from cells with mTOR inhibition bind better to NUFIP1-ZNHIT3 than those from cells in full media. Ribosomes were purified from HEK-293T cells in full media conditions or treated with 250 nM Torin1 for 1 hour. The FLAG-NUFIP1–HA-ZNHIT3 complex was immobilized on FLAG affinity beads and equal amounts of ribosomes were added. Proteins captured by the FLAG affinity beads were analyzed by immunoblotting. HA-METAP2 was purified from cells in full media or treated with 250 nM Torin1 for 1 hour and served as a negative control.

nutrient-insensitive mTORC1 signaling, amino acid starvation did not reduce the abundance of ribosomal proteins, whereas Torin1 still did (fig. S6C). Thus, mTORC1 likely mediates the loss of ribosomal proteins caused by mTOR inhibition.

Given that NUFIP1 binds LC3B and also makes an mTORC1-regulated association with ribosomes, we hypothesized that NUFIP1 is required for the degradation of ribosomes via autophagy, a process that has been termed ribophagy in yeast (*27*). Indeed, in multiple cell types, loss of NUFIP1 prevented the depletion of ribosomal proteins caused by nutrient deprivation or Torin1 treatment (Fig. 4B and fig. S6, D to G).

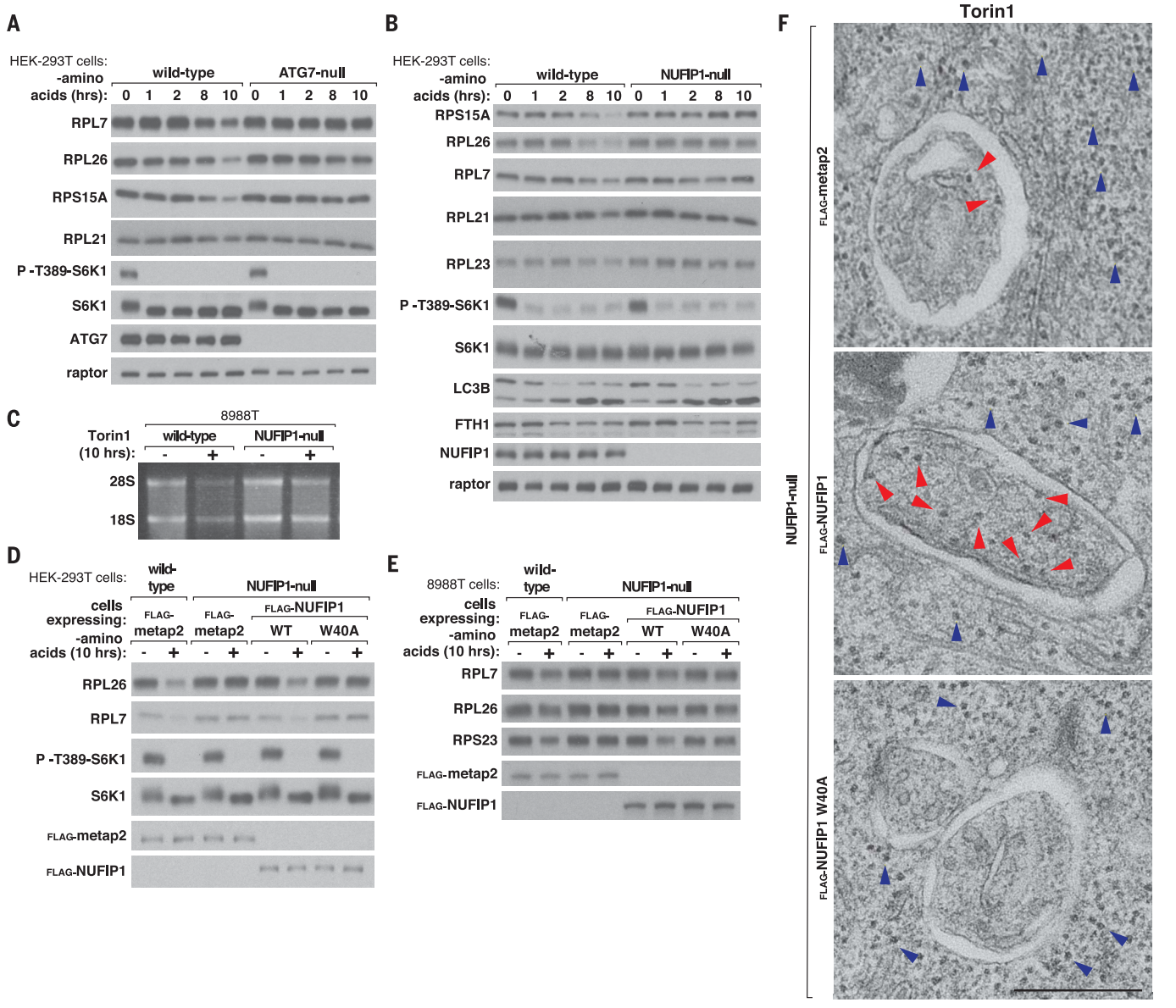

Fig. 4. NUFIP1 is required for ribophagy. (**A**) ATG7 loss suppresses the degradation of ribosomes caused by amino acid starvation. Wild-type or ATG7-null HEK-293T cells were deprived of amino acids for the indicated time points. Cell lysates were analyzed by immunoblotting for the total levels and phosphorylation states of the indicated proteins. (**B**) Loss of NUFIP1 inhibits the degradation of ribosomes caused by amino acid starvation. Wild-type or NUFIP1-null HEK-293T cells were deprived of amino acids for the indicated time points. Cell lysates were analyzed by immunoblotting for the total levels and phosphorylation states of the indicated proteins. (**C**) Loss of NUFIP1 inhibits the loss of 28*S* and 18*S* rRNA caused by mTOR inhibition. Wild-type and NUFIP1-null 8988T cells were treated with 250 nM Torin1 for 10 hours and total RNA was extracted and analyzed on a formaldehyde agarose gel. RNA from equal numbers of cells was loaded in each lane. (**D**) For amino acid starvation to cause ribosomal degradation, NUFIP1 must be able to interact with LC3B. Wild-type or NUFIP1-null HEK-293T cells stably expressing the indicated proteins were deprived of amino acids for 10 hours and analyzed for the total levels and phosphorylation states of the indicated proteins. (**E**) For amino acid starvation to cause ribosomal degradation, NUFIP1 must interact with LC3B. Wild-type or NUFIP1-null 8988T cells stably expressing the indicated proteins were treated as in (B). (**F**) Autophagosomes from HEK-293T cells lacking NUFIP1 or expressing the LC3B-binding W40A mutant contain fewer ribosomes than those from control cells. NUFIP1-null HEK-293T cells expressing the control protein metap2, NUFIP1, or NUFIP1 W40A were treated with Torin1 and concanamycin A for 4 hours and analyzed by electron microscopy. Autophagosomes were identified by the presence of a double membrane. Red arrowheads indicate ribosomes inside an autophagosome. Blue arrowheads indicate ribosomes present in the cytoplasm. Scale bar, 500 nm.

Loss of NUFIP1 had no impact on the induction of autophagy, as assessed by LC3B lipidation, nor on the degradation of ferritin, another selective autophagy substrate, whether it was induced by nutrient starvation or by iron chelation (Fig. 4B and fig. S6H). NUFIP1 loss also blocked the Torin1-induced depletion of ribosomal RNA (rRNA) (Fig. 4C). Reexpression at levels near that of the endogenous protein of wild-type NUFIP1, but not of the W40A mutant deficient in LC3B binding, restored the capacity of NUFIP1-null HEK-293T and 8988T cells to degrade ribosomes upon nutrient depletion (Fig. 4, D and E, and fig. S6I). As assessed by electron microscopy, autophagosomes in HEK-293T cells lacking NUFIP1

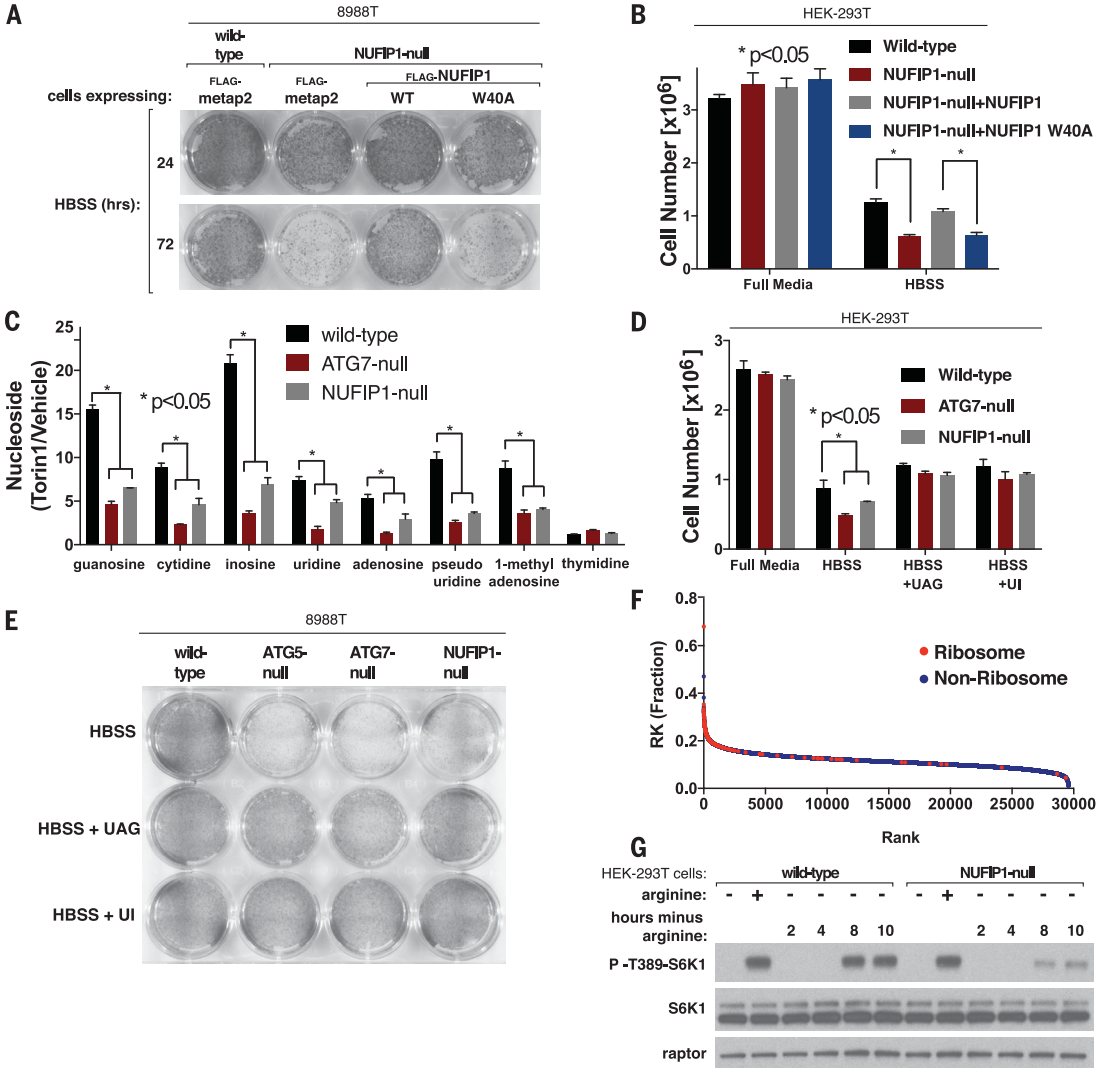

Fig. 5. NUFIP1 is important for cells to survive starvation. (**A**) Loss of NUFIP1 or just its capacity to interact with LC3B impairs cell survival upon nutrient starvation. Wild-type or NUFIP1-null 8988T cells stably expressing the indicated proteins were deprived of nutrients by culturing them in Hanks' balanced salt solution (HBSS); after the indicated times, the surviving cells were stained and imaged. (**B**) NUFIP1 loss or just its capacity to interact with LC3B impairs cell survival upon nutrient starvation. Wild-type or NUFIP1-null HEK-293T cells stably expressing the indicated proteins were deprived of nutrients by HBSS, and after 48 hours the number of surviving cells was quantified by cell counting. Values are normalized relative to cell numbers at the start of the starvation period and are mean ± SD (*P < 0.05; n = 3). (**C**) Loss of NUFIP1 or ATG7 inhibits the increase in nucleosides caused by mTOR inhibition. Data represent relative change in whole-cell concentrations of nucleosides in wild-type, ATG7-null, and NUFIP1-null HEK-293T cells treated with 250 nM Torin1 for 1 hour. Values are mean ± SEM (*P < 0.05; n = 3). (**D**) Nucleoside supplementation rescues the survival defects of ATG7-null and NUFIP1-null HEK-293T cells. Indicated cells were deprived of nutrients by culturing in HBSS with or without the indicated nucleosides (2 mM each). After 48 hours, the number of surviving cells was quantified. Values were normalized relative to cell numbers at the start of the starvation period and are mean ± SD (*P < 0.05; n = 3). (**E**) Nucleoside supplementation rescues the survival defect of ATG5-null, ATG7-null, and NUFIP1-null 8988T cells. Wild-type, ATG5-null, ATG7-null, or NUFIP1-null cells were deprived of nutrients by culturing in HBSS with or without the indicated nucleosides (2 mM each). After 48 hours, the surviving cells were stained and imaged. (**F**) Ribosomes are highly enriched for arginine and lysine. Protein sequences in the UniProt database (including isoforms) were ranked according to their fraction content of arginine and lysine (RK). Ribosomal proteins are shown in red; all other proteins are shown in blue. Mitochondrial ribosomal proteins were not designated as ribosomal in this analysis. (**G**) Loss of NUFIP1 suppresses the reactivation of mTORC1 that occurs after long-term arginine deprivation. Wild-type or NUFIP1 HEK-293T cells were deprived of arginine for 50 min (first two lanes of each set) or the indicated times and, where indicated, restimulated with arginine for 10 min. Cell lysates were analyzed by immunoblotting for the levels and phosphorylation states of the indicated proteins.

or just its LC3B-binding capacity contained far fewer ribosomes than those from control cells (Fig. 4F and fig. S6, J and K). Loss of NUFIP1 did not affect the morphology of the endoplasmic reticulum, mitochondria, or Golgi (fig. S6L).

To test the role of the subcellular localization of NUFIP1 in the induction of ribosome degradation, we generated NUFIP1 mutants lacking either a nuclear localization (NLS) or export (NES) signal and expressed them in NUFIP1-null cells. The NLS mutant localized to the cytoplasm even in cells in full media, but this did not cause ribosome loss. The NLS mutant colocalized to a greater extent with LAMP2 upon Torin1 treatment and restored the capacity of the null cells to degrade ribosomes upon amino acid starvation (fig. S7, A and B). The NES mutant was constitutively nuclear and did not support ribosome degradation even upon nutrient starvation (fig. S7, B and C). Loss of ATG7 or LC3B did not affect the nuclear exit of wild-type NUFIP1 (fig. S7, D and E). Thus, in cells in full media, the presence of NUFIP1 in the cytoplasm is not sufficient to induce ribosome degradation, presumably because mTORC1 inhibition is still needed to promote the interaction of NUFIP1 with ribosomes.

NUFIP1 is important for cells to survive starvation

Because NUFIP1 is required for starvation-induced ribophagy and ribosomes constitute a major fraction of the total cell mass (*28*–*30*), we asked whether NUFIP1 is important for the cellular response to nutrient deprivation. Indeed, loss of NUFIP1 or just its LC3B-binding ability reduced the capacity of multiple cell types to survive nutrient starvation, as measured in clonogenic survival assays or via direct cell counting (Fig. 5, A and B, and fig. S8, A to C). These results suggest that the NUFIP1-mediated degradation of ribosomes supplies metabolites needed for survival during starvation. Consistent with this possibility, loss of either ATG7 or NUFIP1 suppressed the large increase in nucleoside levels [including inosine, which is generated by the deamination of adenosine in lysosomes (*31*)] caused by mTOR inhibition that we recently described (*5*), which suggests that most of this increase results from the lysosomal degradation of rRNA (*32*) (Fig. 5C). The addition of nucleosides to the starvation media rescued the survival defect of the NUFIP1-null cells, and, as previously shown (*33*), of cells lacking the canonical autophagy pathway (Fig. 5, D and E, and fig. S8D).

Starvation of single amino acids acutely inhibits mTORC1 signaling, but over time it reactivates because of the release of endogenous amino acids by the autophagic degradation of proteins. Analysis of the human proteome annotated in the UniProt database (which includes isoforms) revealed that ribosomal proteins are among the most highly enriched for arginine and lysine (Fig. 5F). Because mTORC1 senses lysosomal arginine (and likely lysine) through SLC38A9 (*34*), ribophagy might be important for generating the amino acids necessary for mTORC1 reactivation. Indeed, loss of NUFIP1 severely diminished the reactivation of mTORC1 normally observed after long-term arginine deprivation (Fig. 5G). Thus, NUFIP1-mediated ribophagy contributes to the cellular response to nutrient starvation.

Conclusions

Several properties of NUFIP1 suggest that it functions as an autophagy receptor for ribosomes during starvation-induced ribophagy: (i) It is required for nutrient deprivation to degrade ribosomes, (ii) it binds LC3B and ribosomes, and (iii) a NUFIP1 mutant that does not bind LC3B cannot support ribosomal degradation upon autophagy induction. We propose that NUFIP1 cycles in and out of the nucleus (*14*) (Fig. 2C and fig. S7, A and C), and, upon nutrient starvation, accumulates in the cytoplasm because it binds to ribosomes that acquire an mTORC1-regulated alteration. In the cytoplasm, NUFIP1 transports its ribosome cargo to autophagic vesicles by directly binding LC3B in a fashion that is likely not directly regulated by nutrients and mTORC1. Our NUFIP1 findings suggest that our data set of lysosomal proteins can serve as a resource for future discoveries.

Many questions remain. Our in vitro data indicate that the ribosome is likely altered upon mTORC1 inhibition in a fashion that strengthens its interaction with NUFIP1-ZNHIT3, but the nature of this alteration—whether a post-translational modification, such as the addition of ubiquitin, or the binding of a protein to the ribosome—is unknown. Because NUFIP1-ZNHIT3 most likely interacts with the 60*S* ribosomal subunit and the atomic structure of the human ribosome is available (*35*), it should be possible to determine where NUFIP1-ZNHIT3 interacts. Note that NUFIP1-ZNHIT3 may not bind directly to an established ribosomal protein or the rRNA; other currently unknown proteins may be involved in mediating the interaction.

Our identification of NUFIP1 as an autophagy receptor for ribosomes in mammalian cells adds to the growing list of selective autophagy receptors, including for ferritin, mitochondria, peroxisomes, endoplasmic reticulum, and bacteria (*36*–*43*). We find that ribophagy is an important source of nutrients (particularly nucleosides) upon starvation, and that loss of NUFIP1 decreases the survival of cells under low-nutrient conditions. As RNA-binding proteins, most ribosomal proteins have a high content of basic amino acids, and we find that NUFIP1 is required for the reactivation of mTORC1 that occurs after prolonged arginine starvation. This result suggests that a key role for SLC38A9, which senses lysosomal basic amino acids upstream of mTORC1 (*34*), is to signal the successful degradation of ribosomes in lysosomes to mTORC1.

In the human and mouse cells we have examined, loss of NUFIP1 prevents starvation-induced ribosome degradation, but it is possible that other ribosome receptors or mechanisms for ribosome degradation also exist. For example, recent work suggests that ribosomes can be degraded via bulk autophagy at longer starvation times (24 hours) than those we have examined (*44*). In yeast, it has been proposed that the ubiquitin protease Ubp3p/Bre5p is required for the selective degradation of ribosomes, but it is unclear whether its homologs play such a role in animals (*27*). In growing cells, it is estimated that ribosomes account for ~50% and ~80% of total cellular protein and RNA (*28*–*30*), respectively. Our work identifies a key link between starvation and one of the most abundant nutrient sources in cells.

REFERENCES AND NOTES

1. A. Ballabio, V. Gieselmann, *Biochim. Biophys. Acta* **1793**, 684–696 (2009).
2. F. M. Platt, B. Boland, A. C. van der Spoel, *J. Cell Biol.* **199**, 723–734 (2012).
3. L. Groth-Pedersen, M. Jäättelä, *Cancer Lett.* **332**, 265–274 (2013).
4. R. A. Saxton, D. M. Sabatini, *Cell* **168**, 960–976 (2017).
5. M. Abu-Remaileh *et al.*, *Science* **358**, 807–813 (2017).
6. Y. Sancak *et al.*, *Science* **320**, 1496–1501 (2008).
7. C. Settembre *et al.*, *EMBO J.* **31**, 1095–1108 (2012).
8. A. Roczniak-Ferguson *et al.*, *Sci. Signal.* **5**, ra42 (2012).
9. C. S. Petit, A. Roczniak-Ferguson, S. M. Ferguson, *J. Cell Biol.* **202**, 1107–1122 (2013).
10. J. A. Martina *et al.*, *Sci. Signal.* **7**, ra9 (2014).
11. Z. Y. Tsun *et al.*, *Mol. Cell* **52**, 495–505 (2013).
12. R. P. Murmu *et al.*, *Mol. Cell. Neurosci.* **47**, 191–202 (2011).
13. J. Hirst *et al.*, *Mol. Biol. Cell* **24**, 2558–2569 (2013).
14. B. Bardoni *et al.*, *Exp. Cell Res.* **289**, 95–107 (2003).
15. M. Quinternet *et al.*, *Structure* **24**, 1693–1706 (2016).
16. B. Rothé *et al.*, *Nucleic Acids Res.* **42**, 10731–10747 (2014).
17. S. Boulon *et al.*, *J. Cell Biol.* **180**, 579–595 (2008).
18. K. S. McKeegan, C. M. Debieux, S. Boulon, E. Bertrand, N. J. Watkins, *Mol. Cell. Biol.* **27**, 6782–6793 (2007).
19. M. Quinternet *et al.*, *J. Mol. Biol.* **427**, 2816–2839 (2015).
20. M. Komatsu *et al.*, *J. Cell Biol.* **169**, 425–434 (2005).
21. A. B. Birgisdottir, T. Lamark, T. Johansen, *J. Cell Sci.* **126**, 3237–3247 (2013).
22. M. K. Sung *et al.*, *eLife* **5**, e19105 (2016).
23. M. K. Sung, J. M. Reitsma, M. J. Sweredoski, S. Hess, R. J. Deshaies, *Mol. Biol. Cell* **27**, 2642–2652 (2016).
24. J. R. Warner, *J. Mol. Biol.* **115**, 315–333 (1977).
25. A. D. Mathis *et al.*, *Mol. Cell. Proteomics* **16**, 243–254 (2017).
26. A. R. Kristensen *et al.*, *Mol. Cell. Proteomics* **7**, 2419–2428 (2008).
27. C. Kraft, A. Deplazes, M. Sohrmann, M. Peter, *Nat. Cell Biol.* **10**, 602–610 (2008).
28. J. R. Warner, *Trends Biochem. Sci.* **24**, 437–440 (1999).
29. D. E. Weinberg *et al.*, *Cell Rep.* **14**, 1787–1799 (2016).
30. J. E. Darnell Jr., *Bacteriol. Rev.* **32**, 262–290 (1968).
31. E. R. Lindley, R. L. Pisoni, *Biochem. J.* **290**, 457–462 (1993).
32. H. Huang *et al.*, *EMBO J.* **34**, 154–168 (2015).
33. J. Y. Guo *et al.*, *Genes Dev.* **30**, 1704–1717 (2016).
34. G. A. Wyant *et al.*, *Cell* **171**, 642–654.e12 (2017).
35. S. Klinge, F. Voigts-Hoffmann, M. Leibundgut, N. Ban, *Trends Biochem. Sci.* **37**, 189–198 (2012).
36. A. Khaminets *et al.*, *Nature* **522**, 354–358 (2015).
37. J. D. Mancias, X. Wang, S. P. Gygi, J. W. Harper, A. C. Kimmelman, *Nature* **509**, 105–109 (2014).
38. Y. Wei, W. C. Chiang, R. Sumpter Jr., P. Mishra, B. Levine, *Cell* **168**, 224–238.e10 (2017).
39. Y. C. Wong, E. L. Holzbaur, *Proc. Natl. Acad. Sci. U.S.A.* **111**, E4439–E4448 (2014).
40. E. Deosaran *et al.*, *J. Cell Sci.* **126**, 939–952 (2013).
41. D. A. Tumbarello *et al.*, *PLOS Pathog.* **11**, e1005174 (2015).
42. P. Verlhac *et al.*, *Cell Host Microbe* **17**, 515–525 (2015).
43. T. L. Thurston, G. Ryzhakov, S. Bloor, N. von Muhlinen, F. Randow, *Nat. Immunol.* **10**, 1215–1221 (2009).
44. H. An, J. W. Harper, *Nat. Cell Biol.* **20**, 135–143 (2018).

ACKNOWLEDGMENTS

We thank all members of the Sabatini laboratory for helpful insights, particularly R. L. Wolfson, and the FLI proteomics core facility, in particular J. Kirkpatrick. **Funding:** Supported by NIH grants R01 CA103866, R01 CA129105, and R37 AI47389, U.S. Department of Defense grant W81XWH-15-1-0230, and the Lustgarten Foundation (D.M.S.); U.S. Department of Defense grant W81XWH-15-1-0337 (E.M.F.); an EMBO Long-Term Fellowship

(M.A.-R.); a Saudi Aramco Ibn Khaldun Fellowship for Saudi Women (N.N.L.); an MIT School of Science Fellowship in Cancer Research (G.A.W.); and the FLI proteomics core facility (A.O. and I.H.). The FLI is a member of the Leibniz Association and is financially supported by the Federal Government of Germany and the State of Thuringia. D.M.S. is an investigator of the Howard Hughes Medical Institute. **Author contributions:** G.A.W., M.A.-R., and D.M.S. initiated the project and designed the research plan; G.A.W. and M.A.-R. performed the experiments and analyzed the data with help from E.M.F., N.N.L., and V.D.; A.O. designed the proteomic runs and analyzed the lysosomal proteomic data; C.A.L. and S.H.C. performed LC/MS runs and quantified metabolites; G.A.W. and M.A.-R. wrote the manuscript; and D.M.S. edited it. All the authors approved and edited the manuscript. **Competing interests:** D.M.S. is a founding member of the scientific advisory board, a paid consultant, and a shareholder of Navitor Pharmaceuticals, which is targeting for therapeutic benefit the amino acid sensing pathway upstream of mTORC1. **Data and materials availability:** The mass spectrometry proteomics data have been deposited to the ProteomeXchange Consortium (http://proteomecentral.proteomexchange.org) (*50*) via the PRIDE partner repository (*51*) with the data set identifier PXD009084.

SUPPLEMENTARY MATERIALS

www.sciencemag.org/content/360/6390/751/suppl/DC1
Materials and Methods
Figs. S1 to S8
Tables S1 and S2
References (*45*–*51*)

19 October 2017; accepted 19 March 2018
Published online 26 April 2018
10.1126/science.aar2663

NEPHROLOGY

Single-cell transcriptomics of the mouse kidney reveals potential cellular targets of kidney disease

Jihwan Park,[1]* Rojesh Shrestha,[1]* Chengxiang Qiu,[1] Ayano Kondo,[1] Shizheng Huang,[1] Max Werth,[2] Mingyao Li,[3] Jonathan Barasch,[2] Katalin Suszták[1]†

Our understanding of kidney disease pathogenesis is limited by an incomplete molecular characterization of the cell types responsible for the organ's multiple homeostatic functions. To help fill this knowledge gap, we characterized 57,979 cells from healthy mouse kidneys by using unbiased single-cell RNA sequencing. On the basis of gene expression patterns, we infer that inherited kidney diseases that arise from distinct genetic mutations but share the same phenotypic manifestation originate from the same differentiated cell type. We also found that the collecting duct in kidneys of adult mice generates a spectrum of cell types through a newly identified transitional cell. Computational cell trajectory analysis and in vivo lineage tracing revealed that intercalated cells and principal cells undergo transitions mediated by the Notch signaling pathway. In mouse and human kidney disease, these transitions were shifted toward a principal cell fate and were associated with metabolic acidosis.

The kidney is a highly complex organ that performs many diverse functions that are essential for health. It removes nitrogen, water, and other waste products from the blood. It controls blood electrolytes and acid-base balance, and it secretes hormones that regulate blood composition and blood pressure. The kidney consists of several functionally and anatomically discrete segments. The glomerulus is a specialized group of capillaries that filters the blood and produces the primary filtrate of water and solutes such as sodium, potassium glucose, and bicarbonate. The proximal tubules then reabsorb the majority of the water and electrolytes, whereas solutes such as uric acid, organic anions, potassium, and protons are secreted into the filtrate. The loop of Henle is primarily involved in solute concentration. The distal tubule and the collecting duct are segments where highly regulated solute transport occurs. Thus, each segment is critical for maintaining electrolyte and water homeostasis.

In the past, kidney cells have been annotated on the basis of their function, their anatomical location, or the expression of a small number of marker genes (*1*), yet these classification systems do not fully overlap. An emerging technology called single-cell transcriptional profiling allows investigators to monitor global gene regulation in thousands of individual cells in a single experiment (*2*, *3*). In principle, this technology could answer central questions in kidney biology and disease pathogenesis because it has the potential to provide four distinct types of information.

First, unbiased single-cell clustering can redefine kidney cell types on the basis of only their global transcriptome patterns (*4*). Such analyses have already been applied to other organs (*2*, *5*–*7*) and even to whole multicellular organisms (*8*, *9*). These experiments have identified previously unrecognized cells and have cataloged marker genes for previously defined cells, indicating that this approach has the potential to redefine kidney cell types.

Second, single-cell analysis may help dissect the mechanisms underlying common kidney diseases (*10*, *11*). In general, kidney pathologies have been grouped together by their temporal patterns (acute or chronic) or by their target structures (glomerular versus tubular), which has obscured the underlying biology. Previously obtained bulk transcriptome profiles have generated readouts only for predominant cell populations such as the proximal tubular cells (*12*). Kidney segment–specific RNA-sequencing analysis of the rat kidney has provided useful resources (*13*), but single-cell analysis can potentially further exploit cell type–specific changes and identify previously unrecognized cell types during disease modulation, independent of preconceived cellular definitions.

Third, single-cell analysis may be able to identify fluctuating states of the same cell type. It is generally believed that terminally differentiated cells have limited plasticity. Most cell plasticity in adults has been observed in the context of differentiation of progenitor cells, best described in the blood and intestine (*14*). Such cellular transitions have also been documented during the development of the collecting duct (*15*–*17*). For example, subtypes of intercalated cells (ICs) can change their functional polarity. In addition, stem cell–like populations originating from the principal cell types (PCs) may persist in the adult collecting duct and respond to external stimuli (*18*, *19*), but definition of these plastic cells is lacking.

Fourth, current models of kidney disease cannot distinguish primary cell autonomous responses from secondary cell nonautonomous responses. Single cell–specific gene expression profiles, in contrast, may help identify the readout of disease-associated gene mutations in each cell.

Single-cell profiling and unbiased clustering of mouse kidney cells

We first cataloged mouse kidney cell types in an unbiased manner by using droplet-based single-cell RNA sequencing (*20*). We isolated and sequenced a total of 57,979 cells from whole kidney cell suspensions derived from seven healthy male mice (one kidney per mouse). Using stringent quality controls (*20*), we further analyzed 43,745 cells. Clustering analysis identified 16 distinct cell clusters consisting of as few as 24 cells to as many as 26,482 cells per cluster (the clusters were restricted to a minimum of 20 cells) (Fig. 1A).

We next performed several important quality-control analyses to validate our map. First, we ensured that cells from the seven kidneys were distributed evenly in all 16 clusters and that each cluster contained cells from more than four experiments (fig. S1). Next, we examined the effect of mitochondrial gene content (fig. S2A). The clustering of cells was not affected by mitochondrial gene content (fig. S2, B to E). Furthermore, genes whose expression positively correlated with mitochondrially encoded proteins were associated with solute transport (which requires abundant energy) rather than with cellular stress responses (fig. S3). This indicates that the increased mitochondrial gene count was inherent to specific (proximal and distal tubule) cell types in the kidney. In addition, by testing different clustering methods, we found that most methods identified similar cell groups (fig. S4), expressing the same group of marker genes with limited variations in cell separation. Last, we showed that decreasing the cell number from 40,000 to 10,000, 3000, or 1000 cells (fig. S5A) was associated with increasing uncertainty in cell cluster identification and the loss of rarer cell types (fig. S5, B and C).

Classification of kidney cells based on cell type–specific marker genes

To define the identity of each cell cluster, we generated cluster-specific marker genes by performing differential gene expression analysis (Fig. 1B, fig. S6, and table S1) (*20*). In many cases, the unbiased cluster identifier was a known cell type–specific marker, such as *Kdr* (encoding vascular endothelial growth factor receptor 2) for endothelial cells, *Nphs1* (nephrin) and *Nphs2* (podocin) for podocytes, *Slc12a1* (Na-K-2Cl cotransporter) for the ascending loop of Henle, and *Slc12a3* (thiazide-sensitive sodium chloride cotransporter) for the distal convoluted

[1]Renal Electrolyte and Hypertension Division, Department of Medicine and Genetics, University of Pennsylvania, Philadelphia, PA 19104, USA. [2]Renal Division, Department of Medicine, Columbia University, New York, NY 10032, USA. [3]Department of Biostatistics, Epidemiology and Informatics, University of Pennsylvania, Philadelphia, PA 19104, USA.
*These authors contributed equally to this work.
†Corresponding author. Email: ksusztak@pennmedicine.upenn.edu

tubule (Fig. 1B). Immune cells and endothelial cell clusters separated from epithelial cells, but the ureteric bud–derived (clusters 6 to 8) and metanephric mesenchyme–derived (clusters 2 to 5) epithelial clusters were more closely aligned (Fig. 1A). Although some of the markers were already known, we identified a large number of additional markers, including *Cdkn1c* and *Bcam* for podocytes (Fig. 1B and fig. S6B). Further analysis identified eight subclusters within clusters 1, 3, and 7 (Fig. 1C and tables S2 and S3). Cluster 1 separated into endothelial cells; pericyte, vascular smooth muscle, and mesangial-like cells; and descending loop of Henle (DLH) cells. Cluster 3 (proximal tubules) separated into S1, S2, and S3 segments or proximal convoluted and straight segments (fig. S7). ICs (cluster 7) separated into types A and B.

To reliably assign a specific cell type to each cell cluster, we first correlated our gene expression results with bulk RNA-sequencing data from microdissected rat kidney segments (fig. S8) and microarray data on human immune cell types (fig. S9). To further validate our clustering analysis, we used Nphs2^{Cre}mT/mG, Scl^{Cre}mT/mG, and Cdh16^{Cre}mT/mG mice as reporter lines to mark podocytes, endothelium, and tubule cells with green fluorescent protein (GFP). The GFP expression in these models confirmed the proposed cell identity of our cell clusters (fig. S10). Altogether, our single-cell transcriptome atlas provides a molecular definition of 18 previously defined kidney and immune cell types, as well as three newly defined cell types.

Mendelian disease genes show cell type specificity

We next tested the hypothesis that hereditary kidney diseases that are characterized by the same phenotypic manifestations originate from the same cell type. We also explored whether the functions of specific cell types in the mouse kidney could be inferred from the expression pattern of human genes whose loss of function results in kidney disease. We found that the mouse homologs of 21 of 29 genes that have been associated with monogenic inheritance of proteinuria in humans were expressed in only one cell type—namely, the podocyte of the glomerulus (Fig. 2A and fig. S11). Although earlier studies have implicated defects in endothelial cells and proximal tubules in the development of proteinuria, and functional and structural changes in these cell types can be seen in patients with proteinuria, our results unequivocally show that podocyte dysfunction is the principal reason for proteinuria (*21*). As another example, we found that the mouse homologs of genes associated with renal tubule acidosis (RTA) in humans were expressed only by ICs of the collecting duct, confirming the major role of these cells in acid-base homeostasis (Fig. 2A). Furthermore, mouse homologs of genes that have been implicated in blood pressure regulation through analysis of human Mendelian diseases, such as *Wnk4*, *Wnk1*, *Klh3*, and *Slc12a3*, were expressed specifically in the distal convoluted tubule, whereas *Nr3c2*, *Scnn1b*, *Scnn1g*, and *Hsd11b2* were specifically expressed by PCs of the collecting duct (Fig. 2A and figs. S11 and S13).

Following the same logic, we annotated the expression of putative complex-trait disease genes that have been associated with blood pressure, chronic kidney disease (CKD) and serum metabolite levels, nephrolithiasis (e.g., *Slc34a1*), and RTA (e.g., *Atp6v1b1*) (Fig. 2B and figs. S12 and S13) (*22*–*24*). We found that most genes

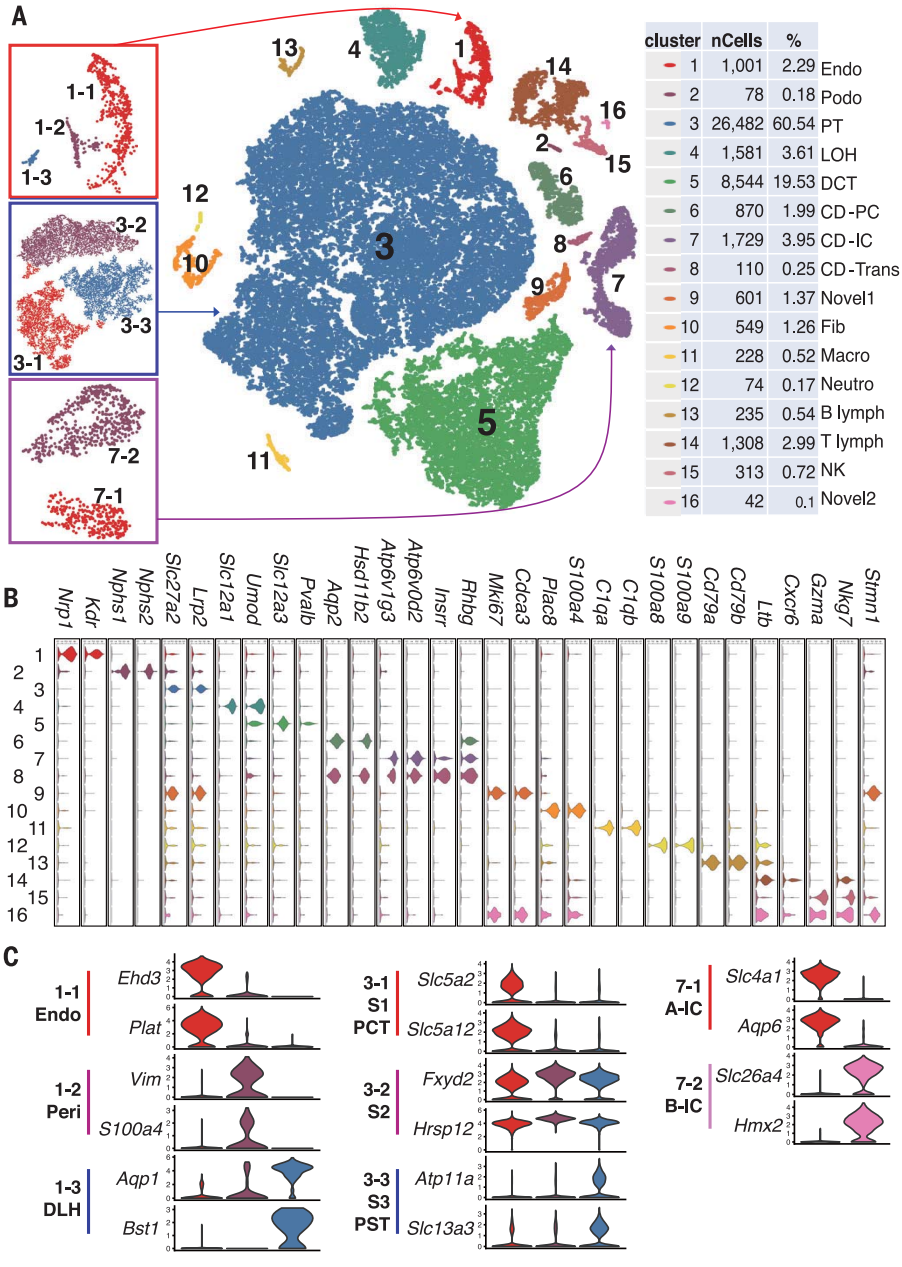

Fig. 1. Cell diversity in mouse kidney cells delineated by single-cell transcriptomic analysis. (**A**) Unsupervised clustering demonstrates 16 distinct cell types shown in a *t*-distributed stochastic neighbor embedding (tSNE) map (center). Left panels are subclusters of clusters 1, 3, and 7. Percentages of assigned cell types are summarized in the right panel. Endo, containing endothelial, vascular, and descending loop of Henle; Podo, podocyte; PT, proximal tubule; LOH, ascending loop of Henle; DCT, distal convoluted tubule; CD-PC, collecting duct principal cell; CD-IC, collecting duct intercalated cell; CD-Trans, collecting duct transitional cell; Fib, fibroblast; Macro, macrophage; Neutro, neutrophil; lymph, lymphocyte; NK, natural killer cell. (**B** and **C**) Violin plots showing the expression levels of representative marker genes across the 16 main clusters. The *y* axis shows the log-scale normalized read count. (C) Cluster 1 [from (A), left] separates into endothelial cells (Endo), pericytes and vascular smooth muscle cells (Peri), and descending loop of Henle (DLH) cells. Cluster 3 (proximal tubules) separates into S1, S2, and S3 segments or proximal convoluted tubules (PCT) and proximal straight tubules (PST). In cluster 7, intercalated cells (ICs) separate into types A and B.

implicated in these traits were expressed only in a single cell type, such as collecting duct cells (RTA) or proximal tubule cells (nephrolithiasis). The expression of genes associated with plasma metabolite levels—such as *Slc17a3* (uric acid), *Slc51a* (bile acid), and *Slc16a9* (carnitine) (*22*–*24*)—and CKD showed strong enrichment for proximal tubule–specific expression, whereas blood pressure–associated genes were mostly expressed in collecting duct cells. Thus, our single-cell transcriptomic analysis highlights specific cells responsible for specific kidney-related disorders, as well as the critical functions of these cells.

Identification of a previously unrecognized cell type in the collecting duct

The collecting duct of the kidney differs from all other kidney epithelia because it originates from the ureteric bud and not from the metanephric mesenchyme. This compartment is composed of at least three distinct cell types: the PCs, which are responsible for sodium, water reabsorption, and potassium secretion, and the type A and B ICs, which are responsible for acid and alkali secretion, respectively. We identified the genes encoding aquaporin 2 (*Aqp2*) and H^+-ATPase (H^+-dependent adenosine triphosphatase) subunit (*Atp6v1g3*) as the key marker genes for clusters 6 and 7, defining these clusters as PCs and ICs (Figs. 1 and 3, A and B).

Unexpectedly, our single-cell profiling identified a third cell cluster. This cell cluster (cluster 8) expressed markers of both ICs and PCs ("double-positive cells"; Fig. 3, A and B) and additional cell type–specific markers. We performed double immunofluorescence staining and in situ hybridization with probes for *Aqp2* and *Atp6v1b1* (Fig. 3C) and cell type–specific markers such as *Parm1* and *Sec23b* (Fig. 3, D to F, and fig. S14) to validate the existence of this cell type.

To further investigate this unexpected cell type, we used the Monocle toolkit to perform cell trajectory analysis using pseudotime reconstitution of clusters 6 to 8 (*20*). We found that the newly identified cells were located between PCs and ICs, suggesting that cluster 8 is a transitional cell type (Fig. 3G). Transitional cells showed low expression levels of stress response genes and cell cycle genes, and these cells were present in all batches of our kidney isolates (figs. S15 and S16), excluding the possibility that they were injured cells, a proliferating subtype of collecting duct cells, or an artifact. Furthermore, cell trajectory analysis separated ICs into types A and B and PCs into their subtypes (PCs in the collecting duct and connecting tubule), as previously identified (Fig. 3G and fig. S17) (*7*, *25*). These results indicate that the collecting duct contains not only PCs and ICs but a third distinct, transitional cell type; this raises the possibility that ICs and PCs represent two ends of a spectrum of cellular phenotypes and that they may undergo cellular transitions.

Fluorescent lineage tracing confirms plasticity of collecting duct cells

We next examined whether transitional cells could be identified by conventional in vivo lineage tracing and whether they match our computational characterization. We generated mice that carry a lineage tag in differentiated PCs ($Aqp2^{Cre}$mT/mG) or in differentiated ICs ($Atp6^{Cre}$mT/mG) (Fig. 3, H and I). We performed triple immunofluorescence labeling in these animals by staining for GFP (all cells of a specific marker origin), AQP2 (PCs), and ATP6V1B1 (ICs). As expected, we found that most of the GFP-positive cells were also AQP2-positive in the $Aqp2^{Cre}$mT/mG mice. A subset of the GFP-positive cells expressed ATP6V1B1, an IC marker, but not AQP2. A smaller subset was double-positive for ATP6V1B1 and AQP2. Among the $Aqp2^{Cre}$mT/mG GFP-positive cells, 61.6% were AQP2-positive, 29.2% were ATP6V1B1-positive, and 9.2% were double-positive for AQP2 and ATP6V1B1 (Fig. 3H). Similar analyses were performed with the $Atp6^{Cre}$mT/mG lineage, which showed that double-positive (AQP2

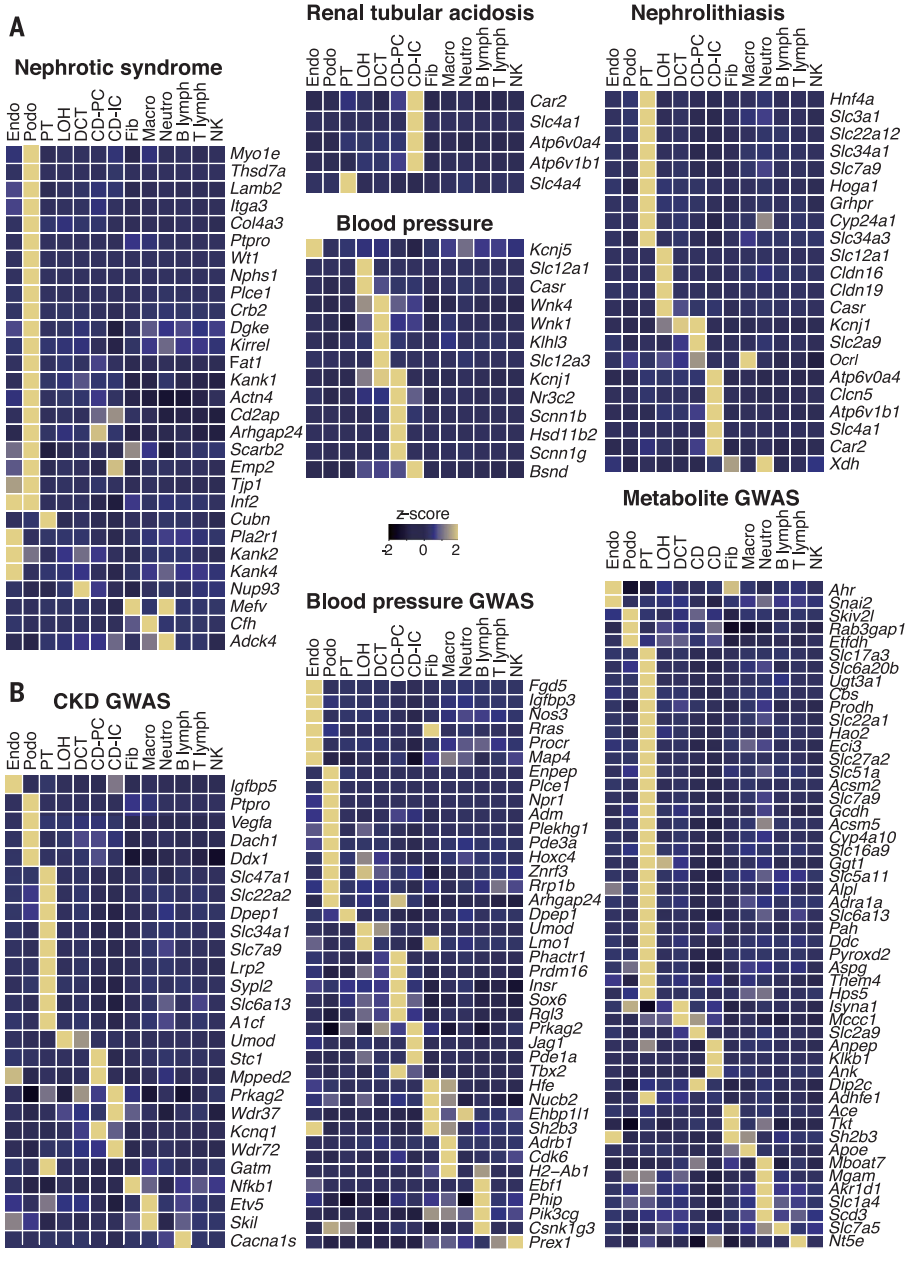

Fig. 2. Discrete human disease phenotypes are due to mutations in single specific cell types. Single cell–type specific average expression of human (**A**) monogenic disease genes and (**B**) complex-trait genes identified by genome-wide association studies. Mean expression values of the genes were calculated in each cluster. The color scheme is based on *z*-score distribution; the map only shows genes with maximum *z*-scores > 2. In the heatmap, each row represents one gene, and each column is a single cell type (defined in Fig. 1). The full list of cell types and genes is shown in figs. S11 and S12.

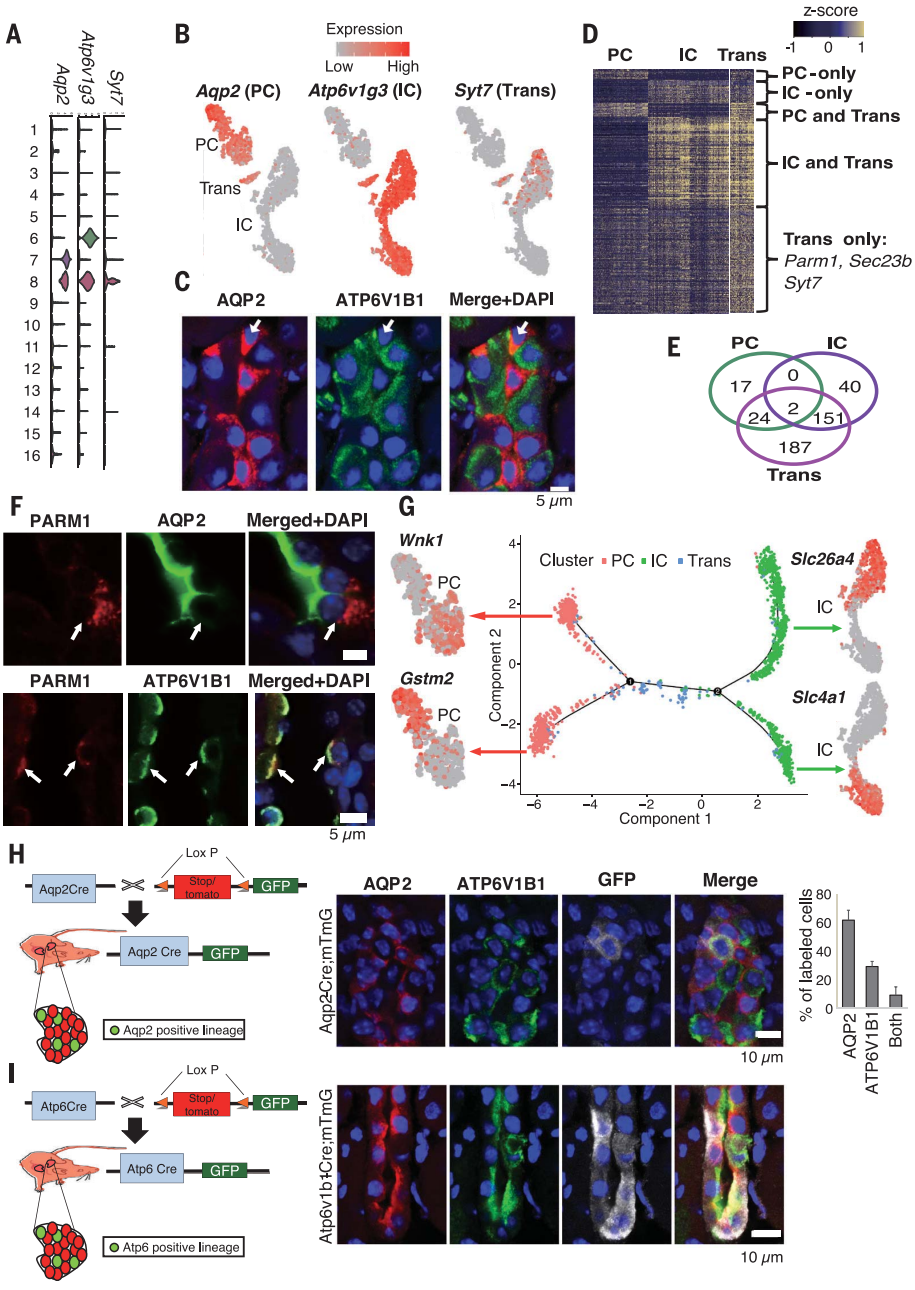

Fig. 3. Identification of a transitional cell type and a conversion process in the kidney collecting duct. (**A**) The expression levels of marker genes across the 16 clusters. The *y* axis shows the log-scale normalized read count. (**B**) Gene expression levels in PCs (*Aqp2*), ICs (*Atp6v1g3*), and transitional cells (*Syt7*), demonstrated by a tSNE plot. (**C**) Representative immunofluorescence images of AQP2 (PC marker), ATP6V1B1 (IC marker), and DAPI (4′,6-diamidino-2-phenylindole) in the kidney collecting duct. The arrow indicates the transitional PC-IC cell type expressing AQP2 and ATP6V1B1. (**D**) Heatmap showing the expression levels of differentially expressed genes in collecting duct cell types. The color scheme is based on *z*-score distribution. (**E**) Venn diagram showing the overlaps of differentially expressed genes between PCs, ICs, and the newly identified cell type. (**F**) Immunofluorescence staining for PARM1 (transitional cell–specific) and AQP2 (upper panels) or ATP6V1B1 (lower panels) in the kidney collecting duct. "Double-positive" cells are shown by the arrows. (**G**) Ordering single cells along a cell conversion trajectory using Monocle. Three collecting duct cell clusters were used for ordering and plotted in low-dimensional space with different colors. The tSNE plots next to the trajectory map show differentially expressed genes in the corresponding cell lineages. (**H**) Aqp2^{Cre}mT/mG mouse model used for lineage tracing of AQP2-positive cells (left) and immunofluorescence staining for GFP, ATP6V1B1, and AQP2 (right). The far-right panel shows the quantification of GFP-positive cells (mean ± SD; *n* = 3). AQP2-driven GFP (white) is found in PCs (red and white) and ICs (green and white). (**I**) Atp6^{Cre}mT/mG mouse model used for lineage tracing of ATP6ase-positive cells (left) and immunofluorescence staining for GFP, ATP6V1B1, and AQP2 in Atp6^{Cre}mT/mG mice (right). ATP6V1B1-driven GFP (white) is found in PCs (red and white), ICs (green and white), and transitional cells (red, green, and white).

and ATP6V1B1–positive) transitional cells and ATP6V1B1-negative true PCs can originate from ATP6V1B1-positive ICs (Fig. 3I).

To determine whether cell proliferation might be responsible for this cell plasticity, we calculated the expression levels of cell cycle–regulated genes in the single-cell transcriptome and in cell trajectory maps. We found that only clusters 9 and 16 (newly identified cell types 1 and 2), not any of the collecting duct clusters, expressed high levels of the cell cycle genes (fig. S18). This suggests that cluster 8 is likely to be a transitional cell population and not a proliferating progenitor cell. Thus, in vivo lineage tracing analysis confirmed transitions of PCs and ICs not only during development (*15*–*17*) but also in the adult collecting duct through a newly identified transitional cell type.

Collecting duct cell plasticity, driven by Notch signaling, results in abnormal cell populations in CKD

For further analysis of the plasticity of collecting duct cells, we identified genes whose expression levels change during transitions of PCs and ICs (fig. S19, A and B) (*20*). PCs showed enriched expression of genes associated with cell adhesion, water homeostasis, and salt transport, whereas ICs showed enriched expression of genes associated with ATP hydrolysis and synthesis, coupled proton transport, and oxidation-reduction processes (fig. S19C). The gene expression patterns revealed that the Notch signaling pathway was activated during the transition of ICs to PCs. Notch regulates the cellular identity of neighboring cells by the expression of either Notch ligands or Notch receptors. Alternating expression of ligands and receptors creates a signal-sending cell (Notch-off) and a signal-receiving cell (Notch-on). Genes encoding Notch ligands, such as *Jag1*, were highly expressed by ICs, whereas their expression levels were low in PCs (Fig. 4A). In contrast, PCs showed high expression levels of Notch2 receptor and its transcriptional target *Hes1* (which encodes a transcription factor), suggesting that PCs are the Notch signal–receiving cells in the collecting duct. Immunofluorescence studies confirmed

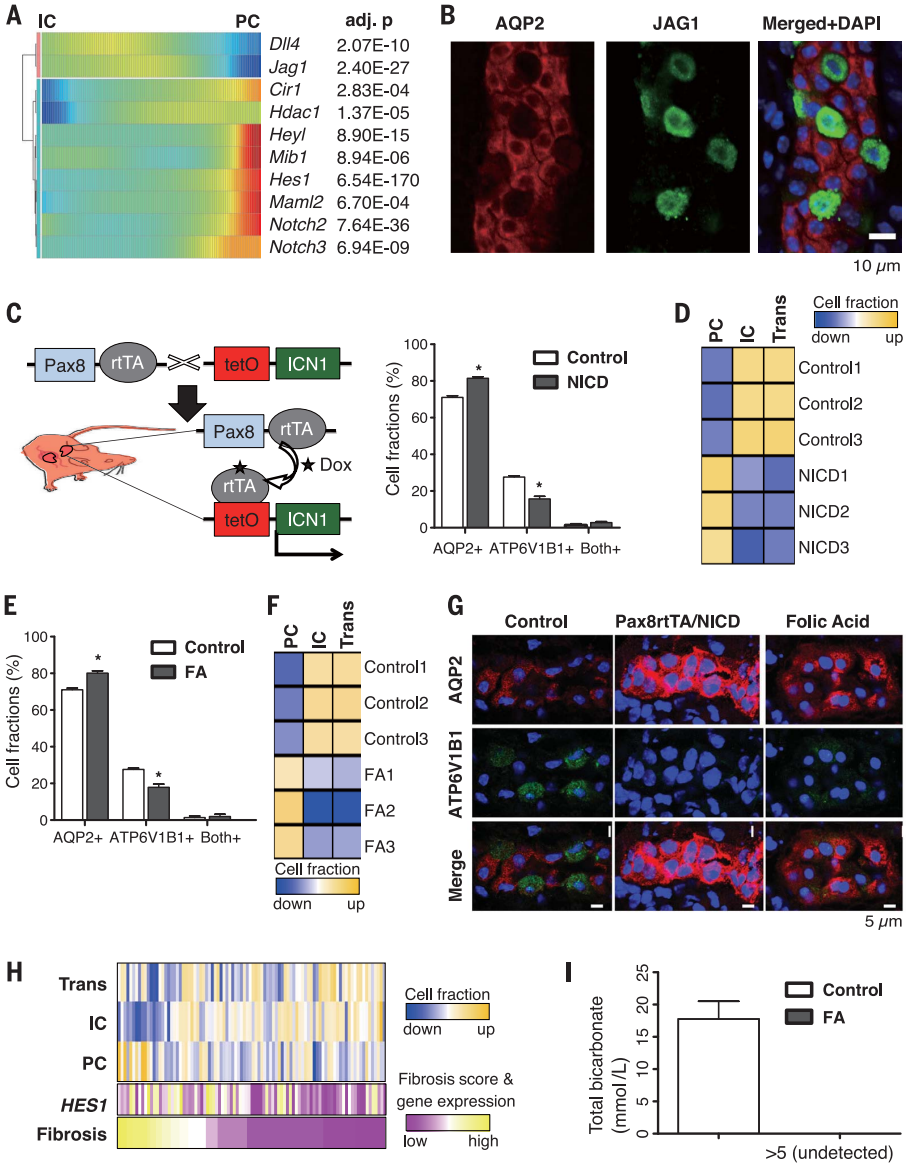

Fig. 4. The IC-to-PC transition is driven by Notch ligand and receptor expression. (**A**) Transcriptional profiles demonstrating the spectrum of expression of Notch genes in the collecting duct. Cells are ordered in pseudotime, and color represents expression levels. (**B**) Double immunofluorescence staining for AQP2 (red) and JAG1 (green) in the kidney collecting duct. (**C**) Generation of mice with inducible expression of Notch (ICN1) in kidney tubules (left). Dox, doxycycline. Excess AQP2-positive cells and reciprocally decreased ATP6V1B1-positive cells are found in Pax8rtTA/NICD tubules (mean ± SD; n = 3) (right). *P < 0.01. (**D**) In silico deconvolution of mouse kidney bulk RNA profiling data. Wild-type and Pax8rtTA/NICD samples were used for analysis. (**E**) Immunofluorescence quantification of cells labeled with AQP2 and ATP6V1B1 in control mice and a mouse model of CKD induced by folic acid (FA) (mean ± SD; n = 3). *P < 0.01. (**F**) In silico deconvolution of mouse kidney bulk RNA profiling. Control and kidney samples from FA-injected mice were used for analysis. (**G**) Immunofluorescence staining for AQP2 and ATP6V1B1 in control, Pax8rtTA/NICD, and FA-induced mouse model collecting ducts. AQP2-positive cells are abundant in the latter two and, conversely, ATP6V1B1-positive cells disappear. (**H**) In silico deconvolution of bulk RNA profiling data derived from kidney biopsy samples of patients with CKD (n = 91). The histological fibrosis scores and *HES1* expression levels for the corresponding samples are also shown. (**I**) Total serum bicarbonate levels in control mice and in mice with FA-induced kidney fibrosis (mean ± SD; n = 5).

exclusive expression of the Notch ligand JAG1 in the ICs (Fig. 4B).

To examine whether Notch signaling drives the IC-to-PC cell transition, we generated Pax8rtTA/NICD mice, which enable inducible transgenic expression of the conserved Notch intracellular domain portion of the receptor, specifically in differentiated kidney tubule cells (Fig. 4C). This experimental model allowed us to study only the IC-to-PC transitions occurring in adult mice, as opposed to those occurring during embryogenesis (*15*). We found that Notch expression disrupted cellular patterning. The number of cells expressing the PC marker AQP2 was increased, whereas the number of cells expressing the IC marker ATP6V1B1 and the type A IC marker ADGRF5 was reduced in parallel (Fig. 4, C and G, and fig. S20). The Notch-mediated transition appeared nearly complete, given that the cells also expressed multiple PC markers, including AQP3 and HSD11B2 (figs. S21 and S22). Last, in silico deconvolution analysis of bulk RNA-profiling data, examining marker gene expression, was performed for control and Pax8rtTA/NICD mice (*20*) to estimate the proportion of ICs and PCs in the collecting duct. The data were consistent with the results of our lineage tracing experiments (Fig. 4D). Collectively, these data indicate that Notch receptor expression and signaling are sufficient to drive the IC-to-PC transition in the collecting duct of the adult kidney.

Because increased Notch expression has been reported in patients with and animal models of kidney disease (*26*, *27*), we examined whether disease states disrupt the relative numbers of PCs and ICs. In a mouse model of CKD induced by folic acid (FA), which shows structural and functional damage resembling that seen in human CKD, we found a loss of the typical alternating patterns of ICs and PCs. We observed an increase in AQP2-positive cells and a decrease in ATP6V1B1-positive cells (as well as ADGRF5-positive type A ICs) compared with untreated mice (Fig. 4, E and G, and fig. S20). Computational cell deconvolution analysis of bulk RNA sequencing and analysis of marker gene expression in control and FA-induced kidney disease models yielded data consistent with a shift from IC to PC fate (Fig. 4F and fig. S23). Using cell markers identified in mice, we performed computational deconvolution analysis of kidney biopsy samples from 91 patients with hypertensive and diabetic CKD (fig. S24). Again, we found that in comparison with healthy samples, the diseased tissue samples showed a higher ratio of PCs to ICs (Fig. 4H and fig. S25), consistent with increased Notch signaling and *HES1* expression (that is indicative of active Notch signaling) in these samples. The shift toward PCs did not correlate with increased expression of cell proliferation–associated genes in PCs or with increased expression of cell death–associated genes in ICs (fig. S25).

Last, we analyzed whether the increased IC-to-PC transition that we observed in the mouse model of CKD (Fig. 4C) and in kidney biopsy samples from patients with CKD (Fig. 4H) had a functional consequence. ICs are uniquely associated with acid secretion in the kidney because they express H^+-transporting genes. Conversely, mutations in genes encoding proton pumps such as ATP6V1B1 cause metabolic acidosis, an accumulation of acid in many compartments of the body (fig. S19C and Fig. 2A). We found that total blood CO_2 levels (composite measure of serum bicarbonate and partial pressure of CO_2) were significantly reduced in the FA-induced kidney disease mouse model, consistent with metabolic acidosis (Fig. 4I). Together, these data show that (i) the IC-to-PC transition is mediated by Notch ligand (IC) and receptor (PC) expression and (ii) a shift toward the PC fate is the likely cause of metabolic acidosis in mouse models of and patients with CKD.

Discussion

Efforts to describe the cell types that make up the kidney date back to the invention of the microscope. Over the past century, a kidney cell annotation has been developed that is based on the organ's functions of transporting water and different types of salts. Here, we provide a molecular definition of cell types in the mouse kidney obtained by single-cell RNA sequencing of 57,979 cells. At this resolution, we distinguished 21 major cell types defined by quantitative gene expression; these cells included almost all previously described cell types, newly defined transitional cells in the collecting duct, and two additional undefined cells (clusters 9 and 16; Fig. 1). Our work complements previous efforts that have applied this technology to the kidney. Single-cell sequencing has been used to study fetal mouse kidneys and sorted kidney segments (*7*, *28*, *29*), and a recent study identified kidney cell composition changes in patients with lupus nephritis (*30*).

Our kidney cell atlas provides insight into kidney function and disease pathogenesis. It demonstrates that the expression of monogenic kidney disease genes is restricted to a single cell type. Therefore, most genetic diseases of the kidney can be traced to single cell types. In this light, each cell type appears to make a nonredundant contribution to a specific type of kidney disease. In contrast, previous transcriptomic studies identified changes in multiple cell types, using aggregated data from different kidney diseases. Last, it appears that the single-cell transcriptomics data can be used to infer cell type–specific function in vivo at the organismal level.

The atlas also highlights the role of the collecting duct system of the kidney in health and disease. The expression of genes harboring mutations associated with human disorders such as metabolic acidosis, CKD, and high blood pressure is specifically localized to this kidney segment. One of the most striking results of our analysis of the mouse kidney was the identification of an unexpected cell type related to the well-known ICs and PCs. Computational and lineage tracing analyses indicated that cells of this type are most likely transitional cells and that the number and patterning of ICs and PCs are controlled by Notch signaling in adult mice. This finding suggests that the Notch pathway may play a role in CKD. We speculate that the transition between PCs and ICs is a constitutive process that is activated in disease conditions, because our cell trajectory analysis demonstrates that the transitions occur at low frequency in healthy mice. PCs may be irreplaceable, considering that they are responsible for sodium and water balance and are involved in the regulation of serum potassium levels (*31*). Elevated serum potassium can cause fatal cardiac conduction abnormalities in patients with chronic kidney failure. On the other hand, acid accumulation owing to the loss of ICs can be partially compensated by regulating the respiratory rate, and, as a result, the organism can maintain near-normal serum pH. Perhaps this rationale explains the preservation or even expansion of PCs, unlike ICs, in disease states.

We have generated a comprehensive cell atlas of the mouse kidney, identified cell type–specific markers along with previously unrecognized cell types, and uncovered unexpected cell plasticity. This information will enhance our understanding of normal kidney function and disease development.

REFERENCES AND NOTES

1. W. Kriz, L. Bankir; The Renal Commission of the International Union of Physiological Sciences (IUPS), *Kidney Int.* **33**, 1–7 (1988).
2. E. Z. Macosko *et al.*, *Cell* **161**, 1202–1214 (2015).
3. G. X. Zheng *et al.*, *Nat. Commun.* **8**, 14049 (2017).
4. O. Rozenblatt-Rosen, M. J. T. Stubbington, A. Regev, S. A. Teichmann, *Nature* **550**, 451–453 (2017).
5. M. J. T. Stubbington, O. Rozenblatt-Rosen, A. Regev, S. A. Teichmann, *Science* **358**, 58–63 (2017).
6. E. Lein, L. E. Borm, S. Linnarsson, *Science* **358**, 64–69 (2017).
7. L. Chen *et al.*, *Proc. Natl. Acad. Sci. U.S.A.* **114**, E9989–E9998 (2017).
8. N. Karaiskos *et al.*, *Science* **358**, 194–199 (2017).
9. J. Cao *et al.*, *Science* **357**, 661–667 (2017).
10. F. Hildebrandt, *Lancet* **375**, 1287–1295 (2010).
11. L. F. Menezes, G. G. Germino, *Wiley Interdiscip. Rev. Syst. Biol. Med.* **7**, 39–52 (2015).
12. H. M. Kang *et al.*, *Nat. Med.* **21**, 37–46 (2015).
13. J. W. Lee, C. L. Chou, M. A. Knepper, *J. Am. Soc. Nephrol.* **26**, 2669–2677 (2015).
14. M. Chang-Panesso, B. D. Humphreys, *Nat. Rev. Nephrol.* **13**, 39–46 (2017).
15. M. Werth *et al.*, *eLife* **6**, e24265 (2017).
16. H. Wu *et al.*, *J. Am. Soc. Nephrol.* **24**, 243–252 (2013).
17. H. W. Jeong *et al.*, *J. Clin. Invest.* **119**, 3290–3300 (2009).
18. J. Li *et al.*, *J. Am. Soc. Nephrol.* **26**, 81–94 (2015).
19. G. J. Schwartz, J. Barasch, Q. Al-Awqati, *Nature* **318**, 368–371 (1985).
20. See supplementary materials.
21. L. Malaga-Dieguez, K. Susztak, *J. Clin. Invest.* **123**, 4996–4999 (2013).
22. C. Pattaro *et al.*, *Nat. Commun.* **7**, 10023 (2016).
23. H. R. Warren *et al.*, *Nat. Genet.* **49**, 403–415 (2017).
24. S. Y. Shin *et al.*, *Nat. Genet.* **46**, 543–550 (2014).
25. P. A. Welling, *Annu. Rev. Physiol.* **78**, 415–435 (2016).
26. B. Bielesz *et al.*, *J. Clin. Invest.* **120**, 4040–4054 (2010).
27. M. T. Sweetwyne *et al.*, *Diabetes* **64**, 4099–4111 (2015).
28. Y. Lu, Y. Ye, Q. Yang, S. Shi, *Kidney Int.* **92**, 504–513 (2017).
29. M. Adam, A. S. Potter, S. S. Potter, *Development* **144**, 3625–3632 (2017).
30. E. Der *et al.*, *JCI Insight* **2**, e93009 (2017).
31. P. A. Welling, *Semin. Nephrol.* **33**, 215–228 (2013).

ACKNOWLEDGMENTS

Funding: Work in the Susztak laboratory is supported by NIH NIDDK R01 DK076077, DK087635, DK105821, and DP3 DK108220. J.P. is supported by American Diabetes Association Training grant #1-17-PDF-036. M.W. and J.B. are supported by NIH 1U54DK104309-01, NIH 2R01DK073462, UG3 DK114926-01, and a Columbia Precision Medicine Pilot Award. **Author contributions:** J.P. performed computational analysis with assistance from C.Q. and M.L., R.S. generated sequencing data with assistance from J.P. and A.K., R.S. and M.W. performed experiments with assistance from S.H., K.S. designed the research, and K.S., J.P. and J.B. wrote the paper. **Competing interests:** The authors declare no competing interests. **Data and materials availability:** Processed and raw data can be downloaded from NCBI GEO (accession number GSE107585).

SUPPLEMENTARY MATERIALS

www.sciencemag.org/content/360/6390/758/suppl/DC1
Materials and Methods
Figs. S1 to S25
Tables S1 to S3
References (*32*–*39*)

13 October 2017; accepted 27 March 2018
Published online 5 April 2018
10.1126/science.aar2131

REPORT

QUANTUM MATERIALS

Elastic strain engineering for ultralow mechanical dissipation

A. H. Ghadimi,[1]* S. A. Fedorov,[1]* N. J. Engelsen,[1]* M. J. Bereyhi,[1] R. Schilling,[1] D. J. Wilson,[2]† T. J. Kippenberg[1]†

Extreme stresses can be produced in nanoscale structures; this feature has been used to realize enhanced materials properties, such as the high mobility of silicon in modern transistors. We show how nanoscale stress can be used to realize exceptionally low mechanical dissipation when combined with "soft-clamping"—a form of phononic engineering. Specifically, using a nonuniform phononic crystal pattern, we colocalize the strain and flexural motion of a free-standing silicon nitride nanobeam. Ringdown measurements at room temperature reveal string-like vibrational modes with quality (*Q*) factors as high as 800 million and *Q* × frequency exceeding 10^{15} hertz. These results illustrate a promising route for engineering ultracoherent nanomechanical devices.

Elastic strain engineering uses stress to realize unusual material properties (*1*). For instance, stress can enhance the electron mobility of a semiconductor, enabling more efficient solar cells (*2*) and smaller, faster transistors (*3*). In mechanical engineering, the pursuit of resonators with low dissipation (*4*) has led to studies of a complementary strain engineering technique known as dissipation dilution, whereby the stiffness of a stressed material is effectively increased without added loss (*5*–*8*). Unlike most bulk mechanical properties, dissipation dilution can improve with reduced device dimensions, implying that smaller-mass resonators can have higher quality factors *Q*. This unusual scaling is responsible for the anomalously high *Q* of Si_3N_4 nanomechanical resonators (*8*–*11*) and has led to the emergence of "quantum-coherent" resonators with thermal decoherence times $\hbar Q/k_B T$ longer than one vibrational period (where $\hbar$, k_B, and T are the reduced Planck constant, Boltzmann constant, and bath temperature, respectively).

Whereas elastic strain engineering commonly relies on extreme inhomogeneous stresses produced by nanoscale deformation (*12*) [e.g., by lithographic patterning (*13*, *14*) or nano-indentation (*15*)], nearly all studies of dissipation dilution have focused on materials under weak, uniform stress produced during material synthesis. The main challenge in bridging these two approaches is to identify strategies to colocalize stress and mechanical motion at the nanoscale. Our strategy, based on phononic crystal patterning, is conceptually simple and entirely material-independent (Fig. 1): By weakly corrugating a prestressed nanobeam, we create a band gap for localizing its flexural modes around a central defect. By tapering the beam, we colocalize these modes with a region of enhanced stress. Reduced motion near the supports ["soft-clamping" (*8*)] results in higher dissipation dilution, while enhanced stress increases both dilution and mode frequency. We implemented this approach on tapered beams with extremely high aspect ratios (as long as 7 mm and as thin as 20 nm) made of 1.1 GPa–prestressed Si_3N_4, and achieved local stresses as high as 3.8 GPa.

To illustrate the basic features of our approach, we first consider a model for dissipation dilution of a nonuniform beam of length L, thickness h, and variable width $w(x)$. Following an anelastic approach successfully applied to uniform nanobeams (*6*, *7*) and nanomembranes (*16*), we partition the potential energy of the beam U into two components: a dissipative component due to bending, $U_E = \frac{1}{2} E_0 \int_0^L I(x)[u''(x)]^2 dx$, and a conservative component due to elongation, $U_\sigma = \frac{1}{2} \mathcal{T} \int_0^L [u'(x)]^2 dx$, where $u(x)$ is the vibrational mode shape, $I(x) = (1/12)w(x)h^3$ is the geometric moment of inertia, E_0 is the Young's modulus, $\mathcal{T} = hw(x)\sigma(x)$ is the tension, and $\sigma(x)$ is the axial stress of the beam, respectively. The *Q* enhancement due to stress (the dissipation "dilution factor") is given by the participation ratio of the lossy potential (*5*–*7*):

$$\frac{Q}{Q_0} = 1 + \frac{U_\sigma}{U_E} \approx \frac{12}{E_0 h^2} \cdot \frac{\int_0^L [u'(x)]^2 dx}{\int_0^L \sigma^{-1}(x)[u''(x)]^2 dx} \quad (1)$$

where Q_0 is the intrinsic (undiluted) quality factor. For the familiar case of a uniform beam with a string-like mode shape described by $u(x) \propto \sin(\pi n x/L)$, where n is the mode number, Eq. 1 implies that

$$\frac{Q}{Q_0} \approx \frac{3}{\pi^2} \frac{\sigma^2}{E_0 h^2 \rho f^2} \quad (2)$$

where ρ is the material density and $f = (n/L)\sqrt{\sigma/\rho}$ is the mode frequency. Nearly all stressed nanomechanical resonators studied to date have operated far below this limit. The main reason for this discrepancy is clamping loss; for example, in the case of a doubly clamped beam, boundary

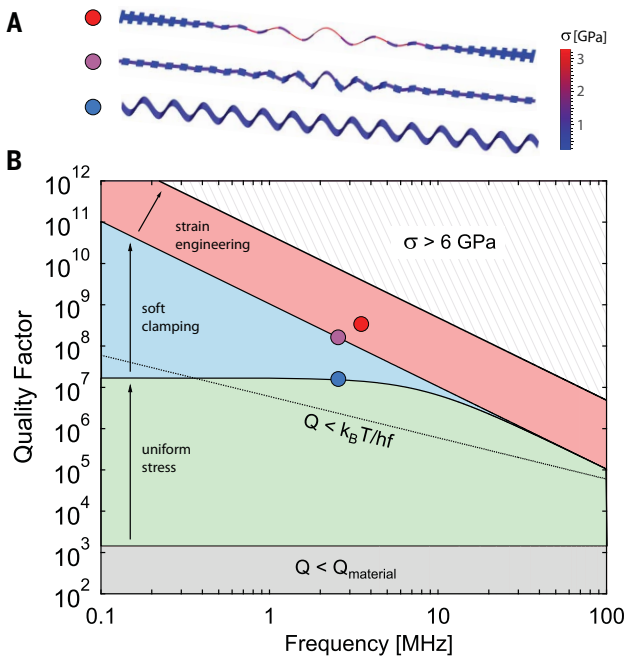

Fig. 1. Ultrahigh-*Q* nanobeams through dissipation dilution. (**A**) Mode shapes representing three strategies to enhance the *Q* of a nanobeam via dissipation dilution. From bottom to top: uniform stress, soft-clamping, and geometric strain engineering. Color scale represents axial stress σ. (**B**) *Q* versus mode frequency (*f*) accessible for a 20-nm-thick Si_3N_4 nanobeam, following Eq. 3. Gray region: *Q*(*f*) of an unstressed beam, limited by material loss. Green region: *Q*(*f*) of a 3-mm-long uniform beam with σ < 1 GPa. Blue region: *Q*(*f*) accessible by soft-clamping. Red region: *Q*(*f*) accessible by soft-clamping and strain engineering. Hatched region (upper right) is forbidden by the material yield strength. Solid circles correspond to measurements described in the main text.

[1]Institute of Physics, École Polytechnique Fédérale de Lausanne, 1015 Lausanne, Switzerland. [2]IBM Research–Zurich, 8803 Rüschlikon, Switzerland.
*These authors contributed equally to this work.
†Corresponding author. Email: daw@zurich.ibm.com (D.J.W.); tobias.kippenberg@epfl.ch (T.J.K.)

conditions $u'(x_0) = u(x_0) = 0$ require that the vibrational mode shape exhibit extra curvature [$u''(x)$] near the supports ($x_0 = 0, L$), resulting in a reduced dilution factor of the form

$$\frac{Q}{Q_0} \approx \left(\underbrace{2\lambda}_{\text{supports}} + \underbrace{\pi^2 n^2 \lambda^2}_{\text{antinodes}} \right)^{-1} \quad (3)$$

(*7*, *17*), where $\lambda = (h/L)\sqrt{1/(12\varepsilon)}$ in units of axial strain $\varepsilon = \sigma/E$.

The uniform beam model (Eq. 3) gives several rules of thumb for maximizing the Q (or $Q \times f$ product) of a stressed nanomechanical resonator; namely, Q is typically highest for the fundamental mode ($n = 1$) and can be increased by increasing the aspect ratio (L/h) or stress. By contrast, $Q \times f$ is typically larger for high-order modes. Both strategies have been explored for a wide variety of beam- and membrane-like geometries (*17*, *18*). A third approach, recently demonstrated with a membrane (*8*), is to use periodic micropatterning [a phononic crystal (PnC)] to localize the mode shape away from the supports. By this soft-clamping approach, the leading term in Eq. 3 can be suppressed, giving access to the performance of an ideal clamp-free resonator (Eq. 2).

Complementary to soft-clamping, our approach consists of colocalizing the mode shape with a region of geometrically enhanced stress, making use of the tension balance relation $\sigma(x) = T/[w(x)h]$ [similar to microbridge structures (*13*, *14*)]. Inhomogeneous stress has been exploited before to increase the $Q \times f$ product of a nanomechanical resonator (*19*); however, performance was in this case limited by rigid clamping. Combining geometrically enhanced stress with soft-clamping can lead to improved performance: For example, Eq. 2 suggests that the Q (for a fixed f) of a typical 1 GPa–prestressed Si_3N_4 nanobeam can be enhanced by a factor of 50 before the stress in the thinnest part of the beam reaches the yield strength of Si_3N_4 ($\sigma_{yield} \approx 6$ GPa). This material limit, described by Eq. 2 with $\sigma = \sigma_{yield}$ and illustrated by the hatched region in Fig. 1, can be shown to apply to an arbitrary beam profile $w(x)$ (*20*). In gaining access to it, the main caveat of our approach is the small area in which the stress is enhanced, which implies that high-order flexural modes must be used to achieve sufficient colocalization.

Devices were patterned on 20-nm-thick films of high-stress Si_3N_4 ($E_0 \approx 250$ GPa, $\sigma_0 \approx 1.1$ GPa) grown by low-pressure chemical vapor deposition on a Si wafer. A multistep release process (*20*) was used to suspend beams as long as 7 mm, enabling aspect ratios as high as 3.5×10^5 and dilution factors in excess of $(2\lambda)^{-1} \approx 3 \times 10^4$. PnCs were realized by corrugating beams with a simple step-like unit cell (length L_c, minor width w_{min}, major width $w_{max} \approx 2w_{min}$) (Fig. 2A). A uniform defect of length L_d was patterned at the center of each beam to define the position of localized modes. Colocalization of stress with these modes is achieved by adiabatically tapering the width of successive unit cells toward the defect according to a Gaussian envelope function (*20*).

Localized modes of PnC nanobeams ("1D phononic crystals") have already been widely studied, as their ultralow mass and sparse mode spectrum make them highly promising for sensing applications. However, in contrast to 2D (membrane-like) resonators (*8*), ultrahigh Q in 1D PnCs has not been reported to date because of a focus on unstrained materials (*21*) and/or highly confined (high-curvature) modes (*18*) limited by radiation loss. With this discrepancy in mind, we first embarked on a study of uniform (untapered) PnC nanobeams, focusing on localized modes of our high–aspect ratio devices.

An experiment demonstrating soft-clamped 1D nanomechanical resonators is shown in Fig. 3. We studied 2.6-mm-long devices with unit cells of length $L_c = 100$ μm and width $w_{min(max)} = 0.5 \pm 0.1$ μm. To characterize these devices, we carried out thermal noise and ringdown measurements in vacuo ($<10^{-6}$ mbar) using a lensed-fiber interferometer (*20*). As a consequence of their simple geometry, mode frequencies (inferred from thermal noise spectra; Fig. 3E) were found to agree well with a numerical solution to the 1D Euler-Bernoulli equation (*20*). Particularly striking is the sparse mode spectrum inside the band gap, visualized by compiling spectra of beams with different defect lengths (Fig. 3F). A single defect mode appears to move in and out of the band gap as the defect length is varied. This mode is expected to be localized and therefore to have a reduced effective mass m. Comparing the area under thermal noise peaks and estimating the physical beam mass to be $m_0 = 100$ pg, we infer that indeed $m \approx 5$ pg $<< m_0$ (*20*). This value is in good agreement with the mode profile obtained from the Euler-Bernoulli equation (Fig. 3G) and is smaller than that of an equivalent 2D localized mode by roughly two orders of magnitude.

In accordance with Eq. 3, we also observed a marked increase in the Q of localized modes. To

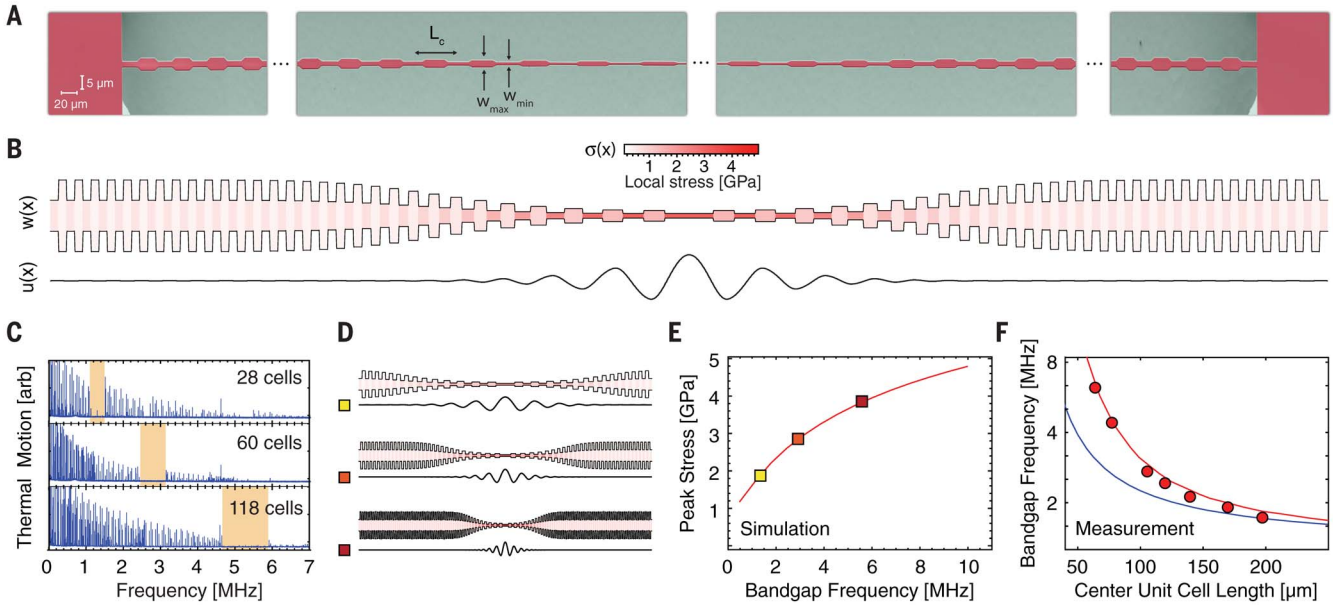

Fig. 2. Strain-engineered 1D phononic crystals. (**A**) Scanning electron microscopy (SEM) image of a tapered PnC nanobeam, vertically scaled for perspective. (**B**) Width/stress profile and defect mode shape of a device with 60 unit cells. (**C**) Thermal displacement spectrum of 4-mm-long devices. Band gaps are highlighted in orange. (**D**) Width/stress profiles of the devices in (C). (**E**) Simulation of peak stress versus band gap frequency f_{bg} for the devices shown in (D). (**F**) Measurements of f_{bg} versus length of the central unit cell (parameterizing the taper length). Red and blue lines are models with and without accounting for stress localization, respectively (see text).

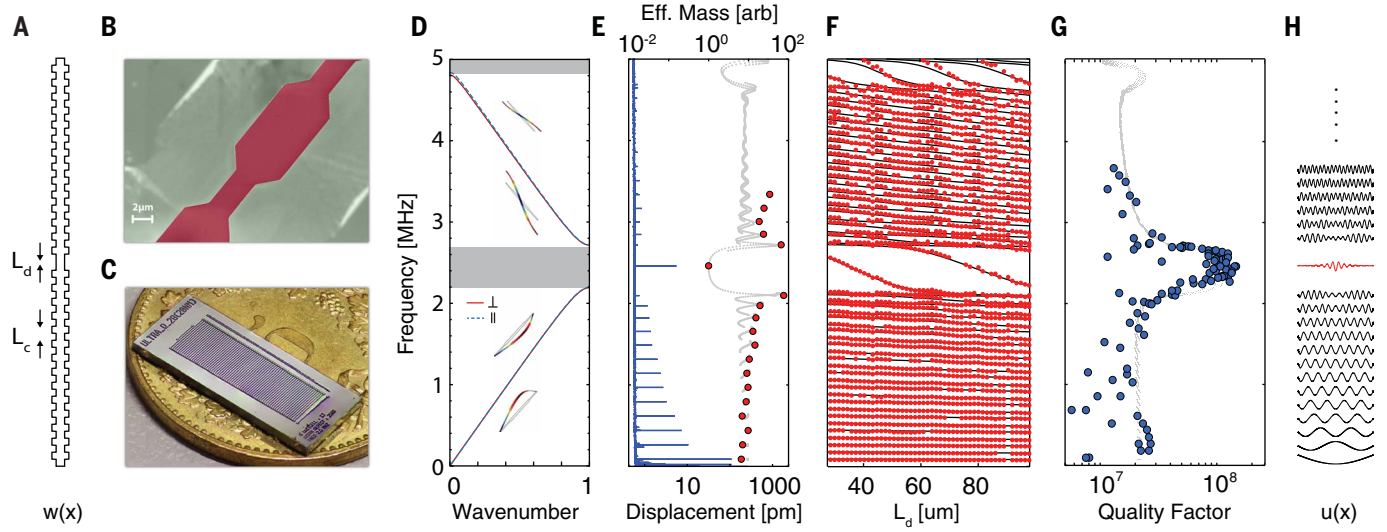

Fig. 3. "Soft-clamped" 1D nanomechanical resonators. (**A**) Schematic of a phononic crystal nanobeam with central defect. See text for details. (**B**) SEM image of a unit cell. (**C**) Optical image of a sample chip with 76 beams, each with a different defect length. (**D**) Band diagram showing in-plane (||) and out-of-plane (⊥) normal modes of a unit cell. (**E**) Displacement spectrum (blue) of a single beam, scaled to the theoretical root mean square thermal displacement of the defect mode, $\sqrt{k_B T/m_d(2\pi f)^2} \approx 6$ pm. Overlaid are effective mass coefficients m/m_d (red circles) inferred from the area beneath noise peaks. The gray curve is a model based on mode shapes in (H), used to estimate $m_d \approx 5$ pm (*20*). (**F**) Frequency spectra of multiple beams with different defect lengths. Black lines are a solution to the Euler-Bernoulli equation. (**G**) Compilation of Q measurements for a subset of the modes in (F), overlaid with a model based on Eq. 1. (**H**) Mode shapes obtained from the Euler-Bernoulli equation.

visualize this enhancement, we compiled measurements of Q versus mode frequency for 40 beams of different defect length (Fig. 3G). Outside the band gap, we find that $Q(f)$ is consistent with that of a uniform beam, asymptoting at low mode order ($n < \sim 20$) to $Q \approx 2 \times 10^7$, implying $Q_0 \approx 2\lambda Q \approx 1500$. Inside the band gap ($n \approx 26$), Q approaches that of an idealized clamp-free beam [$Q \approx Q_0/(\pi n\lambda)^2 \approx 10^8$]. The transition between these two regimes agrees well with a full model (gray dots in Fig. 3G) based on Eq. 1. In Fig. 4A we highlight the 19-s ringdown of a 2.46-MHz defect mode, corresponding to $Q = 1.5 \times 10^8$ and $Q \times f = 3.7 \times 10^{14}$ Hz.

Having established near-ideal soft-clamping of uniform nanobeams, we next studied the performance of strain-engineered (tapered) nanobeams. A set of 4- and 7-mm-long tapered PnC nanobeams was fabricated with the length of the taper varied so as to tune the stress at the center of the beam $\sigma(x_c)$ from 2 to 4 GPa (Fig. 2, D and E). We note that for our tapering strategy, the width of the beam center $w(x_c)$ is fixed, so that the stress is tuned by changing the equilibrium tension $\mathcal{T}$ (*20*). Moreover, for each taper length the soft-clamped mode is engineered to be well localized inside the thin taper region by tuning the pitch of unit cells. Measurements of band gap frequency f_{bg} versus length of the central unit cell length $L_{c,0}$ (parameterizing the taper length) corroborate enhanced stress through correspondence with the theoretical scaling $f_{bg} \propto \sqrt{\sigma(x_c)}/L_{c,0}$ (Fig. 2E).

The Q factors of uniform and tapered PnC nanobeams are compared in Fig. 4. Blue circles correspond to the measurements in Fig. 3G; red circles are compiled for localized modes of 4-mm-long tapered beams with various peak stresses, corresponding to $f_{bg} = 1$ to 6 MHz. According to a full model (*20*), $Q(f_{bg})$ should in principle trace out a line of constant $Q \times f \approx 10^{15}$ Hz, exceeding the clamp-free limit of a uniform beam ($Q \times f \propto 1/f$) for sufficiently high frequency. We observe this behavior with an unexplained ~30% reduction, with Q factors exceeding the clamp-free model by a factor of up to 3 and reaching absolute values high as 3×10^8. Although theoretically this Q should be accessible by soft-clamping alone at lower frequency, our strain-engineering strategy gives access to higher $Q \times f$, reaching a value as high as 8.1×10^{14} Hz for the 3.2-MHz mode of a 4-mm-long device. Higher Q and $Q \times f$ factors were achieved using longer beams (red squares in Fig. 4C). In Fig. 4A we highlight the 190-s ringdown of a 7-mm-long device excited in its 1.33-MHz defect mode, corresponding to $Q = 8.0 \times 10^8$ and $Q \times f = 1.1 \times 10^{15}$ Hz. We note that at this low damping rate ($f/Q \sim 1$ mHz), photothermal effects become important. Stroboscopic ringdowns (Fig. 4, A and B) confirm that photothermal damping contributes less than 5% uncertainty (*20*).

Realization of $Q \times f \sim 10^{15}$ in a mechanical oscillator with m on the order of picograms has numerous intriguing implications. First, such an oscillator is an exquisite force sensor. For example, localized modes of the beam outlined in Fig. 3 are limited by thermal noise to a sensitivity of $\sqrt{8\pi k_B T m f/Q} \approx 3(\mathrm{aN}/\sqrt{\mathrm{Hz}})$ at $f \sim 2.5$ MHz and $T = 300$ K. This value is on par with a typical atomic force microscope cantilever operating at a frequency and absolute temperature two orders of magnitude lower (*22*), creating new opportunities for applications such as high-speed force microscopy (*23*). Of practical importance is that the reported devices also exhibit an exceptionally strong thermal displacement of $\sqrt{k_B TQ/(4\pi^3 m f^3)} \sim \mathrm{nm}/\sqrt{\mathrm{Hz}}$, accessible by rudimentary detection techniques such as deflectometry. Indeed, their zero-point motion $\sqrt{\hbar Q/(2\pi^2 m f^2)} \sim \mathrm{pm}/\sqrt{\mathrm{Hz}}$ is orders of magnitude larger than the sensitivity of modern microcavity-based optical interferometers (*24*), offering possibilities in the field of quantum measurement and control (*25*). A fascinating prospect is to use measurement-based feedback to cool such an oscillator to its ground state from room temperature (*26*). A basic requirement is that the oscillator undergo a single oscillation in the thermal decoherence time $\hbar Q/k_B T$. The devices reported are exceptional in this respect, capable of performing $(2\pi Q \times f)/(k_B T/\hbar) > 100$ coherent oscillations at room temperature.

Looking forward, the performance of our devices seems far from exhausted. First, the dilution factors we have achieved are still an order of magnitude below the limit set by the yield stress of Si_3N_4. Our results may thus benefit from more aggressive strain engineering. [For example, Si microbridges have been fabricated with local stresses as high as 7.6 GPa (*14*).] We also emphasize that higher aspect ratios offer a direct route to higher Q. The aspect ratios of our longest beams ($L/h = 3.5 \times 10^5$) appear to be anomalously high for a suspended thin film, including 2D materials (*27*); however, Si_3N_4 membranes with centimeter-scale dimensions have recently been reported (*28*), hinting at a trend toward more extreme devices. Finally, we note that the source of intrinsic loss in our devices is unknown, although it is likely due to

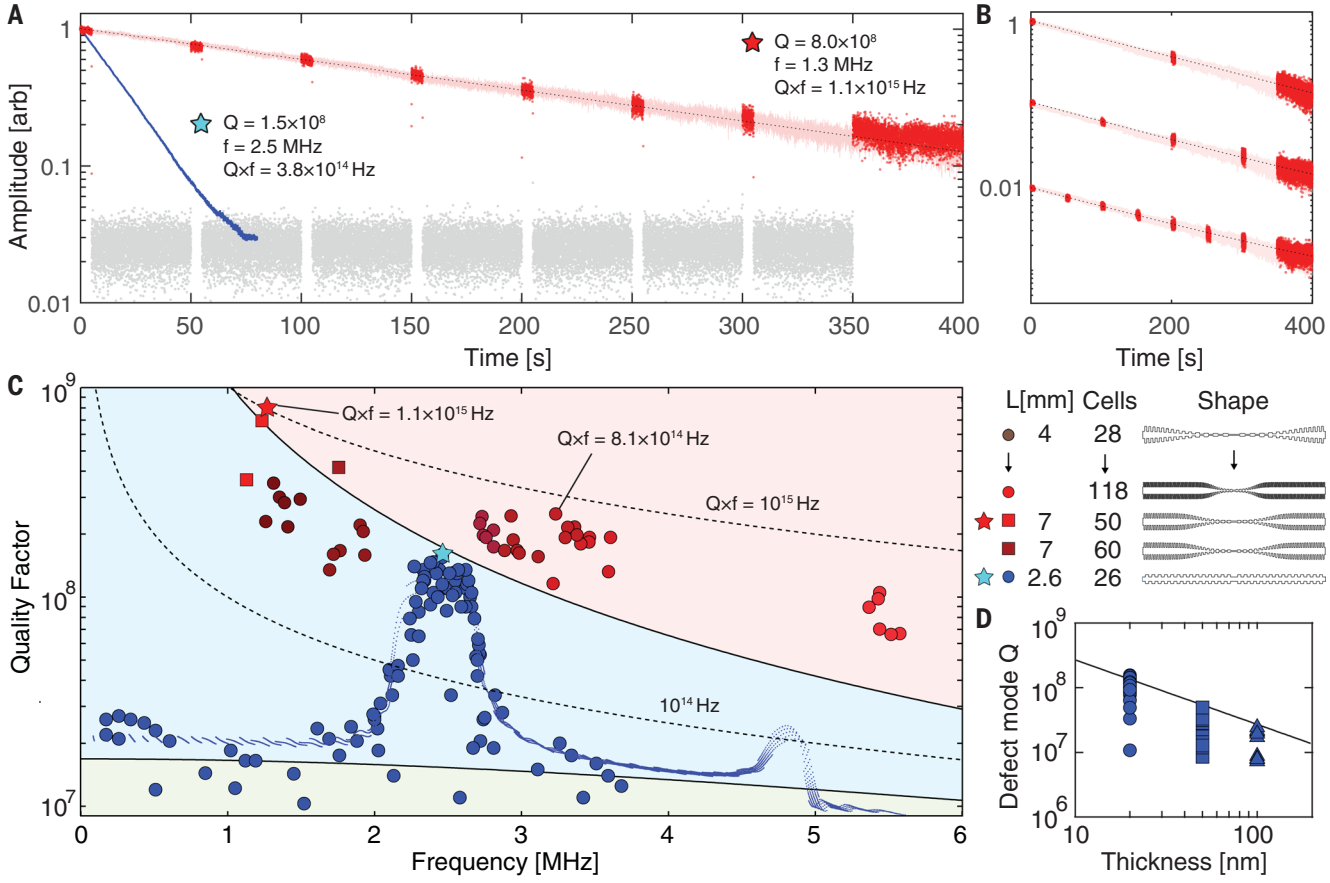

Fig. 4. Enhancing the quality factor of a soft-clamped nanobeam by strain engineering. (**A**) Interferometric ringdown of a 7-mm-long, 20-nm-thick tapered PnC nanobeam excited in its 1.33-MHz defect mode (pink). Dotted line is an exponential fit with a decay time of 190 s. The inferred Q of 8.0×10^8 is indicated by a red star in (C). Overlaid is a stroboscopic ringdown with measurement-on and measurement-off intervals in red and gray, respectively. (**B**) Fits to stroboscopic ringdowns with different duty cycles yield the same Q to within 5%, suggesting that photothermal damping is negligible. Also shown in (A) is a ringdown of a uniform PnC nanobeam [cyan star in (C)]. (**C**) Q versus mode frequency of PnC nanobeams with different geometries. Blue points correspond to modes of the uniform PnC nanobeam described in Fig. 3. Red points correspond to defect modes of tapered beams. Color groups include the highest five Q factors recorded for different beams. Blue dots are a numerical model based on Eq. 1. (**D**) Compilation of defect mode Q for uniform PnC nanobeams (Fig. 3) of different thickness. Overlaid is a model with $Q_0 = 6900 \cdot h/(100\ \text{nm})$, consistent with surface loss.

surface imperfections (*17*). To test this hypothesis, we compiled defect Qs for beams with thicknesses h = 20, 50, and 100 nm (Fig. 4D). The inferred thickness dependence of the intrinsic Q, $Q_0 \approx 6900 \cdot h/100$ nm, is indeed a signature of surface loss and agrees well in absolute terms with a recent meta-study on Si_3N_4 nanomechanical resonators (*17*). Remarkably, the $Q \propto Q_0/h^2$ scaling of soft-clamped resonators (*8*) preserves the advantage of thinner devices even in the presence of surface loss. It therefore seems appealing to apply our approach to epitaxially strained crystalline thin films (*29*), which can have Q_0 values two orders of magnitude larger than amorphous films at temperatures below 10 K (*30*).

REFERENCES AND NOTES

1. J. Li, Z. Shan, E. Ma, *MRS Bull.* **39**, 108–114 (2014).
2. J. Feng, X. Qian, C.-W. Huang, J. Li, *Nat. Photonics* **6**, 866–872 (2012).
3. P. Chidambaram, C. Bowen, S. Chakravarthi, C. Machala, R. Wise, *IEEE Trans. Electron Dev.* **53**, 944–964 (2006).
4. V. B. Braginsky, *Systems with Small Dissipation* (Univ. of Chicago Press, 1985).
5. G. I. González, P. R. Saulson, *J. Acoust. Soc. Am.* **96**, 207–212 (1994).
6. Q. P. Unterreithmeier, T. Faust, J. P. Kotthaus, *Phys. Rev. Lett.* **105**, 027205 (2010).
7. S. Schmid, K. D. Jensen, K. H. Nielsen, A. Boisen, *Phys. Rev. B* **84**, 165307 (2011).
8. Y. Tsaturyan, A. Barg, E. S. Polzik, A. Schliesser, *Nat. Nanotechnol.* **12**, 776–783 (2017).
9. D. R. Southworth *et al.*, *Phys. Rev. Lett.* **102**, 225503 (2009).
10. D. J. Wilson, C. A. Regal, S. B. Papp, H. J. Kimble, *Phys. Rev. Lett.* **103**, 207204 (2009).
11. S. Chakram, Y. S. Patil, L. Chang, M. Vengalattore, *Phys. Rev. Lett.* **112**, 127201 (2014).
12. D. Yu, J. Feng, J. Hone, *MRS Bull.* **39**, 157–162 (2014).
13. M. Süess *et al.*, *Nat. Photonics* **7**, 466–472 (2013).
14. R. A. Minamisawa *et al.*, *Nat. Commun.* **3**, 1096 (2012).
15. A. Castellanos-Gomez *et al.*, *Nano Lett.* **13**, 5361–5366 (2013).
16. P.-L. Yu, T. P. Purdy, C. A. Regal, *Phys. Rev. Lett.* **108**, 083603 (2012).
17. L. G. Villanueva, S. Schmid, *Phys. Rev. Lett.* **113**, 227201 (2014).
18. A. H. Ghadimi, D. J. Wilson, T. J. Kippenberg, *Nano Lett.* **17**, 3501–3505 (2017).
19. R. Zhang *et al.*, *Appl. Phys. Lett.* **107**, 131110 (2015).
20. See supplementary materials.
21. J. Chan, A. H. Safavi-Naeini, J. T. Hill, S. Meenehan, O. Painter, *Appl. Phys. Lett.* **101**, 081115 (2012).
22. M. Poggio, C. L. Degen, H. J. Mamin, D. Rugar, *Phys. Rev. Lett.* **99**, 017201 (2007).
23. M. Poggio, C. L. Degen, *Nanotechnology* **21**, 342001 (2010).
24. M. Aspelmeyer, T. J. Kippenberg, F. Marquardt, *Rev. Mod. Phys.* **86**, 1391–1452 (2014).
25. D. J. Wilson *et al.*, *Nature* **524**, 325–329 (2015).
26. Y.-C. Liu *et al.*, *Phys. Rev. A* **91**, 013824 (2015).
27. R. A. Barton *et al.*, *Nano Lett.* **11**, 1232–1236 (2011).
28. J. P. Moura, R. A. Norte, J. Guo, C. Schäfermeier, S. Gröblacher, arXiv:1707.08128 [physics.optics] (25 July 2017).
29. G. D. Cole *et al.*, *Appl. Phys. Lett.* **104**, 201908 (2014).
30. G. D. Cole, W. Zhang, M. J. Martin, J. Ye, M. Aspelmeyer, *Nat. Photonics* **7**, 644–650 (2013).

ACKNOWLEDGMENTS

We thank H. Schütz and E. Mansouri for valuable contributions during the initial phase of the experiment. **Funding:** Supported by the EU Horizon 2020 Research and Innovation Program under grant agreement 732894 (FET Proactive HOT) and the SNF Cavity Quantum Optomechanics project (grant 163387); MSCA ETN-OMT grant 722923 (M.J.B.); ERC AdG QuREM grant 320966 (T.J.K.); and DARPA seedling grant HR0011181003. All samples

were fabricated at the Center for MicroNanoTechnology (CMi) at EPFL. **Author contributions:** Device design and simulation was led by A.H.G. and S.A.F. with early support from R.S.; devices were fabricated by A.H.G. and M.J.B.; S.A.F. developed the semi-analytical model; all authors contributed to measurements and/or development of the experimental apparatus; data analysis was led by N.J.E., S.A.F., and D.J.W. with support from A.H.G. and M.J.B.; the manuscript was initially drafted by D.J.W. and S.A.F. with support from N.J.E.; D.J.W., S.A.F., N.J.E., A.H.G., M.J.B., and T.J.K. all participated in editing of the final manuscript and supporting information; and D.J.W. and T.J.K. supervised the project. **Competing interests:** None declared. **Data and materials availability:** Data and data analysis code are available through Zonedo at doi:10.5281/zenodo.1202322. All other data needed to evaluate the conclusions in the paper are present in the paper or the supplementary materials.

SUPPLEMENTARY MATERIALS

www.sciencemag.org/content/360/6390/764/suppl/DC1
Supplementary Text
Figs. S1 to S12

8 December 2017; accepted 28 March 2018
Published online 12 April 2018
10.1126/science.aar6939

LIQUID CRYSTALS

Hybrid molecular-colloidal liquid crystals

Haridas Mundoor,[1] Sungoh Park,[1] Bohdan Senyuk,[1] Henricus H. Wensink,[2] Ivan I. Smalyukh[1,3,4]*

Order and fluidity often coexist, with examples ranging from biological membranes to liquid crystals, but the symmetry of these soft-matter systems is typically higher than that of the constituent building blocks. We dispersed micrometer-long inorganic colloidal rods in a nematic liquid crystalline fluid of molecular rods. Both types of uniaxial building blocks, while freely diffusing, interact to form an orthorhombic nematic fluid, in which like-sized rods are roughly parallel to each other and the molecular ordering direction is orthogonal to that of colloidal rods. A coarse-grained model explains the experimental temperature-concentration phase diagram with one biaxial and two uniaxial nematic phases, as well as the orientational distributions of rods. Displaying properties of biaxial optical crystals, these hybrid molecular-colloidal fluids can be switched by electric and magnetic fields.

A vast variety of anisotropic building blocks, such as organic molecules, filamentous viruses, and graphene flakes, self-organize to form nematic liquid crystals (NLCs) (*1*). NLCs can flow because of the lack of correlation in positions of their freely diffusing building blocks, such as rodlike molecules (*1*). However, the long-range average orientational order of such rods along a direction dubbed "director" yields anisotropic properties typically associated with crystalline solids (*1*). These nonpolar uniaxial NLCs exhibit the $D_{\infty h}$ point group symmetry, but fluidity and order could also coexist in fundamentally different ways (*1*). The most sought-after structures are orthorhombic, optically biaxial NLCs, which were envisaged as nematic fluids of brick-shaped building blocks (*2*), with long-range orientational order of both long and short axes of the bricks along the mutually orthogonal directors. Most strategies to realize such NLCs in micellar (*3*), small-molecule (*4*), polymeric (*5*), colloidal (*6*), and other systems (*7*) relied on the designs of bricklike and other biaxial building blocks. We show that such biaxial NLCs can be formed by rodlike building blocks in a hybrid molecular-colloidal soft-matter system.

Small-molecule NLCs are often used as host media to form colloidal dispersions (*8*). However, colloidal particles are typically spheres or weakly shape-anisotropic rods and discs treated to induce strong boundary conditions to harness the elastic interactions for self-assembly with well-defined relative positions and orientations of anisotropic inclusions coupled to the nematic director (*9*–*11*). We used bare, charged inorganic colloidal nanorods with high aspect ratios; these nanorods spontaneously form their own nematic states when dispersed in both isotropic and nematic phases of the NLC host. The average direction of ordering of nanorods is orthogonal to that of the small molecules in the nematic phase (Fig. 1). Analytical modeling of interactions between colloidal rods and the anisotropic molecular interactions at their surfaces explains the temperature-concentration phase diagram and experimental orientational distributions in the hybrid molecular-colloidal NLC. Within the orthorhombic phase, owing to anisotropic interactions, the molecular host induces a biaxial orientational distribution of the nanorods, which, in turn, induce biaxiality in the molecular host.

Hydrothermally synthesized (*12*) nanorods were pre-engineered for luminescence-based imaging of their orientations (*13*). The rods were treated with hydrochloric acid to achieve a length-to-diameter aspect ratio between 40 and 110 via slow etching (Fig. 1, B and C, and fig. S1) and then dispersed in a pentylcyanobiphenyl (5CB) NLC (*13*). These dispersions were infiltrated into glass cells (about 2.5 cm by 2.5 cm) with 10- to 60-μm gap thickness or rectangular capillaries (0.2 mm by 2.0 mm). Monodomain NLC samples were obtained by treating the inner surfaces of cells and capillaries for perpendicular or tangential boundary conditions for the director $\mathbf{n}_m$ describing the average orientation of molecules. Gravity and electrophoresis were used to concentrate nanorods (*13*). Within dispersions, surfaces of bare nanorods spontaneously induced weak perpendicular boundary conditions for $\mathbf{n}_m$. Surface charging of individual nanorods was controlled within $Z^*e \approx +(50 \text{ to } 250)e$ (where e is the elementary charge and Z^* is the number of effective elementary charges on a nanorod's surface) and characterized by probing the electrophoretic mobility of the rods. Debye screening length (ξ_D) in the nonpolar 5CB NLC was varied from 0.1 to 2.1 μm. Phase diagrams for $\xi_D \approx 120$ nm and $Z^*e \approx +250e$ (*13*) showed no dependence on capillary or cell dimensions.

Nanorods tend to orient orthogonally to $\mathbf{n}_m$ (Fig. 1). They induce weak elastic distortions of molecular alignment, in contrast to microparticles (*11*, *14*), which induce bulk defects, but similar to other nanoparticles with soft perpendicular surface boundary conditions (*15*, *16*) (Fig. 1D and fig. S2). To minimize the overall free energy, elastic distortions compete with the cost of deviations of $\mathbf{n}_m$ away from the local perpendicular boundary conditions at the particles' surfaces (Fig. 1D) (*13*). The biaxial molecular-colloidal NLC (Fig. 1, A to E) arises from the host-mediated electrostatic and elastic interactions between nanorods at modestly high colloidal volume fractions ϕ_c, which spontaneously select the direction of colloidal ordering $\mathbf{n}_c$ from a manifold of orientations defined by a plane orthogonal to $\mathbf{n}_m$. In a cell with $\mathbf{n}_m$ orthogonal to substrates (Fig. 1, E to G), $\mathbf{n}_c$ spontaneously aligns parallel to substrates and its orientation can be controlled by electric and magnetic fields. In a cell with in-plane $\mathbf{n}_m$, $\mathbf{n}_c$ spontaneously aligns orthogonally to substrates (Fig. 1H) but can be switched to the in-plane orientation orthogonal to $\mathbf{n}_m$ by a 50- to 100-mT magnetic field normal to the substrates (Fig. 1I) (*13*). Rotation of samples placed between crossed polarizers around $\mathbf{n}_m$ yields minima of transmitted intensity when $\mathbf{n}_c$ is either parallel or perpendicular to crossed polarizers (Fig. 1F) and a maximum when $\mathbf{n}_c$ is at 45° (Fig. 1G). Rotation around $\mathbf{n}_c$ yields minima of transmitted intensity when $\mathbf{n}_m$ is parallel or perpendicular to polarizers (Fig. 1J) and a maximum when $\mathbf{n}_m$ is at 45° (Fig. 1K). Luminescence imaging (Fig. 1, E, H, and I, and movies S1 and S2) reveals that nanorods freely diffuse while exhibiting orientational order but no positional order (Fig. 1A).

The biaxial D_{2h} orthorhombic symmetry of our molecular-colloidal NLC is characterized by a triplet of directors: $\mathbf{n}_m$, $\mathbf{n}_c$, and $\mathbf{n}_\perp$ orthogonal to both $\mathbf{n}_m$ and $\mathbf{n}_c$ (Fig. 2). Nanorods are uniaxial solid nanocrystals with an optical axis along their long axis and extraordinary and ordinary refractive indices $N_{ec} = 1.46$ and $N_{oc} = 1.49$ (*17*). In the absence of colloidal inclusions, the molecular host is also a uniaxial crystal with indices $N_{em} = 1.74$ and $N_{om} = 1.54$ (*18*). However, the molecular-colloidal composite NLC is a biaxial optical crystal with three principal refractive indices and an optical indicatrix (Fig. 2B). These emergent properties arise both from the orthogonal alignment of $\mathbf{n}_m$ and $\mathbf{n}_c$ and also from the low symmetry of orientational distributions of molecular and colloidal rods due to anisotropic interactions between them (e.g., colloidal rods locally perturb orientations of molecular rods, as shown in Figs. 1D and 2A). Using a Berek compensator inserted between crossed polarizers after the NLC in the geometries depicted in Fig. 1, G and K, we measured the two characteristic optical anisotropies of the biaxial NLC at different ϕ_c:

[1]Department of Physics and Soft Materials Research Center, University of Colorado, Boulder, CO 80309, USA. [2]Laboratoire de Physique des Solides, CNRS, Université Paris-Sud, Université Paris-Saclay, 91405 Orsay, France. [3]Department of Electrical, Computer, and Energy Engineering, Materials Science and Engineering Program, University of Colorado, Boulder, CO 80309, USA. [4]Renewable and Sustainable Energy Institute, National Renewable Energy Laboratory and University of Colorado, Boulder, CO 80309, USA.
*Corresponding author. Email: ivan.smalyukh@colorado.edu

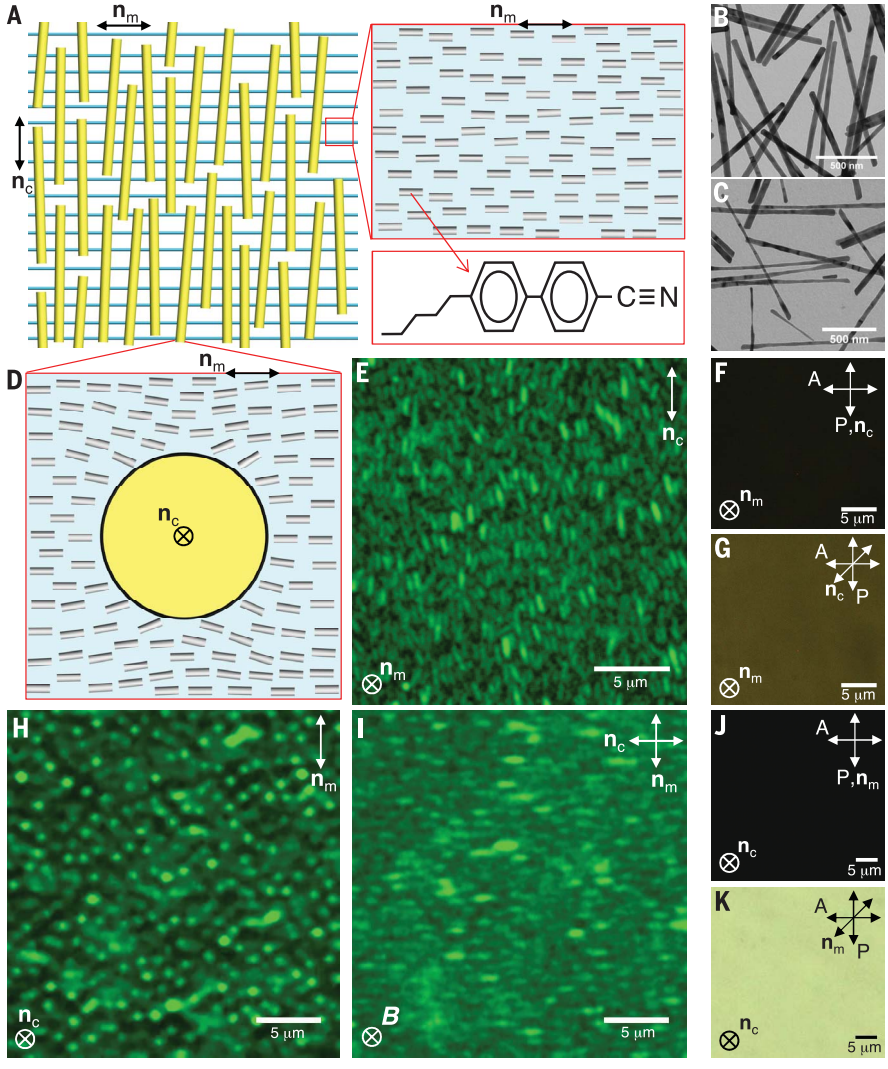

Fig. 1. Structure and characterization of an orthorhombic biaxial NLC. (**A**) Schematic representation of the hybrid molecular-colloidal NLC, with the insets showing (top right) molecular ordering and (bottom right) chemical structure of a 5CB molecule. (**B** and **C**) Transmission electron micrographs of nanorods (B) before and (C) after acid treatment. (**D**) Schematic representation of distortions of the molecular alignment around a nanorod with soft perpendicular boundary conditions. (**E**) Upconversion-based luminescence confocal microscopy image of the nanorods, showing their alignment along $\mathbf{n}_c$, orthogonal to $\mathbf{n}_m$. (**F** and **G**) Polarizing optical micrographs of a biaxial NLC between crossed polarizer P and analyzer A when $\mathbf{n}_c$ is at (F) 0° and (G) 45° with respect to P. (**H** and **I**) Confocal luminescence images of nanorods in a biaxial NLC when the particles are (H) aligned perpendicular to $\mathbf{n}_m$ and then (I) switched with a magnetic field **B** applied perpendicular to $\mathbf{n}_m$ and substrates. (**J** and **K**) Polarizing optical micrograph of a biaxial NLC viewed between crossed polarizers when $\mathbf{n}_m$ is at (J) 0° and (K) 45° with respect to P.

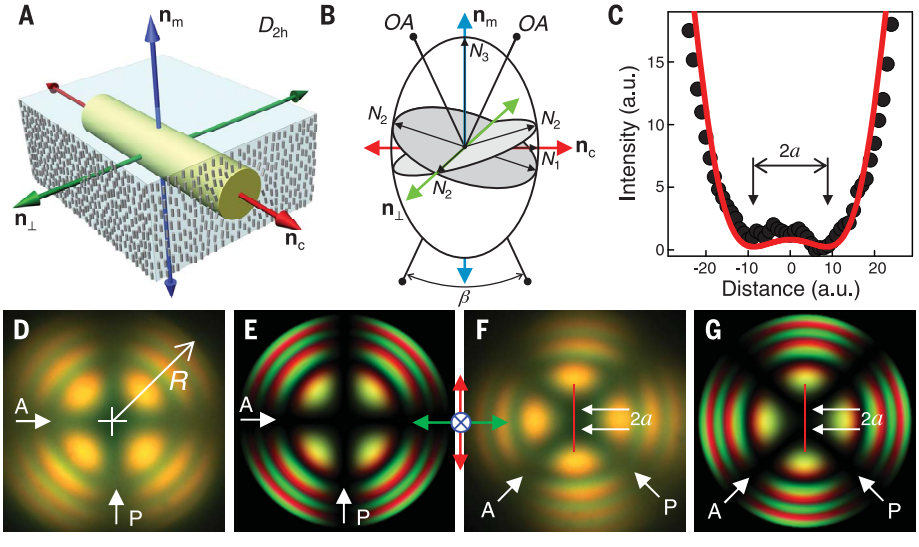

Fig. 2. Optical properties and conoscopic images of a biaxial NLC. (**A**) Schematic representation of a coarse-grained building block of the NLC formed by a nanorod in a molecular nematic host. Three double arrows (red, green, and blue) depict the triplet of directors. (**B**) Optical indicatrix of a biaxial NLC with orthorhombic symmetry. The optical axes, at an angle β to each other, are designated "OA" and confined to the plane formed by $\mathbf{n}_c$ and $\mathbf{n}_m$. (**C**) Experimental (black circles) and computer-simulated (red line) intensity profiles along the red lines in the conoscopy images shown in (F) and (G), respectively. a.u., arbitrary units. (**D** to **G**) Conoscopy images obtained experimentally [(D) and (F)] and via computer simulations [(E) and (G)] for the orientations of the plane containing the two optical axes parallel to the polarizer P [(D) and (E)] and at 45° to it [(F) and (G)], as marked on the images. A, analyzer. The ratio $a/R \approx 0.059$ (where $2a$ is the closest distance between split isogyres and R is the radius of the conoscopic image) obtained from the images is consistent with refractive index measurements (*13*).

$\Delta N_{21} = N_2 - N_1 = (0.4 \text{ to } 1.1) \times 10^{-3}$ and $\Delta N_{31} = N_3 - N_1 \approx 0.2$. Values of $\Delta N_{31} >> \Delta N_{21}$ are common for biaxial optical crystals in both solid-state (*19*) and soft-matter (*7*, *20*) systems, where typical biaxial birefringence is ~10^{-3}. Experimental conoscopic images, produced by optical interference of diverging light rays traveling through a biaxial NLC (*19*), match the ones simulated with the use of separately measured ΔN_{21} and ΔN_{31} (Fig. 2, D to G). For $\mathbf{n}_m$ along the microscope's axis and the NLC's plane containing optical axes oriented at 45° to the crossed polarizers, conoscopic patterns of birefringent colors display splitting of dark bands (isogyres) characteristic of biaxial crystals (Fig. 2, C, F, and G) (*7*, *19*), producing an estimate of the angle $\beta \approx 5.9°$ between the optical axes.

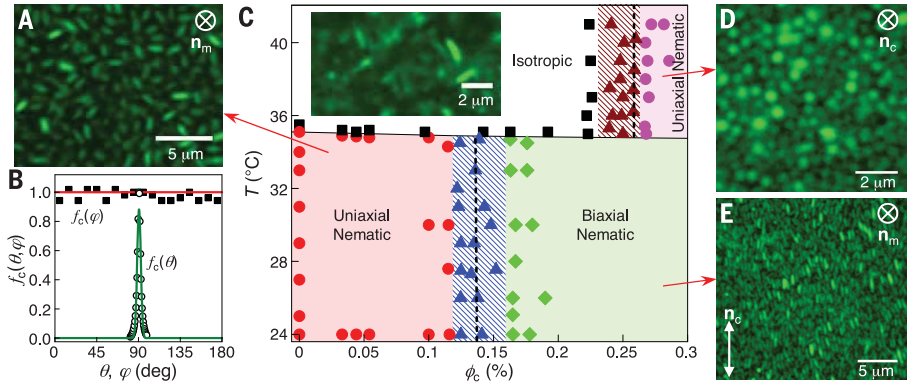

Fig. 3. Phase diagram of a hybrid molecular-colloidal NLC. (**A**) Confocal luminescence image of nanorods in 5CB at $\phi_c \approx 0.054\%$ at room temperature. (**B**) $f_c(\theta, \varphi)$ versus θ and φ at $\phi_c \approx 0.025\%$, obtained by normalizing the maximum values of functions that fit experimental distributions. (**C**) Phase diagram of the hybrid molecular-colloidal system exhibiting uniaxial nematic, isotropic, biaxial nematic, and colloidal uniaxial phases. The inset is a confocal luminescence image of nanorods in a disordered state at $\phi_c \approx 0.1\%$ and T = 38°C. Red arrows indicate confocal luminescence images corresponding to different parts of the diagram. Dashed vertical lines denote theoretical predictions for ϕ_{cUB} and ϕ_{cIN}. (**D**) Confocal luminescence image of the colloidal uniaxial nematic state formed by nanorods at $\phi_c \approx 0.272\%$ and T = 40°C. (**E**) Confocal luminescence image showing nanorods in the biaxial phase at $\phi_c \approx 0.172\%$ at room temperature.

We separately characterize orientational distribution functions $f_{c,m}$ that quantify probabilities of different orientations of colloids and molecules (denoted by "c" and "m") (Fig. 4). From the experimental $f_{c,m}$, we extract order parameters $S_{c,m}$ and $\Delta_{c,m}$ associated with colloidal and molecular rods to quantify their degree of ordering and biaxiality, respectively

$$S_{c,m} = \int_0^{2\pi} d\varphi \int_{-1}^{1} d(\cos\theta) f_{c,m}(\theta, \varphi) P_2(\cos\theta) \quad (1)$$

$$\Delta_{c,m} = \int_0^{2\pi} d\varphi \int_{-1}^{1} d(\cos\theta) f_{c,m}(\theta, \varphi) D(\theta, \varphi) \quad (2)$$

where θ and φ are polar and azimuthal angles, respectively, describing molecular or colloidal orientations defined with respect to $\mathbf{n}_m$; $P_2(\cos\theta) = \frac{1}{2}(3\cos^2\theta - 1)$; and $D(\theta, \varphi) = \sin^2\theta\cos 2\varphi$. Using polarized Raman spectroscopy (fig. S3), we find that S_m in the biaxial phase is slightly lower than S_m of pristine 5CB (Fig. 4A). Moreover, the nanorod-induced biaxiality Δ_m = 0.01 to 0.04 shows a trend of increasing with T, opposite to that of S_m, though both parameters abruptly drop to zero at T^* (Fig. 4A). These findings are consistent with polarized three-photon-absorption–based fluorescence from the biphenyl groups of molecules characterized for both pure 5CB and the biaxial phase of the hybrid NLC (fig. S4). Direct luminescence imaging of nanorods

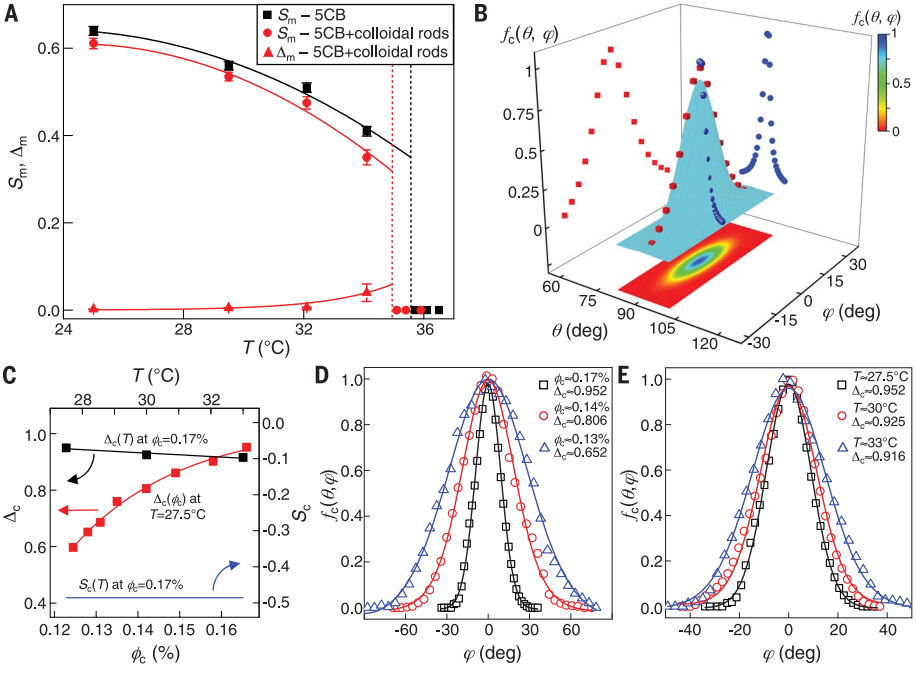

Fig. 4. Order parameters and orientational distributions. (**A**) S_m versus T for pure 5CB (black squares) and S_m (red circles) and Δ_m (red triangles) for a biaxial phase at $\phi_c = 0.17\%$ characterized by using Raman spectroscopy (*13*). (**B**) $f_c(\theta, \varphi)$ versus angles θ (blue symbols) and φ (red symbols) describing orientations of nanorods in a biaxial phase at $\phi_c = 0.176\%$ and T = 27.5°C. (**C**) Dependencies of Δ_c (black squares) and S_c (blue curve) on temperature at $\phi_c = 0.17\%$ and variation of Δ_c (red squares) with ϕ_c at room temperature. Arrows indicate the vertical axes corresponding to the curves. (**D**) $f_c(\theta, \varphi)$ versus φ at room temperature and $\phi_c = 0.17\%$ (black squares), 0.14% (red circles), and 0.13% (blue triangles). (**E**) $f_c(\theta, \varphi)$ versus φ at $\phi_c = 0.17\%$ and T = 27.5°C (black squares), 30°C (red circles), and 33°C (blue triangles).

reveals their biaxial orientational distributions at different T and ϕ_c (Fig. 4, B to E), as well as facile electric and magnetic switching of $\mathbf{n}_c$ (fig. S5). In the vicinity of ϕ_{cUB}, we detected only small changes of $S_c \approx -0.49$ but find that Δ_c jumps from zero to ≈0.6 at $\phi_c \approx 0.12\%$ (in the beginning of the two-phase coexistence) and then increases with ϕ_c to ≈0.95 at $\phi_c > 0.16\%$ in the biaxial phase (Fig. 4C). Orientational distribution functions are biaxial for both molecular and colloidal rods, though biaxiality of colloidal ordering is much stronger than the weak induced biaxiality in molecular ordering (Fig. 4). The biaxial NLC is not merely a superposition of two uniaxial nematic molecular and colloidal states with orthogonal ordering directions. Anisotropic molecular interactions at interfaces of orientationally ordered nanorods lift the uniaxial symmetry of molecular order and, simultaneously, induce biaxiality in the distribution of colloidal nanorod orientations. Tensorial order parameters describing this behavior of molecules and colloids, $\mathbf{Q}_{m,c} = \mathrm{diag}\{S_{m,c}, (\Delta_{m,c} - S_{m,c})/2, -(\Delta_{m,c} + S_{m,c})/2\}$, determine physical properties—such as the optical anisotropies characterized in Figs. 1 and 2—of the biaxial NLC.

Nematic order of pure 5CB emerges from anisotropic van der Waals interactions between molecules (*1*), which are barely affected by the addition of nanorods, so that T^* decreases by only ~1°C with increasing $\phi_c < 0.3\%$ (Fig. 3C). The isotropic-nematic transition of charged nanorods with an effective aspect ratio l_{eff} upon increasing ϕ_c at $T > T^*$ due to electrostatic-modified steric interactions is also well understood (*21*, *22*). Above $\phi_{cIN} \approx 4/l_{eff}$, consistent with the Onsager's theory, this order emerges upon maximizing the overall entropy of nanorods, which (despite lowering the number of states associated with rotational degrees of freedom) corresponds to an orientationally ordered state with low excluded volume and, thus, a large number of positional states accessible to nanorods. At $T < T^*$ and $\phi_c > \phi_{cUB}$, nanorods align with long axes, on average, orthogonal to $\mathbf{n}_m$ to minimize the free energy of the molecular nematic host (*23*, *24*). The scalar order parameter $S_c \approx -0.49$ (*13*), obtained from the experimental orientational distribution, is consistent with a model describing the anisotropic orientational distribution of nanorods in the presence of an aligning potential due to the nematic host (*23*, *24*). By bringing individual nanorods within highly dilute dispersions near each other using laser tweezers, we find that they interact repulsively (fig. S6 and movie S4), showing no correlations in terms of their relative positions or orientations, which suggests that the colloidal ordering along $\mathbf{n}_c$ at $\phi_c > \phi_{cUB}$ emerges from Onsager-type collective behavior, though modified by direct interactions of nanorods with the nematic host and electrostatic repulsions. Because nanorod orientations in a molecular nematic host are effectively constrained to the plane orthogonal to $\mathbf{n}_m$, their degrees of freedom are reduced compared with those of isotropic hosts, so that ordering along $\mathbf{n}_c$ emerges at $\phi_{cUB} < \phi_{cIN}$ (Fig. 3C). For nanorods with soft boundary conditions, the orientational distribution function f_c derived using these assumptions reads (*13*)

$$f_c(\theta, \varphi) \propto \exp\left[\left(\frac{5}{4}\phi_c l_{eff} S_c - \sigma\right) P_2(\cos\theta)\right] \times \left[1 + \frac{15}{16}\phi_c l_{eff} \Delta_c D(\theta, \varphi)\right] \quad (3)$$

where σ is a dimensionless parameter describing the strength of nanorod interaction with the molecular nematic host. The order parameters S_c and Δ_c are determined from fitting experimental data (Fig. 4B). This yields Onsager-type ordering along $\mathbf{n}_c$ at $\phi_{cUB} \approx 32[1 + 2/(3\sigma)]/(15 l_{eff})$. Since σ is large even in the limit of weak boundary conditions on nanorod surfaces, $\phi_{cUB} \approx 32/(15 l_{eff})$, so that $\phi_{cIN}/\phi_{cUB} \approx 1.9$. Despite many assumptions and neglecting the anisotropy of dielectric constants within the NLC, which modifies electrostatic interactions, the prediction $\phi_{cIN}/\phi_{cUB} \approx 1.9$ and the values of ϕ_{cIN} and ϕ_{cUB} agree with those experimentally determined for independently measured Z^*e, ξ_D, and other parameters (Fig. 3C and figs. S7 to S9) (*25*, *26*).

We have described a hybrid molecular-colloidal soft-matter system with orthorhombic biaxial orientational order and fluidity. Formed solely from uniaxial rodlike building blocks, this molecular-colloidal complex fluid features an unexpected self-organization into a biaxial NLC with the D_{2h} point group symmetry.

REFERENCES AND NOTES

1. P. M. Chaikin, T. C. Lubensky, *Principles of Condensed Matter Physics* (Cambridge Univ. Press, 1995).
2. M. J. Freiser, *Phys. Rev. Lett.* **24**, 1041–1043 (1970).
3. L. J. Yu, A. Saupe, *Phys. Rev. Lett.* **45**, 1000–1003 (1980).
4. B. R. Acharya, A. Primak, S. Kumar, *Phys. Rev. Lett.* **92**, 145506 (2004).
5. K. Severing, K. Saalwächter, *Phys. Rev. Lett.* **92**, 125501 (2004).
6. E. van den Pol, A. V. Petukhov, D. M. E. Thies-Weesie, D. V. Byelov, G. J. Vroege, *Phys. Rev. Lett.* **103**, 258301 (2009).
7. G. R. Luckhurst, T. J. Sluckin, Eds., *Biaxial Nematic Liquid Crystals: Theory, Simulation and Experiment* (Wiley, 2015).
8. P. Poulin, H. Stark, T. C. Lubensky, D. A. Weitz, *Science* **275**, 1770–1773 (1997).
9. H. Mundoor, B. Senyuk, I. I. Smalyukh, *Science* **352**, 69–73 (2016).
10. Q. Liu, Y. Yuan, I. I. Smalyukh, *Nano Lett.* **14**, 4071–4077 (2014).
11. T. C. Lubensky, D. Pettey, N. Currier, H. Stark, *Phys. Rev. E* **57**, 610–625 (1998).
12. L. Wang, Y. Li, *Chem. Mater.* **19**, 727–734 (2007).
13. Materials and methods are available as supplementary materials.
14. B. Senyuk *et al.*, *Nature* **493**, 200–205 (2013).
15. R. W. Ruhwandl, E. M. Terentjev, *Phys. Rev. E* **56**, 5561–5565 (1997).
16. V. Tomar *et al.*, *Langmuir* **28**, 6124–6131 (2012).
17. D. Knowles, A. Cassanho, H. P. Jenssen, in *OSA Proceedings on Tunable Solid State Lasers*, M. L. Shand, H. P. Jenssen, Eds. [OSA Proceedings Series, Optical Society of America (OSA), 1989], vol. 5, pp. 139–145.
18. P. G. de Gennes, J. Prost, *The Physics of Liquid Crystals* (Clarendon Press, ed. 2, 1993).
19. E. E. Wahlstrom, *Optical Crystallography* (Wiley, ed. 4, 1969).
20. Y. Galerne *et al.*, *J. Chem. Phys.* **84**, 1732–1734 (1986).
21. L. Onsager, *Ann. N. Y. Acad. Sci.* **51**, 627–659 (1949).
22. G. J. Vroege, H. N. W. Lekkerkerker, *Rep. Prog. Phys.* **55**, 1241–1309 (1992).
23. Q. Liu *et al.*, *Phys. Rev. E* **89**, 052505 (2014).
24. Q. Liu *et al.*, *Phys. Rev. Lett.* **109**, 088301 (2012).
25. S. K. Sainis, J. W. Merrill, E. R. Dufresne, *Langmuir* **24**, 13334–13337 (2008).
26. A. Yethiraj, A. van Blaaderen, *Nature* **421**, 513–517 (2003).

ACKNOWLEDGMENTS

We thank P. Davidson, B. Fleury, Q. Liu, T. Lubensky, and L. Radzihovsky for discussions and technical assistance. **Funding:** This research was supported by the U.S. Department of Energy, Office of Basic Energy Sciences, Division of Materials Sciences and Engineering, under award ER46921, contract DE-SC0010305 with the University of Colorado at Boulder. **Author contributions:** H.M., S.P., B.S., and I.I.S. performed experiments and analyzed data. H.H.W. and I.I.S. developed theoretical models describing molecular-colloidal interactions and phase behavior. H.H.W. performed numerical calculations. I.I.S. conceived of the project, designed experiments, acquired funding, and wrote the manuscript, with the input from all authors. **Competing interests:** The authors declare no competing interests. **Data and materials availability:** All data are reported in the main text and supplementary materials.

SUPPLEMENTARY MATERIALS

www.sciencemag.org/content/360/6390/768/suppl/DC1
Materials and Methods
Figs. S1 to S9
Additional Data
References (*27*–*34*)
Movies S1 to S4
Data for Figure Plots

12 September 2017; accepted 13 April 2018
10.1126/science.aap9359

INORGANIC MATERIALS

Extraordinary plasticity of an inorganic semiconductor in darkness

Yu Oshima,[1] Atsutomo Nakamura,[1]* Katsuyuki Matsunaga[1,2]*

Inorganic semiconductors generally tend to fail in a brittle manner. Here, we report that extraordinary "plasticity" can take place in an inorganic semiconductor if the deformation is carried out "in complete darkness." Room-temperature deformation tests of zinc sulfide (ZnS) were performed under varying light conditions. ZnS crystals immediately fractured when they deformed under light irradiation. In contrast, it was found that ZnS crystals can be plastically deformed up to a deformation strain of ε_t = 45% in complete darkness. In addition, the optical bandgap of the deformed ZnS crystals was distinctly decreased after deformation. These results suggest that dislocations in ZnS become mobile in complete darkness and that multiplied dislocations can affect the optical bandgap over the whole crystal. Inorganic semiconductors are not necessarily intrinsically brittle.

Development of shapeable high-strength materials has been essential to the improvement of advanced civilizations. Therefore, from an historical perspective, we have a broad interest in how materials deform and why materials exhibit failure. Inorganic semiconducting materials tend to fail in a brittle manner when subjected to an external force exceeding their fracture strength (*1*, *2*). The brittleness is generally thought to originate from strong ionic and/or directional covalent bonds of inorganic semiconductors. However, easily shapeable strong and tough inorganic semiconductors are required as smart electronic components in a variety of electronic applications are becoming increasingly important (*2*–*4*). Because the poor mechanical properties of inorganic semiconductors limit their application range, it is of interest to understand how such materials deform and why they exhibit brittle failure. The plastic deformation properties of crystalline inorganic materials are controlled by motion of dislocations, which are topological line defects in crystals (*5*). Recently, dislocations have become of interest because they can be used to induce characteristic functional properties that are not found in bulk (*6*–*10*). On the other hand, fracture properties of crystalline materials are controlled by nucleation and extension of microcracks.

Electrons and holes can be excited in semiconducting materials when irradiated using light having the appropriate wavelength (*11*). These photoexcited electrons and holes will in turn affect the electrical properties of semiconducting materials, which then can exhibit electric conductivity. However, little is known about the influence of light irradiation on the brittle character of semiconducting materials. In particular, plasticity (*12*, *13*) in complete darkness without light exposure has not been taken into consideration so far. This paper focused on the mechanical strength and fracture properties in complete darkness concerning the cubic form of sphalerite ZnS, a representative II-VI semiconductor. This is in part because large-size single crystals suitable for deformation tests are readily available for ZnS. ZnS is used as a luminescent material (*14*), an infrared optical material (*15*), and a photocatalyst (*16*) due to its electric and optical properties having a bandgap, E_g, in the range 3.6 to 3.7 eV (*11*, *17*). We performed room-temperature deformation tests on single-crystal ZnS samples (fig. S1) under controlled light conditions, after which the deformation substructure was characterized using a combination of optical microscopy, conventional transmission electron microscopy (CTEM), and scanning transmission electron microscopy (STEM). The light-absorption properties were also evaluated using a spectrophotometer. (*18*) We found extraordinary plasticity of ZnS when deformed in complete darkness, as well as a drastic decrease in the optical bandgap.

Figure 1A shows stress-strain curves obtained during deformation tests under different conditions: white light (sample C), ultraviolet (UV) light (sample D), and in complete darkness (samples E, F, and G after varying deformation strain). Specimens fractured immediately after yielding during plastic deformation under white and UV light conditions. This behavior is expected because inorganic semiconductors are brittle. Conversely, it was found that specimens undergoing plastic deformation in complete darkness result in stable plastic deformation up to a deformation strain of ε_t = 45%, with limited work-hardening rates. In addition, the flow stress was smaller in samples deformed in complete darkness compared with samples deformed under white and UV light. (See supplementary

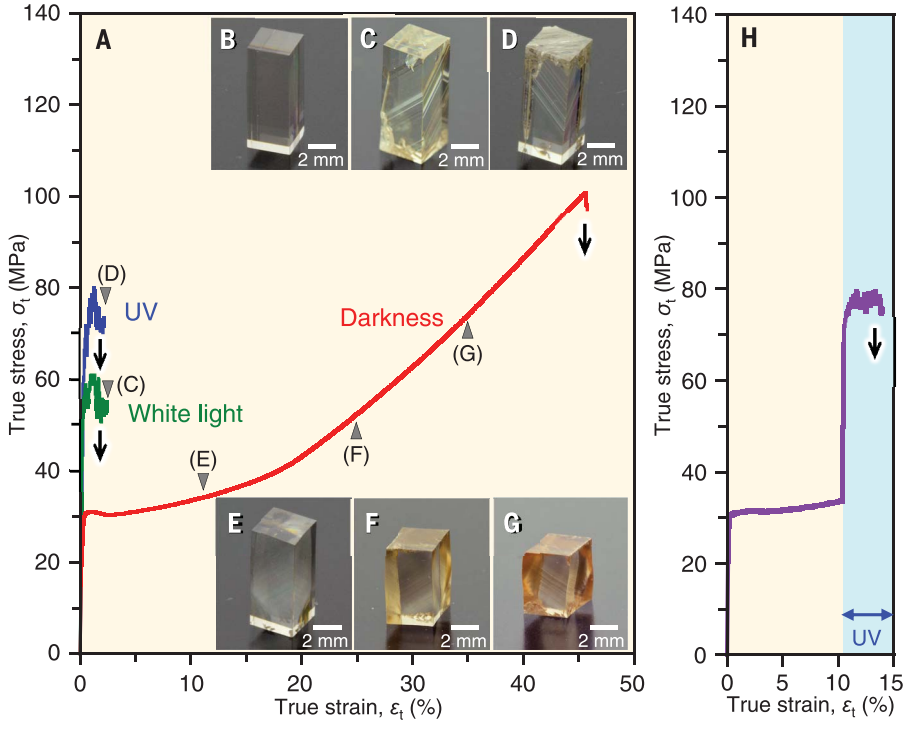

Fig. 1. Characterizations of plastic deformation. (**A**) Stress-strain curves of ZnS single crystals under white or UV light (365 nm) or in complete darkness. (**B**) An undeformed specimen. (**C** and **D**) The specimens deformed under (C) white light-emitting diode (LED) light and (D) UV LED light (365 nm). (**E** to **G**) The specimens deformed up to (E) ε_t = 11%, (F) ε_t = 25%, and (G) ε_t = 35% in complete darkness. (**H**) A stress-strain curve obtained by a deformation in complete darkness up to ε_t = 10% and the subsequent deformation under UV light.

[1]Department of Materials Physics, Nagoya University, Furo-cho, Chikusa-ku, Nagoya 464-8603, Japan. [2]Nanostructures Research Laboratory, Japan Fine Ceramics Center, 2-4-1, Mutsuno, Atsuta-ku, Nagoya 456-8587, Japan.
***Corresponding author. Email: anaka@nagoya-u.jp (A.N.); kmatsunaga@nagoya-u.jp (K.M.)**

text 1 and 2 with figs. S2 to S4 for other characteristics of deformation in complete darkness.) Thus, specimens exhibited extraordinary plasticity without fracture when deformed in complete darkness, despite the fact that inorganic semiconductors are brittle when deformed under regular light conditions. Figure 1, B to G, shows the shapes, surface morphologies, and colors of an undeformed specimen and the deformed specimens. It can be seen that distinct slip lines and an evidence of deformation twinning appear on the surfaces of the specimens deformed under white and UV light conditions (Fig. 1, C and D), whereas faint fine slip lines appear in samples deformed in complete darkness (Fig. 1, E to G). (See supplementary text 3 with fig. S5 for the detailed topographic structures of the surfaces.) The difference in the surface morphologies suggests that the deformation mechanism is different depending on the light condition. It was also found that the color of samples deformed in complete darkness gradually changed from colorless to orange as a function of the deformation strain, suggesting that the optical bandgap of the specimens depends on the deformation strain. The effect of light exposure on the fracture property is also demonstrated in Fig. 1H, showing a sample first deformed in complete darkness and, after about 10% deformation strain, being exposed to UV light, leading to brittle failure. It can be seen that the enhanced plasticity in complete darkness is easily reversed to the ordinary brittle behavior by deformation under UV light conditions.

Figure 2A shows the light-absorption characteristics of an undeformed specimen and specimens deformed to ε_t = 11, 25, and 35% plastic strain in complete darkness. Given that ZnS is a direct transition semiconductor (*1*, *17*, *19*), the optical bandgaps of the undeformed specimen and the specimen deformed up to ε_t = 35% plastic strain in complete darkness are estimated to be 3.52 eV and 2.92 eV, respectively. Figure 2B shows a shift in optical bandgap as a function of deformation strain. It is notable that the optical bandgap was lowered by 0.6 eV due to plastic deformation of ε_t = 35% in complete darkness. This shift could be due to dislocations introduced in the deformed specimens because the dislocation cores could have different band structures (*20*–*22*) with respect to the dislocation-free region. In fact, density functional theory (DFT) calculations (Fig. 3, A and B) [see materials and methods 2 with figs. S6 and S7 (*18*)] showed that calculated bandgaps of the perfect crystal of ZnS and the dislocation-core region are 2.72 eV and 1.88 eV, respectively. The bandgap of the dislocation-core region was lower by 0.84 eV than that in the perfect crystal. This trend corresponds well to the observed shift of optical bandgap by plastic deformation, although underestimation of the bandgaps is a general feature of standard DFT calculations. The bandgap narrowing can be explained by formation of extra energy levels at the bandgap edge in the presence of dislocations. The further bandgap shift and the shape change in the bandgap edge with rising strain may arise from dislocation multiplication.

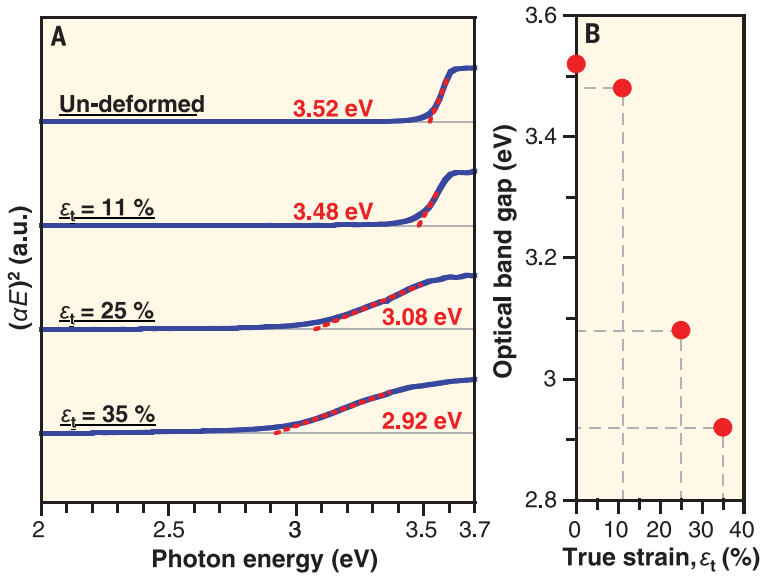

Fig. 2. Light-absorption characteristics. (**A**) An undeformed specimen and the specimens deformed up to ε_t = 11%, 25%, and 35% in complete darkness. Here the α and E in the vertical axis of $(\alpha E)^2$ represent the absorption coefficient and the photon energy, respectively. (**B**) A shift in optical bandgap as a function of deformation strain.

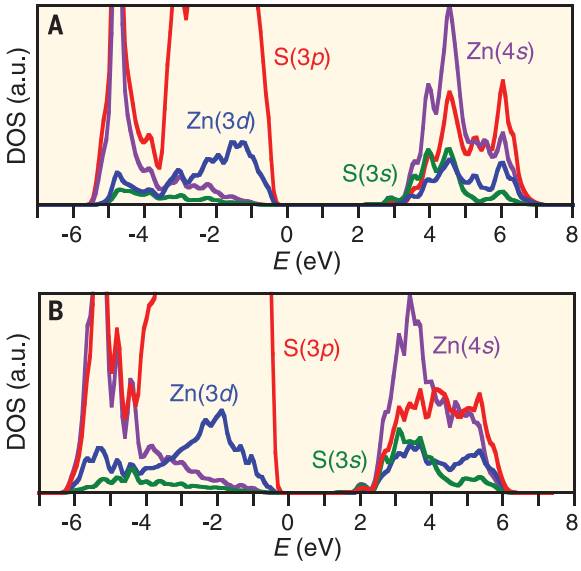

Fig. 3. Characteristic band structure at the dislocation core. (**A**) Density of states (DOS) around the valence band obtained by DFT calculations for the perfect bulk. (**B**) DOS for the dislocation-core region.

Figure 4, A and B, shows bright-field STEM images for the undeformed specimen and the specimen deformed in complete darkness up to a plastic strain of ε_t = 25%, respectively. It can be seen that the dislocation density before plastic deformation is considerably lower (less than 1×10^7 cm^{-2}), whereas that of the deformed specimen at ε_t = 25% increased up to as large as 5×10^8 cm^{-2}. Conventional electron diffraction contrast imaging (see supplementary text 4 with fig. S8) indicated that dislocations in the specimens have the Burgers vector of $\frac{1}{2}\langle 01\bar{1}\rangle$ on the {111} primary slip plane. Because the dislocation density was further raised up to a plastic strain of ε_t = 35%, the plastic deformation in complete darkness is caused by glide and multiplication of dislocations belonging to the primary slip system. Also, since the grown-in dislocation substructure in undeformed specimens has a low density of dislocations, the shift in the optical bandgap results from the multiplied dislocations. In contrast, it was found that the specimens deformed under light irradiation accompany a number of twins (Fig. 4, C and D, and fig. S5, A to C), suggesting that the plastic deformation under light irradiation involves deformation twinning.

The different plastic deformation behaviors with or without light irradiation should be closely related to dislocation characters. Dislocations

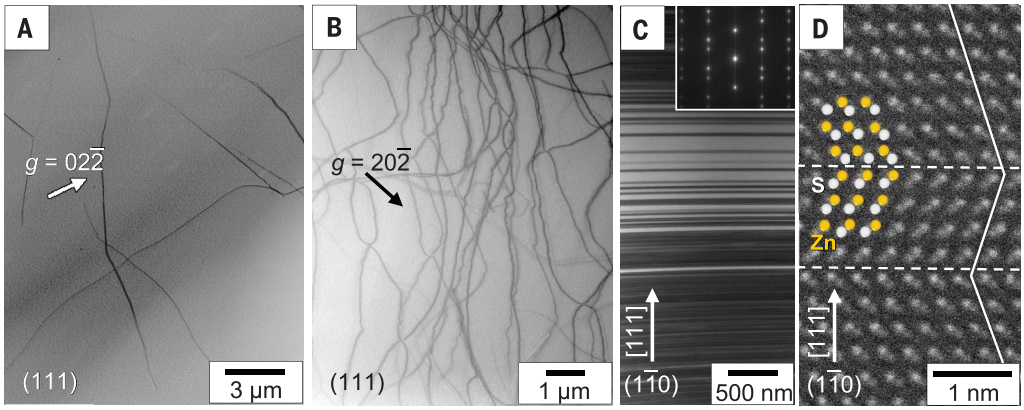

Fig. 4. Characterizations of microstructures in undeformed and deformed specimens. (**A** and **B**) Typical bright-field STEM images of an undeformed specimen and the specimen deformed in complete darkness up to ε_t = 25%, respectively. The images in (A) and (B) were obtained using UHVEM (JEOL JEM-1000KRS, 1000 kV), which makes it possible to observe large areas of dislocation substructure at low magnification. (**C**) A bright-field TEM image of a twinning region in the specimen deformed up to ε_t = 2.0% under UV light. (**D**) A typical high-angle annular dark field STEM (HAADF-STEM) image of a crystal twin in the same specimen as in (C). The image in (D) was obtained using an atomic resolution electron microscope equipped with a spherical aberration corrector (JEOL JEM-ARM200F, 200 kV).

induced in ZnS in darkness dissociate into two partial dislocations (see supplementary text 4). Glide motion of a set of the two partials can bring about large slip deformations, as observed in darkness. In contrast, when one of the partials is much more mobile than the other, ZnS can undergo deformation twinning (*23*) (see supplementary text 5 with fig. S9).

As stated above, dislocation cores in ZnS have a smaller bandgap than the dislocation-free region, and accordingly electrons or holes excited by light irradiation can be trapped at extra energy levels around the bandgap edge of the dislocation cores. Consequently, the partial dislocations can be negatively or positively charged by electrons or holes. A charge state of each partial likely depends on its detailed atomic structure at the core (see supplementary text 5). Additionally, since motion of a charged dislocation corresponds to local charge transportation (*5*), the dislocation mobility may be limited by dragging of the surrounding charge cloud compensating the dislocation charge (*24*). Therefore, different charge states of the two partial dislocations in ZnS can cause a large difference in their mobilities, resulting in the observed deformation twinning. In some inorganic semiconductors, in fact, the hardness and flow deformation stress were reported to be influenced by photons (*25*–*31*), the so-called photoplastic effect, but the previous studies were not aware of the extraordinary plasticity under the nonlighting condition.

In conclusion, it has been shown that cubic ZnS crystals deformed in complete darkness exhibit extraordinary plasticity even at room temperature. The reduced optical bandgap of the deformed crystals by 0.6 eV is thought to arise from the smaller bandgap at the dislocation core. Under light irradiation, on the other hand, the crystals immediately fractured after yielding. It is interesting to find out that the inorganic semiconductor can exhibit extraordinary plasticity when it deforms in complete darkness. This suggests that the mechanical strength and fracture properties in inorganic semiconductors may be controlled by exposure to light. Additionally, the behavior of dislocations plays a critical role in most synthesis and processing of crystalline materials—e.g., film synthesis and epitaxial crystal growth—and that such processes also could be affected by light exposure.

REFERENCES AND NOTES

1. D. B. Holt, B. G. Yacobi, *Extended Defects in Semiconductors: Electronic Properties, Device Effects and Structures* (Cambridge Univ. Press, Cambridge, 2014).
2. S. Wang, Y. Huang, J. A. Rogers, *IEEE Trans. Compon. Packaging Manuf. Technol.* **5**, 1201–1218 (2015).
3. Y.-H. Kim *et al.*, *Nature* **489**, 128–132 (2012).
4. C. Wang, R. Cheng, L. Liao, X. Duan, *Nano Today* **8**, 514–530 (2013).
5. P. M. Anderson, J. P. Hirth, J. Lothe, *Theory of Dislocations* (Cambridge Univ. Press, Cambridge, ed. 3, 2017).
6. A. Nakamura, K. Matsunaga, J. Tohma, T. Yamamoto, Y. Ikuhara, *Nat. Mater.* **2**, 453–456 (2003).
7. K. Szot, W. Speier, G. Bihlmayer, R. Waser, *Nat. Mater.* **5**, 312–320 (2006).
8. Y. Ran, Y. Zhang, A. Vishwanath, *Nat. Phys.* **5**, 298–303 (2009).
9. T. Shimada, T. Xu, Y. Araki, J. Wang, T. Kitamura, *Nano Lett.* **17**, 2674–2680 (2017).
10. C. Elbaum, *Phys. Rev. Lett.* **32**, 376–379 (1974).
11. M. D. McCluskey, E. E. Haller, *Dopants and Defects in Semiconductors* (CRC Press, Boca Raton, 2012).
12. J. Chakrabarty, *Theory of Plasticity* (Elsevier Butterworth-Heinemann, Oxford, ed. 3, 2006).
13. A. Rusinko, K. Rusinko, *Plasticity and Creep of Metals* (Springer, Berlin, 2011).
14. C. Feldmann, T. Jüstel, C. R. Ronda, P. J. Schmidt, *Adv. Funct. Mater.* **13**, 511–516 (2003).
15. L. Thamizhmani, A. K. Azad, J. Dai, W. Zhang, *Appl. Phys. Lett.* **86**, 131111 (2005).
16. M. Sharma, T. Jain, S. Singh, O. P. Pandey, *Sol. Energy* **86**, 626–633 (2012).
17. U. Rössler, Ed., *II-VI and I-VII Compounds; Semimagnetic Compounds* (Springer, Berlin, 1999).
18. Materials and methods are available as supplementary materials.
19. D. Vogel, P. Krüger, J. Pollmann, *Phys. Rev. B* **54**, 5495–5511 (1996).
20. Y. G. Shreter *et al.*, *J. Cryst. Growth* **159**, 883–888 (1996).
21. I. Yonenaga, Y. Ohno, T. Yao, K. Edagawa, *J. Cryst. Growth* **403**, 72–76 (2014).
22. A. Nakamura *et al.*, *Philos. Mag.* **97**, 1281–1310 (2017).
23. P. Pirouz, *Scr. Metall.* **23**, 401–406 (1989).
24. R. W. Whitworth, *Adv. Phys.* **24**, 203–304 (1975).
25. L. Carlsson, C. Svensson, *Solid State Commun.* **7**, 177–179 (1969).
26. C. N. Ahlquist, M. J. Carroll, P. Stroempl, *J. Phys. Chem. Solids* **33**, 337–342 (1972).
27. K. Maeda, O. Ueda, Y. Murayama, K. Sakamoto, *J. Phys. Chem. Solids* **38**, 1173–1179 (1977).
28. Y. A. Osip'yan, V. F. Petrenko, A. V. Zaretskiĭ, R. W. Whitworth, *Adv. Phys.* **35**, 115–188 (1986).
29. K. Maeda, S. Takeuchi, in *Dislocations in Solids*, F. R. N. Nabarro, M. S. Duesbery, Eds. (North-Holland, Amsterdam, 1996), vol. 10, chap. 54.
30. S. Koubaiti, J. J. Couderc, C. Levade, G. Vanderschaeve, *Mater. Sci. Eng. A* **234–236**, 865–868 (1997).
31. Y. A. Osip'yan, R. A. Vardanian, in *Crystal Lattice Defects & Dislocation Dynamics*, R. A. Vardanian, Ed. (Nova Science Publishers, New York, 2000), pp. 149–187.

ACKNOWLEDGMENTS

The authors thank Y. Kurokawa at Nagoya University for lending his expertise on the application of spectrophotometry. The authors acknowledge R. Nagahara and T. Yokoi for technical assistance with theoretical calculations. The authors also express their deep appreciation to K. P. D. Lagerlöf, K. Toyoura, and E. Tochigi for fruitful discussion on the effect of photons on the plastic properties of ZnS. STEM observations in this work were conducted at Nagoya University, supported by Nanotechnology Platform Program of MEXT, Japan. We are grateful to S. Arai for technical assistance with the ultra-high voltage electron microscopy (UHVEM) experiments. **Funding:** This work was mainly supported by Japan Society for the Promotion of Science (JSPS) KAKENHI grant numbers JP16K14414 and JP17H06094. A part of this study was supported by JSPS KAKENHI grant numbers JP15H04145, JP15K14122, and JP17K18983. A.N. also thanks Iketani Science and Technology Foundation for financial support (0281050-A). **Author contributions:** K.M. and A.N. conceived the research idea, and A.N. designed the experiments. Y.O. and A.N. performed the experiments and analyzed the data. K.M. gave advice about the experiments and performed DFT calculations. All the authors discussed the results and wrote the paper. **Competing interests:** Authors declare no competing interests. **Data and materials availability:** All data are available in the main text or the supplementary materials.

SUPPLEMENTARY MATERIALS

www.sciencemag.org/content/360/6390/772/suppl/DC1
Materials and Methods
Supplementary Text
Figs. S1 to S9
References (*32*–*48*)

29 November 2017; accepted 26 March 2018
10.1126/science.aar6035

NANOTHERMOMETRY

Imaging of nonlocal hot-electron energy dissipation via shot noise

Qianchun Weng,[1,4]* Susumu Komiyama,[1,5]* Le Yang,[2] Zhenghua An,[2,3]† Pingping Chen,[1] Svend-Age Biehs,[6] Yusuke Kajihara,[4] Wei Lu[1]†

In modern microelectronic devices, hot electrons accelerate, scatter, and dissipate energy in nanoscale dimensions. Despite recent progress in nanothermometry, direct real-space mapping of hot-electron energy dissipation is challenging because existing techniques are restricted to probing the lattice rather than the electrons. We realize electronic nanothermometry by measuring local current fluctuations, or shot noise, associated with ultrafast hot-electron kinetic processes (~21 terahertz). Exploiting a scanning and contact-free tungsten tip as a local noise probe, we directly visualize hot-electron distributions before their thermal equilibration with the host gallium arsenide/aluminium gallium arsenide crystal lattice. With nanoconstriction devices, we reveal unexpected nonlocal energy dissipation at room temperature, which is reminiscent of ballistic transport of low-temperature quantum conductors.

In modern downscaled microelectronics, current-carrying charges are locally driven far from equilibrium, and the associated heat dissipation is seen as a major concern for future development (*1*). Optimizing nanoscale thermal management by understanding and controlling hot-carrier kinetics is needed to make progress in post–Moore-era nanoelectronics (*1*, *2*). Particularly, understanding the mechanism of heat exchange between the electron and lattice systems is desirable in order to approach ideal device functionality (*1*–*3*). Meanwhile, the excess energy of hot electrons along with a variety of their rich interactions provide a number of promising applications, such as hot luminescent light sources (*4*, *5*), broadband photodetectors (*6*), highly efficient solar cells (*7*), thermoelectric devices (*8*), and plasmon-enhanced photochemistry (*9*). However, it remains extremely challenging to directly map hot electrons in real space with nanoscale resolution (*10*). Pump-probe techniques (*11*, *12*) provide a powerful tool for probing ultrafast transient phenomena with highest resolutions, both in spatial and temporal domains, but cannot be applied to study electronic devices in operating steady state. Sensitive nanothermometry techniques have been developed recently such as scanning thermal microscope (*13*), microscopic Raman spectroscopy (*14*), and plasmon resonance microscopy (*15*). The effective temperature of nonequilibrium electrons, however, is difficult to access with these techniques because electronic nanothermometry is fundamentally hindered by the fact that the heat capacity of electrons is intrinsically small: It is typically several orders of magnitude less than that of the lattice (*16*). Hot electrons are hence easily disturbed by probe-induced local heat flow in most of the nanothermometry techniques.

As a sensitive probe of the electron system, we focus on current fluctuations induced by nonequilibrium electrons, or shot noise (*17*), which has proven to contain nanoscopic information of electron motion not obtained from standard resistance measurements (*17*–*20*). Despite decades of extensive studies, the real-space characteristics of shot noise have been unknown because the existing noise probes were physically immobile (*21*, *22*). In addition, experiments have not been able to access noise frequencies higher than a few hundred gigahertz (*20*), which is far below the typical intrinsic scattering rate of hot electrons; thus, important signatures of ultrafast phenomena have remained obscure.

Here, we visualize hot electrons via shot noise by using a scattering type scanning near-field optical microscope (s-SNOM) (*23*–*26*) called the scanning noise microscope (SNoiM) [Fig. 1A and section 1 of (*27*)]. Current fluctuations induced by nonequilibrium electrons generate fluctuating electromagnetic (EM) evanescent fields on the material surface. In our SNoiM, a sharp metal tip scatters the fluctuating EM evanescent fields to be collected by a confocal microscope and detected with an ultrahighly sensitive sensor called a charge-sensitive infrared phototransistor (*28*). The frequency bandwidth of detection is $\omega/2\pi$ = 21.3 ± 0.7 THz, which is well away from the surface phonon polariton resonance frequencies of the host crystal, so that the measurement is relatively insensitive to phonons. The spatial resolution of the image is ~50 nm. The fluctuating EM evanescent fields detected by SNoiM are, in general, excited not only by nonequilibrium current fluctuation (excess noise) (*17*) but also by thermal current fluctuation in thermal equilibrium conditions (Nyquist noise) (*22*, *29*): The excess noise is specifically termed shot noise if it is caused by nonequilibrium charge carriers. The excellent imaging capability and sensitivity of SNoiM have been proven in recent experiments on metals (*26*).

Below, we will call the signal coming from the tip-scattered EM evanescent fields the passive near-field (NF) signal. In the measurements, the small NF signal component has to be distinguished from a much stronger component associated with the unwanted far-field (FF) background radiation. To this end, two different methods were applied [section 1 of (*27*)]. In one method, the tip height is modulated at f = 5 Hz as a square wave alternating between h and $h + \Delta h$, where Δh = 100 nm throughout this work. The difference signal, $V_{sig}(h) - V_{sig}(h + \Delta h)$, is obtained by demodulating the detector output at fundamental frequency (5 Hz). This difference signal practically equals the signal $V_{sig}(h)$ at h because the NF signal intensity rapidly decreases with increasing h so that $V_{sig}(h + \Delta h)$ can be practically ignored for Δh = 100 nm. In the other method, the bias voltage applied to the device is modulated as a square wave alternating between 0 and V_b at 5 Hz, while the tip height h is not modulated, and the signal is obtained by demodulating the detector output at 5 Hz.

We study small conductors harboring a quasi–two-dimensional electron gas (2DEG), in which energy injection can be highly localized in real space, making hot-electron effects explicit, as theoretically predicted (*30*). The devices with narrow constriction (Fig. 1B and fig. S2) are fabricated in a GaAs/AlGaAs quantum well structure with a 2DEG layer buried 13 nm below the surface [sections 2 and 3 of (*27*)]. Figure 1C shows a two-dimensional (2D) image of the NF signal intensity obtained through the tip-height modulation method with h = 10 nm and bias voltage of V_b = +6 V. In and around the constriction, the region of high NF signal expands toward the downstream side of the electron flow (the positive voltage side). Figure 1D shows that the asymmetric feature is reversed in the opposite polarity of bias voltage (V_b = −6 V), suggesting that the effect is intrinsic, rather than being caused by sample inhomogeneity.

We have cross-checked the signal by applying the V_b-modulation method (0V and ±6 V) with the tip height fixed at h = 10 nm; the obtained 2D images (fig. S3) and those of Fig. 1, C and D, were in close agreement. For all the signals reported below, the two methods were found to yield signals that were nearly equal to each other in amplitude and qualitative features [see section 1 of (*27*) for a discussion]. This indicates that the signals are free from the unwanted FF radiation component and that the thermally generated components are negligible; therefore, the signal

[1]National Laboratory for Infrared Physics, Shanghai Institute of Technical Physics, The Chinese Academy of Sciences, Shanghai 200083, PR China. [2]State Key Laboratory of Surface Physics, Institute for Nanoelectronic Devices and Quantum Computing, and Key Laboratory of Micro and Nano Photonics Structures (Ministry of Education), Department of Physics, Fudan University, Shanghai 200433, PR China. [3]Collaborative Innovation Center of Advanced Microstructures, Nanjing 210093, PR China. [4]Institute of Industrial Science, The University of Tokyo, Komaba 4-6-1, Meguro-ku, Tokyo, 153-8505, Japan. [5]Department of Basic Science, The University of Tokyo, Komaba 3-8-1, Meguro-ku, Tokyo, 153-8902, Japan. [6]Institut für Physik, Carl von Ossietzky Universität, D-26111 Oldenburg, Germany.
*These authors contributed equally to this work.
†Corresponding author. Email: anzhenghua@fudan.edu.cn (Z.A.); luwei@mail.sitp.ac.cn (W.L.)

is caused by the current-induced current fluctuation or excess noise [section 1 of (*27*)]. The excess noise originates from either heated 2DEG or heated lattice. To distinguish between the two, we note that the experimentally obtained images of the NF signal are confined within the mesa structure where the 2DEG is present, with a sharp cut-off edge at the boundary [fig. S5B and section 4 of (*27*)]. This indicates that the origin of the signal is the 2DEG because lattice heating (or nonequilibrium phonon distribution) would not be confined to the mesa structure, and the border of the heated region would have to be substantially smoothed by diffusion of phonons over a relaxation length (200 to 300 nm) (*31*). Thus, the NF signal is ascribed to the shot noise caused by heated 2DEG; this conclusion is strongly supported by theoretical estimates [sections 5 and 6 of (*27*)].

The second important feature is the rapid decay of the NF signal with increasing h (Fig. 1E), where the NF signal is taken via V_b-modulation and is plotted against h. The decay curve is well reproduced with a theoretical predicted curve obtained by combining the hot-electron concept with the electromagnetic local density of states (EM-LDOS) (*32*) of the fluctuating EM evanescent fields [fig. S8 and sections 5 to 7 of (*27*)].

Figure 2, A to F, displays images of the NF signal obtained by modulating the tip height with h = 10 nm and shows how the hot-electron distribution evolves with increasing V_b. NF signals caused by hot electrons are discernible when V_b reaches ~0.8 V, and their distribution expands toward the downstream side of the constriction when V_b exceeds ~4.0 V. At higher values of V_b, a distinct hot spot develops outside the constriction (Fig. 2F for V_b ~ 8.0 V); the signal intensity increases as the electrons move away from the constriction, creating the hottest spot at a distance 200 to 300 nm away from the constriction. This feature is elucidated in Fig. 2G, which shows a distinct maximum peak of the NF signal intensity developing at a position ($y \approx +250$ nm) shifted from the constriction for 5 V < V_b. The nonlocal feature of power dissipation, along with the current-voltage characteristics similar to those described above, have been found in devices with different constriction patterns and crystallographic orientations, suggesting the intrinsic nature of the phenomena [fig. S4 and section 4 of (*27*)]. Above V_b ~ 4.0 V, the current saturates (Fig. 2H). Interestingly, the NF signal intensity at the constriction center ($y \approx 0$) is saturated in step with the current saturation, but the one at the off-centered hot spot ($y \approx +250$ nm) continues to increase. The NF signal intensity for $V_b < 3$ V is roughly proportional to the current I, which is consistent with the conventional theory of shot noise, $\langle S_{shot} \rangle \propto 2e|I|$ (where e is the unit charge). The lack of saturation of the signal intensity at the shifted hot spot for $V_b > 4$ V suggests that specific hot-electron processes play a role, as will be discussed later.

The discrepancy between the noise profile and the electric field distribution is confirmed in additional experiments, where electrostatic potential distribution around the constriction is studied by biasing the metal tip in scanning gate microscopy (SGM) [fig. S10 and section 8 of (*27*)]. A region of high electric fields is found to be concentrated symmetrically in a narrow region around the constriction, roughly defined by $|y| <$ 250 nm. The hot-electron distribution (Fig. 2, D to F), therefore, develops beyond the region of high electric fields. SGM measurements show that the electric field at the constriction reaches $E_c \approx 104$ kV/cm for $V_b = 9.0$ V. The E_c values have been derived as a function of V_b in an independent method, yielding results consistent with SGM (fig. S11).

For materials in thermal equilibrium (*23*–*26*), NF signals have been quantitatively understood in the theoretical framework based on the EM-LDOS for thermally excited fluctuating EM evanescent fields (Nyquist noise) [section 5 of (*27*)]. In nonequilibrium conditions, rigorous theory is not available in general. However, the "hot-electron concept" (*17*, *18*) is applicable in our system, and the knowledge established in thermal equilibrium can be employed as the first-order approximation by considering an effective electron temperature T_e [section 6 of (*27*)]. In our GaAs devices, the exchange of energy and momentum among electrons is so efficient as to nearly establish a quasi-equilibrium state within the electron system. It then follows that the resulting nonequilibrium distribution function of electrons is approximated by the equilibrium Fermi distribution function characterized by an effective electron temperature T_e, and many physical quantities can be derived approximately by noting only the effective temperature T_e. Particularly, the shot noise is approximated by the Nyquist noise at $T = T_e$ and is known by the term hot-electron shot noise (*17*, *18*). In this work, T_e is estimated from the NF signal intensity (see color scales in Figs. 1 and 2) and provides an approximate measure of the average kinetic energy of electrons $\langle \varepsilon \rangle \equiv (3/2)\, k_B T_e$ [section 7 of (*27*)]. The estimated values—T_e = 2200 to 2500 K or $\langle \varepsilon \rangle$ = 280 to 320 meV at the hot spot (Fig. 2F)—are consistent, within the accuracy of estimation (± 7%), with the noise temperature reported in microwave noise measurements on short channel n-GaAs devices (*20*) and with the values $\langle \varepsilon \rangle$ = 300 to 550 meV predicted in Monte Carlo simulations (*33*), both at an electric field $E \approx 100$ kV/cm [section 7 of (*27*)].

The nonlocal feature in this work is reminiscent of the phase-coherent transport through low-dimensional conductors (*34*) or ballistic transport through quantum point contacts at low temperatures (*35*), where energy is dissipated in reservoirs rather than in conductors themselves. The simplest interpretation is therefore to assume purely ballistic motion of electrons passing through the constricted region. Nonlocal energy dissipation is expected to occur in diffusive transport as well (*36*), because electrons necessarily travel a certain distance after acceleration until they release excess energy to the lattice by phonon emission. Indeed, it is a commonly expected feature in most of modern high-speed short-channel transistors (*37*).

We quantitatively model electron transport through the constriction by taking into account relevant transport parameters [section 3 of (*27*)]. When electrons approach and enter the constricted region from the negative-voltage side, they are accelerated by the electric fields. When the accelerated electrons pass through and exit from the constriction, they, in turn, cool down

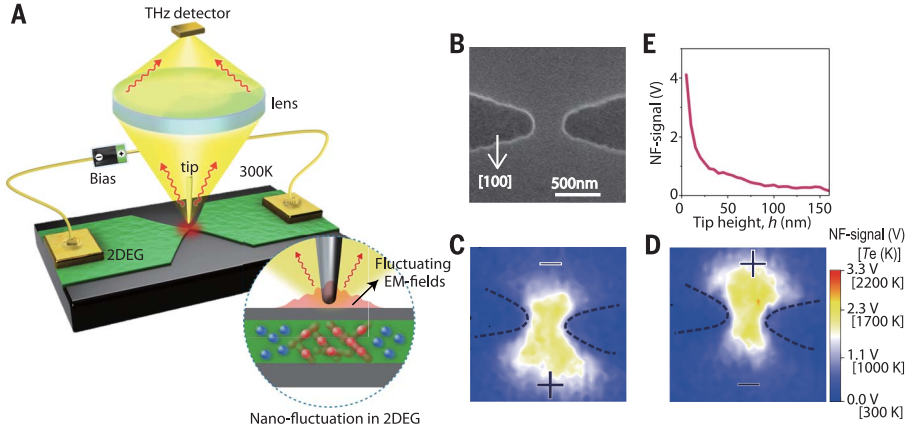

Fig. 1. Nanoscale mapping of ultrahigh-frequency excess noise (21.3 ± 0.7 THz) with scanning noise microscope (SNoiM). (**A**) Schematic representation of the experimental setup of SNoiM [section 1 of (*27*)]. (**B**) SEM image of the nanodevice with a constriction fabricated in a GaAs/AlGaAs quantum well (QW) structure. (**C** and **D**) Two-dimensional real-space images of the NF signal intensity (excess noise), for opposite bias polarities (±6 V). The horizontal and vertical scales are those of the SEM image of (B). The NF signals are taken by modulating the tip height. The color scale is given by the signal amplitude V (detector output) as well as by the effective electron temperature T_e (K) [section 7 of (*27*)]. The electric field at the constriction is estimated to be $E_c \approx 62$ kV/cm for $V_b = 6.0$ V. (**E**) Decay profile of the NF signal with increasing the tip-height h from 5 nm to 150 nm, taken at the center of constriction with $V_b = 6$ V. The signal is obtained by modulating V_b between 0 and 6 V without modulating the tip height.

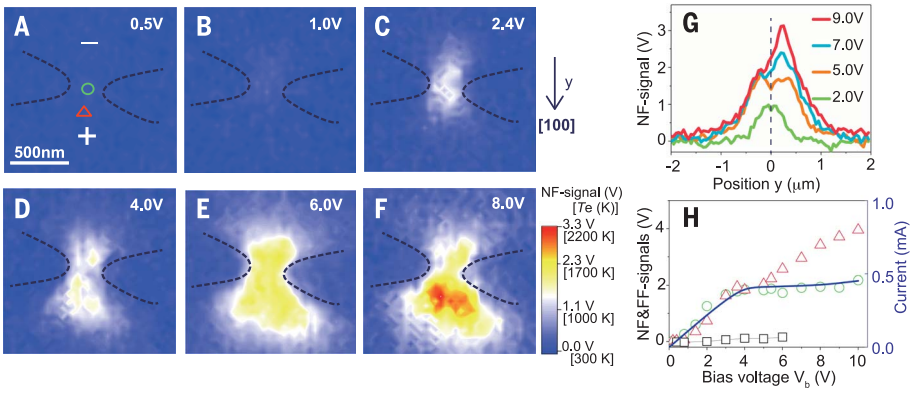

Fig. 2. Evolution of the excess noise distribution with increasing bias voltage, V_b. (**A** to **F**) Two-dimensional images obtained by modulating the tip height. The crystallographic orientation is *y*//[100]. (**G**) One-dimensional profile of the NF signal intensity in the *y* direction, where $y = 0$ corresponds to the center point of the constriction marked by the green circle in Fig. 2A. The data are taken by modulating V_b. (**H**) The solid line shows the current versus V_b curve. Green circles and red triangles show, respectively, the NF signals (excess noise intensities) at the positions marked by o ($y = 0$) and Δ ($y = +250$ nm) in Fig. 2A. The data are taken by modulating V_b. The black squares plot the FF signal, obtained by modulating V_b without using the tip, showing that the current-induced FF component is less than a few percent of the NF signal.

by releasing their excess energy to the lattice. The cooling-down process is, however, relatively slow because the energy relaxation time due to electron-phonon interaction is relatively long ($\tau_{e\text{-}ph} \approx 1.1$ ps). The energetic electrons, on the other hand, pass through the constricted region at high velocities, $v_d \approx (1.9 \text{ to } 2.1) \times 10^5$ m/s (velocity overshoot) (*20*, *38*). It follows that the energetic electrons drift a large distance, $L_{drift,e\text{-}ph} = v_d\tau_{e\text{-}ph} = 210$ to 230 nm, before being equilibrated with the lattice.

The feature of nonlocal energy dissipation is enhanced further by the transfer of hot electrons to upper satellite valleys (*20*, *33*) [section 9 of (*27*)]. It is well known that hot electrons transfer from the Γ-valley to the satellite X- and/or L-valleys at high electric fields (*20*). The effective mass of electrons in the upper valleys is much larger than in Γ-valley, so conductance is reduced, causing the saturation of current *I* for 4.0 V < V_b or 15 kV/cm < E_c (Fig. 2H and figs. S4 and S11). In our system, electron transfer to X-valleys lying above the Γ-valley by $\Delta\varepsilon_{\Gamma X} \approx 550$ meV is important (*20*). The upper valleys serve as a storage for energetic electrons and intensify the feature of nonlocal power dissipation as described below.

A representative experimental image of hot electrons is shown in Fig. 3A, and a detailed interpretation of the nonlocal transport is illustrated in Fig. 3, B to D. The average kinetic energy and the fractional ratio of population of electrons in the Γ-valley are denoted, respectively, by $\langle\varepsilon_\Gamma\rangle$ and n_Γ. As the electrons approach the constriction from the source side (α, −250 nm < *y* < 0 in Fig. 3A), the rapidly increasing electric fields accelerate the electrons (α in Fig. 3B), and the electrons increasingly transfer to the X-valleys (α in Fig. 3C). The average energy, $\langle\varepsilon_\Gamma\rangle$, thereby increases, whereas the fractional population, n_Γ, decreases (α, −250 nm < *y* < 0 in Fig. 3D). At the center of the constriction (β, $y \approx 0$ in Fig. 3, C and D), $\langle\varepsilon_\Gamma\rangle$ reaches maximum, whereas n_Γ falls to a minimum, $n_{\Gamma,c} = 0.3$ to 0.23 for $V_b = 6.0$ to 9.0 V ($E_c = 60$ to 120 kV/cm) (fig. S11). Despite the small $n_{\Gamma,c}$ value, the current through the constriction is dominated by the Γ-valley electrons because their "overshoot" drift velocity $v_{d,\Gamma} \approx (1.9 \text{ to } 2.1) \times 10^5$ m/s is much higher than the drift velocity of X-valley electrons. On the downstream side of the constriction, the electric field *E* decreases rapidly with increasing *y* (γ in Fig. 3B). The average energy $\langle\varepsilon_\Gamma\rangle$ accordingly decreases, but the decrease is slow because (i) the longitudinal-optical-phonon emission process is relatively slow ($\tau_{e\text{-}ph} \approx 1.1$ ps) and (ii) the electrons stored in the X-valleys are now transferred back to the Γ-valley, supplying energetic electrons in the Γ-valley (γ in Fig. 3C). Therefore, n_Γ rapidly recovers the low-field value ($n_\Gamma \approx 1$), but $\langle\varepsilon_\Gamma\rangle$ decreases much more slowly with increasing *y* ($0 < y < 250$ nm in Fig. 3D).

The excess noise is generated primarily by the Γ-valley electrons because their average kinetic energy $\langle\varepsilon_\Gamma\rangle$ is much higher than that of X-valley electrons $\langle\varepsilon_X\rangle$ (*34*). The noise power density is an increasing function of both $\langle\varepsilon_\Gamma\rangle$ and n_Γ, and we simply assume $P_n = n_\Gamma\langle\varepsilon_\Gamma\rangle$ to give a plausible measure of the noise intensity. The profile of P_n (Fig. 3D) reproduces the corresponding experimental feature (Fig. 2G) fairly well, yielding a prominent maximum peak at a location displaced ($y \approx 250$ nm) from the constriction. The saturation of noise intensity at the center point of the constriction (Fig. 2H, $y = 0$) stems from the fact that the increase in $\langle\varepsilon_{\Gamma,c}\rangle$ with increasing V_b (E_c) is compensated by the decrease in $n_{\Gamma,c}$. The lack of saturation at the shifted hot spot (Fig. 2H, $y = 250$ nm) is a consequence of the fact that $n_{\Gamma,c}$ at $y \approx 250$ nm does not decrease substantially so that the effect of $\langle\varepsilon_{\Gamma,c}\rangle$ increase is uncompensated.

SNoiM is applicable to any microelectronics devices of semiconductors, semimetals, and metals. In addition, it can be applied to explore a variety of exotic modes of charge-carrier dynamics in emerging material systems such as graphene (*39*), topological conductors, Weyl semimetals, and anomalous Hall-effect conductors. The target of SNoiM is not restricted to electron systems: For example, by detecting the noise in the frequency band of the surface phonon polariton resonance of the host crystal, the lattice dynamics will be exclusively probed. The sensitivity of our system, limited by the fluctuation of

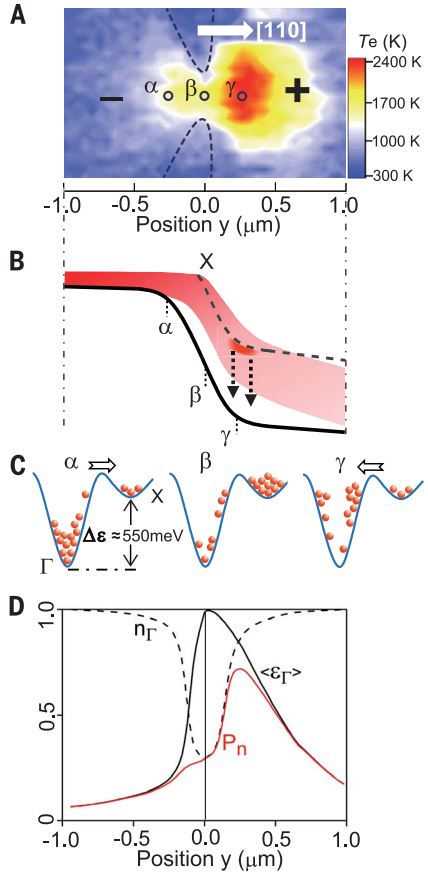

Fig. 3. Hot-electron kinetics in the vicinity of constriction. (**A**) Experimentally obtained image of the hot-electron distribution for $V_b = 9.0$ V ($E_c \approx 120$ kV/cm), taken in a different device from the one shown in Figs. 1 and 2. The data are taken by modulating the tip height with $h = 10$ nm. (**B**) Schematic representation of the electrostatic potential energy of the bottom of the conduction band: The solid line shows the Γ-valley and the broken line the X-valley. Shading shows the distribution of electrons. (**C**) Relative population of electrons in the Γ- and the X-valleys, respectively, at positions α, β, and γ in (A) and (B). (**D**) A sketch of the variation of n_Γ, $\langle\varepsilon_\Gamma\rangle$, and $P_n = n_\Gamma\langle\varepsilon_\Gamma\rangle$ along the *y* axis for $V_b = 6.0$ to 9.0 V, where $n_\Gamma \equiv N_\Gamma/N$ (N_Γ, the density of Γ-valley electrons; N, the total density of electrons) is the relative population of Γ-valley electrons, $\langle\varepsilon_\Gamma\rangle$ is the average kinetic energy of Γ-valley electrons, and $P_n = n_\Gamma\langle\varepsilon_\Gamma\rangle$ is a measure of the excess noise intensity.

background FF radiation, will be dramatically improved at cryogenic temperatures, making measurements in photon-counting mode possible (*40*). The fact that SNoiM should be operable over a range of temperatures with a tunable detection wavelength provides an advantage over most of existing nanothermometry techniques (*41*).

REFERENCES AND NOTES

1. M. M. Waldrop, *Nature* **530**, 144–147 (2016).
2. Y. Dubi, M. Di Ventra, *Rev. Mod. Phys.* **83**, 131–155 (2011).
3. J. Lee *et al.*, *Nat. Nanotechnol.* **9**, 101–105 (2014).
4. C. H. Cho, C. O. Aspetti, J. Park, R. Agarwal, *Nat. Photonics* **7**, 285–289 (2013).
5. M. Troccoli *et al.*, *Nature* **433**, 845–848 (2005).
6. N. M. Gabor *et al.*, *Science* **334**, 648–652 (2011).
7. D. J. Farrell, H. Sodabanlu, Y. Wang, M. Sugiyama, Y. Okada, *Nat. Commun.* **6**, 8685 (2015).
8. X. Cai *et al.*, *Nat. Nanotechnol.* **9**, 814–819 (2014).
9. Y. Zhai *et al.*, *Nat. Mater.* **15**, 889–895 (2016).
10. R. Chau, B. Doyle, S. Datta, J. Kavalieros, K. Zhang, *Nat. Mater.* **6**, 810–812 (2007).
11. E. Najafi, V. Ivanov, A. Zewail, M. Bernardi, *Nat. Commun.* **8**, 15177 (2017).
12. V. Jelic *et al.*, *Nat. Phys.* **13**, 591–598 (2017).
13. F. Menges *et al.*, *Nat. Commun.* **7**, 10874 (2016).
14. J. S. Reparaz *et al.*, *Rev. Sci. Instrum.* **85**, 034901 (2014).
15. M. Mecklenburg *et al.*, *Science* **347**, 629–632 (2015).
16. J. Y. Park, L. R. Baker, G. A. Somorjai, *Chem. Rev.* **115**, 2781–2817 (2015).
17. Y. M. Blanter, M. Büttiker, *Phys. Rep.* **336**, 1–166 (2000).
18. A. H. Steinbach, J. M. Martinis, M. H. Devoret, *Phys. Rev. Lett.* **76**, 3806–3809 (1996).
19. V. Bareikis, J. Liberis, I. Matulioniene, A. Matulionis, P. Sakalas, *IEEE Trans. Electron Dev.* **41**, 2050–2060 (1994).
20. V. Aninkevičius *et al.*, *Phys. Rev. B* **53**, 6893–6895 (1996).
21. E. S. Tikhonov *et al.*, *Sci. Rep.* **6**, 30621 (2016).
22. S. Kolkowitz *et al.*, *Science* **347**, 1129–1132 (2015).
23. Y. Kajihara, K. Kosaka, S. Komiyama, *Opt. Express* **19**, 7695–7704 (2011).
24. K. T. Lin, S. Komiyama, Y. Kajihara, *Opt. Lett.* **41**, 484–487 (2016).
25. K.-T. Lin, S. Komiyama, S. Kim, K. I. Kawamura, Y. Kajihara, *Rev. Sci. Instrum.* **88**, 013706 (2017).
26. S. Komiyama, Y. Kajihara, K. Kosaka, T. Ueda, Z. An, [cond-mat.mes-hall] (4 Jan 2016); available at https://arxiv.org/abs/1601.00368.
27. Materials and methods are available as supplementary materials.
28. S. Komiyama, *IEEE J. Sel. Top. Quantum Electron.* **17**, 54–66 (2011).
29. H. Nyquist, *Phys. Rev.* **32**, 110–113 (1928).
30. R. D'Agosta, N. Sai, M. Di Ventra, *Nano Lett.* **6**, 2935–2938 (2006).
31. L. Zeng *et al.*, *Sci. Rep.* **5**, 17131 (2015).
32. K. Joulain, R. Carminati, J.-P. Mulet, J.-J. Greffet, *Phys. Rev. B* **68**, 245405 (2003).
33. J. Požela, A. Reklaitis, *Solid-State Electron.* **23**, 927–933 (1980).
34. M. Büttiker, *Phys. Rev. Lett.* **57**, 1761–1764 (1986).
35. E. Tekman, S. Ciraci, *Phys. Rev. B* **42**, 9098–9103 (1990).
36. H. Pothier, S. Guéron, N. O. Birge, D. Esteve, M. H. Devoret, *Phys. Rev. Lett.* **79**, 3490–3493 (1997).
37. J. Schleeh *et al.*, *Nat. Mater.* **14**, 187–192 (2015).
38. S. L. Teitel, J. W. Wilkins, *IEEE Trans. Electron Dev.* **ED-30**, 150–153 (1983).
39. K. T. Lin *et al.*, IEEE *Xplore*; available at http://ieeexplore.ieee.org/document/8067243/).
40. K. Ikushima, in *Frontiers in Optical Methods, Springer Series in Optical Sciences*, K. Shudo, I. Katayam, Eds. (Springer Series in Optical Sciences, 2013), vol. 180, chap. 11.
41. D. Halbertal *et al.*, *Nature* **539**, 407–410 (2016).

ACKNOWLEDGMENTS

Z.A. thanks C. M. Hu, L. Zhou, S. W. Wu, and Y. F. Mei for helpful discussions. Part of the experimental work was carried out in Fudan Nanofabrication Laboratory. **Funding:** We acknowledge the research support from the National Natural Science Foundation of China under grant nos. 11427807/11634012/11674070, National Key Research Program of China under grant no. 2016YFA0302000, and Shanghai Science and Technology Committee under grant no. 16JC1400400. S.K. acknowledges support by the Chinese Academy of Sciences Visiting Professorships for Senior International Scientists. Q.W. is an International Research Fellow of the Japan Society for the Promotion of Science (JSPS). Y.K. acknowledges support from Collaborative Research Based on Industrial Demand by Japan Science and Technology Agency. **Author contributions:** S.K., Q.W., and Z.A. conceived the idea, analyzed the data, and cowrote the manuscript, with constant discussion with W.L. The SNoiM was constructed by Q.W. and Z.A. following the advice and the design of Y.K. and S.K. The experiments were carried out by Q.W. on nanodevices fabricated by L.Y. in the wafers grown by P.C. The simulation calculation of EM-LDOS was done by S.-A.B. The research projects were cosupervised by Z.A. and W.L. **Competing interests:** The authors declare no competing financial interests. **Data and materials availability:** All data needed to evaluate the conclusions in the paper are present in the paper and/or the supplementary materials. Spreadsheet data can be found at http://doi.org/10.5281/zenodo.1186949.

SUPPLEMENTARY MATERIALS

www.sciencemag.org/content/360/6390/775/suppl/DC1
Materials and Methods
Supplementary Text
Figs. S1 to S11
References (*42*–*57*)

16 February 2017; resubmitted 19 October 2017
Accepted 12 March 2018
Published online 29 March 2018
10.1126/science.aam9991

THERMOELECTRICS

3D charge and 2D phonon transports leading to high out-of-plane *ZT* in n-type SnSe crystals

Cheng Chang,[1] Minghui Wu,[2] Dongsheng He,[2] Yanling Pei,[1] Chao-Feng Wu,[3] Xuefeng Wu,[2] Hulei Yu,[4] Fangyuan Zhu,[5] Kedong Wang,[2] Yue Chen,[4] Li Huang,[2] Jing-Feng Li,[3] Jiaqing He,[2]* Li-Dong Zhao[1]*

Thermoelectric technology enables the harvest of waste heat and its direct conversion into electricity. The conversion efficiency is determined by the materials figure of merit *ZT*. Here we show a maximum *ZT* of ~2.8 ± 0.5 at 773 kelvin in n-type tin selenide (SnSe) crystals out of plane. The thermal conductivity in layered SnSe crystals is the lowest in the out-of-plane direction [two-dimensional (2D) phonon transport]. We doped SnSe with bromine to make n-type SnSe crystals with the overlapping interlayer charge density (3D charge transport). A continuous phase transition increases the symmetry and diverges two converged conduction bands. These two factors improve carrier mobility, while preserving a large Seebeck coefficient. Our findings can be applied in 2D layered materials and provide a new strategy to enhance out-of-plane electrical transport properties without degrading thermal properties.

Thermoelectric technology, which converts heat into electricity, provides a promising route to environmentally friendly power generation through the harvest of industrial waste heat (*1*, *2*). The conversion efficiency of thermoelectric materials is determined by the dimensionless figure of merit $ZT = [(S^2\sigma)/\kappa]T$, where S, σ, κ, and T are the Seebeck coefficient, electrical conductivity, thermal conductivity, and absolute temperature, respectively. However, the complex interrelationships among thermoelectric parameters prevent us from maximizing the *ZT* value and conversion efficiency (*3*, *4*). To date, various approaches have been adopted to optimize these critical thermoelectric parameters, such as enhancing the electrical transport properties (power factor, $S^2\sigma$) through engineering band structures (*5*–*7*), lowering the thermal conductivity through scattering all-scale length phonons (*8*), and seeking potential materials with low thermal conductivity (*9*, *10*). Impressive achievements have been made in various thermoelectric systems on the basis of these strategies, including bismuth (*11*), lead (*8*, *12*), tin (*13*) and copper (*14*) chalcogenides; germanium silicides (*15*); Zintl phase (*16*); skutterudite (*17*); half-Heusler (*18*); and magnesium-based systems (*19*–*21*).

Over the past decade, bulk crystals with two-dimensional (2D) layered structures have been studied because of their strongly anisotropic transport features. High thermoelectric performance along the in-plane direction was primarily achieved by improving charge-carrier mobility (*22*–*24*). However, the out-of-plane properties have garnered less attention because electrical transport is always impeded by the 2D interlayers. Out-of-plane thermal conductivities in 2D layered materials are sufficiently low enough that they approach the amorphous limit (*25*, *26*). Enhancing the out-of-plane electrical properties may result in excellent thermoelectric performance in this direction.

Very low thermal conductivity due to strong anharmonic and anisotropic bonding was found along the in-plane direction of p-type SnSe crystals with a 2D layered structure (*27*–*29*). After hole doping, SnSe shows an exceptionally high power factor enabled by its multiple valence bands (*28*, *30*). These results reveal that p-type SnSe is a remarkable compound with promising thermoelectric performance. However, the discrepancy of in-plane thermal conductivity observed in fully dense SnSe crystals seems to conclude that the thermal conductivity was underestimated owing to low sample density (*31*). On the contrary, the ultralow thermal conductivity observed in the fully dense SnSe crystals revealed the story to be more complicated (*32*). The continued reports elucidate the thermal conductivity discrepancy, clarifying that the low thermal conductivity in SnSe is sensitive to the vast off-stoichiometric defects (*33*), much softer van der Waals–like Se–Sn bonding (*34*), polycrystalline oxidations (*35*), crystal cracks (*36*), and so on. These investigations on in-plane thermal conductivity are enriching the physical and chemical stories behind SnSe.

Compared to its in-plane thermal conductivity, SnSe exhibits a more steady and even lower thermal conductivity along the out-of-plane direction (*27*, *28*, *32*), which motivated us to investigate its power factor. We synthesized n-type SnSe crystals through the temperature gradient method and bromine doping (figs. S1 and S2). We found that the conduction bands of n-type SnSe have much more complex behavior

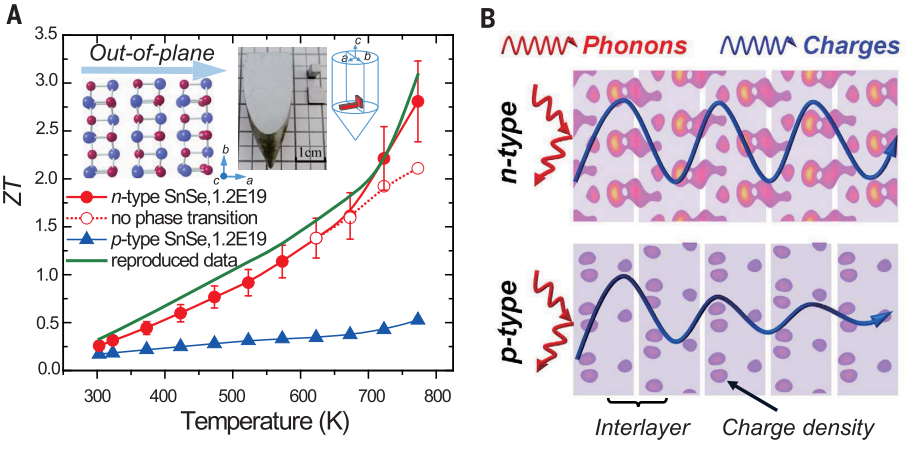

Fig. 1. *ZT* values as a function of temperature and a schematic of phonon and charge transport in n- and p-type SnSe crystals along the out-of-plane direction. (**A**) *ZT* values for p- and n-type SnSe with and without phase transition; the high performance of n-type SnSe is well reproduced by third parties (green line, test reports are provided in the supplementary materials). Inset images show the SnSe crystal structure (blue, Sn atoms; red, Se atoms) with the investigated out-of-plane direction. The typical sample cleaved along the (100) plane and the diagram show how the crystals are cut for measurements (inset images, from left to right). 1.2E19, carrier concentration of ~1.2 × 10^{19} cm^{-3}. (**B**) Schematic out-of-plane charge and phonon transports in n- and p-type SnSe. The colored dots represent the charge densities. The gray blocks represent the two-atom-thick SnSe slabs along the out-of-plane direction (*a* axis) of SnSe.

[1]School of Materials Science and Engineering, Beihang University, Beijing 100191, China. [2]Department of Physics, Southern University of Science and Technology, Shenzhen 518055, China. [3]Key Laboratory of New Ceramics and Fine Processing, School of Materials Science and Engineering, Tsinghua University, Beijing 100084, China. [4]Department of Mechanical Engineering, The University of Hong Kong, Hong Kong SAR, China. [5]Shanghai Institute of Applied Physics, Chinese Academy of Sciences, Shanghai 201204, China.
***Corresponding author. Email: he.jq@sustc.edu.cn (J.H.); zhaolidong@buaa.edu.cn (L.-D.Z.)**

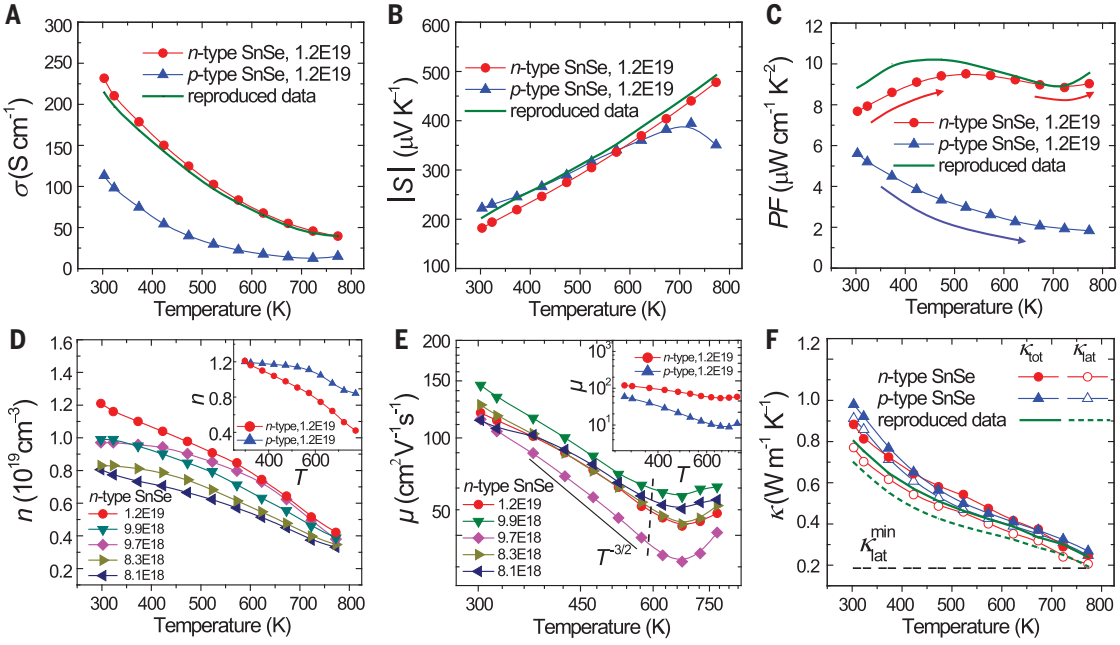

Fig. 2. Thermoelectric properties as a function of temperature for the out-of-plane n- and p-type SnSe crystals. (**A**) Electrical conductivity. (**B**) Seebeck coefficient. (**C**) Power factor (PF). (**D**) Hall carrier concentrations and (**E**) carrier mobilities, where both insets compare n- and p-type SnSe. (**F**) Total and lattice thermal conductivities. The dashed black line is the out-of-plane minimum lattice thermal conductivity. The reproduced data provided by third parties (green lines) for the high-performance n-type SnSe are also plotted for comparison.

owing to a temperature-dependent continuous phase transition from *Pnma* to *Cmcm*, which leads to an outstanding temperature-independent power factor and a maximum ZT (ZT_{max}) of ~2.8 at 773 K along the out-of-plane direction. We obtained independent tests from third-party inspection institutions to verify the high performance and reproducibility [Fig. 1A, green line (*37*)].

The high performance we achieved for n-type SnSe is explained by two cumulative features. First, density functional theory (DFT) calculations and scanning tunneling microscopy (STM) observations indicate that delocalized Sn and Se p electrons near the conduction band minimum (CBM) contribute to more orbital overlap along the out-of-plane direction. When the carrier concentration is fixed at ~1.2×10^{19} cm^{-3}, in contrast to p-type SnSe, the charge density of n-type SnSe overlaps to fill the crystal-structure interlayers. The overlapped charge density can facilitate electron transport through the interlayers, resulting in an expected ZT_{max} of ~2.1 at 773 K for n-type SnSe. By contrast, the ZT_{max} is ~0.5 at 773 K for p-type SnSe (Fig. 1A). Second, high-temperature synchrotron radiation x-ray diffraction (SR-XRD) indicates a continuous phase transition from *Pnma* to *Cmcm* starting at ~600 K before the critical temperature (800 K) in SnSe. This apparently continuous phase transition in n-type SnSe leads to an increased symmetry in the crystal structure, which is further confirmed by in situ spherical aberration–corrected transmission electron microscopy (Cs-corrected TEM). This phase transition also results in the divergence of two converged conduction bands at ~600 K. In contrast to the band convergence, the band divergence decreases the average inertial band mass and thus leads to higher carrier mobility. The changes in the band structure due to the continuous phase transition further increase ZT_{max} from 2.1 to 2.8 at 773 K (Fig. 1A). Collectively, our findings show that the out-of-plane electrical transport properties in n-type SnSe are comparable to those along the in-plane direction (3D charge transport) (Fig. 1B), which has rarely been observed in bulk materials with a 2D structure (*38*, *39*). For comparison, we measured thermoelectric properties as a function of temperature along the in-plane and out-of-plane directions for both p- and n-type SnSe crystals (fig. S3).

To clarify the origin of the huge difference in the out-of-plane thermoelectric performance between the n- and p-type SnSe crystals, we compared the transport properties of the n- and p-type SnSe crystals with the same carrier concentration of ~1.2×10^{19} cm^{-3} (abbreviated 1.21E19, Fig. 2). The electrical conductivity of n-type SnSe is twofold higher than that of p-type SnSe (Fig. 2A), indicating a twofold-higher carrier mobility. At room temperature, the Seebeck coefficient of approximately –180 μV K^{-1} for n-type SnSe is lower than that of p-type SnSe, which is +210 μV K^{-1} (Fig. 2B), indicating a lower effective mass for the n-type crystal. Interestingly, with an increasing temperature, the magnitude of the n-type Seebeck coefficient increases faster and higher than the p-type Seebeck coefficients above ~600 K. This indicates that the conduction band structure is much more complex than that of the valence bands as the temperature increases (*28*). The power factor for p-type SnSe declines monotonically with rising temperature. By contrast, the power factor for n-type SnSe preserves a high value of ~9.0 μW cm^{-1} K^{-2} over the entire temperature range. Finally, the power factor at 773 K for n-type SnSe is five times that of p-type SnSe (Fig. 2C). The carrier concentrations for n-type SnSe show a decreasing trend with increasing temperature (Fig. 2D) and a more pronounced decline than those of p-type SnSe (Fig. 2D, inset), which is consistent with the higher carrier mobility in n-type SnSe (Fig. 2E, inset). Particularly, a distinct rise in the carrier mobility above ~600 K is observed in all n-type SnSe with different carrier concentrations (Fig. 2E), which contributes to higher electrical transport properties above 600 K. The strong anharmonic and anisotropic bonding of SnSe leads to very low thermal conductivity (*27*, *28*, *32*, *40*), which is expected to be even lower along the out-of-plane direction of SnSe owing to strong interlayer phonon scattering. Indeed, both the total and lattice thermal conductivities (κ_{tot} and κ_{lat}) along the out-of-plane direction for both the n- and p-type SnSe crystals are extremely low (Fig. 2F and fig. S4), which even reach a minimum lattice thermal conductivity (κ_{lat}^{min}) as low as 0.18 W m^{-1} K^{-1} at 773 K. These thermoelectric transport properties show good reproducibility by varying the carrier concentration (figs. S5 and S6). Moreover, the highest performance also shows good thermal stability upon temperature changes (fig. S7) and excellent reproducibility through cross-checking in independent inspections [Fig. 2, A to C and F (*37*)].

The twofold-higher n-type out-of-plane electrical conductivity originates from the higher carrier mobility, which indicates that electron transport is facilitated through the interlayers. We investigated the charge density for both types of SnSe along both the out-of-plane (*ab* plane) and in-plane (*bc* plane) directions to determine the origins of the high carrier mobility (Fig. 3A). We investigated the density of states (DOS) near the band edges through DFT calculations [Fig. 3B, (*37*)]. Our calculations reveal that the anisotropies of the charge density in n- and p-type SnSe are dominated by the partial

DOS of Sn (p) and Se (p), respectively. Specifically, in the valence band maximum (VBM), Se (p_z) largely contributes to the total DOS, whereas Sn (p_x) predominately contributes to the total DOS in the CBM. These contributions indicate that the charge density tends to distribute within the in-plane direction in p-type SnSe and along the out-of-plane direction in n-type SnSe. Our DFT calculations further indicate the distinct overlaps of the electron orbitals in the out-of-plane direction of n-type SnSe, which form electrical conduction pathways (Fig. 3C). However, the charge densities mainly distribute along the in-plane direction in p-type SnSe (Fig. 3D). The features in n-type SnSe become more pronounced with increasing temperature (figs. S8 and S9). We further verify the charge-density differences between n- and p-type SnSe through scanning tunneling spectroscopy (STS) and STM images. The dI/dV curves describe the partial DOS distributed along the *kx* direction (*41*), where I is current and V is voltage, which corresponds to the out-of-plane direction in SnSe (Fig. 3E). The sharp slope near the CBM and gradual slope near the VBM are in good accordance with the DOS calculations (Fig. 3B). We visualized the charge density distribution in the *bc* plane using the contrast STM image and dI/dV mapping, where a large difference in charge density results in strong contrast. The low contrast in the images of n-type SnSe (Fig. 3, F and G) indicates an extended charge density distribution, whereas the stronger contrast in p-type SnSe (Fig. 3, H and I) shows a localized preference in the charge density distribution. This is consistent with the DFT calculations in the *bc* plane (Fig. 3, C and D). In summary, overlapping charge density fills the interlayers in n-type SnSe, explaining the high carrier mobility out of plane. By contrast, the charge density for p-type SnSe prefers to fill the in-plane intralayers (*42*, *43*).

The dynamic structural behavior of SnSe at 800 K involves a reversible phase transition from *Pnma* to *Cmcm*, and the highly symmetric *Cmcm* phase can enhance carrier mobility and preserve the high power factor of SnSe (*44*). To directly capture the structural evolution of SnSe as a function of temperature, we conducted in situ Cs-corrected TEM heating experiments for both n- and p-type SnSe. We tilted both samples along the [010] direction (Fig. 4A). The Sn and Se columns are displayed as brighter and dimmer dots, clearly resolved from the [010] direction. At room temperature, the SnSe unit cell consists of two SnSe bilayers with Se atoms in a different planes from the Sn atoms. This lowers the symmetry of the crystal structure. With an increasing temperature, the Se atoms gradually move closer to the nearest Sn layers in n-type SnSe. We quantitatively identified the atomic column positions with a peak-finding program (*37*) and used the d/D ratio to determine symmetry (Fig. 4B), where d and D are the Se intralayer and Se interlayer distances, respectively (an intralayer corresponds to a two-atom-thick SnSe slab along the a axis). Initially, the Se-Se layer distance follows a *d-D-d-D* sequence along the out-of-plane direction, where d and D are approximately 0.25 and 0.34 nm, respectively (figs. S10 to S12). After heating, in n-type SnSe, the d/D ratio increases with increasing temperature, which indicates an increase in the symmetry (Fig. 4C). This behavior is particularly obvious above ~600 K for n-type SnSe. We observed the same phenomenon through high-temperature SR-XRD (fig. S13). We obtained lattice parameters (fig. S14) and atomic positions (tables S1 and S2) for a range of temperatures (*37*). The d/D ratio we calculated from SR-XRD agrees with that from the in situ TEM, indicating the larger movement of Se atoms and thus higher symmetry in n-type SnSe. Collectively, the SR-XRD results indicate a continuous phase transition initializing at ~600 K, and the experimental Cs-corrected TEM observations confirmed that this continuous phase transition is much more pronounced in n-type SnSe. We believe enhanced carrier mobility is related to the high symmetry in the crystal structure of n-type SnSe.

We performed DFT calculations based on the temperature-dependent crystal structures (figs. S15 and S16) to clarify the Seebeck coefficient enhancements above ~600 K in n-type SnSe. Our DFT calculations indicate that the lowest CBM lies in the Γ-Y direction (Fig. 5A, CBM1), whereas the second CBM is located at point Γ (Fig. 5A, CBM2). The energy offset for these two conduction bands is ~0.10 eV at room temperature, and as the temperature increases, the energy offset narrows and reaches a minimum value of ~0.04 eV at about 600 K. Above this temperature, the energy gap sharply rises and then returns to ~0.10 eV again at 773 K (Fig. 5B). Converging band structures can enhance thermoelectric performance by enhancing the effective mass through introduction of additional band degeneracy (N_v) from heavy band contributions

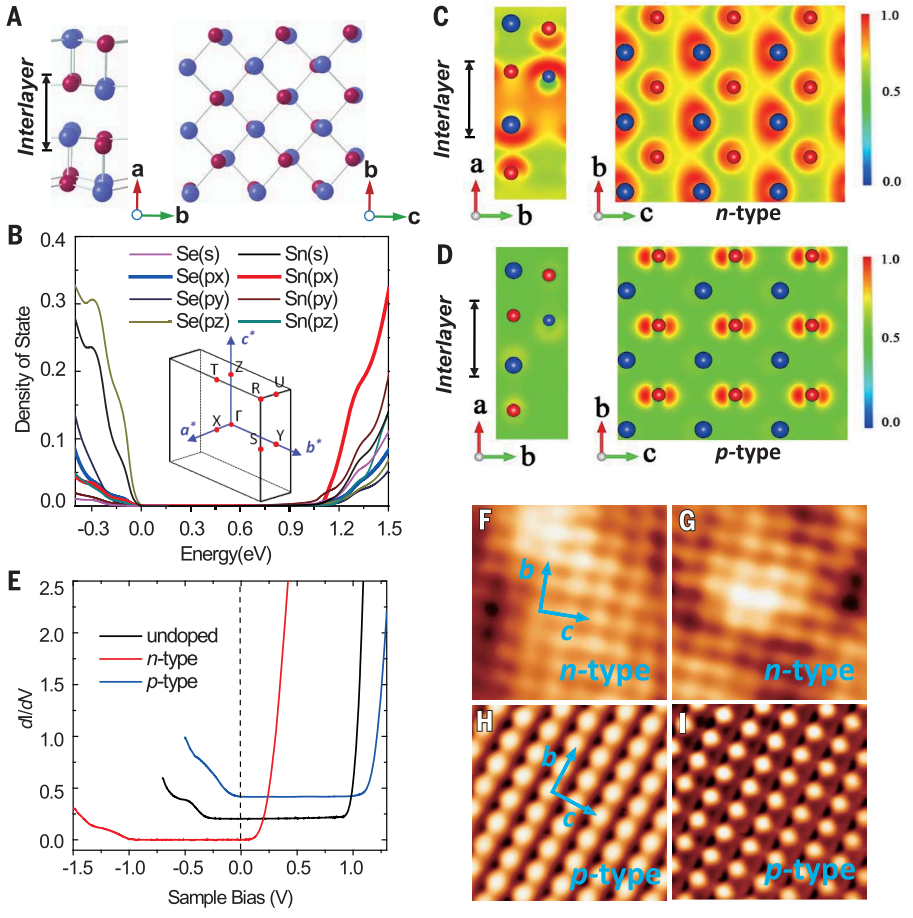

Fig. 3. Crystal structures, DOS, and charge density of n- and p-type SnSe. (**A**) Crystal structures of SnSe in the *ab* and *bc* planes. (**B**) Projected DOS of SnSe near the CBM and VBM ~0.4 eV. The Fermi level is shifted to zero. The inset diagram shows the Brillouin zone of SnSe. Calculated charge densities of (**C**) n- and (**D**) p-type SnSe in the *ab* and *bc* planes, given by wave functions around ~0.2 eV for the CBM and VBM, respectively. The color scale indicates the normalized charge density. (**E**) STS of the undoped, n-type, and p-type SnSe crystals. The spectra are vertically shifted for clarity. STM images and corresponding dI/dV mapping for the (**F** and **G**) n- and (**H** and **I**) p-type SnSe crystals in the *bc* plane. Image sizes are 3 nm by 3 nm. STM and dI/dV mapping are taken at sample biases of 0.4 and −0.2 V for the n- and p-type SnSe crystals, respectively.

(*6*, *7*). However, increasing the effective mass usually deteriorates the carrier mobility (*45*). Distinct band structures are desirable if they can balance the effective mass and carrier mobility. We found that the conduction bands of n-type SnSe experience energy convergence and divergence within 0.10 eV as the temperature increases. We expect the conduction band divergence to improve the carrier mobility by reducing N_v. Indeed, the distinct conduction band structures in n-type SnSe lead to optimization of both the Seebeck coefficient and carrier mobility, which are critical to preserving a higher power factor (Fig. 2F).

To investigate the Seebeck coefficient enhancements, we conducted Seebeck coefficient calculations as a function of carrier concentration at different temperatures on the basis of the single-band model (Fig. 5C). At room temperature, the experimentally observed Seebeck coefficients with different carrier concentrations

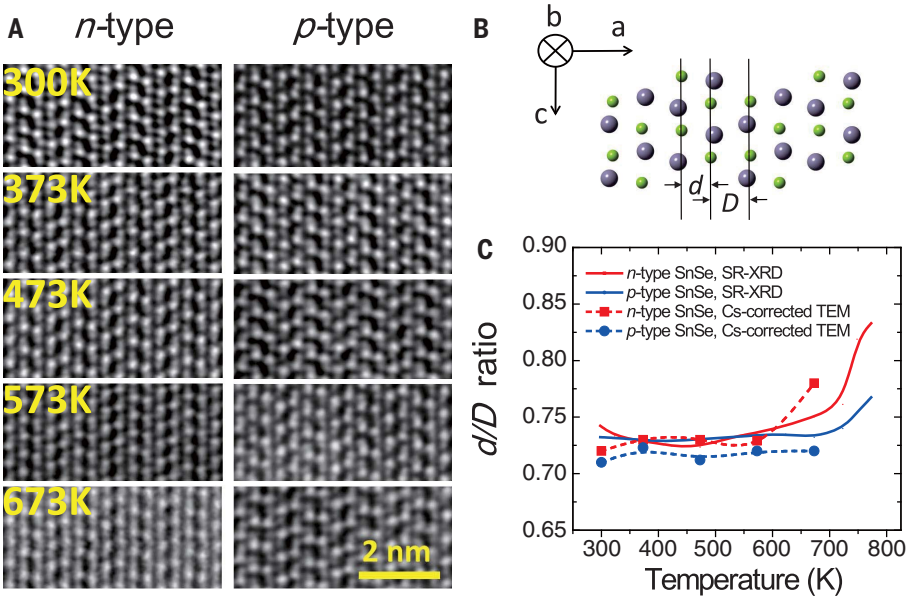

Fig. 4. In situ Cs-corrected TEM, the Se displacements detected by Cs-corrected TEM, and SR-XRD of n- and p-type SnSe. (**A**) High-angle annular dark-field scanning transmission electron microscopy images of n- and p-type SnSe at increasing temperatures as viewed along the *b* axis. Owing to the Z contrast of the Cs-corrected TEM image, brighter dots are Sn columns and dimmer dots are Se columns. (**B**) Atomic model of SnSe viewed along the *b* axis; blue atoms are Sn, and green atoms are Se. (**C**) The *d*/*D* ratio of the n- and p-type SnSe crystals with rising temperature. The markedly increasing *d*/*D* ratio after ~600 K derived from both Cs-corrected TEM (dotted lines) and SR-XRD (solid lines) indicates that n-type SnSe tends to easily undergo a continuous phase transition from *Pnma* to *Cmcm*.

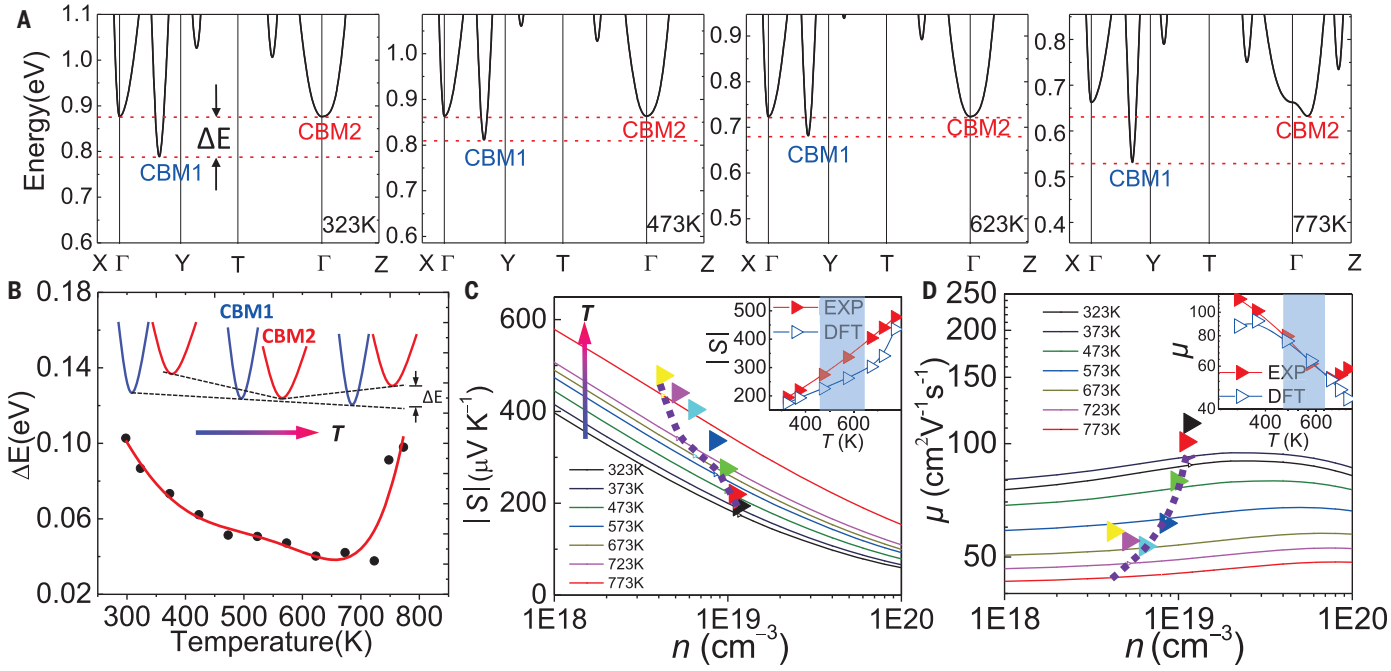

Fig. 5. DFT-calculated band structures, Seebeck coefficients, and carrier mobilities of n-type SnSe with rising temperature. (**A**) Electronic band structures at 323, 473, 623, and 773 K. (**B**) The changing energy gap (Δ*E*) between CBM1 and CBM2 at elevated temperature. Inset diagram indicates that the two conduction bands experience convergence and then divergence with rising temperature. Comparisons of the experimental and calculated (**C**) Seebeck coefficients and (**D**) carrier mobilities as a function of carrier concentration with rising temperature. The triangles are the experimental values, which are compared to the calculated values (string of purple squares) with the same carrier concentrations. Both the Seebeck coefficient and carrier mobility can be optimized through band convergence and divergence. The insets show the deviations of experimental and calculated Seebeck coefficient and carrier mobility as a function of temperature, with the blue regions indicating the temperature range before the conduction band divergence.

are consistent with the Pisarenko relation (fig. S17), which indicates that the single-band characteristics dominate carrier transport at low temperature. However, with rising temperature, the experimental Seebeck coefficients gradually deviate to higher values compared to the calculated Seebeck coefficients (Fig. 5C, inset). The deviation maximizes at ~600 K, indicative of the greatest amount of band convergence. Above ~600 K, the contribution of CBM2 declined owing to band divergence, leading to a smaller deviation between the experimental and calculated values, which agrees with the observed considerable rise in carrier mobility at about 600 K (Fig. 5D). Considering the band convergence, the experimentally observed Seebeck coefficients in the middle temperature range agree with the calculated results. Meanwhile, the notable carrier mobility rise is attributed to the band divergence, which occurs above 600 K. Interestingly, our results indicate that the continuous phase transition that starts at 600 K can enhance the power factor and the final *ZT* value (fig. S18).

Utilizing the ultralow thermal conductivity of out-of-plane SnSe along with an outstanding power factor, we realized a ZT_{max} ~ 2.8 at 773 K in out-of-plane n-type SnSe crystals. We initially selected the very low lattice thermal conductivity in the out-of-plane direction of SnSe crystals. Then, we optimized the carrier mobility and Seebeck coefficient by modifying the temperature-dependent crystal and band structures deriving from the continuous phase transition. Our results open prospects for new strategies to improve the out-of-plane electrical transport properties in 2D layered materials, while maintaining low thermal conductivity.

REFERENCES AND NOTES

1. C. Uher, Ed., *Materials Aspect of Thermoelectricity* (CRC Press, 2017).
2. J. He, T. M. Tritt, *Science* **357**, eaak9997 (2017).
3. X. Zhang, L. D. Zhao, *J. Materiomics* **1**, 92–105 (2015).
4. G. Tan, L. D. Zhao, M. G. Kanatzidis, *Chem. Rev.* **116**, 12123–12149 (2016).
5. J. P. Heremans *et al*., *Science* **321**, 554–557 (2008).
6. Y. Pei *et al*., *Nature* **473**, 66–69 (2011).
7. W. Liu *et al*., *Phys. Rev. Lett.* **108**, 166601 (2012).
8. K. Biswas *et al*., *Nature* **489**, 414–418 (2012).
9. D. T. Morelli, V. Jovovic, J. P. Heremans, *Phys. Rev. Lett.* **101**, 035901 (2008).
10. L. D. Zhao *et al*., *Energy Environ. Sci.* **7**, 2900–2924 (2014).
11. B. Poudel *et al*., *Science* **320**, 634–638 (2008).
12. K. F. Hsu *et al*., *Science* **303**, 818–821 (2004).
13. H. Wu *et al*., *Energy Environ. Sci.* **8**, 3298–3312 (2015).
14. H. Liu *et al*., *Nat. Mater.* **11**, 422–425 (2012).
15. N. Mingo, D. Hauser, N. P. Kobayashi, M. Plissonnier, A. Shakouri, *Nano Lett.* **9**, 711–715 (2009).
16. E. S. Toberer, A. F. May, G. J. Snyder, *Chem. Mater.* **22**, 624–634 (2010).
17. W. Zhao *et al*., *Nature* **549**, 247–251 (2017).
18. T. J. Zhu, C. G. Fu, H. H. Xie, Y. T. Liu, X. B. Zhao, *Adv. Energy Mater.* **5**, 1500588 (2015).
19. H. Zhao *et al*., *Nano Energy* **7**, 97–103 (2014).
20. J. Zhang *et al*., *Nat. Commun.* **8**, 13901 (2017).
21. J. Shuai *et al*., *Energy Environ. Sci.* **10**, 799–807 (2017).
22. N. Thu Huong *et al*., *J. Alloys Compd.* **368**, 44–50 (2004).
23. J. S. Rhyee *et al*., *Nature* **459**, 965–968 (2009).
24. I. Terasaki, Y. Sasago, K. Uchinokura, *Phys. Rev. B* **56**, R12685–R12687 (1997).
25. C. Chiritescu *et al*., *Science* **315**, 351–353 (2007).
26. C. Wan *et al*., *Sci. Technol. Adv. Mater.* **11**, 044306 (2010).
27. L. D. Zhao *et al*., *Nature* **508**, 373–377 (2014).
28. L. D. Zhao *et al*., *Science* **351**, 141–144 (2016).
29. C. W. Li *et al*., *Nat. Phys.* **11**, 1063–1069 (2015).
30. K. L. Peng *et al*., *Energy Environ. Sci.* **9**, 454–460 (2016).
31. P. C. Wei *et al*., *Nature* **539**, E1–E2 (2016).
32. A. T. Duong *et al*., *Nat. Commun.* **7**, 13713 (2016).
33. D. Wu *et al*., *Nano Energy* **35**, 321–330 (2017).
34. G. Li *et al*., *Chem. Mater.* **29**, 2382–2389 (2017).
35. Y. X. Chen *et al*., *Adv. Funct. Mater.* **26**, 6836–6845 (2016).
36. L. D. Zhao, C. Chang, G. Tan, M. G. Kanatzidis, *Energy Environ. Sci.* **9**, 3044–3060 (2016).
37. Materials, methods, and test reports are available as supplementary materials.
38. Y. L. Pei, C. Zhang, J. Li, J. Sui, *J. Alloys Compd.* **566**, 50–53 (2013).
39. K. Biswas, L. D. Zhao, M. G. Kanatzidis, *Adv. Energy Mater.* **2**, 634–638 (2012).
40. C. C. Lin, R. Lydia, J. H. Yun, H. S. Lee, J. S. Rhyee, *Chem. Mater.* **29**, 5344–5352 (2017).
41. M. Iavarone *et al*., *Phys. Rev. Lett.* **89**, 187002 (2002).
42. K. Kutorasinski, B. Wiendlocha, S. Kaprzyk, J. Tobola, *Phys. Rev. B* **91**, 205201 (2015).
43. J. Yang, G. Zhang, G. Yang, C. Wang, Y. X. Wang, *J. Alloys Compd.* **644**, 615–620 (2015).
44. A. Dewandre *et al*., *Phys. Rev. Lett.* **117**, 276601 (2016).
45. Y. Pei, H. Wang, G. J. Snyder, *Adv. Mater.* **24**, 6125–6135 (2012).

ACKNOWLEDGMENTS

The authors thank BL14B1 (Shanghai Synchrotron Radiation Facility) for the SR-XRD experiments. **Funding:** This work was supported by the National Natural Science Foundation of China (51571007, 51772012, 11474176, 51602143, 11574128, and 51788104), the Beijing Municipal Science and Technology Commission (Z171100002017002), the Shenzhen Peacock Plan team (KQTD2016022619565991), and the 111 Project (B17002). J.H. is grateful for the Pico Center at SUSTech, supported by the Presidential fund and Development and Reform Commission of Shenzhen Municipality, and also for support from the Natural Science Foundation of Guangdong Province (grant no. 2015A030308001), the leading talents of Guangdong Province Program (grant no. 00201517). H.Y. and Y.C. are grateful for financial support from the Early Career Scheme of the Research Grants Council (27202516). **Author contributions:** C.C. and L.-D.Z. synthesized the samples, designed and carried out the experiments, analyzed the results, and wrote the paper. M.W., H.Y., Y.C., and L.H. carried out the DFT calculations. C.-F.W. and J.-F.L. carried out the Hall measurements. J.-F.L. provided helpful discussion. X.W. and K.W. carried out STM and STS measurements. D.H. and J.H. conducted microscopy experiments and confirmed the thermoelectric transport properties. Y.P. confirmed the thermal transport properties. F.Z. and C.C. carried out the high-temperature SR-XRDs and Rietveld refinements. All authors conceived the experiments, analyzed the results, and coedited the manuscript. **Competing interests:** The authors declare no competing interests. **Data and materials availability:** All data are available in the manuscript or the supplementary materials. Test reports are also available in the supplementary materials.

SUPPLEMENTARY MATERIALS

www.sciencemag.org/content/360/6390/778/suppl/DC1
Materials and Methods
Figs. S1 to S18
Tables S1 to S6
References (*46*–*56*)

9 October 2017; resubmitted 26 October 2017
Accepted 30 March 2018
10.1126/science.aaq1479

ELECTROCHEMISTRY

CO_2 electroreduction to ethylene via hydroxide-mediated copper catalysis at an abrupt interface

Cao-Thang Dinh,[1]* Thomas Burdyny,[2]* Md Golam Kibria,[1]* Ali Seifitokaldani,[1]* Christine M. Gabardo,[2] F. Pelayo García de Arquer,[1] Amirreza Kiani,[1] Jonathan P. Edwards,[2] Phil De Luna,[3] Oleksandr S. Bushuyev,[1] Chengqin Zou,[1,4] Rafael Quintero-Bermudez,[1] Yuanjie Pang,[2] David Sinton,[2] Edward H. Sargent[1]†

Carbon dioxide (CO_2) electroreduction could provide a useful source of ethylene, but low conversion efficiency, low production rates, and low catalyst stability limit current systems. Here we report that a copper electrocatalyst at an abrupt reaction interface in an alkaline electrolyte reduces CO_2 to ethylene with 70% faradaic efficiency at a potential of −0.55 volts versus a reversible hydrogen electrode (RHE). Hydroxide ions on or near the copper surface lower the CO_2 reduction and carbon monoxide (CO)–CO coupling activation energy barriers; as a result, onset of ethylene evolution at −0.165 volts versus an RHE in 10 molar potassium hydroxide occurs almost simultaneously with CO production. Operational stability was enhanced via the introduction of a polymer-based gas diffusion layer that sandwiches the reaction interface between separate hydrophobic and conductive supports, providing constant ethylene selectivity for an initial 150 operating hours.

The efficient electrochemical conversion of carbon dioxide (CO_2) into valuable carbon-based fuels and feedstocks enables the urgently needed storage of intermittent renewable electricity and, ultimately, a net reduction of greenhouse gas emissions (*1*–*5*). Much effort has been devoted to advance the prospects of producing ethylene, a chemical feedstock in high demand, from CO_2 electroreduction (*6*–*13*). The CO_2 reduction reaction (CO_2-RR) has reached lower activation overpotentials and increased faradaic efficiencies via tuning of catalyst morphologies (*4*, *5*, *10*, *14*, *15*), manipulation of oxidation states (*3*, *16*, *17*), and introduction of dopants (*2*, *18*–*20*). For CO_2 conversion to ethylene, Cu oxide catalysts have achieved peak faradaic efficiencies of 60% by suppressing competing reactions and operating in a narrow reaction window (*13*, *21*–*23*). Separately, ethylene currents of 150 mA cm^{-2} have been achieved at selectivities of 36% and potentials of −0.58 V versus a reversible hydrogen electrode (RHE) on Cu nanoparticles in a flow cell configuration with alkaline electrolytes (*12*).

Despite advances in individual metrics (table S1), large negative potentials are required to reach substantial ethylene selectivities, in part because of the 200- to 300-mV overpotential gap between the formation of necessary CO intermediates and that of ethylene (*24*). Additionally, selective ethylene production has not yet been sustained at commercially relevant current densities (>100 mA cm^{-2}). Stable and highly selective ethylene production at lower overpotentials is urgently needed to enable the renewable electricity–powered synthesis of fuels and feedstocks.

We first pursued experimental and theoretical insights into the direct influence of hydroxide (OH^-) ions, as distinct from bulk pH effects alone, on CO_2 reduction at a Cu catalyst surface. In CO_2 reduction applications, metal oxides have been proposed as active sites even when present in residual or subsurface forms (*16*, *25*, *26*). Hydroxide ions adsorbed or proximate to metal catalysts may play a similar role in modulating active catalytic sites. Further, the reaction rate of the competing hydrogen evolution reaction is suppressed in alkaline electrolytes because of slow kinetics of the first water reduction step (the Volmer step), lowering adsorbed hydrogen surface coverage and influencing the subsequent Heyrovsky and Tafel steps (*27*–*30*).

The direct molecular effects of hydroxide on CO_2 reduction have yet to be studied in detail, in part because canonical H-shaped electrochemical architectures (H cells) are limited by the low availability of CO_2 at pH >10 in aqueous electrolytes. CO_2 dissolved in an alkaline electrolyte will rapidly react, forming a neutral-pH carbonate mixture. Although high-pH conditions can be locally generated in H cells via rapid proton consumption [first from proton reduction, then from water reduction (*31*)], this operation provides information about production at high currents and does not directly elucidate CO_2 reduction onset potentials.

In contrast, a gas diffusion layer positioned immediately adjacent to the catalyst layer allows for CO_2 to diffuse a short distance to the catalyst surface and react before it is converted to bicarbonate. Thus, it is possible for CO_2 reduction to occur under alkaline conditions. We took the view that a flow cell in which the catalyst is deposited onto a gas diffusion layer has the potential to substantially increase the local concentration of gaseous CO_2 and enable clarification of the influence of hydroxides in CO_2-RRs.

We deposited a 100-nm-thick Cu catalyst onto a carbon-based gas diffusion layer (fig. S1), allowing CO_2 reduction under extremely alkaline conditions with the benefit of diffusion of CO_2 across the gas-liquid interface (Fig. 1A). In an Ar environment, the onset potential for H_2 remained relatively constant in the KOH concentration range of 1 to 10 M (Fig. 1B). In a CO_2 environment, the onset potential for the CO_2-RR shifted markedly to more positive potentials with increasing KOH concentrations (Fig. 1B). A similar experiment on a hydrogen-evolving catalyst showed only a minor anodic shift when Ar was replaced by CO_2 (fig. S2), agreeing well with the applied Nernst shift as predicted by a reaction-diffusion model (fig. S3). In 10 M KOH, formation of CO was then observed at a potential 140 mV lower, close to the thermodynamic potential of −0.11 V versus an RHE (Fig. 1C), and the reaction reached >50% selectivity at −0.18 V. Notably, ethylene formation in 10 M KOH occurred at similar potentials: We detected ethylene at applied potentials as low as −0.165 V versus an RHE, only 0.245 V higher than the thermodynamic CO_2-to-ethylene electroreduction potential. This observation is in contrast to our findings with 1 M KOH and prior reports in which the onset potentials of CO and C_2H_4 formation were separated by 200 to 300 mV (*12*, *24*), with one reported ethylene onset occurring at −0.34 V versus an RHE (*9*).

Tafel analyses (Fig. 1E) of ethylene production from CO_2 on the Cu catalyst gave slopes of 135 and 65 mV decade $(dec)^{-1}$ in 1 and 10 M KOH, respectively. Similar slopes for ethylene were also observed in CO reduction on the Cu catalyst (fig. S4), suggesting that the increased hydroxide concentration changes the overall rate-determining step. In contrast to the case of the CO_2-RR, however, the ethylene onset potential when ethylene is produced directly from CO does not shift to lower potentials, implying a further and distinct effect of hydroxide on reaction kinetics.

In the CO_2-RR the onset potential gap between CO and C_2H_4 is attributed to the need to build up coverage of surface-adsorbed CO (*CO) across the catalyst surface before CO dimerization becomes energetically favorable. As the electrolyte pH is increased, the penetration distance of CO_2 into the electrolyte is notably diminished through direct interaction with hydroxide molecules—a point revealed from a reaction-diffusion model analysis (Fig. 1D) analogous to studies presented in prior reports (*32*). In 10 M KOH, the CO_2 present in the electrolyte

[1]Department of Electrical and Computer Engineering, University of Toronto, 10 King's College Road, Toronto, ON M5S 3G4, Canada. [2]Department of Mechanical and Industrial Engineering, University of Toronto, 5 King's College Road, Toronto, ON M5S 3G8, Canada. [3]Department of Materials Science Engineering, University of Toronto, 184 College Street, Toronto, ON M5S 3E4, Canada. [4]Institute of New-Energy Materials, School of Materials Science and Engineering, Tianjin University, Tianjin 300072, China.
*These authors contributed equally to this work.
†Corresponding author. Email: ted.sargent@utoronto.ca

resides mainly within the first 120 nm of the catalyst layer. This arrangement requires CO_2 reduction to take place near an abrupt reaction interface, in contrast with the more distributed reaction interface feasible in 1 M KOH. With little competition from H_2 at these potentials (Fig. 1B), the more localized, and hence concentrated, CO_2 reaction intensity boosts *CO coverage even at modestly negative potentials. This effect improves the reaction kinetics for CO dimerization. This hydroxide-mediated abrupt reaction interface then kinetically allows CO and C_2H_4 to form at similarly low potentials (Fig. 1C). The observed 300-mV shift in ethylene formation from 1 to 10 M KOH is also larger than the pH-dependent shift (59.1 mV/pH unit) observed both experimentally and theoretically for CO reduction to ethylene, where the initial CO_2-to-CO step is avoided (*33*–*36*).

We characterized the catalyst during and after CO_2-RRs in different electrolytes. We used scanning electron microscopy (SEM), transmission electron microscopy (TEM), and in situ x-ray absorption spectroscopy (XAS). In situ XAS of 100-nm samples (fig. S5) showed that at the open-circuit potential, Cu becomes oxidized when submerged in 5 M KOH, most likely via formation of surface hydroxides. However, when a negative potential of −0.16 or −0.96 V versus an RHE is applied, the observed spectra closely match those of fully-reduced pristine Cu foil (fig. S5). We conclude that, under the applied reducing potential used during the CO_2-RR, the surface is primarily Cu^0 and remains consistent over the range of potentials and concentrations of interest. The SEM and TEM characterization of the sample after CO_2-RRs in 1, 5, and 10 M KOH electrolyte showed similar Cu morphologies and crystalline structures, from which we argue that structure morphology did not play a predominant role in the enhanced CO_2-RR we observed at high KOH concentrations (figs. S1 and S6).

To supplement these experimental findings, we used density functional theory (DFT) to assess the impact of hydroxide ions on the thermodynamic and activation energy barriers of the CO dimerization step. CO dimerization is the rate-determining step for C_2 products at high pHs and low applied potentials (*22*, *35*). We performed this analysis on Cu(111), (100), and (110) surfaces, including explicit water molecules in the computational studies (figs. S7 to S10 and tables S2 to S11). The DFT results suggest that the presence of hydroxide lowers the binding energy of CO on the Cu surface. On all surfaces, hydroxide is found to also increase the charge imbalance between carbon atoms in adsorbed OCCO, further stabilizing this intermediate through a stronger dipole attraction within OCCO. The combined differences lead to an overall decrease in the activation energy barrier for the CO dimerization step, lowering the energy barrier by 156 meV on Cu(100) with an OH^- surface coverage of two OH^- ions per 16 Cu atoms [a 2/16 monolayer (ML)] (fig. S9).

With the decreased Tafel slope and matching onset potentials of CO and C_2H_4 in 10 M KOH, high ethylene selectivities at low overpotentials become feasible. By increasing the reaction rate over a fixed electrochemically active surface area, we can control the relative kinetics of CO desorption and dimerization to drive ethylene formation. As seen in Fig. 1D, the abrupt reaction interface and the use of high KOH concentrations contribute to achieving this goal by limiting CO_2 penetration to a fraction of the catalyst layer, reducing the specific active area where the CO_2-RR occurs. Therefore, we sought to similarly constrain the electrochemically active surface

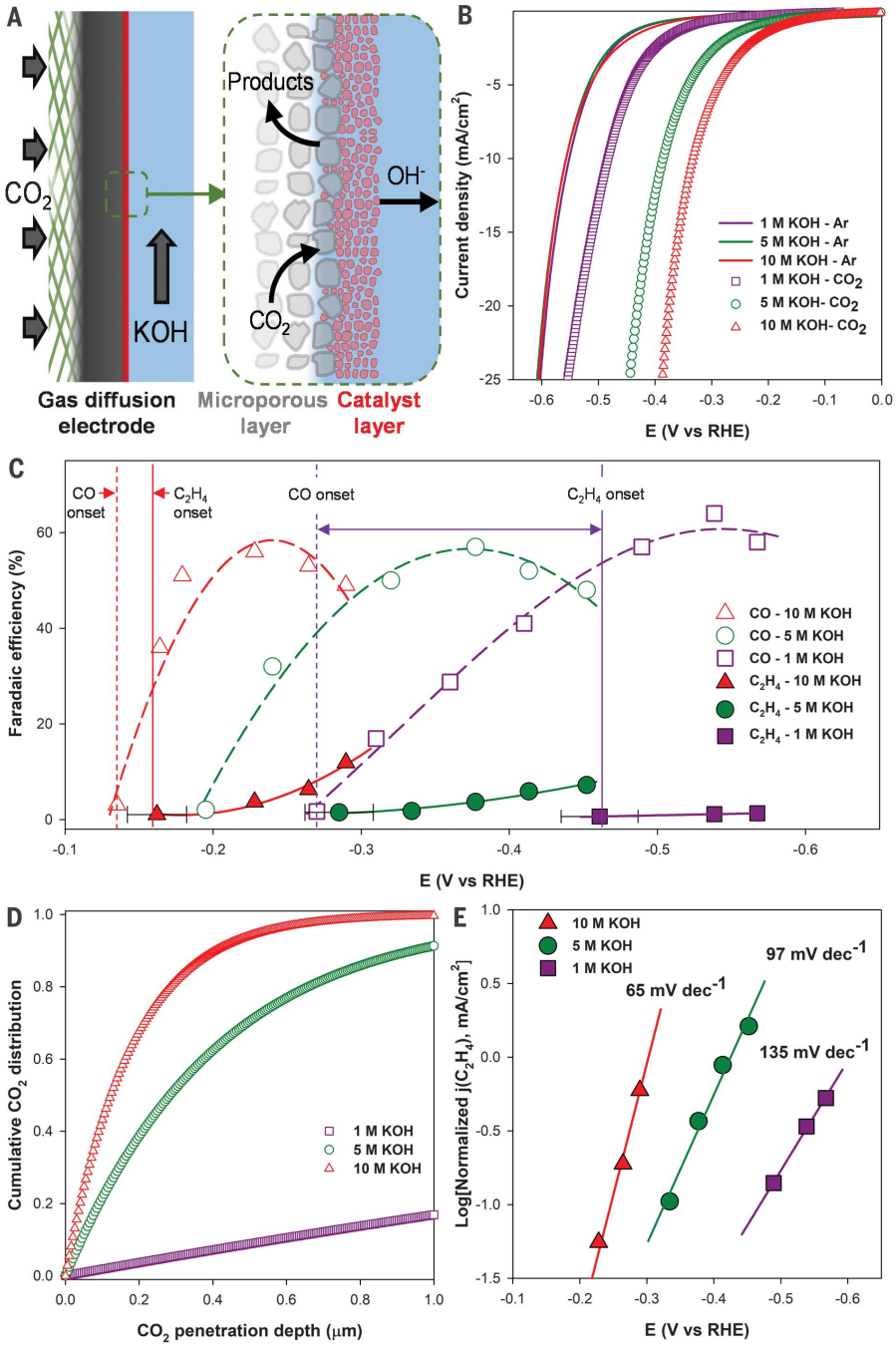

Fig. 1. Experimental studies of the effect of hydroxide on CO_2 reduction, hydrogen evolution, and CO-CO coupling. (**A**) Schematic of the cathode portion of a gas diffusion electrode for CO_2. (**B**) Linear sweep voltammetry scan in various KOH electrolyte concentrations showing low overpotential CO_2 reduction in high KOH concentrations. E, electrode potential. (**C**) C_2H_4 and CO faradaic efficiencies showing the reduction of C_2H_4 onset potential with increasing KOH concentrations. Values are means, and error bars indicate SD (n = 3 replicates). (**D**) Modeling of the cumulative CO_2 distribution across the catalyst layer at 0 mA cm^{-2} and different KOH concentrations. (**E**) Partial ethylene current densities and Tafel slope with increasing KOH concentrations. j, electric current density.

area of the catalyst layer by using thermal evaporation to tune the thickness of the CO_2 reduction interface in the flow cell configuration (Fig. 1A). We used deposition thicknesses of 10 and 25 nm and compared with a thermally deposited thickness of 1000 nm, all deposited on a carbon-based gas diffusion layer. For further comparison, we deposited commercial Cu nanoparticles (particle size, <50 nm) at a loading concentration of 1000 μg/cm^2 by using a drop-casting technique. We characterized nanoparticle size and surface morphology by SEM and scanning TEM for particle sizes ranging from 15 to 40 nm (figs. S11 and S12). Ex situ x-ray photoelectron spectroscopy (XPS) of all three samples showed the presence of C, Cu, and O (fig. S13). The Cu peaks indicated a mixture of metallic Cu and Cu^{2+}. X-ray powder diffraction confirmed the crystalline structure of the samples. The catalyst loadings, analyzed with the use of inductively coupled plasma atomic emission spectrometry (ICP-AES), were ~11, 28, and 1100 μg for the thermally deposited 10-, 25-, and 1000-nm samples, respectively. In CO_2-RR tests in an H cell configuration using 0.1 M $KHCO_3$ electrolyte, these samples exhibited C_2H_4 faradaic efficiency comparable to that of reported Cu and oxide-derived Cu catalysts (fig. S14 and table S13).

The CO_2-RR activities of the Cu samples were evaluated in the flow cell reactor with 10 M KOH (Fig. 2A and figs. S15 to S17). At less-negative potentials (−0.4 V versus an RHE and potentials closer to zero), the samples showed similar slopes, indicative of similar levels of intrinsic activity. The two thicker samples showed higher current densities than the 10- and 25-nm samples at similar potentials, indicating that the higher catalyst loading distributes the reaction beyond 25 nm, as predicted in Fig. 1D. At more-negative potentials, however, the reaction rates on the thinner samples were higher than those on the thicker samples, resulting in similar current densities at −0.54 V versus an RHE. When we analyzed product selectivities in 10 M KOH, we found that the samples showed optimal ethylene production in the current range of 225 to 275 mA cm^{-2} (Fig. 2B), as CO selectivity decreased with current density (fig. S16). Both the 10- and 25-nm samples showed an ethylene faradaic efficiency higher than 60%, with the 25-nm sample peaking at 66% ethylene and exhibiting ethanol at 11% and acetate at 6% (figs. S16 and S17). Overall, the 25-nm sample showed a total C_2 selectivity of 83% at 275 mA cm^{-2} and a low potential of −0.54 V versus an RHE, corresponding to a half-cell ethylene conversion efficiency of 44% (table S1). The 25-nm narrow reaction interface also enabled a high ethylene mass activity of 6.5 A mg^{-1} (table S1 and fig. S16).

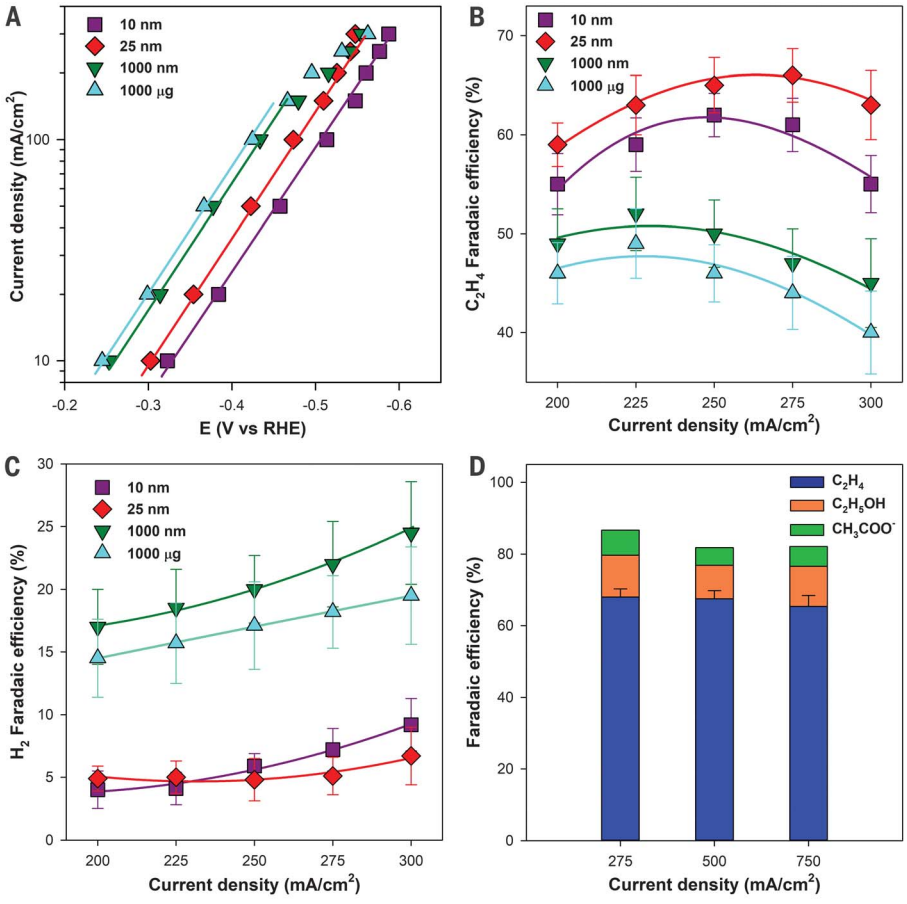

Fig. 2. Hydroxide-mediated CO_2 reduction performance on abrupt reaction interface catalysts. (**A**) Geometric reduction current density as a function of applied potential with 10 M KOH electrolyte on Cu samples of varying thickness. The 10-, 25-, and 1000-nm samples were thermally deposited, and the 1000-μg sample used drop-casted nanoparticles. (**B**) C_2H_4 faradaic efficiencies in the current density range of 200 to 300 mA cm^{-2}, showing the increased C_2H_4 selectivity of the abrupt reaction interface samples (10 and 25 nm) compared with that of thicker samples (1000 nm and 1000 μg) that allow for a more distributed reaction. (**C**) H_2 faradaic efficiencies showing lower H_2 generation on abrupt interface catalysts. (**D**) Optimization of electrolyte for high C_2H_4 selectivity on a 25-nm sample: 10 M KOH (at 275 mA cm^{-2}), 5.5 M KOH with 4 M KI (at 500 mA cm^{-2}), and 3.5 M KOH with 5 M KI (at 750 mA cm^{-2}). Values are means, and error bars indicate SD (n = 3 replicates).

The higher CO_2 reduction selectivities achieved on the thinner catalyst layers were attributable in part to a decrease in H_2 production as a proportion of the total current density, from >15% in the case of the 1000-nm sample to only 5% (Fig. 2C). As shown in Fig. 1B, with the aid of a large CO_2 supply and a low applied potential, CO_2 reduction is favored over H_2 evolution. At higher currents and potentials, the CO_2-RR can also suppress H_2 evolution by occupying surface sites. In highly alkaline conditions, however, a portion of the 1000-nm catalyst layer is largely devoid of CO_2 (Fig. 1D and fig. S3), leaving H_2 evolution as the only possible reaction pathway in this region at higher potentials. These results indicate the need to limit the thickness of the catalyst layer at higher current densities and potentials to prevent unwanted H_2 evolution. The effect of reduced CO_2 availability on CO_2-RR selectivity could also be observed at non–CO_2-limited current densities in 1 M KOH on the 25-nm sample by lowering the partial pressure of CO_2 in the gas phase (fig. S18).

Although the most efficient ethylene production occurred in 10 M KOH, similar ethylene selectivities were achieved at higher partial current densities with a thinner catalyst layer and lower KOH concentrations. By using a thin catalyst to create a catalyst-mediated abrupt reaction interface for the CO_2-RR, we could partially replicate the effect of using 10 M KOH to create a hydroxide-mediated abrupt reaction interface (Fig. 1D). Using a catalyst thickness of 25 nm, we achieved ethylene selectivities of 66, 65, and 63% at total current densities of 275, 500, and 750 mA cm^{-2} in KOH concentrations of 10, 5.5, and 3.5 M, respectively; in each case KI was added to replace the missing potassium (Fig. 2D). KI was chosen because iodide in the electrolyte is known to increase CO_2 reduction activity by accelerating the hydrogenation of the key adsorbed CO intermediate (*37*). We then achieved an ethylene partial current density of

473 mA cm^{-2} at only −0.67 V versus an RHE (fig. S19).

Although high electrochemical performance is achieved with the traditional carbon-based gas diffusion layer architecture, the stability of catalysts on these substrates was poor. The carbon-based gas diffusion electrode degrades (fig. S20) within 1 hour of continuous CO_2-RR operation, regardless of catalyst thickness (25 and 1000 nm) or electrolyte concentration (1 and 7 M KOH). We studied the stability of the carbon-based gas diffusion electrode itself by carrying out electroreduction on a gas diffusion layer without a Cu catalyst. The results show that the oxygen content in the gas diffusion layer doubled and that the surface of carbon turned from hydrophobic to hydrophilic when a negative potential of −0.4 to −0.8 V versus an RHE was applied (fig. S21). We concluded that the instability of the Cu on a carbon-based gas diffusion electrode arose because the gas diffusion layer became flooded as its hydrophobicity was lost during operation. Once the gas diffusion layer floods, the pathways for the diffusion of CO_2 in the gas phase toward the catalyst become obstructed and high CO_2 reduction currents can no longer be sustained.

To improve stability, we sought to develop a new electrode configuration that decoupled the hydrophobic and current collection requirements of traditional carbon-based gas diffusion layers (Fig. 1A). Instead of relying on a single multifunctional layer, we separated the polytetrafluoroethylene (PTFE) and carbon nanoparticles (NPs) into two layers that sandwich our Cu catalyst while maintaining an abrupt reaction interface (Fig. 3A). In this configuration (graphite/carbon NPs/Cu/PTFE electrode) the pure PTFE layer acts as a more stable hydrophobic gas diffusion layer that prevents flooding, and the presence of carbon NPs and graphite stabilizes the Cu catalyst surface. To fabricate the new polymer-based gas diffusion electrode, we sputtered a Cu catalyst layer onto a porous PTFE membrane with a pore size of 220 nm (Fig. 3C). Carbon black nanoparticles were then spray-coated on top to electrically connect the catalyst layer and provide a uniform distribution of current density over the geometric surface (fig. S22). An added graphite layer acted as an overall support and current collector. The thin Cu layer is seen sandwiched between the two layers in a cross-sectional SEM image showing that the abrupt CO_2 reaction interface is conserved in this configuration (Fig. 3B). XPS characterization (fig. S22) revealed that the sample consisted mainly of Cu^0 and Cu^{2+}.

The new electrode showed high CO_2-RR selectivity relative to H_2 evolution in 7 M KOH, similar to the carbon-based gas diffusion electrode (table S13). Although the addition of the carbon NPs between Cu and graphite did not affect the total current density (fig. S23), the ethylene faradaic efficiency rose to 70% (Fig. 3D). The additional carbon support may contribute to a more even distribution of current across the Cu electrode while inhibiting the diffusion of OH^- to the bulk electrolyte, further diminishing CO production to 3% (fig. S23). To evaluate the possibility that carbon NPs could act as a carbon source, we performed the CO_2-RR with isotopic $^{13}CO_2$ as the feedstock. The data show that all of the produced ethylene was derived from $^{13}CO_2$ (fig. S24).

The new graphite/carbon NPs/Cu/PTFE electrode operated for 150 hours without a loss in ethylene selectivity at current densities between

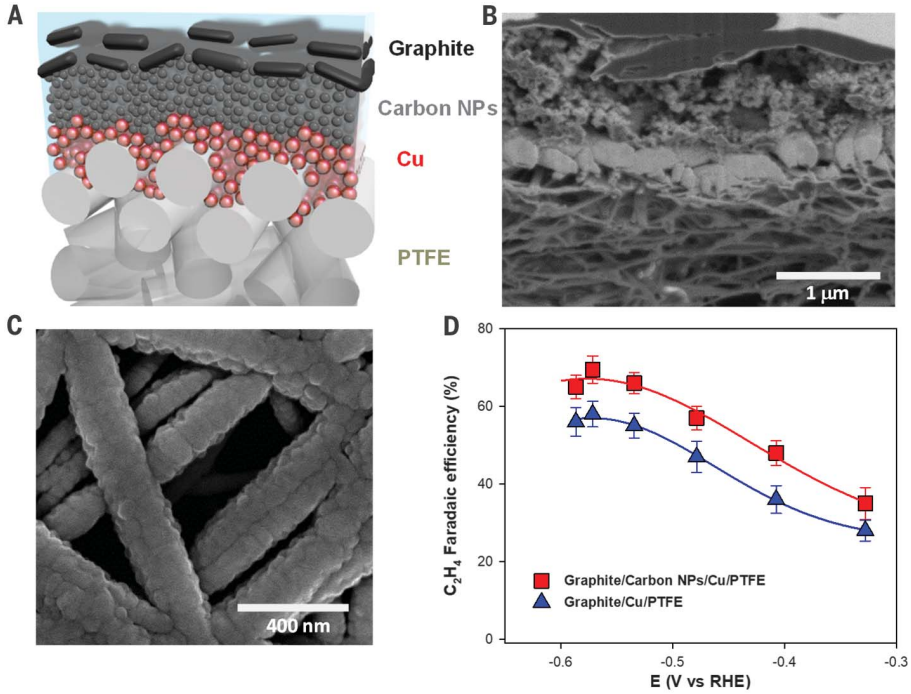

Fig. 3. Structure and performance of the polymer-based gas diffusion electrode. (**A**) Schematic illustration of the graphite/carbon NPs/Cu/PTFE electrode. (**B**) Cross-sectional SEM image of a fabricated graphite/carbon NPs/Cu/PTFE electrode. (**C**) SEM image of Cu nanoparticles sputtered on the PTFE membrane. (**D**) Comparison of ethylene faradaic efficiencies on graphite/carbon NPs/Cu/PTFE and graphite/Cu/PTFE electrodes for CO_2-RR in 7 M KOH electrolyte. Values are means, and error bars indicate SD (n = 3 replicates).

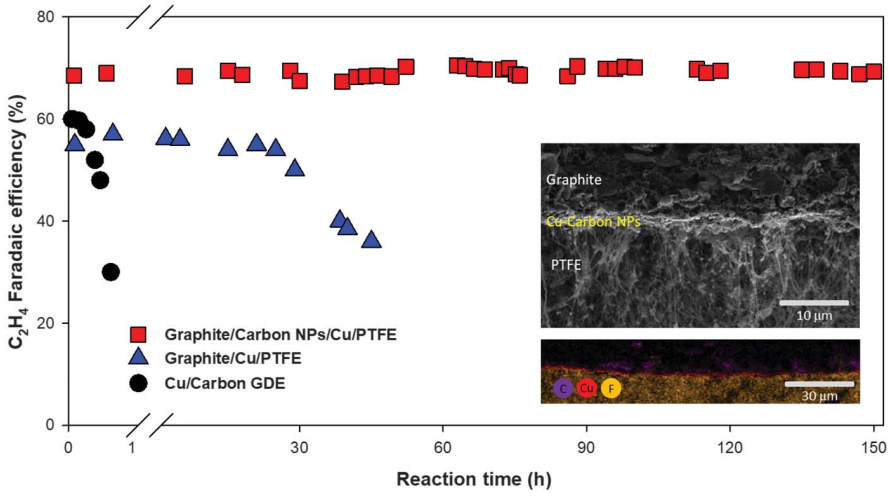

Fig. 4. Stability test of the polymer-based electrode. Long-term performance test of CO_2 reduction to ethylene in 7 M KOH showing high selectivity stability of the graphite/carbon NPs/Cu/PTFE electrode compared with that of a traditional carbon-based gas diffusion electrode (GDE). The stability of a graphite/Cu/PTFE electrode is shown for comparison to highlight the importance of the carbon NPs as a contacting and stabilizing layer. Insets show the cross-section SEM and energy-dispersive x-ray spectroscopy mapping of the sample after 150 hours of continuous CO_2 reduction operation. The stability test was performed at a constant applied voltage of −0.55 V versus the RHE. The current gradually decreased from 100 to 75 mA cm^{-2} over 150 hours of operation.

75 and 100 mA cm^{-2} (Fig. 4 and fig. S25). This performance demonstrates a 300-fold increase in the operating lifetime compared with that of the Cu/carbon gas diffusion layer. The graphite/carbon NPs/Cu/PTFE design also provided longer, higher, and more consistent ethylene selectivities than the same electrode configuration without carbon NPs because of the more mechanically and electrically connected catalyst layer (figs. S25 and S26). Because CO_2 conversion to hydrocarbons is usually carried out at very negative potentials (such as −1 V versus an RHE), material restructuring—even in milder electrolytes and at lower operating currents—can occur over time, and few catalysts have demonstrated sustained high ethylene selectivities over 1 hour of operation (table S13). We propose that the low overpotential required in our system may contribute to avoiding excessive surface reconstruction (*38*) and may be a factor in the observed stable selectivity for ethylene. The observed decrease in current density on the graphite/carbon NPs/Cu/PTFE catalyst over extended operating times is equivalent to a 20-mV increase in potential (fig. S23).

The new electrode configuration shows promise as an easy-to-construct and highly stable system that is compatible with a variety of different catalysts and operating conditions, as demonstrated here by the long-term stability in 7 M KOH. Stable testing in highly alkaline conditions is also important practically, as a high-conductivity electrolyte will likely be required to reduce ohmic losses and boost the overall efficiency of an entire cell. Operating in 10 M KOH versus 0.1 M $KHCO_3$, for instance, results in a decrease in ohmic overpotentials by a factor of 47.

We combined the graphite/carbon NPs/Cu/PTFE cathode with a $NiFeO_x$ (*39*) oxygen evolution catalyst (fig. S27) to perform a full-cell operation in 7 M KOH electrolyte (fig. S28). The system delivers a full-cell energy efficiency for conversion to ethylene of 34% [without the benefit of ohmic resistance (*i*R) correction] at an applied voltage of 2.4 V and an average current density of 110 mA cm^{-2} over 1 hour of operation.

The concept of forming an abrupt reaction interface at a catalyst in highly alkaline media enabled advances in the combination of ethylene electroproduction current density, selectivity, and operating lifetime. The resultant electrical-to-chemical power conversion efficiency, when coupled with the operating stability, indicates a promising platform for CO_2 reduction applications.

REFERENCES AND NOTES

1. M. Schreier *et al.*, *Nat. Energy* **2**, 17087 (2017).
2. S. Lin *et al.*, *Science* **349**, 1208–1213 (2015).
3. S. Gao *et al.*, *Nature* **529**, 68–71 (2016).
4. R. Kas *et al.*, *Nat. Commun.* **7**, 10748 (2016).
5. M. Liu *et al.*, *Nature* **537**, 382–386 (2016).
6. K. D. Yang *et al.*, *Angew. Chem. Int. Ed.* **56**, 796–800 (2017).
7. A. Loiudice *et al.*, *Angew. Chem. Int. Ed.* **55**, 5789–5792 (2016).
8. F. S. Roberts, K. P. Kuhl, A. Nilsson, *Angew. Chem. Int. Ed.* **54**, 5179–5182 (2015).
9. T. T. Hoang, S. Ma, J. I. Gold, P. J. Kenis, A. A. Gewirth, *ACS Catal.* **7**, 3313–3321 (2017).
10. C. Reller *et al.*, *Adv. Energy Mater.* **7**, 1602114 (2017).
11. J. Wu *et al.*, *Nat. Commun.* **7**, 13869 (2016).
12. S. Ma *et al.*, *J. Power Sources* **301**, 219–228 (2016).
13. H. Mistry *et al.*, *Nat. Commun.* **7**, 12123 (2016).
14. Y. Li *et al.*, *Nano Lett.* **17**, 1312–1317 (2017).
15. P. De Luna *et al.*, *Nat. Catal.* **1**, 103–110 (2018).
16. Y. Chen, C. W. Li, M. W. Kanan, *J. Am. Chem. Soc.* **134**, 19969–19972 (2012).
17. D. Ren *et al.*, *ACS Catal.* **5**, 2814–2821 (2015).
18. J. Wu *et al.*, *ACS Nano* **9**, 5364–5371 (2015).
19. D. Kim *et al.*, *J. Am. Chem. Soc.* **139**, 8329–8336 (2017).
20. S. Ma *et al.*, *J. Am. Chem. Soc.* **139**, 47–50 (2017).
21. R. Kas, R. Kortlever, H. Yilmaz, M. T. M. Koper, G. Mul, *ChemElectroChem* **2**, 354–358 (2015).
22. H. Xiao, T. Cheng, W. A. Goddard 3rd, R. Sundararaman, *J. Am. Chem. Soc.* **138**, 483–486 (2016).
23. Y. Lum, B. Yue, P. Lobaccaro, A. T. Bell, J. W. Ager, *J. Phys. Chem. C* **121**, 14191–14203 (2017).
24. Y. Huang, A. D. Handoko, P. Hirunsit, B. S. Yeo, *ACS Catal.* **7**, 1749–1756 (2017).
25. M. Favaro *et al.*, *Proc. Natl. Acad. Sci. U.S.A.* **114**, 6706–6711 (2017).
26. C. Liu *et al.*, *J. Phys. Chem. C* **121**, 25010–25017 (2017).
27. R. Subbaraman *et al.*, *Science* **334**, 1256–1260 (2011).
28. Y. Y. Birdja, M. T. M. Koper, *J. Am. Chem. Soc.* **139**, 2030–2034 (2017).
29. V. R. Stamenkovic, D. Strmcnik, P. P. Lopes, N. M. Markovic, *Nat. Mater.* **16**, 57–69 (2016).
30. W. Sheng, M. Myint, J. G. Chen, Y. Yan, *Energy Environ. Sci.* **6**, 1509–1512 (2013).
31. H. Ooka, M. C. Figueiredo, M. T. M. Koper, *Langmuir* **33**, 9307–9313 (2017).
32. N. Gupta, M. Gattrell, B. MacDougall, *J. Appl. Electrochem.* **36**, 161–172 (2006).
33. K. J. P. Schouten, Z. Qin, E. Pérez Gallent, M. T. M. Koper, *J. Am. Chem. Soc.* **134**, 9864–9867 (2012).
34. J. H. Montoya, C. Shi, K. Chan, J. K. Nørskov, *J. Phys. Chem. Lett.* **6**, 2032–2037 (2015).
35. J. D. Goodpaster, A. T. Bell, M. Head-Gordon, *J. Phys. Chem. Lett.* **7**, 1471–1477 (2016).
36. K. J. P. Schouten, E. Pérez Gallent, M. T. M. Koper, *J. Electroanal. Chem.* **716**, 53–57 (2014).
37. A. S. Varela, W. Ju, T. Reier, P. Strasser, *ACS Catal.* **6**, 2136–2144 (2016).
38. Y.-G. Kim *et al.*, *J. Electroanal. Chem.* **780**, 290–295 (2016).
39. X. Lu, C. Zhao, *Nat. Commun.* **6**, 6616 (2015).

ACKNOWLEDGMENTS

We thank D. Kopilovic and R. Wolowiec for electrochemical cell design and setup and C. S. Tan and A. Proppe for high-resolution TEM and XPS measurements. We thank Y. Hu for XAS support. **Funding:** This work was financially supported by TOTAL American Services, the Connaught Fund, the Ontario Research Fund: Research Excellence Program, the Natural Sciences and Engineering Research Council (NSERC) of Canada, and the CIFAR Bio-Inspired Solar Energy program. All DFT computations were performed on the IBM BlueGene/Q supercomputer with support from the Southern Ontario Smart Computing Innovation Platform (SOSCIP). SOSCIP is funded by the Federal Economic Development Agency of Southern Ontario, the Province of Ontario, IBM Canada, Ontario Centres of Excellence, Mitacs and 15 Ontario academic member institutions. We acknowledge the Toronto Nanofabrication Centre (TNFC) and the Ontario Centre for the Characterization of Advanced Materials (OCCAM) for sample preparation and characterization facilities. X-ray spectroscopy measurements were performed at the Canadian Light Source (SXRMB beamline). A.S. thanks Fonds de Recherche du Quebec–Nature et Technologies (FRQNT) for support in the form of a postdoctoral fellowship award. M.G.K. acknowledges a Banting postdoctoral fellowship from the government of Canada. T.B. thanks Hatch for a graduate scholarship for sustainable energy research. J.P.E. thanks NSERC, Hatch, and the government of Ontario for their support through graduate scholarships. P.D.L thanks NSERC for financial support in the form of the Canada Graduate Scholarship–Doctoral (CGS-D) award. C.M.G. and O.S.B. thank NSERC for financial support in the form of a postdoctoral fellowship. C.Z. acknowledges support from the International Academic Exchange Fund for Joint Ph.D. Students from Tianjin University. **Author contributions:** E.H.S. and D.S. supervised the project. C.-T.D., T.B., M.G.K., and A.S. designed and carried out all of the experiments. A.S. carried out the DFT simulation. T.B. carried out the reaction-diffusion simulation. M.G.K., F.P.G.D.A., and A.K. prepared the evaporated catalysts. P.D.L. and O.S.B. performed the XAS measurements. C.Z. performed the ICP-AES analysis. C.M.G. and Y.P. performed the SEM measurements. R.Q.-B. carried out the XPS analysis. C.-T.D. and J.P.E. designed the electrodes and electrochemical cells. All authors discussed the results and assisted during manuscript preparation. **Competing interests:** C.-T.D., T.B., M.G.K., A.S., D.S., and E.H.S. of the University of Toronto have filed provisional patent application no. 62522925 regarding the preparation of an abrupt catalyst interface for CO_2 reduction. **Data and materials availability:** All data are reported in the main text and supplementary materials.

SUPPLEMENTARY MATERIALS

www.sciencemag.org/content/360/6390/783/suppl/DC1
Materials and Methods
Figs. S1 to S28
Tables S1 to S13
References (*40*–*58*)

3 January 2018; accepted 3 April 2018
10.1126/science.aas9100

PROTECTED AREAS

One-third of global protected land is under intense human pressure

Kendall R. Jones,[1,2]* Oscar Venter,[3] Richard A. Fuller,[2,4] James R. Allan,[1,2] Sean L. Maxwell,[1,2] Pablo Jose Negret,[1,2] James E. M. Watson[1,2,5]

In an era of massive biodiversity loss, the greatest conservation success story has been the growth of protected land globally. Protected areas are the primary defense against biodiversity loss, but extensive human activity within their boundaries can undermine this. Using the most comprehensive global map of human pressure, we show that 6 million square kilometers (32.8%) of protected land is under intense human pressure. For protected areas designated before the Convention on Biological Diversity was ratified in 1992, 55% have since experienced human pressure increases. These increases were lowest in large, strict protected areas, showing that they are potentially effective, at least in some nations. Transparent reporting on human pressure within protected areas is now critical, as are global targets aimed at efforts required to halt biodiversity loss.

In response to massive worldwide biodiversity loss (*1*), the global extent of protected land has roughly doubled in size since the 1992 Earth Summit in Rio de Janeiro, Brazil, with more than 202,000 protected areas now covering 14.7% of the world's terrestrial area (*2*). The recent expansion has been closely associated with Aichi Biodiversity Target 11, which mandates the inclusion of at least 17% of terrestrial areas in effectively managed and ecologically representative protected areas by 2020 (*3*). Protected areas have various management objectives, ranging from strict biodiversity conservation areas [International Union for Conservation of Nature (IUCN) categories I and II] to zones permitting certain human activities and sustainable resource extraction (IUCN categories III to VI), but the primary objective of all protected areas with an IUCN category is to conserve nature (*4*). As such, maintaining the ecological integrity and natural condition of these areas is essential to ensure the protection of species, habitats, and the ecological and evolutionary processes that sustain them (*3*).

The increasing growth and overall extent of protected areas is deservedly celebrated as a conservation success story (*5*), and there is no doubt that well-managed protected areas can preserve biodiversity (*6*, *7*). However, despite the clear relationship between human activities and biodiversity decline (*8*), and the prevalence of these activities inside many protected areas (*9*), there has been only one global assessment of multiple human pressures within protected areas (*10*). This study mapped human pressure at a coarse scale, considered only a small subset of global protected areas (n = 8950), and did not consider many important human pressures, such as roads and navigable waterways (*11*), livestock grazing (*12*), and urbanization (*13*). A comprehensive analysis of cumulative human pressure within protected areas, and how this has changed since the Convention on Biological Diversity was ratified in 1992, is necessary to assess how human pressure inside protected areas may impede progress toward international conservation targets (*3*).

Here we use the most comprehensive global map of human pressure on the environment [the human footprint; (*14*)] to quantify the extent and intensity of human pressure within protected areas and how this has changed since 1992. The human footprint provides a single pressure metric that combines data on built environments, intensive agriculture, pasture lands, human population density, nighttime lights, roads, railways, and navigable waterways (*14*). The presence of these pressures is directly linked to constraints on and declines in biodiversity (*8*, *15*, *16*). We delineate areas of intense human pressure in protected areas (human footprint ≥ 4; see methods) and explore how excluding these areas would affect measurements of progress toward Aichi Biodiversity Target 11. We also assess the impact of protected-area size and IUCN management category on patterns of human pressure within protected areas.

We find that the average human footprint score within protected areas is 3.3, almost 50% lower than the global mean of 6.16 (*14*). Despite this, human activities are prevalent across many protected areas, with only 42% of protected land free of any measurable human pressure (figs. S1 and S2). Areas under intense human pressure make up 32.8% (6,005,249 km^2) of global protected land (Fig. 1), and more than half (57%) of all protected

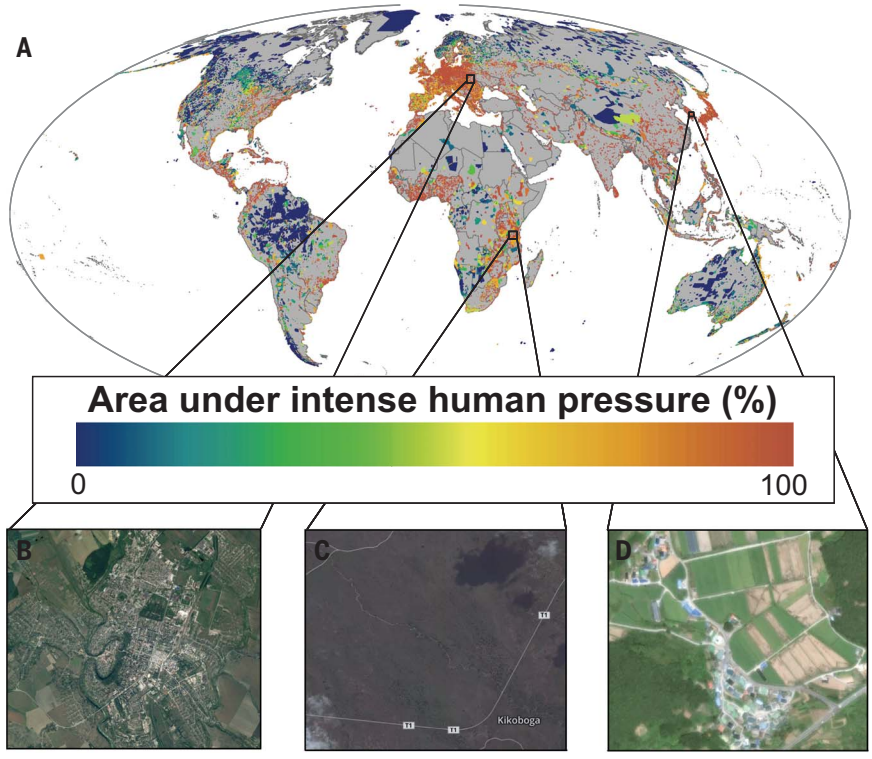

Fig. 1. Human pressure within protected areas. (**A**) Proportion of each protected area that is subject to intense human pressure, spanning from low (blue) to high (orange) levels. (**B**) Kamianets-Podilskyi, a city within Podolskie Tovtry National Park, Ukraine. (**C**) Major roads fragment habitat within Mikumi National Park, Tanzania. (**D**) Agriculture and buildings within Dadohaehaesang National Park, South Korea. [Photo credits: Google Earth]

[1]School of Earth and Environmental Sciences, The University of Queensland, St. Lucia, Queensland 4072, Australia. [2]Centre for Conservation and Biodiversity Science, The University of Queensland, St. Lucia, Queensland 4072, Australia. [3]Ecosystem Science and Management Program, University of Northern British Columbia, Prince George, British Columbia V2N 4Z9, Canada. [4]School of Biological Sciences, University of Queensland, Brisbane, Queensland 4072, Australia. [5]Wildlife Conservation Society, Global Conservation Program, Bronx, NY 10460, USA.
*Corresponding author. Email: k.jones10@uq.edu.au

areas contain only land under intense human pressure (concentrated in western Europe, southern Asia, and Africa; Fig. 1). Just 4334 protected areas (10% of analyzed areas; see methods) are completely free of intense human pressure (Fig. 1), and these primarily occur in remote areas of high-latitude nations, such as Russia and Canada.

Protected areas with strict biodiversity conservation objectives (IUCN categories I and II) are subject to significantly lower levels of human pressure (Kruskal-Wallis test; $H = 5045.2$, $P < 0.001$; fig. S3A), and a lower proportion of their area under is intense human pressure (Kruskal-Wallis test; $H = 4609.6$, $P < 0.001$; fig. S3B), compared to those permitting a wider range of human activities (Table 1). This effect is not sensitive to the threshold used to determine intense human pressure (fig. S4), and there are still a considerable number of less-strict protected areas (IUCN categories III to VI) under low human pressure (fig. S4). Smaller protected areas are much more likely to have high levels of human pressure than larger protected areas (Fig. 2; linear regression, t value = –58.02, $P < 0.001$). Nonetheless, many small protected areas contain low human pressure (Fig. 2), and they can be crucial for providing habitat in highly modified landscapes (*17*). This is especially true in protected areas where biodiversity has persisted under high human influence and traditional management practices (IUCN category VI) can maintain biodiversity values (*18*).

Mean human pressure has increased substantially since the Earth Summit, both worldwide [9% increase; (*14*)] and within protected areas (6% increase; table S1). Human pressure increased in 55% (n = 11,390) of protected areas designated in or before 1993, with substantial increases (mean human footprint increase > 1) occurring in 10% (n = 3966; fig. S5). Although strict protected areas (IUCN categories I and II) have the lowest current levels of human pressure, IUCN management category does not appear to affect the rate at which human pressure has increased (table S1). Protected areas designated after 1993 have a lower level of intense human pressure within their borders, compared to those designated in or before 1993, suggesting that recent protected-area establishment may be targeting a higher percentage of area under low human pressure (Table 1).

The most concerning increases in human pressure are in those landscapes that were intact when a protected area was designated. Within protected areas designated during or before 1993, 280,000 km^2 of land has changed from a low– to an intense–human pressure category (table S1). Strict protected areas (IUCN categories I and II) lost far less of their low-pressure land than non-strict protected areas (3.6 versus 8%; fig. S6), and, by far, the largest losses occurred in those without an IUCN category (17%; fig. S6).

Human pressure inside protected areas is likely compromising national progress toward Convention on Biological Diversity obligations. Almost three-quarters of nations (n = 137, 70%) have >50% of their protected land under intense human pressure (fig. S7 and table S2). If one assumes that protected land under intense human pressure does not contribute toward conservation targets, we show that 74 of the 111 nations that have reached a level of 17% protected-area coverage would drop out of that list (fig. S7 and table S2). Moreover, the protection of some biomes (for example, mangroves and temperate forests) would decrease by >70% (Fig. 3A). Although 301 (38% of) ecoregions (ecologically

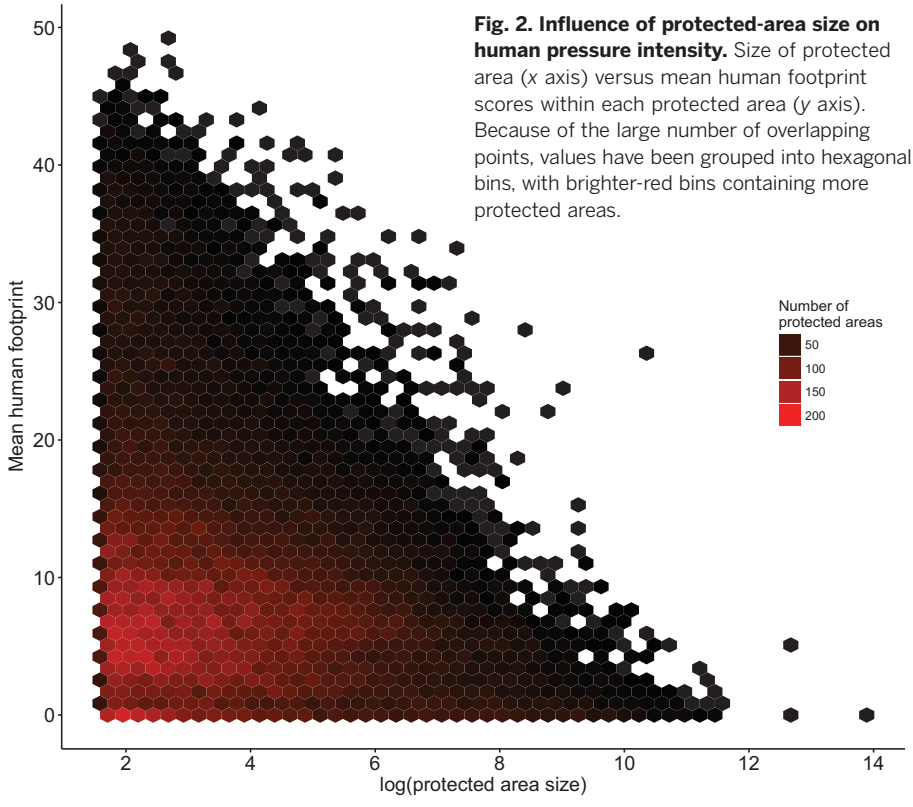

Fig. 2. Influence of protected-area size on human pressure intensity. Size of protected area (x axis) versus mean human footprint scores within each protected area (y axis). Because of the large number of overlapping points, values have been grouped into hexagonal bins, with brighter-red bins containing more protected areas.

Table 1. Influence of protected-area category on current human pressure. Strict biodiversity conservation areas (IUCN categories I and II) contain lower levels of human pressure than protected areas that permit a broader range of activities (for example, nonindustrial resource use; IUCN categories III to VI). NA represents those protected areas without an assigned IUCN category. Protected areas smaller than 5 km^2 are excluded.

IUCN category	Number of protected areas (area in km^2)	Mean human footprint	Area under intense pressure (%)
I	3,992 (2,089,560)	1.27	12.4
II	3,628 (4,529,337)	2.12	24.1
III	1,672 (199,062)	2.42	24.0
IV	7,412 (2,410,055)	3.68	36.6
V	8,378 (2,557,816)	5.21	45.8
VI	2,365 (2,859,949)	2.4	26.4
NA	14,481 (4,502,128)	4.38	44.2
All protected areas	41,928 (19,147,911)	3.26	32.8
Protected areas established before 1993	22,046 (11,048,058)	3.36	34.9
Protected areas established after 1993	19,882 (8,099,852)	3.13	29.7

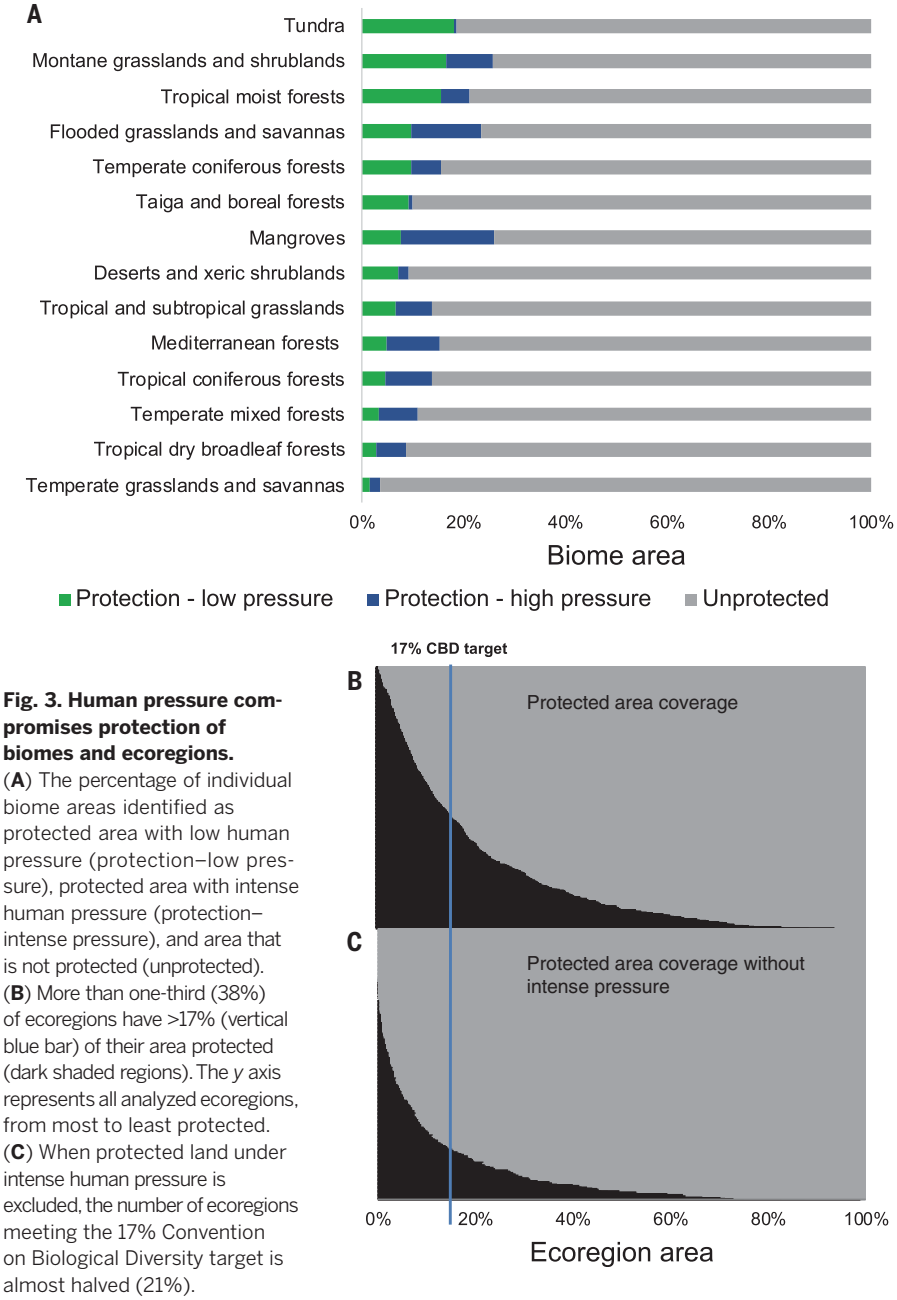

Fig. 3. Human pressure compromises protection of biomes and ecoregions. (**A**) The percentage of individual biome areas identified as protected area with low human pressure (protection–low pressure), protected area with intense human pressure (protection–intense pressure), and area that is not protected (unprotected). (**B**) More than one-third (38%) of ecoregions have >17% (vertical blue bar) of their area protected (dark shaded regions). The *y* axis represents all analyzed ecoregions, from most to least protected. (**C**) When protected land under intense human pressure is excluded, the number of ecoregions meeting the 17% Convention on Biological Diversity target is almost halved (21%).

similar areas) currently have more than 17% coverage inside protected areas (Fig. 3B), excluding land subject to intense human pressure would almost halve this (n = 167, 21%; Fig. 3C). These results make a clear case that nations reporting solely on the area of protected land may be overestimating the true level of protection for biodiversity and highlight the need for international reporting on protected areas to include robust, reproducible measures of human pressure and ecological condition (*5*). It is also important to note that we are unable to capture the full range of human impacts on biodiversity, such as ecological shifts associated with changing climate and disturbance regimes (*19*), which should also be incorporated into measures of protected-area condition.

Although we show that human pressure may be compromising the conservation value of protected lands worldwide, we are not suggesting that high-pressure protected areas be degazzetted (abolished) or defunded. On the contrary, it is crucial that nations recognize the profound conservation gains that can be realized by "upgrading" (increasing the strictness of protection zones) and restoring degraded protected areas, while respecting the needs of local people (*20*). A crucial part of this will be combatting the chronic underfunding of protected areas worldwide, which will require recognizing and quantifying the return on investment that well-managed protected areas provide, through preservation of cultural heritage, improvements in economic and social well-being, and the natural capital they hold (*21*, *22*). Funding could also be increased through mechanisms that allow nations to trade or offset conservation funding and commitments, so wealthy nations can support conservation in poorer nations (*23*). Our finding that there is no relationship between the degree of human pressure and IUCN categories III to VI points to a need for nations to categorize protected areas on the basis of consistent classifications of permitted human activities, which would ensure that IUCN categories better reflect the actual impacts of human activities within protected areas (*24*).

We show that human pressure is prevalent within many protected areas, but our work is subject to three caveats. First, although we explore a scenario in which land under intense human pressure does not contribute toward conservation targets, some aspects of biodiversity can persist in areas of high human pressure [for example, mixed agricultural land (*25*)], and some protected areas are intentionally placed in high-pressure areas. Second, the human footprint does not account for all pressures affecting biodiversity, such as poaching or climate change. This is especially true for developing regions, where activities such as small-scale shifting agriculture and poaching are exerting considerable pressure on biodiversity in many protected areas (*9*). Third, the human footprint measures the pressure humans place on the environment, not the realized state or impact on biodiversity. Further studies investigating how natural systems within protected areas respond to specific human pressures, or assessing the impacts of human pressure on biodiversity within protected areas at a local scale, would provide valuable additional information for measuring progress toward Convention on Biological Diversity commitments.

The Convention on Biological Diversity provides an opportunity to overcome one of society's grandest challenges—halting global biodiversity loss. Many nations report being on track to meet their commitments (*2*), but our analysis suggests that this progress may be undermined by widespread human pressure inside protected areas. As nations continue to expand their protected-area estates, there is clearly an urgent need for them to undertake objective assessments of human pressure and habitat condition within protected areas. These efforts must be combined with better management practices in land beyond protected areas, to ensure that nature conservation goals can be more fully achieved across diverse landscapes in the long term.

REFERENCES AND NOTES

1. A. D. Barnosky *et al.*, *Nature* **471**, 51–57 (2011).
2. UN Environment World Conservation Monitoring Centre, International Union for Conservation of Nature, World Database on Protected Areas (2017); www.protectedplanet.net.
3. Convention on Biological Diversity, "COP 10 decision X/2: strategic plan for biodiversity 2011–2020," 10th Meeting of the Conference of the Parties to the Convention on Biological Diversity, Nagoya, Japan, 18 to 29 October 2010.
4. N. Dudley, S. Stolton, P. Shadie, *Guidelines for Applying Protected Area Management Categories* (International Union for Conservation of Nature, Gland, Switzerland, 2008).

5. J. E. M. Watson *et al*., *Conserv. Biol.* **30**, 243–248 (2016).
6. C. L. Gray *et al*., *Nat. Commun.* **7**, 12306 (2016).
7. B. W. T. Coetzee, K. J. Gaston, S. L. Chown, *PLOS ONE* **9**, e105824 (2014).
8. T. Newbold *et al*., *Nature* **520**, 45–50 (2015).
9. W. F. Laurance *et al*., *Nature* **489**, 290–294 (2012).
10. J. Geldmann, L. N. Joppa, N. D. Burgess, *Conserv. Biol.* **28**, 1604–1616 (2014).
11. W. F. Laurance, M. Goosem, S. G. W. Laurance, *Trends Ecol. Evol.* **24**, 659–669 (2009).
12. J. B. Kauffman, W. C. Krueger, *J. Range Manage.* **37**, 430–438 (1984).
13. M. F. J. Aronson *et al*., *Proc. Biol. Sci.* **281**, 20133330 (2014).
14. O. Venter *et al*., *Nat. Commun.* **7**, 12558 (2016).
15. K. Safi, N. Pettorelli, *Glob. Ecol. Biogeogr.* **19**, 352–362 (2010).
16. M. A. Tucker *et al*., *Science* **359**, 466–469 (2018).
17. T. H. Ricketts *et al*., *Proc. Natl. Acad. Sci. U.S.A.* **102**, 18497–18501 (2005).
18. P. Moguel, V. M. Toledo, *Conserv. Biol.* **13**, 11–21 (1999).
19. B. R. Scheffers *et al*., *Science* **354**, aaf7671 (2016).
20. R. M. Pringle, *Nature* **546**, 91–99 (2017).
21. A. Balmford *et al*., *Science* **297**, 950–953 (2002).
22. J. E. M. Watson, N. Dudley, D. B. Segan, M. Hockings, *Nature* **515**, 67–73 (2014).
23. P. A. Lindsey *et al*., *Glob. Ecol. Conserv.* **10**, 243–252 (2017).
24. B. Horta e Costa *et al*., *Mar. Policy* **72**, 192–198 (2016).
25. B. Phalan, M. Onial, A. Balmford, R. E. Green, *Science* **333**, 1289–1291 (2011).

ACKNOWLEDGMENTS

We are grateful to M. Di Marco, M. Hockings, J. Geldmann, N. Burgess, L. Coad, and the Green Fire Science lab group for providing constructive feedback and discussions around elements of this study. **Funding:** This work was supported by an Australian Government Research Training Program Scholarship. **Author contributions:** K.R.J., O.V., and J.E.M.W. designed the research. K.R.J. performed the analysis. K.R.J., O.V., R.A.F., J.R.A., S.L.M., P.J.N., and J.E.M.W. wrote the manuscript. **Competing interests:** None declared. **Data and materials availability:** The revised human footprint data are available for download from http://datadryad.org/resource/doi:10.5061/dryad.052q5. Protected-area data are available for download from www.protectedplanet.net/. Ecoregional data are available for download from www.worldwildlife.org/publications/terrestrial-ecoregions-of-the-world. Country-, ecoregion-, and biome-level protected area–coverage statistics are available for download from www.protectedplanet.net/c/protected-planet-report-2016/protected-planet-report-2016–data–maps-figures. All other data needed to evaluate the conclusions in the paper are present in the paper or the supplementary materials.

SUPPLEMENTARY MATERIALS

www.sciencemag.org/content/360/6390/788/suppl/DC1
Materials and Methods
Figs. S1 to S7
Tables S1 to S2
References (*26*–*36*)

14 September 2017; accepted 29 March 2018
10.1126/science.aap9565

CLIMATE CHANGE

The projected effect on insects, vertebrates, and plants of limiting global warming to 1.5°C rather than 2°C

R. Warren,[1]* J. Price,[1] E. Graham,[2] N. Forstenhaeusler,[1] J. VanDerWal[2]

In the Paris Agreement on Climate Change, the United Nations is pursuing efforts to limit global warming to 1.5°C, whereas earlier aspirations focused on a 2°C limit. With current pledges, corresponding to ~3.2°C warming, climatically determined geographic range losses of >50% are projected in ~49% of insects, 44% of plants, and 26% of vertebrates. At 2°C, this falls to 18% of insects, 16% of plants, and 8% of vertebrates and at 1.5°C, to 6% of insects, 8% of plants, and 4% of vertebrates. When warming is limited to 1.5°C as compared with 2°C, numbers of species projected to lose >50% of their range are reduced by ~66% in insects and by ~50% in plants and vertebrates.

Climate change poses risks to biodiversity through a number of mechanisms (*1*–*3*). The United Nations Framework Convention on Climate Change (UNFCCC) Paris Agreement aims to limit global warming to "well below 2°C" above preindustrial levels and to "pursue efforts" to limit it to 1.5°C. Previous policy-relevant research on the risks climate change poses to biodiversity focused on quantifying the benefits of limiting warming to 2°C above preindustrial levels in terms of avoided range loss (*4*). Studies of the potential effects of climate change on insects generally focused on small groups only [e.g., (*5*–*8*)], although some studies covered a family of insects in a single country [e.g., Australian butterflies (*9*)].

Here we quantify the difference that avoiding an additional 0.5°C warming (from 2° to 1.5°C) by 2100 would make for biodiversity in terms of avoided changes in climatically determined range size (loss or gain, hereafter "range size"). We provide a global assessment of the potential impacts of climate change on the range sizes of more than 115,000 terrestrial species, including more than 34,000 insects and other invertebrates not included in previous global-scale studies of climate change and biodiversity [(*4*, *10*)].

This work builds on the earlier study with a number of notable updates and improvements (*4*, *11*): the inclusion of insects, which are particularly important for healthy ecosystem functioning (*12*); a near-tripling of the number of species studied; a nearly five times higher spatial resolution [allowing the inclusion of species with ranges approximately one-fifth the size of those in a previous analysis (*4*)]; and a set of new climate change scenarios and models. We also specifically looked at warming levels specific to current policy efforts, including a scenario in which countries make no further emission reductions after achieving the first Nationally Determined Contributions in 2030, hereafter referred to as "current pledges," corresponding to the upper end of a warming range of 2.6° to 3.2°C (http://www.wri.org/) (*13*); and with a scenario with little or no climate change mitigation and a warming of 4.5°C [all temperatures relative to preindustrial (*11*)].

Two complementary metrics are used to compare climate change scenario outcomes for the taxa studied: metric 1, the proportion of species losing >50% of their current climatically determined range, providing a broad-brush indicator of biodiversity range loss comparable with previous studies; and metric 2, the total integrated range loss, providing a complementary indicator of biodiversity range loss that allows the full range of outcomes within taxa to be examined. It has a maximum value of 1, which corresponds to 100% range loss in all species and gives the magnitude of range loss across all species in a taxon.

Constraining warming to 1.5°C instead of 2°C reduces the number of plant and vertebrate species exposed to >50% projected range loss by ~50% (Fig. 1 and table S2) for all taxa explored (although the benefits are slightly smaller for reptiles). However, for insects (and more broadly, invertebrates), the risks are reduced by ~66%. Overall, the risks at 4.5°C warming are 8 to 10 times larger than those at 1.5°C warming.

With current pledges (~3.2°C), projected geographic range losses of >50% occur in 49% (31 to 65%) of the insects, 44% (29 to 63%) of the plants, and 26% (16 to 40%) of the vertebrates. At 2°C, these are reduced by 60 to 70%, to 18% (6 to 35%) of the insects, 16% (9 to 28%) of the plants, and 8% (4 to 16%) of the vertebrates. At 1.5°C, this is reduced further to 6% (1 to 18%) of the insects, 8% (4 to 15%) of the plants, and 4% (2 to 9%) of the vertebrates (table S2). Overall, insects are exposed to greater potential climatic range loss than any other animal group (Fig. 1) and also benefit the most if warming is constrained to 1.5°C rather than 2°C. Among insect orders, Diptera, Coleoptera, and Hemiptera show the greatest potential range loss and Odonata the lowest (fig. S1).

Our findings support earlier literature projecting large increases in range loss and extinction risk potentially associated with warming (*14*, *15*). The shapes of the range loss curves (Fig. 2) provide additional information about numbers of species losing large proportions of their range, showing how these change from concave at 1.5°C to convex by 3.2°C, reflecting increasing risks. For insects (fig. S2), this change in form is particularly strong, which indicates more rapid increases in risk.

Under current pledges (3.2°C), the projected total integrated range loss is 43% (30 to 55%) in the insects, 46% (36 to 57%) in the plants, and 21% (9 to 34%) in the vertebrates. At 2°C, this is reduced by 30 to 60% to 27% (16 to 37%) in the insects, 30% (23 to 38%) in the plants, and 10% (1 to 20%) in the vertebrates; and at 1.5°C, to 20% (11 to 28%) in the insects, 24% (18 to 30%) in the plants, and 6% (−1 to 14%) in the vertebrates (table S3). This metric thus also indicates that insects and plants are the groups with the greatest exposure, closely followed by amphibians, and also that insects benefit the most from constraining warming to 1.5°C rather than 2°C. Our results also show that there is still appreciable climatic range loss at 1.5°C warming, despite the relatively small proportions of species for which range loss of >50% is projected (Fig. 2, figs. S2 and S3, and table S3).

Figure 1, figs. S1 and S3, and tables S4 and S5 include corresponding projections for the alternative assumption of no dispersal. Without dispersal, Lepidoptera and Odonata appears more vulnerable to climate change than otherwise (figs. S2 and S3); as do Aves and Mammalia (fig. S2), indicating how critical dispersal is for potential climate change adaptation for these taxa. Figure 2, fig. S2, and table S6 also indicate the small proportions of species gaining range size via dispersal. Except for Odonata, the proportions gaining more than half their range are vastly greater than the proportions losing over half, except at 1.5°C warming. In this case, when dispersal is included, the proportions of Mammalia and Aves species gaining or losing >50% of their climatic range is similar at 1.5°C (table S6), and the total integrated range loss is also close to zero (Fig. 2 and table S3). Odonata shows a very different climate response to any other taxa, with the number of species gaining range appearing to be balanced by the loss at all levels of warming, and indeed slightly negative values of integrated range loss (table S3).

Figures S4 and S5 show that among Lepidoptera, moths are at greater risk than butterflies, and moths benefit considerably more than butterflies if warming is constrained to 1.5°C rather than 2°C, a finding consistent with a recent attribution study relating 48% of moth population declines in the United Kingdom to climate change (*16*). Projected risks for key insect crop pollinator families (Apidae, Syrphidae, and Calliphoridae; i.e., bees, hoverflies, and blowflies) are also (figs. S4 and S5) greatly reduced.

[1]Tyndall Centre for Climate Change Research, School of Environmental Sciences, University of East Anglia, Norwich NR4 7TJ, UK. [2]College of Science and Engineering, James Cook University, Townsville, Australia.
*Corresponding author. Email: r.warren@uea.ac.uk

Figure 3 indicates the geographical distribution of the benefits of limiting warming to 1.5°C as compared with 2°C, and 2°C compared with 3.2°C in plants, vertebrates, and insects. Areas benefiting the most from constraining warming are Southern Africa, parts of the Amazon, Europe, and Australia. Figure S6 indicates the projected changes in species richness globally at the four levels of warming (1.5°, 2°, 3.2°, 4.5°C above preindustrial levels) and, where appropriate, (for animals) including or excluding realistic dispersal. Areas where potential species richness declines the most due to climate change of 3.2° and 4.5°C are Southern Africa, Australia, and the high Arctic.

We find substantial benefits to limiting warming to 1.5°C above preindustrial levels as compared with 2°C by 2100. The number of insect species projected to lose >50% of their range is reduced by about 66%, whereas the number of plant and animal species projected to lose more than half their range is reduced by ~50%. Hence, successful implementation of the Paris Agreement could lead to substantial benefits for global terrestrial biodiversity. Risks to biodiversity generally increase linearly with increased global temperature rises of between 1.5° and 4.5°C warming irrespective of the metric used (figs. S7 and S8). The projected risks of warming are in general greater for most invertebrates, plants, amphibians, and reptiles than for mammals, birds, and a few of the insect groups studied, owing to their slower dispersal rates. Because range loss may increase extinction risk, it follows that limiting warming to 1.5°C rather than 2°C also reduces extinction risk, and the reduction associated with limiting warming to 1.5°C rather than 3.2°C is greater still.

However, restricting warming to 1.5°C may be difficult. Of the 166 climate change mitigation scenarios assessed (*17*), 87% of those limiting warming to less than 2°C with >66% probability incorporate "negative emissions technology," typically large-scale bioenergy with carbon capture and storage (BECCS) (*18*). If primary bioenergy is used to supply BECCS, up to 18% of the land surface could be required by the end of the century (*19*); or 24 to 36% of the current arable cropland (*20*). Competition for land between bioenergy and agriculture could intensify, potentially leading to indirect land-use change and ecosystems conversion to cropland (*21*–*23*), unless conservation measures are in place and enforced. It could also lead to agricultural intensification, potentially leading to declines in insect populations (*24*). Hence, to realize the projected benefits to biodiversity quantified here, we introduce the term "Article 2 compliant mitigation." This puts into practice the need to allow "ecosystems to adapt naturally" to climate change; requiring careful design and expansion of existing protected area networks to allow species to persist and disperse with warming in tandem with mitigation activities. New studies are exploring scenarios in which BECCS is produced from secondary biofuels, or in which there are dietary changes in humans, resulting in greatly

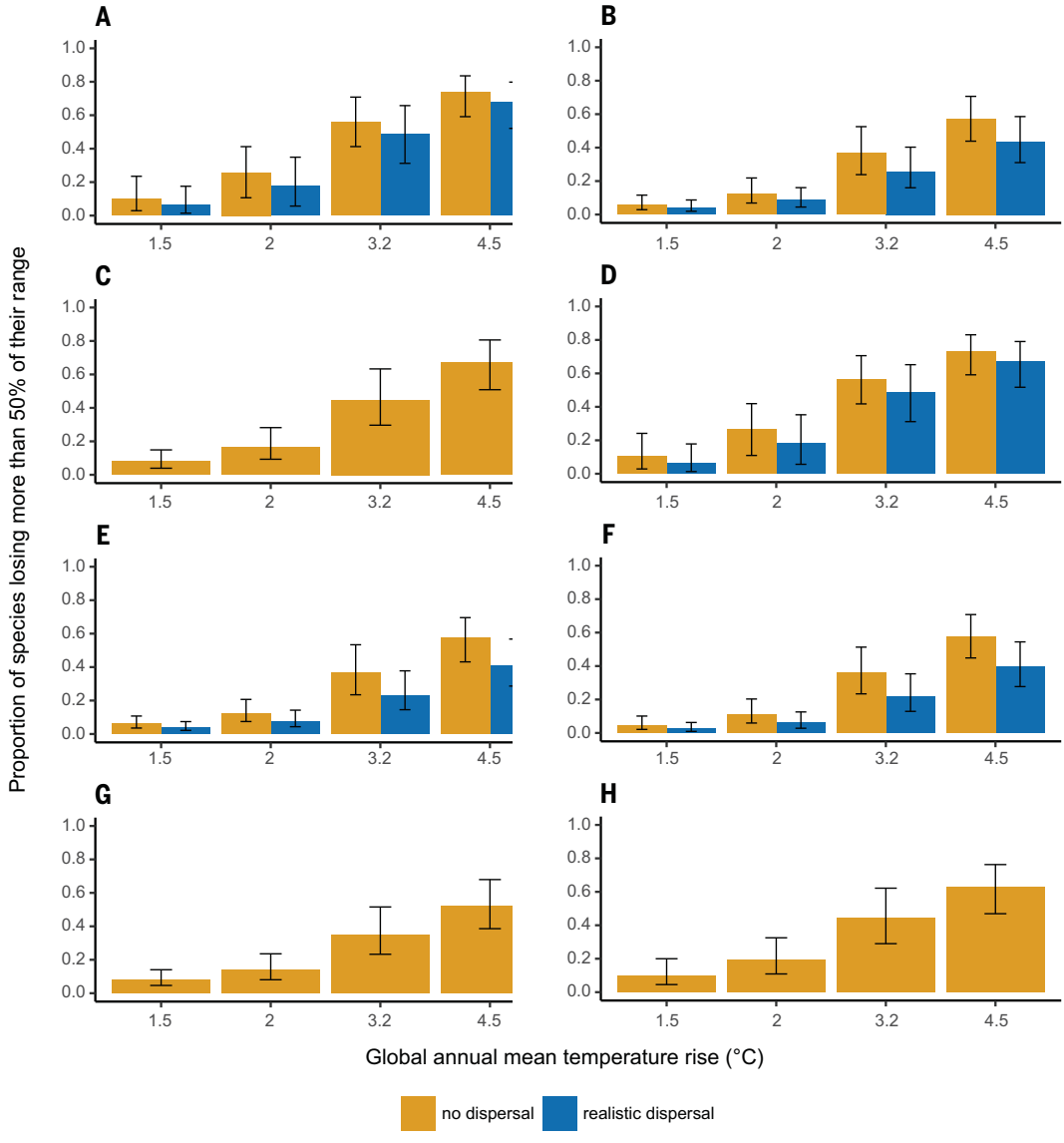

Fig. 1. The proportion of modeled species losing more than half their climatically determined range by 2100 at specific levels of global warming. (**A**) Invertebrates (*n* = 34,104), (**B**) Chordata (*n* = 12,640), (**C**) Plantae (*n* = 73,224), (**D**) Insecta (*n* = 31,536), (**E**) Mammalia (*n* = 1769), (**F**) Aves (*n* = 7966), (**G**) Reptilia (*n* = 1850), and (**H**) Amphibia (*n* = 1055). Colors: Including (blue) and excluding (orange) realistic dispersal. Data are presented as the mean projection across 21 alternative climate model patterns with error bars indicating the 10 to 90% range.

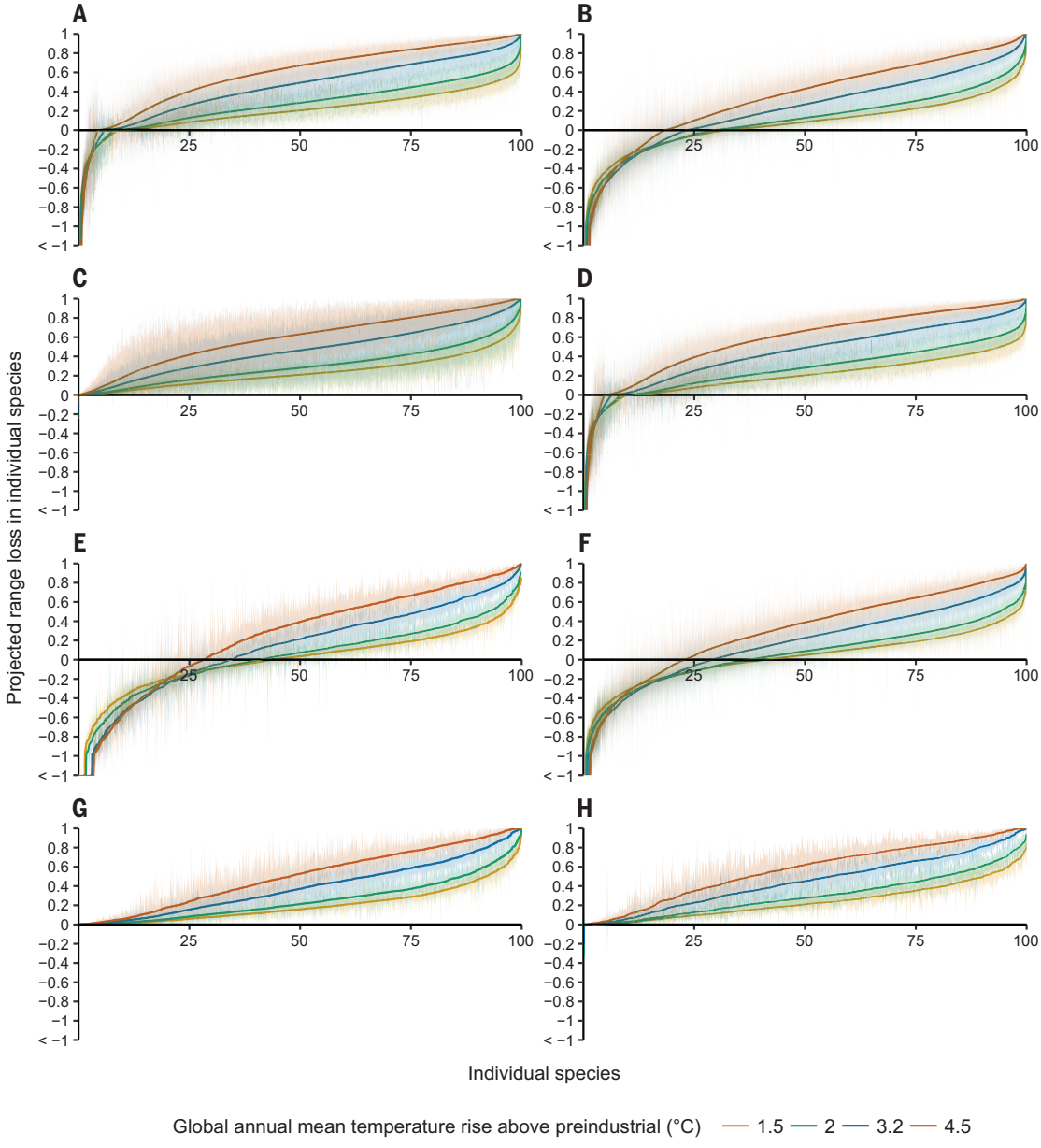

Fig. 2. Projected climatically determined range loss by 2100 for all species at specific levels of global warming. (**A**) Invertebrates (*n* = 34,104), (**B**) Chordata (*n* = 12,640), (**C**) Plantae (*n* = 73,224), (**D**) Insecta (*n* = 31,536), (**E**) Mammalia (*n* = 1769), (**F**) Aves (*n* = 7966), (**G**) Reptilia (*n* = 1850), and (**H**) Amphibia (*n* = 1055). The proportion ranges from +1 (100% loss) to −1 (100% gain); values <−1 indicate more than 100% gain. *X* axes represent the 0th to 100th percentile of species arranged in order of increasing range loss, normalized by the number modeled in the taxon. Losses for each species are shown as mean and 10 to 90% range across regional climate model patterns as in Fig. 1.

reduced effects of indirect land-use change (*25*). The implications of "overshoot" scenarios in which temperatures exceed a particular level and later return to it are provided in the supplementary materials (*11*).

This study has focused on a comparison of benefits of reaching 1.5°C versus 2°C warming by 2100. On other time scales, the risks associated with reaching these alternative levels of warming will depend on the time scale: The earlier a particular level of warming is reached, the greater the risks, because species will have less time to disperse naturally to track their climate envelope, and society will have less time to expand protected area networks or otherwise facilitate movement. Mitigation, therefore, "buys time" for adaptation.

Caveats notwithstanding (*11*), our results are generally considered to likely be conservative, in particular in light of the lack of consideration of the potential disruption of predator-prey, plant-pollinator, mutualistic, or other species-species interactions (*2*, *26*) and the limited evidence that mutualisms may or may not be substituted under climate change (*27*). Such disruptions may lead to losses of ecosystem functioning, particularly important given the finding that projected range losses in insects and plants may, in many places, exceed those for birds and mammals that have a greater ability to disperse naturally to track their geographically shifting climate envelope. Additionally, lack of consideration of potential risks associated with extreme weather events, projected to become more frequent and intense in many regions (*28*, *29*) or fire regimes (*11*), may lead to impacts potentially occurring sooner than models project.

These projected declines in climatically determined ranges of species would be expected to have a concomitant effect on ecosystem functioning and the delivery of important provisioning and regulating ecosystem services and the maintenance of human well-being (*30*). Recently, declines of 76 to 82% in flying insect populations have been reported in Germany over the past 27 years (*24*); and, globally, 67% of the invertebrates studied showed a 45% abundance decline (*31*). If these observations are representative of global trends, any projected declines arising from climate change would add to those observed. Such declines would reduce ecosystem

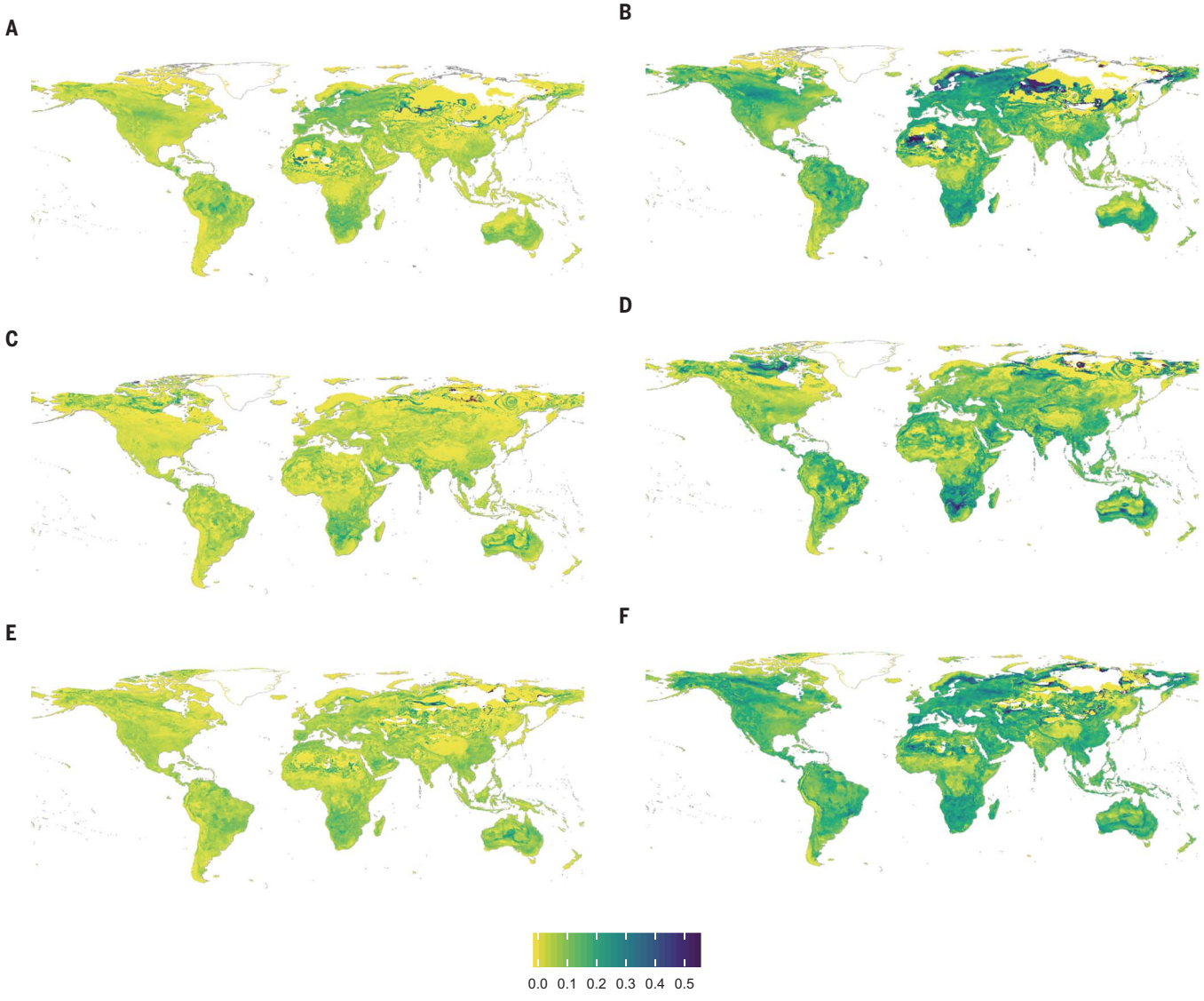

Fig. 3. Benefits of global annual mean temperature rise in terms of avoided species richness loss. (**A** and **B**) Insecta, (**C** and **D**) Chordata, and (**E** and **F**) Plantae without dispersal. (A, C, E) 1.5°C versus 2°C; (D, E, F) 2°C versus 3.2°C.

services with concomitant implications for plant survival (*29*, *30*). Insects are also key to food provisioning for higher trophic levels and perform other key functions in ecosystems such as detritivory, herbivory, and nutrient cycling (*28*, *32*, *33*). Hence, risks to these vital ecosystem functions and services performed by insects are substantially smaller if global warming is constrained to 1.5°C above preindustrial levels as compared with 2°C.

REFERENCES AND NOTES

1. T. L. Root *et al.*, *Nature* **421**, 57–60 (2003).
2. A. Fischlin *et al.*, in *Climate Change 2007: Impacts, Adaptation and Vulnerability. Contribution of Working Group II to the Fourth Assessment Report of the Intergovernmental Panel on Climate Change*, M. L. Parry, O. F. Canziani, J. P. Palutikof, P. J. van der Linden, C. E. Hanson, Eds. (Cambridge Univ. Press, Cambridge, 2007), pp. 211–272.
3. E. Post *et al.*, *Science* **341**, 519–524 (2013).
4. R. Warren *et al.*, *Nat. Clim. Chang.* **3**, 678–682 (2013).
5. M. C. Fitzpatrick *et al.*, *Ecography* **34**, 836–847 (2011).
6. T. C. Giannini *et al.*, *Ecol. Modell.* **244**, 127–131 (2012).
7. V. G. Ferro, P. Lemes, A. S. Melo, R. Loyola, *PLOS ONE* **9**, e107792 (2014).
8. T.-S. Kwon, C. M. Lee, T. W. Kim, S.-S. Kim, J. H. Sung, *J. Asia-Pacific Biodiversity* **7**, e133–e155 (2014).
9. L. J. Beaumont, L. Hughes, *Glob. Change Biol.* **8**, 954–971 (2002).
10. W. B. Foden *et al.*, *PLOS ONE* **8**, e65427 (2013).
11. Supplementary text is available in the supplementary materials.
12. W. W. Weisser, E. Siemann, in *Insects and Ecosystem Function*, W. W. Weisser, E. Siemann, Eds. (Springer Berlin Heidelberg, Berlin, Heidelberg, 2008), pp. 3–24.
13. J. Rogelj *et al.*, *Nature* **534**, 631–639 (2016).
14. C. D. Thomas *et al.*, *Nature* **427**, 145–148 (2004).
15. M. C. Urban, *Science* **348**, 571–573 (2015).
16. B. Martay *et al.*, *Ecography* **40**, 1139–1151 (2017).
17. L. Clarke *et al.*, in *Climate Change 2014: Mitigation of Climate Change. Contribution of Working Group III to the Fifth Assessment Report of the Intergovernmental Panel of Climate Change*, O. Edenhofer *et al.*, Eds. (Cambridge Univ. Press, Cambridge, UK, 2014).
18. P. Smith *et al.*, *Nat. Clim. Chang.* **6**, 42–50 (2015).
19. A. Wiltshire, T. Davies-Barnard, "Planetary limits to BECCS negative emissions" (AVOID2 WPD.2a Report 1, 2015); available at www.avoid.uk.net/2015/07/planetary-limits-to-beccs-negative-emissions-d2a/.
20. A. Popp *et al.*, *Clim. Change* **123**, 495–509 (2014).
21. M. Tavoni, R. Socolow, *Clim. Change* **118**, 1–14 (2013).
22. P. Smith *et al.*, *Glob. Change Biol.* **19**, 2285–2302 (2013).
23. P. Smith, J. Price, A. Molotoks, R. Warren, Y. Malhi, *Philos. Trans. R. Soc. A* **376**, 20160456 (2018).
24. C. A. Hallmann *et al.*, *PLOS ONE* **12**, e0185809 (2017).
25. D. P. Van Vuuren, A. Hof, D. Gernaat, M.-S. de Boer, "Limiting global temperature to 1.5°C: implications for carbon budgets, emissions and energy pathways" (PBL Netherlands Environmental Assessment Agency, 2017).
26. R. J. Warren 2nd, M. A. Bradford, *Glob. Change Biol.* **20**, 466–474 (2014).
27. C. Parmesan, A. Williams-Anderson, M. Moskwik, A. S. Mikheyev, M. C. Singer, *J. Insect Conserv.* **19**, 185–204 (2015).
28. O. McDermott Long *et al.*, *J. Anim. Ecol.* **86**, 108–116 (2017).
29. T. H. Oliver *et al.*, *Nat. Clim. Chang.* **5**, 941–945 (2015).
30. K. J. Gaston, R. A. Fuller, *Trends Ecol. Evol.* **23**, 14–19 (2008).
31. R. Dirzo *et al.*, *Science* **345**, 401–406 (2014).

32. J. C. Biesmeijer *et al.*, *Science* **313**, 351–354 (2006).
33. K. L. Stuble *et al.*, *PeerJ* **2**, e286 (2014).

ACKNOWLEDGMENTS

The model computing and data storage are part of a near-decade-long partnership with the eResearch Centre at James Cook University. We acknowledge I. Atkinson and his staff for their long collaboration on the Wallace Initiative. We thank A. Franco for comments on an earlier draft of the manuscript. **Funding:** This work was funded by the UK Natural Environment Research Council (NERC) grant no. NE/P014992/1.

Author contributions: All authors contributed to the paper and to all aspects of the work, but the main roles of the team members were as follows: R.W. wrote the paper and managed the NERC project; J.P., R.W., and J.V. designed the original experiments; E.G., J.P., and J.V. prepared the data, ran the models, and analyzed the output data; N.F. helped analyze the data and prepare the figures. The team are members of the Wallace Initiative collaboration led by J.P. **Competing interests:** The authors have no competing interests. **Data and materials availability:** The data are available from wallaceinitiative.org, or by request to datasharing@wallaceinitiative.org.

SUPPLEMENTARY MATERIALS

www.sciencemag.org/content/360/6390/791/suppl/DC1
Materials and Methods
Supplementary Text
Figs. S1 to S8
Tables S1 to S6
References (*34*–*55*)

1 November 2017; accepted 12 April 2018
10.1126/science.aar3646

MICROBIOTA

Gut microbiota utilize immunoglobulin A for mucosal colonization

G. P. Donaldson,[1]* M. S. Ladinsky,[1] K. B. Yu,[1] J. G. Sanders,[2,3] B. B. Yoo,[1] W.-C. Chou,[4] M. E. Conner,[5] A. M. Earl,[4] R. Knight,[2,3] P. J. Bjorkman,[1] S. K. Mazmanian[1]*

The immune system responds vigorously to microbial infection while permitting lifelong colonization by the microbiome. Mechanisms that facilitate the establishment and stability of the gut microbiota remain poorly described. We found that a regulatory system in the prominent human commensal *Bacteroides fragilis* modulates its surface architecture to invite binding of immunoglobulin A (IgA) in mice. Specific immune recognition facilitated bacterial adherence to cultured intestinal epithelial cells and intimate association with the gut mucosal surface in vivo. The IgA response was required for *B. fragilis* (and other commensal species) to occupy a defined mucosal niche that mediates stable colonization of the gut through exclusion of exogenous competitors. Therefore, in addition to its role in pathogen clearance, we propose that IgA responses can be co-opted by the microbiome to engender robust host-microbial symbiosis.

At birth, ecological and evolutionary processes commence to assemble a complex microbial consortium in the animal gut. Community composition of the adult human gut microbiome is remarkably stable during health, despite day-to-day variability in diet and diverse environmental exposures. Instability, or dysbiosis, may be involved in the etiology of a variety of immune, metabolic, and neurologic diseases (*1*, *2*). Longitudinal sequencing studies indicate that a majority of bacterial strains persist within an individual for years (*3*), and for most species there is a single, persistently dominant strain (*4*) (termed "single-strain stability"). Mucus and components of the innate and adaptive immune systems are thought to influence microbiome stability, independently of diet. For example, immunoglobulin A (IgA), the main antibody isotype secreted in the gut, shapes the composition of the intestinal microbiome via currently unknown mechanisms (*5*–*8*). IgA deficiency in mice increases interindividual variability in the microbiome (*9*) and decreases diversity (*10*, *11*). The direct effects of IgA on bacteria have largely been studied in the context of enteric infection by pathogens (*12*). However, early studies of IgA in the healthy gut found that the majority of live bacterial cells in feces are bound by IgA (*13*), reflecting a steady-state IgA response to persistent indigenous microbes (*14*). Studies show that IgA promotes adherence of commensal bacteria to tissue-cultured intestinal epithelial cells (*15*, *16*), although the in vivo implications of this observation are unclear. Furthermore, lack of IgA, the most common human immunodeficiency, does not affect lifespan and only modestly increases susceptibility to respiratory and gastrointestinal infections (*17*); hence, it remains a mystery why the immune system evolved to invest the considerable energy needed to produce several grams of IgA daily (*18*).

Bacteroides fragilis is an important member of the human gut microbiome, with beneficial properties that ameliorate inflammatory and behavioral symptoms in preclinical animal models (*19*–*22*). This commensal exhibits remarkable single-strain stability (*23*, *24*) and enriched colonization of the gut mucosal surface relative to other species (*25*). To explore physical features of *B. fragilis* interaction with the host epithelium, we used transmission electron microscopy (TEM) to visualize colonic tissues of monocolonized mice. *B. fragilis* commonly formed discrete aggregates of tightly packed cells on the apical epithelial surface (Fig. 1A) and penetrated the glycocalyx layer of transmembrane mucins, nearly contacting the microvilli (Fig. 1B and fig. S1, A and B). Intact *B. fragilis* cells were also found nestled in the ducts of the crypts of Lieberkühn (Fig. 1C and fig. S1C). We previously identified a genetic locus in *B. fragilis*, named the commensal colonization factors (*ccfABCDE*), which is necessary for colonization of colonic crypts (*26*). To assess how these genes affect bacterial localization to the mucosal surface, we monocolonized mice with a *ccfCDE* (Δ*ccf*) mutant. TEM showed that *B. fragilis* Δ*ccf* was found only as sparse, individual cells within the epithelial mucosa, excluded from contact with the glycocalyx (Fig. 1, D and E); unlike wild-type *B. fragilis*, it was never observed in aggregates (Fig. 1F). The *B. fragilis* burden in the colon lumen was identical between strains (fig. S2A), which suggests that the CCF system is required specifically for bacterial aggregation within mucus.

High-resolution tomograms of bacterial cells in vivo revealed the presence of a thick, fuzzy capsule layer covering wild-type *B. fragilis* (Fig. 1G), which was significantly reduced in *B. fragilis* Δ*ccf* (Fig. 1, H and I). We sought to investigate the bacterial physiology underlying this ultrastructural change and its potential corresponding effects on colonization. The *ccf* locus is highly induced during gut colonization (*26*) and bacterial growth in mucin O-glycans (*27*), indicating that the CCF system may sense a specific host-derived glycan. The *ccf* genes are homologous to polysaccharide utilization systems in which a sigma factor (*ccfA*) is activated by extracellular glycan sensing (*28*); thus, we hypothesized that *ccfA* may activate genes involved in mucosal colonization. We overexpressed *ccfA* in *B. fragilis* and assessed global gene expression by RNA sequencing (RNA-seq) during in vitro growth [without overexpression, *ccf* is poorly expressed in culture (*26*)]. Of the non-*ccf* genes regulated by *ccfA*, 24 of 25 genes mapped to the biosynthesis loci for capsular polysaccharides A and C (PSA and PSC) (Fig. 2, A and B, and table S1). Correspondingly, *ccf* mutation decreased expression of PSC and increased expression of PSA in vivo (Fig. 2C). Although phase variation of capsular polysaccharides is known to influence the general in vivo fitness of *B. fragilis* (*29*, *30*), these studies identify a pathway for transcriptional regulation of specific polysaccharides in the context of mucosal colonization.

We modeled single-strain stability using a horizontal transmission assay, wherein co-housing animals respectively harboring isogenic strains of wild-type *B. fragilis* resulted in minimal strain transmission from one animal to another (Fig. 2D and fig. S2A). This intraspecies colonization resistance is provided through bacterial occupation of a species-specific nutrient or spatial niche (*26*). However, as previously reported (*26*), when mice were colonized initially with *B. fragilis* Δ*ccf*, animals were permissive to co-colonization by wild-type *B. fragilis* after co-housing (Fig. 2E and fig. S2B), indicating a CCF-dependent defect in niche saturation. Mice harboring a mutant in the biosynthesis genes for PSC (ΔPSC) showed highly variable co-colonization by wild-type bacteria (Fig. 2F and fig. S2C). We observed an unexpected increase in expression of the PSB biosynthesis genes in this mutant (Fig. 2H), which may compensate for the loss of PSC.

We generated a strain defective in synthesizing both PSB and PSC (ΔPSB/C), and mice mono-associated with the double mutant were consistently unable to maintain colonization resistance (Fig. 2G and fig. S2, D to F), even though the strain retained *ccf* expression (fig. S2G). Despite lack of competition in a monocolonized setting and equal levels of colonization in the colon lumen (fig. S2H), the *B. fragilis* Δ*ccf* and ΔPSB/C strains were defective in colonization of the ascending colon mucus (Fig. 2I), reflecting impaired saturation of the mucosal niche.

[1]Department of Biology and Biological Engineering, California Institute of Technology, Pasadena, CA 91125, USA. [2]Department of Pediatrics, University of California, San Diego, CA 92110, USA. [3]Department of Computer Science and Engineering, University of California, San Diego, CA 92093, USA. [4]Infectious Disease and Microbiome Program, Broad Institute of MIT and Harvard, Cambridge, MA 02142, USA. [5]Department of Molecular Virology and Microbiology, Baylor College of Medicine, Houston, TX 77030, USA.
*Corresponding author. Email: gdonalds@caltech.edu (G.P.D.); sarkis@caltech.edu (S.K.M.)

Accordingly, when we used TEM to image the ΔPSB/C strain in vivo, although the capsule was not as thin as in *B. fragilis* Δ*ccf* (fig. S2, I and J), the hallmark epithelial aggregation phenotype was abrogated relative to wild-type bacteria (fig. S2, K and L). Therefore, we conclude that the CCF system regulates capsule expression to mediate *B. fragilis* mucosal colonization and single-strain stability.

To investigate host responses contributing to mucosal colonization, we defined the transcriptome of the ascending colon during colonization with wild-type *B. fragilis* or *B. fragilis* Δ*ccf*. Remarkably, 7 of the 14 differentially expressed genes encoded Ig variable chains (Fig. 3A and table S2). We did not observe any elevation of immune responses in Δ*ccf*-colonized mice (fig. S3A), indicating that changes in mucosal association

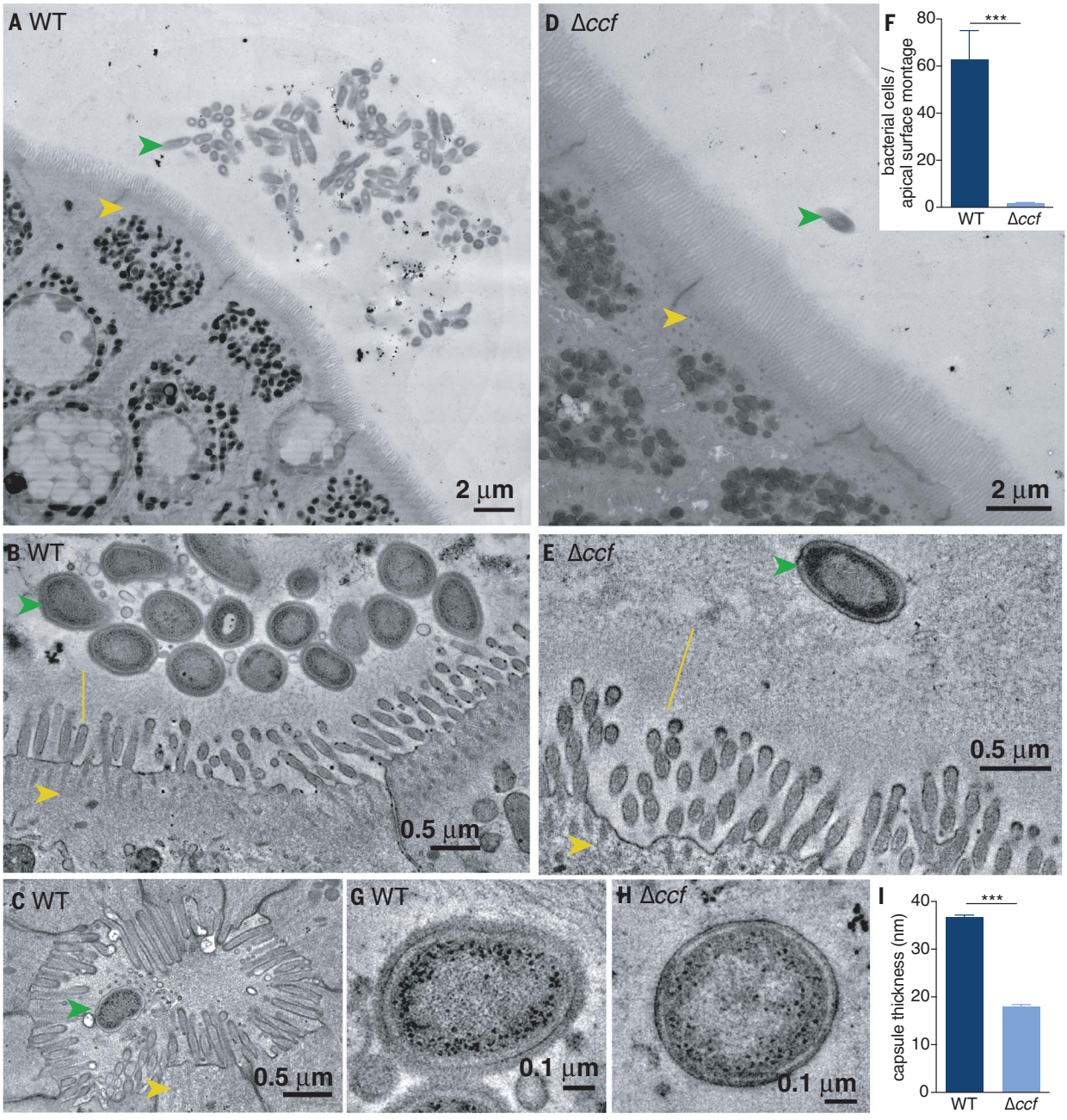

Fig. 1. *Bacteroides fragilis* resides as aggregates on the colon epithelium in a CCF-dependent manner. (**A** and **B**) Representative TEM projection (A) and high-resolution tomogram (B) of epithelial-associated wild-type (WT) *B. fragilis* in monocolonized mice. Under nonpathogenic conditions, ascending colons of mice harbored aggregates of *B. fragilis* (green arrowheads) that made tight associations with the glycocalyx (yellow line) overlying intestinal epithelial cells (yellow arrowheads). (**C**) Tomogram of wild-type *B. fragilis* penetrating deep into the duct of a crypt of Lieberkühn. (**D** and **E**) Representative TEM projection (D) and tomogram (E) of epithelial-associated *B. fragilis* Δ*ccf*. The absence of the CCF system abrogated formation of bacterial aggregates and prevented intimate association with the glycocalyx (n = 3 mice per group, about 1 mm of epithelium scanned per mouse). (**F**) Quantification of bacterial cells per projection montage [(A) and (D)] of epithelial-associated bacteria (mean ± SEM, unpaired t test, n = 7, 8 images from 4 mice per group). (**G** and **H**) Tomograms of the bacterial surface of wild-type *B. fragilis* (G) and *B. fragilis* Δ*ccf* (H) revealed a thick fuzzy capsule for wild-type bacteria residing in the colons of mice. (**I**) Measurement of capsule thickness (mean ± SEM, unpaired t test, n = 10 cells from 3 mice per group). ***$P < 0.001$.

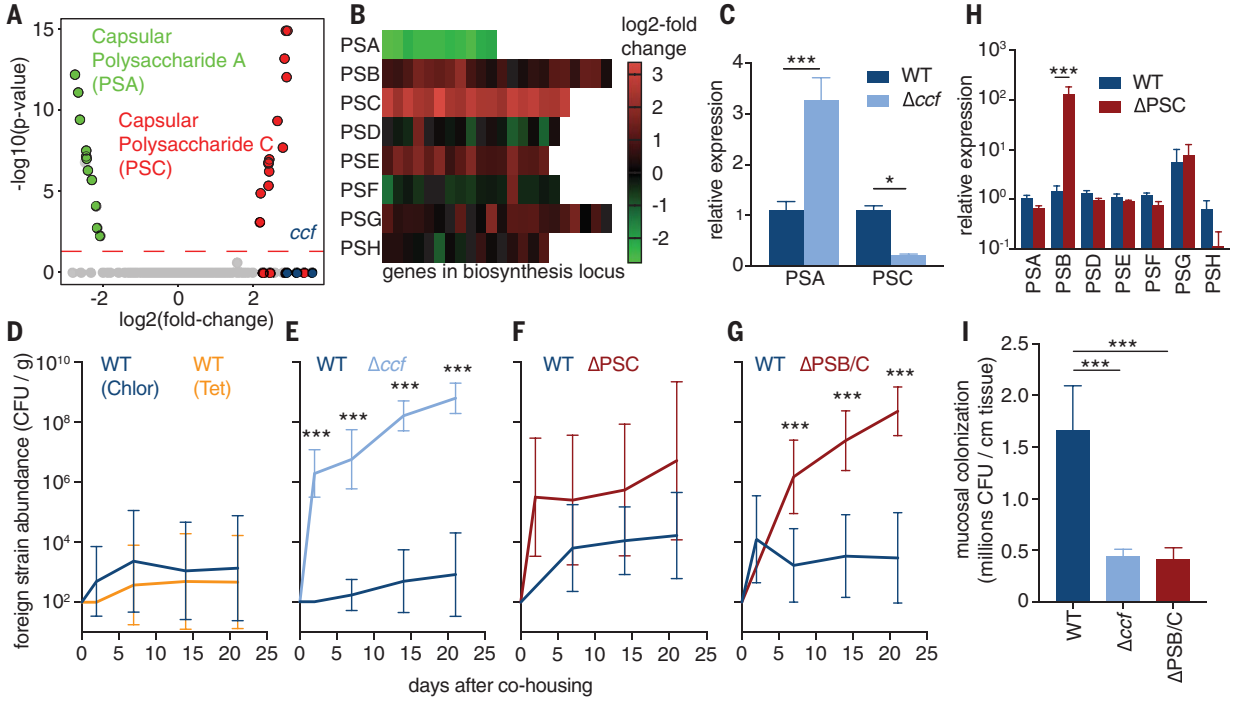

Fig. 2. Specific capsular polysaccharides, regulated by *ccf*, are necessary for single-strain stability. (**A**) RNA-seq gene expression analysis of *B. fragilis* overexpressing *ccfA* during laboratory culture growth, relative to empty vector control (n = 3). Green, PSA genes; red, PSC genes; blue, *ccf* genes. (**B**) Heat map of expression levels for all capsular polysaccharide loci in *B. fragilis* after *ccfA* overexpression during growth in culture. (**C**) Relative expression using quantitative reverse transcription polymerase chain reaction (qRT-PCR; ΔΔCt normalized to gyrase) of RNA from colon lumen contents of mice monocolonized with *B. fragilis* or *B. fragilis* Δ*ccf* [mean ± SEM, Sidak two-way analysis of variance (ANOVA), n = 4]. (**D** to **G**) Abundance of foreign strains exchanged between pairs of co-housed mice each monocolonized with the indicated strains, in colony-forming units (CFU) per gram of feces [Sidak repeated-measures two-way ANOVA on log-transformed data, geometric mean and 95% confidence interval (CI), n = 9 to 12 pairs per plot]. (**H**) Relative expression levels of capsular polysaccharides analyzed by qRT-PCR (ΔΔCt normalized to gyrase) of RNA from colon lumen contents of mice monocolonized with *B. fragilis* or *B. fragilis* ΔPSC (mean ± SEM, Sidak two-way ANOVA, n = 3 for wild type, 4 for ΔPSC). (**I**) Plating of CFU from ascending colon mucus of mice monocolonized with *B. fragilis* strains (mean ± SEM, Tukey ANOVA, n = 8). *P < 0.05, ***P < 0.001.

are not caused by inflammation. Accordingly, we tested whether capsular polysaccharide regulation by *ccf* affects IgA recognition of bacteria (*31*–*33*). In fecal samples from monocolonized animals, wild-type *B. fragilis* was highly coated with IgA, which was significantly diminished in Δ*ccf* and ΔPSB/C strains (Fig. 3, B and C, and fig. S4A). We observed no difference between these strains in the induction of total fecal IgA (Fig. 3D), reflecting equivalent stimulation of nonspecific IgA production (*10*, *34*, *35*). To test bacteria-specific responses, we evaluated IgA that had been extracted from feces of mice monocolonized with *B. fragilis* for binding to bacteria recovered from monocolonized *Rag1*$^{-/-}$ mice (in vivo–adapted, yet IgA-free bacteria). Western blots of bacterial lysates showed that strong IgA reactivity to capsular polysaccharides was abrogated in the Δ*ccf* and ΔPSB/C strains (Fig. 3, E and F). Although IgA can be polyreactive (*10*, *34*, *35*), binding to lysates of *Bacteroides* was species-specific (fig. S4B) and required induction of IgA after bacterial colonization (fig. S4, C and D). Accordingly, in a whole-bacteria binding assay, IgA induced by wild-type bacteria maximally coated wild-type *B. fragilis*, unlike the Δ*ccf* and ΔPSB/C strains (Fig. 3G). IgA induced by *B. fragilis* Δ*ccf* exhibited reduced binding to wild-type bacteria (Fig. 3G). The addition of IgA to in vivo–adapted, IgA-free bacteria increased adherence of *B. fragilis* to intestinal epithelial cells in tissue culture (Fig. 3H), yet had no effect on bacterial viability (fig. S4E). Cell lines known to produce more mucus (*36*) exhibited a greater capacity for IgA-enhanced *B. fragilis* adherence (fig. S4F), consistent with prior work showing that IgA binds mucus (*36*–*38*). IgA-enhanced adherence was decreased whether targeted bacteria lacked *ccf* or PSB/C, or whether the IgA tested was induced by a *ccf* mutant or by *B. thetaiotaomicron* (Fig. 3H and fig. S4G). Whereas pathogenic bacteria elaborate capsular polysaccharides for immune evasion, these results suggest that *B. fragilis* deploys specific capsules for immune attraction, potentially enabling stable mucosal colonization.

We determined whether IgA coating promotes *B. fragilis* colonization in mice. Under the horizontal transmission paradigm, *Rag1*$^{-/-}$ mice colonized with wild-type *B. fragilis* were readily co-colonized by an isogenic strain from a co-housed animal (fig. S5, A and B), showing loss of colonization resistance in the absence of adaptive immunity. We next treated wild-type mice with an antibody to CD20 (fig. S5C) (*39*) to deplete B cells (fig. S5, D to F), thus reducing total fecal IgA levels (fig. S5G) and eliminating IgA coating of wild-type *B. fragilis* during monocolonization (Fig. 4A). IgA recovered from isotype control–treated mice that had been monocolonized with *B. fragilis* promoted adherence of wild-type bacteria to epithelial cells in vitro, whereas IgA from anti-CD20–treated mice had no effect despite being exposed to *B. fragilis* antigens (Fig. 4B). In the horizontal transmission assay, B cell–depleted mice monocolonized with *B. fragilis* were readily invaded by wild-type bacteria, whereas isotype control–injected animals retained colonization resistance (Fig. 4C and fig. S5H). Therefore, active B cell responses to *B. fragilis* colonization enhance single-strain stability.

Because B cell depletion eliminates all antibody isotypes, germ-free IgA$^{-/-}$ mice (*40*) were generated and monocolonized with *B. fragilis*. We did not observe compensatory coating by IgM (fig. S6A). In a horizontal transmission assay with wild-type (BALB/c) and IgA$^{-/-}$ mice, lack of IgA allowed co-colonization by challenge strains (Fig. 4D and fig. S6, B to D), indicating that IgA specifically contributes to single-strain stability. This feature was reproduced in mice with a full microbial community "spiked" with genetically marked *B. fragilis* strains (fig. S6, E and F),

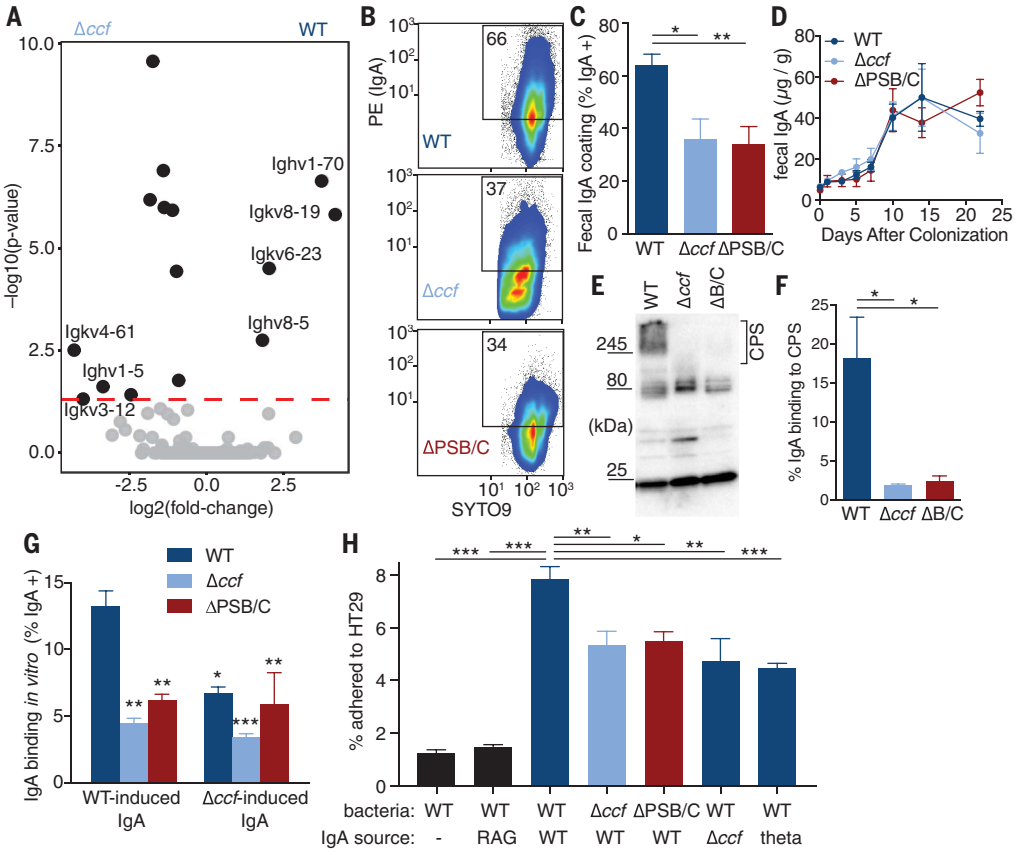

Fig. 3. *B. fragilis* induces a specific IgA response, dependent on *ccf* regulation of surface capsular polysaccharides, which enhances epithelial adherence. (**A**) RNA-seq gene expression analysis of RNA recovered from whole ascending colon tissue of mice monocolonized with *B. fragilis* or *B. fragilis* Δ*ccf* ($n = 3$). (**B**) Flow cytometry plots of *B. fragilis* from feces of monocolonized mice identified with a nuclear stain (SYTO9) and stained with an anti-IgA phycoerythrin (PE)–conjugated antibody. (**C**) Quantification of IgA coating of *B. fragilis* from feces of mice monocolonized with various strains (mean ± SEM, Tukey ANOVA, $n = 11$ or 12). (**D**) Enzyme-linked immunosorbent assay for total fecal IgA in monocolonized mice (mean ± SEM, Sidak repeated-measures two-way ANOVA, not significant, $n = 4$). (**E**) Bacterial lysates from feces of monocolonized *Rag1*$^{-/-}$ mice probed in Western blots with fecal IgA from *B. fragilis* monocolonized mice. (**F**) Quantification of the proportional signal from IgA binding to capsular polysaccharides (CPS) (>245 kDa) (mean ± SEM, Tukey ANOVA, $n = 3$ mice). (**G**) Binding of fecal IgA extracted from monocolonized mice to various strains of *B. fragilis*. Source of IgA is mice colonized with either wild-type *B. fragilis* or *B. fragilis* Δ*ccf*. Because *ccf* is expressed in vivo, IgA-free bacteria from feces of monocolonized *Rag1*$^{-/-}$ mice were used as the target for IgA binding (mean ± SEM, Tukey two-way ANOVA; asterisks denote significant differences from wild-type bacteria with wild-type IgA, $n = 3$). (**H**) In vitro epithelial cell (HT29) adherence assay using IgA extracted from Swiss Webster mice (or *Rag1*$^{-/-}$, second column) monocolonized with *B. fragilis* or *B. thetaiotaomicron* (theta, last column). IgA-free but in vivo–adapted bacteria were isolated from monocolonized *Rag1*$^{-/-}$ mice (mean ± SEM, Tukey ANOVA, $n = 4$ mice as the source of bacteria). $^{*}P < 0.05$, $^{**}P < 0.01$, $^{***}P < 0.001$.

revealing that single-strain stability of an individual bacterial species occurs in the context of a complex community. Monocolonized IgA$^{-/-}$ mice harbored reduced levels of live bacteria in the colon mucus relative to wild-type mice (Fig. 4E), although they had greater numbers of bacteria in the colon lumen (fig. S6G). TEM images of ascending colon tissues reveal that in IgA$^{-/-}$ animals, wild-type *B. fragilis* failed to aggregate on the epithelial surface (Fig. 4, F and G), similar to the *ccf* and PSB/C mutants in wild-type animals. *B. fragilis* cells also formed aggregates in feces in the presence of IgA (fig. S7), indicating that enhanced mucosal colonization may be due to increased aggregation or growth (*41*) within mucus. These findings converge to support a model whereby *ccf* regulates expression of specific capsular polysaccharides to attract IgA binding, allowing for robust mucosal colonization and single-strain stability.

Beyond *B. fragilis*, we tested whether IgA shapes a complex microbiome after controlled introduction of mouse microbiota to germ-free BALB/c or IgA$^{-/-}$ mice. One month after colonization, despite similar microbiome profiles in feces of both mouse genotypes (fig. S8A), we observed differences for specific taxa (table S3). We also identified a defect in community stratification between the colonic mucus and lumen of IgA$^{-/-}$ mice (Fig. 4H and fig. S8B); this result indicates that IgA is required to individualize microbiome profiles between these two anatomic locations. Remarkably, a highly mucus-enriched exact sequence variant, mapping uniquely to *B. fragilis*, was significantly decreased in the mucus of IgA$^{-/-}$ mice relative to BALB/c mice (Fig. 4I and fig. S9A), naturally supporting our observations from monocolonized mice. To extend this analysis to other microbial species, we identified Rikenellaceae, *Blautia* sp., and segmented filamentous bacteria as being highly IgA-coated (fig. S9B) (*35*), and we assessed the abundance of these taxa in the colonic or ileal mucus. *Blautia* sp. and segmented filamentous bacteria displayed increased mucosal association in the absence of IgA (Fig. 4I) (*42*), demonstrating that IgA can protect the intestinal barrier. However, similar to *B. fragilis*, Rikenellaceae were highly abundant in colon mucus and were significantly depleted in IgA$^{-/-}$ mice (Fig. 4I). We conclude that IgA-enhanced mucosal colonization occurs within complex communities for multiple strains of *B. fragilis* and other species of the gut microbiome.

Classically viewed, the immune system evolved to prevent microbial colonization. However, our findings show that animals tolerate a complex microbiome; moreover, in the case of *B. fragilis*, its intimate association with its mammalian host is (paradoxically) enabled when an immune response is provoked. Related commensal bacteria may also benefit from actively engaging IgA during symbiosis, as *Rag2*$^{-/-}$ mice devoid of adaptive immunity harbor fewer *Bacteroides* (*43*) and both B cell–deficient and IgA$^{-/-}$ animals display decreased colonization by the Bacteroidaceae family (*44*). IgA has been previously shown to increase adherence of *Escherichia coli* (*15*), *Bifidobacterium lactis*, and *Lactobacillus rhamnosus* (*16*) to tissue-cultured epithelial cells, which suggests that these microorganisms may also benefit from IgA to establish a mucosal bacterial community.

Mucosal microbiome instability or loss of immunomodulatory species may underlie the link between IgA deficiency and autoimmune diseases in humans (*45*). Whereas IgA-coated bacteria from individuals with inflammatory bowel disease (*46*) or nutritional deficiencies (*47*) exacerbate respective

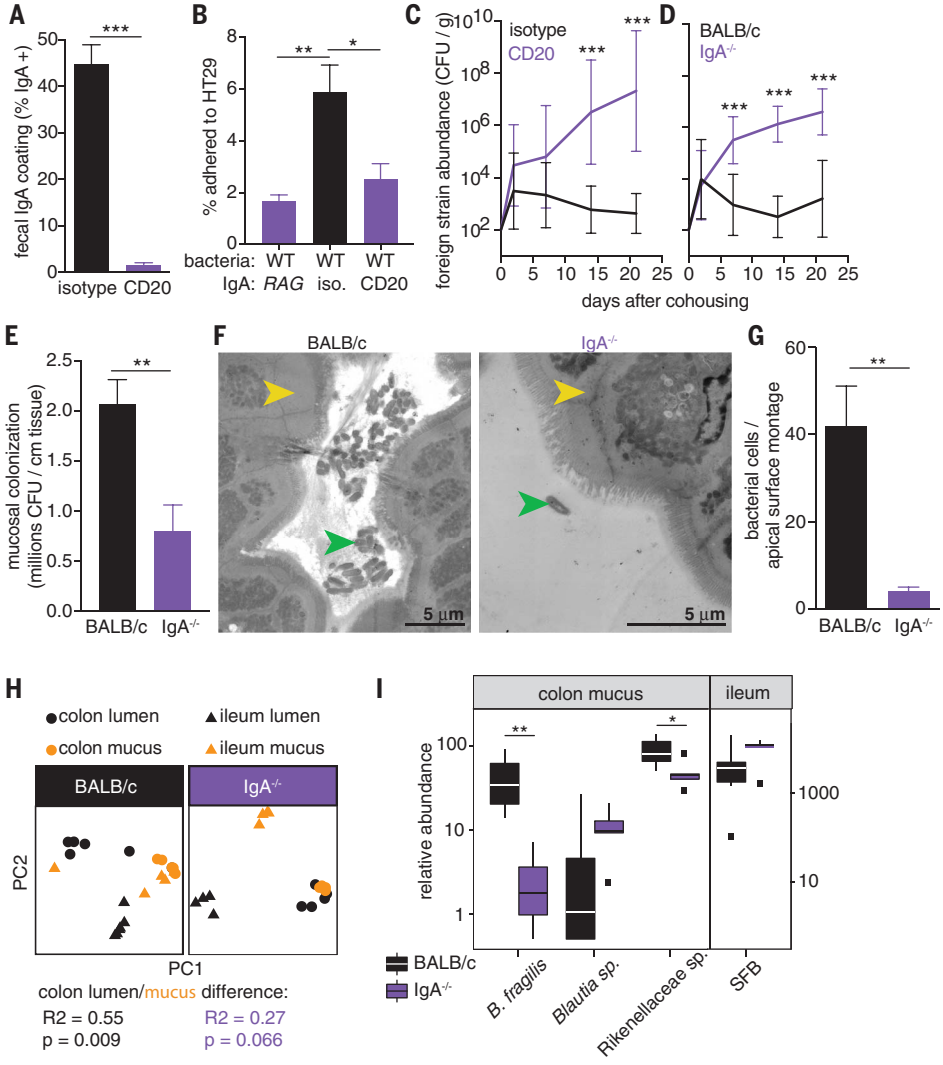

Fig. 4. IgA production in vivo is necessary for single-strain stability, mucosal colonization, and epithelial aggregation. (**A**) IgA coating of wild-type *B. fragilis* in feces after injection of anti-CD20 or isotype control antibody (mean ± SEM, unpaired *t* test, $n = 8$). (**B**) Epithelial cell (HT29) adherence assay of wild-type *B. fragilis* incubated with IgA extracted from the indicated monocolonized mice (mean ± SEM, Tukey ANOVA, $n = 4$ mice as the source of bacteria). (**C**) Abundance of foreign strains exchanged between pairs of wild-type *B. fragilis* monocolonized mice treated with anti-CD20 or an isotype control (geometric mean and 95% CI, Sidak repeated-measures two-way ANOVA on log-transformed data, $n = 10$). (**D**) Foreign strains exchanged between pairs of BALB/c and BALB/c $IgA^{-/-}$ mice monocolonized with wild-type *B. fragilis* (geometric mean and 95% CI, Sidak repeated-measures two-way ANOVA on log-transformed data, $n = 9$). (**E**) CFU plating of ascending colon mucus of wild-type and $IgA^{-/-}$ mice monocolonized with wild-type *B. fragilis* (mean ± SEM, unpaired *t* test, $n = 9$). (**F**) Representative TEM projections of ascending colon (yellow arrowhead: epithelial cell) from mice monocolonized with wild-type *B. fragilis* (green arrowhead) ($n = 3$ mice per group, about 1 mm epithelium scanned per mouse). (**G**) Quantification of bacterial cells per projection montage (mean ± SEM, unpaired *t* test, $n = 7$, 6 images from 3 mice per group). (**H**) Principal coordinates analyses of weighed UniFrac distances of 16*S* community profiles of ex–germ-free BALB/c and BALB/c $IgA^{-/-}$ mice transplanted with a complex mouse microbiota (Adonis test within colon for lumen/mucus difference). (**I**) Relative abundance of *B. fragilis* and highly IgA-coated exact sequence variants in ex–germ-free mice. SFB, segmented filamentous bacteria (median and interquartile range). $^{*}P < 0.05$, $^{**}P < 0.01$, $^{***}P < 0.001$.

pathologies in mice, IgA-coated bacteria from healthy humans protect mice from disease (*47*). We propose that during health, IgA fosters mucosal colonization of microbiota with beneficial properties (*9*), whereas disease states may induce (or be caused by) IgA responses to pathogens or pathobionts that disrupt healthy microbiome equilibria. Indeed, computational models indicate that IgA can both maintain indigenous mucosal populations and clear invasive pathogens (*48*). In addition to serving as a defense system, adaptive immunity apparently evolved to engender intimate association with members of the gut microbiome.

REFERENCES AND NOTES

1. A. B. Hall, A. C. Tolonen, R. J. Xavier, *Nat. Rev. Genet.* **18**, 690–699 (2017).
2. T. C. Fung, C. A. Olson, E. Y. Hsiao, *Nat. Neurosci.* **20**, 145–155 (2017).
3. J. J. Faith *et al.*, *Science* **341**, 1237439 (2013).
4. D. T. Truong, A. Tett, E. Pasolli, C. Huttenhower, N. Segata, *Genome Res.* gr.216242.116 (2017).
5. S. Fagarasan *et al.*, *Science* **298**, 1424–1427 (2002).
6. S. Kawamoto *et al.*, *Science* **336**, 485–489 (2012).
7. A. J. Macpherson, Y. Köller, K. D. McCoy, *Trends Immunol.* **36**, 460–470 (2015).
8. J. L. Kubinak, J. L. Round, *Nat. Rev. Immunol.* **16**, 767–774 (2016).
9. J. L. Kubinak *et al.*, *Cell Host Microbe* **17**, 153–163 (2015).
10. F. Fransen *et al.*, *Immunity* **43**, 527–540 (2015).
11. S. Kawamoto *et al.*, *Immunity* **41**, 152–165 (2014).
12. N. J. Mantis, S. J. Forbes, *Immunol. Invest.* **39**, 383–406 (2010).
13. L. A. van der Waaij, P. C. Limburg, G. Mesander, D. van der Waaij, *Gut* **38**, 348–354 (1996).
14. K. E. Shroff, K. Meslin, J. J. Cebra, *Infect. Immun.* **63**, 3904–3913 (1995).
15. R. R. Bollinger *et al.*, *Immunology* **109**, 580–587 (2003).
16. A. Mathias *et al.*, *J. Biol. Chem.* **285**, 33906–33913 (2010).
17. L. Yel, *J. Clin. Immunol.* **30**, 10–16 (2010).
18. M. E. Conley, D. L. Delacroix, *Ann. Intern. Med.* **106**, 892–899 (1987).
19. S. K. Mazmanian, J. L. Round, D. L. Kasper, *Nature* **453**, 620–625 (2008).
20. J. Ochoa-Repáraz *et al.*, *J. Immunol.* **185**, 4101–4108 (2010).
21. E. Y. Hsiao *et al.*, *Cell* **155**, 1451–1463 (2013).
22. H. Chu *et al.*, *Science* **352**, 1116–1120 (2016).
23. M. Scholz *et al.*, *Nat. Methods* **13**, 435–438 (2016).
24. M. Yassour *et al.*, *Sci. Transl. Med.* **8**, 343ra81 (2016).
25. K. Yasuda *et al.*, *Cell Host Microbe* **17**, 385–391 (2015).
26. S. M. Lee *et al.*, *Nature* **501**, 426–429 (2013).
27. N. A. Pudlo *et al.*, *mBio* **6**, e01282–e15 (2015).
28. E. C. Martens, R. Roth, J. E. Heuser, J. I. Gordon, *J. Biol. Chem.* **284**, 18445–18457 (2009).
29. M. J. Coyne, M. Chatzidaki-Livanis, L. C. Paoletti, L. E. Comstock, *Proc. Natl. Acad. Sci. U.S.A.* **105**, 13099–13104 (2008).
30. C. H. Liu, S. M. Lee, J. M. Vanlare, D. L. Kasper, S. K. Mazmanian, *Proc. Natl. Acad. Sci. U.S.A.* **105**, 3951–3956 (2008).
31. D. A. Peterson, N. P. McNulty, J. L. Guruge, J. I. Gordon, *Cell Host Microbe* **2**, 328–339 (2007).
32. N. L. Zitomersky, M. J. Coyne, L. E. Comstock, *Infect. Immun.* **79**, 2012–2020 (2011).
33. K. Moor *et al.*, *Nat. Protoc.* **11**, 1531–1553 (2016).
34. M. Shimoda, Y. Inoue, N. Azuma, C. Kanno, *Immunology* **97**, 9–17 (1999).
35. J. J. Bunker *et al.*, *Science* **358**, eaan6619 (2017).
36. H. L. Gibbins, G. B. Proctor, G. E. Yakubov, S. Wilson, G. H. Carpenter, *PLOS ONE* **10**, e0119677 (2015).
37. A. R. Biesbrock, M. S. Reddy, M. J. Levine, *Infect. Immun.* **59**, 3492–3497 (1991).
38. A. Phalipon *et al.*, *Immunity* **17**, 107–115 (2002).
39. G. Sarikonda *et al.*, *PLOS ONE* **8**, e54712 (2013).
40. S. E. Blutt, A. D. Miller, S. L. Salmon, D. W. Metzger, M. E. Conner, *Mucosal Immunol.* **5**, 712–719 (2012).
41. K. Moor *et al.*, *Nature* **544**, 498–502 (2017).
42. K. Suzuki *et al.*, *Proc. Natl. Acad. Sci. U.S.A.* **101**, 1981–1986 (2004).
43. J. Barroso-Batista, J. Demengeot, I. Gordo, *Nat. Commun.* **6**, 8945 (2015).
44. J. Mirpuri *et al.*, *Gut Microbes* **5**, 28–39 (2014).
45. K. Singh, C. Chang, M. E. Gershwin, *Autoimmun. Rev.* **13**, 163–177 (2014).
46. N. W. Palm *et al.*, *Cell* **158**, 1000–1010 (2014).

47. A. L. Kau *et al*., *Sci. Transl. Med.* **7**, 276ra24 (2015).
48. K. McLoughlin, J. Schluter, S. Rakoff-Nahoum, A. L. Smith, K. R. Foster, *Cell Host Microbe* **19**, 550–559 (2016).

ACKNOWLEDGMENTS

We thank E. Hsiao, J. Round, H. Chu, and members of the Mazmanian laboratory for critical review of this manuscript. The anti-CD20 antibody was provided under an MTA from Genentech. $IgA^{-/-}$ mice were originally generated at Baylor College of Medicine, and an MTA was required to obtain them. We thank T. Thron, the Caltech Office of Laboratory Animal Resources, Caltech Genomics Laboratory, and Caltech Flow Cytometry Facility for technical support. **Funding:** Supported by NIH training grant 5T32 GM07616 and NSF Graduate Research Fellowship DGE-1144469 (G.P.D.), NIH grant U19AI110818 to the Broad Institute, NIH grants P50 GM082545 and AI04123 (P.J.B.), and NIH grants GM099535 and DK083633 and the Heritage Medical Research Institute (S.K.M.). **Author contributions:** G.P.D. and S.K.M. conceived the study and designed experiments; G.P.D. performed most of the experiments; M.S.L. performed electron microscopy; K.B.Y. and B.B.Y. performed mouse and tissue culture experiments; J.G.S. analyzed 16*S* sequencing data; W.C.C. analyzed RNA-seq data; S.K.M., P.J.B., R.K., A.M.E., and M.E.C. supervised research and provided guidance on analysis and interpretations; G.P.D. and S.K.M. wrote the paper; and all authors edited the manuscript. **Competing interests:** The authors declare no competing interests. **Data and materials availability:** All data and code to understand and assess the conclusions of this research are available in the main text and supplementary materials, as well as EMBL-EBI accession ERP107727 and NCBI Bioproject accessions PRJNA445716 and PRJNA438372.

SUPPLEMENTARY MATERIALS

www.sciencemag.org/content/360/6390/795/suppl/DC1
Materials and Methods
Figs. S1 to S9
Tables S1 to S5
References (*49*–*69*)

29 September 2017; accepted 29 March 2018
Published online 3 May 2018
10.1126/science.aaq0926

GENE REGULATION

SLAM-seq defines direct gene-regulatory functions of the BRD4-MYC axis

Matthias Muhar,[1] Anja Ebert,[1] Tobias Neumann,[1] Christian Umkehrer,[1] Julian Jude,[1] Corinna Wieshofer,[2] Philipp Rescheneder,[3] Jesse J. Lipp,[1] Veronika A. Herzog,[4] Brian Reichholf,[4] David A. Cisneros,[1] Thomas Hoffmann,[1] Moritz F. Schlapansky,[1] Pooja Bhat,[4] Arndt von Haeseler,[3] Thomas Köcher,[5] Anna C. Obenauf,[1] Johannes Popow,[2] Stefan L. Ameres,[4]* Johannes Zuber[1,6]*

Defining direct targets of transcription factors and regulatory pathways is key to understanding their roles in physiology and disease. We combined SLAM-seq [thiol(SH)–linked alkylation for the metabolic sequencing of RNA], a method for direct quantification of newly synthesized messenger RNAs (mRNAs), with pharmacological and chemical-genetic perturbation in order to define regulatory functions of two transcriptional hubs in cancer, BRD4 and MYC, and to interrogate direct responses to BET bromodomain inhibitors (BETis). We found that BRD4 acts as general coactivator of RNA polymerase II–dependent transcription, which is broadly repressed upon high-dose BETi treatment. At doses triggering selective effects in leukemia, BETis deregulate a small set of hypersensitive targets including MYC. In contrast to BRD4, MYC primarily acts as a selective transcriptional activator controlling metabolic processes such as ribosome biogenesis and de novo purine synthesis. Our study establishes a simple and scalable strategy to identify direct transcriptional targets of any gene or pathway.

Transcription factors (TFs) and chromatin regulators govern the identity and fate of a cell, and their mutation or dysregulation drives cancer and other human diseases (*1*). Epigenetic regulators that maintain aberrant cell states have emerged as accessible entry points for targeted therapies (*2*). Among these, BET bromodomain inhibitors (BETis) have shown activity in preclinical models of leukemia and other cancers (*2*, *3*), yet underlying mechanisms remain poorly understood. Although BETis interfere with multiple BET proteins, therapeutic effects have mainly been attributed to displacement of BRD4 from acetylated histones and repression of its target genes. In hematopoietic malignancies, BETis commonly trigger repression of *MYC* (*4*–*6*), an oncogenic TF that is overexpressed in up to 70% of human cancers (*7*).

Defining direct targets of transcriptional regulators such as BRD4 and MYC is critical, both for understanding their cellular function and for therapy development. However, deciphering direct regulatory relationships remains challenging because genomic binding of a factor does not predict regulatory functions on neighboring genes, whereas conventional expression analyses after gene perturbation preclude a clear distinction between direct and indirect effects owing to vast differences in mRNA and protein half-lives (fig. S1A) (*8*, *9*). An ideal strategy for defining direct transcriptional targets would combine rapid protein perturbation and subsequent measurement of changes in mRNA output at time scales that preclude secondary effects.

Thiol(SH)–linked alkylation for the metabolic sequencing of RNA (SLAM-seq) enables the direct quantification of 4-thiouridine (4sU)–labeled mRNAs within the total mRNA pool (*10*). This is achieved through alkylation of the thiol group in 4sU (fig. S1B), which prompts misincorporation of G during reverse transcription, enabling the detection of 4sU as thymine-to-cytosine (T>C) conversion in 3′-end mRNA-sequencing. To test the suitability of SLAM-seq for detecting immediate and global changes in mRNA production, we measured responses to inhibition of CDK9, a cyclin-dependent kinase globally required for releasing RNA polymerase II (Pol2) from promoter-proximal pausing (*11*). To this end, we treated human K562 leukemia cells with the CDK inhibitor flavopiridol and performed SLAM-seq after 45 min of 4sU labeling (fig. S1C). As expected, only a few transcripts showed deregulation at the total mRNA level, whereas transcripts containing T>C conversions were broadly repressed (fig. S1, D and E). We further optimized the setup to eliminate noise introduced by polymerase chain reaction and sequencing errors (fig. S1F) and to maximize the recovery of labeled reads (fig. S1G). To test whether SLAM-seq captures more specific transcriptional responses, we treated K562 cells with small-molecule inhibitors of their driving oncogene BCR-ABL, as well as the kinases Mek and Akt, which act in distinct signaling cascades downstream of BCR-ABL (fig. S2A) (*12*). SLAM-seq revealed prominent immediate responses to these inhibitors (fig. S2, B and C) that were not biased by mRNA half-lives (fig. S2D). Combined inhibition of Mek and Akt approximated to effects of BCR-ABL inhibition, recapitulating their function as key effector pathways of BCR-ABL (fig. S2, E and F). Together, these pilot studies establish SLAM-seq as a rapid and scalable approach for probing direct transcriptional responses to drug treatment.

To generalize this approach for investigating the vast number of regulators for which, as in the case of BRD4, no selective inhibitors are available, we sought to combine SLAM-seq with chemical-genetic protein degradation (Fig. 1A). To achieve sufficiently rapid kinetics, we used the auxin-inducible degron (AID) system reported to degrade AID-tagged proteins within less than 1 hour (*13*). Specifically, we introduced a minimal AID-tag into the BRD4 locus of K562 cells (Fig. 1B) and transduced homozygous knock-in clones with a lentiviral vector expressing the rice F-box protein transport inhibitor response 1 (Tir1), which mediates ubiquitination of AID-tagged proteins upon treatment with IAA (indole-3-acetic acid). IAA treatment of edited cells triggered a highly specific and near-complete degradation of BRD4 within 30 min (Fig. 1B; fig. S3, A to C; and table S1). Whereas introduction of the tag or Tir1 expression and IAA treatment were well tolerated, prolonged BRD4 degradation strongly suppressed cell proliferation (fig. S3, D and E) in line with its essential function (*14*).

SLAM-seq after acute BRD4 degradation and 60 min of 4sU labeling revealed a global downregulation of transcription (Fig. 1C and fig. S3F), similar to effects of CDK9 inhibition. These effects are not due to displacement of core transcriptional machinery because loss of BRD4 did not impair chromatin binding of factors involved in transcriptional initiation (TBP1 and MED1) or pause-release and elongation (CDK9, Cyclin T1, and SPT5) (Fig. 1D). Whereas initiation-associated phosphorylation of Pol2 at serine 5 (S5) of its C-terminal repeat domain was unaffected, BRD4 degradation led to a marked reduction of elongation-associated serine 2 (S2)–phosphorylated Pol2, indicating a defect in promoter proximal pause release. Spike-in controlled chromatin immunoprecipitation (ChIP)–sequencing upon BRD4 degradation showed an accumulation of total and S5-phosphorylated Pol2 levels at active transcription start sites (TSSs), whereas total, S5-, and S2-phophorylated Pol2 were reduced throughout gene bodies (Fig. 1, E and F, and fig. S4). These results are in line with a recent report showing a widespread reduction of transcription upon pan-BET protein degradation independent of CDK9 recruitment (*15*) and convincingly show that BRD4 globally controls transcription by promoting the release of stalled Pol2.

Although these findings are consistent with the promiscuous binding of BRD4 to active TSS

[1]Research Institute of Molecular Pathology (IMP), Vienna BioCenter (VBC), 1030 Vienna, Austria. [2]Boehringer Ingelheim–Regional Center Vienna GmbH and Company KG, 1121 Vienna, Austria. [3]Center for Integrative Bioinformatics Vienna, Max F. Perutz Laboratories, University of Vienna and Medical University of Vienna, 1030 Vienna, Austria. [4]Institute of Molecular Biotechnology of the Austrian Academy of Sciences (IMBA), VBC, 1030 Vienna, Austria. [5]Vienna Biocenter Core Facilities (VBCF), 1030 Vienna, Austria. [6]Medical University of Vienna, VBC, 1030 Vienna, Austria.
*Corresponding author. Email: johannes.zuber@imp.ac.at (J.Z.); stefan.ameres@imba.oeaw.ac.at (S.L.A.)

(*16*), they contrast with selective effects of BETis, which have been widely reported based on results of conventional expression analyses. To define immediate transcriptional responses to BETis, we performed SLAM-seq after treatment with different doses of the BETi JQ1 (*17*) in K562 and human MV4-11 acute myeloid leukemia (AML) cells. In both cell types, high-dose JQ1 treatment (1 or 5 μM) broadly suppressed transcription (Fig. 2A and fig. S5A) and globally reduced Pol2-S2 phosphorylation (fig. S5B) similar to effects observed after BRD4 degradation, showing that global transcriptional functions of BRD4 are BET bromodomain–dependent. Effects of high-dose BETis on Pol2-S2 phosphorylation were recapitulated after knockdown of BRD4 but not BRD2 or BRD3 (fig. S5, C and D), indicating that global effects of BETis are primarily mediated by BRD4 inhibition and cannot be compensated by other BET proteins.

Because JQ1 doses above 1 μM vastly exceed growth-inhibitory concentrations in AML and other sensitive cell lines, we explored direct transcriptional responses to a more selective dose of 200 nM, which triggers strong antileukemic effects in a wide range of AML models (*4*). In K562 cells, one of few BETi-insensitive leukemia cell lines, 200 nM JQ1 induced a selective deregulation of a small number of transcripts (Fig. 2B). Treatment of two highly sensitive AML cell lines with the same dose triggered transcriptional responses that were comparable in scale (Fig. 2B and fig. S6, A and B) and affected a similar set of BETi-hypersensitive transcripts, including *MYC* and other genes known to be essential in myeloid leukemia cells (Fig. 2C and fig. S6, C and D)

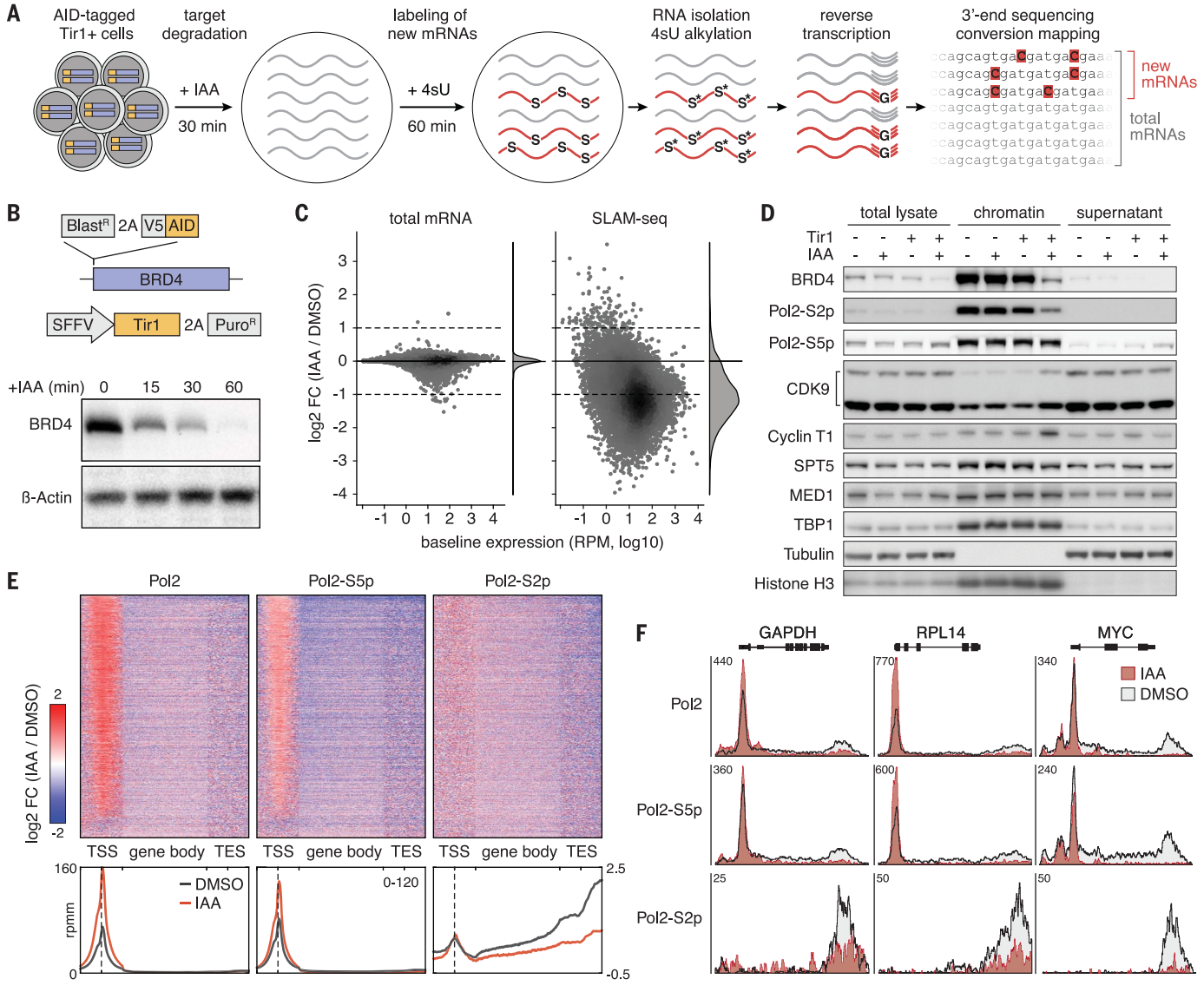

Fig. 1. Global transcriptional control by BRD4. (**A**) Sample workflow of a SLAM-seq experiment mapping direct transcriptional responses to degradation of AID-tagged proteins. (**B**) Schematic of the AID-BRD4 knock-in allele and Tir1 delivery vector SOP (pRRL-SFFV-Tir1-3xMYC-tag-T2A-Puro). Immunoblotting of BRD4 in K562$^{AID\text{-}BRD4}$+Tir1 cells treated with 100 μM IAA for the indicated time points. (**C**) Changes in the abundance of total and newly synthesized mRNAs (detected in SLAM-seq based on T>C conversions) in K562$^{AID\text{-}BRD4}$+Tir1 cells treated with IAA for 30 min followed by 4sU labeling over 60 min. FC, fold-change. (**D**) Immunoblotting of indicated transcriptional core regulators and controls in total cell lysate, chromatin fraction, and supernatant of K562$^{AID\text{-}BRD4}$+Tir1 cells treated with IAA for 60 min. (**E**) Spike-in controlled ChIP-seq of hypophosphorylated, S2-phosphorylated, and S5-phosphorylated Pol2 in K562$^{AID\text{-}BRD4}$+Tir1 cells treated with IAA for 60 min. Heatmaps and density diagrams show change of signals across genes at transcription start sites (TSS, ± 1 kb), gene bodies (scaled), and transcription end sites (TES, ± 1 kb). A density scale from low (blue) to high (red) is shown. rpmm, reads per million mapped reads. (**F**) Changes of Pol2 occupancy upon BRD4 degradation shown in (E) for indicated genes.

(*14*). These findings are in line with the notion that sensitivity to BETis at the cellular level is determined by secondary adaptation rather than differences in the primary transcriptional response (*18*, *19*). We also noted a small set of genes that were commonly up-regulated after BET inhibition or BRD4 degradation (fig. S6E) through mechanisms that remain elusive. Collectively, our results reveal a profound dose-dependency of direct responses to BETis and show that therapeutically active doses trigger antileukemic effects by deregulating a small set of hypersensitive genes.

We next explored whether the BETi hypersensitivity of certain transcripts simply reflects a pronounced sensitivity to interference with general Pol2 pause-release machinery. To test this, we used SLAM-seq to compare transcriptional responses to BET inhibition (200 nM JQ1) to effects triggered by different doses of the selective CDK9 inhibitor NVP-2 (*20*). Whereas high-dose CDK9 inhibition (60 nM NVP-2) globally suppressed transcription, an intermediate dose (6 nM NVP-2) triggered selective transcriptional responses that were distinct from the conserved response to BETis (Fig. 2, D and E, and fig. S7, A and B). Because CDK9 and BET inhibitors display strong synergistic effects (fig. S7, C and D) (*20*), we sought to investigate transcriptional responses underlying this phenomenon. In contrast to selective effects seen after single-agent treatment, combining intermediate doses of JQ1 and NVP-2 triggered a global loss of transcription similar to high-dose CDK9 inhibition (Fig. 2, D and E, and fig. S7A). These observations hold true in a genetically distinct AML cell line (fig. S7, E and F), suggesting that the therapeutic synergy between BETis and CDK9i is largely based on synergistic suppression of global transcription, raising concerns about toxicities of this combination. These results also suggest that therapeutically active doses of CDK9 and BET inhibitors exploit different bottlenecks in Pol2 pause-release to trigger selective transcriptional responses.

To investigate whether BETi hypersensitivity is determined by specific chromatin features at

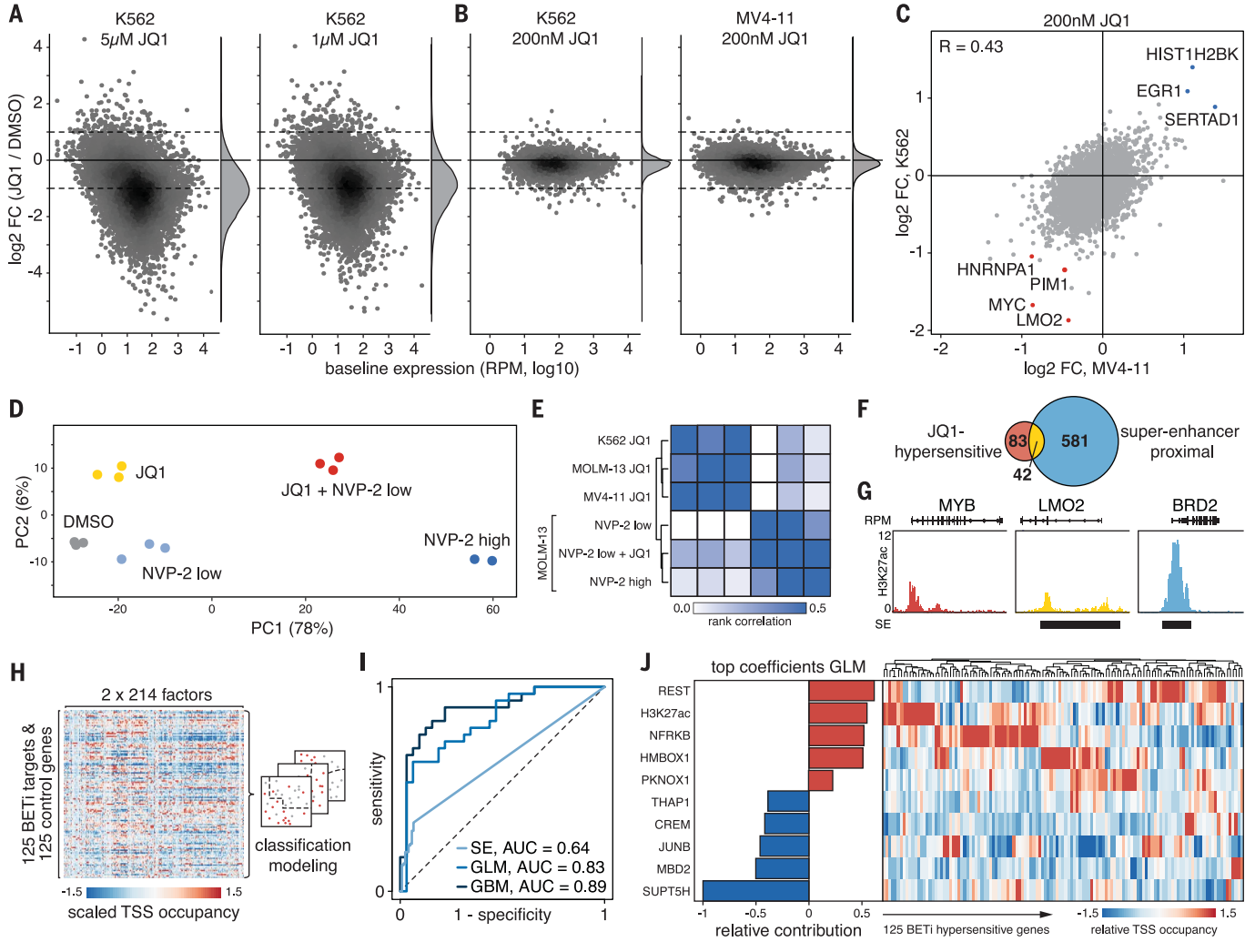

Fig. 2. Dose dependency and determinants of responses to BETis. (**A**) SLAM-seq responses of K562 cells treated with indicated doses of JQ1 for 30 min before 4sU labeling for 60 min. (**B**) SLAM-seq responses of K562 and MV4-11 cells treated with 200 nM JQ1 as in (A). (**C**) Pairwise comparison of SLAM-seq responses to JQ1 shown in (B). *R*, Pearson correlation coefficient. (**D**) Principal component analysis of SLAM-seq profiles from MOLM-13 cells treated with JQ1 or NVP-2 as in (A). (**E**) Heatmap and hierarchical clustering of Spearman's rank correlations between SLAM-seq responses to JQ1 and NVP-2 in indicated cell lines. (**F**) Venn diagram showing overlap between BETi-hypersensitive genes and published superenhancer targets in K562 cells. (**G**) Sample tracks of H3K27ac ChIP-seq with superenhancer (SE) annotation exemplifying categories in (F). (**H**) Simplified model generation workflow for classifying BETi-hypersensitive genes based on 214 chromatin signatures. (**I**) ROC curve for classification of BETi-hypersensitive genes by means of superenhancer assignment or two independent chromatin signature–based models assessed on a held-out test set. (**J**) Relative contribution of the strongest positive and negative predictors to the GLM shown in (I) based on normalized model coefficients. Heatmap shows relative ChIP-seq densities of these factors at TSS of 125 BETi-hypersensitive genes.

target genes, we first tested whether BRD4 occupancy levels at TSS or their accessibility to BETis could distinguish direct BETi targets [false discovery rate (FDR) ≤ 0.1, $\log_2$–fold-change (FC) ≤ −0.7] from an equally sized cohort of unresponsive genes with identical baseline expression (FDR ≤ 0.1, −0.1 ≤ $\log_2$FC ≤ 0.1) (fig. S8A). Whereas chromatin occupancy of BRD4 did not predict BETi-hypersensitive target genes [area under the receiver operating characteristic (ROC) curve (AUC) 0.52] (fig. S8B), recently reported chromatin binding levels of BETi measured with Click-seq could partly account for BETi responses (AUC 0.63) (fig. S8C), suggesting that differences in drug accessibility contribute to selective BETi effects. Another model attributes transcriptional and therapeutic effects of BETis to their ability to selectively suppress superenhancers (*16*). This notion has been challenged by a recent study that identified H3K27ac-based regulatory potential as a superior predictor of BETi targets (*21*). Because these studies relied on conventional RNA sequencing (RNA-seq) after prolonged drug treatment, we reevaluated both models using SLAM-seq

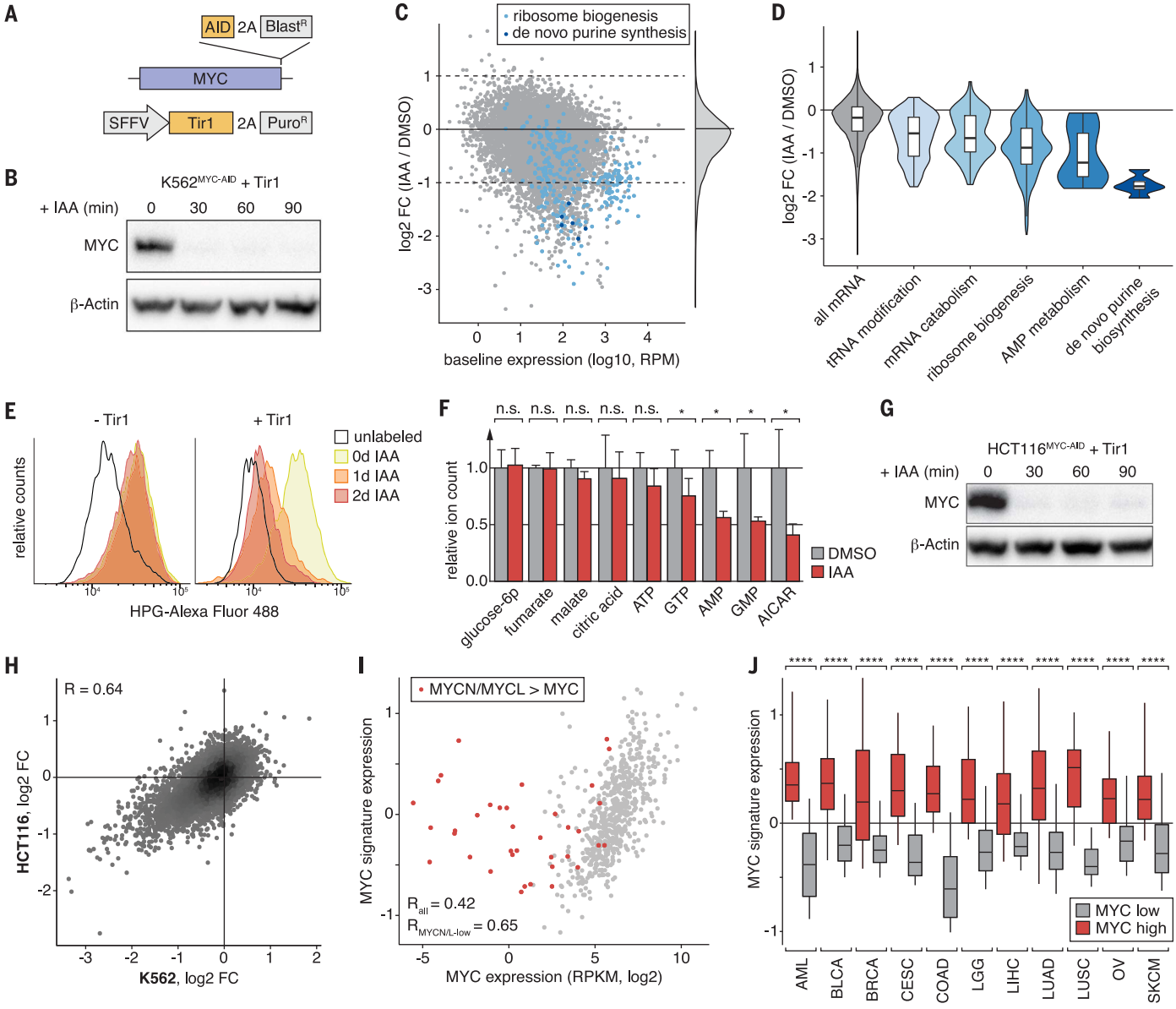

Fig. 3. MYC is a selective transcriptional activator of genes involved in biosynthesis processes. (**A**) Schematic of the MYC-AID knock-in allele and Tir1 delivery vector. (**B**) Immunoblotting of MYC in K562$^{MYC\text{-}AID}$+Tir1 cells treated with IAA. (**C**) SLAM-seq profile after MYC degradation in K562$^{MYC\text{-}AID}$+Tir1 cells (30 min IAA treatment, 60 min 4sU labeling). Highlighted are ribosome biogenesis factors (light blue) and de novo purine synthesis enzymes (dark blue). (**D**) Violin plots depicting SLAM-seq responses of significantly enriched gene ontology classes (Fisher's exact test, FDR-corrected). (**E**) Measurement of global protein synthesis by means of L-homopropargylglycine (HPG) incorporation and flow cytometry in K562$^{MYC\text{-}AID}$ cells treated with IAA. (**F**) Targeted mass spectrometry quantification of indicated metabolites in K562$^{MYC\text{-}AID}$+Tir1 cells after 48 hours of IAA treatment. Bars show means of results from three independent experiments. Error bars indicate 1 SD. n.s., not signficant. *P < 0.05 (Student's t test). (**G**) MYC-immunoblotting in HCT116$^{MYC\text{-}AID}$+Tir1 cells as in (B). (**H**) Comparison of SLAM-seq responses in K562$^{MYC\text{-}AID}$+Tir1 and HCT116$^{MYC\text{-}AID}$+Tir1 cells. (**I**) Expression of *MYC* compared with a signature of the top 100 common MYC-dependent transcripts in (H) across 672 cancer cell lines. (**J**) MYC-target signature expression across 5583 patient samples separated according to high (top 20%) or low (bottom 20%) MYC expression and cancer type. ****P < 0.0001 (Wilcoxon's rank-sum test).

profiles. Both the H3K27ac-based regulatory potential of genes as well as their association with superenhancers (*22*) predicted hypersensitivity to BETis with modest accuracy (AUC 0.66 and 0.64, respectively) (fig. S8B). However, two-thirds of BETi-sensitive genes could not be assigned to superenhancers, and the vast majority of expressed superenhancer-associated genes did not respond to BETi treatment (Fig. 2, F and G). These observations hold true in other leukemia cell lines (fig. S8D) and show that the sensitivity to BET inhibition is associated with, but not determined by, the presence of superenhancers, suggesting that more complex factors underlie this phenomenon.

To further explore determinants of BETi hypersensitivity, we took advantage of extensive profiling data available for K562 cells (*23*, *24*) and devised an unbiased approach for modeling combinatorial modes of gene regulation. Specifically, we extracted signals of 214 ChIP- and methylome-sequencing experiments within 500 and 2000 base pairs (bp) around the TSS of BETi-sensitive and -unresponsive genes and used this data to train various classification models that were later evaluated based on held-out test genes (Fig. 2H and fig. S8E). This approach yielded multiple classifiers that predicted BETi sensitivity with high fidelity (AUC > 0.8) (Fig. 2I and fig. S8F), among them a generalized linear model (GLM) derived through elastic net regression. Reanalyzing coefficients of this model revealed that several factors, including high levels of TSS-proximal REST and H3K27ac, are associated with BETi hypersensitivity, whereas high occupancy of SUPT5H (SPT5), itself a regulator of elongation (*25*, *26*), was the strongest negative predictor (Fig. 2J and fig. S9A). Unsupervised clustering revealed that predictive TFs and cofactors are enriched only at distinct subclusters of BETi-sensitive or -unresponsive genes (Fig. 2J and fig. S9B), suggesting that the transcriptional response to BETis is determined by locus-specific regulators and cannot be predicted on the basis of a single unifying chromatin factor.

Therapeutic effects of BETis are likely mediated through deregulation of multiple hypersensitive genes. Although repression of MYC has been identified as a common and relevant effector mechanism in leukemia (*4*), direct regulatory functions of MYC remain under debate. Previous reports have described activating or repressive effects of MYC on specific target genes, whereas other studies suggest that MYC acts as a general transcriptional amplifier (*27*–*31*). To test these models, we sought to measure direct changes in mRNA output after acute loss of endogenous MYC. We therefore engineered an AID-tag into the endogenous *MYC* locus of K562 cells (Fig. 3A and fig. S10), which in homozygous Tir1-expressing clones allowed for rapid degradation of MYC within less than 30 min (Fig. 3B). We then used SLAM-seq to quantify the output of newly synthesized mRNAs over 60 min after MYC degradation. In contrast to degradation of BRD4, acute loss of MYC resulted in highly specific rather than global changes in mRNA production (Fig. 3C). These were dominated by repressive effects on 712 genes, whereas only 15 mRNAs were strongly up-regulated (fig. S11A). Hence, in K562 cells, MYC does not act as a direct repressor or general amplifier of transcription but predominantly functions as a transcriptional activator of specific target genes.

Because MYC is known to occupy most active promoters (*27*), we next investigated how MYC exerts selective transcriptional activation despite ubiquitous binding. To this end, we trained classification models to predict MYC-dependent transcripts (FDR ≤ 0.1, $\log_2$FC ≤ −1) based on different ChIP-seq signals at their promoter. Elastic net regression yielded a simple GLM that was highly predictive of MYC-dependent gene regulation (AUC 0.91) (fig. S11B). The strongest contributor in this model was the abundance of MYC itself (fig. S11C). Although the presence of MYC at promoters determined by conventional peak calling fails to identify MYC-sensitive transcripts, binding levels of MYC or its cofactor MAX predict MYC-dependent gene regulation with intermediate accuracy (AUC 0.76 and 0.74, respectively) (fig. S11, D and E). These results suggest that genes directly activated by MYC are defined by strong binding of MYC and by further modulation through additional factors such as MNT, NKRF, TBL1XR1, EP300, and YY1.

To investigate the cellular function of MYC-dependent gene regulation, we performed gene ontology analysis of direct MYC target genes in K562 cells. Acute MYC degradation predominantly led to down-regulation of genes associated with protein and nucleotide biosynthesis, including 36% of all ribosome biogenesis factors, key regulators in adenosine 5′-monophosphate (AMP) metabolism, and all six enzymes of the de novo purine synthesis pathway (Fig. 3, C and D, and table S2). MYC degradation progressively impaired protein synthesis (Fig. 3E) and led to a strong reduction in cellular AMP and guanosine 5′-monophosphate (GMP) levels as well as their upstream intermediate aminoimidazole carboxamide ribonucleotide (AICAR) before the onset of cell proliferation defects (Fig. 3F and fig. S12, A and B). MYC's role as a direct regulator of key enzymes in protein and nucleotide biosynthesis—as well as several subunits of RNA polymerases I, II, and III (fig. S12C)—provide an explanation for the reported increase in total cellular RNA upon MYC overexpression and support the notion that these effects are secondary rather than due to global transcriptional effects (*32*).

To test whether direct transcriptional functions of MYC are conserved in other cellular contexts, we introduced homozygous AID-tags into the *MYC* locus of HCT116 human colon carcinoma cells. As with K562 cells, IAA treatment of TIR1-expressing $HCT116^{MYC\text{-}AID}$ cells triggered complete degradation of MYC within less than 30 min (Fig. 3G). SLAM-seq profiling revealed a selective transcriptional response (Fig. 3H and fig. S12D) that affected the same cellular processes (fig. S12E) and correlated with effects observed in K562 cells [Pearson correlation coefficient (R) = 0.64] (Fig. 3H). To test whether the conservation of MYC targets extends to other cancer types, we derived a signature of the 100 most strongly down-regulated genes in SLAM-seq (table S3) and compared its expression with *MYC* levels in a panel of 672 cancer cell lines (*33*). Expression of *MYC* and our MYC target signature correlated well (Fig. 3I), except for a small fraction of outliers. All of these express high levels of *MYCN* or *MYCL* (fig. S13A), indicating that *MYC* paralogs have redundant functions in the regulation of core MYC targets. Our signature of direct MYC targets was also strongly correlated with *MYC* levels in publicly available RNA-seq profiles from 5583 primary patient samples across 11 major human cancers (Fig. 3J and fig. S13B) (*34*). Together, these findings suggest that MYC drives expression of a conserved set of transcriptional targets, which should be considered as entry points for blocking its oncogenic functions.

In summary, combining rapid chemical-genetic perturbation and SLAM-seq establishes a simple yet powerful strategy for probing specific and global direct functions of TFs and cofactors. Using this approach, we functionally characterize BRD4, a protein widely studied as a regulator of lineage- and disease-associated expression programs, as a general cofactor in transcriptional pause-release. We also found that MYC, which has previously been implicated as a global transcriptional amplifier, activates a confined and conserved set of target genes to fuel basic anabolic processes, particularly protein and nucleotide biosynthesis. More generally, by enabling the direct quantification of changes in mRNA output, SLAM-seq provides a simple, robust, and scalable method for defining direct transcriptional responses to any perturbation and thereby exploring the regulatory wiring of a cell.

REFERENCES AND NOTES

1. T. I. Lee, R. A. Young, *Cell* **152**, 1237–1251 (2013).
2. P. A. Jones, J.-P. J. Issa, S. Baylin, *Nat. Rev. Genet.* **17**, 630–641 (2016).
3. J. Shi, C. R. Vakoc, *Mol. Cell* **54**, 728–736 (2014).
4. J. Zuber *et al.*, *Nature* **478**, 524–528 (2011).
5. J. E. Delmore *et al.*, *Cell* **146**, 904–917 (2011).
6. M. A. Dawson *et al.*, *Nature* **478**, 529–533 (2011).
7. C. V. Dang, *Cell* **149**, 22–35 (2012).
8. B. E. Housden *et al.*, *Nat. Rev. Genet.* **18**, 24–40 (2017).
9. B. Schwanhäusser *et al.*, *Nature* **473**, 337–342 (2011).
10. V. A. Herzog *et al.*, *Nat. Methods* **14**, 1198–1204 (2017).
11. P. B. Rahl *et al.*, *Cell* **141**, 432–445 (2010).
12. R. Ren, *Nat. Rev. Cancer* **5**, 172–183 (2005).
13. K. Nishimura, T. Fukagawa, H. Takisawa, T. Kakimoto, M. Kanemaki, *Nat. Methods* **6**, 917–922 (2009).
14. T. Wang *et al.*, *Science* **350**, 1096–1101 (2015).
15. G. E. Winter *et al.*, *Mol. Cell* **67**, 5–18.e19 (2017).
16. J. Lovén *et al.*, *Cell* **153**, 320–334 (2013).
17. P. Filippakopoulos *et al.*, *Nature* **468**, 1067–1073 (2010).
18. P. Rathert *et al.*, *Nature* **525**, 543–547 (2015).
19. C. Y. Fong *et al.*, *Nature* **525**, 538–542 (2015).
20. H. Lu *et al.*, *eLife* **4**, 1–26 (2015).
21. S. Wang *et al.*, *Genome Res.* **26**, 1417–1429 (2016).
22. D. Hnisz *et al.*, *Cell* **155**, 934–947 (2013).
23. ENCODE Project Consortium, *Nature* **489**, 57–74 (2012).
24. S. Mei *et al.*, *Nucleic Acids Res.* **45** (D1), D658–D662 (2017).
25. T. Wada *et al.*, *Genes Dev.* **12**, 343–356 (1998).
26. A. Shetty *et al.*, *Mol. Cell* **66**, 77–88.e5 (2017).
27. C. Y. Lin *et al.*, *Cell* **151**, 56–67 (2012).
28. Z. Nie *et al.*, *Cell* **151**, 68–79 (2012).
29. A. Sabò *et al.*, *Nature* **511**, 488–492 (2014).
30. S. Walz *et al.*, *Nature* **511**, 483–487 (2014).

31. F. Lorenzin *et al.*, *eLife* **5**, 1–35 (2016).
32. T. R. Kress, A. Sabò, B. Amati, *Nat. Rev. Cancer* **15**, 593–607 (2015).
33. C. Klijn *et al.*, *Nat. Biotechnol.* **33**, 306–312 (2015).
34. R. L. Grossman *et al.*, *N. Engl. J. Med.* **375**, 1109–1112 (2016).

ACKNOWLEDGMENTS

We are grateful to all members of the Zuber and Ameres laboratories and A. Stark, F. Muerdter, M. Rath, and D. Kaiser for experimental advice and helpful discussions. We thank A. Sommer, I. Tamir, and the VBCF-NGS team (www.vbcf.ac.at) for deep sequencing services; G. Dürnberger, K. Mechtler, E. Roitinger, and M. Schutzbier at the IMP/IMBA protein biochemistry core facility for performing mass spectrometry–based proteomics; and the IMP/IMBA bio-optics and molecular biology services for continuous support. **Funding:** This work was funded by Starting Grants of the European Research Council to J.Z. (ERC-StG-336860) and S.L.A. (ERC-StG-338252) and the Austrian Science Fund (SFB grants F4710 and F4322, Y-733-B22 START and W127-B09). M.M. is recipient of a DOC fellowship of the Austrian Academy of Sciences. Research at the IMP is generously supported by Boehringer Ingelheim. VBCF is funded by the City of Vienna through the Vienna Business Agency. **Author contributions:** M.M., S.L.A., and J.Z. conceived and planned this project. M.M., A.E., C.U., C.W., T.K., and J.P. designed and conducted experiments. M.M., A.E., T.N., S.L.A., and J.Z. analyzed and interpreted original and publicly available data. T.N. established and performed deep sequencing data analyses. J.J., P.R., V.A.H., B.R., D.A.C., T.H., P.B., and M.F.S. established critical reagents and methodology. J.J.L., A.v.H., A.C.O., and J.P. provided critical input on experimental designs and data analyses. M.M. and J.Z. cowrote the manuscript with input from coauthors. **Competing interests:** S.L.A., B.R., V.A.H., J.Z., and M.M. are inventors on patent application EU17166629.0-1403 submitted by the IMBA that covers methods for the modification and identification of nucleic acids, which have been licensed to Lexogen GmbH. **Data and materials availability:** All deep sequencing data are available through GEO (www.ncbi.nlm.nih.gov/geo) under the accession code GSE111463. Materials will be provided upon request under a materials transfer agreement with IMP.

SUPPLEMENTARY MATERIALS

www.sciencemag.org/content/360/6390/800/suppl/DC1
Materials and Methods
Figs. S1 to S13
Tables S1 to S10
References (*35*–*45*)

5 July 2017; resubmitted 8 February 2018
Accepted 21 March 2018
Published online 5 April 2018
10.1126/science.aao2793

PINS

RESTORING HOPE

Since the first Deep Brain Stimulation initiative of Tsinghua Univeristy in 2000, PINS Medical has gradually established a multinational corporation with headquarter based in Beijing and international business center in Singapore. As an innovative high-tech enterprise with focus on neuromodulation, a variety of clinical products have been developed to date, which include stimulators for deep brain, vagus nerve, spinal cord and sacral nerve stimulation therapies. PINS Medical devotes itself to providing cutting-edge treatments for patients who suffer from neurological disorders such as Parkinson's Disease, Epilepsy, Chronic Pain and OAB, etc.

As part of the "National Engineering Laboratory for Neuromodulation", PINS Medical works in close cooperation with Tsinghua University and the numerous affiliated clinical centers, becoming a center of attraction for a wide range of professional talents in areas of clinical research, innovative R&D and business management. Since 2008, PINS Medical has developed rapidly in becoming a leading brand in neuromodulation within the Chinese market, due to the success of its creative research platform that efficiency links basic research, R&D of novel products, clinical testing and market entry.

With an outstanding reputation as a high-tech healthcare corporation, PINS Medical has a primary mission for providing innovative, high-quality products and services for patients to improve quality of life. PINS, which stands for Programmable Implanted Neuromodulation Stimulator, is also an abbreviation of "Patient Is No.1 alwayS". This clearly presents the goal of PINS Medical for "restoring hope", not simply as an innovation company but also across society to citizens.

Looking into the future with the continuous rise in incidence of neuropsychiatric disorders and increased social burden across the globe, PINS Medical along with local governments, research centers, companies and top academic scientists, are now developing and promoting innovative therapies worldwide.

www.pinsmedical.com info@pinsmedical.cn

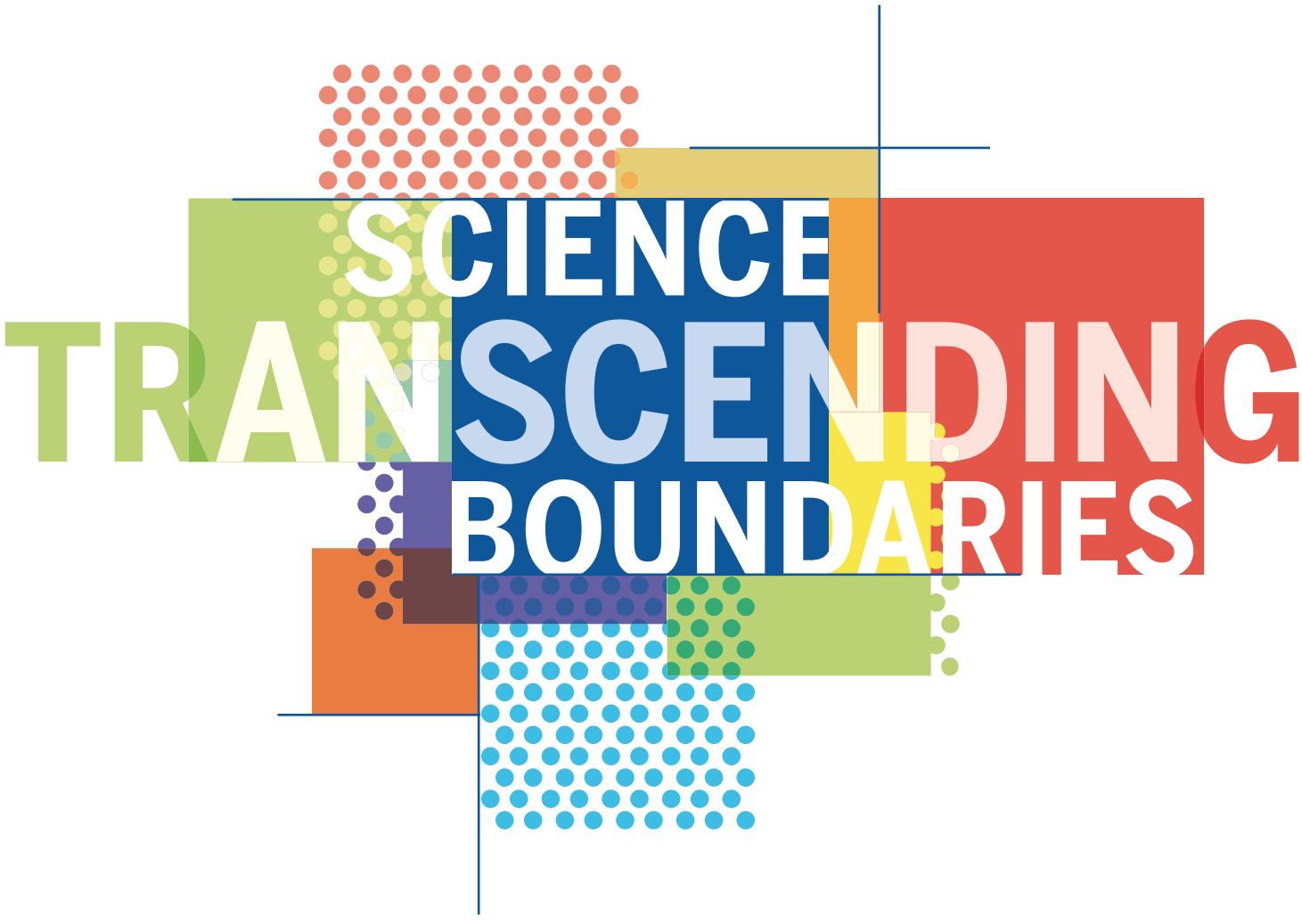

AAAS
ANNUAL MEETING
Washington, DC | Feb. 14–18, 2019

Sponsorship and Exhibit Spaces Now Available

Enhance your visibility at the AAAS Annual Meeting, the world's largest and most widely reported general scientific gathering. Don't miss this chance for your research, products, and services to grab the attention of researchers, scientists, engineers, journalists, policymakers, educators, students, hiring managers and funding agencies.

Join us in the nation's capital!

aaas.org/meetings

Lundbeck Foundation
calls for nominations for

THE BRAIN PRIZE 2019

Nominations must be received by 1 September 2018

The prize of € 1 million is awarded to researchers for outstanding contributions to neuroscience – from basic to clinical.

The Brain Prize is open to researchers around the world.

Nominations will be reviewed by the Selection Committee:

Anders Björklund, Sweden, Chairman
Joseph Coyle, USA
Geoffrey Donnan, Australia
Catherine Dulac, USA
Story Landis, USA
Richard Morris, United Kingdom, Vice-Chairman
Mu-ming Poo, China
Philip Scheltens, The Netherlands
Irene Tracey, United Kingdom

Lundbeck Foundation encourages diversity in nominees.

For the nomination form and details of the nomination procedure, please visit www.thebrainprize.org.

THE BRAIN PRIZE
Lundbeck Foundation

eppendorf & Science

PRIZE FOR NEURO BIOLOGY

2017 Winner
Flavio Donato, Ph.D.
Kavli Institute
Norwegian University of
Science and Technology

For research on how neural networks mature during development to represent space in the brain

Application Deadline
June 15, 2018

Call for Entries

Eppendorf & Science Prize for Neurobiology
The annual Eppendorf & Science Prize for Neurobiology is an international award which honors young scientists for their outstanding contributions to neurobiological research based on methods of molecular and cell biology. The winner and finalists are selected by a committee of independent scientists, chaired by *Science's* Senior Editor, Dr. Peter Stern. To be eligible, you must be 35 years of age or younger.

As the Grand Prize Winner, you could be next to receive
> Prize money of US$25,000
> Publication of your work in *Science*
> Full support to attend the Prize Ceremony held in conjunction with the Annual Meeting of the Society for Neuroscience in the USA
> 10-year AAAS membership and online subscription to *Science*
> Complimentary products worth US$1,000 from Eppendorf
> An invitation to visit Eppendorf in Hamburg, Germany

It's easy to apply! Learn more at:

www.eppendorf.com/prize

eppendorf Science AAAS

6 powerful propellers

to accelerate expert science and technology solutions in life science

Our mission is to collaborate with the global scientific community to solve the toughest problems in life science. To achieve this, we have brought together the world's leading Life Science brands to create a world-class portfolio: Millipore®, SAFC®, BioReliance®, Sigma-Aldrich®, Milli-Q® and Supelco®.

A science and technology ecosystem

MilliporeSigma has brought together the world's leading Life Science brands to solve the toughest problems in life science. In particular, you may be interested in the following brands:

Sigma-Aldrich® continues to develop its broad portfolio of state-of-the-art lab and production materials, paired with technical support and scientific partnerships.
Milli-Q® offers a continually pioneering range of intuitive, easy-to-use lab water instruments that seamlessly integrate into your daily work.
Millipore® provides proven preparation, separation, filtration and testing products and technologies.
Supelco® continues to be a trusted resource for accurate and reliable analytical products, developed by analytical chemists, for analytical chemists.

Support you can count on

At MilliporeSigma, we offer a world-class portfolio with over 300,000 high-quality products and services – from research to commercial manufacturing.

With 19,000 life science employees in 66 countries across the globe, we have 130 distribution centers and 10 global customer collaboration facilities across North America, Europe, Asia and Latin America.

Customer-centric innovation

We are dedicated to putting our customers first, and by collaborating we can help advance life science. Together, we can improve and expand global access to health with unparallelled services and support under one banner.

Seamless access

With 24/7 customer support, an efficient ordering and delivery service, and an unmatched e-commerce platform, you get exactly what you need, when you need it.

A sharper look

As part of the exciting life science restructure, we are refreshing our existing packaging design and labeling to better serve you and reflect the vibrant nature of our business and vision.

Let us help you

Find out how we collaborate to solve your toughest problems at SigmaAldrich.com/advancinglifescience

#howwesolve

The life science business of Merck KGaA, Darmstadt, Germany operates as MilliporeSigma in the U.S. and Canada.

MilliporeSigma

THE 6 SHARPEST PERSPECTIVES

for focused science and technology solutions in life science

Millipore®
Proven Preparation, Separation, Filtration & Testing Products

SAFC®
Tailored Pharma & Biopharma Raw Material Solutions

BioReliance®
Expert Pharma & Biopharma Manufacturing & Testing Services

Sigma-Aldrich®
State-of-the-Art Lab & Production Materials

Milli-Q®
Pioneering Lab Water Solutions

Supelco®
Trusted Analytical Products

MilliporeSigma has brought together the world's leading Life Science brands, so whatever your life science problem, you can benefit from our expert products and services.

To find out how MilliporeSigma can help you work, visit SigmaAldrich.com/advancinglifescience

#howwesolve

The life science business of Merck KGaA, Darmstadt, Germany operates as MilliporeSigma in the U.S. and Canada.

MilliporeSigma

CALL FOR PAPERS

SPJ
SCIENCE PARTNER JOURNALS

spj.ScienceMag.org/research

Research

OFFICIAL JOURNAL OF CAST

An Open Access Journal

Research is a comprehensive, interdisciplinary, and selective **Open Access journal from the China Association of Science and Technology (CAST)**, published quarterly and distributed by the **American Association for the Advancement of Science (AAAS)**. *Research* provides an international platform for academic exchange, research collaboration, and technological advancements. The journal will publish fundamental research in the life and physical sciences as well as important findings or issues in engineering and applied science.

The Science Partner Journals (SPJ) program was established by AAAS, the nonprofit publisher of the *Science* family of journals. The SPJ program features high-quality, online-only open access publications produced in collaboration with international research institutions, foundations, funders and societies. Through these collaborations, AAAS expands its efforts to communicate science broadly and for the benefit of all people by providing top-tier international research organizations with the technology, visibility and publishing expertise that AAAS is uniquely positioned **to offer as the world's largest general science membership society**.

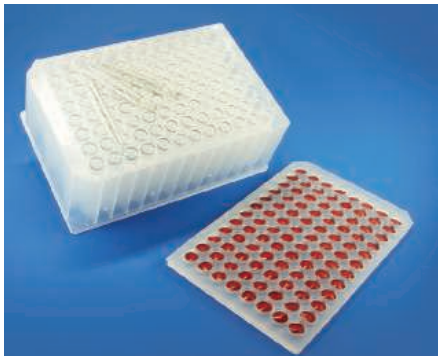

Glass Vial Deep-Well Plate

The new glass vial deep-well plate from Porvair Sciences is designed to ensure that absolutely no extractables or leachates are present in a withdrawn sample, thereby removing the risk of false peaks in sensitive UHPLC and mass spectrometry applications. This product combines 1 mL × 96 tapered- or flat-bottomed glass vials held firmly in each well of a 2 mL × 96 deep-well plate. These plates are less costly than solid glass plates and are precisely manufactured to comply with ANSI/SLAS dimensions, to ensure complete compatibility with automated equipment. Complimented by a snug-fitting silicone cap mat that seals each vial individually with a prescored septum, the glass vial deep-well plates allow an autosampler to pierce each septum and withdraw sample from each sealed vial with high precision and reproducibility.

Porvair Sciences
For info: +44-(0)-1978-666222
www.porvair-sciences.com

siRNA Kit

The Trilencer-27 siRNA kit contains Dicer–Substrate duplexes that provide two critical improvements over the use of traditional 2-mer small interfering RNA (siRNA) designs. 27-mer siRNA takes advantage of the natural processing by Dicer, producing 10-fold higher potency and specificity than shorter 21-mer RNA interference (RNAi) forms. 27-mer siRNA duplexes also evade the radar of the mammalian interferon response when expressed in mammalian cells, and initiate strong, specific gene silencing. Because of its optimal design, 27-mer siRNA has the assets of improved efficacy and minimal interferon response. The kit, which comes with three gene-specific siRNAs and one negative control, provides genome-wide coverage against human, mouse, and rat messenger RNA. It guarantees greater than 70% gene knockdown.

OriGene
For info: 888-267-4436
www.origene.com/sirna

IDO Pathway Research Products

AMS Biotechnology (AMSBIO) offers numerous IDO pathway research (*IDO1, IDO2*, and *TDO* genes) products. Researchers are trying to identify the complex mechanisms that enable cancer cells to evade the host's immune system. Cancer cells use the indoleamine 2,3-dioxygenase (IDO) pathway to suppress the host's immune response in order to facilitate survival, growth, invasion, and metastasis of malignant cells. The IDO pathway is active in many tumors, providing a direct defense against T-cell attack. It is also active in many antigen-presenting cells, resulting in peripheral tolerance to tumor-associated antigens. AMSBIO offers Inhibitor Screening Assay Kits designed to measure IDO1, IDO2, and TDO enzyme inhibition. In addition, the company has stable recombinant HEK293 cell lines for monitoring IDO1 and TDO pathway activity, and screening for activators or inhibitors of IDO1 and TDO. For studying enzyme kinetics, substrate specificity, and screening inhibitors, AMSBIO also offers human and mouse IDO1, IDO2, and TDO His-tagged proteins.

AMS Biotechnology
For info: +44-(0)-1235-828-200
www.amsbio.com/ido-pathway.aspx

CRISPR/Cas9 Mouse Model Generation Services

While it's tempting to try to save costs by doing it yourself, generating a new mouse model using CRISPR comes with many challenges that are sometimes unpredictable. These can lengthen a simple knockout project by several months if not managed correctly. By letting the Jackson Laboratory (JAX) take the hassle out of generating your new mouse strain, you enable your lab staff to focus on more important things, like performing experiments and getting papers published. There is no need to backcross your new model to make it congenic. We can generate the model you need on the genetic background you want. We've generated models in a variety of strain backgrounds, including BALB/cJ, C57BL/6J, C57BL/6NJ, FVB/NJ, NOD/ShiLtJ, and NSG, and are adding new strains regularly. From conditional knockouts to reporter insertions and difficult genetic backgrounds, JAX has 80-plus years' experience generating complex models. Save time and money by letting the experts build your model in the most efficient way possible.

The Jackson Laboratory
For info: 800-422-6423
www.jax.org

Network Analyzer

The DIRIS Q800 network analyzer boasts unparalleled quality compared to other analyzers on the European market, and is IEC 62586-2 Class A certified. The electrical energy that powers a network or facility is subject to pollution or interference stemming from a variety of sources. This interference can have severe consequences for sensitive equipment connected to the network, and can sometimes cause outages that adversely affect the operation of critical facilities, including industrial production lines, data centers, infrastructures, health care centers, and more generally, lighting and safety systems in public-access buildings, among others. The analyzer identifies the sources of failure before they reach a critical point for the application, so that any potential preventive maintenance operations can be performed in time to guarantee availability of the required electric power. Besides anticipating power failures, the DIRIS Q800 optimizes the power facility as part of an energy-efficiency initiative.

Socomec
For info: +33-(0)-3-88-57-41-41
www.socomec.co.in

Electronically submit your new product description or product literature information! Go to www.sciencemag.org/about/new-products-section for more information.

Newly offered instrumentation, apparatus, and laboratory materials of interest to researchers in all disciplines in academic, industrial, and governmental organizations are featured in this space. Emphasis is given to purpose, chief characteristics, and availability of products and materials. Endorsement by *Science* or AAAS of any products or materials mentioned is not implied. Additional information may be obtained from the manufacturer or supplier.

NEW ENGLAND BioLabs® Inc.

be INSPIRED
drive DISCOVERY
stay GENUINE

We've spread our wings.

Monarch® Nucleic Acid Purification Kits Now available for DNA & RNA

Designed with sustainability in mind, Monarch® Nucleic Acid Purification Kits are the perfect complement to many molecular biology workflows. Available for DNA & RNA purification, with buffers and columns available separately, Monarch kits are optimized for excellent performance, convenience and value. Quickly and easily recover highly pure, intact DNA and RNA in minutes. Available kits include:

- Monarch Plasmid Miniprep Kit
- Monarch DNA Gel Extraction Kit
- Monarch PCR & DNA Cleanup Kit (5 µg)
- **NEW** MONARCH TOTAL RNA MINIPREP KIT – optimized for use with a variety of sample types, including cells, tissues, blood, and more

Make the change and migrate to Monarch today.

Interested in trying a sample of our new Monarch Total RNA Miniprep Kit?

Learn more at
NEBMonarch.com

JOB FOCUS: MICROBIOLOGY

POSTDOCTORAL FELLOWSHIP IN IMMUNOLOGY

Postdoctoral fellowship is available to pursue research supported by NIH grants. Studies will address the epigenomic and microbiomic effects of plant products such as resveratrol, indoles and cannabinoids on inflammation, autoimmunity and cancer. Other projects include studies on the role of CD44, estrogens and dioxins on immune response. Ph.D. in any biomedical sciences is required with preference given to experience in Immunology. Send curriculum vitae and 3 references to Dr. Mitzi Nagarkatti, Chair of Department of Pathology, Microbiology and Immunology, University of South Carolina School of Medicine, Columbia, SC 29208 or apply to website: **http://uscjobs.sc.edu/postings/30519**. *USC Columbia is an EOAA Employer and encourages applications from women and minorities.*

POSITIONS OPEN

Postdoctoral Position

A postdoctoral position is available at the University of Maryland School of Medicine to model inherited lipid storage diseases using iPSC technology. The candidate should have a Ph.D., experience in Cell/Molecular Biology, excellent oral and written communication skills, and be able to work independently. Experience in hESC/iPSC technology and hematopoietic/neuronal development is desirable. Salary is commensurate with experience. To apply, send a Curriculum Vitae and contact information for 3 references to **Dr. Ricardo A. Feldman** at e-mail: **rfeldman@som.umaryland.edu**.

The “Talent-Attraction Storm” Sweeping China

Just as the craze for artificial intelligence and blockchain technology is escalating in the global venture capital investment community, a “talent-attraction storm” is sweeping across China.

In March 2018, the municipal government of China’s capital, Beijing, known for its high housing prices and the difficulty faced by migrants in settling there, passed two acts: “Some Measures on the Optimization of Talent Services, Promotion of Scientific and Technological Innovation, and the Advancement of High-Tech Industries” and “The Management of the Talent-Attraction Campaign in Beijing (Pilot).” The former act aims to increase China’s acquisition of global talent through adopting more aggressive policies for talent attraction, financial incentives (housing, medical care, and education for children), and talent assessment as well as the protection of intellectual property and the reinforcement of knowledge transfer. It also includes a “green card” scheme for high-level talents, which stipulates that experts chosen from the Thousand Talents Plan and winners of major scientific and technological awards can be given immediate residency; outstanding overseas talents can apply for positions as chief scientists of Beijing’s major R&D institutes; permanent Chinese residence permits can be issued in 50 working days; and household registration permits for spouses and children of high-level talents can be issued quickly.

Soon after Beijing announced these new policies, Shanghai, with a GDP of over RMB 3 trillion (USD 478.1 million) in 2017 (the highest in China), decided to follow suit. On March 26, Shanghai held a “Talents Work Conference,” which was presented on such a large scale that Li Qiang, the Communist Party Secretary of Shanghai, openly advocated this effort to attract expertise. During the convention, he emphasized that: “we can never pay too much attention to the role played by talent in Shanghai’s development.” He demanded that the city “move faster to build a competitive talent system, and work harder to construct a world-class development environment so as to create a ‘Peak Talents’ project.’’ An act passed by the Shanghai government at the same time, “Action on the Peak Talents Project,” not only makes clear the city’ s emphasis on attracting talent in areas including cosmology and astronomy, photonics science and technology, life Sciences and biomedicine, and neuroscience and artificial intelligence, but also proposes providing “custom policy” for every talent who is recruited, implementing an accepted system for regulating talent acquisition, and setting up standardized norms that would give full authority to top talent to recruit staff, allocate funds, and target the direction of scientific research-a sure sign of Shanghai’s determination to succeed in this endeavor.

Shixin Wang
Deputy Editor-in-Chief of China Education Online

Shanghai has boasted the highest attraction index for talent in China for several years. The excess of talent available to the city has allowed it to become inactive in the work of attracting new talent. So what has made the city adopt these urgent stimulus measures? The answer, beyond doubt, is fierce competition. Over the past few years, the most important element of China's urban development has been to bring in new enterprises, which were expected to increase overall employment and the growth rate of GDP and tax revenue. However, in today's situation, talent attraction has become more prominent, and talent is now seen as the most essential factor in the development of cites and commerce.

There are clear signs that China's traditional first-tier cities (Beijing, Shanghai, Guangzhou, and Shenzhen) are facing strong challenges from the so-called "new first-tier cities" (Chengdu, Wuhan, Nanjing, Xi'an, etc.) in terms of drawing talent. In 2017, those cities launched several programs to attract talent both at home and abroad, which is definitely a sign of "brain drain" for traditional first-tier cities that are now troubled by the problems mentioned above, such as the high cost of housing and challenging conditions for incoming migrants.

According to the spring 2018 "Research Report on the Job-Hopping Index of White-Collar Workers" issued by a domestic website focused on human resources, Chengdu, Hangzhou and Wuhan (among other new first-tier cities) for the first time surpassed the traditional first-tier cities in bringing in talent, which is exemplified by the fact that more and more white collar workers are job hopping to new first-tier cities.

The intense scramble to acquire talent has even spread to second- and third-tier cities, and even institutions at the district and county level have entered this fierce competition. The Xiaoshan District of Hangzhou, for example, has issued an announcement that winners of key awards such as the Nobel Prize and the Turing Award, and world-class scientists (including academicians from the United States and the United Kingdom, and academicians of the Chinese Academy of Sciences and Chinese Academy of Engineering) can receive a grant of up to RMB 100 million (USD 15.9 million), among other benefits.

China's intensified effort to attract talent is clearly good news for its colleges and universities, which are the major participants in the country's plan to build world-class universities and first-class disciplines.

Universities in China are offering competitive salaries, often commensurate with what could be expected in the UK or the US.

Treatment like this for high-level talent is commonly seen in China-not counting accommodation subsidies, research startup funds, and children's educational arrangements. That makes sense, because as the fundamental source for urban talent, colleges and universities are also the most important reservoir of top talent for the country. Propelled by the "Double-First Class" plan, colleges and universities have become more and more eager to acquire top experts. That fact, combined with the talent-attraction policies of major cities and corresponding projects implemented by local governments, has brought a "halo effect" to the attraction campaign.

However, apart from the necessary requirements of a doctoral degree, colleges and universities are more concerned with whether talent meets or almost meets the standards of the Thousand Talents Plan and the Thousand Youth Talents Plan.

The Thousand Talents Plan, also known as the "Recruitment Program of Global Experts", is closely tied to China's national development strategy and aims at attracting thousands of experts to national key innovation projects, disciplines and laboratories, as well as central enterprises, state-owned financial institutions, and various high-tech industrial parks, for the purpose of making major breakthroughs in key technologies, developing high-tech industries, and advancing emerging disciplines. The "Recruitment Program for Young Professionals," a division of the Thousand Talents Plan, mainly targets those under 40 years of age who hold a Ph.D. in the field of natural science or engineering technology granted by prestigious overseas universities; work experience of more than three years with overseas teaching and research institutions is required. It should be noted that, if accepted, current employees of overseas universities, scientific institutions and enterprise development laboratories should return to China to work on a full-time basis. The "Recruitment Program for Foreign Experts," another part of the Thousand Talents Plan is a long-term program focusing on non-Chinese foreign experts who can work more than nine months per year in China for three consecutive years.

According to statistics, since the implementation of the Thousand Talents Plan in 2008, talent-attraction programs in all regions and departments have brought in more than 50,000 top experts from overseas, the highest number recorded since the founding of the People's Republic of China.

From China's central government to down to the municipal level, from colleges and universities to scientific research institutions, everyone has reached a consensus: Talent is China's most important resource. With the rapid development of the Chinese economy and the consistent promotion of human-resource development there, talent-attraction programs are now in a much more prominent position. To quote a recent headline in one of China's mainstream newspapers: "Talents, Coming for the Best Times!"

Certainly, since talent acquisition policies in China are changing quickly, a huge information gap between employers and overseas talent cannot be avoided. Nevertheless, AcaBridge, China's most professional platform promoting employment and entrepreneurship for high-level talent both at home and abroad, would love to bridge this gap. Those interested in working in China can contact us at consultant@acabridge.edu.cn. We provide a "one-stop" service, so you can learn about open positions in China, contact employers there, and communicate with people who can help you get here. For more information, please visit www.edu.cn/jjrcxm.

Faculty Recruitment of Overseas Talents Beijing Institute of Technology

Beijing Institute of Technology (BIT) announces recruitment for talented applicants for full-time tenured faculty positions in the broad areas of sciences and engineering, including but not limited to: aerospace engineering, mechanical engineering, optoelectronics, electronics and informatics, automation, computer science and technology, material science and engineering, chemistry and chemical engineering, life science and bio-engineering, mathematics and statistics, physics, management and economics. Successful candidates are expected to establish research labs in the corresponding academic schools and to interact with diverse faculty across disciplines. This hiring initiative is a part of the National "Thousand Talents Program", "Outstanding Young Faculty Program", and BIT's tenure tracked faculty program. These programs intend to attract international candidates addressing important research issues and contributing to the signature research areas of the university.

BIT, founded in 1940, has always been a leading institution of science and technology in China. In 2016-2017, BIT was ranked among the Top 400 in QS World Universities Ranking, as well as the 15th among the Chinese universities in the above rankings. The fundamental research on engineering, material science, chemistry, physics, computer, mathematics and social science in BIT is among the top 1% in ESI ranking.

I.Requirements for Positions of National "Thousand Talents Program"

1.Positions Supported by the National "Young Thousand Talents Program"

(1)The applicants are required to hold a Ph. D. and have at least three years overseas research experience in world-class universities, research institutes, or top-ranking overseas companies. Applicants with overseas experience and who are now working in China for less than one year will also be considered.

(2)Exceptional candidates under the age of 40 who have made outstanding research discoveries will be considered as individual cases.

2.Other Positions Supported by the National"Thousand Talents Program"

The candidates are required to hold a professor position or equivalent position at world-class universities or research institutions. And for the Innovative Talents Project , Applicants must be under the age of 55, for the Overseas Experts Project, applications must be under the age of 65.

II.Requirements for Positions at Tenure-tracked Program

1.The applicants are required to hold a Ph. D. and have more than 2 years-experience at world-class universities or research institutions, under the age of 35 for associate professor and 32 for assistant professor.

2.The applicants are required to have expertise about the latest development in the research area with highly recognized research achievements, show potential for being future academic leaders to develop new research directions, and be supported by high-level papers as the first author or corresponding author.

III.Payment and Benefits

1. Recipients of the National "Young Thousand Talents Program"will receive:

(1)Professorship and Ph.D. supervisor, with special enrollment quotas for graduate students

(2)A subsidy of 2-6 million RMB for research funding and laboratory space provided by BIT.

(3)Annual salary is 420,000 RMB (insurance and accumulation fund paid by BIT not included).

(4)Opportunity of buying a new flat of one sitting room and two bedrooms with a discount of 1 million RMB compared to the market price or a subsidy of 2 million RMB. Assistance of housing during the transition period will be provided.

(5)Assistance in the placement of children and spouse for educational and job opportunities.

(6)International travel expenses will be covered for the interview, with recommendations to other positions if not recruited.

2. Other projects in National "Thousand Talents Program"

BIT supports various projects on the basis of payment from the government, appoints entrants as professors and Ph. D. supervisors, provides adequate research start-up funds, competitive salary and other material benefits, helps to arrange assistants, office and laboratories, and supports the entrant to establish research teams.

3.Tenure-tracked Program

Recipients of the Associate Professorship will receive:

(1) Professorship and Ph. D. supervisor, with special enrollment quotas for graduate students.

(2) Annual salary is 360,000 RMB (Insurance and accumulation fund paid by BIT not included).

(3) Research start-up funds of 600,000 RMB.

(4) Assistance in the placement of children's educational opportunities.

Recipients of the Assistant Professorship will receive:

(1) Associate-professorship and supervisor of master's degree students, with special enrollment quotas for graduate students, and will qualify to apply for Ph. D. supervisor.

(2) Annual salary is 300,000 RMB (Insurance and accumulation fund paid by BIT not included).

(3) Research start-up funds of 400,000 RMB.

(4) Assistance in the placement of children's educational opportunities.

IV.Application Instructions

Applicants for the National "Thousand Talents Program" should send their CVs and the complete representative published works to the BIT HR Office. Applicants for the Outstanding Young Faculty Program should send their CVs and 5 representative published works, quotations and comments by others, and future working plans to the BIT HR Office. Please state the position being applied for in the subject line of the email.

For any issues related to the "Thousand Talents Program" and the "Outstanding Young Faculty Program", please contact:
Mrs. Xia Yinqiu or **Mr. Fan Shicheng**
Tel.: +86-10-68914243
+86-10-68914546
Email: bitrcb@bit.edu.cn
For more information about the "Thousand Talents Program" and the "Outstanding Young Teachers Program", please visit: http://zhaopin.bit.edu.cn/

Call for Global Talents
Recruitment Information of Nankai University

About Nankai University

Located in the city of Tianjin, 30 minutes away from Beijing by high-speed rail, Nankai University is a multidisciplinary Project 985 & 211 university and "Double First Class University" under the direct jurisdiction of the Ministry of Education. It features a balance between the Humanities and the Sciences, a solid foundation and a combination of application and creativity. Besides its main campus in Balitai, Nankai University also has a campus in Jinnan District and TEDA College in Tianjin Economic-Technological Development Area. With the support of the Ministry of Education and Tianjin municipal government, the new campus in Jinnan District was officially put to use in 2015, with a scale of 1.5 million square meters to accommodate 37,000 students.

Recently, Tianjin municipal government released a series of policies to attract and cultivate scholars. High-level scholars who come to work full-time in Tianjin will receive an award of up to 2,000,000 RMB and a research fund of up to 10,000,000 RMB. Tianjin will also provide awards and scientific research fund, a better platform for international exchange programs as well as support of the education of the scholar's children.

Nankai University is providing the following honorable positions for global talents:

1. Hundred High-level Talents Support Program of Nankai University

This program targets academicians, professors and associate professors of "National Thousand Talents Program", distinguished professors of "Chang Jiang Scholars Program" and other high-level talents programs. The applicants should be well-established and highly innovative scientists with outstanding academic records and leadership. Successful applicants will be offered an annual salary of 650,000-1,200,000 RMB (pre-tax), research fund of 500,000-12,000,000 RMB for natural sciences and engineering or 500,000 RMB for humanities and social sciences and housing subsidy and settling-in allowance of 600,000-3,000,000 RMB. The colleges will provide corresponding support such as allowance, scientific research fund as well as laboratory and office.

2. Hundred Young Academic Leaders Program of Nankai University

This program targets "National Thousand Young Talents Program", young academics of "Chang Jiang Scholars Program", and other excellent young scholars in humanities, social sciences and natural sciences. Successful applicants will be offered an annual salary of 400,000-700,000 RMB (pre-tax), research fund of 500,000 -1,000,000RMB for natural sciences and engineering or 200,000-500,000 RMB for humanities and social sciences and housing subsidy and settling-in allowance of 200,000-1,400,000 RMB. The colleges will provide corresponding support such as allowance, scientific research fund as well as laboratory and office.

3. Other Positions (Professor / Associate Professor / Lecturer / Postdoctoral Researcher / Visiting Professor)

Please visit http://www.nankai.edu.cn/2018/0309/c157a91627/page.htm

The applicants should send their curriculum vitae to: Mr. Wang or Ms. Yang, Office of Human Resources, Nankai University, 38 Tongyan Road, Haihe Educational Park, Jinnan District, Tianjin, China, 300350;

Tel: 0086-22-8535-8595, 0086-22-8535-8586;

Website: http://rsc.nankai.edu.cn;

Email: nkuniversity@nankai.edu.cn.

4. 2018 International Talent Forum in Nankai University

Nankai will organize the third International Talent Forum in 2018, which aims to recruit more staff of international background. The forum involves a variety of activities including speeches, seminars, sightseeing tours and so on. Nankai will invite international renowned scholars, alumni, and potential young scholars to join the forum for exchange and cooperation. Nankai will provide necessary transportation fare and accommodation. Information of the forums is as follows:

Time	Subject	Contact
May 20-21	Environment	Haiyong Wang envwanghy@nankai.edu.cn
June 12	Micro-nano optics, ultrafast optics, fiber optics, THz optics, etc.	Weiwei Liu liuweiwei@nankai.edu.cn
June 13-17 July 10	Entrepreneurship, innovation, strategy, etc.	Yinan Jiang & Jun Yang jiangyinan@nankai.edu.cn, nkyangjun@163.com
June 29-July 1	Tourism-related research areas	Shan Wang & Shuling Liang nkutourism@126.com
July	Microbiology	Kai Jiao tedacollege@nankai.edu.cn
July 6	History	Nan Xie lsxyrs@nankai.edu.cn
Oct. 12-14	Photovoltaic research frontiers from materials to applications	Xiaodan Zhang & Yi Ding xdzhang@nankai.edu.cn tingyee@163.com
Nov. 7-9	Pharmacy, biology, chemistry and other interdisciplinary topics	Yongwei Hao haoyongwei@nankai.edu.cn
Dec. 15	Economics	Hao Lan ecojobs@nankai.edu.cn

If you would like to join the sub-forum(s), please feel free to contact us. Nankai University is also recruiting staff from abroad in more than ten events around the world.

Harbin Institute of Technology, Shenzhen (HITSZ) Recruiting Members or Candidates of Thousand Young Talents Program

Founded in 1920, Harbin Institute of Technology (HIT), which is under the Ministry of Industry and Information Technology, is a national key university that provides multidisciplinary studies in science and technology. It offers specializations in science, engineering, management, arts, economics, law, and many other fields. It is a member of the C9 League and is one of the first universities to be part of Project 985 and one in list of "Double First-Class" University project. In the engineering field, HIT ranked No.2 in China and No.6 in the world according to US NEWS 2018.

Together with the Shenzhen Municipal Government, HIT created Harbin Institute of Technology, Shenzhen (HITSZ), which was established in 2002 as HIT Shenzhen Graduate School and currently serves as a key campus of HIT. HITSZ provides full-time undergraduate and postgraduate education. Till 2020, HIT will realize the aim of constructing an excellent university with one hundred years history also with a feature of 'Chinese Characteristics, World-class, HIT Qualification'. At the same time, HITSZ will carry on the new responsibility of constructing a unique campus which matches the world-class level.

With a brand-new look, HITSZ will follow the HIT tradition, keep on the philosophy of high starting point, high standard to attract more international excellent talents and carry forward the Shenzhen spirit to serve as a contributor to national and regional economic and social development.

Fields Open for Recruitment:

(1) Aeronautical and Astronautical Science and Technology
(2) Computer Science and Technology
(3) Electronic Science and Technology
(4) Information and Communication Engineering
(5) Materials Science and Engineering
(6) Environmental Science and Engineering
(7) Management Science and Engineering
(8) Control Science and Engineering
(9) Civil Engineering
(10) Mechanical Engineering
(11) Biomedical Engineering
(12) Power Engineering and Engineering Thermophysics
(13) Mechanics
(14) Mathematics
(15) Chemistry
(16) Physics
(17) Biology
(18) Architecture
(19) Design
(20) Business Administration
(21) Marine Science
(22) Practical Economics
(23) Urban and Rural Planning
(24) Sociology
(25) Space Science and Technology

Basic Requirements:

(1) Applicants whose research fields are in natural science and engineering technology should be under 40 years old;
(2) Applicants should have acquired a doctoral degree, and have over three years' overseas research and working experience (not including working experience abroad with employment relations remained in China);
(3)Applicants should have a permanent teaching or research position in overseas universities, research institutions and enterprises of high prestige;
(4) Generally, applicants should not have a full-time position in China at the time of application. However, if applicants are already holding a position in China, it should be less than one year that they returned from abroad;
(5) Applicants should work full-time in China once employed.

Salary and Benefits:

For members of "Thousand Young Talents Program" (Currency in RMB):

(1) Salary: approximately 700,000 per year (pre-tax) with a title of professor.
(2) Funds for research: up to 4,500,000-8,500,000, including 1,000,000-3,000,000 (Nation), 500,000 (Guangdong Province) and 3,000,000-5,000,000(Shenzhen).
(3) Living allowance: up to 2,750,000, including a central finance subsidy of 500,000, the Guangdong provincial finance will also grant 250,000 and Shenzhen will grant 2,000,000.
(4) The university will provide the recruited with assistance in their children's entry into kindergarten, primary school and middle school in Shenzhen.

Additionally, if members are successfully hired, within the limited budget, our university will afford flight ticket and 3 nights of designated hotel when they come to register.

Contact Information:

Human Resources Department of HITSZ
Contact person: YANG Zhixi
Tel: 0755-26033365
E-mail: hrsz@hit.edu.cn

哈爾濱工業大學(深圳)
HARBIN INSTITUTE OF TECHNOLOGY, SHENZHEN

Recruitment of School of Physics in Sun Yat-sen University

中山大學 SUN YAT-SEN UNIVERSITY

Sun Yat-sen University (SYSU), located in Guangzhou in Southern China, is one of the mostly acclaimed top 10 universities in Mainland China. It was ranked at the 8th position by the U.S. News and the Times Higher Education in 2017. The physics program of SYSU was established at the very beginning with the establishment of SYSU in 1924 by Dr. Sun Yat-sen and was restructured into the School of Physics in 2015. We are located in the south campus of SYSU in Guangzhou besides the beautiful Pearl River. Enjoying the long history of the SYSU physics program since its establishment, the school has strong teams in theoretical physics, condensed matter physics, optics, and high energy physics. We have also recently set up research groups working in soft condensed matter and biophysics, energy physics, and a few other cross discipline fields. Thanks to the fast development of SYSU and the school with the strong supports in higher education from the central government, we are actively recruiting high level talents in all the disciplines all over the world. We have open positions in the following disciplines for talents at different stages of their careers. Our school will provide internationally competitive startups, salaries and relocation fees. We welcome all applicants who want to further their careers at SYSU!

I Disciplines Open for Recruitment

Condensed matter physics
Theoretical physics
Optics
High energy physics
Soft matter and biophysics
Energy physics
Neutron science and technology
Ultrafast Intense Laser Technology

II Recruiting positions and treatments

1. National Thousand Talents Program and Thousand Young Talents Program

(1) Applicants should apply for and obtain the titles from National Thousand Talents Program or Thousand Young Talents Program by the support of our university or other institutions.

(2) Applicants obtained the titles from National Thousand Talents Program or Thousand Young Talents Program can be employed as professors or associate professors.

2. "Top 100 Talents" Program of Sun Yat-sen University

(1)Leading talents

Applicants under 50 years old holding professors, associated professors, or equivalent positions in high level universities with notable scientific achievements.

(2)Outstanding young and middle-aged talents

Applicants under 40 years old with good publication records, well-recognized scientific achievements, clear research directions, superior scientific attainments, and great development potential.

(3)Young academic talents

Applicants under 35 years old with significant academic achievements, good development potential, and innovative capabilities.

Positions are given according to the competence of the applicants and demands of the disciplines. Research startup funding, competitive salaries, housing subsidies, transitional housing, and children's school admission are provided.

3. Research fellows and postdoctoral fellows

(1)Research fellows

Applicants should be postdoctoral researchers, outstanding Ph.Ds from top level universities, lecturers, or holding equivalent positions under 38 years old.

(2) Postdoctoral fellows

Applicants under 35 years old obtained their doctorates within the past three years.

Research fellows and postdoctoral fellows with prominent achievements could apply for positions of associate professors and above by competition.

III Application procedures

We welcome you to attend the 2018 International Young Scholars Zhuhai Forum of SYSU. The forum will be held from Jun 8-11, 2018. Please click the follow link to get more information: http://survey.sysu.edu.cn/cn/registration/iysf2018cn

Applicants may contact us via email or telephone, and provide personal academic resumes, research plans, and three recommendation letters.

Contact address: No. 135, West Xingang Road, Haizhu District, Guangzhou, 510275

Contact:

Shuang Liang (Secretary)
Email: lshuang5@mail.sysu.edu.cn
Tel: +86- 20-84113293

Yue Zheng (Dean)
Email: zhengy35@mail.sysu.edu.cn
Website: http://spe.sysu.edu.cn/node/2254

Thousands of reasons
to stay abroad,
but one decision to
return to the roots.

Overseas Scholar's Visit to Top Chinese Universities —— Chinese Universities Forums

For more information, please check www.edu.cn/zgx

▶ **10,000+ academic job vacancies in China**
▶ **Free one-to-one consultation service**

Send your CV to
consultant@acabridge.edu.cn

Outstanding young scholars are welcomed to apply for "The Recruitment Program for Young Professionals" of Beijing Jiaotong University(BJTU). In addition, BJTU will hold the First International Young Scholars "Learn and Practice" Forum in Beijing from July 15 to July 17, 2018 and extend its sincere invitation to excellent young scholars from both home and abroad. For more details please click on the link below.

http://www.bjtu.edu.cn/tzgg/152118.htm

BJTU's Invitation of Outstanding Applicants for "The Recruitment Program for Young Professionals"

Ⅰ. Disciplines

Traffic and Transportation Engineering, Information and Communication Engineering, System Science, Computer Science and Technology, Business Administration, Applied Economics, Civil Engineering, Mechanical Engineering, Electrical Engineering, etc.

Ⅱ. Supporting Conditions

"The Recruitment Program for Young Professionals" is included in the"Outstanding Hundred Talents Plan" of Beijing Jiaotong University and its awardees will be supported accordingly. Competitive salary and superior working and living conditions will be offered.

Ⅲ. Contact Us

Mr. Zhang: +86+10-51685138
Mrs. Yun: +86+10-51683432
E-mail: rczp@bjtu.edu.cn
Home Page: http://www.bjtu.edu.cn/
Address: Talent Program Office, Personnel Department, Beijing Jiaotong University, No.3 Shangyuancun, Haidian District, Beijing, P.R.China
Zip Code: 100044

1000 Talents Global Recruitment Program Southern University of Science and Technology

Southern University of Science and Technology (SUSTech) in Shenzhen, China is seeking outstanding candidates for the "1000 Talents Global Recruitment Program" sponsored by the Central Government of China. Applications are invited for all major science and engineering disciplines. Successful applicants will be appointed to the faculty of SUSTech at a level commensurate with each applicant's background and experience, from tenure-track assistant professor to tenured chair professor.

SUSTech offers a generous salary and startup package for "1000 Talents Global Recruitment Program" recipients, including: a) world-wide competitive starting salary; b) a living subsidy of 2.75 million RMB for "1000 Young Talents" and 4.5 million RMB for "1000 Talents" or "Foreign 1000 Talents" over 3-5 years; c) a start-up fund of up to 12 million RMB; d) PI system and tenure-track system; e) housing allowance up to 8000 RMB per month; and f) social insurance and welfare.

Applicants should have a Ph.D. degree in a relevant science or engineering field. Applicants for "1000 Talents Global Recruitment Program" should be a professor or a senior researcher. Applicants for "1000 Young Talents Global Recruitment Program" should have three years or more of oversea post-doctoral research or work experience. Applicants must have a proven track record of high-quality peer-reviewed academic publications. They must also have excellent communication skills and the capacity to teach in English.

If interested, please apply through the website at http://talent.sustc.edu.cn/en/enindex.aspx.

Contact person:
Ms. Jing Long, Mr. Lan Ge
Phone: +86-755-88010968
+86-755-88010945
Email: talents@sustc.edu.cn
http://www.sustc.edu.cn

"Jinan Double Hundred Talents Plan" Recruiting Members (Candidates) Of the "Thousand Young Talents Program"

Jinan University (JNU) is one of China's "One Hundred Key Universities of 21st Century"(the "211 Project") . As the first university established by the State for overseas Chinese students, JNU currently has the largest number of overseas and foreign students and is honored as the "top university for overseas Chinese". Abiding by the motto of "loyalty, sincerity, integrity and respect", the university is committed to cultivating talents with the excellent traditional Chinese moralities and culture. JNU was selected to the "High-level University Construction Program" by Guangdong provincial government In Jun 2015 and was selected to participate in the National "Double-First Class" initiative of first-class disciplines construction by Ministry of Education of PRC in Sep 2017. So far, disciplines of JNU including engineering science, chemistry, clinical medicine, pharmacology & toxicology, materials science, biology & biochemistry, agriculture science, environmental science / ecology have ranked the top 1% of ESI.

Disciplines Open for Recruitment

Pharmaceutical science, science of Chinese pharmacology, biology, biomedical engineering, basic medicine, clinical medicine, Chinese medicine, integrative medicine, stomatology, public health and preventive medicine, nursing, ecology, environmental science and engineering, chemistry, physics, food science and engineering, materials science and engineering, mechanics, civil engineering, architecture, optical Engineering, computer science and technology, information and communication engineering, electronic science and technology, cyberspace security, software engineering, mathematics, electrical Engineering, journalism, philosophy, Chinese language and literature, China history, world history, foreign language and literature, theoretical economics, applied economics, business management, management science and engineering, public administration, psychology, law, International relations , Marxist theory, art, physical science and so on.

Basic Requirements

1. Members of the "Thousand Young Talents Program".
2. Candidates of the "Thousand Young Talents Program" (candidates of the discipline of finance not included). Applicants should meet the following requirements:
(1) Applicants whose research fields are in natural science and engineering technology should be under 40 years old (up to June.1 of the year of application, the same below);
(2) Applicants should have acquired a doctoral degree, and have over 36 months' running overseas research and working experience (not including working experience abroad with employment relations remained in China).
(3) Generally, applicants should not have a full-time position in China at the time of application. However, if applicants are already holding a position in China, it should be less than one year that they returned from abroad.
(4) Once employed, applicants should work full time at least 3 years in China.

Package of Salary & Benefits

JNU will provide recruited members and candidates of "Thousand Young Talents Program" with a competitive package of salary and benefits based on the job position.

1.For members of "Thousand Young Talents Program":

(1) Salary: no less than ¥500,000 per year (pre-tax).
(2) Supporting funds for research: ¥1,000,000-3,000,000. Encourage the application of the Guangdong Innovation Team for the introduction of planned projects (5-7 team members, 20 million research funds).
(3) Housing/settling allowance: no less than ¥2,000,000(pre-tax). Another set of lake view elevator turnover room on campus for rent.
(4) Recruited members will be directly employed as a senior professional.
(5) Recruited members will have the priority to recruit PhD students, post-doctors and research assistants.
(6) The university will provide applicants assistance in their children's entry into kindergarten, primary school and middle school in Guangzhou.
(7) Members will enjoy the one-stop service for high-level talents.
(8) The university will provide a job for the spouse of members.
(9) Each new recruit is entitled to a central finance subsidy of ¥500,000and a research fund ranging from ¥1,000,000 to ¥3,000,000, which, once ratified, will be allocated according to schedule. The Guangdong provincial finance will also grant the recruit a living allowance of ¥250,000 and a supportive fund of ¥500, 000.

2.Candidates having successfully passed the university review process can sign an employment contract of intent, and apply for the "Thousand Young Talents Program" membership in the name of Jinan University. Candidates who have entered into the defense session are entitled to the following salary and benefits:

(1)Salary: no less than ¥400,000 per year (pre-tax).
(2)Supporting funds for research: no less than ¥1,000,000. Encourage the application of the Guangdong Innovation Team for the introduction of planned projects (5-7 team members, 20 million research funds).
(3) Housing/settling allowance: no less than ¥1,000,000 (pre-tax). Another set of lake view elevator turnover room on campus for rent if well-off.
(4)Recruited members will have the priority to recruit PhD students and research assistants.
(5)The university will provide applicants assistance in their children's entry into kindergarten, primary school and middle school in Guangzhou.
(6)Recruited members will enjoy the one-stop service for high-level talents.
(7)If recruited members are enrolled into the "Thousand Talents Program", they are entitled to all the pay and benefits offered by the university to members of this program.

Materials to be Submitted for Application:

(1) One copy of CV;
(2) The full text of two representative papers;

Please send them to the contact of each institute.

Scan the QR code above for contact information

Contact Information

Home page of Personnel Department, Jinan University (https://hrdam.jnu.edu.cn/)
Tel: 0086-20-85227283 (fax available), 0086-20-85223525
Contacts: Mr. Tong, Mr. Liu
Email: otalents@jnu.edu.cn
Address: No. 601, Huangpu Avenue West, Guangzhou, Guangdong, PRC
Post Code: 510632

Talents At Home And Abroad Are Invited By Harbin Engineering University For "Recruitment Program of Global Young Experts"

Harbin Engineering University is located along the beautiful Songhua River – Harbin, the "Ice City" in the North. The University is a national key university, one of the first batch of universities being selected in the national "211 Project" construction, entering the construction of national "Innovation Platform For Superiority Subjects" project, and setting up graduate school. In 2017, relying on its distinct "three ocean disciplines and one nuclear discipline" (shipping industry, navy equipment, oceanographic engineering and nuclear application) characteristic advantages, the University is incorporated in the construction of "state-class universities and world-class disciplines". All talents, no matter at home or abroad, are welcomed to Harbin Engineering University.

I. Posts and Condition

1. Major in natural science or engineering technology, no more than 40 years old;
2. PHD obtained, as well as at least 3 years of working experience in overseas scientific research;
3. Working as the official teaching or scientific research position in famous overseas universities, scientific research institution or enterprise and research institution;
4. Tip-top talent among peers engaging in the scientific research field, with the development potential of becoming the academic and technical leader of this field;
5. After the application is approved, the applicant must return home and work as full time. In general, the applicant should have no working experience in China; if not, the time should be within one year.

For the candidate with excellent performances, his age and position time will not be the limitation.

II. Remuneration and Conditions

Following remunerations are available for the candidates of "Recruitment Program of Global Young Experts":

1. To be employed as the professor (third level) and doctoral supervisor;
2. The university provides at least RMB 500,000 Yuan annual salary and RMB 300,000 Yuan settling-in allowance;
3. The central government provides the one-time subsidy for RMB 500,000 Yuan;
4. The central government provides the scientific research funds of RMB 1,000,000 – 3,000,000 Yuan ; and the university supports the scientific research startup funds at 1:1, and supports to establish the academic team;
5. The university provides one house for at least 80 square meters or RMB 1-1.5 million Yuan house-purchase subsidy;
6. To assist to solve the employment of your spouse, preferentially arrange you children to study in the provincial top class kindergarten, primary and middle school.
7. The candidate who has received the"Recruitment Program of Global Young Experts"review but failed to be selected can also enjoy the above mentioned remuneration according to the academic level after being discussed by the university.

III. Application Method

Please send your resume to rencai@hrbeu.edu.cn, we will contact with you timely.

Contact information
Contact person: You Dandan
Tel: +86-451-82518061
Email: rencai@hrbeu.edu.cn

Join Us-Chang'an University Recruitment Notice

Chang'an University, directly affiliated to the Ministry of Education of the People's Republic of China, is the national "211 Project" key construction university, national "985 preponderant Discipline Innovation Platform" and the national first-class disciplines construction university. It covers an area of more than 3,745 mu (approximately 250 hectares), which is located in Xi'an, a famous historical and cultural city. The university comprises two teaching campuses and two practice bases. The main campus is adjacent to the Big Wild Goose Pagoda of Xi'an, the Weishui campus is located in the Xi'an Economic and Technological Development Zone. For more than 60 years, Chang'an University has evolved into an influential comprehensive higher institution in China, with engineering as its main discipline focus, combining engineering with sciences, and with multidisciplinary development in economy, management and humanities.

Chang'an University attaches great importance to the talents team construction. To achieve the goal of building a high-level university, it further increases the introduction, cultivation and supporting of high-level talents and also strengthens the selection and employment of excellent PhD graduates both at home and abroad. As a continuously expanding institution, we are seeking to recruit talents in natural science, engineering technology, management, humanities, social sciences and newly-developing interdisciplinary professional and technical personnel, especially in the field of traffic engineering, land resources and environment and constructional engineering.

Positions

1. The 1000 Talents Plan (Long-term Program, Short-term Program, Young Program and Foreign Scholar Program)
2. Changjiang Scholar Program (Specially-Appointed Professors,Visiting Professors and Young Changjiang Scholars
3. The 1000 Talents Plan of Shaanxi Province (Long-term Program, Short-term Program, Young Program and Foreign Scholar Program)
4. Chang'an Scholar Support Program(Specially-Appointed and Visiting Professors)
5. Outstanding doctoral and postdoctoral graduates at home and abroad

Offering

We provide an international platform and environment, excellent start-up endowment, enormous working spaces, advanced facilities and competitive salaries.

Contact us:

Talents Plan Recruitment:
He Yanfei
Tel: (+ 86-29) 82334069
E-mail: rcb@chd.edu.cn

PhD. and Postdoctoral Graduates Recruitment:
Sun Lin
Tel: (+ 86-29) 82334137
E-mail: rsczp@chd.edu.cn

Address: Middle-section of Nan'er Huan Road Xi'an, ShaanXi Province, 710064, China

Recruitment Announcement of Xi'an University of Science and Technology

Xi'an University of Science and Technology (XUST) is a university co-constructed by the State Administration of Production Safety Supervision and Management and The People's Government of Shaanxi Province. As one of the key high-level universities in Shaanxi as well as in the middle western areas of China, XUST is an important training base and scientific research center which cultivates professionals of geology, mining, safety science and engineering. Located in Xi'an, the capital city of Shaanxi Province, XUST has two campuses: the head one located in Yanta District and the new one in Lintong District. XUST owns 19 colleges and departments, 6 post-doctoral centers, 7 first-level disciplines and 40 second-level disciplines to award doctoral degree, 25 first-level disciplines and 107 second-level disciplines to award master's degree, 18 cultivation programs on Master of Engineering, 1 program to award master's degree of MBA and 1 program to award master's degree of MPAcc as well as 56 undergraduate programs. Featured in Mining, Geology, and the relevant disciplines, it has now grown into a well-rounded university with 23,000 full-time students, integrating the primary subject of engineering with other subjects of science, literature, management, law, economics and art.

● ***If you are a candidate of the National Recruitment Program of Global Experts("the Thousand Talents Plan") under the age of 55...***

We will offer you:

1.An on-campus apartment of 190 ㎡(free of charge) and disposable settling-in allowance of RMB 2.2 million yuan; or RMB 3.2 million yuan as disposable subsidy. (Both plans include a one-off start-up package of RMB 1 million yuan from the nation's central budget)
2. Sufficient amount of research and lab construction fund for talents of different disciplines-RMB 10-15 million yuan for Engineering, RMB 3-5 million yuan for Science and RMB 2-3 million yuan for Humanities.
3. The title of Second-level Professor and doctoral supervisor, provided with salary and benefits conforming to national regulations and extra negotiated wages in terms of employment contract.
4. The quota for postgraduate enrollment, a teaching and scientific research group of 10 members, an assistant as well as a car for work.
5. Relocation of spouse.

● ***If you are a candidate of the National Recruitment Program for Young Professionals under the age of 45...***

We will offer you:

1.An on-campus apartment of 160 ㎡(free of charge) and disposable settling-in allowance of RMB 1.3 million yuan; or RMB 2.1 million yuan as disposable subsidy. (Both plans include a one-off start-up package of RMB 0.5 million yuan from the nation's central budget)
2. Sufficient amount of research and lab construction fund for talents of different disciplines: RMB 3-7 million yuan for Engineering, RMB 2.5-4 million yuan for Science and RMB 1.3-3.6 million yuan for Humanities (including research subsidies of RMB 1-3 million yuan from the central budget throughout the process of the program according to the level and quality).
3. The title of Forth-level Professor or higher position (with identified professorship) and doctoral supervisor, provided with salary and benefits conforming to national regulations and extra negotiated wages in terms of employment contract.
4. The quota for postgraduate enrollment, a teaching and scientific research group of 5-7 members, an assistant as well as a car for work.
5. Relocation of spouse.

How to contact us

1. Sending your CV via e-mail: xkdrcb@xust.edu.cn. (Please name your CV file in the following format: name - specialized field -graduated school.)
2. Contacting us via WeChat: 78024224
3. Tel: +86 29 83856208

Guangzhou University Seeking Faculty Applicants for the National "Thousand Young Talents Plan"

About us

Guangzhou University is a comprehensive university named after the national key central city of Guangzhou. Guangzhou University has two campuses - the University Town campus and the Gui Huagang Campus in downtown Guangzhou. Boasting rich teaching resources and state-of-the-art scientific and research facilities, the University enrolls 33,974 students including undergraduate and graduate students, PhD candidates and post-doctoral candidates.

Guangzhou University employs 3,000 faculty and staff which includes 1,169 professors or associate professors. Our prestigious faculty include 4 full-time and 6 dual-employed academicians of CAS&CAE, 1 full-time and 1 short-time employed academicians of ATSE, 5 Yangtze River Scholars, 12 experts awarded with The National Science Fund for Distinguished Young Scholars, and 8 experts of the Thousand Talents Plan. With these outstanding research fellows, Guangzhou University has been contracted to various Chinese national key research projects, such as the 973 Project, the 863 Project and receiving grants for major humanitarian and social sciences programs, such as the National Natural Science Foundation Projects and the National Social Science Fund Projects.

Guangzhou University is dedicated to developing itself into a leading university complementing the status and development of Guangzhou city.

Recruitment Disciplines

Mathematics, Physics, Chemistry, Astronomy, Geography, Atmospheric science, Geology, Biology, Systems Science, Ecology, Statistics, Mechanics, Mechanical Engineering, Optical Engineering, Materials Science and Engineering, Electrical Engineering, Electronic Science and Technology, Information and Communication Engineering, Control Science and Engineering, Computer Science and Technology , Architecture, Civil Engineering, Surveying and Mapping Science and Engineering, Chemical Engineering and Technology, Geological Resources and Geological Engineering, Environmental Science and Engineering, Biomedical Engineering, Food Science and Engineering, Urban and Rural Planning, Landscape Architecture, Software Engineering, Bioengineering, Safety Science and Engineering.

Key Development Fields of Guangzhou University

Intelligent Manufacturing, Mobile Data Science and Engineering (including Advanced Technology on Cyber Space and Intelligent Software), Geography of Southern China, Sustainable Urban Development and Living Environment, Development of Urban Underground Resources and Space in the Pearl River Delta, Life Science and Human Health which includes sophisticated Gene Editing Engineering.

Qualifications and Requirements

- Applicants should be under 40 years old.
- Applicants should hold a PhD degree and have worked overseas with scientific research experience of over three years.
- Applicants should hold an official teaching or research position at a prestigious overseas university, research institution or a research department in a renowned company. Applicants should also be a leading figure among their peers in their research field and have the potential to be an academic or technical pioneer.
- Applicants should have not worked full-time in China. For those returning to China, applicants should have lived in China for no more than a year.

For newly PhD graduates with outstanding research during their study, limits on age, working experiences and other qualifications can be further reviewed.

Salary and Benefits

- An annual salary of at least 800,000 RMB provided by Guangzhou University.
- An after-tax housing subsidy of over 2 million RMB provided by Guangzhou University.
- Startup research funds of over 3 million RMB provided by Guangzhou University.
- Assistance in building a research team.
- Temporary residence, apartment or a rental subsidy of 4,000 RMB will be provided for three years.
- Assistance in children's schooling.
- Other benefits provided by national, Guangdong provincial and Guangzhou municipal government.

Material Required from Applicants

- A resume with the applicant's educational background, work experience, major achievements and personal contact information.
- Teaching and research plan.
- A catalogue of all applicant papers published noting the first author and correspondent author. In the catalogue, three to five representative papers should be presented in full length. Reference materials for major achievements are also needed.
- Recommendation letters from three prestigious experts should be submitted. In the recommendation letter, name and e-mail address of the expert and where he or she works should be noted.
- Any other relevant materials that the applicant believes to be beneficial.

Guangzhou University recruits outstanding faculty to apply for the National "Thousand Young Talents Plan" throughout the year.

For Further Information:

Contacts: Mr. TAN Jinghua (Chinese) and Ms. XU Duotian (English)
Tel: 0086-20-39341749 / 20-39366462
Fax: 0086-20-39366216
E-mail: gdrsc@gzhu.edu.cn
xu_dt@gzhu.edu.cn
Website: http://www.gzhu.edu.cn
Address:
Department of Human Resources, Guangzhou University
230 Waihuan Xi Road
Guangzhou Higher Education Mega Center
Guangzhou, 510006
Guangdong Province, People's Republic of China

Dr. Chen Xiaohong
President of HNUC,Academician of Chinese Academy of Engineering

Faculty needed by Hunan University of Commerce

Hunan University of Commerce (HNUC) was founded in 1949 and located in the historically and culturally renowned city of Changsha, capital city of Hunan Province. It enjoys convenient communications and beautiful environments with picturesque Yuelu Mountain to the south and rippling Xiang River to the east. It is a full-time provincial university to deliver both bachelor and master degrees. It was appraised as Excellence in the Undergraduate Teaching Quality Evaluation Program by the National Education Ministry in 2007. During the last three years, the university has won various honors such as one of the "Applied Universities of Industry-Education Project of the National Thirteenth-Five-year Plan"; one of the first batch of "Top 100 Model Universities of Deepening Innovation and Entrepreneurship Education Reform"; the National Innovation and Entrepreneurship Base of Practical Education and one of the National Top 50 Universities of Innovation and Entrepreneurship. Three major disciplines of the university ---Theoretical Economics, Applied Economics and Business Administration---entered the top 25% of China's best disciplines by Shanghai Soft Science Ranking in 2017, and was ranked 19 among financial and economic universities by CUAA as well.

The university is developing in high speed. All kinds of talents from home and abroad are welcome.

I. Targets

1. Professors who have acquired long-term tenures or corresponding posts in domestic and overseas well- known universities or research institutions or associate professors with doctoral degrees under the age of 45 or corresponding posts are welcome.
2. High quality PhDs graduated from well-known universities or research institutes both home and abroad under the age of 35 or candidates who will graduate before 30th December 2018 are welcome.
3. Scholars who have achieved already certain academic achievements in some fields, or have obvious academic potential with excellent academic and professional ethics are welcome.

II. Requirements and Treatments

1.Disciplinary (or Direction) chiefs

1) Majors:

Theoretical Economics; Applied Economics;Management Science and Engineering; Business Administration; Accounting; Computer Science and Technology; Electronics and Information Engineering; Big Data Analysis; Artificial Intelligence (AI); Cloud Computing; Mobile Internet Development and Application; Internet of Things; Applied Mathematics; Marxist Theory.

2) Employ Modes and Treatments:

Mode 1: Full-time

Academicians; A-level awardees of the "National Thousand Talents Project"; awardees of the "National Ten-Thousand Talents Project": salary, settling-in allowance, housing subsidies and other relevant matters are negotiable.

Distinguished/Chair Professors of the "Changjiang Scholar"; awardees of National Distinguished Young Scholars Fund; leading scholars from the "National Ten-Thousand Talents Project"; awardees of the "National Thousand Talents Project"; National-level Selectee of "Hundreds, Thousands of Talents Project"; chief scientists of the 973 Program; and awardees of "Hundred Talents Project" of Chinese Academy of Sciences:

① one-two million RMB for annual salary;
② a settling-in allowance of 160 square meter housing and purchase subsidies;

young chief scientists of the 973 Program; young leading scholars from "Ten-Thousand Talents Project"; "Young Changjiang Scholars"; awardees of "Young Thousand Talents Project"; awardees of National Distinguished Young Scholars Fund; and awardees of the "Provincial Furong Scholar":

① 0.5-0.8 million RMB for annual salary;
② a settling-in allowance of 140 square meter housing and purchase subsidies.

Overseas professors by annual salary system:

① 0.5-1million RMB for annual salary;
② 0.3 million RMB for research start-up and international exchange fee; ③ 10,000 RMB for moving expenses; ④ 20,000 RMB for housing subsidies per year, if makeshift shelter unavailable during the period of employment.

Overseas associate professors by annual salary system:

① 0.4-0.6 million RMB for annual salary; ② 0.3 million RMB for research start- up and international exchange fee; ③ 10,000 RMB for a settling-in subsidy; ④ 20,000 RMB for housing subsidies per year, if makeshift shelter unavailable during the period of employment.

2. Scholars with Doctorates

Majors:

Economics; E-business; Finance; Insurance; Management Science and Engineering; Business Administration; Accounting; Tourism Management; Public Administration; Urban Management; Engineering Management; Computer Science and Technology; Electronic and Information Engineering; Big Data Analysis; Artificial Intelligence; Cloud Computing; Mobile Internet Development and Application; Internet of Things; Statistics; Applied Mathematics; English, French; Philosophy; Art and Design; Physical Education; etc.

Treatments

① 150,000 RMB of settling-in allowance and housing subsidies; ② 100,000 RMB for research start-up fee; ③ additional 50,000 to 100,000 RMB for rare talents in such majors as Accounting , Finance, Big Data Analysis; Artificial Intelligence; Cloud Computing; Mobile Internet Development and Application; Internet of Things; ④ 10,000 RMB of moving expenses; ⑤ rising to basic level associate professor' s salary after passing annual assessment after two years' work.

Mode 2: Part-time

Negotiable.

III. Application:

Send the following materials to the email rc88688001@163.com of the university's Talents Employment Office: Resume (including personal basic information and achievements), two letters of recommendation from two professors (If applicants are PhD candidates or will graduate in 2018, one of the letters should be provided by his/her doctoral supervisor.) All relevant materials should be true and valid, any falsifier will be disqualified.

Contact: Mr. Yuan
Tel: +86 731 88688001
E-mail: rc88688001@163.com
Address: Personnel Division of Hunan University of Commerce, 569#, Yuelu Ave., Changsha city, Hunan Province, P. R. China (Zip Code: 410205)

南昌工程学院
NANCHANG INSTITUTE OF TECHNOLOGY

Recruitment Announcement for 2018 Academic Leaders of Nanchang Institute of Technology (NIT)

I. NIT Profile

NIT is a public undergraduate institution jointly built by People's Government of Jiangxi Province and the Ministry of Water Resources. NIT is dominated by engineering with multi-disciplinary coordinated development of economics, management, liberal arts, science, agriculture, and etc. Located in the provincial capital city of Jiangxi, Nanchang City, it is formerly known as Jiangxi Institute of Water Conservancy and Electric Power founded in 1958. In September 2011, NIT was approved by the Ministry of Education of China as a higher institution for "Excellent Engineer Education Program" and we started the enrollment of postgraduate students of professional master's degree in September 2012. NIT was approved to establish postdoctoral innovation practice base of Jiangxi in 2015 and was granted master's degree conferment unit in 2017. The discipline, water conservancy engineering, was selected as one of the "First-class Discipline of Higher Institutions in Jiangxi".

II. Target: academic leaders

III. Disciplines: water conservancy engineering, management sciences and engineering, power engineering, architectural and civil engineering, electronic and communication engineering

IV. Benefits

(1) NIT provides a talent fund of ￥0.5-2 million, a research start-up fund of ￥0.5-10 million, basic yearly salary of no less than ￥300-600 thousand;
(2) NIT offers assistance to build an academic team equipped with assistants and provides necessary office and other facilities for teaching and research. Benefits for the introduction of talent team should be negotiated separately.
(3) A platform construction fund will be provided;
(4) NIT provides on campus a 120m2 apartment (equipped with general living facilities ,no property right, free of rent);
(5) Spouse's job should be negotiated personally;
(6) Academic leaders' benefits and assessment should be subjected to the determination of NIT after argumentation.
(7) Eligible people can be recommended to apply for "'Thousand-people Plan' of Jiangxi Province for Introducing High-level Talents for Innovation and Entrepreneurship", and the selected people will enjoy relevant supporting and funding policies (please refer for details to "Double-thousand Plan" application website http://218.64.59.32/egrantweb).

Contact Person: REN Changqin
Tel:+86-(0) 791-88126554
Email: rsc@nit.edu.cn
Website: www.nit.edu.cn

Southwest Jiaotong University, Chengdu, China Invites Applications for Academic Positions

Southwest Jiaotong University (SWJTU), founded in 1896, is one of the oldest institutions of high learning in China. In its proud legacy of 120 years, the University has been dedicated to Chinese higher education and has proudly nurtured generations of engineering and scientific leaders. As the most comprehensive leading research university in transportation, SWJTU is world-renown for pioneering the Chinese railway transportation engineering and industry, and for its leading contributions to the development of Chinese high-speed rail system. For its sustained excellence and prominence, the University is placed among the key, elite multidisciplinary "211" and "985" Tier-1 universities directly administered by the Chinese Ministry of Education. We offer comprehensive education and research programs in 19 faculties and institutes/centers, covering diverse disciplines in engineering, sciences, arts, and management leading from undergraduate to doctoral degrees. The University boasts 2,600 outstanding academic staffs, 15 doctoral/ 43 master/ 75 undergraduate programs and 11 post-doctoral stations, supported by more than 30 cutting edge key laboratories at the national and provincial levels.

Located strategically in Chengdu, the capital of Sichuan province—the China's dynamically growing West, SWJTU is blessed with rich heritage, unparallel vibrancy, and a beautiful campus. "Prosperous and plentiful ever now and then, the City flourishes in hibiscus blossoms in no end," as so known, Chengdu has been long renowned for its historical and cultural heritage, and for its natural beauty and abundance. As a major cultural and economical center and a transportation hub, the City offers first-class cultural experience, education, employment, cuisine and living environment. Leveraging on these unique advantages and the University's strengths, SWJTU is vigorously implementing its strategic plan "Developing and Strengthening SWJTU: Attracting and Cultivating Talents". We earnestly look forward to your joining our legacy and contributing to the University's continuing excellence.

More information is available at http://www.swjtu.edu.cn/

Openings in

Civil Engineering/Surveying Science and Engineering/Mechanical Engineering
Science of Transportation and Logics/ Science of Information and Communication
Electrical Engineering/Computer Science and Technology
Materials Science and Technology/Mechanics/ Management Science and Technology
Managing Technology and Innovation/Environmental Science/Architecture
Physics Science/ Mathematics Science/Life Science/Medical Science
Chemical Science/Humanities and Social Science

Salary and Fringe Benefits

Salary will be highly competitive, commensurate with qualifications and experiences. The University offers a comprehensive fringe benefit package for eligible appointees, including relocation allowances, subsidy of rental residence, start-up funds for research. The University is committed to proving assistance in establishing scientific platform and research group as well as international-level training and promotion.

The University also assists the eligible appointees in child education. Special arrangements are open for discussion for exceptional appointees.

How to Apply

Interested candidates should send a full resume, copies of academic credentials, a publication list with abstracts of selected publications, a research plan, a teaching statement, together with names of three references to Human Resources Department Southwest Jiaotong University Western Park of High-Tech Zone Chengdu, Sichuan Province, China 611756

Tel: +86-28-66366202

Email: talent@swjtu.edu.cn

For inquiries, please contact Ms. Ye Zeng or Mr. Jian Wu at the above addresses.

2018 Overseas Career Fair for Chinese Universities in Australia

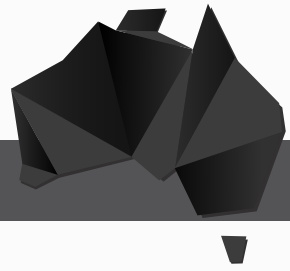

Thousands of academic job vacancies are in fast-developing China.

Job Fairs in Australia		
May 25th	16:10-19:10 (Local Time)	The University of Adelaide
May 26th	13:30-16:30 (Local Time)	The University of Melbourne
May 27th	13:30-16:30 (Local Time)	Monash University
Global Virtual Job Fair		
May 27th	08:00-20:00 (Beijing Time)	http://www.edu.cn/cv

Participation Approach

Please submit your resume to zhaojia@eol.cn

Job Vacancies

in China's Universities and Institutes Please visit http://www.acabridge.cn/

Pre-registration Now Open

UNIVERSITY of MARYLAND
SCHOOL OF MEDICINE

DEPARTMENT OF MICROBIOLOGY & IMMUNOLOGY AND CENTER FOR VACCINE DEVELOPMENT FACULTY POSITION

Baltimore, Maryland

The Department of Microbiology & Immunology and the Center for Vaccine Development of the Institute for Global Health at the University of Maryland School of Medicine is recruiting new or established investigators with actively funded research programs in viral vaccines and pathogenesis studies. Highly qualified individuals will be considered for tenure-track positions at the rank of **Assistant**, **Associate** or full **Professor**.

The Department and the School of Medicine have significant strengths in microbial pathogenesis, vaccine development, HIV biology, genome sciences, inflammation, innate and adaptive immunity, clinical infectious diseases and international research and training. The Department offers excellent laboratory facilities, competitive salary and startup packages, and access to numerous core facilities including state-of-the-art BSL3 and ABSL3 facilities. **We are particularly interested in candidates with experience in developing vaccines against viral pathogens.**

Successful candidates are expected to maintain active research programs and participate in department teaching and service opportunities.

Interested applicants are invited to submit their applications using the following link:

https://umb.taleo.net/careersection/jobdetail.ftl?job=180000MH&lang=en#.Wt3h8DFq-Rw.email

Consideration of candidates will begin upon receipt of applications and will continue until a suitable candidate is identified.

The University of Maryland, Baltimore is an Equal Opportunity/ Affirmative Action Employer. Minorities, women, individuals with disabilities, and protected veterans are encouraged to apply.

LSU Health NEW ORLEANS
School of Medicine

FACULTY POSITION
Department of Microbiology, Immunology & Parasitology

The Department of Microbiology, Immunology and Parasitology in the School of Medicine at LSU Health Sciences Center in New Orleans, LA invites applications for a full-time, tenure-track position in Bacteriology at the academic rank of Assistant or Associate Professor. Applicants should hold a Ph.D., M.D. or equivalent degree. Special consideration will be given to candidates with outstanding records of research accomplishment in bacterial genomics, pathogenesis of bacterial infections, host-bacteria interactions, vaccine development against bacterial disease, or microbiomes, who complement existing areas of research strength, including Chlamydia/STI and mycobacteria. The Department has a highly interactive faculty in the disciplines of bacteriology, virology, mycology, parasitology, and immunology. Information on the department can be viewed at: **http://www.medschool.lsuhsc.edu/microbiology/**.

The appointee will be expected to maintain an active, extramurally funded research program, engage in collaborative research efforts, serve on institutional and peer-review committees, mentor PhD and MD/PhD graduate students and postdoctoral fellows, and participate in graduate and undergraduate teaching programs. Collaborative opportunities are available for interaction with researchers in basic science and clinical departments, and in Centers of Excellence at the University, who engage in microbiology, immunology and genome research. This position is supported by state-of-the-art infrastructure, including core laboratories in genomics, proteomics, bioinformatics, imaging, flow cytometry, and a BSL-3 facility. The successful candidate will have significant laboratory space, a competitive salary, and an excellent start-up package commensurate with qualifications and experience.

LSUHSC encourages women and minority candidates to submit applications for this position. Applicants should submit their curriculum vitae that includes previous and current research support, teaching experience, a statement of research plans, e-prints of three representative publications, and the complete contact information of three professional references. LSU Health is an Equal Opportunity Employer for females, minorities, individuals with disabilities and protected veterans.

UCL

UCL MRC Laboratory for Molecular Cell Biology

London

Director of the MRC LMCB and Professor of Molecular Cell Biology

Full Time

The appointment will be on UCL Grade Professorial

Salary: Competitive salary on the professorial scale, inclusive of London Allowance.

Applications are invited for the post of Director of the MRC Laboratory for Molecular Cell Biology and Professor for Molecular Cell Biology at UCL in London.

Founded by the MRC and UCL in 1993, the MRC LMCB is a research Institute with a strong international reputation for research excellence focused on elucidating fundamental mechanisms underlying cell and tissue biology. Consisting of around 20 research groups, it is a highly collaborative research environment situated at the heart of the central UCL campus. The new Director will build on LMCB's world-leading research portfolio, and provide strategic leadership and a compelling scientific vision for the next phase of its development.

The successful applicant will have an outstanding research track record that should complement the Institute's strengths. S/he will have proven leadership experience, excellent communication and interpersonal skills and the ability to foster collaborative work within the institute and beyond. The appointee will be expected to attract research funding and to articulate a clear and compelling vision for the support and further development of the LMCB's cutting-edge technology development platforms, and for post-graduate training in cell biology. The post holder will also mentor staff in keeping with the main scientific mission of the LMCB. The LMCB is a Division within the UCL Faculty of Life Sciences and s/he should have the ability to work as part of a strong and collaborative Faculty team.

The Director represents a key appointment for UCL and the MRC, and is central to the continuance and further development of research in molecular cell biology in the UK. Only candidates with the appropriate research background and senior management experience will be considered. The Director will be a Professorial appointment at UCL. Salary will be at a level appropriate to the international standing of the successful applicant. For further information about the MRC LMCB, please see http://www.ucl.ac.uk/lmcb/

For further information about this post, please see job description on www.ucl.ac.uk/jobs and search on Reference Number 1724138.

For informal enquiries, please contact Professor Mark Marsh (Director, MRC LMCB, m.marsh@ucl.ac.uk).

For queries regarding the application process, please contact Ms Claire Hebblethwaite (c.hebblethwaite@ucl.ac.uk).

For further details about the vacancy and how to apply online please go to https://www.ucl.ac.uk/human-resources/working-ucl/jobs-ucl and search on Reference Number 1724138.

Please be sure to attach a copy of your CV, a statement of research interests and vision for the future direction of the MRC LMCB at UCL and the contact details (including e-mail addresses) for three academic referees who are leading figures in your field of research including at least one based outside your own country of residence.

Closing Date: 10 June 2018
Latest time for the submission of applications: 23:59
Interview Date: To be held throughout June and July 2018 (TBC)

We particularly welcome female applicants and those from an ethnic minority, as they are under-represented within UCL at this level.

We will consider applications to work on a part-time, flexible and job share

By **Barbara A. Wanchisen**

There's no shame in leaving

Surrounded by half-unpacked boxes in my new home, alone in a new city, and just starting to get a feel for a new job, I was plagued by suspicions that I had made the wrong choice. Maybe the naysayers were right. Maybe I was crazy to leave my tenured post in the Midwest, not to mention my friends and colleagues, for a job as the executive director of a small nonprofit organization in Washington, D.C. But I had spent a lifetime in academia, and I was excited to explore this new world.

I had started thinking about leaving academia shortly after receiving tenure 7 years earlier. I had achieved the ultimate prize for most academics, but I feared boredom—and eventually felt it. I tried to push those uneasy feelings away and find peace in my research and service to the university. But satisfaction was fleeting. By the time a sabbatical rolled around, I had decided that I needed to try something entirely different.

I wasn't sure exactly what that should be, but I figured that applying for yearlong fellowships that required a Ph.D. would be a good start. Most of these were in public policy, and I envisioned using my scientific approach to help address policy issues as a natural extension of my experience doing basic research. So, I submitted my applications—and watched the rejections stack up.

"I had spent a lifetime in academia, and I was excited to explore this new world."

Then a friend suggested that I contact my congressperson for help. Surely he wouldn't talk to me, I thought. Even if he did, he wouldn't have a clue as to what I should do. But to my surprise, he agreed to a phone call. After I gave my speech about who I was and what I wanted to do, he simply asked, "Do you want to come work with me on a peace initiative?" At first, I was speechless. Then I blurted something like, "Yes, yes, yes!"

I had to make a new life and figure out how to fit into this fast-paced world, where many of my colleagues were the same age as the students I had been teaching. I was encouraged, however, when I met people like me but a step further: scientists who had found happiness in "nontraditional" jobs. When my sabbatical ended, I returned to my university post, but my experience had confirmed that it was time for me to find another career path. I had made many friends over the years and built a laboratory from the ground up, but something in me said that it's now or never.

A few months later, I got a call about a job in Washington, D.C. With the wind at my back, the interview felt like one of the easiest I had ever done, which I took to mean that the job would be a good fit. When I got the offer, I didn't hesitate to take it.

The transition had its challenges. At my university, I had been established and respected; now, I felt like I was starting over. But it didn't take too long to develop a vibrant new community, and I felt renewed energy for my work. At times, it was scary to be doing something that felt so foreign, but the skills and approaches that I had honed in academia helped me figure out how to get the job done. And a few years in this first job led me to an even more fulfilling position, at a different organization, which I have now held for more than a decade.

In talking to other faculty members over the years, I found that some wished they had other career options, but most keep such thoughts to themselves. It is simply in the culture of academia to covet a tenured position. But if unhappy academics would move out of those jobs, opening niches for newer Ph.D. recipients, the world could be a happier place. We tell students to take risks and try new things, and there is nothing like doing it yourself to see how hard that can be—but also how rewarding. Above all, there is no shame in wanting to leave academia, no matter your career stage, and then actually doing it. ■

Barbara A. Wanchisen is the director of the Board on Behavioral, Cognitive, and Sensory Sciences at the National Academies of Sciences, Engineering, and Medicine in Washington, D.C. Do you have an interesting career story? Send it to SciCareerEditor@aaas.org.